

# Surface-Functionalized Gold and Silver Nanoparticles Based on Thioether-Poly(glycidol) for Potential Biomedical Application – Impact on Stability, Protein Corona Formation and Biodistribution

Dissertation zur Erlangung des naturwissenschaftlichen Doktorgrades  
der Julius-Maximilians-Universität Würzburg

vorgelegt von

**Johanna Späth, geb. Lutz**

aus Schweinfurt

Würzburg 2023



Eingereicht bei der Fakultät für Chemie und Pharmazie am

\_\_\_\_\_

Gutachter der schriftlichen Arbeit

1. Gutachter: \_\_\_\_\_

2. Gutachter: \_\_\_\_\_

Prüfer des öffentlichen Promotionskolloquiums

1. Prüfer: \_\_\_\_\_

2. Prüfer: \_\_\_\_\_

3. Prüfer: \_\_\_\_\_

Datum des öffentlichen Promotionskolloquiums

\_\_\_\_\_

Doktorurkunde ausgestellt am

\_\_\_\_\_



This work was conducted from October 2016 till March 2021 at the Department for Functional Materials in Medicine and Dentistry (FMZ) at the Institute of Functional Materials and Biofabrication at the University of Würzburg (Würzburg, Germany) under the supervision of Prof. Dr. rer. nat. Jürgen Groll.

---

**“If we don’t change, we don’t grow.  
If we don’t grow, we aren’t really living.”**

Gail Sheehy



## List of publications

### As first author:

- Lutz, J., Albrecht, K., Groll, J., Thioether-Polymer Coating for Colloidal Stabilization of Silver Nanoparticles, *Adv. NanoBiomed Res.* **2021**, 2000074.
- Späth, J., Yu, Y., Wolf A.-K., Beilhack A. Albrecht, K., Groll, J., Impact of Surface Functionality on Biodistribution in Silkworms. Submitted at the time of thesis submission.
- Späth, J., Keller, T., Seifert, A., Albrecht, K., Groll, J., Protein Corona Composition on Hydrophobic Functionalized Poly(glycidol) Coated Gold Nanoparticles and Their Impact on Macrophage Uptake. Submitted at the time of thesis submission.

### As co-author:

- Feineis, S., Lutz, J., Hefele, L., Albrecht K., Endl, E., Groll, J., Thioether-Polyglycidol as Multivalent and Multifunctional Coating System for Gold Nanoparticles, *Adv. Mater.* **2018**, 30, 1704972.
- Rudnitzki, F., Feineis, S., Rahmazzadeh, R., Lutz, J., Endl, E., Groll, J., Hüttmann, G., siRNA release from gold nanoparticles by nanosecond pulsed laser irradiation and analysis of the involved temperature increase, *J. Biophotonics* **2018**, e201700329.

## Author contributions to the original published first author research articles

**Publication** (complete reference):

**Lutz, J.**, Albrecht, K., Groll, J., Thioether-Polymer Coating for Colloidal Stabilization of Silver Nanoparticles, *Adv. NanoBiomed Res.* **2021**, 2000074.

DOI: <https://doi.org/10.1002/anbr.202000074>

Contributor	Contribution
Johanna Späth, geb. Lutz	Designed research; performed the research; performed all experiments and analyzed all data, wrote the manuscript
Krystyna Albrecht	Designed research; revised and provided feedback on the manuscript
Jürgen Groll	Designed research; revised and provided feedback on the manuscript

**Publication** (complete reference):

**Späth, J.**, Yu, Y., Wolf A.-K., Beilhack A. Albrecht, K., Groll, J., Impact of Surface Functionality on Biodistribution in Silkworms. Submitted at the time of thesis submission.

Contributor	Contribution
Johanna Späth	Designed research; performed the research; performed all experiments except of silkworm rearing, intra-hemolymph injection of AuNP solutions and silkworm dissection; analyzed all data; wrote the manuscript
Yidong Yu	Performed silkworm rearing, intra-hemolymph injection of AuNP solutions and silkworm dissection; revised and provided feedback on the manuscript
Ann-Katrin Wolf	Support in rearing, intra-hemolymph injection of AuNP solutions and silkworm dissection
Andreas Beilhack	Revised and provided feedback on the manuscript
Krystyna Albrecht	Designed research; revised and provided feedback on the manuscript
Jürgen Groll	Designed research; revised and provided feedback on the manuscript



**Publication** (complete reference):

Späth, J., Keller, T., Seifert, A., Albrecht, K., Groll, J., Protein Corona Composition on Hydrophobic Functionalized Polyglycidol Coated Gold Nanoparticles and Their Impact on Macrophage Uptake. Submitted at the time of thesis submission.

Contributor	Contribution
Johanna Späth	Designed research; performed the research; performed all experiments except of SDS-PAGE and LC-MS/MS measurements and analyzed all data; wrote the manuscript
Thorsten Keller	Performed SDS-PAGE analysis; revised and provided feedback on the manuscript
Annika Seifert	Provided macrophage isolation from buffy coats
Krystyna Albrecht	Designed research; revised and provided feedback on the manuscript
Jürgen Groll	Designed research; revised and provided feedback on the manuscript



## Affidavit / Eidesstattliche Erklärung

### Affidavit

I hereby confirm that my thesis entitled "Surface-Functionalized Gold and Silver Nanoparticles Based on Thioether-Poly(glycidol) for Potential Biomedical Application – Impact on Stability, Protein Corona Formation and Biodistribution" is the result of my own work. I did not receive any help or support from commercial consultants. All sources and / or materials applied are listed and specified in the thesis.

Furthermore, I confirm that this thesis has not yet been submitted as part of another examination process neither in identical nor in similar form.

Würzburg,

\_\_\_\_\_  
Place, Date

\_\_\_\_\_  
Signature

### Eidesstattliche Erklärung

Hiermit erkläre ich an Eides statt, die Dissertation „Surface-Functionalized Gold and Silver Nanoparticles Based on Thioether-Poly(glycidol) for Potential Biomedical Application – Impact on Stability, Protein Corona Formation and Biodistribution“ eigenständig, d.h. insbesondere selbständig und ohne Hilfe eines kommerziellen Promotionsberaters, angefertigt und keine anderen als die von mir angegebenen Quellen und Hilfsmittel verwendet zu haben.

Ich erkläre außerdem, dass die Dissertation weder in gleicher noch in ähnlicher Form bereits in einem anderen Prüfungsverfahren vorgelegen hat.

Würzburg,

\_\_\_\_\_  
Ort, Datum

\_\_\_\_\_  
Unterschrift



# Table of Contents

List of abbreviations and symbols .....	VII
<b>1 Motivation .....</b>	<b>1</b>
<b>2 State of knowledge .....</b>	<b>7</b>
2.1 Colloidal chemistry of noble metal nanoparticles (NPs) .....	9
2.1.1 Optical and electronical properties .....	9
2.1.2 Application of gold nanoparticles (AuNPs) and silver nanoparticles (AgNPs) .....	11
2.1.3 Stability of colloidal particles .....	15
2.1.3.1 DLVO theory.....	16
2.1.3.2 Electrostatic stabilization .....	17
2.1.3.3 Steric stabilization .....	19
2.1.3.4 Steric stabilization via polymer adsorption .....	23
2.1.3.5 Sulfur-metal NPs bonding models.....	25
2.2 Interaction of NPs with biological systems.....	30
2.2.1 Protein Corona .....	30
2.2.1.1 Parameters influencing protein binding on NPs .....	30
2.2.1.2 Stealth polymers .....	33
2.2.2 Cellular uptake of NPs by immune cells .....	35
2.2.3 Influence of adsorbed proteins on cellular uptake.....	38
2.3 Biodistribution of AuNPs – in vivo research .....	41
2.3.1 NP surface functionalization affect biodistribution .....	41
2.3.2 Silkworms as alternative to mammals .....	43
<b>3 Results and discussion.....</b>	<b>45</b>
3.1 Colloidal stability of thiol- and thioether-polymer-coated AgNPs.....	47
3.1.1 Synthesis of thiol- and thioether-polymers .....	49
3.1.1.1 Monovalent PEG .....	49
3.1.1.2 Multivalent PGs.....	52
3.1.2 AgNP surface modification with thiol- and thioether-polymers.....	58

3.1.2.1	Citrate-stabilized AgNPs.....	59
3.1.2.2	Adsorption of thiol- and thioether-polymers on citrate-AgNPs.....	60
3.1.2.3	Investigation of polymer surface coverage and conformation on AgNPs .....	63
3.1.2.3.1	Quantification of polymer amount per AgNP via micro-TGA measurements.....	63
3.1.2.3.2	Determination of the polymeric arrangement of MeO-PEG-SH and MeO-PEG-SPentyl on AgNPs.....	67
3.1.2.3.3	Possible polymeric arrangement of P(G <sub>50</sub> -CO-SH <sub>6</sub> ) and P(G <sub>50</sub> -CO-SEt <sub>6</sub> ) on AgNPs.....	69
3.1.3	Stabilization efficacy of thiol- and thioether-polymer-modified AgNPs .....	70
3.1.3.1	Binding kinetics study .....	71
3.1.3.2	Colloidal stability studies.....	72
3.2	Protein corona composition on hydrophobic functionalized PG-coated AuNPs and their impact on macrophage uptake.....	77
3.2.1	Multifunctional, amphiphilic PGs bearing different hydrophobic moieties....	78
3.2.1.1	Synthesis of alkyl-functionalized PGs .....	80
3.2.1.2	Synthesis of cholesteryl-functionalized PGs.....	82
3.2.1.3	Critical Aggregation Concentration (CAC) of hydrophobic functionalized PGs .....	91
3.2.2	Au surface modification with hydrophobic functionalized PGs.....	97
3.2.2.1	Citrate-stabilized AuNPs.....	98
3.2.2.2	Adsorption of alkyl- and cholesteryl-functionalized PGs on citrate-AuNPs .....	100
3.2.2.2.1	Determination of optimal polymer concentration for aggregate-free NPs via DLS .....	101
3.2.2.2.2	Determination of optimal polymer concentration by addition of a salt solution.....	104
3.2.2.2.3	Characterization of alkyl- and cholesteryl-functionalized AuNPs .....	110
3.2.3	Serum protein adsorption on citrate-, alkyl- and cholesteryl-modified AuNPs .....	117
3.2.3.1	Characterization of AuNPs after HS incubation .....	117

3.2.3.2	Quantification of total protein amount on AuNPs .....	122
3.2.3.3	Quantification of protein pattern .....	124
3.2.3.4	Investigation of protein corona composition of various coated AuNPs .....	126
3.2.3.5	Macrophage uptake of AuNPs with known protein corona composition .....	135
3.3	Impact of surface functionality on biodistribution of AuNPs in silkworms .....	141
3.3.1	PGs bearing charged functionalities .....	142
3.3.1.1	Synthesis of amine-functionalized PG .....	142
3.3.1.1	Synthesis of carboxyl-functionalized PG .....	144
3.3.2	Adsorption of PEG and PG carrying various functionalities on citrate- AuNPs .....	147
3.3.3	Biodistribution and accumulation of AuNPs in silkworms .....	150
<b>4</b>	<b>Summary / Zusammenfassung.....</b>	<b>155</b>
4.1	Summary .....	156
4.2	Zusammenfassung .....	162
<b>5</b>	<b>Experimental section.....</b>	<b>169</b>
5.1	Materials and Methods.....	170
5.1.1	Materials.....	170
5.1.2	Methods .....	172
5.1.2.1	Working techniques .....	172
5.1.2.2	UV-light triggered reactions.....	172
5.1.2.3	Material purification via dialysis and lyophilization .....	172
5.1.2.4	<sup>1</sup> H-NMR spectroscopy .....	172
5.1.2.5	FT-IR spectroscopy .....	173
5.1.2.6	Raman spectroscopy .....	173
5.1.2.7	SEC analysis .....	173
5.1.2.8	Ellman Assay .....	174
5.1.2.9	TNBSA Assay.....	175
5.1.2.10	ICP-MS.....	175
5.1.2.11	SEM .....	175

5.1.2.12	DLS and zeta potential .....	176
5.1.2.13	UV-Vis spectroscopy .....	176
5.1.2.14	Micro-TGA.....	176
5.1.2.15	Micro-BCA assay .....	176
5.1.2.16	SDS-PAGE and Coomassie Brilliant Blue G-250 staining.....	177
5.1.2.17	LC-MS/MS .....	178
5.1.2.18	Macrophage isolation .....	179
5.1.2.19	AuNP uptake into macrophages .....	180
5.1.2.20	Live-Dead staining.....	180
5.1.2.21	Silkworm rearing and intra-hemolymph injection of AuNP solutions...	181
5.1.2.22	Silkworm dissection .....	181
5.1.2.23	Au content in silkworm tissues .....	182
5.1.2.24	Statistical analysis .....	182
5.2	Polymer synthesis and AgNP functionalization .....	183
5.2.1	Citrate-AgNPs .....	183
5.2.1.1	Handling and characterization of citrate-AgNPs.....	183
5.2.1.2	Polymer functionalization of citrate-AgNPs.....	183
5.2.2	MeO-PEG-SH .....	184
5.2.2.1	Ag–MeO-PEG-SH.....	184
5.2.3	MeO-PEG-SPentyl.....	185
5.2.3.1	Ag–MeO-PEG-SPentyl .....	186
5.2.4	EEGE .....	186
5.2.5	P(EEGE <sub>50</sub> -CO-AGE <sub>6/12</sub> ) .....	187
5.2.6	P(G <sub>50</sub> -CO-AGE <sub>6/12</sub> ) .....	189
5.2.7	P(G <sub>50</sub> -CO-SH <sub>6</sub> ) .....	191
5.2.7.1	Ag–P(G <sub>50</sub> -CO-SH <sub>6</sub> ).....	192
5.2.8	P(G <sub>50</sub> -CO-SEt <sub>6</sub> ) .....	193
5.2.8.1	Ag–P(G <sub>50</sub> -CO-SEt <sub>6</sub> ).....	194
5.3	Studies of thiol- and thioether-polymer-modified AgNPs.....	195
5.3.1	Binding kinetics study .....	195
5.3.2	Colloidal stability studies .....	195
5.4	Polymer synthesis and AuNP functionalization.....	196



5.4.1	Citrate-AuNPs .....	196
5.4.1.1	Handling and characterization of citrate-AuNPs.....	196
5.4.1.2	Polymer functionalization of citrate-AuNPs.....	197
5.4.1.3	Calculation of surface area .....	198
5.4.1.4	Incubation with human serum (HS) .....	198
5.4.2	P(G <sub>50-co</sub> -SEt <sub>11-co</sub> -SPent <sub>1</sub> ) .....	199
5.4.2.1	Au-P(G <sub>50-co</sub> -SEt <sub>11-co</sub> -SPent <sub>1</sub> ).....	200
5.4.2.2	Au-P(G <sub>50-co</sub> -SEt <sub>11-co</sub> -SPent <sub>1</sub> )-HS .....	200
5.4.3	P(G <sub>50-co</sub> -SEt <sub>10-co</sub> -SPent <sub>2</sub> ) .....	201
5.4.3.1	Au-P(G <sub>50-co</sub> -SEt <sub>10-co</sub> -SPent <sub>2</sub> ).....	202
5.4.3.2	Au-P(G <sub>50-co</sub> -SEt <sub>10-co</sub> -SPent <sub>2</sub> )-HS .....	202
5.4.4	P(G <sub>50-co</sub> -SEt <sub>9-co</sub> -SPent <sub>3</sub> ).....	203
5.4.4.1	Au-P(G <sub>50-co</sub> -SEt <sub>9-co</sub> -SPent <sub>3</sub> ).....	204
5.4.4.2	Au-P(G <sub>50-co</sub> -SEt <sub>9-co</sub> -SPent <sub>3</sub> )-HS.....	204
5.4.5	P(G <sub>50-co</sub> -SEt <sub>8-co</sub> -SPent <sub>4</sub> ).....	205
5.4.5.1	Au-P(G <sub>50-co</sub> -SEt <sub>8-co</sub> -SPent <sub>4</sub> ).....	206
5.4.5.2	Au-P(G <sub>50-co</sub> -SEt <sub>8-co</sub> -SPent <sub>4</sub> )-HS.....	206
5.4.6	P(G <sub>50-co</sub> -SEt <sub>11-co</sub> -SDec <sub>1</sub> ).....	207
5.4.6.1	Au-P(G <sub>50-co</sub> -SEt <sub>11-co</sub> -SDec <sub>1</sub> ).....	208
5.4.6.2	Au-P(G <sub>50-co</sub> -SEt <sub>11-co</sub> -SDec <sub>1</sub> )-HS.....	208
5.4.7	P(G <sub>50-co</sub> -SEt <sub>10-co</sub> -SDec <sub>2</sub> ).....	209
5.4.7.1	Au-P(G <sub>50-co</sub> -SEt <sub>10-co</sub> -SDec <sub>2</sub> ).....	210
5.4.7.2	Au-P(G <sub>50-co</sub> -SEt <sub>10-co</sub> -SDec <sub>2</sub> )-HS.....	210
5.4.8	P(G <sub>50-co</sub> -SEt <sub>9-co</sub> -SDec <sub>3</sub> ) .....	211
5.4.8.1	Au-P(G <sub>50-co</sub> -SEt <sub>9-co</sub> -SDec <sub>3</sub> ) .....	212
5.4.8.2	Au-P(G <sub>50-co</sub> -SEt <sub>9-co</sub> -SDec <sub>3</sub> )-HS.....	212
5.4.9	P(G <sub>50-co</sub> -SEt <sub>8-co</sub> -SDec <sub>4</sub> ) .....	213
5.4.9.1	Au-P(G <sub>50-co</sub> -SEt <sub>8-co</sub> -SDec <sub>4</sub> ) .....	214
5.4.9.2	Au-P(G <sub>50-co</sub> -SEt <sub>8-co</sub> -SDec <sub>4</sub> )-HS.....	214
5.4.10	P(G <sub>50-co</sub> -SEt <sub>11-co</sub> -SPentadec <sub>1</sub> ).....	215
5.4.10.1	Au-P(G <sub>50-co</sub> -SEt <sub>11-co</sub> -SPentadec <sub>1</sub> ).....	216
5.4.10.2	Au-P(G <sub>50-co</sub> -SEt <sub>11-co</sub> -SPentadec <sub>1</sub> )-HS.....	216

5.4.11	P(G <sub>50</sub> - <i>co</i> -SEt <sub>10</sub> - <i>co</i> -SPentadec <sub>2</sub> ).....	217
5.4.11.1	Au-P(G <sub>50</sub> - <i>co</i> -SEt <sub>10</sub> - <i>co</i> -SPentadec <sub>2</sub> ).....	218
5.4.11.2	Au-P(G <sub>50</sub> - <i>co</i> -SEt <sub>10</sub> - <i>co</i> -SPentadec <sub>2</sub> )-HS.....	218
5.4.12	P(G <sub>50</sub> - <i>co</i> -SEt <sub>9</sub> - <i>co</i> -SPentadec <sub>3</sub> ).....	219
5.4.12.1	Au-P(G <sub>50</sub> - <i>co</i> -SEt <sub>9</sub> - <i>co</i> -SPentadec <sub>3</sub> ).....	220
5.4.12.2	Au-P(G <sub>50</sub> - <i>co</i> -SEt <sub>9</sub> - <i>co</i> -SPentadec <sub>3</sub> )-HS.....	220
5.4.13	P(G <sub>50</sub> - <i>co</i> -SEt <sub>8</sub> - <i>co</i> -SPentadec <sub>4</sub> ).....	221
5.4.13.1	Au-P(G <sub>50</sub> - <i>co</i> -SEt <sub>8</sub> - <i>co</i> -SPentadec <sub>4</sub> ).....	222
5.4.13.2	Au-P(G <sub>50</sub> - <i>co</i> -SEt <sub>8</sub> - <i>co</i> -SPentadec <sub>4</sub> )-HS.....	222
5.4.14	Carboxyl-functionalized Cholesterol (Chol-COOH).....	223
5.4.15	P(G <sub>50</sub> - <i>co</i> -SEt <sub>5.5</sub> - <i>co</i> -NH <sub>2(0.5)</sub> ).....	225
5.4.16	P(G <sub>50</sub> - <i>co</i> -SEt <sub>5.5</sub> - <i>co</i> -Chol <sub>0.5</sub> ).....	226
5.4.16.1	Au-P(G <sub>50</sub> - <i>co</i> -SEt <sub>5.5</sub> - <i>co</i> -Chol <sub>0.5</sub> ).....	227
5.4.16.2	Au-P(G <sub>50</sub> - <i>co</i> -SEt <sub>5.5</sub> - <i>co</i> -Chol <sub>0.5</sub> )-HS.....	227
5.4.17	P(G <sub>50</sub> - <i>co</i> -SEt <sub>5.5</sub> - <i>co</i> -SPEG-NH <sub>2(0.5)</sub> ).....	228
5.4.18	P(G <sub>50</sub> - <i>co</i> -SEt <sub>5.5</sub> - <i>co</i> -SPEG-Chol <sub>0.5</sub> ).....	229
5.4.18.1	Au-P(G <sub>50</sub> - <i>co</i> -SEt <sub>5.5</sub> - <i>co</i> -SPEG-Chol <sub>0.5</sub> ).....	230
5.4.18.2	Au-P(G <sub>50</sub> - <i>co</i> -SEt <sub>5.5</sub> - <i>co</i> -SPEG-Chol <sub>0.5</sub> )-HS.....	230
5.4.19	P(G <sub>50</sub> - <i>co</i> -SEt <sub>5</sub> - <i>co</i> -NH <sub>2(1)</sub> ).....	231
5.4.19.1	Au-P(G <sub>50</sub> - <i>co</i> -SEt <sub>5</sub> - <i>co</i> -NH <sub>2(1)</sub> ).....	232
5.4.20	P(G <sub>50</sub> - <i>co</i> -SEt <sub>5</sub> - <i>co</i> -COOH <sub>1</sub> ).....	232
5.4.20.1	Au-P(G <sub>50</sub> - <i>co</i> -SEt <sub>5</sub> - <i>co</i> -COOH <sub>1</sub> ).....	233
5.5	Full list of hard corona proteins adsorbed on 15 nm AuNPs identified by LC-MS/MS analysis.....	234
<b>6</b>	<b>References.....</b>	<b>247</b>

## List of abbreviations and symbols

Abbreviation	Meaning
Ag	Silver
AGC	Automatic gain control
AgNPs	Silver nanoparticles
AGE	Allyl glycidyl ether
APS	Ammonium persulfate
Ar	Argon
ATR	Attenuated total reflection
a. u.	Arbitrary units
Au	Gold
AuNPs	Gold nanoparticles
Bis-Tris	Bis(2-hydroxyethyl)amino-tris(hydroxymethyl)methane
br	Broad (for NMR assignment)
BSA	Bovine serum albumin
C	Carbons (for NMR assignment)
CAC	Critical aggregation concentration
CaH <sub>2</sub>	Calcium hydrate
Calcein AM	Calcein acetoxymethyl ester
CC	Carbon-carbon single bond
C=C	Carbon-carbon double bond; allyl
CH	Methine
CH <sub>2</sub>	Methylene
CH <sub>3</sub>	Methyl
Chol	Cholesteryl
Chol-COOH	Carboxy-functionalized cholesterol
CO	Carbon-oxide single bond
C=O	Carbonyl
COC	Ether
(C=O)NH	Carboxamide
(C=O)O <sup>-</sup>	Carboxylate
COOH	Carboxylic acid
(C=O)OH	Carboxylic acid
(C=O)OR	Carboxylic acid ester
CO <sub>2</sub>	Carbon dioxide
CS	Dialkylsulfide
CDCl <sub>3</sub>	Deuterated chloroform
CHCl <sub>3</sub>	Chloroform
C5	Pentyl

C10	Decyl
C15	Pentadecyl
d	Day(s); Doublet (for NMR assignment)
<i>d</i>	Hydrodynamic diameter
dd	Doublet of doublet (for NMR assignment)
DCM	Dichloromethane
DCR	Derived count rate
DLS	Dynamic light scattering
DLVO	Derjaguin-Landau-Verwey-Overbeek
DMAP	4-(Dimethylamino)pyridine
DMEM	Dulbecco's modified Eagle medium
DMF	<i>N,N</i> -Dimethylformamide
DMPA	2,2-Dimethoxy-2-phenylacetophenon
DMSO	Dimethyl sulfoxide
DNA	Deoxyribonucleic acid
D <sub>2</sub> O	Deuterium oxide
DTNB	5,5'-dithiobis(2-nitrobenzoic acid); Ellman's reagent
DTT	Dithiothreitol
DVB	Divinyl benzene
EDC	<i>N</i> -(3-Dimethylaminopropyl)- <i>N'</i> -ethylcarbodiimide hydrochloride
EDL	Electric double layer
EEGE	Ethoxyethyl glycidyl ether
e.g.	Exempli gratia (for example)
<i>et al.</i>	Et alii (and others)
Et <sub>2</sub> O	Diethylether
EtOH	Ethanol
EtSH	Ethanethiol
FCS	Fetal calf serum
FT-IR	Fourier-transform infrared
g	Gravitational force
G	Glycidol
GSH	γ-L-Glutamyl-L-cysteinyl-glycin, L-glutathione reduced
h	Hour(s)
H	Hydrogen; Protons (for NMR assignment)
HCD	Higher energy collisional dissociation
HCl	Hydrochloric acid
HNO <sub>3</sub>	Nitric acid
hPL	Human platelet lysate
H <sub>2</sub> O	Water; deionized water
H <sub>2</sub> O <sub>2</sub>	Hydrogen peroxide

HPLC	High performance liquid chromatography
HS	Human serum
HSA	Human serum albumin
HS-PEG-NH <sub>2</sub>	Alpha-mercapto-omega-amino poly(ethylene glycol)
iBAQ	Intensity based absolute quantification
ICP-MS	Inductively-coupled-plasma mass-spectrometry
i.e.	Id est (that is)
I2959	2-Hydroxy-1-[4-(hydroxyethoxy)-phenyl]-2-methyl-1-propanone
KCl	Potassium chloride
kcps	kilo counts per second
KH <sub>2</sub> PO <sub>4</sub>	Potassium dihydrogen phosphate
KOH	Potassium hydroxide
KO <sup>t</sup> Bu	Potassium <i>tert</i> -butoxide
LALS	Low angle light scattering
LC-MS/MS	Liquid chromatography tandem mass spectrometry
LiBr	Lithium bromide
m	Multiplet (for NMR assignment)
MALS	Multi angle light scattering
MeOH	Methanol
MeO-PEG-SH	Poly(ethylene glycol) methyl ether thiol
MgSO <sub>4</sub>	Magnesium sulfate
MHz	Megahertz
Micro-BCA	Micro-bicinchoninic acid
Micro-TGA	Micro-thermogravimetric analysis
$\bar{M}_n$	Number-averaged molar mass
MS/MS	Tandem mass spectrometry
$\bar{M}_w$	Weight-averaged molar mass
MWCO	Molecular-weight cut off
N <sub>2</sub>	Nitrogen
NaBH <sub>4</sub>	Sodium borohydride
NaCl	Sodium chloride
NaHCO <sub>3</sub>	Sodium hydrogen carbonate
NH <sub>4</sub> HCO <sub>3</sub>	Ammonium hydrogencarbonate
(NH <sub>4</sub> ) <sub>2</sub> SO <sub>4</sub>	Ammonium sulfate
Na <sub>2</sub> HPO <sub>4</sub>	Disodium hydrogen phosphate
Na <sub>2</sub> HPO <sub>4</sub> ·12H <sub>2</sub> O	Disodium hydrogen phosphate dodecahydrate
NaOH	Sodium hydroxide
NaKHPO <sub>4</sub> ·12H <sub>2</sub> O	Sodium phosphate dibasic dodecahydrate
NaN <sub>3</sub>	Sodium azide
NaNO <sub>3</sub>	Sodium nitrate

NH	Amide
NH <sub>2</sub>	Amine
NHS	<i>N</i> -Hydroxysuccinimide
NMR	Nuclear magnetic resonance
NPs	Nanoparticles
O <sub>2</sub>	Oxygen
OH	Hydroxyl
PB	Phosphate buffer
PBS	Phosphate-buffered saline
PDI	Polydispersity index
PEEP	Poly(ethyl ethylene phosphate)
PEG	Poly(ethylene glycol); MeO-PEG-SH
PEGylation	Functionalization with PEG ligands
Pen-Strep	Penicillin-streptomycin
PG	Poly(glycidol)
PG1	P(G <sub>50</sub> - <i>co</i> -SEt <sub>11</sub> - <i>co</i> -SPent <sub>1</sub> )
PG2	P(G <sub>50</sub> - <i>co</i> -SEt <sub>10</sub> - <i>co</i> -SPent <sub>2</sub> )
PG3	P(G <sub>50</sub> - <i>co</i> -SEt <sub>9</sub> - <i>co</i> -SPent <sub>3</sub> )
PG4	P(G <sub>50</sub> - <i>co</i> -SEt <sub>8</sub> - <i>co</i> -SPent <sub>4</sub> )
PG5	P(G <sub>50</sub> - <i>co</i> -SEt <sub>11</sub> - <i>co</i> -SDec <sub>1</sub> )
PG6	P(G <sub>50</sub> - <i>co</i> -SEt <sub>10</sub> - <i>co</i> -SDec <sub>2</sub> )
PG7	P(G <sub>50</sub> - <i>co</i> -SEt <sub>9</sub> - <i>co</i> -SDec <sub>3</sub> )
PG8	P(G <sub>50</sub> - <i>co</i> -SEt <sub>8</sub> - <i>co</i> -SDec <sub>4</sub> )
PG9	P(G <sub>50</sub> - <i>co</i> -SEt <sub>11</sub> - <i>co</i> -SPentadec <sub>1</sub> )
PG10	P(G <sub>50</sub> - <i>co</i> -SEt <sub>10</sub> - <i>co</i> -SPentadec <sub>2</sub> )
PG11	P(G <sub>50</sub> - <i>co</i> -SEt <sub>9</sub> - <i>co</i> -SPentadec <sub>3</sub> )
PG12	P(G <sub>50</sub> - <i>co</i> -SEt <sub>8</sub> - <i>co</i> -SPentadec <sub>4</sub> )
PG13	P(G <sub>50</sub> - <i>co</i> -SEt <sub>5.5</sub> - <i>co</i> -Chol <sub>0.5</sub> )
PG14	P(G <sub>50</sub> - <i>co</i> -SEt <sub>5.5</sub> - <i>co</i> -SPEG-Chol <sub>0.5</sub> )
PG(Alkyl)	P(G <sub>50</sub> - <i>co</i> -SEt <sub>10</sub> - <i>co</i> -SDec <sub>2</sub> )
PG(+)	P(G <sub>50</sub> - <i>co</i> -SEt <sub>5</sub> - <i>co</i> -NH <sub>2</sub> ( <sub>1</sub> ))
PG(-)	P(G <sub>50</sub> - <i>co</i> -SEt <sub>5</sub> - <i>co</i> -COOH <sub>1</sub> )
PGylation	Functionalization with PG ligands
pH	Negative logarithmic value of the hydrogen ion concentration
PHDCA	Poly(hexadecyl-cyanoacrylate)
PMMA	Poly(methyl methacrylate)
POx	Poly(2-oxazoline)
PS	Polystyrene
PTFE	Poly(tetrafluoroethylene)
<i>p</i> TsOH	Toluene-4-sulfonic acid monohydrate
PVP	Poly(vinyl pyrrolidone)

q	Quartet (for NMR assignment)
quin	Quintet (for NMR assignment)
R	Rest
RALS	Right angle light scattering
RI	Refractive index
RPMI	Roswell Park Memorial Institute
RT	Room temperature
s	Singlet (for NMR assignment)
S	Sulfur
SDec	Thiododecyl
SDS	Sodium dodecyl sulfate
SDS-PAGE	Sodium dodecyl sulfate polyacrylamide gel electrophoresis
SEC	Size exclusion chromatography
SEM	Scanning electron microscopy
SEt	Thioethyl
SH	Thiol
siRNA	Small interfering ribonucleic acid
SPent	Thiopentyl
SPentadec	Thiopentadecyl
SPR	Surface plasmon resonance
SR	Thioether
styrene-DVB	Styrene-divinyl benzene
t	Triplet (for NMR assignment)
<sup>t</sup> Bu	<i>Tert</i> -Butyl
TCEP	Tris(2-carboxyethyl)phosphine hydrochloride
TEM	Transmission electron microscopy
TEMED	<i>N,N,N',N'</i> -Tetramethyl ethylenediamine
TGA	Thermogravimetric analysis
TMS	Tetramethylsilane
TNBSA	2,4,6-trinitrobenzene sulfonic acid
THF	Tetrahydrofuran
Tris-HCl	Tris-Hydrochloride
UV	Ultraviolet
UV-Vis	Ultraviolet and visible light
vs.	Versus

The abbreviations of proteins are not listed separately here due to their large number, but can be found in **Table 80** in **Section 5.5**.

Symbol	Meaning
$\mathcal{D}$	Dispersity
$\delta$	Chemical shift (NMR spectroscopy)
$\zeta$	Zeta potential
$\tilde{\nu}$	Wavenumber
hv	Light

Formular symbol	Meaning
$M_w$	Molecular weight
$N_A$	Avogadro constant
$r, r$	Radius
$R_f$	Flory radius
$M_w$	Molecular weight
$\rho$	Density
$\alpha$	Length of one monomer
$n$	Number of monomer units
$\sigma$	Grafting density
$D_{grafting}$	Distance between two PEG chains
V	Volume of a sphere
A	Surface area of a sphere

Mathematical unit	Meaning
Å	Angstrom
cm	Centimeter
cm <sup>-1</sup>	Inverse centimeters
cm <sup>2</sup>	Square centimeter
cm <sup>3</sup>	Cubic centimeter
Da	Dalton
dL	Deciliter
g	Gram
Hz	Hertz
K	Kelvin
kDa	Kilodalton
kJ	Kilojoule
L	Liter
M	Molar; molarity
mbar	Millibar
mg	Miligram



min	Minute(s)
mL	Milliliter
mm	Millimeter
mM	Millimolar
mmol	Millimole
mV	Millivolts
mW	Milliwatt
m/z	Mass-to-charge ratio
nL	Nanoliter
nm	Nanometer
nm <sup>2</sup>	Square nanometer
pg	Picogram
ppm	Parts per million
rpm	Revolutions per minute
V	Volt
v/v	Volume per volume
W	Watt
wt%	Weight percentage
w/v	Weight per volume
μg	Microgram
μL	Microliter
μm	Micrometer
μM	Micromolar
μmol	Micromole
°	Degree
°C	Degree Celsius
%	Percent



---

# 1 Motivation

---

## 1 Motivation

Due to their interesting chemical, physical, and biological properties, colloidal solutions consisting of gold nanoparticles (AuNPs) or silver nanoparticles (AgNPs) attracted enormous attention in nanotechnology and biomedicine. While AgNPs showed a wide range of applications such as biosensor materials, drug delivery systems, dental restorative materials, antimicrobial agents, for wound healing or in cosmetics,<sup>[1]</sup> AuNPs were used for instance as contrast agent<sup>[2]</sup>, in photothermal therapy<sup>[3]</sup> or for drug delivery<sup>[4,5]</sup>. Ensuring the broad applicability of these particles, the stabilization efficacy plays a crucial role, as aggregation leads to a loss of their unique properties. Thus, it is relevant for enhancing the stability of such nanoparticles (NPs) by attaching capping agents with high affinity to the surface, which consequently generate a barrier to aggregation.

Steric stabilization and biocompatibilization of these noble metal NPs are usually achieved through ligand-exchange reactions especially with thiol-based molecules, such as alkyl thiols<sup>[6]</sup> or the commonly used thiol-terminated poly(ethylene glycol) (PEG)<sup>[7,8]</sup>. In particular polymer functionalization is known to protect the particles against aggregation and yielded in improved colloidal stability. This in turn affects the biodistribution, as reducing the aggregation tendency enhances their mobility in the bloodstream.<sup>[9,10]</sup> In this regard, biocompatible polymers such as PEG<sup>[8,11,12]</sup> have been widely used for enhancing the physiological particle stabilization, also since PEG is found to be a suitable candidate for drug delivery and provides a number of favorable properties for use as a ligand on NP conjugates for medical and biological applications.<sup>[13-15]</sup> Even though thiol-terminated PEG is the established gold-standard, this procedure has disadvantages, since the highly nucleophilic and oxidative character of thiols limits the possibilities introducing functional groups and provokes polymeric crosslinking.<sup>[16]</sup> Consequently, in the last few years, more focus is put on the attachment of chemical inert thioethers to the particles surface. Hereby especially the author's working group provided major contribution to the stabilization efficacy of AuNPs modified with the thioether analog of the well-established gold standard MeO-PEG-SH as well as with a multivalent equivalent, linear side-chain functionalized poly(glycidol) (PG) with multiple thiol or ethylthioether.<sup>[17]</sup>

Ensuring that noble metal NPs can fulfill their biomedical application it is essential not only to optimize the colloidal stabilization, but also to prevent these nanocarriers from being recognized as foreign substances by phagocytes and thus being rapidly removed and

cleared from the bloodstream. Rather, a prolonged circulation in the bloodstream has to be ensured reaching their desired target site in the body.

The propensity of NPs to remain in circulation depends on several properties such as size, shape, surface charge as well as surface functionalization of the particles.<sup>[18-20]</sup> In addition, the protein corona, which is formed spontaneously and rapidly upon NPs enter the body and come into contact with the body fluid, plays a crucial role in biodistribution, as proteins bound to the surface of the NPs are known to influence their clearance by affecting the uptake in immune cells. The composition of the protein corona is in turn dependent on various factors such as the biological source<sup>[21]</sup>, the exposure time<sup>[22]</sup> as well as the physiochemical properties of the nanocarrier<sup>[23,24]</sup>, including NP material, size and shape, and surface chemistry. Hence, understanding the protein corona is quite challenging, however, the interactions between NPs and proteins is a decisive aspect in the development of targeted nanomaterials. NP surface functionalization, e.g. coating with polymers, has a significant impact in the protein corona composition, whereas functionalization with PEG ligands (PEGylation) is considered as the gold standard for NPs' surface modification in the biomedical field application. Due to the PEG's stealth properties, such coatings ensure prolonged NP circulation in the bloodstream.<sup>[25,26]</sup> Additionally, reduced nonspecific protein adsorption affects further the biodistribution and enables specific organ targeting.<sup>[27,28]</sup> Other promising polymers for stealth coating include poly(2-oxazoline)s (POx)<sup>[29]</sup>, poly(ethyl ethylene phosphate)s (PEEPs)<sup>[30]</sup>, poly(vinyl pyrrolidone)s (PVPs)<sup>[31]</sup>, or PGs<sup>[32]</sup>. Latter is a more attractive alternative to PEG not only due to the similar chemical structure, but especially due to its possibility for multifunctionalization, whereas PG coating shows comparable or more reduced protein adsorption.<sup>[33,34]</sup> In addition, PG is known to inhibit non-specific interaction with opsonins and thus avoid phagocytosis and increase blood circulation time.<sup>[35,36]</sup>

To date, animal models are still indispensable for studying biodistribution and elimination of nanomaterials. However, the use of mammals for in vivo experiments faces various challenges including increasing regulatory hurdles and costs. In order to overcome these obstacles, several invertebrate animal models have been proposed as alternatives to mammalian models for preliminary in vivo studies in the last years, such as fruit flies (*Drosophila melanogaster*)<sup>[37]</sup>, larvae of the greater wax moths (*Galleria mellonella*)<sup>[38]</sup>,

## 1 Motivation

and especially silkworm larvae (*Bombyx mori*)<sup>[39-41]</sup>. Latter are of great interest due to similarities between silkworm's hemolymph and mammals blood, similar specialized major organ compartments, as well as common pharmacokinetics and a conserved innate immune system.<sup>[42,43]</sup> However, so far, only a limited number of studies report the biodistribution of NPs in silkworms compared to well-studied mammals.

This **thesis followed three aims**. First, thioethers, especially multivalent thioethers based on PG, aimed to be established as a promising coating platform for AgNPs, providing high colloidal stability. For this purpose, AgNPs coated with mono- and multivalent thiol- and thioether-polymers are prepared to systematically investigate the adsorption kinetics onto the silver (Ag) surface as well as the colloidal stability after exposure to different conditions relevant for biomedical application, such as freeze-drying and treatment under physiological conditions. As multivalent thioether-PG is already proven as a promising candidate for AuNP modification and stabilization, the second aim was to examine the stealth behavior of PG, side-chain functionalized with various hydrophobic units, to gain a deeper understanding of AuNP surface functionalization in terms of protein adsorption and their subsequent cellular uptake by human macrophages, which are important components of the immune defense and play an essential role in the clearance of foreign substances from the bloodstream. Lastly, the aim was to validate larvae of the domestic silkworm *Bombyx mori* as an alternative invertebrate model for preliminary in vivo research, using AuNPs with various surface chemistry.

**Chapter 2** provides an overview in the theoretical background and current state of research relating to this thesis. First, general information about colloidal systems is given, such as the optical properties of noble metal NPs, their application in biomedical field, as well as a deeper introduction of the colloidal stability. This also includes the current state of the art on sulfur-metal bonding models with comparison of thiol and thioethers on both gold (Au) and Ag. The interaction of NPs with biological systems is thereafter described, starting with a deeper insight into the protein corona and how it is affected, information on NP uptake by immune cells, and how adsorbed proteins influence cellular uptake. Finally, the influence of surface functionalization of NPs on in vivo biodistribution is explained, followed by the introduction of silkworms as possible alternatives to mammals for in vivo experiments.

The results of this thesis and their discussion are given in **Chapter 3**, which is divided into three main sections. Firstly, the colloidal stabilization efficacy of thioether-polymer coated AgNPs in comparison to thiol-functionalized ones is investigated, using particles modified with mono- and multivalent thiol- and thioether-polymers (see **Section 3.1**). In this section, first the synthesis and characterization of monovalent thiol- and thioether-terminated PEG as well as of the multifunctional PG analogues is presented. Surface modification of citrate-stabilized AgNPs with the aforementioned mono- and multivalent sulfur-containing polymers was carried out by ligand exchange reaction and is proven by various methods. In addition, polymer surface coverage and configuration on AgNPs is examined. Afterwards, the stabilization efficacy of particles functionalized with the previously mentioned mono- and multivalent sulfur-containing polymers is investigated through exposure to conditions provoking aggregation.

The second **Section 3.2** focuses on protein corona composition on varyingly sized AuNPs coated with various multifunctional, amphiphilic PGs bearing different hydrophobic moieties, and its impact on macrophage uptake. The experimental procedures for all alkyl- and cholesteryl-functionalized polymer synthesis and their characterization are described first and the critical aggregation concentration (CAC) of these multivalent polymers is investigated. Then, intensive examination on AuNP incubation with polymeric solutions of various molar concentrations is conducted to figure out the molarity, which is high enough resulting in high stability, even after salt treatment, and simultaneously low enough to prevent aggregation by bridging flocculation. Subsequently, full characterization of successful adsorption of the synthesized multifunctional polymers on 15 nm and 30 nm AuNPs is provided. After incubation of the aforementioned modified AuNPs with human serum (HS), HS-incubated particles are characterized and attached proteins are quantitatively and qualitatively analyzed. Finally, AuNP uptake by macrophages is evaluated in terms of adsorbed or blocked proteins as a result of surface functionalization.

Lastly, the aim of **Section 3.3** is to study the biodistribution and accumulation of AuNPs with different surface functionalities in silkworm larvae as an alternative to mammals. This section starts with the synthesis and characterization of the used polymers, followed by modification of AuNPs with different surface coatings: one PEG-based modification and three PG-coatings with slightly hydrophobic functionalization, as well as positively and

## 1 Motivation

negatively charges. Finally, the toxicity of the four differently polymer-functionalized AuNPs in silkworms is evaluated and a first comparison of these AuNPs with respect to their biodistribution in silkworm organs following intra-hemolymph injection is presented.

**Chapter 4** provides a summary of the thesis in English and German language.

The experimental section including materials and methods used in this thesis is presented in **Chapter 5**. This section additionally provides detailed information on each performed experiment, including full characterization of the polymers and correspondingly polymer-coated and protein-bound NPs.



---

## 2 State of knowledge

---

## 2 State of knowledge

Parts of **Section 2.1** were published as original research article (Johanna Lutz, Krystyna Albrecht, Jürgen Groll, Thioether-Polymer Coating for Colloidal Stabilization of Silver Nanoparticles in *Advanced NanoBiomed Research* 2021, 2000074), reproduced from reference<sup>[44]</sup> as an open access article distributed under the Creative Commons Attribution 4.0 International License (CC BY 4.0), which permits unrestricted use, distribution, and reproduction in any medium.

Copyright (2021) The Authors. *Advanced NanoBiomed Research* published by Wiley-VCH GmbH.

The article is based on the work of the author of this thesis, Johanna Späth, geb. Lutz, who conducted all experiments and data evaluation and wrote the manuscript.

Parts of **Section 2.2** are written in the form of an original research article (Johanna Späth, Thorsten Keller, Annika Seifert, Krystyna Albrecht, Jürgen Groll, Protein Corona Composition on Hydrophobic Functionalized Polyglycidol Coated Gold Nanoparticles and Their Impact on Macrophage Uptake) and has been submitted to a peer-reviewed journal by the time of the submission of this thesis. The chapter is thus intended to be published in the near future. To improve readability, figures from the supplementary information have been integrated into the main article in this thesis.

The article is based on the work of the author of this thesis, Johanna Späth, who conducted most of the experiments and data evaluation, wrote the manuscript and will hold the first authorship after publication.

Parts of **Section 2.3** are written in the form of an original research article (Johanna Späth, Yidong Yu, Ann-Katrin Wolf, Andreas Beilhack, Jürgen Groll, Krystyna Albrecht, Impact of Surface Functionality on Biodistribution of AuNPs in Silkworms) and has been submitted to a peer-reviewed journal by the time of the submission of this thesis. The chapter is thus intended to be published in the near future. To improve readability, figures from the supplementary information have been integrated into the main article in this thesis.

The article is based on the work of the author of this thesis, Johanna Späth, who conducted most of the experiments and data evaluation, wrote the manuscript and will hold the first authorship after publication.

### 2.1 Colloidal chemistry of noble metal nanoparticles (NPs)

The most famous and oldest surviving example using metallic NPs is the so-called Lycurgus cup<sup>[45]</sup>, created by ancient Romans. Depending on the angle of light incidence, the glass cage cup changes the color from red to green. While in transmission the glass appears red, it shows a greenish color in reflected light. The appearance of the different colors related to the direction of light illumination could finally be understood after a very long time, as researchers discovered tiny amounts of colloidal AuNPs and AgNPs in the glass, allowing the explanation of the color change phenomenon by the optical scattering of the metal NPs on the sidewall.<sup>[46,47]</sup>

In the following, the optical properties of colloidal metal NPs are described in detail, whereupon the stability of these NPs as well as their surface functionalization are discussed.

#### 2.1.1 Optical and electronical properties

The beginning of colloidal research in view of the coloring properties of noble metal NPs was conducted by Michael Faraday<sup>[48]</sup> and was further developed by Lorenz<sup>[49]</sup>, Maxwell<sup>[50]</sup> and especially by Gustav Mie<sup>[51]</sup>. Mie succeeded in 1908 the exact calculation of Maxwell's equation for the absorption and scattering behavior of an electromagnetic wave on one single spherical particle, based on the phenomenological description of the material properties by the dielectric function. Finally, the introduction of the electron band theory for metals by Kreibitz *et al.*, provided the physical interpretation of the optical properties and permitted an association of the Mie-absorption with the collective plasmon oscillation.<sup>[52,53]</sup> The interaction of metallic NPs with light causes a collective oscillation of the conduction band by excitation of the free electrons resulting in a charge shift of the electron cloud (see **Figure 1**). The charge separation is compensated by the Coulomb attraction between the opposite charges of the electrons and the nuclei, resulting in oscillation. This oscillation frequency strongly depends on various factors regarding the particle surface, such as the size and shape of the particles, the surrounding medium as well as the surface coating, and is therefore called surface plasmon resonance (SPR).<sup>[54,55]</sup>

## 2 State of knowledge

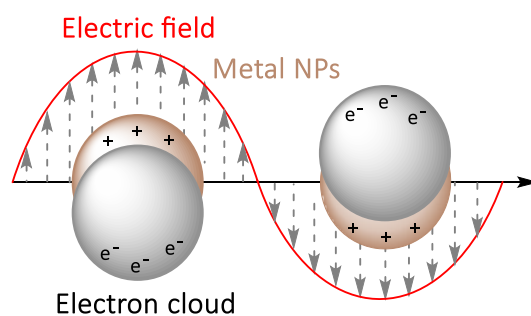


**Figure 1.** Schematic illustration of the plasmonic oscillation for a spherical metal NP, showing the displacement of the electron cloud upon interaction with an electromagnetic wave, adapted from Kelly *et al.*<sup>[55]</sup>.

Metallic NPs of Ag or Au display a localized SPR in the visible range due to the energetic location of the d-d-transitions, resulting in the characteristic yellow or red color, respectively. As their SPR bands are dependent of the size of the particle, AgNPs with particle diameters between 10 nm and 100 nm show SPR wavelengths around 392-493 nm, whereas the plasmon band of AuNPs with same sizes appears at 517 nm to 575 nm.<sup>[56,57]</sup> **Figure 2a** displays the size dependency of spherical AuNPs, presenting a red-shifting and broadening of the SPR band by increasing the particle size. Furthermore, this shift to higher wavelength could also be observed after surface modification of the particles, as shown in **Figure 2b**. In this case, a significant red-shift of 6 nm compared to the unmodified particles indicates the adsorption of aptamers to 25 nm AuNPs, caused by ligand-dependent changes in the electron density on the surface of the NPs.<sup>[58,59]</sup>

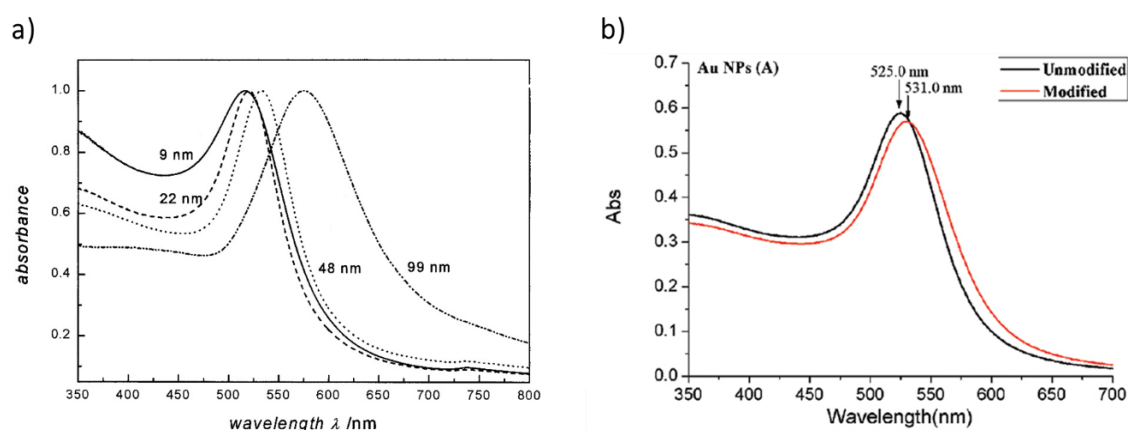


**Figure 2.** a) UV-Vis absorbance spectra of AuNPs with particle diameter between 9 nm and 99 nm, showing a size dependent SPR shift. Reprinted from reference<sup>[57]</sup>, Copyright (1999), with permission from American Chemical Society. b) UV-Vis absorption spectra of unmodified and modified AuNPs, displaying an obvious SPR red-shift after surface functionalization. Reprinted from reference<sup>[58]</sup>, Copyright (2016), with permission from Wolters Kluwer Medknow Publications.

Furthermore, it is known that the SPR frequency depends on the morphology of the nanoparticles. While spherical NPs exhibit one single SPR, a structure change for example to Au nanorods or Ag nanocubes leads to the appearance of two or even more absorption bands.<sup>[60,61]</sup> However, since the current thesis exclusively focuses on spherical metal NPs, the correlation of SPR and the particle shape will not be discussed in more detail.

The dielectric properties of the NPs environment are not only affected by size, shape, and surface modification but also by the surrounding medium. An increase of the refractive index (RI) of the solvent, causes a shift in the extinction spectrum to higher wavelength. More specifically, using solutions with RIs between 1.336 and 1.602 leads to a SPR red-shifting from 520 nm up to 545 nm and a color changing of the colloidal solution, which is not attributed to aggregation.<sup>[62]</sup>

The optical properties of metallic NPs are also dependent on particles distances and changed completely by interaction of various NPs with each other. Hence, an intensity decrease or broadening of the original extinction peak, or even a secondary, red-shifted band may occur, as in the extreme case of aggregation, which also involves a color change from red to blue for AuNPs as well as from a yellow to a brownish solution for AgNPs. This can be explained by the delocalization of the electron cloud over all neighboring particles, leading to a SPR shift to lower energies and consequently to higher wavelength.<sup>[63,64]</sup>

### 2.1.2 Application of gold nanoparticles (AuNPs) and silver nanoparticles (AgNPs)

Owing to their unique physico-chemical, optical, and electronic properties, metal NPs have been exploited for a wide range of applications in diagnostics, imaging, delivery, and therapy (see **Figure 3**). The broadening of the SPR band as well as the visual detection of the color change from red to blue upon aggregation show, for instance, benefit in Au-based diagnostic assays, especially for the detection of nonamplified hepatitis C virus.<sup>[65]</sup> In addition, the intense optical properties of AuNPs and AgNPs are utilized in various biodiagnostics, e.g. in an urine pregnancy test<sup>[66]</sup> or for the detection of SARS-CoV-2<sup>[67,68]</sup>.

## 2 State of knowledge

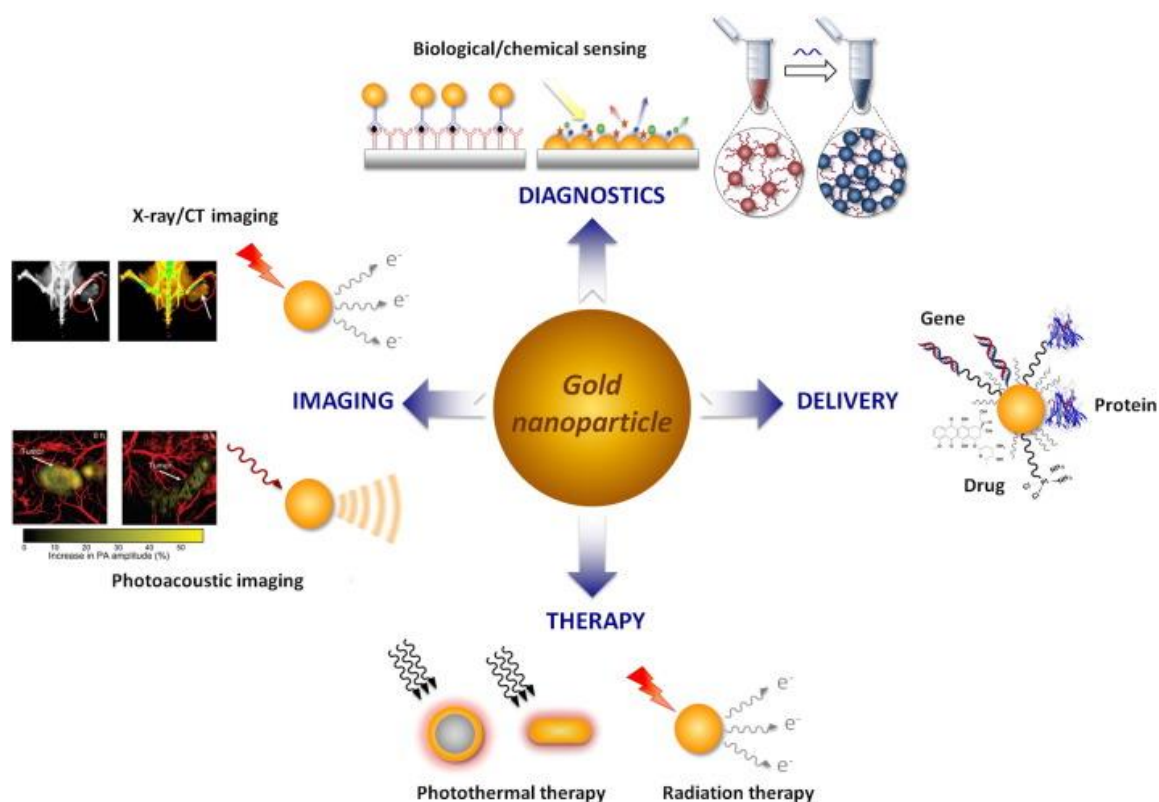


**Figure 3.** Biomedical applications of AuNPs. Owing to their unique physico-chemical, optical, and electronic properties, AuNPs have been exploited for a wide range of applications in diagnostics, imaging, delivery, and therapy. Reprinted from reference<sup>[69]</sup>, Copyright (2017), with permission from Elsevier.

Besides the usage as optical biosensors, metallic NPs found application in diagnostic methods such as visualization and cell imaging due to their light-scattering properties. Nanosystems consisting of silica nanospheres with a Ag layer, for example, were used as contrast agent for photoacoustic and ultrasound imaging of breast and pancreatic cancer cells.<sup>[70]</sup> Moreover, El-Sayed *et al.*<sup>[2]</sup> presented visualization of cancer cells by dark-field scattering microscopy using AuNPs conjugated to antibodies which only bind to cancerous cells. After cellular imaging, these NPs were applied for photothermal therapy by killing cancer cells upon irradiation with 514 nm light, which is near to their absorption maximum. The use of AuNPs for photothermal destruction of cancer cells is based on the fact that the particles strongly absorb light at their SPR, being nearly 100% converted into heat within picoseconds, which is then released to the surrounding environment and is sufficient to cause cellular damage.<sup>[71]</sup> Combining diagnostic imaging and therapy by, for instance, photothermal treatment of cancer cells, known as theranostic, makes particles based on Au and Ag attractive candidates for biomedical application. In addition to the large number of publications using nanogold as photothermal agent for cancer treatment<sup>[3,72,73]</sup>, AgNP-

based nanosystems have also been explored in cancer detection, diagnosis and photothermal therapy<sup>[74-76]</sup>. However, their application in cancer therapy is not limited to their photothermal properties, but noble metal NPs are also of great interest for targeted drug delivery.

Drug delivery systems based on NPs offer the ability to entrap and transport poorly soluble or unstable drugs, not only improving their solubility and in vivo stability, but also their biocompatibility and circulation time in the body. All these aspects are crucial for enhancing the efficacy and enabling accumulation at a disease site.<sup>[77]</sup> Due to their ease of surface functionalization, and their high affinity to various anchoring groups like phosphine, carboxylic, amine and especially thiol units,<sup>[78,79]</sup> a variety of biomolecules such as small interfering ribonucleic acid (siRNA)<sup>[80,81]</sup>, deoxyribonucleic acid (DNA)<sup>[82,83]</sup>, proteins<sup>[84,85]</sup> or drugs<sup>[4,86,87]</sup> can be attached directly to the NPs (see **Figure 4**). Thereby, biomolecules can bind via hydrophobic entrapment or by electrostatic interaction if the biomolecule bears no anchoring group, or by covalent interactions if the biomolecules have been chemically modified with moieties having high affinity to the particle surface.<sup>[88]</sup> Chen *et al.*<sup>[89]</sup> bound the anti-cancer drug methotrexate onto Au nanospheres and investigated the cytotoxic and antitumor effect compared to free methotrexate. The results showed, that drug-coated AuNPs exhibited a higher cytotoxic effect as well as a faster and higher accumulation in tumor cells than free methotrexate. Higher efficacy of combining nanomaterials with drugs could also be observed for AgNPs, presenting an increased amoebicidal effect against *Acanthamoeba* infection compared to drug alone due to multivalent drug binding.<sup>[90]</sup> However, direct binding to the NP surface is limited due to the reason that not all biomolecules possess a functional group having high affinity to the particle surface, and especially binding of hydrophobic drugs may lead to aggregation. Moreover, unfunctionalized NPs, which are commonly covered with citrate, are not stable in biological medium, but only in neutral aqueous solution,<sup>[91,92]</sup> being not a good precondition for biological application.

## 2 State of knowledge

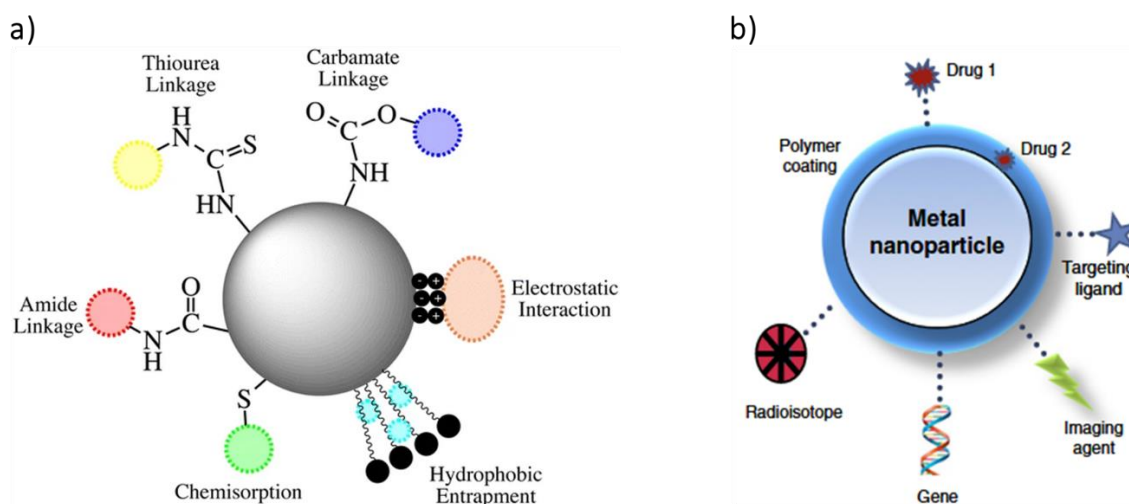


**Figure 4.** a) Functionalization strategies of NPs by covalent linkage and non-covalent conjugation. Reprinted from reference<sup>[88]</sup>, Copyright (2014), with permission from Springer Nature. b) Designing metal NPs for biomedical application by functionalization with various biomolecules. Reprinted from reference<sup>[93]</sup>, Copyright (2015), with permission from Elsevier.

Hence, besides drug attachment via surface complexation, therapeutics can further be bound covalently to functional groups of modified NPs. In these cases, biocompatible hydrophilic polymers were mainly used as capping agents, as they are known to protect the particles against aggregation, improve the stability and biocompatibility, lead to enhanced biodistribution due to reduced opsonization, and thus ensure effective targeting.<sup>[9]</sup> For example, AuNPs were coated with poly(ethylene glycol) (PEG) terminated with a thiol for Au-S-Linkage, and with a carboxylate functionality to complex platinum-based anticancer drugs, used for killing lung cancer cells.<sup>[94]</sup> Furthermore, Abdelfattah *et al.*<sup>[14]</sup> firstly covered the AgNP surface with PEG followed by loading with doxorubicin. This nanosystem was demonstrated to be an efficient drug carrier with high drug loading enabling sustained and selective drug delivery to the target site. In addition to these examples, PEG is commonly used as a hydrophilic protecting layer for nanocarriers<sup>[13]</sup> and is discussed in more detail in **Section 2.2.1.2**.

Effective drug release from NPs can be triggered via external or internal stimuli, such as photothermally modulated<sup>[95]</sup> or pH-triggered release of drugs<sup>[96]</sup>, or by place exchange reactions<sup>[97]</sup>, as demonstrated by Hong *et al.* using a glutathione-mediated intracellular release.

Besides targeted drug-delivery and drug release, there is also the possibility of simultaneous labeling and targeting to identify cancerous tumors at an early stage.<sup>[98]</sup>



Moreover, Mukherjee *et al.*<sup>[99]</sup> biosynthesized colloidal AgNPs showing high biocompatibility, as well as antibacterial and anticancer activity. In addition, these particles can be used as imaging agent as they indicate a bright red fluorescence signal that allows detection and localization of the NPs inside the cancer cells.

Conclusively, the variable surface modification, the possibility of multifunctionalization, and their unique optical and electronic properties make Ag and Au nanoparticles of great interest for theranostic nanomedicine, combining multiple functions discussed above like targeting, labeling, imaging, and therapy.<sup>[93,100,101]</sup> The aforementioned applications of nanoparticles in nanotechnology and medicine are basically related to the binding of various molecules, whereby the stability is of major importance in order to ensure increased blood circulation time, enhanced biodistribution and consequently reach disease sites. Therefore, the influence of surface functionalization on the stability of AgNPs was investigated thoroughly later in this thesis (see **Section 3.1**).<sup>[44]</sup> A detailed study on the stabilization efficacy of various thiol- and thioether-modified AuNPs was previously published.<sup>[17]</sup> Based on the obtained results of excellent colloidal stability of multifunctional thioether-AuNPs, different thioether-poly(glycidol) (PG)-coated AuNPs were investigated in **Section 3.2** focusing on protein binding and macrophage internalization in order to draw conclusions on their potential use as nanocarriers for biomedical applications. Furthermore, initial experiments were conducted to examine the biodistribution and blood retention time of Au-based nanocarriers with different surface coatings in silkworms used as an alternative to mammals (see **Section 3.3**).

### 2.1.3 Stability of colloidal particles

As mentioned before, colloidal solutions consisting of AgNPs and AuNPs attracted enormous attention in nanotechnology and biomedicine due to their interesting chemical, physical and biological properties. While AgNPs exhibited a wide range of applications such as biosensor materials, drug delivery systems, dental restorative materials, antimicrobial agents, for wound healing or in cosmetics,<sup>[1,102,103]</sup> AuNPs were used for instance as contrast agent<sup>[2]</sup>, in photothermal therapy<sup>[3]</sup> or for drug delivery<sup>[4,5]</sup>, as described thoroughly in the previous section. Ensuring the broad applicability of these metallic NPs, the stabilization efficacy plays a crucial role as aggregation leads to a loss of their unique

## 2 State of knowledge

properties. Thus, it is relevant enhancing the stability of such particles in dispersion by attaching capping agents with high affinity to the surface which consequently generate a barrier to aggregation.

### 2.1.3.1 DLVO theory

Colloidal particles undergo Brownian motion in solution, preventing the particles from sedimenting, but also induces random collision of individual particles with each other and with solvent molecules. Hence, the colloidal stability is driven by interactions between the particles and solvent molecules, as well as by the interparticle behavior itself, arising from different forces between the particles once in immediate vicinity. According to the Derjaguin-Landau-Verwey-Overbeek (DLVO) theory, two types of particle-particle interactions play a crucial role: van der Waals interactions, acting attractively between two identical particles, and electrostatic interaction, affecting as a repulsive force. To ensure the stability of the NPs, the repulsive interaction needs always to be stronger than the attractive one.<sup>[104,105]</sup> It should be noted, however, that DLVO theory only considers particle-particle interaction and not the particle-solvent interaction, and is therefore not directly suitable for many AuNP conjugates.

In general, colloidal particles are in a thermodynamic unfavorable state owing to their nanoscale size, meaning a large surface area and a large surface energy.<sup>[106]</sup> Thus, NPs try to leave this state by agglomeration, due to attractive von der Waals forces induced by their short interparticle distance, since attraction increases rapidly with decreasing particle distance. In order to suppress the aggregation process, counteracting repulsive forces are necessary, which can be achieved by modifying the NP surface, either by electrostatic or steric stabilization of the colloids, as thoroughly described in the next sections.<sup>[107,108]</sup> **Figure 5** schematically shows the force balancing between attractive van der Waals interactions and repulsive forces due to electrostatic or steric modification of the NP surface to obtain stable NP dispersions.

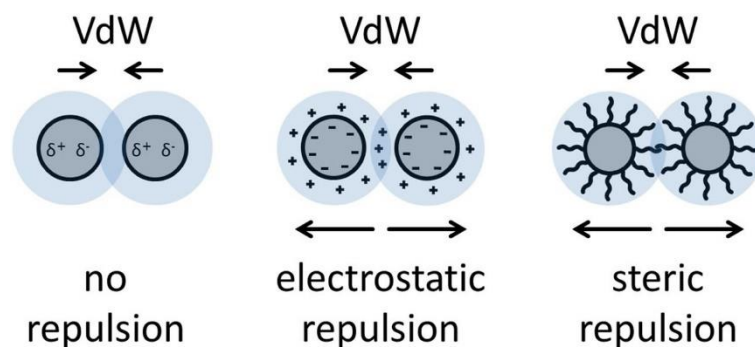


**Figure 5.** Stabilization of dispersed NPs by force balancing of attractive van der Waals interaction and repulsive electrostatic or steric forces. Reprinted from reference<sup>[108]</sup>, Copyright (2020), with permission from Elsevier.

### 2.1.3.2 Electrostatic stabilization

Noble metal NPs are commonly prepared by chemical reduction of the corresponding metal ions with salts via nucleation and growth process. Already in 1951, Turkevich *et al.*<sup>[109]</sup> revealed a facile synthesis of spherical AuNPs by gold salt reduction using sodium citrate as reducing agent, which was further improved by Frens *et al.*<sup>[110]</sup> allowing an adjusted size control by varying the relative citrate to gold ratio. Based on this kinetically controlled seeded growth method, the NP synthesis is well-established over the time, enabling to prepare monodisperse spherical AuNPs with a narrow size distribution and particle sizes ranging from 10 to 200 nm as well as under 10 nm.<sup>[111,112]</sup> Based on the synthesis of AuNPs by Turkevich, stable AgNPs are formed by citrate reduction of silver salts, particularly silver nitrate, in aqueous solutions.<sup>[113]</sup>

As citrate acts not only as reducing agent throughout these synthesis, but also as stabilizing agent, colloidal AuNPs and AgNPs are normally stabilized by charges.<sup>[109,114]</sup> In order to balance the net charge of the system, adsorption of citrate ions from dispersion media on the particle surface leads to the attraction of oppositely charged ions from the solution, resulting in the formation of an electric double layer (EDL). This EDL is consisting of an inner layer of counter-ions directly on the particle surface (Stern layer), and an outer, more diffuse layer of loosely associated ions of opposite net charge from the dispersant. If two of such particles are in immediate vicinity, the EDLs overlap, resulting in repulsion of the two particles. This Coulombic repulsion of such two neighboring particles with same surface charge hinders their approach and thus prevent aggregation.<sup>[107,115]</sup> **Figure 6a** displays the formation of an EDL on a negative charged NP and its electrostatic interaction potential, which decreases exponentially with distance from the particle surface.

## 2 State of knowledge

As described previously in **Section 2.1.3.1**, the electrostatic force of the EDL is counteracting to the attractive van der Waals interaction to prevent agglomeration. Thus, according to the DLVO theory, the total interaction energy between two particles is obtained to be the sum of van der Waals and EDL interaction energies. **Figure 6b** schematically shows a potential energy diagram of the DLVO interaction consisting of EDL (red line) and van der Waals interaction energies (blue line), as well as the resulting total interaction energies (black line) as a function of particle distance. The curve of the total interaction potential shows a maximum representing the aggregation barrier which is an important criterion for the colloidal stability. The larger this barrier is, the higher the stability of the colloidal dispersion, because for aggregation to occur, two particles would have to overcome this energy barrier during collision.<sup>[107,108]</sup>

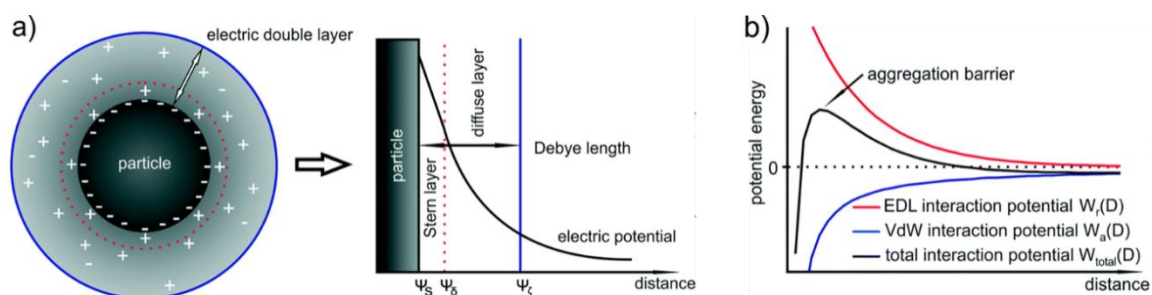


**Figure 6.** a) Electrical double layer (EDL) on a negatively charged NP surface by counter-ions from the solution and its potential energy curve. b) Schematic energy diagram of the particle-particle interaction according to the DLVO theory consisting of van der Waals and electrostatic interactions due to the EDL. Reprinted from reference<sup>[107]</sup>, Copyright (2015), with permission from Royal Society of Chemistry.

However, the total interaction potential is influenced by different factors like temperature and the ionic strength of the solvent. By increasing the ion concentration, for instance, more oppositely charged ions directly deposit as a compact layer on the particle surface, resulting in a compression of the Stern EDL and thus a shortening of the interaction radius. Consequently, the decrease of the EDL induces particle aggregation due to a lower aggregation energy barrier.<sup>[108]</sup>

Owing to the high sensitivity of electrostatic stabilized particles towards ionic strength, the applicability of these colloidal systems is enormously hindered. It is known that citrate-capped NPs usually show only good stabilities in aqueous solutions and tend to aggregate in biological environments due to the presence of proteins and especially the high ion

content, making these charge stabilized particles generally unsuitable for most biomedical applications.<sup>[11,116]</sup>

To overcome the environmental influenced aggregation behavior of electrostatic stabilized NPs, functional organic molecules such as polymers can be adsorbed on the particle surface, resulting in steric stabilization of the colloid, which is discussed in more detail in the following sections. However, electrostatic interactions provide the advantage that, for instance, oppositely charged biomolecules such as peptides, antibodies, and DNA can be non-covalently attached to the NPs without previous chemical modification, and thus without affecting the biomolecule's native, active form.<sup>[88]</sup>

### **2.1.3.3 Steric stabilization**

Agglomeration of NPs can not only be prevented by the formation of an EDL, but also by steric shielding of the colloids. In case of steric stabilization, a solution of organic substances is added to the dispersed NPs, allowing their adsorption on the NP surface, and thus preventing the particles from approaching each other due to the formation of this protective ligand shell. When two such capped particles come close, the ligand layers get compressed, resulting in a loss of mobility of the attached ligands as well as a limitation of their possible configurations. Consequently, this entails an entropy decrease which makes NP association unfavorable and causes a repulsive effect.<sup>[105,117]</sup> Hence, the adsorbed ligands enhance the stability by changing the surface properties, arising additional forces between two particles like steric forces as well as hydrophilic and hydrophobic interactions that counteract the van der Waals interactions, as depicted in **Figure 5**. This is referred to as the extended DLVO theory, wherein the energy potential is defined as the sum of the van der Waals, electrostatic, and steric potentials. The strength of the steric force depends on various conditions, such as the solubility of the ligands, the ligand concentration, the particle size, but also on the ligands themselves and their behavior in the solvent.<sup>[118,119]</sup> In the next section, steric stabilization of NPs with polymers as ligands is further discussed and some of the above factors are considered in more detail.

As previously mentioned, the particle surface can easily be modified with biomolecules by direct electrostatic coupling<sup>[78,120]</sup> or especially with functional organic ligands like polymers by ligand exchange reactions<sup>[17,121,122]</sup> provoking steric stabilization. In contrast

## 2 State of knowledge

to non-covalent (electrostatic) linkage to the NP surface, covalent attachment generally provides higher stability and better reproducibility of functionalization. The ligand exchange is caused by the labile binding of the citrate ions (hard Lewis base) to the Au or Ag surface (soft Lewis acids)<sup>[123]</sup>, inducing linkage of ligands modified with an anchor group that has high affinity to the NP surface, like carboxylates, amines, phosphines, and especially thiol-based ones under formation of a strong metal-sulfur bond<sup>[78,79]</sup>.

In 1994, Brust *et al.*<sup>[124]</sup> examined the synthesis of thiol-modified AuNPs using a two-phase system to allow simultaneous adsorption of self-assembled dodecanethiol monolayers during Au cluster growth (see **Figure 7a**). Using this method according to Brust, a variety of studies present direct insertion of thiols on noble metal NPs during particle formation. For instance, various alkyl-thiols with different chain length were attached to Au colloids<sup>[125]</sup>, while another working group focused on AgNP and AuNP stabilization by thiol-protection with poly(phenylacetylene-*co*-allylmercaptan)<sup>[126]</sup>.

In addition to the in situ thiolation during particle synthesis, there are a large number of publications on the linkage of thiol-based molecules by ligand exchange reaction, as depicted in **Figure 7c**, which represents a simple way of ligand attachment. This also enables the attachment of ligands to the NP surface that cannot be adsorbed in situ during colloid formation, for example due to incompatibilities with the synthesis conditions.<sup>[127]</sup> Bellino *et al.*<sup>[128]</sup>, for instance, performed derivatization of citrate-stabilized AuNPs with 3-mercaptopropane sulfonate and 2-mercaptoethylamine hydrochloride and investigated their adsorption kinetics. Furthermore, different alkanethiols with chain length of 2 to 14 CH<sub>2</sub> units were attached to AuNPs and AgNPs with different sizes to investigate their stabilization efficacy. It was demonstrated that the colloidal stability increases as a function of alkanethiol chain length and particle size.<sup>[6]</sup> Even the thiol-containing amino acids cysteine, homocysteine and glutathione, which are known to be involved in a number of diseases such as rheumatoid arthritis, AIDS and heart disease<sup>[129]</sup>, could be bound to AuNPs and AgNPs by ligand exchange reaction of the citrate capping agent.<sup>[130,131]</sup>

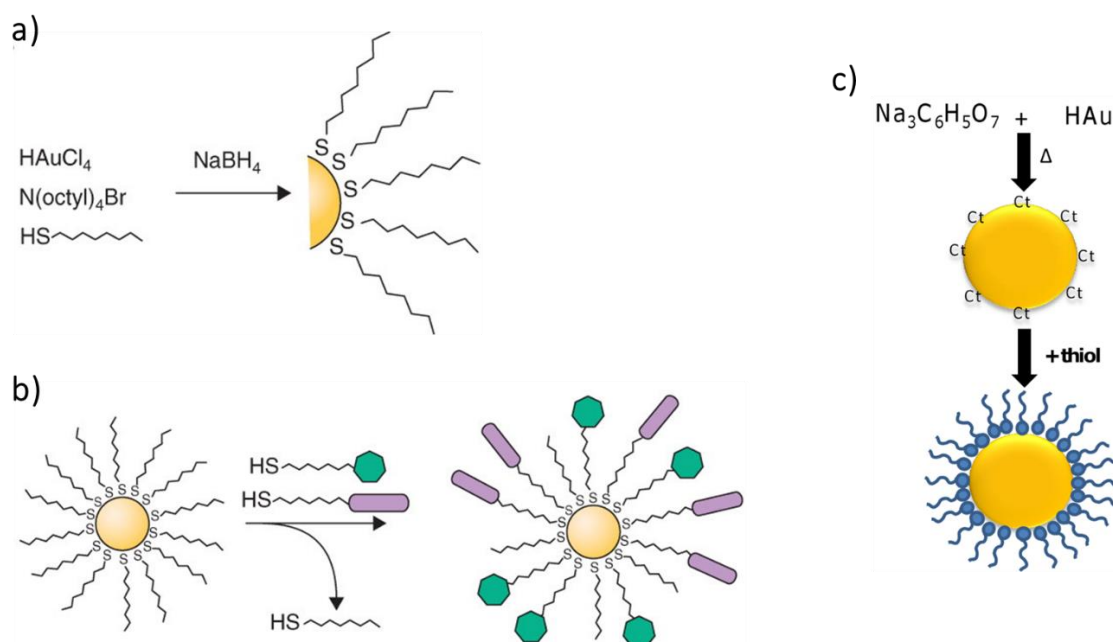


**Figure 7.** a) Synthesis of thiol-modified AuNPs according to Brust-Schiffrin method, enabling direct insertion of thiols on noble metal NPs during particle formation. b) Place exchange reaction of various thiol-terminated molecules on NPs. Both reprinted from reference<sup>[132]</sup>, Copyright (2010), with permission from Taylor & Francis. c) Synthesis of citrate-capped particles by Turkevich Method and subsequent ligand exchange reaction with thiols resulting in thiol-functionalized NPs. Reprinted from reference<sup>[133]</sup>, Copyright (2015), with permission from PLoS ONE.

In addition to ligand exchange reactions between citrate and thiol-ligands on noble metal surfaces, several working groups examined ligand exchange of phosphine-modified<sup>[134]</sup>, amine-protected<sup>[121]</sup> or even thiol-stabilized NPs<sup>[135-137]</sup> with other thiol-functionalities, as shown in **Figure 7b**. Here, either the entire ligand shell can be replaced by incoming ligands or only some of the ligands can be exchanged. This place exchange can be ascribed, for instance, to the higher affinity of thiols to silver and gold surfaces compared to phosphines or amines. Thereby, and in the case of the thiol-thiol exchange, the replacement is highly dependent on various factors such as the particle size, the solvent, the ligand concentration, and the structure of the ligands.<sup>[121,127]</sup> In this regard, Hostetler *et al.*<sup>[138]</sup> showed that short-chain ligands are more easily exchanged and those with longer chain lengths are preferentially tethered, attributed to stabilization by chain-chain interaction. They further investigated the influence of the concentration between the functionalized colloids and the incoming ligands. At low concentration of incoming ligands, almost no place exchange occurred, whereas at higher concentration, more than 60% of ligands were exchanged. Beyond a certain point, increasing the concentration had no further impact on the number of exchanged ligands.

## 2 State of knowledge

Besides thiol stabilization, which has been the most examined, other sulfur-containing compounds such as disulfides or thioethers are also reported to stabilize noble metal nanoparticles.<sup>[139-144]</sup> However, in the majority of these studies, sulfides or disulfides were attached in situ during particle synthesis rather than by ligand exchange from citrate-stabilized NPs, which is the basis of the present thesis.

The large number of the just mentioned publications, demonstrates that almost any molecule bearing a sulfur unit can bind to the surface of metal NPs. In **Section 2.1.3.5**, the binding of sulfur-containing compounds to Au and Ag surfaces is studied more extensively. Moreover, thiol-functional polymers, especially biocompatible polymers such as poly( $\epsilon$ -caprolactone)<sup>[145]</sup>, polyamidoamines<sup>[146]</sup> and PEG<sup>[8,11,12,147]</sup> have often been used for enhancing the physiological particle stabilization and knowing to be suitable candidates for drug delivery. Thiol-terminated PEG (MeO-PEG-SH) are the gold standard for the coating and biofunctionalization of NPs. However, the highly nucleophilic and oxidative character of thiols limits the possibilities introducing functional groups and provokes polymeric crosslinking.<sup>[148]</sup> Consequently, in the last few years, more focus is put on the attachment of chemical inert thioethers to the particles surface. In particular, the author's working group provided major contribution to the stabilization efficacy of AuNPs modified with the thioether analog of the well-established gold standard MeO-PEG-SH as well as with a multivalent equivalent.<sup>[17]</sup> Unlike in case of AuNPs, nearly no study have considered thioether-containing polymers as possible coating system for AgNPs, so this was investigated within this thesis (see **Section 3.1**) and has already been published.<sup>[44]</sup>

Once steric stabilization of NPs has been successfully achieved by ligand exchange of the citrate ions, further modification and functionalization can occur, representing an essential tool for biomedical applications. Thus, a variety of biofunctional molecules can bind covalently or via simple hydrophobic or electrostatic interactions, as depicted in **Figure 4**. For covalent bonding of biomolecules, it is advantageous that the surface functionalities are bifunctional, i.e., possess a terminal functional group in addition to the anchoring group.<sup>[78,79]</sup> In this thesis, exclusively the hydrophobic interaction between polymer protected AuNPs and proteins is of interest.



### 2.1.3.4 Steric stabilization via polymer adsorption

Steric stabilization of noble metal NPs with polymers are of great interest, as polymer functionalization protect the particles against aggregation and yielded in improved colloidal stability. This in turn affects the biodistribution, as reducing the aggregation tendency enhances their mobility in the bloodstream.<sup>[9,10]</sup> As mentioned above, the gold standard for coating and biofunctionalization of NPs is MeO-PEG-SH, not only due to the high affinity of the terminal sulfur moiety, but also as PEG provides a number of favorable properties (see **Section 2.2.1.2**) for use as a ligand on NP conjugates for medical and biological applications.<sup>[13-15]</sup>

Due to its amphiphilic character, PEG is well soluble in various organic solvents, and in particular water represents an excellent solvent, in which the polymer is strongly hydrated as a random coil.<sup>[149]</sup> However, upon binding via the terminal end group, the non-adsorbed polymer chains extend out from the particle surface in a good solvent in order to maximize the polymer conformations, resulting in a repulsive force. In a poor solvent, polymers may adopt a different configuration, reducing the surface repulsion or even allowing attractive forces to predominate.<sup>[150]</sup>

Besides, monofunctional PEG can adopt different conformations on the NP surface which is dependent on the grafting density (see **Figure 8a**). At low grafting densities, terminally anchored polymers adopt a so-called mushroom configuration, yielding in a thin polymer shell, whereby the polymer chains are widely spaced and can hardly interact with each other. Contrary, a large grafting density leads to a brush conformation resulting in a thicker PEG shell. This elongated structure occurs due to the favored minimization of chain-chain interaction of the large number of polymers present at the particle surface, since the polymer chains repel each other in good solvents.<sup>[118,151]</sup> Later in this work, these conformations will be addressed more thoroughly by determining the arrangement of thiol- and thioether-functionalized PEG on AgNPs in **Section 3.1.2.3.2**.

## 2 State of knowledge

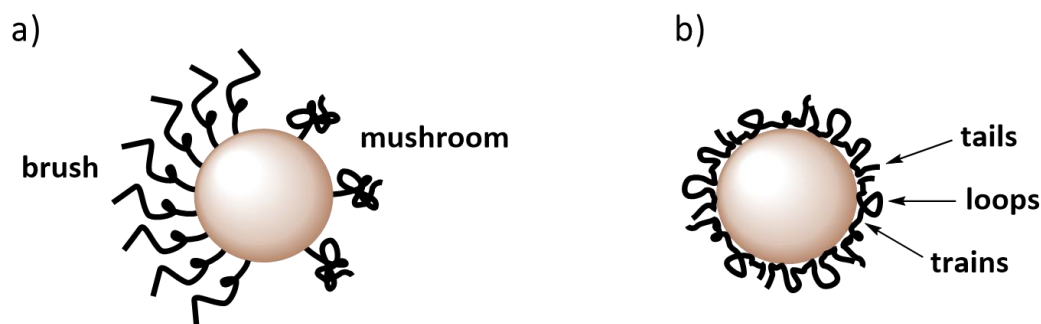


**Figure 8.** Arrangement of polymers on a particle surface. a) Brush and mushroom conformation formed by endgrafted polymers with a terminal anchor group or a terminal sequence as in block copolymers. b) Train-loop-tail configuration formed by linear homopolymers or random copolymers containing multiple anchor regions distributed along the backbone.

In contrast to the well-ordered conformation of PEG, which is also adopted by block copolymers bearing a terminal sequence with high affinity to the NP surface, other structures exist for linear homopolymers or random copolymers containing multiple anchor units. In a good solvent, these polymers adopt a coil configuration and upon binding to the particles via multiple anchor groups, a structure of a number of trains and loops as well as of two tails will be formed. As depicted in **Figure 8b**, trains are polymer segments adsorbed to the NPs, tails are the non-adsorbed ends of the polymer chains that protruded from the surface, and loops are non-adsorbed polymer sequences between the trains and the tails spreading out into the solution.<sup>[152]</sup> Such an arrangement on a NP surface could be found for homopolymers like PVP<sup>[153]</sup> and poly(vinyl alcohol)<sup>[154]</sup>. Hence, it can also be assumed that the copolymer PG used for particle stabilization in this work adopts a train-loop-tail configuration on AgNPs and AuNPs.<sup>[17]</sup>

Furthermore, the surface curvature has an impact on the polymer configuration. In case of polymers that show brush arrangement, an increase in surface curvature results in a decrease in chain-chain interactions, which in turn leads to an increased polymer surface coverage and a reduction of the layer thickness.<sup>[155]</sup> A decreased layer thickness with an increased surface curvature was also observed for polymers adsorbing in a train-loop-tail conformation.<sup>[156]</sup>

Overall, however, steric stabilization is only effective when the polymer layer on the NP surface is uniform and completely occupied, not exhibiting any gaps. Incomplete coverage of the particle surface may cause attraction of the colloids even in a good solvent. Furthermore, in particular long-chain and high molecular weight polymers having multiple

anchor groups may interact with more than one NP with a patchy surface coverage leading to aggregation, which is referred to as bridging flocculation.<sup>[157]</sup>

### 2.1.3.5 Sulfur-metal NPs bonding models

Protection of surfaces and NPs of gold and silver with compounds containing sulfur, especially thiols, is widely used and extensively studied. The focus of these studies was on the functionalization and stabilization of NPs for biomedical applications rather than on understanding the structure of the ligand shells and the entire binding process. For noble metal surfaces, more detailed investigations on the structural properties as well as the adsorption behavior of thiols and sulfides are found.<sup>[6,7,27,79,158-161]</sup>

Sulfur-containing ligands spontaneously form self-assembled monolayers upon adsorption onto Au substrates, as illustrated in **Figure 9**, with thiols exhibiting a more ordered structure than dialkyl sulfides and thiols forming a thicker ligand shell than dialkyl sulfides.<sup>[161]</sup> In consequence, a weaker metal-thioether bond is often reported in literature compared to the adsorption of thiol molecules. The ordering and stability, however, is not only dependent on the anchor group, but mainly on the exact molecular composition of the sulfur-containing ligand.<sup>[159,162]</sup> Upon adsorption of alkanethiols on Ag, structurally related monolayers as on Au are formed, but differ in details of their orientation (see **Figure 9b**).<sup>[163]</sup> Schlenoff *et al.*<sup>[164]</sup>, for instance, reported a 30 ° tilt angle and interchain spacing of 5.0 Å for the binding of alkanethiols on Au surfaces, whereas alkyl chains on silver were oriented more upright with a tilt of 13 ° and exhibited a packing distance of 4.1 Å.

Besides the structural studies, different approaches regarding the binding process of sulfur-containing ligands to metal surfaces exist in literature. Using various spectroscopic methods, Nuzzo *et al.*<sup>[165]</sup> have demonstrated that the S-H bond remain intact after methanethiol binding to gold. In contrast, some other research groups report that thiol compounds adsorb to the Au surface via a chemical bond (chemisorption) provoked by S-H bond cleavage, resulting in a stable, covalent Au-S bond with a slightly polar character and elimination of molecular hydrogen. Consequently, thiols adsorb as corresponding thiolates on metal surfaces composed of Au or Ag.<sup>[166-168]</sup>

## 2 State of knowledge

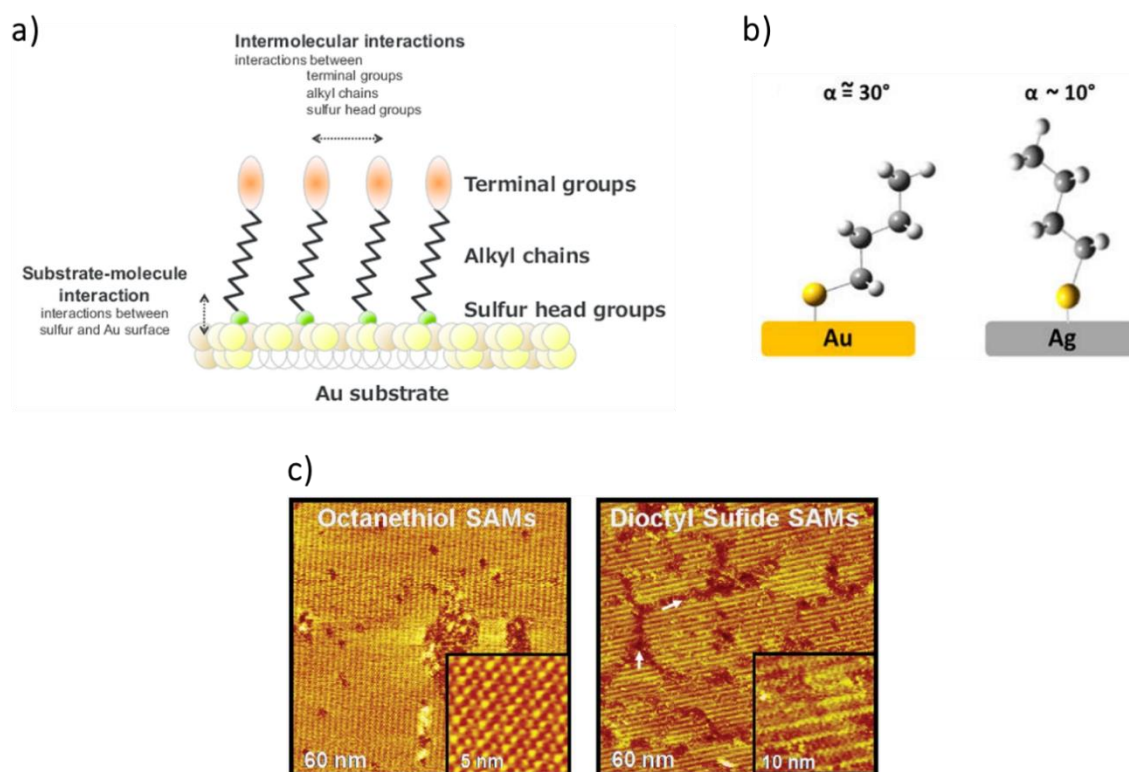


**Figure 9.** a) Illustration of a self-assembled monolayer of an alkanethiol on an Au substrate and its interactions. Reprinted from reference<sup>[169]</sup>, Copyright (2011), with permission from Current Physical Chemistry, Bentham Science Publishers. b) Schematic illustration of a self-assembled molecule on an Au and Ag surface, achieving different tilt angles. Reprinted from reference<sup>[163]</sup>, Copyright (2015), with permission from MDPI. c) Scanning tunneling microscopy images of self-assembled monolayers on gold surfaces formed by octanethiol and dioctyl sulfide, resulting in different packing structure. Reprinted from reference<sup>[170]</sup>, Copyright (2015), with permission from John Wiley and Sons.

Here, Au-S desorption energies around 126 kJ/mol arise, irrespective of the type of thiols.<sup>[159]</sup> In addition to chemisorption, also physisorption, caused by van der Waals or steric interactions between organic moieties like alkyl units, plays a crucial role in the bonding strength (see **Figure 9a**). CH<sub>2</sub> units contribute 6.2 kJ/mol (linear) and 8.1 kJ/mol (cyclic) to the physisorption energy, respectively, while the contribution of CH<sub>3</sub> groups is 15.5 kJ/mol.<sup>[171]</sup> Consequently, both chemisorption as well as inter- and intra-chain interactions determine the arrangement of ligands on the surface and the packing density, and are responsible for their stability.<sup>[166]</sup>

Despite the thorough contributions on thiol adsorption on gold, there were only limited investigations on binding process on silver. It is indicated that thiols chemisorb on Ag surfaces as thiolates under formation of a stable Ag-S bond, having an ionic character, while the Au-S bond is more covalent.<sup>[172]</sup> In literature, two times lower bond strengths were found for thiol ligands on Ag surfaces compared to a gold-sulfur bond.<sup>[173]</sup> According to

Bryant and Pemberton, the different bond strengths are an explanation for the different character of Ag-S and Au-S bond as well as for the different orientation and tilting of the chains of thiol molecules adsorbed on the metal surface, as previously mentioned.<sup>[160]</sup>

For thioethers, Zhong and Porter<sup>[174]</sup>, provided evidence that C-S bond cleavage occurs under electrochemical conditions during the spontaneous attachment of various organosulfides to Au. In addition, C-S scission of diphenyl sulfide and dibenzyl sulfide adsorbed on silver films was verified by surface-enhanced Raman scattering.<sup>[175]</sup> On the other hand, several research groups demonstrated that the C-S bond remained intact during binding to the Au surface and was not cleaved, thus thioethers do not chemisorb but are only stabilized by physisorption.<sup>[161,176-179]</sup> Due to the fact that dialkyl sulfides only physisorb, a weaker interaction between the sulfur anchor unit and the metal surface is expected compared to the binding of thiols. For diethyl sulfide and dibutyl sulfide, adsorption energies of 68 kJ/mol and 86 kJ/mol, respectively, were reported, attributed to physisorption only. In contrast, butanethiol, for instance, featured a higher energy due to a contribution of the chemisorption of the sulfur group (127 kJ/mol) and a contribution of the physisorption of the alkyl chain (68 kJ/mol).<sup>[159]</sup>

As just mentioned, extensive investigations on the formation of monolayers of thiols and dialkyl sulfides on planar Au and Ag surfaces can be found in the literature, showing differences in surface structure and adsorption process dependent on the organosulfur component and the metal surface. However, discrepancies exist with regard to the adsorption structure, wherein most publications report S-H bond cleavage upon binding of thiols, whereas the C-S bond is not cleaved in the case of thioethers. Despite the numerous detailed studies, however, the exact mechanism of this process has not yet been fully understood. Particularly for organosulfur-coated NPs, most researchers only focused on NP functionalization and stabilization and their biomedical application, and thus little is known about the understanding of the structure, the chemical composition of the metal-sulfur interface of NPs and the energetics of monolayer formation.

Using various spectroscopic data, Hostetler *et al.*<sup>[180]</sup> demonstrated that the overall structure of alkanethiols adsorbed on small Au clusters is analogous to planar surfaces and that the physical and spectroscopic properties of the ligand shells of alkanethiols on the Au(111) surfaces of particles with diameters > 4.4 nm resemble to those on flat substrates.

## 2 State of knowledge

This may be due to the fact that above a diameter of 4.4 nm the Au(111) faces dominate the particle surface, which is as well the most important crystal surface of planar gold substrates. In addition, it is known that thiols also adsorb as thiolates on colloidal particles caused by S-H bond cleavage.<sup>[181]</sup> Similarly, for the adsorption of alkanethiols to AgNPs, comparable tilt angles and arrangements were found as on planar Ag surfaces.<sup>[182]</sup> Thiol-functionalized AuNPs showed higher stability than their silver analogue<sup>[6]</sup>, which is in agreement with the larger Au-S than Ag-S binding strength on planar substrates. Moreover, dialkyl sulfides were reported to form a weaker bond to metal NPs than thiol ligands<sup>[139,183]</sup>, as already observed on flat substrates. This general statement of a weaker thioether-metal bond, however, has been refuted by a detailed study on AuNPs<sup>[17]</sup> as well as on AgNPs<sup>[44]</sup> as described in **Section 3.1**. Nevertheless, the detailed research of sulfur-containing ligands on planar substrates provides a valuable basis for experiments on NPs. Thus, the knowledge gained from studies on metal-sulfur binding and surface chemistry of organosulfurs on planar Au and Ag substrates could be profitably transferred to studies on NPs, as, for example, some research groups have demonstrated for investigations on the reduction of nonspecific protein adsorption due to PEGylation.<sup>[184-186]</sup> Despite the similarities, there are also differences between thiol molecules adsorbing to Au(111) and to AuNPs, making a precise elucidation of the sulfur-Au interface still unclear. Especially the surface curvature, the existing surface defects, and the different coverage densities suggest that not all findings can be applied one-to-one to particle surfaces.<sup>[182,187]</sup>

Finally, the chemical bonding scenario of Au with sulfur-containing ligands is discussed more precisely. The valence electron configuration of Au ( $d^{10}s^1$ ) allows interaction with neighboring atoms either via a pair of d electrons or a single s electron. For the bonding of thiols to Au, both bonding scenarios are displayed in **Figure 10a**. According to Reimers *et al.*, the interaction of a p electron of sulfur with a single s electron of Au leads to an Au(I)-thiolate species, whereas an Au(0)-thiyl scenario results when the d electron pair of Au is involved in the interaction. The latter is a rather unusual arrangement, since the d orbital of Au is fully occupied and consequently relatively unreactive. In addition, the d orbital of Au is energetically much lower than the s-bonding orbital, which results in only a small amount of electron density being transferred from Au to S.<sup>[188]</sup> Therefore, it is usually

expected that the attachment of sulfur-containing compounds to Au surfaces leads to Au(I)-thiolates.<sup>[166,189-192]</sup>

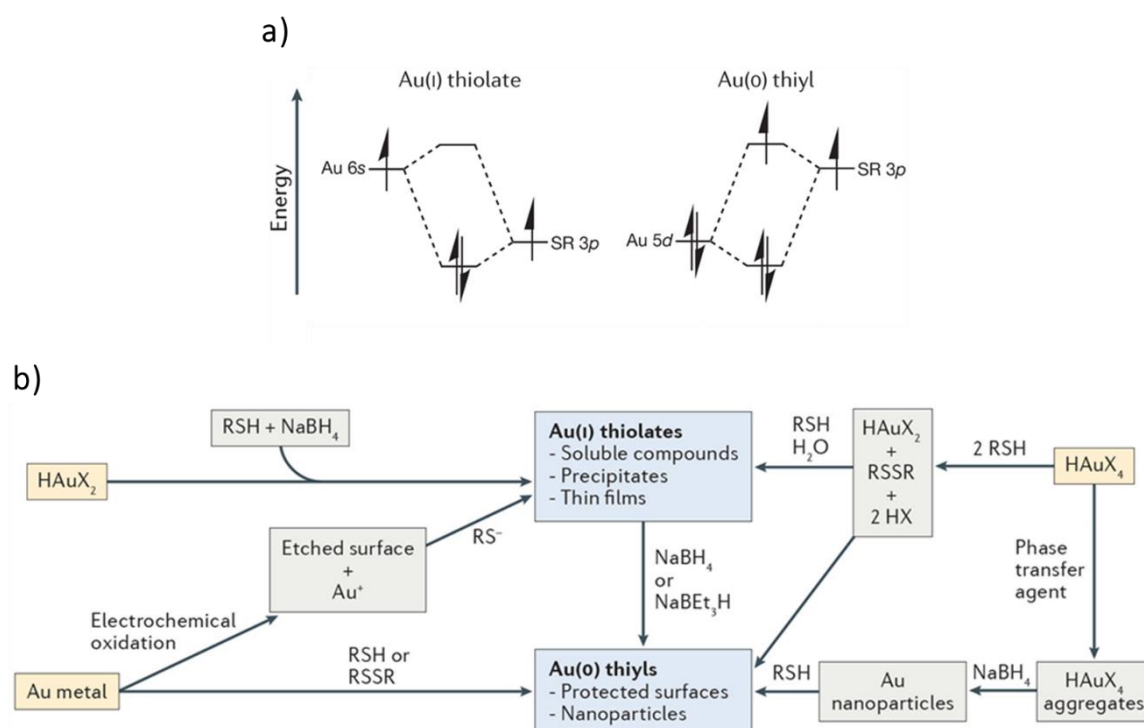


**Figure 10.** a) Frontier orbital interactions of Au-S bonds in chemical bonding scenarios of Au(I)-thiolate and Au(0)-thiyl. b) Synthetic pathways to Au(I)-thiolate species and Au(0)-thiyl species. Reprinted from reference<sup>[193]</sup>, Copyright (2017), with permission from Springer Nature.

However, Reimers *et al.* demonstrated that the predominant binding scenario of an Au-S bond is not always Au(I)-thiolate. Rather, the occurrence of Au(I)-thiolate and Au(0)-thiyl species is dependent on the reaction pathway, how and in which process sulfur-containing compounds interact with Au (see **Figure 10b**), because, as described previously, sulfur functionalities can be introduced by direct synthesis according to the method of Brust or by ligand exchange to the particle surface. **Figure 10b**, for instance, shows that the introduction of thiols or disulfides onto Au metals without the presence of reducing agents or electrochemical oxidation leads to the formation of Au(0)-thiyl. Most relevant for the present work, however, is that thiols that attach directly to and stabilize already formed AuNPs exhibit an Au(0)-thiyl character. Thus, there is no covalent contribution to the bonding. Hence this Au(0)-thiyl species is also described as non-bonding, and in this case stabilization occurs by dispersive interactions, in which all electrons of the atoms are involved. Consequently, van der Waals interactions are the critical forces for both physisorption and surface species chemisorbed to NP.<sup>[188,193]</sup>

## 2 State of knowledge

### 2.2 Interaction of NPs with biological systems

Ensuring that noble metal NPs can meet their biomedical application for instance as contrast agent<sup>[103,194]</sup>, in photothermal therapy<sup>[75,195]</sup> or for drug delivery<sup>[102,196]</sup> (presented in detail in **Section 2.1.2**), it is essential to prevent these nanocarriers from being recognized as foreign bodies by phagocytes and thus being rapidly removed and cleared from the bloodstream.

#### 2.2.1 Protein Corona

Upon NPs entering the body, they get into contact with thousands of blood proteins varying in abundances over a broad concentration range from 5 pg/mL to 50 mg/mL<sup>[197]</sup>, which spontaneously and rapidly leads to protein coverage of the particle surface due to physical and chemical interactions between the surface and the biomolecules<sup>[198,199]</sup>. This so called protein corona is consistent of proteins binding with high affinity to the nanomaterials surface (hard corona) as well as of loosely bound proteins (soft corona), which can be replaced easily by other proteins of the biological source.<sup>[200]</sup> Since proteins of the hard corona are tightly bound showing long-term and irreversible adsorption, it is suggested that the hard corona plays a more important role in the biological behavior than the soft corona.<sup>[201]</sup> In addition, hard corona proteins are considered to be most essential for understanding the interaction with cells and NP-protein complexes<sup>[202]</sup>, thus most studies only focus on investigations on the hard corona.

##### *2.2.1.1 Parameters influencing protein binding on NPs*

The composition of the protein corona is dependent on various factors such as the biological source<sup>[21,203]</sup>, the exposure time<sup>[22,204]</sup> as well as the physiochemical properties of the nanocarrier<sup>[23,24,205,206]</sup>, including NP material, size and shape, and surface chemistry.

After incubation of silica and polystyrene NP with plasma, both 200 nm in size, different protein corona compositions were obtained.<sup>[207]</sup> Differences in adsorbed proteins were further found for varying sizes and shapes of the nanocarrier, despite the same core material. Curvature and size of NPs are known to affect protein orientation and structure of the bound proteins<sup>[208]</sup> and that the thickness of the protein corona increases with increasing particle size, as demonstrated by Piella *et al.*<sup>[209]</sup> for AuNPs ranging from



3.5-150 nm. In addition, on 50 nm AuNPs, a lower number of bound proteins was identified compared to 30 nm AuNPs.<sup>[210]</sup>

Since protein-NP interactions, driven by various forces like van der Waals interactions, coulomb forces, H-bond or hydrophobic interactions, play a significant role in protein corona formation,<sup>[198]</sup> the surface chemistry is another important parameter. Increasing the surface charge density of negatively charged particles, for instance, lead to enhanced protein adsorption.<sup>[211]</sup> This working group additionally reported a predominant binding of proteins with an isoelectric point < 5.5 on positively charged NPs, whereas particles with a negatively charge preferentially bound proteins with isoelectric points > 5.5.<sup>[212]</sup>

However, besides the surface charge, especially NP surface functionalization such as coating with polymers is known to have a crucial effect on protein corona composition, with PEG being the most studied polymer, which is considered in more detail in the next **Section 2.2.1.2**. Particles modified with PEG resulted in a reduced adsorption of the protein complement C3 (C3) and an increase in gelsolin (GSN) binding compared to citrate- and phosphine-capped AuNPs. In general, a lower total protein binding was observed for PEG-coated NPs.<sup>[213]</sup> Furthermore, the working group of Walkey *et al.*<sup>[27]</sup> studied the protein corona on AuNPs with various PEG grafting densities and found a grafting density dependent reduction in adsorbed proteins, as illustrated in **Figure 11**. They further demonstrated that the protein C3 shows high affinity to citrate-AuNPs, while this protein is less abundant in the protein corona of PEGylated particles. In addition to this example of blocking a certain protein with hydrophilic PEG, Schöttler *et al.*<sup>[30]</sup> displayed the possibility of selective adsorption of the protein clusterin (Apolipoprotein J, APOJ) induced by PEEP surface functionalization of polystyrene NPs, resulting in reduced macrophage internalization. Cell uptake of NPs and the influence of protein corona composition on cellular uptake will be discussed more thoroughly in **Section 2.2.2**.

## 2 State of knowledge

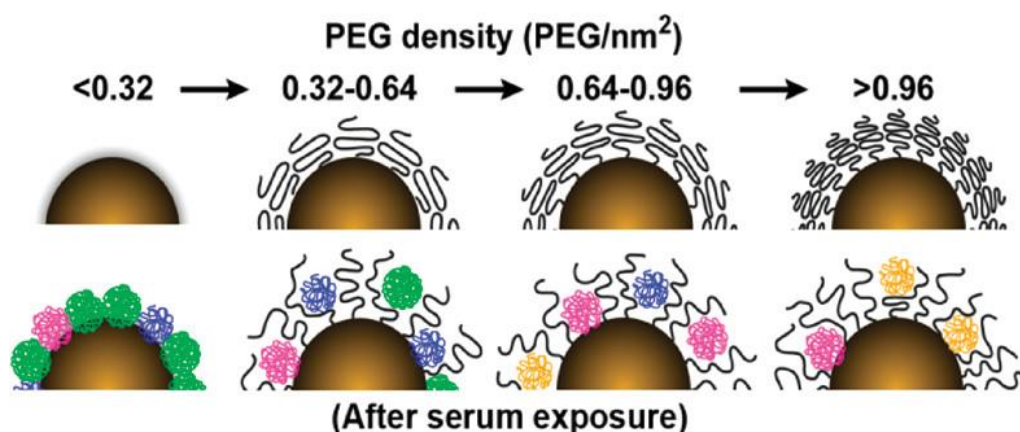


**Figure 11.** Schematic illustration of protein adsorption on AuNPs with various PEG grafting densities, showing a reduced binding of proteins with an increase in PEG density. Reprinted from reference<sup>[27]</sup>, Copyright (2012), with permission from American Chemical Society.

Besides coating NPs with hydrophilic polymers, surface hydrophobicity is known to influence the protein corona formation and composition, showing increased adsorption of proteins on hydrophobic nanomaterials compared to hydrophilic ones.<sup>[214,215]</sup> Yu *et al.*<sup>[216]</sup> not only demonstrated the attachment of a larger number of proteins to hydrophobic surfaces, but furthermore that small and negatively charged proteins preferably bound. More precisely, adsorption of hemoglobin fetal subunit beta and of human serum albumin (HSA) increased with increasing hydrophobicity, while less vitronectin (VTN) and antithrombin III (SERPINC1) was detected. High enrichment of HSA on hydrophobic surfaces is in agreement with investigations from other working groups.<sup>[217]</sup>

Only few investigations on protein binding and cellular uptake were found on particles functionalized with copolymers composed of a hydrophilic and a hydrophobic moiety. Kim *et al.*<sup>[218]</sup>, for instance, studied the protein adsorption on hydrophobic poly(hexadecylcyanoacrylate) (PHDCA) particles compared to NPs functionalized with a copolymer consisting of hydrophilic PEG and hydrophobic PHDCA. A higher amount of adsorbed proteins on pure PHDCA particles is shown, which is in accordance with the beforementioned findings of enhanced protein binding due to hydrophobicity. HSA is most abundant in both protein coronas, representing nearly the same fraction. In contrast, some proteins, such as apolipoprotein A-I (APOA1), was enriched on more hydrophobic NPs, while apolipoprotein E (APOE) and apolipoprotein B-100 (APOB-100) was adsorbed with higher affinity to PEG-PHDCA particles. Furthermore, Zhang *et al.*<sup>[219]</sup>, indicated no

significant difference of protein corona composition of AuNPs coated with polymers with various hydrophilic-to-hydrophobic ratios, except of pure hydrophilic AuNPs.

Due to the large number of factors that have an impact on protein adsorption, the protein corona is quite complex and not easy to understand. Especially with respect to surface functionalization, it has to be noted that coating of the NPs usually implies a change in size, surface charge and particle composition, which in turn affects protein binding.

### **2.2.1.2 Stealth polymers**

As mentioned above, MeO-PEG-SH is the most common used polymer for stabilization and biocompatibilization. The covalent binding of PEG is known as PEGylation and was first described in 1977 by Davies and Abuchowsky<sup>[220,221]</sup>, which provided new opportunities in pharmacology and medicine. Since then, PEG is one of the most studied ligands for functionalization of nanomaterials due to its favorable properties for biological and medical applications. Here, the fact that PEG is non-toxic, inert and the possibility of structural variability regarding chain length and terminal functionalization play a crucial role.<sup>[222-224]</sup> PEG is not only used as a conjugate for therapeutically relevant proteins, but also for modification of drugs improving their in vivo performance, as PEGylation alters the physicochemical properties of the biomolecules resulting in changed elimination kinetics.<sup>[224-227]</sup> In addition, there are a large number of publications on the attachment of PEG to nanomaterials, exhibiting reduced phagocytosis and simultaneously an increased blood circulation time, which, for instance, enables the transport of drug-loaded nanosystems to their target tissue.<sup>[228-230]</sup> This may be explained by the fact that the hydrophilicity of PEG improves water solubility, thus reducing the aggregation tendency and enhancing its mobility in the bloodstream. Additionally, as described in **Section 2.1.3.3**, PEG sterically stabilizes the NPs, enabling sufficient stabilization in biological environment in the first place. However, most relevant seems to be that PEG coating strongly reduces nonspecific adsorption of proteins and peptides and consequently suppresses opsonization (see **Figure 12**). Thus, the NPs are prevented from being recognized by macrophages, allowing a longer retention time in the blood.<sup>[186,231]</sup> Since the PEG shell acts as a kind of magic hood, PEG is further known as stealth polymer and represents to date the gold standard of non-ionic hydrophilic polymers with stealth behavior. Even though the

## 2 State of knowledge

mechanism of nonspecific protein adsorption of PEG-coated materials is not yet fully understood, researchers demonstrated dependency of stealth properties on chain length, grafting density, and the conformation of PEG chains on the surface.<sup>[232-235]</sup>

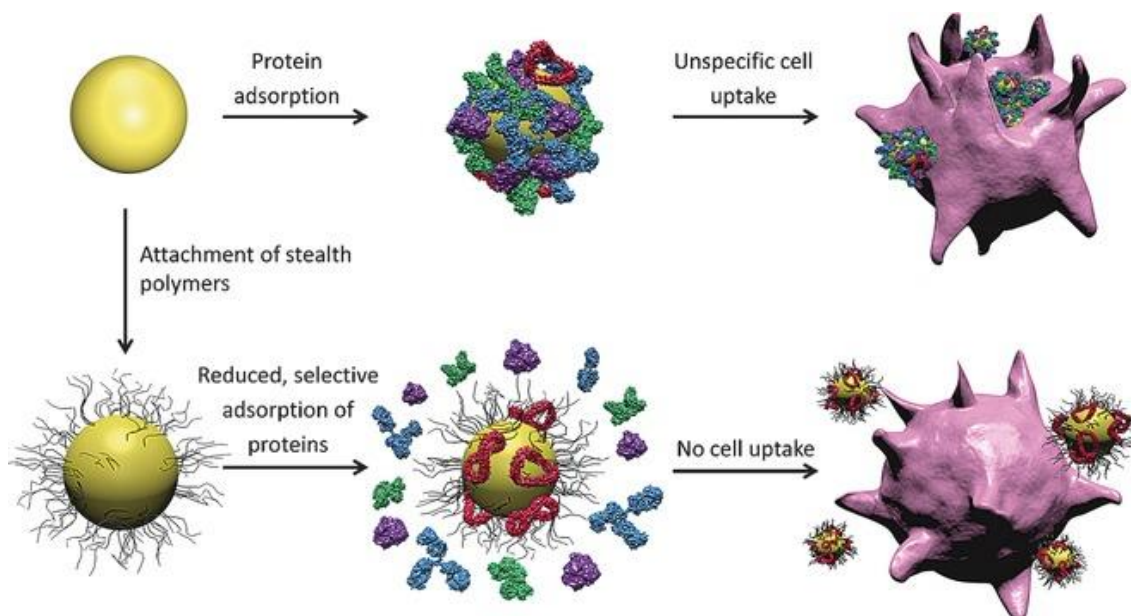


**Figure 12.** Protein corona formation on ungrafted and with a stealth polymer functionalized particle, and their differences in cell uptake. Reprinted from reference<sup>[24]</sup>, Copyright (2016), with permission from John Wiley and Sons.

Fang *et al.*<sup>[233]</sup> have shown that the amount of adsorbed plasma proteins is significantly reduced by increasing the molecular weights of attached PEG from 2 to 20 kDa. In contrast, coating with low molecular weight PEG of 559 Da also showed effective protein resistance upon reaching a packing density of 1.2 chains/nm<sup>2</sup>.<sup>[236]</sup> Hence, the effect of decreased protein adsorption is not only due to the molecular weight but also to the surface density, showing a reduction in adsorption as PEG coverage increased.<sup>[237]</sup> However, Unsworth *et al.*<sup>[234]</sup> displayed an increased protein resistance up to a certain surface density of 0.5 chains/nm<sup>2</sup>, while above this value adsorption decreased. Providing effective stealth properties, an optimal PEG packing density has to be achieved, which is different for each PEG, as well as each surface and protein source. PEG chains have to be densely packed on the material surface, which is related to the configuration of PEG. Low surface coverage leads to a mushroom-like structure, whereby proteins have enough space to bind in the interstices resulting in elimination from the systemic circulation. Contrary, higher PEG density creates brush conformation showing usually more suppressed protein

adsorption.<sup>[235]</sup> The different chain configurations of PEG on surfaces and their dependence on packing density will be discussed in more detail in **Section 3.1.2.3**.

Although covalently attachment of PEG is the gold standard to reduce nonspecific protein adsorption, by now some researchers focused on potential alternatives. A promising polymer class for stealth coating is POx, attracting attention due to their hydrophilic, non-ionic character, and their high biocompatibility.<sup>[29,238]</sup> Furthermore, Schöttler *et al.*<sup>[30]</sup> investigated the protein resistance to NP surfaces modified with PEEP, displaying a reduced and non-specific protein binding after exposure to human plasma, similarly to PEG, with a selective adsorption of APOJ. Other innovative polymers representing good alternatives to PEG are PVP<sup>[31]</sup>, polyacrylamides<sup>[239]</sup>, polycarbonates<sup>[240]</sup> or PGs<sup>[32]</sup>. Latter is a more attractive alternative not only due to the similar chemical structure, but especially due to its possibility for multifunctionalization, whereas PG coating is comparable or more useful in preventing protein adsorption than PEG.<sup>[33,34]</sup> In addition, PG is known to reduce non-specific interaction with opsonins and thus avoid phagocytosis and increase blood retention time.<sup>[35,36,241]</sup> Despite the investigations of reduced protein adsorption and cell resistance of PG-coated Au substrates<sup>[33,34,242]</sup>, to the best of the author's knowledge, there is nearly no study on protein corona and cellular uptake on AuNPs functionalized with PG. Due to the opportunity of combining stealth properties with introduction of additional functionalities, PG is used in this work as basis for coating AuNPs.

Nevertheless, all these stealth polymers cannot completely prevent protein corona formation, but only reduce the number or amount of adsorbed proteins, and lead to selective binding of proteins. These two aspects contribute to a reduced uptake of such polymer-functionalized NPs by immune cells, as shown in **Figure 12**. In the following two sections of this thesis, the cellular uptake of NPs by immune cells in general and the impact of the composition of the protein corona on cell internalization will be explained in more detail.

### 2.2.2 Cellular uptake of NPs by immune cells

After intravenous administration, NPs, like all foreign substances, are recognized by phagocytic cells of the reticuloendothelial system, predominantly macrophages of the liver (Kupffer cells), and rapidly removed from the bloodstream.<sup>[243]</sup> The application of NPs as a

## 2 State of knowledge

liver contrast agent takes advantage of rapid cell uptake by macrophages. Since fewer macrophages are existent in pathological regions, resulting in a reduced uptake of the contrast agent, healthy and diseased tissues can be clearly distinguished due to the strong contrast.<sup>[194,244]</sup> Conversely, rapid clearance from the bloodstream is a major limitation for other biomedical applications, such as drug administration over a prolonged period of time or targeted drug transport to specific sites in the body, as this prevents the nanocarriers from reaching their target site. For such biomedical applications, it is essential to alter the nanocarriers to enhance their biodistribution and minimize their non-specific cell uptake.<sup>[245]</sup> Thus, understanding the interaction between NPs and cells is a crucial factor for the design of efficient nanocarriers.

Macrophages and other cell types like monocytes and neutrophils utilize NP after penetration into the body via a process called phagocytosis.<sup>[246]</sup> As illustrated in **Figure 13**, phagocytosis occurs in 4 steps - opsonization (A), adhesion and ingestion (B), phagosome formation (C) and phagolysosome formation (D). The first step, the binding of opsonizing proteins, happens before the actual phagocytosis. However, opsonization is the crucial part for NPs to be recognized as a foreign body by macrophages and thus allow phagocytosis to take place. Thereafter, the opsonized particles attach to the cell membrane of macrophages via specific receptors, with the Fc receptor and the complement receptor playing major roles. Receptor binding initiates a signaling cascade mediated by Rad homologous family of guanosine triphosphatase (Rho family of GTPases), which induces actin formation. This leads to the growth of cell surface extensions around the particle, up to the complete surrounding and uptake of the non-cellular material in the cytoplasm. Then, the NP are enclosed in the inside of the cell in so-called phagosomes and are transported by these vesicles through the cytoplasm. Finally, the phagosome merged with another membrane-enveloped vesicle, the lysosome, forming a phagolysosome, where the actual digestion occurs. The inside of the phagolysosome has an acidic environment, caused by protons pumped into the cell interior by membrane-bound adenosine triphosphatase (ATPase), and contains a variety of digestive enzymes that enable digestion of endogenous and exogenous substances.<sup>[247]</sup>

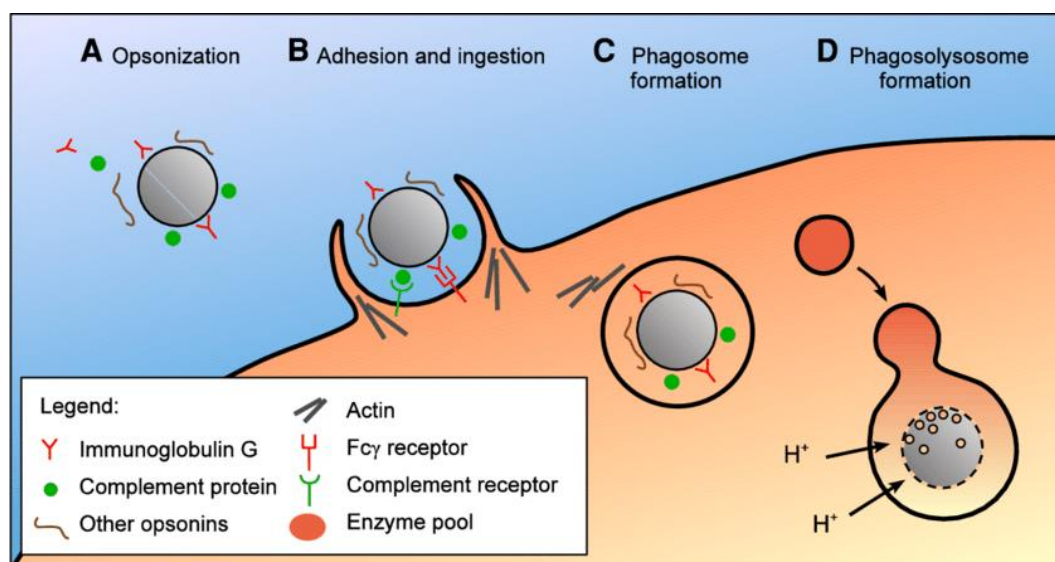


**Figure 13.** Schematic illustration of phagocytosis – opsonization, cell adhesion and uptake of opsonized particles into macrophages. Reprinted from reference<sup>[247]</sup>, Copyright (2009), with permission from Springer Nature.

Cellular uptake of particles is known to be affected by their physicochemical properties such as core material, shape, size, surface charge, hydrophobicity, and surface chemistry.<sup>[19,248]</sup> In addition to the characteristics of the NPs, the cell type has emerged as a further factor influencing the NP-cell interactions.<sup>[249]</sup> However, protein corona, which is formed spontaneously and rapidly after NPs enter the body and come into contact with biological fluids, has the greatest influence on the interaction of NPs with cell membranes and the uptake mechanism. Some groups have shown that the adsorbed proteins prevent NP aggregation, and lead to reduction in non-specific cell uptake and toxicity.<sup>[250,251]</sup> The decrease in cell internalization is often associated with a lowered interaction of NP and cell membrane, caused by a negative zeta potential and a shielding effect against phagocytic cells. Proteins that exhibit such a shielding effect are called dysopsonins.<sup>[24,252]</sup> In contrast, some studies demonstrated concentration-dependent or protein-protein interaction-induced aggregation of NPs, resulting in enhanced cellular uptake.<sup>[253-256]</sup> Furthermore, the protein corona may also contain opsonins that have an opposite effect to dysopsonins and promote internalization of cells of the reticuloendothelial system, because as previously described, phagocytosis of macrophages is driven by opsonization.<sup>[257,258]</sup> Enhanced cell uptake by phagocytes could also be confirmed by specific adsorption of such opsonizing proteins on NPs.<sup>[259]</sup>

## 2 State of knowledge

Thus, in terms of decreased macrophage uptake and consequently prolonged blood circulation time, it appears to be most important which proteins are abundant in the protein corona, as proteins have different biological and molecular functions<sup>[260]</sup>. Due to their functions, corona proteins are able to modulate the nanomaterial-cell-interaction during cellular uptake since the corona proteins represent the primary contact with cells.<sup>[261-263]</sup>

### 2.2.3 Influence of adsorbed proteins on cellular uptake

As stated in **Section 2.2.1**, there are several NP properties that affect the protein corona profile, and protein binding itself induces changes in particle properties such as size and surface charge. These changes as well as the composition of the protein corona have an impact on the internalization process of the particles in macrophages and the biological distribution.

Some investigations showed that non-specific cellular uptake of nanocarriers by phagocytic cells is promoted by opsonizing proteins and that hydrophobic particles were removed faster from the blood than hydrophilic particles due to higher protein binding.<sup>[264,265]</sup> To prevent the particles from rapid clearance from the bloodstream and to achieve their desired targeting effect, thus, it is important to control the protein corona, by reducing the protein adsorption and, most importantly, ensuring specific protein binding.<sup>[245]</sup> In order to decrease the binding of plasma proteins, many research groups focused on coating the nanoparticle surface with protein blocking layers, such as stealth polymers, which has already been reported in **Section 2.2.1.2**. This coating acts as a kind of magic hood and prevents NPs from being recognized by macrophages, resulting in longer blood circulation, not only due to reduced protein binding, but also because only specific proteins were adsorbed to the protected particles and, respectively, the adsorption of certain proteins was selectively suppressed.<sup>[30,186]</sup> In **Figure 14a**, it is seen how particle surface functionalization affects protein binding and how the adsorbed proteins in turn influence their biodistribution.



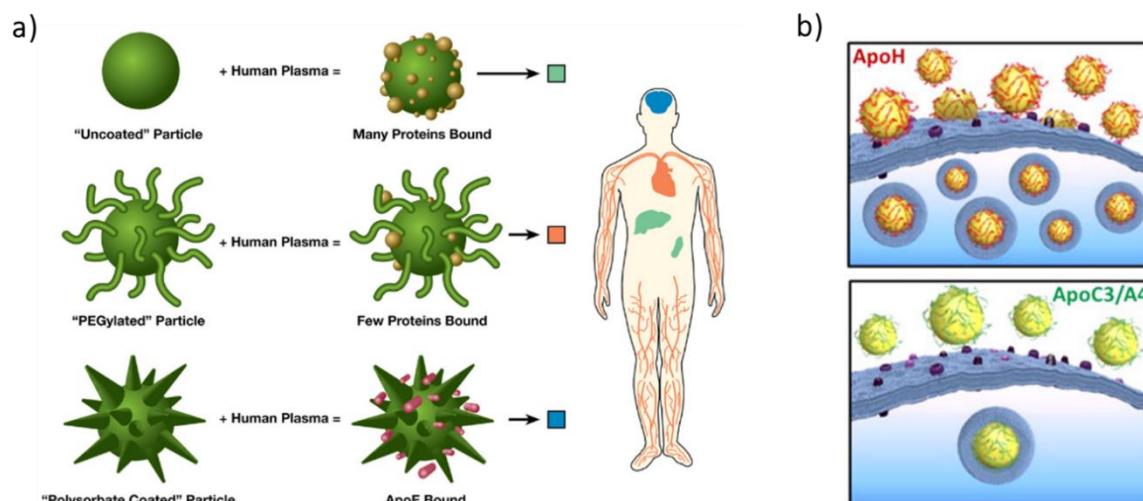


**Figure 14.** a) Biological distribution of various surface-functionalized particles incubated in plasma. Uncoated NPs show high amount of bound protein and thus rapid uptake by macrophages of the liver and spleen. PEGylated particles reveal a stealth effect, causing reduced protein adsorption and longer circulation in the bloodstream. Polysorbate-modified NPs display specific binding of APOE and thus enable particles to cross the blood-brain barrier and accumulate in the brain. Reprinted from reference<sup>[245]</sup>, Copyright (2009), with permission from Elsevier. b) Precoating of NPs with apolipoproteins APOH led to enhanced cellular uptake, while precoating with APOC3/APOA4 resulted in inhibited cell internalization. Reprinted from reference<sup>[266]</sup>, Copyright (2015), with permission from American Chemical Society.

Uptake of NPs by macrophages, is promoted by certain proteins called opsonins, which include, for instance, immunoglobulins, complement factors and fibrinogen. In addition, there are as well dysopsonins, such as albumin and apolipoproteins, which protect the particles from macrophage internalization and cause a long blood circulation time.<sup>[267,268]</sup>

HSA, for instance, which is the most abundant protein in plasma<sup>[269]</sup>, is often used for specific linkage to gold surfaces, since such AuNP-HSA systems are known to improve relevant properties for biomedical and pharmaceutical applications like increased colloidal stability, prolonged retention time, lower toxicity and reduced interaction with plasma proteins.<sup>[270]</sup> Owing to these advantages and the fact that HSA can contribute to transportation and release of drugs<sup>[271,272]</sup> as well as that albumin-based nanomaterials exhibit selective bioaccumulation at disease sites such as tumor cells<sup>[273,274]</sup>, HSA-capped AuNPs are promising for targeted drug delivery<sup>[275-277]</sup>. Upon AuNP incubation with HSA, HSA was determined to be one of the main proteins in the protein corona on citrate-stabilized particles<sup>[278,279]</sup> and is commonly present on other AuNPs, independent of their surface functionality<sup>[213,280-282]</sup>. In literature, inhibited cellular uptake of HSA-enriched NPs is explained by repulsive interactions between anionic HSA and the negative cell surface.<sup>[283]</sup>

## 2 State of knowledge

In addition to HSA, a positive effect of reduced internalization of NPs into phagocytic cells and prolonged circulation time was observed for apolipoproteins C3 (APOC3) and A4 (APOA4).<sup>[266]</sup> Furthermore, high abundance of APOJ in the protein corona of PEG- and especially PEEP-functionalized NPs resulted in inhibited macrophage internalization compared to ungrafted NPs.<sup>[30]</sup> Göppert *et al.*<sup>[284]</sup> further showed that APOE is a protein relevant for delivering drugs to brain tissue since it enables particles to cross the blood-brain barrier (see **Figure 14a**). In contrast, increased cellular uptake in phagocytes was reported for apolipoprotein H (APOH), also known as beta-2-glycoprotein 1. Since this protein binds preferentially to negatively charged surfaces like phospholipids, it is suggested to be the explanation for enhanced adhesion of APOH-loaded NPs with the cell membrane, consisting of a phospholipid double layer. **Figure 14b** schematically depicted the differences in cell internalization for APOH and APOC3/APOA4 pre-coated NPs. However, promoted internalization of APOH-adsorbed NP was only found in phagocytic cells and not in nonphagocytic cells.<sup>[266,285]</sup> Consequently, not all apolipoproteins have a dysopsonizing character per se, making their mode of action in the protein corona more complex.

Immunoglobulins, along with albumins, are the most important and abundant components in blood plasma<sup>[286]</sup>, are part of the immune defense system and promote phagocytosis due to their opsonizing character. Yang *et al.*<sup>[287]</sup> found reduced Immunoglobulin G (IgG) concentration on NPs functionalized with PEG, yielding in decreased cellular uptake. Furthermore, IgG was highly enriched on polystyrene nanospheres incubated in serum, especially after longer incubation time. Here, the three times higher internalization in Kupffer cells of NPs with high IgG concentration indicated enhanced phagocytosis and rapid clearance from the bloodstream.<sup>[288]</sup> As IgG is known to bind to the Fc receptor, which plays an important role in phagocytosis, as mentioned in **Section 2.2.2**, this may explain the facilitated adhesion of IgG-coated particles to the cell membrane of phagocytic cells.<sup>[247]</sup> In addition to Fc receptor-mediated binding, IgG is also able to activate the complement cascade, which then leads to complement receptor-mediated uptake.<sup>[289]</sup>

Besides immunoglobulins, complement proteins are known to influence particle clearance from the immune system. Similar to the binding of the opsonin IgG, Nagayama *et al.*<sup>[288]</sup> also reported a time-dependent increase in protein C3 adsorption to NPs and that the high

abundance of C3 was directly related to the enhanced cell uptake. As already mentioned in an earlier section of this thesis, the protein corona of citrate-AuNPs is highly enriched in protein C3, while PEG-coated particles selectively suppress the adsorption of this complement protein.<sup>[27]</sup> Since C3 promotes the clearance of NPs by macrophages<sup>[290]</sup>, ungrafted AuNPs show higher cellular uptake than PEG-functionalized particles. The increased recognition by macrophages can be attributed to complement proteins such as C3 being opsonins known to enhance phagocytosis, as phagocytic cells express complement receptors.<sup>[247]</sup> C3 is known to play a major role in the complement system, displaying an essential part of the body's immune response. This system consists of a complex complement cascade and has the function of eliminating foreign bodies from the blood or tissue, for example, by opsonizing foreign particles as a precondition for their phagocytosis.<sup>[291]</sup> However, in contrast, lower cellular uptake in a mouse dendritic cell line was observed despite a high enrichment of C3 on hydrophilic functionalized AuNPs.<sup>[219]</sup> Hence, the NP-cell interaction is not only affected by the most abundant protein, instead the total protein corona composition has major impact.

### 2.3 Biodistribution of AuNPs – in vivo research

Biodistribution of NPs plays a crucial role in nanomedicine concerning their applications as drug carriers<sup>[292,293]</sup>, biosensors<sup>[294]</sup>, photothermal therapeutics<sup>[295]</sup>, or for tumor imaging<sup>[296]</sup>, which required the successful accumulation of particles in desired tissues, body fluids or organs. Since NPs, just like all foreign substances in the bloodstream, are eliminated by phagocytes such as macrophages, and consequently have no chance reaching their target site in the body, a prolonged circulation in the bloodstream has to be ensured for applications in nanomedicine. The propensity of NPs to remain in circulation depends on several properties such as size, shape, surface charge as well as surface functionalization of the particles.<sup>[18,20,297-299]</sup>

#### 2.3.1 NP surface functionalization affect biodistribution

In particular, the effect of surface modification and surface charge has been intensively investigated in recent years, showing prolonged retention time for example of zwitterionic NPs.<sup>[300]</sup> In addition, Estevanato *et al.*<sup>[301]</sup> and Qiao *et al.*<sup>[302]</sup> demonstrated improved blood

## 2 State of knowledge

circulation for iron oxide particles modified with dextran and a sulfoxide-containing polymer. However, currently PEGylation is considered as the gold standard for NPs' surface modification in the biomedical field application. Due to the PEG's stealth properties, such coatings ensure prolonged NP's circulation in the bloodstream.<sup>[25,26,303,304]</sup> Additionally, reduced nonspecific protein adsorption affects further the biodistribution and enables specific organ targeting.<sup>[27,28,305]</sup> For example Cho *et al.*<sup>[306]</sup> and Zhang *et al.*<sup>[15]</sup> demonstrated prolonged blood circulation time of PEG-stabilized AuNPs injected in mice. Concerning biodistribution, both studies showed preferential accumulation of AuNPs in the liver and spleen. As mentioned above, also the surface charge affects the biokinetics of AuNPs, resulting in a higher accumulation of positively charged particles in the kidney compared to NPs with negative and neutral surfaces, which presented mostly in the liver and spleen.<sup>[307]</sup> Lee *et al.*<sup>[308]</sup> investigated the effect of different surface functionalities on biodistribution of AuNPs in mice, showing longer retention time in bloodstream for pure PEG-modified AuNPs, while positively and negatively charged NPs coated with a PEG layer on the surface rapidly spread into the organs (see **Figure 15a**). In this case, 32.6 nm sized AuNPs with a negative surface accumulated predominantly in the liver whereas AuNPs (63.7 nm) with a positive surface charge in the spleen. Yet, injection of much smaller particles (2.8 nm diameter) resulted in the highest Au accumulation in the liver for both positively and negatively charged NPs.<sup>[309]</sup> Since surface functionalization and charge are known to affect protein binding, more specifically protein corona composition, which is related to blood retention time as well as organ targeting, there are also several *in vivo* studies investigating the biokinetics of serum protein-conjugated AuNPs.<sup>[310-312]</sup>

**Figure 15b** shows the biokinetics of intravenously injected citrate-AuNPs and AuNPs adsorbed with proteins HSA and APOE, respectively, in blood and liver. It is seen that citrate-coated AuNPs were barely detected in blood directly after injection, while both protein-modified NPs exhibited longer blood circulation times. Furthermore, protein binding, especially with HSA, resulted in inhibited liver uptake compared to citrate-AuNPs.<sup>[310]</sup> These results are consistent in that a longer retention time in the blood implies lower cell uptake, whereas a short blood circulation time indicates increased uptake in phagocytic cells, like macrophages of the liver.<sup>[243]</sup> Taken together, these studies demonstrated noticeable dependencies on particle size, surface functionalization and

charge concerning blood retention time, organ distribution and excretion of AuNPs, which provided useful information for targeted delivery in vivo. However, applying mammalian animal models for such studies, faces several obstacles, particularly increasing ethical issues and high costs.<sup>[313]</sup>

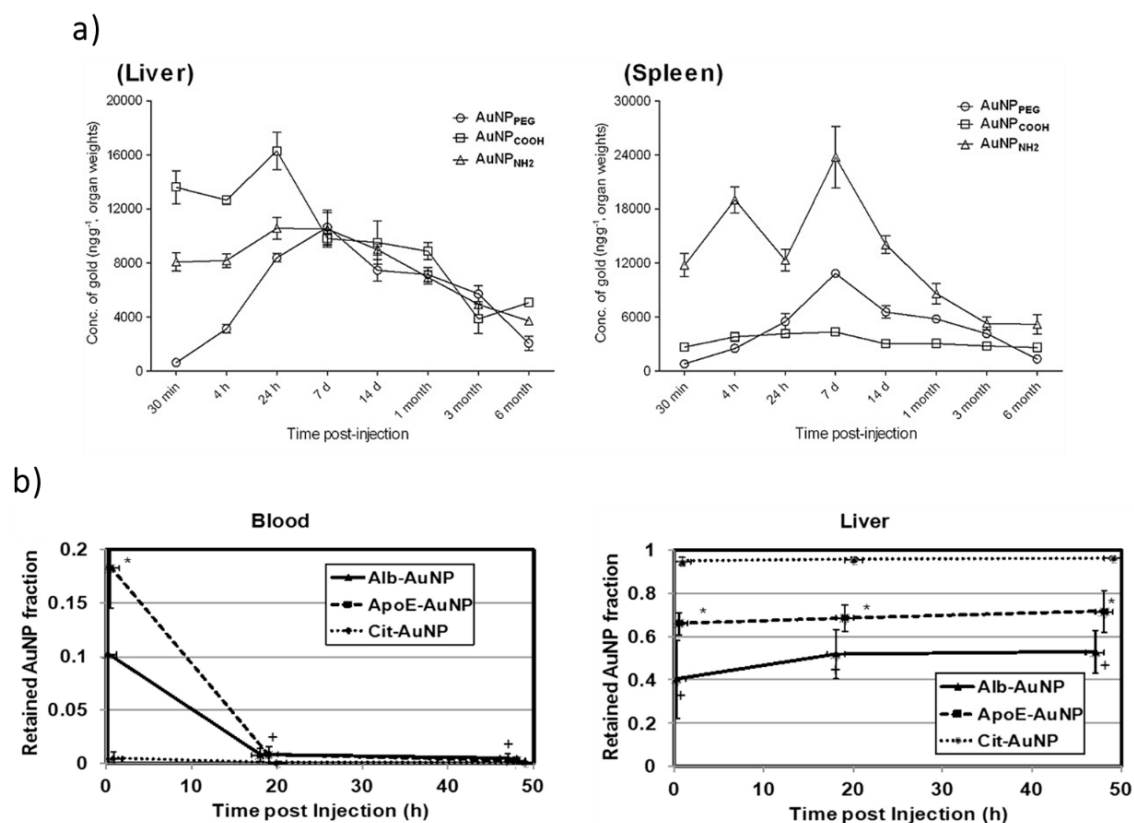


**Figure 15.** a) Distribution pattern of PEG-coated, positively and negatively charged AuNPs in liver and spleen after intravenous injection, showing high accumulation of negatively charged particles in the liver whereas NP with a positive surface accumulated predominantly in the spleen. Reproduced from reference<sup>[308]</sup>, Copyright (2014), with permission from John Wiley and Sons. b) Biokinetics of intravenously injected citrate-AuNPs and AuNPs adsorbed with proteins HSA and APOE, respectively, in blood and liver, demonstrating longer blood retention time for protein-bound particles and lower accumulation in the liver. Reproduced from reference<sup>[310]</sup>, Copyright (2014), with permission from Elsevier.

### 2.3.2 Silkworms as alternative to mammals

In order to overcome these aforementioned obstacles, several invertebrate animal models have been proposed as alternatives to mammalian models for preliminary in vivo studies in the last years, such as fruit flies (*Drosophila melanogaster*)<sup>[37]</sup>, larvae of the greater wax moths (*Galleria mellonella*)<sup>[38]</sup>, and especially silkworm larvae (*Bombyx mori*)<sup>[39-41,314]</sup>. The major advantages of these animal models include less ethical concerns, much lower maintenance costs, and the feasibility of cost- and time-efficient large scale in vivo studies.<sup>[315]</sup> In addition, compared to other invertebrate species, silkworm larvae can only

## 2 State of knowledge

move very slowly, and the adult moths are unable to fly due to long-term domestication. Therefore, silkworm larvae have much lower chance of biohazard. Silkworms are easy to handle due to their larger size (4-5 cm in length), which allows injection of larger volume (up to 50  $\mu\text{L}$ ) with a conventional syringe. Major injection routes include intra-hemolymph and intra-midgut administration, which are comparable to intravenous and oral administration in mammals, respectively.<sup>[316,317]</sup> Furthermore, their body size also enables: (i) easy extraction of hemolymph, which is analogous to the blood of mammals but lacking red blood cells and having a higher concentration of free amino acids<sup>[318]</sup> and (ii) easy dissection to extract tissues and organs, of which, for example, the midgut of silkworms is considered equivalent to the mammalian small and large intestines but also plays a central role in detoxification of exogenous compounds<sup>[42]</sup>. Besides the analogy of the most important organ involved in the metabolic process and elimination of foreign matters, pharmacokinetic parameters of multiple model compounds have been demonstrated to be similar in silkworms vs. in mammals.<sup>[43]</sup> Due to these advantages mentioned above, silkworm models have already been applied in various research areas such as infectious diseases<sup>[317,319]</sup>, antimicrobial drug screening<sup>[320]</sup>, and environmental monitoring<sup>[321]</sup>.

However, despite these similarities between silkworms and mammals, allowing usage of silkworms as a model organism,<sup>[322]</sup> to date only limited number of studies report the biodistribution of NPs in silkworms compared to well-studied mammals, although investigation of biokinetic distribution, as well as knowledge of retention time and clearance, is important for many applications of NPs in nanomedicine<sup>[323-325]</sup>. Ke *et al.*<sup>[326]</sup> and Cheng *et al.*<sup>[327]</sup> analyzed the concentration of Ag and copper (Cu) in various silkworm tissues after feeding the animals with fresh mulberry leaves pre-sprayed with respective NP solutions. In addition, Ma *et al.*<sup>[328]</sup> evaluated the biological effects of Au nanomaterials on growth of silkworms and silk properties by injecting different concentrations of bovine serum albumin (BSA)-modified Au nanoclusters into the hemolymph of silkworms.

---

## 3 Results and discussion

---

### 3 Results and discussion

Parts of **Section 3.1** were published as original research article (Johanna Lutz, Krystyna Albrecht, Jürgen Groll, Thioether-Polymer Coating for Colloidal Stabilization of Silver Nanoparticles in *Advanced NanoBiomed Research* 2021, 2000074), reproduced from reference<sup>[44]</sup> as an open access article distributed under the Creative Commons Attribution 4.0 International License (CC BY 4.0), which permits unrestricted use, distribution, and reproduction in any medium.

Copyright (2021) The Authors. *Advanced NanoBiomed Research* published by Wiley-VCH GmbH.

The article is based on the work of the author of this thesis, Johanna Späth, geb. Lutz, who conducted all experiments and data evaluation and wrote the manuscript.

Parts of **Section 3.2** are written in the form of an original research article (Johanna Späth, Thorsten Keller, Annika Seifert, Krystyna Albrecht, Jürgen Groll, Protein Corona Composition on Hydrophobic Functionalized Polyglycidol Coated Gold Nanoparticles and Their Impact on Macrophage Uptake) and has been submitted to a peer-reviewed journal by the time of the submission of this thesis. The chapter is thus intended to be published in the near future. To improve readability, figures from the supplementary information have been integrated into the main article in this thesis.

The article is based on the work of the author of this thesis, Johanna Späth, who conducted most of the experiments and data evaluation, wrote the manuscript and will hold the first authorship after publication.

Parts of **Section 3.3** are written in the form of an original research article (Johanna Späth, Yidong Yu, Ann-Katrin Wolf, Andreas Beilhack, Jürgen Groll, Krystyna Albrecht, Impact of Surface Functionality on Biodistribution of AuNPs in Silkworms) and has been submitted to a peer-reviewed journal by the time of the submission of this thesis. The chapter is thus intended to be published in the near future. To improve readability, figures from the supplementary information have been integrated into the main article in this thesis.

The article is based on the work of the author of this thesis, Johanna Späth, who conducted most of the experiments and data evaluation, wrote the manuscript and will hold the first authorship after publication.



### 3.1 Colloidal stability of thiol- and thioether-polymer-coated AgNPs

Due to their interesting chemical, physical, and biological properties, colloidal AgNPs attracted enormous attention in nanotechnology and biomedicine, showing a wide range of applications, such as biosensor materials, drug delivery systems, dental restorative materials, antimicrobial agents, for wound healing, or in cosmetics.<sup>[1]</sup> Ensuring the broad applicability of AgNPs, the stabilization efficacy plays a crucial role, as aggregation leads to a loss of their unique properties. Thus, it is relevant for enhancing the stability of such particles by attaching capping agents with high affinity to the surface, which consequently generate a barrier to aggregation. AgNPs are normally stabilized by charges or tenside double layer<sup>[114,329]</sup>, and further stabilization and biocompatibilization of the particles are usually achieved through ligand-exchange reactions especially with PVP<sup>[330,331]</sup> or thiofunctional molecules, often with alkyl thiols<sup>[158,332]</sup> or the commonly used thiol-terminated PEG<sup>[7,333]</sup>. Furthermore, it is recognized that surface modification, for example, with cysteine and other low molecular weight thiols affected the cytotoxicity of silver ions to organism.<sup>[334,335]</sup>

To date, a lot of reports have intensively investigated the interaction of thiols with silver gaining fundamental insights into the adsorption mechanism.<sup>[172,336-338]</sup> As thiols are oxidation sensitive, and the presence of the highly nucleophilic thiols in molecules restricts the possibility to introduce other functional groups,<sup>[16]</sup> it has, thus, examined whether thioether may be used as alternative to thiols for stabilizing Ag colloids. In case of thioethers, the synthesis of silver-thioether complexes<sup>[339,340]</sup> or the attachment on flat Ag surfaces<sup>[341]</sup> is described in the literature, but to the best of my knowledge, there is nearly no study considering thioether-containing polymers as possible coating systems for AgNPs. Pletsch *et al.*<sup>[342]</sup>, for example, reported an in situ method using linear high-molecular poly(propylene sulfide) for conjugation on AgNPs resulting in stabilization of such particles. Unlike in the case of the noble metal silver, in the last few years, there are a large number of investigations on thioether coatings on AuNPs<sup>[343,344]</sup> as an alternative to the well-studied thiols.<sup>[125,345]</sup> Recently, the author's working group presented a thorough contribution on immobilizing mono- and multivalent thiol- and thioether-polymers on AuNPs, yielding high colloidal stability for thioether modification especially for coating with the multivalent system.<sup>[17]</sup>

### 3 Results and discussion

Herein, the question was raised whether functionalization of AgNP with thioether is comparable or even enhances the stabilization efficacy compared with thiols and, particularly, whether the multivalency leads to stable AgNP conjugates even though a weaker sulfur–silver bond is proved compared with the sulfur binding on Au.<sup>[346]</sup> For this, monovalent MeO-PEG-SH and MeO-PEG-SPentyl with multifunctional analogs, linear side-chain functionalized PG with multiple thiol (P(G-co-SH)), or ethylthioether (P(G-co-SEt)) are systematically compared as a coating system for AgNPs. The modified AgNPs were characterized and exposed to conditions provoking aggregation of the NPs, such as centrifugation, treatment at 80°C, freeze-drying, and incubation in buffer and medium. In the literature, there are few contributions to the stability of capped AgNPs in different biological relevant media. However, most studies assessed only the influence of proteins on citrate-stabilized particles<sup>[347,348]</sup> or additionally compared the colloidal stability of citrate-AgNPs with PVP-coated or PEGylated particles<sup>[11,349,350]</sup>, resulting in better stabilities. To date, there have been reports for thiol-terminated PEG attached to AgNPs, but yet no working group was focusing on thioether-polymer adsorption or multivalent systems, respectively.

Throughout this section the colloidal stabilization efficacy of thioether-polymer-coated AgNPs in comparison to thiol-functionalized ones is investigated, using particles modified with mono- and multivalent thiol- and thioether-polymers. For systematic comparison, linear PEG terminated with a single thiol (MeO-PEG-SH) or thioether (MeO-PEG-SPentyl) anchor group, as well as linear side-chain functionalized PG featuring multiple thiol (P(G-co-SH)) or ethylthioether (P(G-co-SEt)) along the linear backbone were used as coating system for AgNPs. To ensure better comparability, PEG and PG having a similar chemical structure and comparable molecular weights (approximately 6000 Da and 5000 Da) were synthesized. The thiol and thioether functionalities were introduced by thiol-ene reaction in the presence of a photo initiator and under irradiation with ultraviolet (UV) light. In this section the successful synthesis of all before mentioned polymers was verified via proton nuclear magnetic resonance (<sup>1</sup>H-NMR), Fourier-transform infrared spectroscopy (FT-IR) and Raman spectroscopy as well as by Ellman assay and size exclusion chromatography (SEC). It was further proven by UV-Vis absorbance, dynamic light scattering (DLS), zeta potential measurements and FT-IR spectroscopy that the thiol- and thioether-polymers

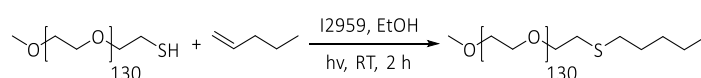
were attached to the NP surface. Micro-thermogravimetric analysis (micro-TGA) was performed quantifying the number of polymer chains per particle. Finally, the colloidal stability of the modified AgNPs was investigated by UV-Vis absorbance measurements after exposure to different conditions provoking aggregation of the particles such as centrifugation, treatment at 80 °C, freeze-drying as well as incubation in buffer and cell culture medium.

### 3.1.1 Synthesis of thiol- and thioether-polymers

In the following section the synthesis and characterization of monovalent thiol- and thioether-terminated PEG as well as of the multifunctional PG analogues were presented.

#### 3.1.1.1 Monovalent PEG

The monovalent thiol-terminated PEG (MeO-PEG-SH) with a molecular weight of 6000 Da was commercially purchased and served as educt for the synthesis of the thioether analogue. MeO-PEG-SPentyl was obtained by thiol-ene reaction of MeO-PEG-SH with an excessive amount of 1-pentene and the photo initiator 2-hydroxy-1-[4-(hydroxyethoxy)-phenyl]-2-methyl-1-propanone (I2959) in ethanol (EtOH) as described in literature (see **Scheme 1**).<sup>[17]</sup> After 2 h of UV irradiation at room temperature (RT), followed by purification via dialysis and lyophilization, MeO-PEG-SPentyl was received as a colorless solid. Both polymers were analyzed by <sup>1</sup>H-NMR, FT-IR and Raman spectroscopy as well as by Ellman assay and SEC measurements (see **Section 5.2.2** and **Section 5.2.3**).



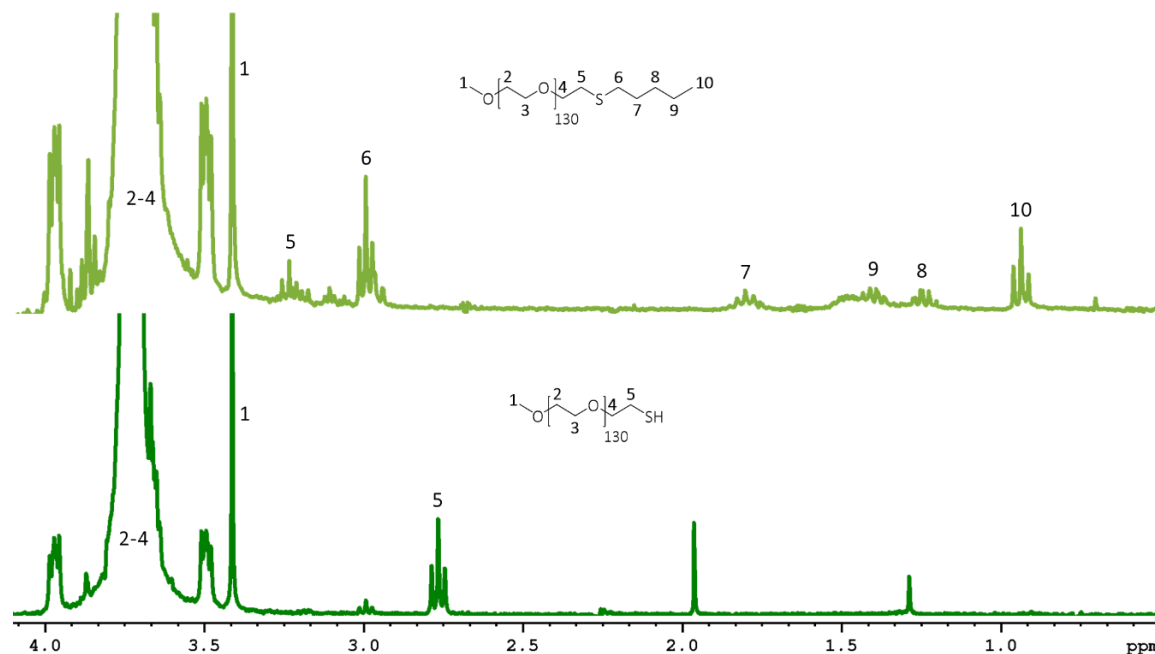
**Scheme 1.** Synthesis of MeO-PEG-SPentyl by thiol-ene reaction of MeO-PEG-SH with 1-pentene.

In the below-mentioned characterization methods both polymers were directly compared by displaying their results in one figure, whereby MeO-PEG-SH was labeled in green and MeO-PEG-SPentyl in light green. Besides, relevant areas were highlighted in light grey.

**Figure 16** shows the <sup>1</sup>H-NMR spectrum of MeO-PEG-SH (bottom) in comparison to MeO-PEG-SPentyl (top). Here, the low field shift of the methylene proton signal H-5 from 2.77 ppm to 2.99 ppm, due to the changed chemical environment of these protons after

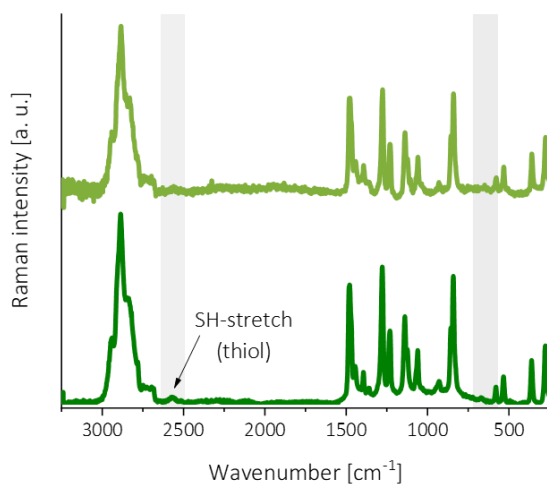
### 3 Results and discussion

binding, as well as the detection of new signals at 2.97 ppm (H-6), 1.85-1.76 ppm (H-7), 1.43-1.36 ppm (H-8), 1.28-1.20 ppm (H-9) and 0.94 ppm (H-10) which belonged to the pentyl chain, indicated a successful reaction.



**Figure 16.** <sup>1</sup>H-NMR spectrum of MeO-PEG-SPentyl (top, light green) compared to MeO-PEG-SH (bottom, green).

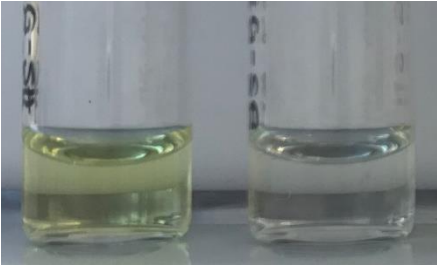
In addition, the conversion of thiol into thioether groups was proven by Raman spectroscopy, as displayed in **Figure 17**. The thiol stretching vibration for MeO-PEG-SH was located at  $2558\text{ cm}^{-1}$ , which was absent in the spectrum of MeO-PEG-SPentyl after thiol-ene reaction. Unlike, the thioether units, which normally showed a characteristic band in the region at  $585\text{-}740\text{ cm}^{-1}$ , could not be detected possibly due to a lower relative Raman intensity of thioethers compared to thiols. In general, the detection of such end groups is challenging as the polymer backbone has a larger mass fraction compared to the terminal units.



**Figure 17.** Raman spectrum of MeO-PEG-SPentyl (top, light green) compared to MeO-PEG-SH (bottom, green).

Furthermore, the number of thiols within MeO-PEG-SH was quantitatively determined by Ellman assay. **Table 1** reveals that the value identified by the assay matched well with this maintained by  $^1\text{H-NMR}$  spectroscopy. The image in the table shows a yellow discoloration for MeO-PEG-SH after reaction with Ellman's reagent, indicating the presence of thiols, while for MeO-PEG-SPentyl no color change could be observed.

**Table 1.** Thiol amount determined by Ellman assay and  $^1\text{H-NMR}$  spectroscopy of MeO-PEG-SH as well as visualization of the presence and absence of thiols within MeO-PEG-SH (left) and MeO-PEG-SPentyl (right) by reaction with Ellman's reagent.

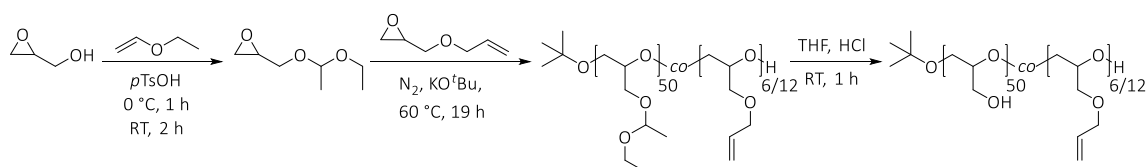
Thiol units per polymer chain		
Ellman assay	$^1\text{H-NMR}$ spectroscopy	
0.8	1	

### 3 Results and discussion

#### 3.1.1.2 Multivalent PGs

The multivalent polymeric system based on linear P(G<sub>50-co</sub>-AGE<sub>6</sub>) was synthesized by copolymerization of the monomers ethoxy ethyl glycidyl ether (EEGE)<sup>[351]</sup> and allyl glycidyl ether (AGE) as described in literature.<sup>[352]</sup> Subsequently, the copolymer P(G<sub>50-co</sub>-AGE<sub>6</sub>) enabled introducing thiol and thioether functionalities to the allyl groups of the PG backbone via thiol-ene reaction, obtaining P(G<sub>50-co</sub>-SH<sub>6</sub>) and P(G<sub>50-co</sub>-SEt<sub>6</sub>).<sup>[17,353]</sup> In this section first the synthesis and characterization of the copolymerization is discussed (see **Scheme 2**), followed by the functionalization with thiol and thioether moieties (see **Scheme 3**).

Receiving linear PG, firstly an acetal protected version of glycidol was synthesized.<sup>[351]</sup> Therefore, ethyl vinyl ether and toluene-4-sulfonic acid monohydrate (*p*TsOH) was added to glycidol under ice cooling. After stirring for 3 h and extraction with saturated sodium hydrogen carbonate (NaHCO<sub>3</sub>) solution, EEGE was purified by drying over calcium hydride (CaH<sub>2</sub>) overnight and fractionated distillation under argon (Ar) atmosphere. EEGE was received as a clear, colorless liquid and analyzed via <sup>1</sup>H-NMR spectroscopy (see **Section 5.2.4**). By living anionic ring opening polymerization of EEGE and AGE under nitrogen (N<sub>2</sub>) atmosphere the linear copolymer P(EEGE-*co*-AGE) was obtained as a brownish oil. The polymerization was initiated with potassium *tert*-butoxide (KO<sup>t</sup>Bu), conducted at 60 °C for 19 h and terminated by the addition of EtOH. In this thesis two different allyl-functionalized PGs with various EEGE to AGE ratios were synthesized, named as P(EEGE<sub>50-co</sub>-AGE<sub>6</sub>) and P(EEGE<sub>50-co</sub>-AGE<sub>12</sub>). The exact amounts of the used substances and the characterization of these polymers via <sup>1</sup>H-NMR, FT-IR and Raman spectroscopy as well as SEC analysis is described in **Section 5.2.5**.



**Scheme 2.** Synthesis of the protected glycidol EEGE followed by anionic copolymerization with AGE (using two different ratios) and subsequent deprotection of P(EEGE<sub>50-co</sub>-AGE<sub>6/12</sub>) under acidic conditions, receiving linear P(G<sub>50-co</sub>-AGE<sub>6/12</sub>).

Afterwards, the acetal protection group within EEGE was removed by treatment with 37% hydrochloric acid (HCl) in tetrahydrofuran (THF) for 1 h at RT. After neutralization and

purification by dialysis and lyophilization, P(G<sub>50-co</sub>-AGE<sub>6</sub>) and P(G<sub>50-co</sub>-AGE<sub>12</sub>) were received as yellowish oils. <sup>1</sup>H-NMR, FT-IR and Raman spectroscopy and SEC analysis verified the successful synthesis.

In **Figure 18** the <sup>1</sup>H-NMR spectra of P(G<sub>50-co</sub>-AGE<sub>6</sub>) (bottom, black) and P(G<sub>50-co</sub>-AGE<sub>12</sub>) (top, grey) are displayed. The ratio of EEGE to AGE was confirmed by correlation of the proton signals of the allyl unit to the backbone signals in PG. A multiplet was present at 6.08-5.96 ppm, corresponding to the methine protons (H-8) of the allyl group and the methylene protons H-9 and H-10 were detected at a chemical shift of 5.37 ppm and 4.14 ppm respectively. Signals at 3.82-3.67 ppm were attributed to the polymer backbone and the singlet at 1.28 ppm was assigned to protons (H-1) of the *tert*-butyl end group.

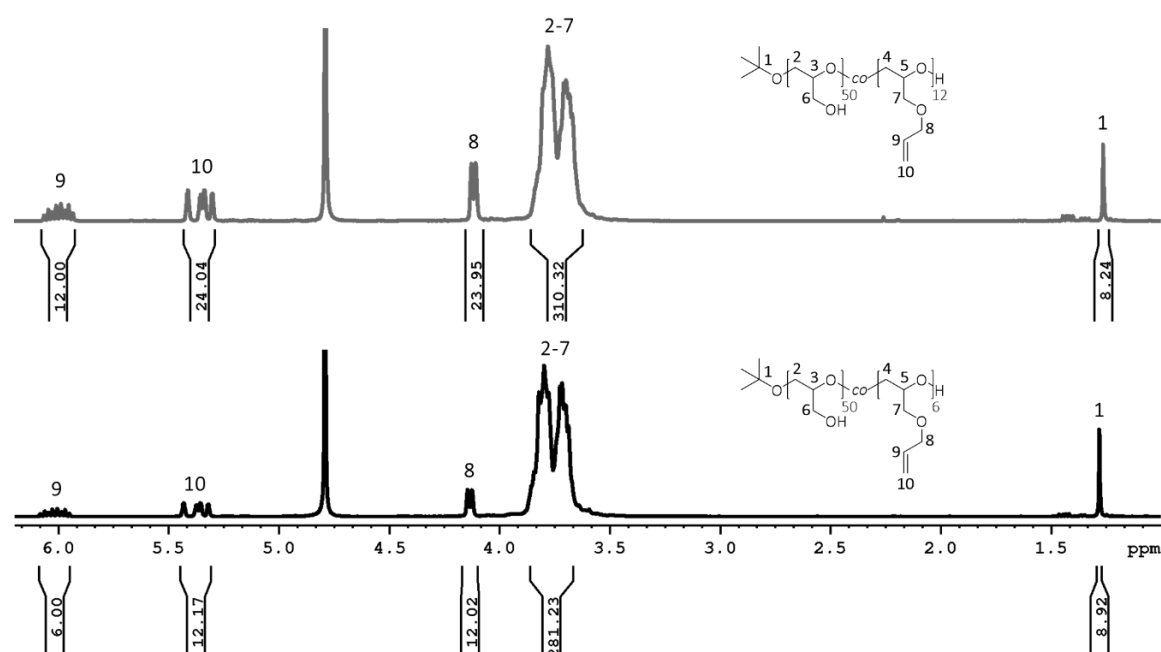


**Figure 18.** <sup>1</sup>H-NMR spectra of P(G<sub>50-co</sub>-AGE<sub>6</sub>) (bottom, black) and P(G<sub>50-co</sub>-AGE<sub>12</sub>) (top, grey).

FT-IR and Raman analysis presented all relevant bands for P(G<sub>50-co</sub>-AGE<sub>6/12</sub>) (see **Figure 19** and **Section 5.2.6**). The figure shows a comparison of the resulted spectra of P(G<sub>50-co</sub>-AGE<sub>6</sub>) and P(G<sub>50-co</sub>-AGE<sub>12</sub>), displaying similar vibrations for both polymers. However, the allylic signal at 1644 cm<sup>-1</sup> and 1646 cm<sup>-1</sup>, respectively, revealed different intensities, indicating that polymers with various numbers of allylic side chains were synthesized.

### 3 Results and discussion

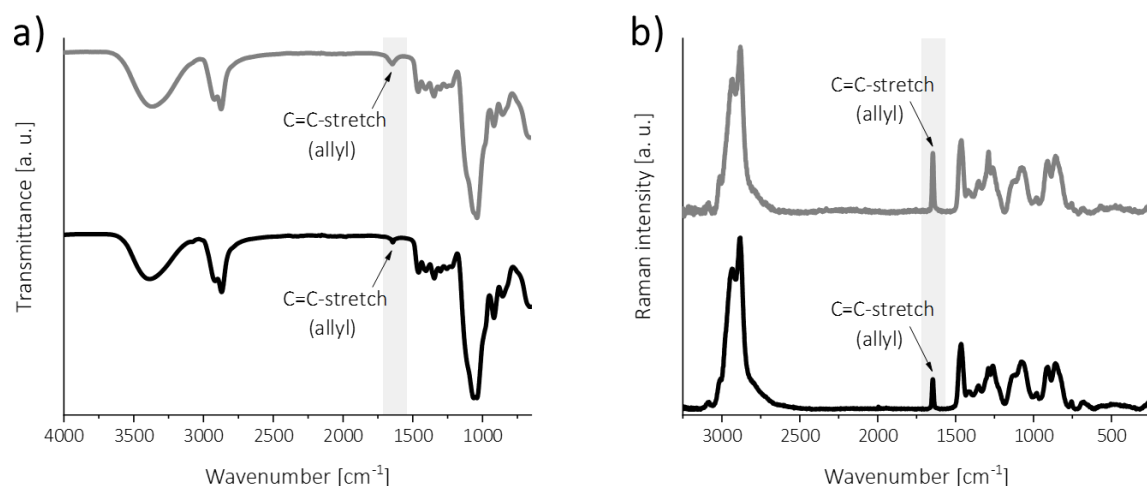


**Figure 19.** a) FT-IR transmittance and b) Raman spectra of P(G<sub>50</sub>-co-AGE<sub>6</sub>) (bottom, black) and P(G<sub>50</sub>-co-AGE<sub>12</sub>) (top, grey), displaying allyl-vibrations with different intensities

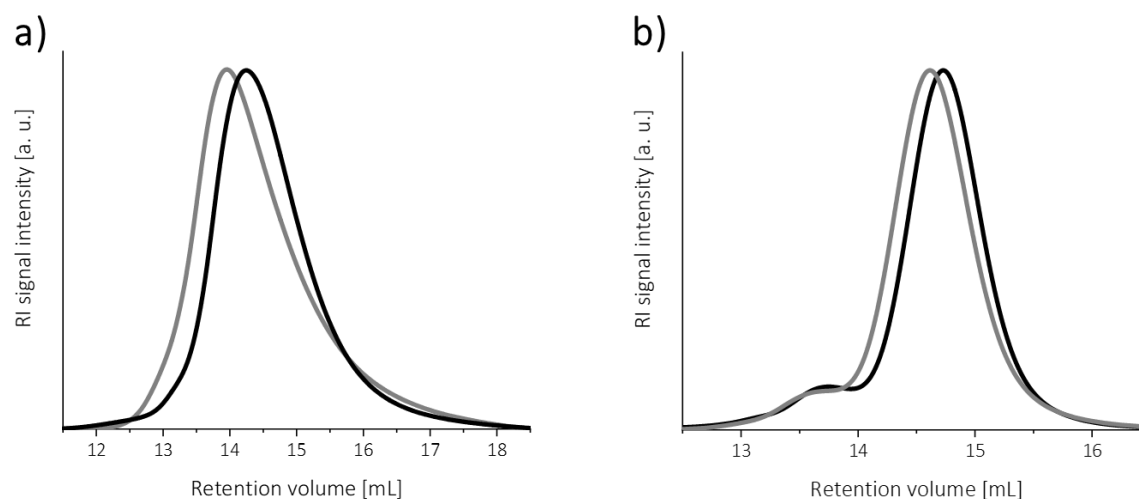
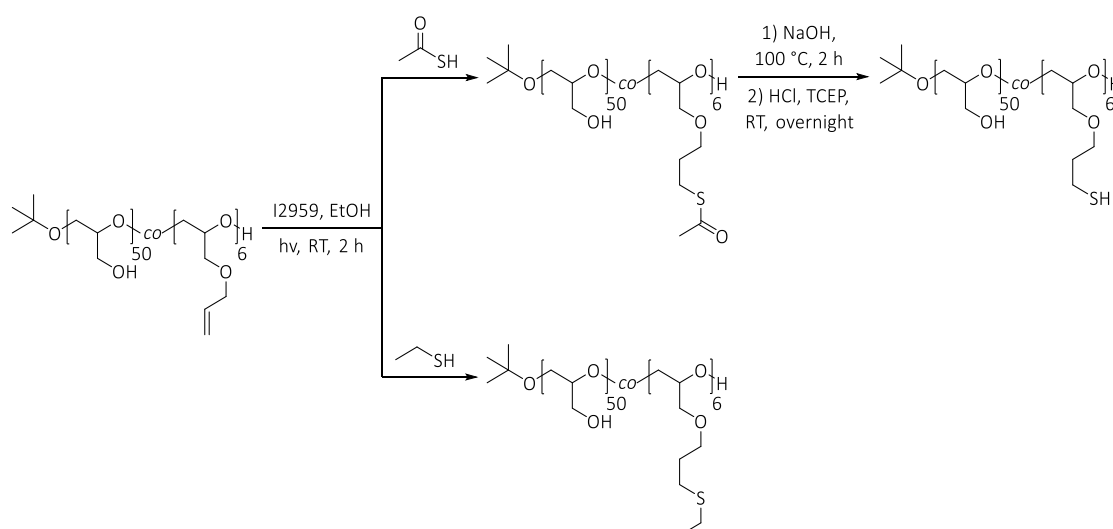


**Figure 20.** SEC elugram of P(G<sub>50</sub>-co-AGE<sub>6</sub>) (black) and P(G<sub>50</sub>-co-AGE<sub>12</sub>) (grey) in a) H<sub>2</sub>O and b) DMF, displaying a monomodal distribution with a low molecular weight tailing for analysis in H<sub>2</sub>O while a bimodal distribution is detected by SEC in DMF.

SEC analysis of the two different allyl-functionalized PGs, displayed in **Figure 20**, revealed a monomodal distribution with a low molecular weight tailing for analysis in deionized water (H<sub>2</sub>O) while a bimodal distribution is detected by SEC in *N,N*-dimethylformamide (DMF). In addition, PGs in DMF exhibited longer retention times than in H<sub>2</sub>O. The different curve progressions and retention times suggest a disparate behavior of the polymers in the used solvents, as well as possible interactions with the column material, which is distinguishable in both SEC systems. Comparing the polymers with the different allyl functionalities, it could be noticed that, unlike as expected, a shorter retention time is demonstrated for polymers with higher allyl functionality in both H<sub>2</sub>O and DMF, maybe as a result of different coiling behaviors due to additional lipophilic side groups.



Based on P(G<sub>50</sub>-co-AGE<sub>6</sub>) thiol and thioether moieties were introduced via thiol-ene reaction, yielding P(G<sub>50</sub>-co-SH<sub>6</sub>) and P(G<sub>50</sub>-co-SEt<sub>6</sub>), as seen in **Scheme 3**. The thiol-modified PG was received by adding thioacetic acid and I2959 to P(G<sub>50</sub>-co-AGE<sub>6</sub>) dissolved in EtOH. After irradiation with UV light for 2 h at RT, the obtained thioester was deprotected under basic conditions followed by reduction with tris(2-carboxyethyl)phosphine hydrochloride (TCEP) and finally purification via dialysis and lyophilization. The thioether analog P(G<sub>50</sub>-co-SEt<sub>6</sub>) was received by two hours UV irradiation of P(G<sub>50</sub>-co-AGE<sub>6</sub>) with the photo initiator I2959 and an excessive amount of ethanethiol (EtSH), and subsequent successive purification. The mercaptan compound EtSH has to be added in large excess due to its high volatility.<sup>[354]</sup> Both multivalent polymers were received as slightly yellow, viscous oils and characterized by <sup>1</sup>H-NMR, FT-IR and Raman spectroscopy as well as by Ellman assay and SEC measurements (see **Section 5.2.7** and **Section 5.2.8**).



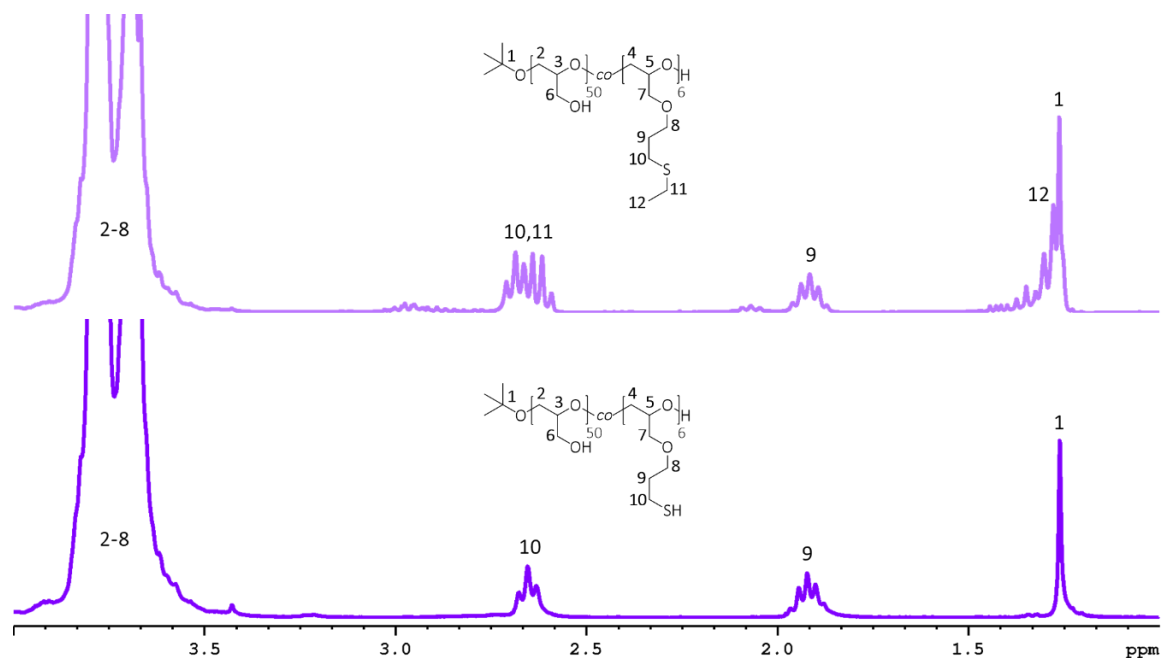
**Scheme 3.** Modification of P(G<sub>50</sub>-co-AGE<sub>6</sub>) with thiol and thioether moieties by thiol-ene reaction, yielding P(G<sub>50</sub>-co-SH<sub>6</sub>) and P(G<sub>50</sub>-co-SEt<sub>6</sub>).

In the analyzation methods presented above, both polymers were directly compared by showing their results in one figure, whereby P(G<sub>50</sub>-co-SH<sub>6</sub>) was marked in purple and P(G<sub>50</sub>-co-SEt<sub>6</sub>) in light purple.

**Figure 21** shows signals at 3.80-3.67 ppm, assigned to the protons H-2-8 of the backbone, and methylene protons of the side chains at 2.71-2.59 ppm (H-10) and 1.92 ppm (H-9), respectively. In case of P(G<sub>50</sub>-co-SEt<sub>6</sub>), the signals appearing at 2.71-2.59 ppm (H-11) and 1.35-1.30 ppm (H-12) attributed to the ethyl chain of the thioether unit. In both spectra

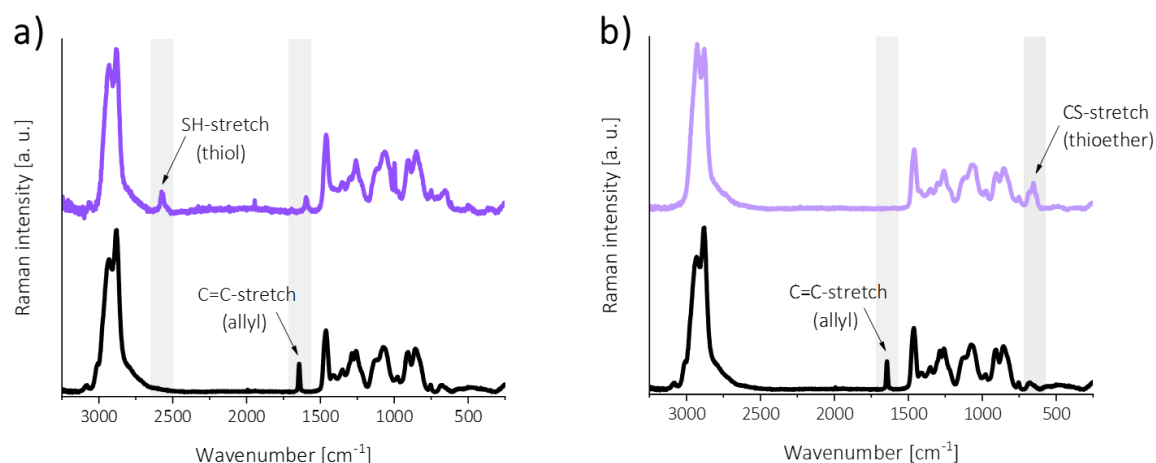
### 3 Results and discussion

the protons (H-1) of the initiating <sup>t</sup>Bu-group were detected at a chemical shift of 1.27 ppm. Integration of the <sup>1</sup>H-NMR signals demonstrated the introduction of six thiol respective thioether units per polymer.



**Figure 21.** <sup>1</sup>H-NMR spectra of P(G<sub>50</sub>-co-SH<sub>6</sub>) (bottom, purple) and P(G<sub>50</sub>-co-SEt<sub>6</sub>) (top, light purple).

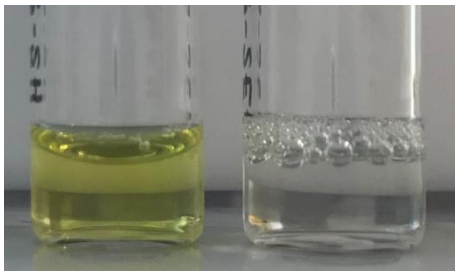
To confirm the presence of thiol and thioether moieties, Raman measurements were performed and displayed in **Figure 22**, with relevant areas highlighted in light grey. In **Figure 22a** the characteristic SH-stretching vibration of the thiol units in P(G<sub>50</sub>-co-SH<sub>6</sub>) was located at a wavenumber of 2565 cm<sup>-1</sup>, whereas in the spectrum of the P(G<sub>50</sub>-co-SEt<sub>6</sub>) (see **Figure 22b**) a band at 654 cm<sup>-1</sup> was attributed to the thioether vibration. An oxidation of the thiols in P(G<sub>50</sub>-co-SH<sub>6</sub>) can be excluded due to bands with negligible intensity in the region of thioether vibration (585-740 cm<sup>-1</sup>). Furthermore, both spectra displayed absence of allylic vibration at a wavelength of 1644 cm<sup>-1</sup>. In contrast to the monovalent system, the detection of the thiol and thioether groups of the multivalent PGs was possible, as the amount of these units in the side chains is higher.



**Figure 22.** a) Raman spectra of P(G<sub>50</sub>-co-SH<sub>6</sub>) (top, purple) and b) of P(G<sub>50</sub>-co-SEt<sub>6</sub>) (top, light purple), both compared to P(G<sub>50</sub>-co-AGE<sub>6</sub>) (bottom, black), displaying the absence of allyl vibration as well as the presence of thiols and thioether stretching, respectively, after thiol-ene reaction.

The presence and absence of thiols was furthermore verified by reaction of P(G<sub>50</sub>-co-SH<sub>6</sub>) and P(G<sub>50</sub>-co-SEt<sub>6</sub>) with Ellman's reagent, resulting in yellow discoloration for thiol-PG, whereas thioether-PG remained colorless (see image in **Table 2**). Here, the yellow color is more intense than this in MeO-PEG-SH, as depicted in **Table 1**, indicating a higher thiol amount in P(G<sub>50</sub>-co-SH<sub>6</sub>). In addition, by Ellman assay, the number of thiols in P(G<sub>50</sub>-co-SH<sub>6</sub>) was analyzed, which is in accordance with the value maintained by <sup>1</sup>H-NMR spectroscopy, as displayed in **Table 2**.

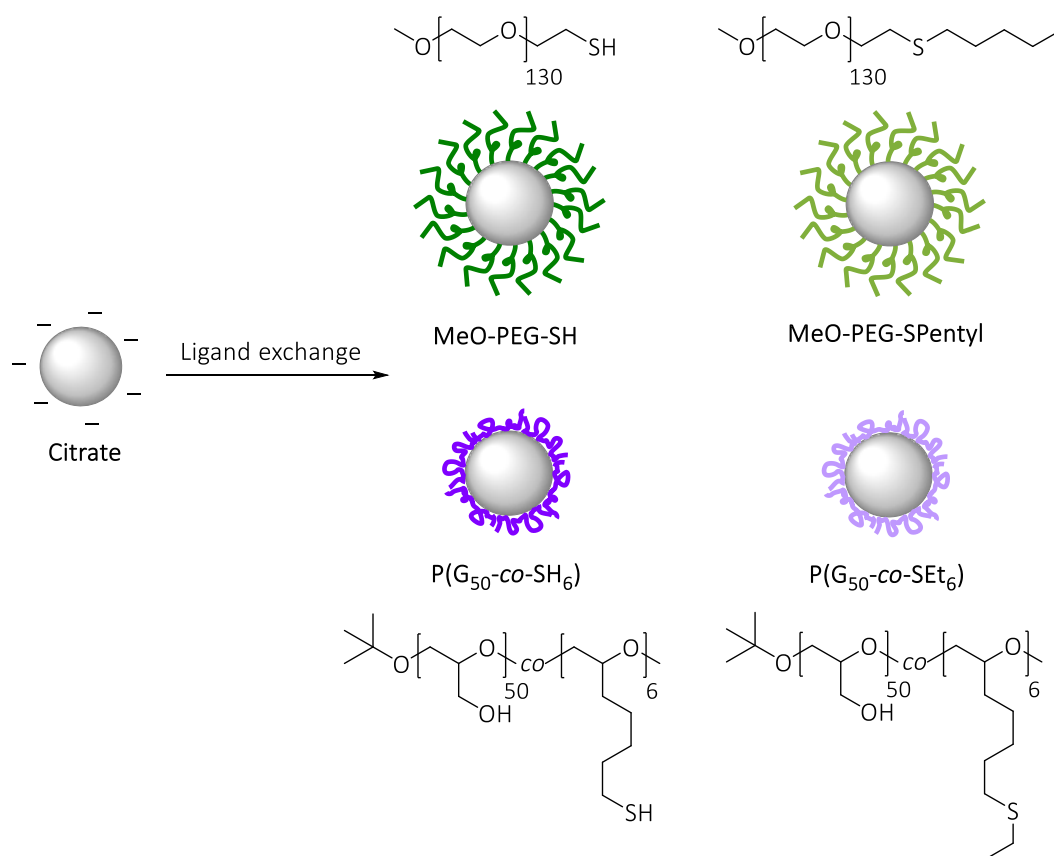
**Table 2.** Thiol amount determined via Ellman assay and <sup>1</sup>H-NMR spectroscopy of P(G<sub>50</sub>-co-SH<sub>6</sub>) as well as visualization of the presence and absence of thiols within P(G<sub>50</sub>-co-SH<sub>6</sub>) (left) and P(G<sub>50</sub>-co-SEt<sub>6</sub>) (right) by reaction with Ellman's reagent.

Thiol units per polymer chain		
Ellman assay	<sup>1</sup> H-NMR spectroscopy	
5.6	6	

### 3 Results and discussion

#### 3.1.2 AgNP surface modification with thiol- and thioether-polymers

Surface modification of citrate-stabilized AgNPs with the aforementioned mono- and multivalent sulfur-containing polymers was carried out by ligand exchange reaction. In this section, first the citrate-AgNPs were investigated via scanning electron microscopy (SEM), UV-Vis absorbance, DLS and zeta potential measurements as well as FT-IR spectroscopy, whereafter the successful polymer attachment was proven by same characterization methods. Besides, micro-TGA was conducted to investigate the amount and the arrangement of thiol- and thioether-polymers on the particle surface. As displayed in **Scheme 4**, citrate-stabilized AgNPs were labeled in grey, AgNPs modified with MeO-PEG-SH in green, MeO-PEG-SPentyl in light green, P(G<sub>50</sub>-co-SH<sub>6</sub>) in purple and P(G<sub>50</sub>-co-SEt<sub>6</sub>) in light purple throughout this section.



**Scheme 4.** Simplified schematization of thiol- and thioether-modified AgNPs received by ligand exchange reaction.

### 3.1.2.1 Citrate-stabilized AgNPs

Spherical AgNPs suspended in a dilute aqueous citrate buffer and with particle diameter of 20 nm were commercially purchased. The citrate stabilization provided long term stability of the NPs and allowed a readily ligand exchange due to weak association of citrate with the particle surface, as already discussed in **Section 2.1.3**. Here, firstly the NP size and shape were analyzed by using SEM imaging (see **Figure 23a**). As consistent with the literature<sup>[355,356]</sup>, it was found that AgNPs are not all perfectly spherical and uniform in size. According to the manufacturer's specification, particle size deviation with less than 13% is realized, resulting in diameters with deviation of  $21.3 \pm 2.7$  nm. In addition, the citrate-stabilized AgNPs were characterized via DLS, UV-Vis absorbance and zeta potential measurements as well as by FT-IR spectroscopy. **Figure 23** shows a characteristic SPR band at 400 nm, a curve progression with a polydispersity index (PDI) of 0.229, a mean hydrodynamic diameter (Z-average)  $d = 26.2 \pm 0.5$  nm and a negative zeta potential value of  $\zeta = -36.5 \pm 2.5$  mV. The just mentioned values are further listed in **Table 3** (see **Section 3.1.2.2**). The negatively charged surface determined by zeta measurements as well as the presence of the C=O stretching vibrations at  $1579\text{ cm}^{-1}$  and  $1393\text{ cm}^{-1}$  assigned to the carboxylate moiety in the FT-IR spectrum (**Figure 23d**), indicated that citrate is used as capping agent. As the particles were dispersed in aqueous solution, the infrared spectrum consisted of a broad OH-stretching band centered at  $3375\text{ cm}^{-1}$ . Besides, according to inductively coupled plasma-mass spectroscopy (ICP-MS) measurements the Ag mass concentration of the purchased particle solution was 19.4 mg/L.

### 3 Results and discussion

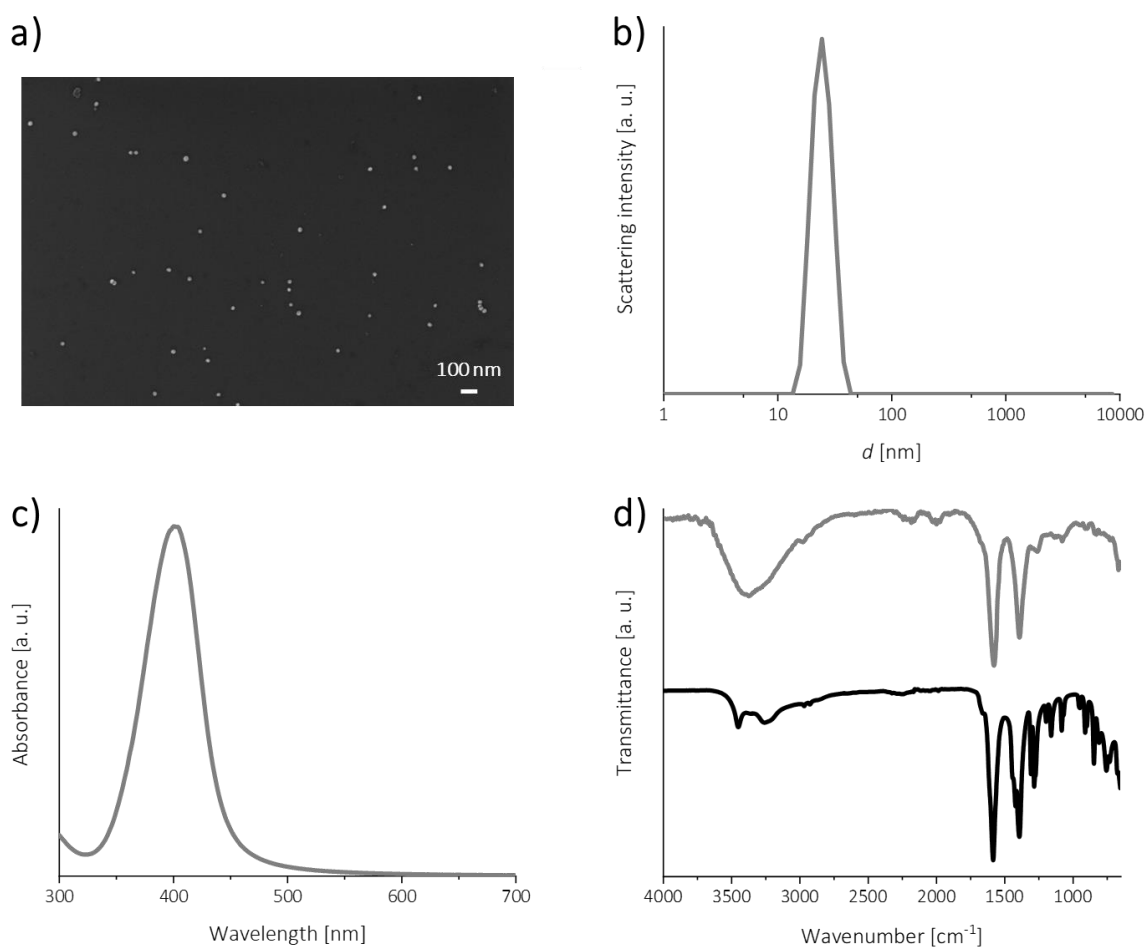


**Figure 23.** a) SEM image, b) DLS and c) UV-Vis absorbance spectrum of citrate-AgNPs as well as d) FT-IR analysis of 20 nm citrate-stabilized AgNPs (top, grey) compared to pure sodium citrate (bottom, black). In the latter case, AgNPs show characteristic C=O stretching as of pure citrate and an additional OH-vibration at  $3375\text{ cm}^{-1}$  due to particle dispersion in water.

#### 3.1.2.2 Adsorption of thiol- and thioether-polymers on citrate-AgNPs

Due to the only negligible electrostatic interaction of the citrate molecules in the NPs surface, the citrate-stabilized AgNPs can easily be modified with the sulfur-containing polymers of **Section 3.1.1** via ligand exchange reaction under formation of a quasi-covalent silver-sulfur bond.<sup>[357]</sup> Such organosulfur molecules possess high affinity to the Ag surface and have been used to stabilize the particles. It is known that the polymer-capped particles (steric stabilization) are more stable than citric acid-modified particles, which were charge stabilized.<sup>[11]</sup> In this study, thiol- and thioether-PEG and -PG having a similar chemical structure and a comparable molecular weight were used for NP functionalization and sterical stabilization. Therefore, 100  $\mu\text{L}$  of the respective polymeric solution (310  $\mu\text{M}$ ) was mixed with 1 mL of the purchased 20 nm citrate-AgNPs at RT. After incubation overnight,

the colloidal solutions were purified by centrifugation (20 000 g, 25 min, 4 °C) and subsequent redispersion in milli-Q H<sub>2</sub>O in order to remove unbound polymers.

Successful attachment of monovalent and multivalent thiol- and thioether-functionalized polymers to the NP surface was confirmed via various spectroscopic data (UV-Vis absorbance, DLS, zeta potential, and FT-IR spectroscopy) as listed in **Table 3**. The red shift (3-7 nm) in the SPR band of the polymer-capped NPs compared with the citrate-stabilized AgNPs (**Figure 24a**) is caused by a change in the dielectric constant at the surface of the particles,<sup>[358]</sup> as thoroughly discussed in **Section 2.1.1**.

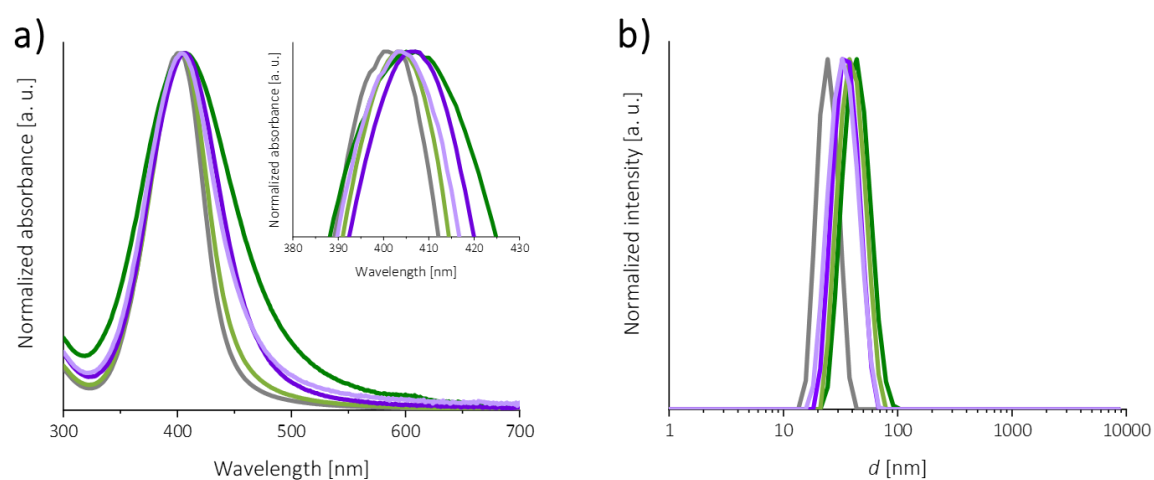


**Figure 24.** a) Normalized UV-Vis absorption and b) DLS spectra of 20 nm citrate-AgNPs (grey) compared to particles functionalized with MeO-PEG-SH (green), MeO-PEG-SPentyl (light green), P(G<sub>50-co</sub>-SH<sub>6</sub>) (purple) and P(G<sub>50-co</sub>-SEt<sub>6</sub>) (light purple), displaying a SPR red-shift and larger *d* values after AgNP polymer coating. The insert in (a) displays an enlarged part of the respective graph with adjusted scaling of both axes, to improve visualization of the SPR shift.

Furthermore, the detection of larger hydrodynamic diameter *d* in the DLS spectra (see **Figure 24b**) indicated the successful binding of these sulfur-containing polymers on the NP surface, whereby the PG coating exhibited a lower hydrodynamic diameter than the functionalization with PEG. The thinner coating layer for PG in contrast to PEG suggested that according to the literature, the polymers display different conformations on the AgNP surface. While, in case of PEG, there can only be an interaction via end group, which lead to a mushroom or brush-like configuration, PG can be possibly multiple bonded to the particle surface showing trains and loops.<sup>[1,153]</sup> A detailed investigation of the polymer-amount attached to AgNPs as well as their arrangement on the surface is described in **Section 3.1.2.3**. Zeta potential measurements of AgNPs before and after polymer coating displayed in **Table 3** show an increase from around -37 mV for citrate-AgNPs to values

### 3 Results and discussion

between -26 mV and -17 mV for polymer-functionalized NPs, verifying the successful attachment with neutral capping agents.

**Table 3.** Values of SPR,  $d$ , PDI and  $\zeta$  of citrate- and polymer-stabilized AgNPs, determined by UV-Vis, DLS and zeta potential measurements.

20 nm AgNPs	SPR [nm]	$d$ [nm]	PDI	$\zeta$ [mV]
Citrate	400	$26.2 \pm 0.5$	0.229	$-36.5 \pm 2.5$
MeO-PEG-SH	407	$48.8 \pm 1.1$	0.111	$-16.8 \pm 1.4$
MeO-PEG-SPentyl	403	$42.8 \pm 0.9$	0.201	$-21.1 \pm 2.7$
P(G <sub>50-co</sub> -SH <sub>6</sub> )	406	$33.5 \pm 0.8$	0.213	$-19.8 \pm 1.3$
P(G <sub>50-co</sub> -SEt <sub>6</sub> )	403	$36.2 \pm 0.8$	0.218	$-25.4 \pm 2.6$

In addition, the comparison of the FT-IR data of polymer-coated AgNPs, pure polymers and citrate-stabilized AgNPs in **Figure 25** suggests a complete ligand exchange as the typical C=O-stretching vibrations of citrate at  $1579\text{ cm}^{-1}$  and  $1393\text{ cm}^{-1}$  were not detected after polymeric functionalization. In fact, the spectra of the polymer-modified AgNPs displayed similar vibration bands like these of the correspondingly pure polymers. These data are shown exemplarily for the monovalent thiol and the multivalent thioether systems in **Figure 25**.

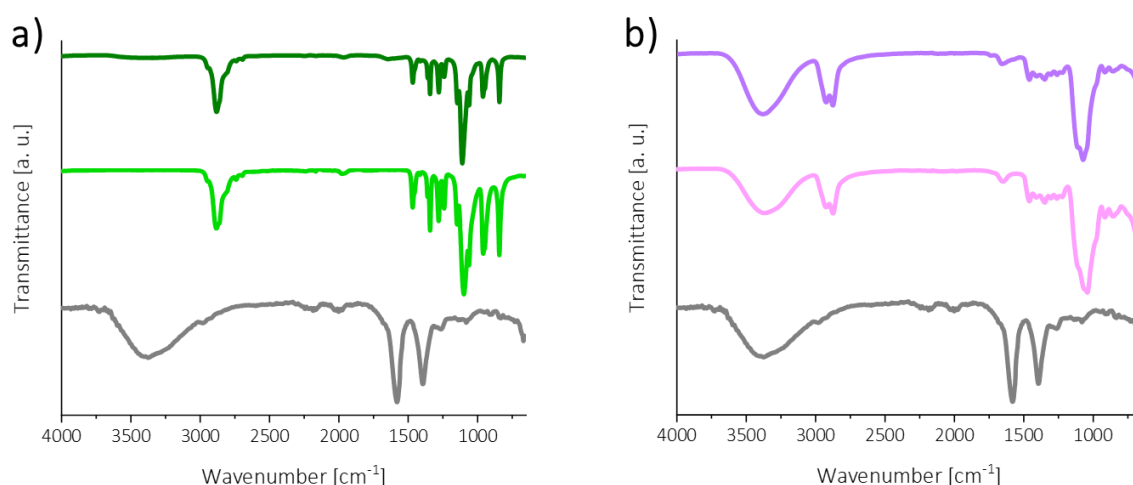


**Figure 25.** FT-IR transmittance spectra of a) Ag-MeO-PEG-SH (top, green) in comparison to pure MeO-PEG-SH (middle, dark green) and citrate-AgNPs (bottom, grey) as well as of b) Ag-P(G<sub>50-co</sub>-SEt<sub>6</sub>) (top, light purple) compared to pure P(G<sub>50-co</sub>-SEt<sub>6</sub>) (middle, light pink) and citrate-AgNPs (bottom, grey).



### 3.1.2.3 Investigation of polymer surface coverage and conformation on AgNPs

As described in **Section 2.1.3.4** steric colloidal stabilization with polymers is dependent on the grafting density, which defines how much polymer chains were attached per nm<sup>2</sup> particles. Thereby, both the number and the location of the anchor groups within the polymer play a decisive role, resulting in different conformations on the NP surface. Throughout this section, the polymer amount per AgNP was first calculated, followed by determination of the arrangement of MeO-PEG-SH and MeO-PEG-SPentyl, as well as suggestions for possible conformation of the multivalent systems P(G<sub>50-co</sub>-SH<sub>6</sub>) and P(G<sub>50-co</sub>-SEt<sub>6</sub>).

#### 3.1.2.3.1 Quantification of polymer amount per AgNP via micro-TGA measurements

Micro-TGA of 20 nm AgNPs functionalized with thiol- and thioether-polymers was conducted to investigate the amount and the arrangement of thiol- and thioether-polymers on the particle surface. Here, the polymer surface coverage was quantified, more specifically the number of polymers per particle, and thus the polymeric configuration on the NP surface. These features do not only affect protein binding and consequently blood circulation time, as described in **Section 2.2**, but also influence the steric stabilization of colloids (see **Section 2.1.3.4**), which is crucial for biological applications of NPs. Manson *et al.*<sup>[359]</sup> investigated the affect of PEG grafting density on AuNP stability in different media, demonstrating enhanced stabilization efficacy by increasing the surface coverage.<sup>[359]</sup> Colloidal stability in water was further presented for NP coating with 1.10 PEG chains per nm<sup>2</sup>, while lower polymer densities resulted in aggregation.<sup>[360]</sup>

By TGA, which is a commonly used method for quantitative analysis of polymer numbers on NPs<sup>[361,362]</sup>, a dried sample of a polymer-functionalized AgNP is heated up at a constant heating rate measuring the polymeric weight loss. Due to the different thermal decomposition of inorganic and organic substances, it is feasible to calculate the polymer to AgNP ratio in wt% and afterwards the surface coverage.

The detailed calculations for quantifying the polymer amount per AgNP as well as the estimation of the polymer configuration on the particle surface are presented in the following. **Figure 26** displays the weight loss spectra of 20 nm AgNPs modified with thiol- and thioether-polymers and their first deviation, showing that the weight loss in the

### 3 Results and discussion

temperature regions of 230-320 °C is considered as PG bound to the silver surface, while PEG ranges from 320-430 °C. These temperature regions were used for calculating the polymer to AgNP ratio.<sup>[8]</sup> The weight loss around 530-580 °C in all samples indicated soot formation due to pyrolysis.

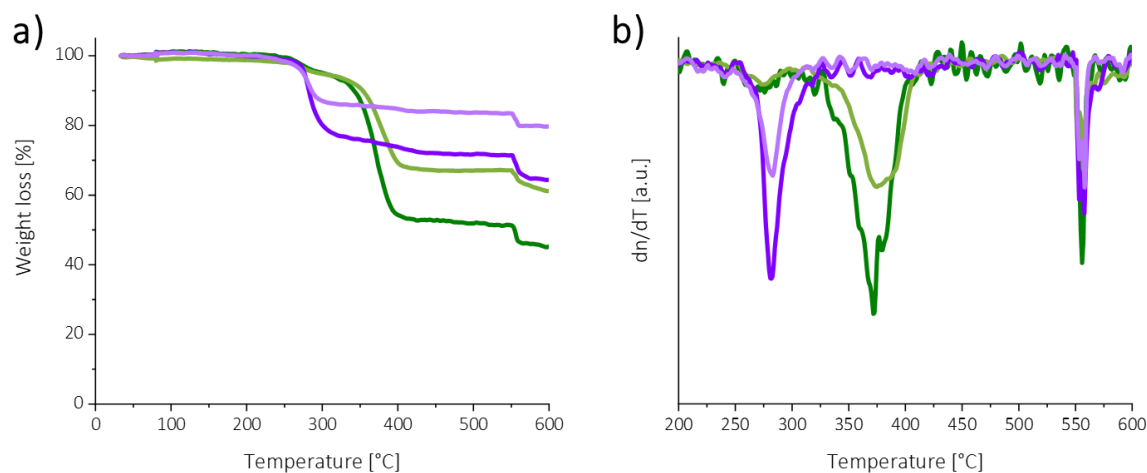


**Figure 26.** a) Weight loss spectra of 20 nm AgNPs modified with MeO-PEG-SH (green), MeO-PEG-SPentyl (light green), P(G<sub>50-co</sub>-SH<sub>6</sub>) (purple) and P(G<sub>50-co</sub>-SEt<sub>6</sub>) (light purple) received from micro-TGA measurements, showing a polymer dependent polymer to AgNP ratio. b) First deviation of the weight loss spectra of AgNPs functionalized with MeO-PEG-SH (green), MeO-PEG-SPentyl (light green), P(G<sub>50-co</sub>-SH<sub>6</sub>) (purple) and P(G<sub>50-co</sub>-SEt<sub>6</sub>) (light purple), showing the temperature regions of 230-320 °C for PG, of 320-430 °C for PEG. These temperature regions were used for calculating the polymer to AgNP ratio.<sup>[8]</sup> The weight loss between 530-580 °C in all samples indicated soot formation due to pyrolysis.

The ratio of polymer to 20 nm AgNP in wt% for thiol- and thioether-polymer functionalized AgNPs, received by micro-TGA measurements, are listed in **Table 4**. Here a polymer dependent polymer to AgNP ratio could be observed, increasing in the order P(G<sub>50-co</sub>-Et<sub>6</sub>) < MeO-PEG-SPentyl ≤ P(G<sub>50-co</sub>-SH<sub>6</sub>) < MeO-PEG-SH.

**Table 4.** Polymer to AgNP ratio in wt%, obtained from micro-TGA measurements.

	MeO-PEG-SH	MeO-PEG-SPentyl	P(G <sub>50-co</sub> -SH <sub>6</sub> )	P(G <sub>50-co</sub> -SEt <sub>6</sub> )
wt% <sub>polymer</sub> / wt% <sub>Ag</sub>	47.4 / 46.2	30.9 / 63.1	34.6 / 65.3	20.0 / 79.9

With these results, the number of polymers per particle were calculated via **Equation 4** which was derived as follows.<sup>[361]</sup> The number of polymers in the total sample were at first derived from wt%<sub>polymer</sub> divided with the polymer mass per chain. Latter was described as quotient of the molecular weight of the polymer  $M_w$  and the Avogadro constant  $N_A$  (see **Equation 1**).

$$\text{Number of polymers in the sample} = \frac{\text{wt}\%_{\text{polymer}}}{\text{Polymer mass per chain}} = \frac{\text{wt}\%_{\text{polymer}}}{M_w} \cdot N_A \quad \text{Equation 1}$$

Then the number of polymers in the total sample was defined as the quotient of the number of polymers per particle and the number of particles in the sample (see **Equation 2**).

$$\text{Number of polymers in the sample} = \frac{\text{Number of polymers per particle}}{\text{Number of particles in the sample}} \quad \text{Equation 2}$$

In turn, the number of particles in the sample was defined as a division of wt%<sub>Ag</sub> and the particle mass. Latter was known as the product of the density of silver ( $\rho_{Ag}$ ) and the volume of one spherical particle ( $4/3\pi r^3$ ) (see **Equation 3**).

$$\text{Number of particles in the sample} = \frac{\text{wt}\%_{Ag}}{\text{Particle mass}} = \frac{\text{wt}\%_{Ag}}{\rho_{Ag} \cdot \frac{4}{3}\pi r^3} \quad \text{Equation 3}$$

By inserting and rearranging of the previous Equations 1-3 yields the following **Equation 4**.

$$\text{Number of polymers per particle} = \frac{\text{wt}\%_{\text{polymer}} \cdot \rho_{Ag} \cdot \frac{4}{3}\pi r^3 \cdot N_A}{\text{wt}\%_{Ag} \cdot M_w} \quad \text{Equation 4}$$

$\rho_{Ag}$  = Density of Ag (10.49 g cm<sup>-3</sup>),  $r$  = Radius of AgNP

$M_w$  = Molecular weight of polymer,  $N_A$  = Avogadro constant

The values obtained from the calculations for the number of polymers per AgNP are listed in **Table 5**. Here it has to be considered that the determined values are based on single measurements and that we have assumed two things. First, an exact polymer molecular weight and no distribution is estimated, and second, the AgNPs are monodisperse and perfectly spherical with a diameter of 20 nm, although it is found in literature that NPs naturally are not uniform in shape and size.<sup>[355,356]</sup> This could also be confirmed by SEM images of the purchased AgNPs (see **Section 3.1.2.1**). However, in calculations where particle size is considered, it is always approximate that the particles are uniformly and perfect spheres, as described in literature.<sup>[363-365]</sup> Therefore, standard deviations were not

### 3 Results and discussion

taken into account in this purpose. Hence, giving such assumptions, the rounded values in **Table 5** should be treated with caution, and instead it is preferable to focus on the trend of a polymer dependent surface coverage.

It could be observed that the number of polymers per particle is higher for PEG than for the corresponding PG owing to their different structures with various numbers of anchor groups resulting in different polymer configuration on the NP surface (see **Section 2.1.3.4**). Due to the differences in the arrangements of monovalent and multivalent polymer systems, a direct comparison of the number of polymers per AgNP between PEG and PG was not suitable, but only of thiol- and thioether-PEG or thiol- and thioether-PG.

**Table 5.** Number of polymers per AgNP, calculated via Equation 4.

	MeO-PEG-SH	MeO-PEG-SPentyl	P(G <sub>50-co</sub> -SH <sub>6</sub> )	P(G <sub>50-co</sub> -SEt <sub>6</sub> )
Number of polymers per AgNP	4500	2100	3000	1400

As seen in **Table 5**, the number of PEG chains grafted to the AgNPs for MeO-PEG-SH was twice as high as for MeO-PEG-SPentyl caused by the size difference of the anchor groups, as thiols (-SH, with a molecular weight of 33 g/mol) claimed less space on the NP surface than the thioether units (-SPentyl, with a molecular weight of 103 g/mol). The higher number of polymer chains of MeO-PEG-SH per AgNP was also reflected in the larger SPR and hydrodynamic diameter of thiol-PEG compared to the thioether analog, as shown in **Table 3**.

Although a larger hydrodynamic diameter was obtained for P(G<sub>50-co</sub>-SEt<sub>6</sub>) than for P(G<sub>50-co</sub>-SH<sub>6</sub>) upon AgNP coating with these polymers, a similar trend as observed for PEG could be noted for the polymer coverage with PG. Here, the number polymers per AgNP is two times higher for thiol-PG than for thioether-PG, even though the size difference between the thiol (-SH, 33 g/mol) and the thioether moieties (-SEt, 61 g/mol) was less distinct. Hence, the difference in polymer coverage was not attributed to the various structures of the anchor groups, but possibly the different affinities of the thiol and thioether units towards silver play a decisive role. In the investigation of thiol- and thioether-polymer based coatings of AuNPs it was already demonstrated that these two anchor groups have different affinities to the Au surface, resulting in differences regarding polymer coverage

as well as colloidal stabilization.<sup>[17]</sup> In contrary to AuNPs, where it was hypothesized that thioether units have a higher affinity to AuNPs than thiols, leading to a larger number of polymers, this could not be confirmed for AgNPs. In case of Ag, the affinity of thiols appears to be stronger than of thioethers, causing in an increased polymer coverage of MeO-PEG-SH and P(G<sub>50-co</sub>-SH<sub>6</sub>) respectively. Whether the larger number of polymers per AgNP is also associated with better stabilities of thiols is discussed in **Section 3.1.3**. Therefore, the functionalized particles were exposed to conditions provoking aggregation such as centrifugation, high temperature, freeze-drying, ionic strength, and pH value, and were analyzed regarding the strength of the thiol-/thioether-silver interaction. Before, however, the arrangement of MeO-PEG-SH and MeO-PEG-SPentyl on the particle surface was investigated in the following.

#### 3.1.2.3.2 Determination of the polymeric arrangement of MeO-PEG-SH and MeO-PEG-SPentyl on AgNPs

According to literature, there are two different configurations of PEG on nanoparticle surfaces - the mushroom and the brush conformation.<sup>[366]</sup> For a better clarification of these regimes, the relation between the coil size (Flory radius  $R_f$ ) of PEG and the average distance between two grafted PEG chains ( $D_{grafting}$ ) has to be considered.  $R_f$  was determined as the product of the length of one monomer ( $\alpha$ ) and the number of monomer units ( $n$ ) for PEG (see **Equation 5**). The factor 3/5 was taken into account as a conformation of grafted linear molecules like PEG was expected displaying larger sizes in a good solvent (especially water) than in bad solvents (e.g. hexane).<sup>[367]</sup> The  $R_f$ -value for MeO-PEG-SH and MeO-PEG-SPentyl was calculated to 6.5 nm.

$$R_f = \alpha n^{\frac{3}{5}} \quad \text{Equation 5}$$

$\alpha$  = Length of one monomer (3.5 Å for PEG)<sup>[368]</sup>

$n$  = Number of monomer units (130 for PEG)

Estimating a mushroom or brush conformation on the particle surface,  $D_{grafting}$  can be calculated using **Equation 7**. First, the grafting density ( $\sigma$ ) has first be determined by dividing the number of polymers per AgNP and the particles surface area ( $4\pi r^2$ ) (see

### 3 Results and discussion

**Equation 6).** For this calculation, a surface area of perfect spherical and uniform NPs was assumed. In literature a mushroom conformation was described for  $D_{grafting} > R_f$  whereas for  $D_{grafting} < R_f$  the polymer showed a brush like configuration.<sup>[369,370]</sup>

$$\sigma = \text{Grafting density} = \frac{\text{Number of polymers per AgNP}}{4\pi r^2} \quad \text{Equation 6}$$

$r = \text{Radius of AgNP (here 10 nm)}$

$$D_{grafting} = 2 \sqrt{\frac{1}{\sigma\pi}} \quad \text{Equation 7}$$

$D_{grafting} = \text{Distance between two PEG chains}$

$\sigma = \text{Grafting density of PEG}$

By using these equations, the grafting density and  $D_{grafting}$  of MeO-PEG-SH and MeO-PEG-SPentyl on AgNPs were calculated, from which the polymeric conformation was deduced. The corresponding values are listed in **Table 6**. Even though the grafting density of thioether-PEG (1.7 polymer chains per nm<sup>2</sup>) is much lower as for the analog thiol ligands (3.6 polymer chains per nm<sup>2</sup>), due to a decreased steric hindrance of the thiol anchor groups, both polymers demonstrated a brush-like configuration on the AgNP surface, as listed in **Table 6**. Comparing the obtained values of  $\sigma$  with literature values, quantifications of PEG grafting densities on various colloidal inorganic NPs were reported within literature, demonstrating values between 0.35 and 14.5 PEG chains per nm<sup>2</sup> on particles with diameter of 2.8 nm to 60 nm and polymers with a molecular weight of 740-5000 Da.<sup>[371,372]</sup> These studies indicated the dependency of NP size and type as well as polymer length, concentration and type on surface coverage. Further factors affecting polymer density, such as incubation time, are known, presenting 0.89-1.8 PEG chains per nm<sup>2</sup> after coating 25 nm AgNPs with 1 kDa PEG at different time points.<sup>[373]</sup> Moreover, within literature various methods like NMR and fluorescence spectroscopy as well as TGA measurements were described, which provide differences in determination of the grafting density.<sup>[372]</sup> Due to this multitude of influences, a comparison of the grafting densities for MeO-PEG-SH and MeO-PEG-SPentyl on 20 nm AgNPs with the literature values is not meaningful. In addition, when calculating the values of  $\sigma$  according to **Equation 6**, it has to be considered that an

exact polymer  $M_w$  as well as particle volume and surface area of perfectly spherical NPs were assumed.

**Table 6.** Determination of a brush conformation for MeO-PEG-SH and MeO-PEG-SPentyl on 20 nm AgNPs by relating  $D_{grafting}$  to  $R_f$ .

	MeO-PEG-SH	MeO-PEG-SPentyl
$\sigma$ [polymer chains per nm <sup>2</sup> ]	3.6	1.7
$D_{grafting}$ [nm]	0.59	0.87
	$D_{grafting} < R_f \rightarrow$ brush conformation	

### 3.1.2.3.3 Possible polymeric arrangement of P(G<sub>50</sub>-co-SH<sub>6</sub>) and P(G<sub>50</sub>-co-SEt<sub>6</sub>) on AgNPs

While in case of PEG there can only be an interaction via end-group, which leads to a mushroom or brush-like conformation, the multivalency of PG has a crucial impact on its arrangement on colloidal surfaces. As described in literature, homopolymers or random-copolymers possessing multiple anchor groups along the polymer chain acquired a configuration including trains, loops and tails (see **Figure 8**).<sup>[1,374-376]</sup> In general, trains were defined as segments directly adsorbed to the surface, loops as non-adsorbed polymer sequences between trains spreading out into the solution, whereby tails are non-adsorbed polymer ends protruded from the particle surface.<sup>[152]</sup> In order to determine the composition of trains, loops and tails, several methods based on conformational statistical analysis were found, as described for polymer adsorption onto flat surfaces as well as on hydrophobic colloids by Fler *et al.*<sup>[377,378]</sup> However, it has to be noted that the train-loop-tail conformation of the aforementioned investigations are generated by linear homopolymers or random copolymers, where each sequence of the polymer adhere with same affinity to the NP surface. Since in case of P(G<sub>50</sub>-co-SH<sub>6</sub>) and P(G<sub>50</sub>-co-SEt<sub>6</sub>) only the thiol and thioether units will specifically bind to the AgNPs, which also exhibit different binding kinetics, these statistical models can not be applied.

So far, polymers with high affinity towards the surface are known to present fewer tails and loops than those adsorbing more weakly, having an impact on the hydrodynamic diameter.<sup>[379]</sup> Thus, based on the size difference of  $d = 33.5 \pm 0.8$  nm for P(G<sub>50</sub>-co-SH<sub>6</sub>) and  $d = 36.2 \pm 0.8$  nm for P(G<sub>50</sub>-co-SEt<sub>6</sub>), it can thus be assumed that thiol-PG possessed a lower

### 3 Results and discussion

amount of loops and tails and bound more strongly to the AgNPs as compared to the corresponding thioether analog. In general, in both cases a relatively small number of extending trails and loops was estimated, since the presence of predominantly long protruding segments would cause a so called bridging flocculation, enhancing particle aggregation.<sup>[105,380]</sup> Such bridging occurred by adsorption of extended polymer sequences onto neighbouring particles, requiring unsaturated areas on the surface of the NPs to which further tails and loops of adjacent particles can attach. Therefore, a dense polymer layer was assumed after coating 20 nm AgNPs with the multivalent PG systems P(G<sub>50</sub>-CO-SH<sub>6</sub>) and P(G<sub>50</sub>-CO-SEt<sub>6</sub>), respectively. The extent to which the suspected differences in the arrangement of PGs to the surface have implications for colloidal stabilities as well as for the strength of polymer-NP interaction, was examined throughout the next section.

#### 3.1.3 Stabilization efficacy of thiol- and thioether-polymer-modified AgNPs

As thoroughly discussed in **Section 2.1.3.3** NPs can sterically be stabilized via polymer adsorption resulting in thermodynamic stability of the colloids. Polymers with high affinity to the particle surface, especially sulfur-compounds, generate a barrier to particle aggregation which consequently lead to enhanced stability. Even though adsorption of sulfur-containing polymers as thiols, thioether or disulfides result in a stable silver-sulfur bond, the chemical differences of the sulfur anchor groups feature different bonding strengths that effects the stabilization efficacy, as precisely described in **Section 2.1.3.5**. Additionally, several factors like the ionic strength or the presence of bio-macromolecules influences the aggregation behavior, as ions or proteins can be attached to the particle surface if the polymer adsorption is not strong enough. Since NP aggregation in turn affects, for instance, the cellular interaction<sup>[381]</sup>, it is mandatory demonstrating the impact of the thiol- and thioether-polymers of **Section 3.1.1** on the colloidal stability of AgNPs. In the following, particles functionalized with the above-mentioned mono- and multivalent sulfur-containing polymers MeO-PEG-SH, MeO-PEG-SPentyl, P(G<sub>50</sub>-CO-SH<sub>6</sub>) and P(G<sub>50</sub>-CO-SEt<sub>6</sub>) were investigated regarding their stabilization efficacy. Before evaluation of the colloidal stability of the thiol- and thioether-polymer-coated AgNPs, an adsorption kinetics study was recorded. The implementation of such studies were previously described.<sup>[17]</sup>



### 3.1.3.1 Binding kinetics study

The binding kinetics of implied polymers onto AgNPs was studied by performing a time-dependent polymeric incubation using different time points ranging from 5 min to 12 h. After stopping the incubation by centrifugation, absorbance measurements were conducted.

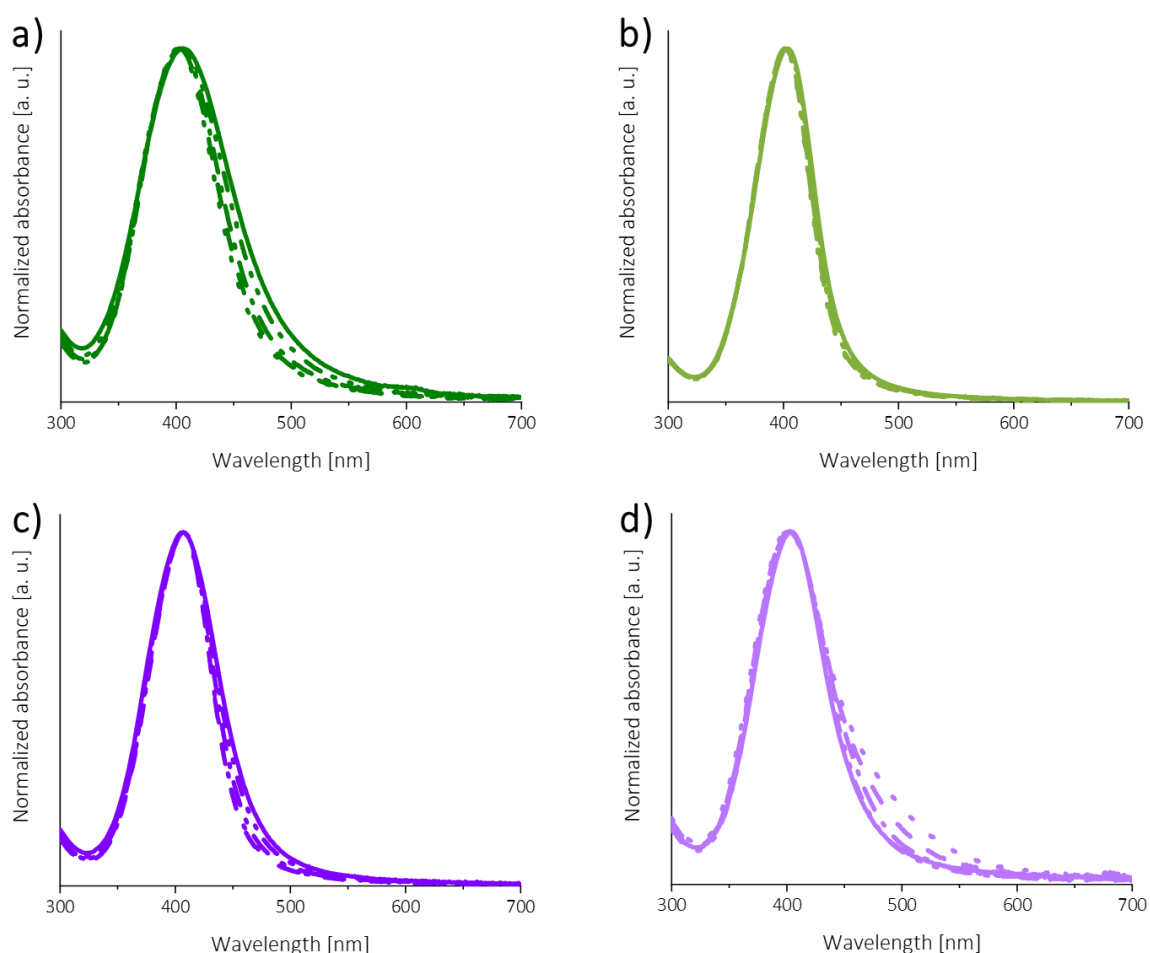


**Figure 27.** Binding kinetics study: UV-Vis spectra of AgNPs coated with a) MeO-PEG-SH (green), b) MeO-PEG-SPentyl (light green), c) P(G<sub>50</sub>-co-SH<sub>6</sub>) (purple) and d) P(G<sub>50</sub>-co-SEt<sub>6</sub>) (light purple) after 5 min (dotted line), 30 min (dashed line), 2 h (dash-dot line), 6 h (dash-dot-dot line) and 12 h (solid line) incubation time.

As displayed in **Figure 27**, the multivalent P(G<sub>50</sub>-co-SEt<sub>6</sub>) needed longer for complete particle passivation than the thiol analog as well as the monovalent polymers, which is in accordance with the literature for monolayer formation of thiol versus thioether on flat metal surfaces.<sup>[382]</sup> However, the longer passivation time has not to be necessarily related to a weaker thioether-silver bond as already verified for AuNPs.<sup>[17]</sup> Barngrover and Aikens found a residue group dependency of the binding energy in silver-sulfur clusters, however, observing no significant differences using chemical and structural similar groups such as

### 3 Results and discussion

hydrogen and methyl groups.<sup>[346]</sup> While an incubation time of at least 2 h was required for P(G<sub>50</sub>-CO-SEt<sub>6</sub>), 5 min incubation was enough reaching steric stabilization for MeO-PEG-SPentyl-functionalized particles, indicating that the initial adsorption is dependent on the ligand structure. In case of the side-chain functionalized PG, a slower ordering respective reorganization process occurs probably due to steric hindrance. The faster thioether passivation of the monovalent system might possibly be further provided by additional stability due to van der Waals interactions of the extended PEG brushes.<sup>[383]</sup>

#### 3.1.3.2 Colloidal stability studies

Besides the study on binding kinetics, the colloidal stabilization efficacy of the different polymer coatings was evaluated. Therefore, the particles were exposed to conditions provoking aggregation, such as centrifugation, high temperature, freeze-drying, treatment in phosphate buffered saline (PBS), and Dulbecco's modified Eagle medium (DMEM) as well as incubation in 5 mM phosphate buffer (PB) with different pH values (4.0, 5.4, 7.4 and 9.4). As AgNPs have a strong SPR band in the UV-Vis spectrum, the stability of coated particles can generally be determined by changes in the curve progression or absorbance intensities.<sup>[11,115]</sup> Thus the colloidal stabilization in percent was analyzed by measuring the absorption before and after each treatment. In addition, this allows providing a statement on the stability in percent (see **Figure 29**), for what the absorbance values at a wavelength of 410 nm, obtained by measurements before (mean 100%) and after, were situated in relation. For this purpose, it was relevant to verify no absorption of the used polymers at the considered wavelength of 410 nm, as displayed in **Figure 28**.

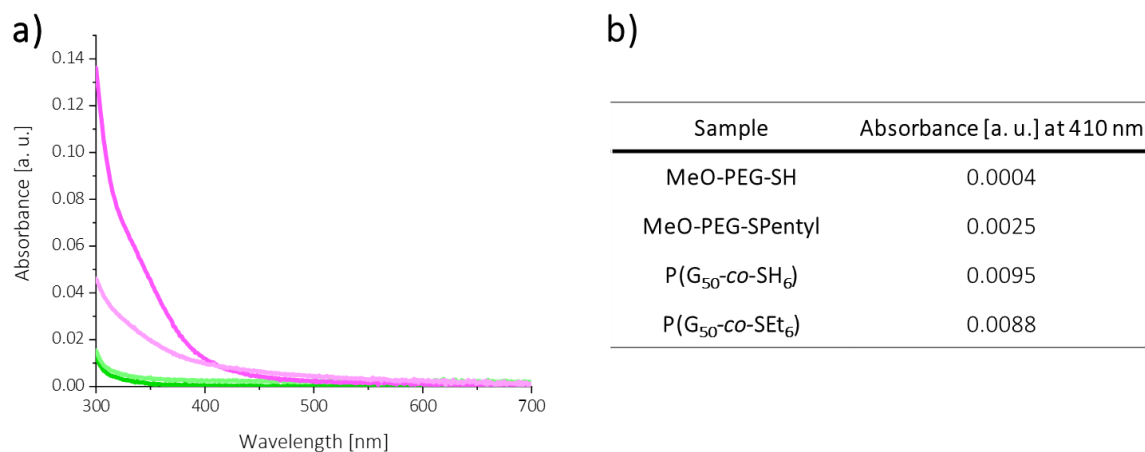


**Figure 28.** a) UV-Vis absorbance spectra and b) absorbance values at a wavelength of 410 nm of MeO-PEG-SH (green), MeO-PEG-SPentyl (shiny green), P(G<sub>50-co</sub>-SH<sub>6</sub>) (pink) and P(G<sub>50-co</sub>-SEt<sub>6</sub>) (light pink) polymer solutions (310 μM).

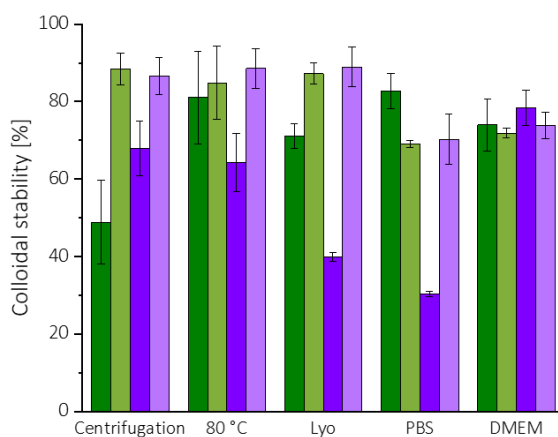


**Figure 29.** Colloidal stability in percentage terms of AgNPs functionalized with MeO-PEG-SH (green), MeO-PEG-SPentyl (light green), P(G<sub>50-co</sub>-SH<sub>6</sub>) (purple) and P(G<sub>50-co</sub>-SEt<sub>6</sub>) (light purple) after centrifugation, temperature treatment at 80 °C, lyophilization (Lyo), and incubation in PBS and DMEM. Error bars represent the deviation from four experiments.

As depicted in **Figure 29**, first, the impact on the colloidal stability after five centrifugation (20 000 g, 25 min, 4 °C) and resuspension cycles was investigated. While there was no notable influence on the stabilization for thioether-polymer coatings, thiol functionalization led to a polymer-dependent decrease, even though the polymer coverage was much higher for thiols than for thioethers, as listed in **Table 5**. The better colloidal stability values indicated a stronger thioether-silver interaction under centrifugation conditions in comparison with the thiol linkage attachment with multivalent P(G<sub>50-co</sub>-SH<sub>6</sub>) ensured good stabilities around 70%, whereas modification with thiol-terminated PEG exhibited a significant particle loss of 51%. In case of thiol-functionalized polymers, the amount of thiol moieties influenced the stabilization efficacy, as a higher number of anchor groups ensured better colloidal stability.

### 3 Results and discussion

In addition, heating up the particle solution to 80 °C for 12 h resulted in good colloidal stabilities for thiol- and thioether-polymer functionalized AgNPs (81-89%) with exception of P(G<sub>50</sub>-CO-SH<sub>6</sub>). In accordance with the centrifugation studies, there was no correlation between the coverage density and the particle stability. Here, the type of the anchor group influenced the stabilization efficacy, indicating a weaker thiol-silver correlation upon high temperatures than the thioether linkage. Due to additional stability of the PEG brushes by van der Waals interactions, the single anchor unit showed less impact on colloidal stability. Furthermore, the stabilization after a lyophilization process, which is an important method improving the long-term stability of NPs relevant for clinical applications<sup>[384]</sup>, was studied. Therefore, the colloidal solutions of the modified particles were deep-frozen followed by removing the ice under reduced pressure. Afterwards, the dried samples were resuspended in milli-Q H<sub>2</sub>O before analyzing the absorbance value at 410 nm. **Figure 29** shows that the stabilization effect was highly dependent on the polymer coating. A thioether functionalization possesses the best colloidal stability of 89% for P(G<sub>50</sub>-CO-SEt<sub>6</sub>) and 87% for MeO-PEG-SPentyl, and also, the monovalent thiol-polymer reached good stabilization values of 71%. In contrast, the AgNPs modified with P(G<sub>50</sub>-CO-SH<sub>6</sub>) resulted in aggregation possibly due to oxidative intermolecular crosslinking between oxidized species of the multiple thiol moieties of two different thiol-PG-functionalized particles. The oxidative effect was less crucial for MeO-PEG-SH due to single end group functionalization, achieving less poor colloidal stabilization.

To investigate the influence of ions and proteins on the colloidal stability, the different polymer-coated AgNPs were incubated for 12 h in PBS and DMEM, the most common medium for cell culture. After centrifugation, the particles were resuspended in PBS and DMEM, respectively. As illustrated in **Figure 29**, AgNPs modified with MeO-PEG-SH reached highest stability values (83%) after treatment in the standard working concentration of 1x PBS, associating with the high number of polymers per particle (see **Table 5**). On the contrary, the polymer coverage has no influence on colloidal stabilization for the other polymer coatings. Instead, both thioether functionalization displayed good stabilities around 70%, whereas the multivalent thiol-polymer showed the worst colloidal stabilization of 30%. In case of PG coating, the type of anchor groups was decisive regarding

the stability of the particles. Here, a lower thiol-silver bonding strength resulted in aggregation enabling adsorption of ions from the salt solution on the particle surface.

Besides the previously discussed stability studies, suspension in DMEM, a complex mixture of proteins, sugars, and amino acids, demonstrated no polymer dependency in view of the stabilization in percentage terms. Here, all coatings resulted in good colloidal stabilities (72-78%) with a slightly improved stabilization for thiol-functionalized AgNPs, which is accompanied with a larger number of polymers on the particle surface.

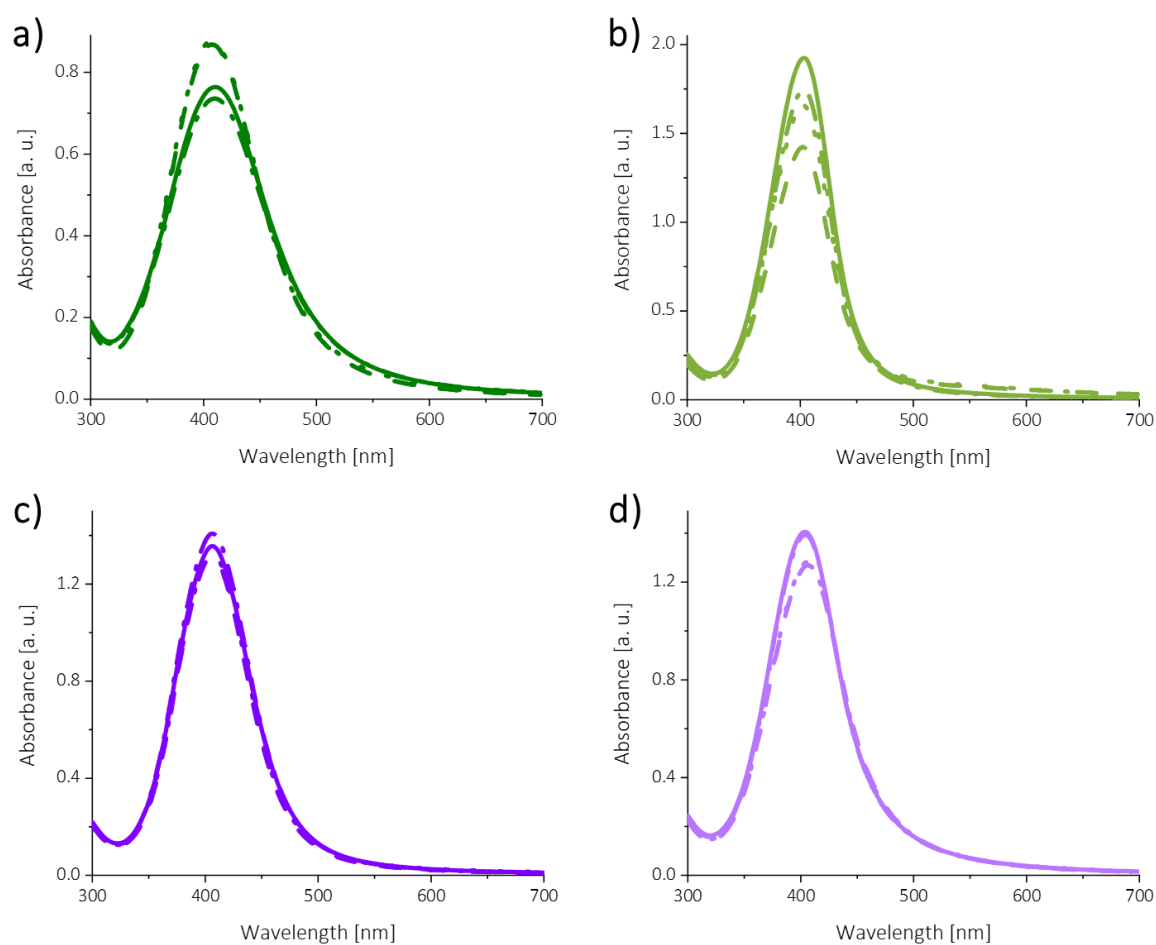


**Figure 30.** UV-Vis spectra of AgNPs functionalized with a) MeO-PEG-SH (green), b) MeO-PEG-SPentyl (light green), c) P(G<sub>50</sub>-co-SH<sub>6</sub>) (purple) and d) P(G<sub>50</sub>-co-SEt<sub>6</sub>) (light purple) after treatment in 5 mM PB with pH values of 4.0 (dashed line), 5.4 (dotted line), 7.4 (solid line) and 9.4 (dashed/dotted line).

Finally, the influence of different pH values on the stabilization effect of coated AgNPs was checked. Therefore, the functionalized particles were suspended in 5 mM PB with the pH values between 4.0 and 9.4, which covers a significant range of ion strength. **Figure 30** shows that only for modification with MeO-PEG-SPentyl, there were major differences in

### 3 Results and discussion

SPR bands, decreasing in the order 7.4 > 9.4 > 5.4 > 4.0. Thiol-PEG-functionalized particles had similar absorbance values for pH 4.0 and 5.4, and an equal band disappearance for higher pH levels. In contrast to this, the multivalent PG coating was more stable in neutral and alkaline buffer than in acidic environment, whereby this effect was less pronounced for AgNPs modified with P(G<sub>50</sub>-CO-SH<sub>6</sub>).

In summary, different physicochemical techniques verified the successful thiol and thioether surface functionalization of AgNPs, while the number of polymer molecules loaded onto the particles as well as the conformation of PEG on the AgNPs surface was quantified via micro-TGA. As previously reported for AuNPs<sup>[17,385]</sup>, thioether binding onto AgNPs was slower than the adsorption of analog thiols. However, the presented study on the colloidal stabilization after centrifugation, high temperature treatment and lyophilization suggested a thermodynamically stronger attachment for thioethers. Also the aim of receiving stability in biological fluids could be reached after coating the AgNPs with these functional polyethers except for particles capped with P(G<sub>50</sub>-CO-SH<sub>6</sub>) suspended in PBS. In all studies using thioether as binding agent, there were nearly similar results for PEGylated and PG-coated particles indicating no substantially stable silver-ligand interactions for multi-dental units. The excellent stabilization efficacy of thioether-coated AgNPs in water as well as the good colloidal stability in biological environment and especially the ability of introducing different chemical or biological functionalities to the backbone of the thioether-PG makes this nanoparticle system of great interest in biomedical applications.

### 3.2 Protein corona composition on hydrophobic functionalized PG-coated AuNPs and their impact on macrophage uptake

For biomedical purpose, apart from the previously discussed AgNPs, particularly AuNPs were used as they have the advantage of not being sensitive to oxidation, leading to higher chemical stability.<sup>[386]</sup> Ensuring that AuNPs can meet their biomedical application for instance as contrast agent<sup>[194]</sup>, in photothermal therapy<sup>[195]</sup> or for drug delivery<sup>[196,387]</sup>, it is essential to prevent these nanocarriers from being recognized as foreign bodies by phagocytes and thus being rapidly removed and cleared from the bloodstream. Upon entering the body, NPs are rapidly covered by proteins, forming a so-called protein corona that affects cell internalization, as thoroughly described in **Section 2.2**. Thus, NP-protein interactions play a crucial role for biomedical application of nanocarriers to transport them at the desired site of action and minimize the non-specific uptake by immune cells.

As it is known that surface functionalization such as coating with polymers, or hydrophobic ligands, as well as the particle size, influences the stability and the protein corona formation and composition,<sup>[8,27,216]</sup> AuNPs with two different sizes (15 nm and 30 nm) coated with multivalent thioether-PG were prepared in this work. Multivalent thioether-PG was used as coating agent as previous studies verified excellent colloidal stability of such surface functionalized AuNPs,<sup>[17]</sup> and because PG is known to be a stealth polymer<sup>[35]</sup>. The different PGs were functionalized with various hydrophobic moieties and differ in their hydrophilic-to-hydrophobic ratio, to investigate the effect of different surface hydrophobicities on serum protein adsorption and their subsequent cellular uptake by human monocyte-derived macrophages. For this purpose, different alkyl functionalities with varying chain lengths as well as cholesteryl units are introduced in PG via side-chain functionalization. Human serum (HS) was utilized as protein source, leading to protein corona formation with varying compositions, examined by different analysis methods. Serum was chosen as protein source because it is most widely used in research due to its advantage of not containing coagulants.<sup>[388]</sup> However, it should be noted that using another protein source, e.g. plasma, may lead to completely different results.<sup>[266,389]</sup> Subsequently, to prove the PG coating results in a stealth behavior of the particles and to investigate the impact of the different adsorbed or blocked proteins in a biological system, the in vitro interaction of the various hydrophobic modified AuNPs with immune cells was studied. Therefore, selected

### 3 Results and discussion

PGylated as well as the citrate-capped particles, before and after incubation with HS, were incubated with human monocyte-derived macrophages. Macrophages were used as they are important components of the immune defense and play an essential role in the clearance of foreign substances from the bloodstream.<sup>[243]</sup>

In this section, first the experimental procedures for all fourteen alkyl- and cholesteryl-functionalized polymer synthesis and their characterization via <sup>1</sup>H-NMR, FT-IR, and Raman spectroscopy, TNBSA assay as well as SEC analysis is described. In addition, these multivalent PGs were investigated regarding their critical aggregation concentration (CAC) via DLS analysis, since it is known that amphiphilic polymers can form soluble aggregates in aqueous solution above a certain concentration.<sup>[390]</sup> Second, studies were carried out to identify the optimal polymer concentration for AuNP functionalization receiving stable and aggregation-free coated particles. After that, the successful adsorption of the synthesized multifunctional polymers on 15 nm and 30 nm AuNPs was further proven by UV-Vis absorbance, DLS, zeta potential measurements and FT-IR spectroscopy. Third, after incubation of modified AuNPs with HS, successful protein adsorption was verified by various spectroscopic methods (UV-Vis, DLS, zeta potential, FT-IR) and attached proteins were quantitatively and qualitatively analyzed by micro-bicinchoninic acid (micro-BCA) assay and one-dimension sodium dodecyl sulfate polyacrylamide gel electrophoresis (SDS-PAGE) as well as label-free liquid chromatography tandem mass spectrometry (LC-MS/MS), respectively. Last, AuNP uptake of previously in detail discussed AuNPs by macrophages was analyzed in terms of adsorbed or blocked proteins as a result of surface functionalization by determining the amount of AuNPs not taken up by cells after 6 h of treatment using ICP-MS analysis.

#### 3.2.1 Multifunctional, amphiphilic PGs bearing different hydrophobic moieties

In this section the synthesis of multifunctional thioether-containing PGs was performed. Since thioethers have the outstanding advantage of having a non-nucleophilic and non-oxidative character, they provide the introduction of any functional mercaptan compound to allyl groups of the PG backbone via thiol-ene reaction.<sup>[391,392]</sup> Here, bimolecular reactions were conducted by adding EtSH and a hydrophobic sulfur-containing compound to the in **Section 3.1.1.2** presented polymers P(G<sub>50</sub>-CO-AGE<sub>6</sub>) and P(G<sub>50</sub>-CO-AGE<sub>12</sub>), respectively,



obtaining amphiphilic copolymers. As hydrophobes, different alkyl functionalities with varying chain lengths as well as cholesterol were used. The fatty acid like alkyl chains were chosen to introduce hydrophobicity in a simple way, since alkyl thiols can easily be attached to PG by UV-triggered thiol-ene reaction.<sup>[17]</sup> In addition, some researchers studied the hemocompatibility of coated substrates with immobilized alkyl chains of different chain length, addressing different proteins that trigger coagulation or complement activation. Fischer *et al.*<sup>[393]</sup>, for instance, showed reduced coagulation activation with increased degree of octadecyl-functionality after blood incubation, as well as decreased binding of complement protein C5a. Even with shorter undecanoyl ligands, this working group observed diminished binding of proteins responsible for complement activation compared to ligands terminated with a hydrophilic hydroxyl group.<sup>[394]</sup> Since human serum albumin (HSA) is known to suppress the binding of certain proteins and to provide good transport function for long-chain free fatty acids in the bloodstream, mainly composed of 16 to 18 carbon atoms, the literature contains some investigations on improved blood compatibility of HSA pre-coated materials.<sup>[395-397]</sup> In this regard, Gonçalves *et al.*<sup>[398]</sup> introduced octadecyl functionalities on gold surfaces modified with 11-Mercapto-1-undecanol and studied the adsorption of HSA alone and in competition to fibrinogen, which is known to promote blood coagulation<sup>[399]</sup>. They showed an increase in HSA binding with the degree of octadecyl immobilization, i.e., hydrophobicity. Upon competitive binding of HSA and fibrinogen with a ratio similar in blood, surfaces with octadecyl functionality of 2.5% and 5% showed low affinity for fibrinogen compared to more hydrophobic or less hydrophobic surfaces. Consequently, the degree of hydrophobicity plays a crucial role for the hemocompatibility, as hydrophobic surfaces are known to show increased blood platelet adhesion due to high binding of fibrinogen<sup>[400]</sup>. Cholesterol was selected as an even more hydrophobic molecule, as it is an essential component of the cell membrane and is known to be transported in the blood by lipoproteins.<sup>[401-403]</sup> Moreover, the protein HSA plays an important role in transportation of cholesterol in the bloodstream, hence the interaction of HSA with cholesterol has been widely studied.<sup>[404-407]</sup> Peng *et al.*<sup>[407]</sup> and Teir *et al.*<sup>[408]</sup> investigated the interaction between HSA and cholesterol by various spectroscopic measurements. Both working groups displayed autofluorescence quenching of HSA with increasing cholesterol content caused by changes around the tryptophan residue due to cholesterol binding. Since the tryptophan residue on HSA is located in subdomain IIA<sup>[409]</sup>, it

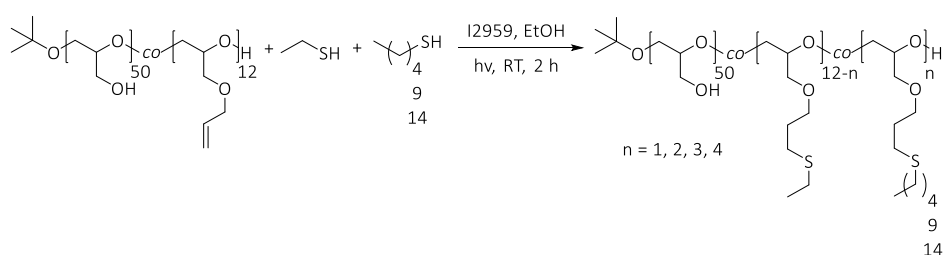
### 3 Results and discussion

is suggested that this is the hydrophobic binding pocket for cholesterol, which is also known as binding site of aromatic and heterocyclic ligands<sup>[410,411]</sup>. Fatty acid binding, on the other hand, involves various other binding sites such as subdomains IIIA and IIIB.<sup>[409,412]</sup>

The successful copolymer synthesis was confirmed by <sup>1</sup>H-NMR, FT-IR and Raman spectroscopy as well as TNBSA assay and SEC analysis. In addition, these PGs were investigated regarding their CAC via DLS analysis, since it is known that amphiphilic polymers can form soluble aggregates in aqueous solution above a certain concentration<sup>[390]</sup>, which has to be avoided to achieve attachment of these amphiphilic polymers to the NP surface.

#### 3.2.1.1 Synthesis of alkyl-functionalized PGs

Alkyl-functionalized PGs were synthesized by thiol-ene reaction of P(G<sub>50</sub>-co-AGE<sub>12</sub>) with EtSH and different alkyl thiols, more specifically 1-pentanethiol, 1-decanethiol and 1-pentadecanethiol (see **Scheme 5**). In this thesis four different multifunctional polymers were prepared for each mentioned alkyl thiol by variation of the EtSH to alkyl thiol ratio, receiving twelve different alkyl-functionalized PGs. The UV-light triggered reaction and subsequent purification by dialysis and lyophilization was conducted as described for P(G<sub>50</sub>-co-SEt<sub>6</sub>) in **Section 3.1.1.2**.



**Scheme 5.** Synthesis of alkyl-functionalized PGs via thiol-ene reaction of P(G<sub>50</sub>-co-AGE<sub>12</sub>) using EtSH and 1-pentane-, 1-decane- as well as 1-pentadecanethiol.

<sup>1</sup>H-NMR, FT-IR and Raman spectroscopy as well as SEC measurements were applied analyzing the obtained alkyl-functionalized polymers (see **Section 5.4.2** to **Section 5.4.13**). Due to the similarity regarding their chemical structure, in the following the characterization will be shown exemplarily for one alkyl-PG, more precisely P(G<sub>50</sub>-co-SEt<sub>10</sub>-co-SDec<sub>2</sub>).

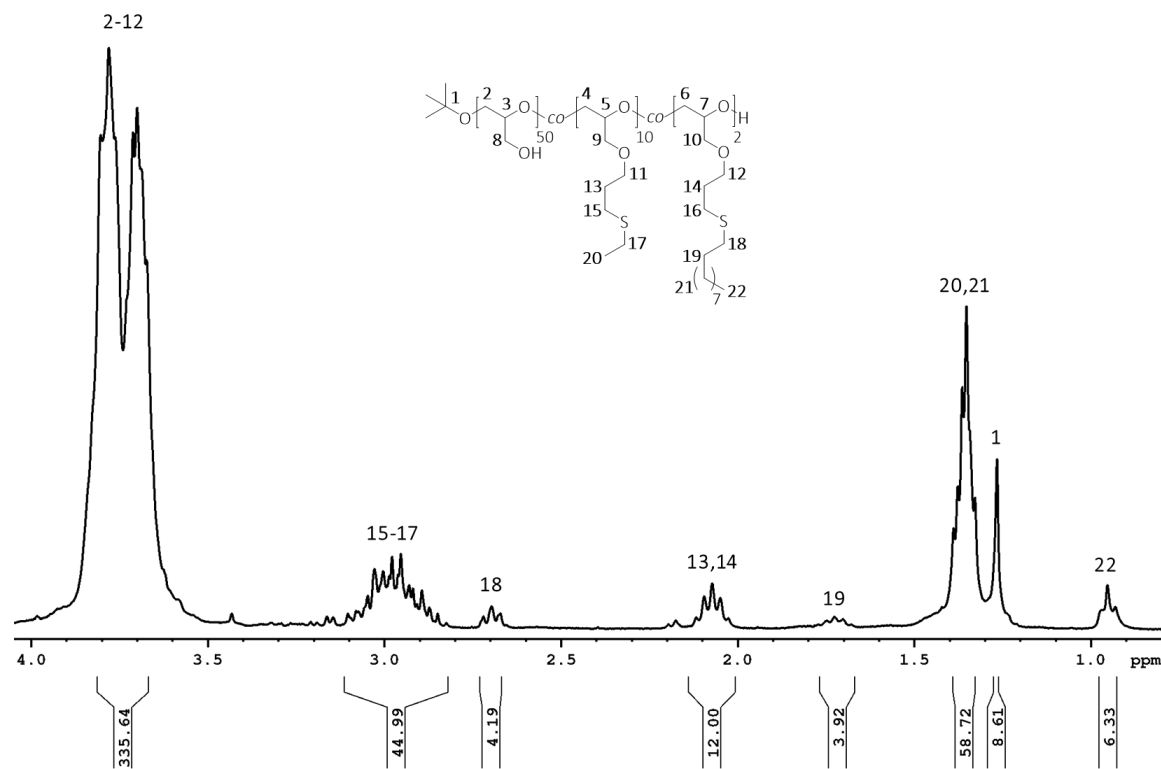


**Figure 31.**  $^1\text{H-NMR}$  spectrum of  $\text{P}(\text{G}_{50}\text{-co-SEt}_{10}\text{-co-SDec}_2)$ , synthesized via bimolecular thiol-ene reaction of  $\text{P}(\text{G}_{50}\text{-co-AGE}_{12})$  with EtSH and 1-decanethiol.

$^1\text{H-NMR}$  spectrum in **Figure 31** shows a multiplet at 3.80-3.67 ppm, corresponding to the polymer backbone. The methylene protons H-15-17, H-18, H-13,14 and H-19 were detected at a chemical shift of 3.10-2.83 ppm, 2.70 ppm, 2.07 ppm and 1.73 ppm. In addition, the signals appearing at 1.39-1.33 ppm were contributed to 20 and 21 position protons, and the *tert*-butyl end group displayed a singlet at 1.27 ppm. The triplet at 0.95 ppm (H-22) revealed that two decyl chains were introduced per polymer backbone. Integrating the  $^1\text{H-NMR}$  signals as well as the fact, that no allylic signals could be detected, confirmed successful thiol-ene reaction.

Total conversion of allyl to thioether groups was further proven by Raman spectroscopy. As depicted in **Figure 32**, the absence of the allylic signal ( $1646\text{ cm}^{-1}$ ) and the presence of the thioether stretching vibration ( $642\text{ cm}^{-1}$ ) indicated a successful functionalization with the thiol compounds. Both relevant Raman bands were highlighted in light grey.

### 3 Results and discussion

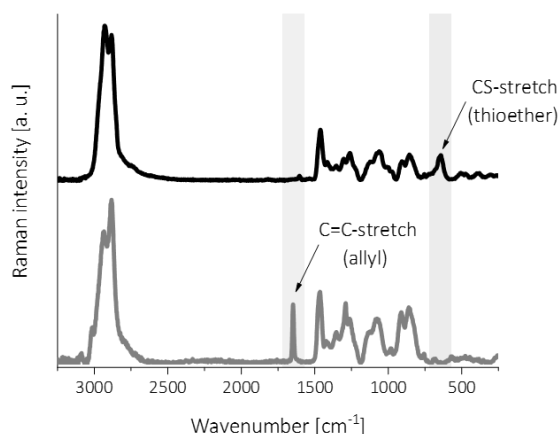


**Figure 32.** Raman spectrum of P(G<sub>50</sub>-co-SEt<sub>10</sub>-co-SDec<sub>2</sub>) (top, black) in comparison to P(G<sub>50</sub>-co-AGE<sub>12</sub>) (bottom, grey), displaying the absence of allyl vibration as well as the presence of thioether stretching after thiol-ene reaction.

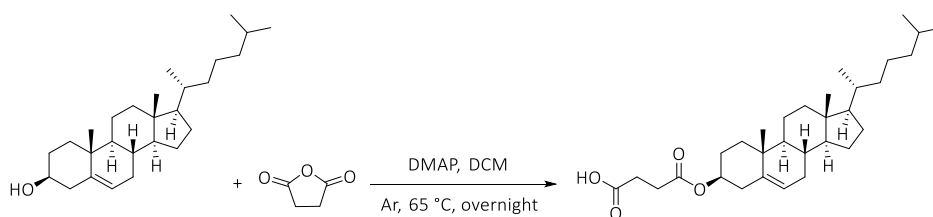
Molecular weight distribution, more precisely values of  $\bar{M}_w$ ,  $\bar{M}_n$  and  $\bar{D}$  of these different alkyl-functionalized PGs obtained by SEC analysis (see **Section 5.4.2** to **Section 5.4.13**) indicated that the side chain functionalities possibly provoke interactions with the SEC column material. Combined with the fact that such amphiphilic polymer form aggregates at the required concentration (see detailed study in **Section 3.2.1.3**), leads to distorted values for  $\bar{M}_w$ ,  $\bar{M}_n$  and  $\bar{D}$ . However, the values received by SEC measurements for the unfunctionalized starting polymer P(G<sub>50</sub>-co-AGE<sub>12</sub>) (SEC (RI, DMF):  $\bar{M}_w$  = 5718 Da,  $\bar{M}_n$  = 4812 Da,  $\bar{D}$  = 1.12) were in good agreement with the expected molecular weight of 5146 Da determined via <sup>1</sup>H-NMR spectroscopy (see **Table 24**).

#### 3.2.1.2 Synthesis of cholesteryl-functionalized PGs

The direct binding of cholesterol in the form of thiocholesterol via thiol-ene reaction, which was sufficiently described in previous sections, was not feasible due to steric hindrance. In order to introduce cholesterol to the PG backbone, the ability of conjugating carboxylic acid directly to primary amines by activation of the carboxyl groups was used. Carbodiimide compounds, as *N*-(3-dimethylaminopropyl)-*N'*-ethylcarbodiimide hydrochloride (EDC), can be utilized activating carboxylic acids to facilitate the crosslinking to primary amines under carboxamide bond formation. Improving the efficiency of this EDC activation process, *N*-hydroxysuccinimide (NHS) was additionally included. Starting from cholesterol, several working steps were necessary enabling the even described attachment.

Based on P(G<sub>50</sub>-CO-AGE<sub>6</sub>), in this section two different amine functionalities were introduced by bimolecular reaction with EtSH and molecules, terminated with a thiol as well as an amine unit (see **Scheme 7**). The obtained polymers were named as P(G<sub>50</sub>-CO-SEt<sub>10</sub>-CO-NH<sub>2(0.5)</sub>) and P(G<sub>50</sub>-CO-SEt<sub>10</sub>-CO-SPEG-NH<sub>2(0.5)</sub>). Thereafter, the carboxylic acid contained cholesteryl unit, termed as Chol-COOH, was attached via activation with the carbodiimide EDC and with assistance of the additive NHS, as shown in **Scheme 8**.

First, Chol-COOH was synthesized by reaction of cholesterol with succinic anhydride in dichloromethane (DCM) in the presence of 4-(dimethylamino) pyridine (DMAP), as displayed in **Scheme 6**. Succinic anhydride was added in a slight excess ensuring the complete reaction of all hydroxy groups. After stirring overnight under reflux and successive purification, Chol-COOH was received as colorless powder with a yield of 82 wt%. The successful anhydride linkage was proven by <sup>1</sup>H-NMR, FT-IR and Raman spectroscopy (see **Section 5.4.14**).



**Scheme 6.** Synthesis of Chol-COOH via reaction of cholesterol and succinic anhydride according to literature of Yang *et al.*<sup>[413]</sup>

The signals in the <sup>1</sup>H-NMR spectrum in **Figure 33** at 5.37 ppm and 4.69-4.58 ppm assigned to the methine protons H-14 and H-16. Two multiplets in the range of 2.70 ppm to 2.58 ppm were attributed to the methylene protons of the succinyl unit, indicating the cleavage of the anhydride. Additionally, all other methylene protons in cholesterol were found between 2.33 ppm and 1.07 ppm. The signals appearing at a chemical shift of 1.02 ppm and 0.91 ppm were contributed to the methyl protons H-7 and H-19, whereas H-1 was detected at 0.86 ppm and H-23 as a singlet at 0.68 ppm.

### 3 Results and discussion

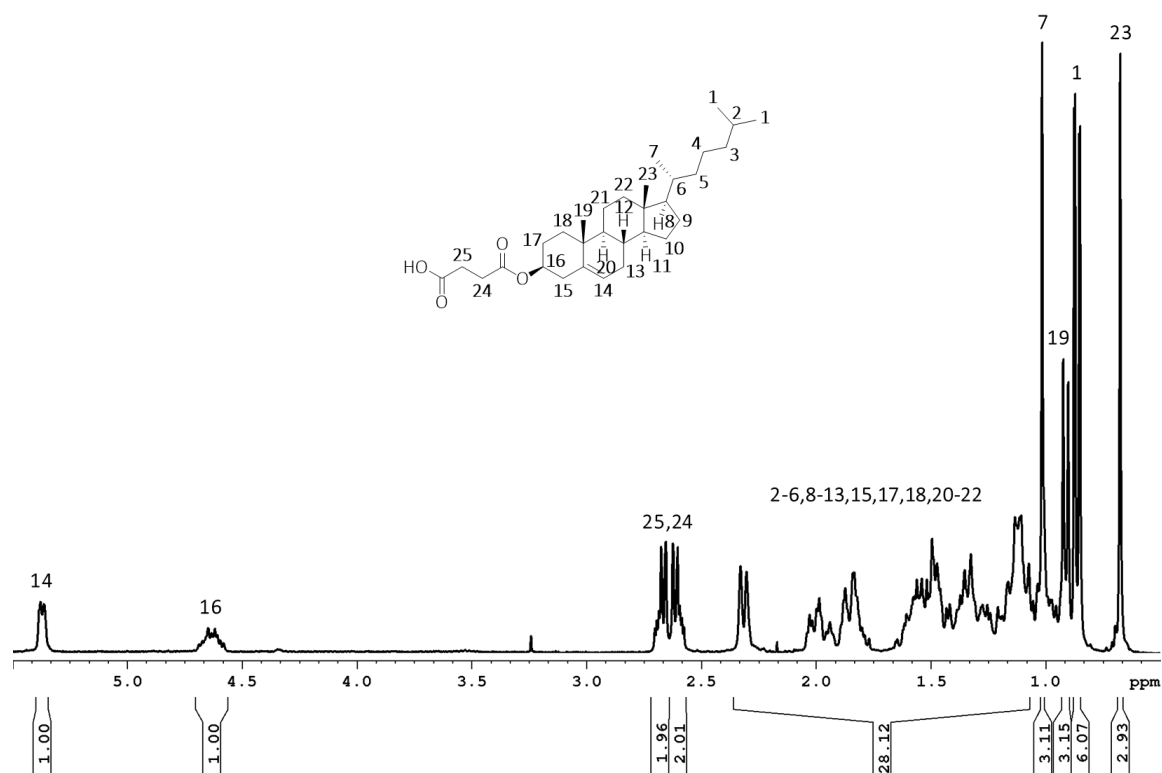


**Figure 33.**  $^1\text{H-NMR}$  spectrum of Chol-COOH, received by reaction of cholesterol with succinic anhydride.

Further FT-IR spectroscopy was performed to detect if Chol-COOH was obtained including a free carboxylic terminal. For clarity, **Figure 34** displays the transmittance spectrum of Chol-COOH (top, orange) compared to the educts cholesterol (middle, black) and succinic anhydride (bottom, grey), whereby relevant band areas were highlighted in light grey. It was observed that the characteristic symmetric and asymmetric C=O vibration bands ( $1859\text{ cm}^{-1}$  and  $1775\text{ cm}^{-1}$ ) of the anhydride functionality not remained intact. Instead, an intensive C=O-stretching band at  $1708\text{ cm}^{-1}$  was present, assigned to the carboxylic acid group, as well as a signal at  $1729\text{ cm}^{-1}$  which correspond to the C=O-stretching vibration of the formed aliphatic ester. In addition, all other vibration bands belonging to Chol-COOH were found at  $3430\text{ cm}^{-1}$  (OH),  $2934\text{-}2867\text{ cm}^{-1}$  (CH,  $\text{CH}_2$ ,  $\text{CH}_3$ ),  $1174\text{ cm}^{-1}$  and  $1025\text{ cm}^{-1}$  (COC) as well as  $957\text{-}737\text{ cm}^{-1}$  (CC).

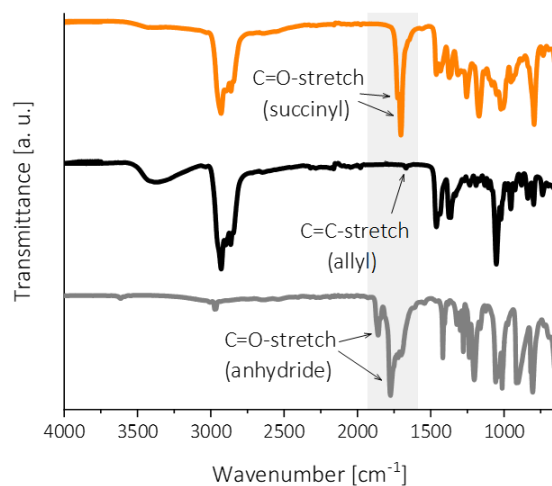
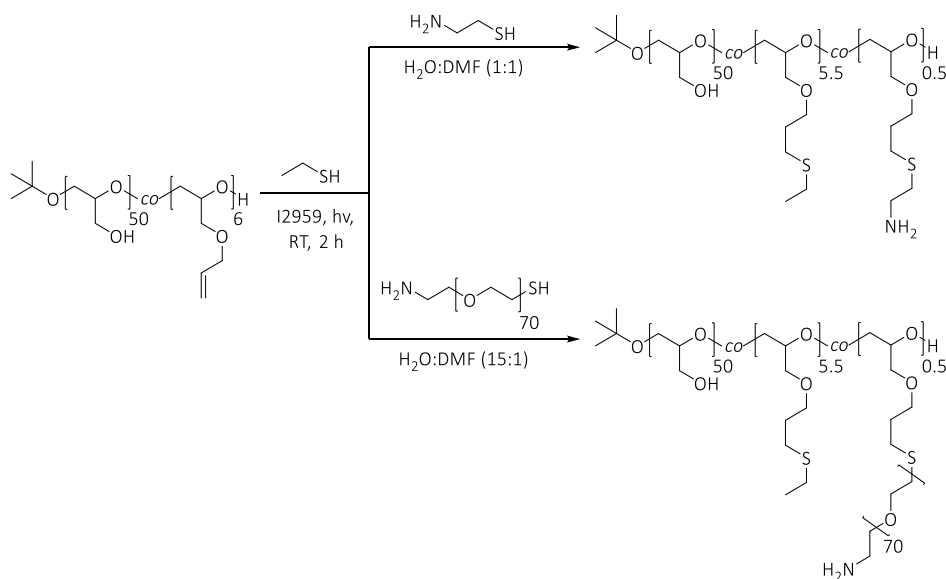


**Figure 34.** FT-IR transmittance spectrum of Chol-COOH (top, orange) in comparison to the educts cholesterol (middle, black) and succinic anhydride (bottom, grey).

Besides the even described carboxylic acid-functionalized compound Chol-COOH a primary amine is needed for the EDC/NHS-activated crosslinking reaction. In order to receive amine-modified PG, a bimolecular thiol-ene reaction of  $P(G_{50-co-AGE_6})$  with EtSH and cysteamine or alpha-mercapto-omega-amino poly(ethylene glycol) (HS-PEG-NH<sub>2</sub>) in a mixture of H<sub>2</sub>O and DMF, initiated by addition of I2959, was conducted (see **Scheme 7**). After two hours stirring at RT and UV irradiation followed by purification via dialysis and lyophilization,  $P(G_{50-co-SEt_{5.5-co-NH_{2(0.5)}}})$  and  $P(G_{50-co-SEt_{5.5-co-SPEG-NH_{2(0.5)}}})$  were obtained as a yellowish oil and a colorless solid, respectively. Only a very small number of amine groups were introduced into the PG to maintain the water solubility of the polymer even after cholesterol functionalization. The PEG linker was used to increase the hydrophilicity of the polymer, ensuring better water solubility, what is especially essential after attachment of the hydrophobic cholesteryl group. Concerning the subsequent AuNP coating with the functionalized polymers, a further effect of the PEG linker was keeping the large hydrophobic compound at distance from the particle surface.

### 3 Results and discussion



**Scheme 7.** Synthesis of P(G<sub>50</sub>-co-SEt<sub>5.5</sub>-co-NH<sub>2(0.5)</sub>) and P(G<sub>50</sub>-co-SEt<sub>5.5</sub>-co-SPEG-NH<sub>2(0.5)</sub>) by bimolecular thiol-ene reaction of P(G<sub>50</sub>-co-AGE<sub>6</sub>) with EtSH and cysteamine or HS-PEG-NH<sub>2</sub>.

The introduction of amine functionalities was proven via <sup>1</sup>H-NMR, FT-IR, Raman and SEC analysis (see **Section 5.4.15** and **Section 5.4.17**). Due to the analogy of P(G<sub>50</sub>-co-SEt<sub>5.5</sub>-co-NH<sub>2(0.5)</sub>) and P(G<sub>50</sub>-co-SEt<sub>5.5</sub>-co-SPEG-NH<sub>2(0.5)</sub>) regarding their chemical structure, hereafter the analyzation will be shown exemplarily for P(G<sub>50</sub>-co-SEt<sub>5.5</sub>-co-NH<sub>2(0.5)</sub>).

In the <sup>1</sup>H-NMR spectrum in **Figure 35** the proton signals of the PG backbone were presented at 3.79-3.65 ppm. The triplet at 3.23 ppm and the quintet at 2.87 ppm were allocated to the methylene protons H-20 and H-18 next to the amine group of the bound cysteamine. Integration of these signals determined an introduction of 0.5 amine moieties per polymer. The spectrum showed further methylene protons (H-15-17 and H-13,14) at a chemical shift of 2.69-2.58 ppm and 1.90 ppm, respectively. The signals between 1.30 ppm and 1.28 ppm were attributed to the methyl protons of the thioethyl units and the *tert*-butyl end group. <sup>1</sup>H-NMR analyzation of the analog P(G<sub>50</sub>-co-SEt<sub>5.5</sub>-co-SPEG-NH<sub>2(0.5)</sub>) also revealed that the polymer carried 0.5 PEG-NH<sub>2</sub> chains (see **Section 5.4.17**).



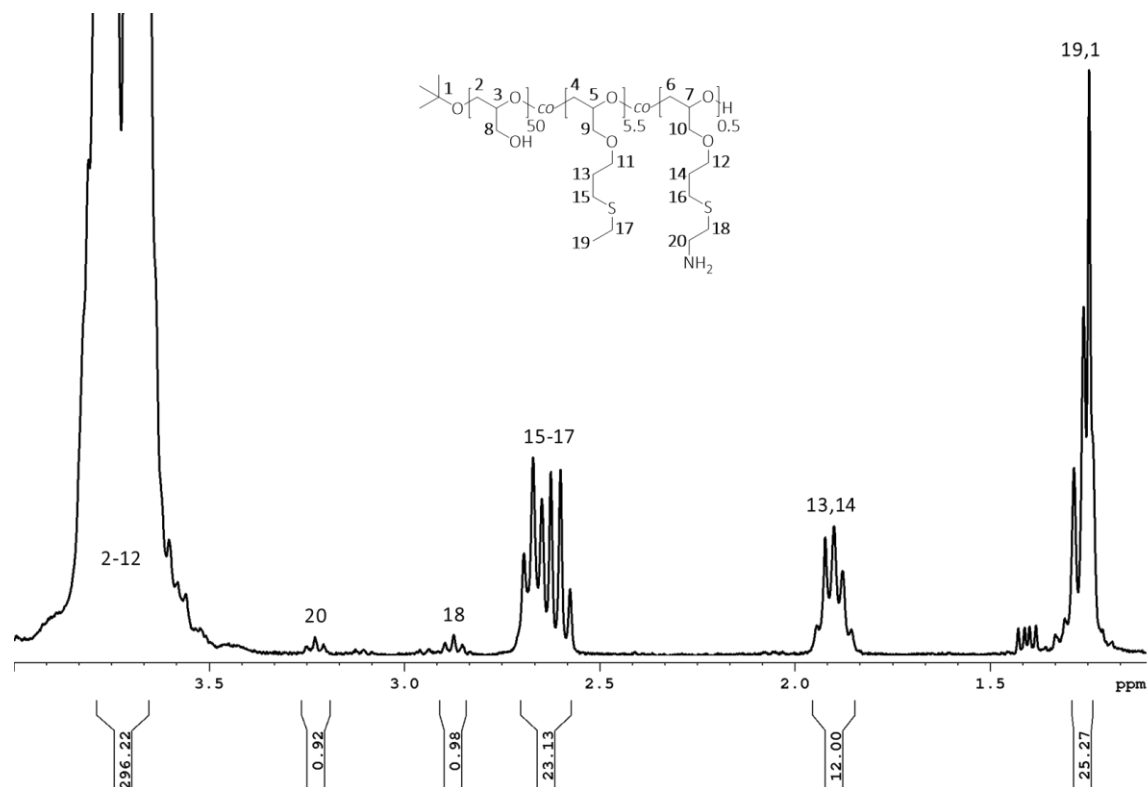


**Figure 35.**  $^1\text{H-NMR}$  spectrum of  $\text{P}(\text{G}_{50}\text{-co-SEt}_{5.5}\text{-co-NH}_{2(0.5)})$ , obtained by bimolecular thiol-ene reaction of  $\text{P}(\text{G}_{50}\text{-co-AGE}_6)$  with EtSH and cysteamine.

Furthermore, the number of amines within these PGs were quantitatively determined by TNBSA assay. **Table 7** reveals that the values identified by the assay matched well with these maintained by  $^1\text{H-NMR}$  spectroscopy.

**Table 7.** Amine amount determined by TNBSA assay and  $^1\text{H-NMR}$  spectroscopy of  $\text{P}(\text{G}_{50}\text{-co-SEt}_{5.5}\text{-co-NH}_{2(0.5)})$  and  $\text{P}(\text{G}_{50}\text{-co-SEt}_{5.5}\text{-co-SPEG-NH}_{2(0.5)})$  copolymers.

Polymer	Amine units per polymer chain	
	TNBSA assay	$^1\text{H-NMR}$ spectroscopy
$\text{P}(\text{G}_{50}\text{-co-SEt}_{5.5}\text{-co-NH}_{2(0.5)})$	0.5	0.5
$\text{P}(\text{G}_{50}\text{-co-SEt}_{5.5}\text{-co-SPEG-NH}_{2(0.5)})$	0.7	0.5

Total conversion of allyl groups was further proven by FT-IR and Raman spectroscopy. In **Figure 36a** no longer detection of the allylic  $\text{C}=\text{C}$  vibration at a wavelength of  $1646\text{ cm}^{-1}$ , but a signal at  $1604\text{ cm}^{-1}$ , assigned to the  $\text{NH}$ -deformation vibration, indicating introduction of amine functionalities. As depicted in **Figure 36b**, the absence of the allylic signal ( $1644\text{ cm}^{-1}$ ) and the presence of the thioether stretching vibration ( $655\text{ cm}^{-1}$ ) indicated a

### 3 Results and discussion

successful functionalization with the thiol compounds. Both relevant FT-IR and Raman bands were highlighted in light grey.

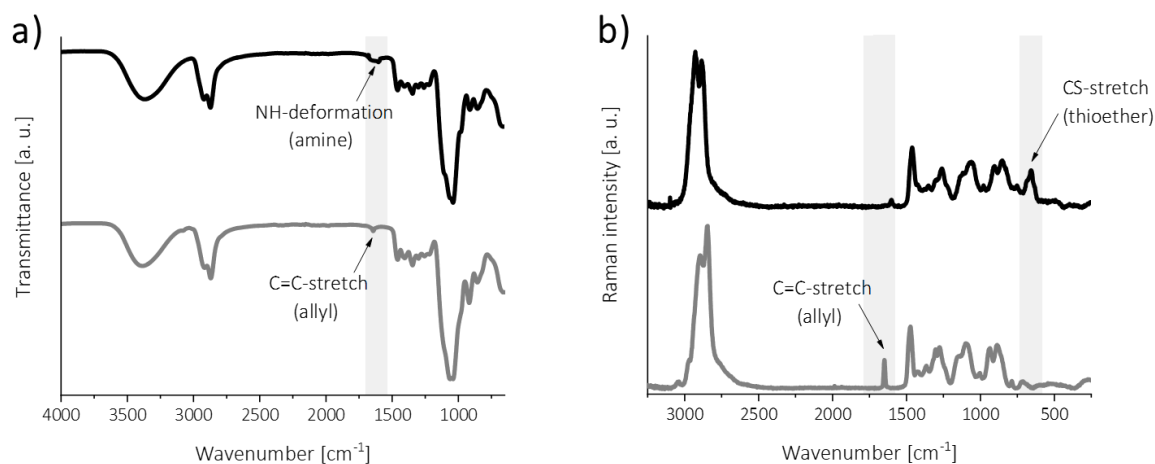
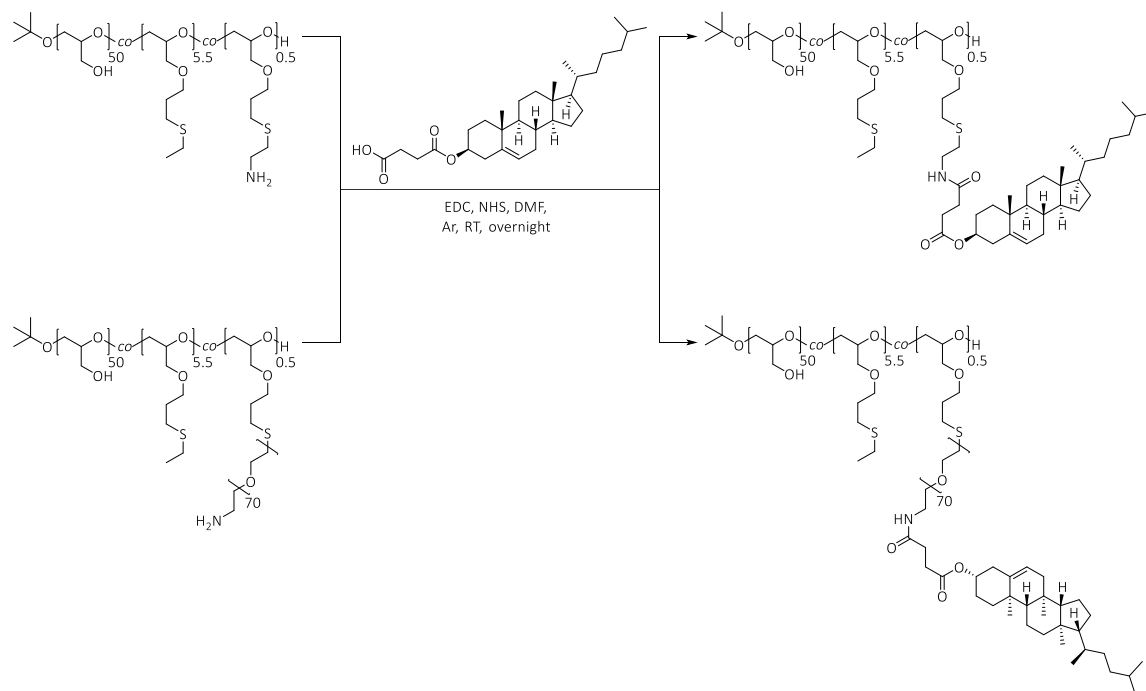


**Figure 36.** a) FT-IR transmittance and b) Raman spectra of P(G<sub>50</sub>-co-SEt<sub>5.5</sub>-co-NH<sub>2(0.5)</sub>) (top, black) in comparison to P(G<sub>50</sub>-co-AGE<sub>6</sub>) (bottom, grey), displaying the absence of allyl vibration as well as the presence of amine and thioether stretching after thiol-ene reaction.

Finally, Chol-COOH was activated by addition of EDC and NHS allowing the resulted carboxylic-activated group to react with the primary amines of the just presented polymers. As displayed in **Scheme 8**, the cholesteryl-functionalized PGs, termed as P(G<sub>50</sub>-co-SEt<sub>5.5</sub>-co-Chol<sub>0.5</sub>) and P(G<sub>50</sub>-co-SEt<sub>5.5</sub>-co-SPEG-Chol<sub>0.5</sub>), were synthesized under exclusion of air via reaction of P(G<sub>50</sub>-co-SEt<sub>5.5</sub>-co-NH<sub>2(0.5)</sub>) or P(G<sub>50</sub>-co-SEt<sub>5.5</sub>-co-SPEG-NH<sub>2(0.5)</sub>) with Chol-COOH in DMF and addition of the activators EDC and NHS. After stirring overnight at RT and successive purification, the polymers were received as greenish solids.



**Scheme 8.** Synthesis of  $P(G_{50}\text{-}co\text{-SEt}_{5.5}\text{-}co\text{-Chol}_{0.5})$  and  $P(G_{50}\text{-}co\text{-SEt}_{5.5}\text{-}co\text{-SPEG-Chol}_{0.5})$  via reaction of  $P(G_{50}\text{-}co\text{-SEt}_{5.5}\text{-}co\text{-NH}_{2(0.5)})$  or  $P(G_{50}\text{-}co\text{-SEt}_{5.5}\text{-}co\text{-SPEG-NH}_{2(0.5)})$  with cholesterol-COOH, activated by addition of EDC and NHS.

The successful conjugation was confirmed by  $^1\text{H-NMR}$  and FT-IR spectroscopy as well as SEC analysis, as shown in **Section 5.4.16** and **Section 5.4.18**. In the following, the investigation will be shown exemplarily for  $P(G_{50}\text{-}co\text{-SEt}_{5.5}\text{-}co\text{-Chol}_{0.5})$ , because of the similarity of both cholesteryl-modified PGs regarding their chemical structure. The relevant areas in the following spectra were highlighted in light grey.

**Figure 37** presents the  $^1\text{H-NMR}$  spectrum in deuterium oxide ( $\text{D}_2\text{O}$ ) of  $P(G_{50}\text{-}co\text{-SEt}_{5.5}\text{-}co\text{-Chol}_{0.5})$  (top, black) compared to  $P(G_{50}\text{-}co\text{-SEt}_{5.5}\text{-}co\text{-NH}_{2(0.5)})$  (bottom, grey). As no signals of the cholesteryl units could be detected in  $\text{D}_2\text{O}$ , a detailed characterization of the cholesteryl-functionalized PG by  $^1\text{H-NMR}$  spectroscopy seemed to be challenging. However, the absence of the proton signals at 3.23 ppm and 2.87 ppm belonging to the methylene groups next to the amine unit indicated cholesterol introduction, since binding changed the environment of these protons provoking a chemical shift. Owing to an overlap of the shifted signals with other proton signals of PG, an exact assignment of these methylene groups in  $P(G_{50}\text{-}co\text{-SEt}_{5.5}\text{-}co\text{-Chol}_{0.5})$  was not feasible, as shown in **Figure 37** (top spectrum). Integration of the signals at 2.70-2.58 ppm attributed to the methylene protons H-15-18 suggested the attachment of cholesteryl units. In addition, investigation of  $P(G_{50}\text{-}co\text{-SEt}_{5.5}\text{-}co\text{-SPEG-Chol}_{0.5})$  via  $^1\text{H-NMR}$  spectroscopy concluded a total conversion of amine

### 3 Results and discussion

groups (see **Section 5.4.18**). Measuring  $^1\text{H-NMR}$  in dimethyl sulfoxide (DMSO) (data not shown) indeed showed proton signals of cholesterol and the polymer backbone, however, an exact assignment of the other relevant proton signals was not possible due to overlapping signals.

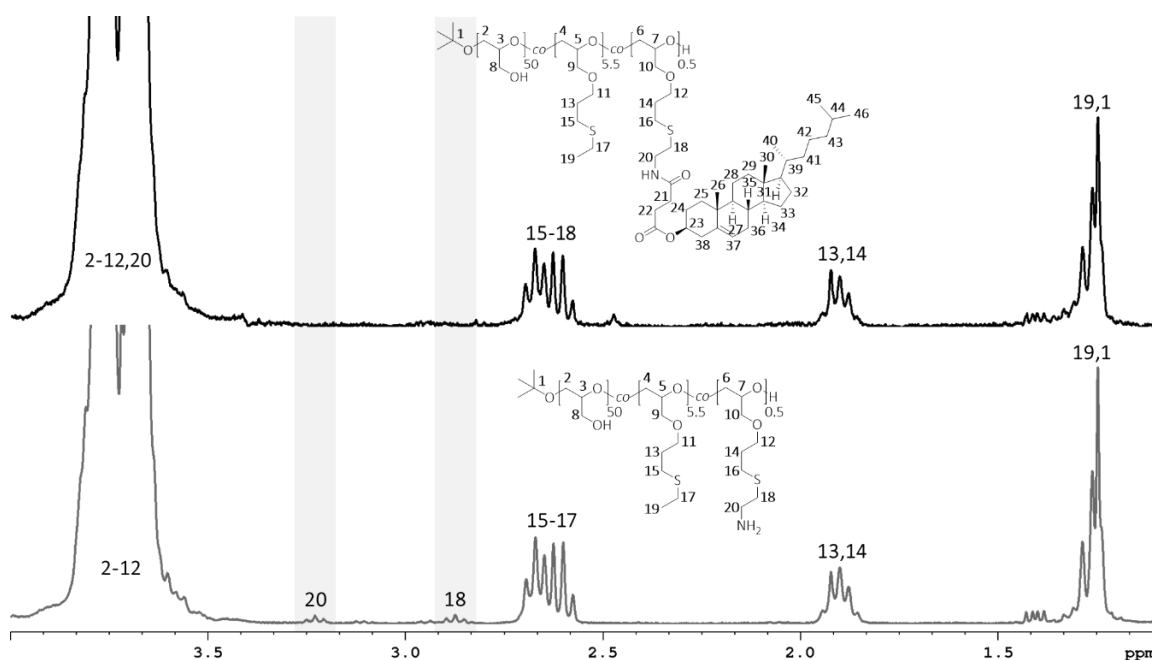


**Figure 37.**  $^1\text{H-NMR}$  spectrum in  $\text{D}_2\text{O}$  of  $\text{P}(\text{G}_{50}\text{-co-SEt}_{5.5}\text{-co-Chol}_{0.5})$  (top, black) in comparison with the educt  $\text{P}(\text{G}_{50}\text{-co-SEt}_{5.5}\text{-co-NH}_{2(0.5)})$  (bottom, grey).

In contrast to characterization by  $^1\text{H-NMR}$  spectroscopy, FT-IR measurements clearly verified successful reaction with Chol-COOH. For better comparison, **Figure 38a** displayed the FT-IR transmittance spectra of  $\text{P}(\text{G}_{50}\text{-co-SEt}_{5.5}\text{-co-Chol}_{0.5})$  (top, orange) as well as of the educts  $\text{P}(\text{G}_{50}\text{-co-SEt}_{5.5}\text{-co-NH}_{2(0.5)})$  (middle, black) and Chol-COOH (bottom, grey). The wavenumber region revealing relevant bands were highlighted in light grey. The detection of the C=O-stretching band at  $1731\text{ cm}^{-1}$  and especially of the C=O-stretching ( $1649\text{ cm}^{-1}$ ) and NH-deformation ( $1588\text{ cm}^{-1}$ ) vibrations corresponding to the formed carboxamide indicated a successful crosslinking between the amine functionalities of  $\text{P}(\text{G}_{50}\text{-co-SEt}_{5.5}\text{-co-NH}_{2(0.5)})$  and the carboxylic acid terminal of Chol-COOH. The absence of the intense carboxylic acid band as seen for Chol-COOH further proved evidence for the binding as well as the carboxamide bond formation. Furthermore, all other bands assigned to  $\text{P}(\text{G}_{50}\text{-co-SEt}_{5.5}\text{-co-Chol}_{0.5})$  were found at  $3383\text{ cm}^{-1}$  (OH),  $2927\text{-}2880\text{ cm}^{-1}$  and  $1465\text{-}1465\text{ cm}^{-1}$  ( $\text{CH}_2$ ,  $\text{CH}_3$ ),  $1060\text{ cm}^{-1}$  (COC) as well as  $962\text{-}842\text{ cm}^{-1}$  (CC). Moreover, Raman measurement of PG after cholesterol binding showed a low intensity band at  $1665\text{ cm}^{-1}$ , attributable to the C=C

vibration of the cholesteryl unit, as seen in **Figure 38b**. Similar results were obtained for the analog polymer  $P(G_{50}\text{-}co\text{-SEt}_{5.5}\text{-SPEG-Chol}_{0.5})$ , whereby a PEG linker was introduced (see **Section 5.4.18**).

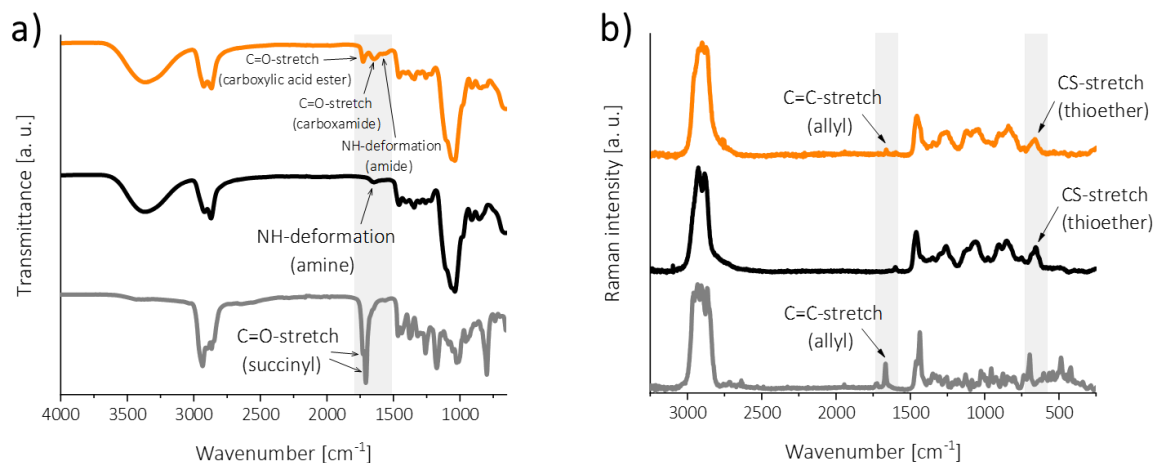


**Figure 38.** a) FT-IR transmittance and b) Raman spectra of  $P(G_{50}\text{-}co\text{-SEt}_{5.5}\text{-}co\text{-Chol}_{0.5})$  (top, orange) in comparison with the educts  $P(G_{50}\text{-}co\text{-SEt}_{5.5}\text{-}co\text{-NH}_{2(0.5)})$  (middle, black) and Chol-COOH (bottom, grey).

In addition, by reaction with TNBSA it was confirmed that no amines were present after binding Chol-COOH to  $P(G_{50}\text{-}co\text{-SEt}_{5.5}\text{-}co\text{-NH}_{2(0.5)})$  and  $P(G_{50}\text{-}co\text{-SEt}_{5.5}\text{-}co\text{-SPEG-NH}_{2(0.5)})$ .

As previously mentioned for the alkyl-functionalized PGs, SEC results of both cholesteryl-functionalized PGs (see **Section 5.4.16** and **Section 5.4.18**) also suggested that the side chain functionalities possibly provoke interactions with the SEC column material. Combined with the fact that such amphiphilic polymer form aggregates at the required concentration (see detailed study in the next section), leads to distorted values for  $\bar{M}_w$ ,  $\bar{M}_n$  and  $\bar{D}$ . However, the values obtained by SEC analysis for the unfunctionalized starting polymer  $P(G_{50}\text{-}co\text{-AGE}_6)$  (SEC (RI, DMF):  $\bar{M}_w = 5198$  Da,  $\bar{M}_n = 4100$  Da,  $\bar{D} = 1.27$ ) were in good agreement with the expected molecular weight of 4461 Da determined via <sup>1</sup>H-NMR spectroscopy (see **Table 24**).

### 3.2.1.3 Critical Aggregation Concentration (CAC) of hydrophobic functionalized PGs

Owing to the amphiphilic character of the before presented multifunctional PGs, containing both a hydrophilic polymer backbone and hydrophobic side chains, the formation of nano-sized micelle-like aggregates in aqueous solution can be induced by intra- or intermolecular hydrophobic interactions. The aggregation behavior of amphiphilic polymers has already been extensively studied. In literature there are some investigations

### 3 Results and discussion

demonstrating dependency of aggregation behavior on various factors such as temperature, ionic strength and concentration.<sup>[390,414,415]</sup> Besides the solution conditions, the physicochemical properties and chemical structure of the polymers particularly affect the formation of aggregates in an aqueous solution, as it is known that self-assembly is driven by different noncovalent forces like hydrogen bonding, van der Waals or hydrophobic interaction, whereby latter has major effect. Riemer *et al.*<sup>[416]</sup> studied the association behavior of polymers with different hydrophobicity by varying the degree of alkyl modifications and the length of the alkyl chains, displaying a correlation between the molecular architecture and the ability forming aggregates. In addition, the self-assembly of amphiphilic polymers with bulky cholesteryl derivatives attached as hydrophobic compound was of great interest, showing contributions of cholesteryl end-capped and side-chain functionalized water-soluble copolymers.<sup>[417,418]</sup> The biotechnology and medicine allowing encapsulation of drugs in the hydrophobic inner core.<sup>[419,420]</sup> However, the advantage of intended self-aggregation used for drug carrying was not relevant in this work. Rather, it was necessary to avoid polymer aggregates to achieve attachment of the amphiphilic polymers to the particle surface via sulfur-gold bond, resulting in NPs with high colloidal stability.

In order to receive detailed information about the self-aggregation of polymeric amphiphiles, several assays including experimental methods such as fluorescence probe technique with pyrene, transmission electron microscopy or light scattering measurements are presented in literature.<sup>[421-423]</sup> All analysis demonstrated that aggregation is dependent on compound concentration, and thus the aim was to determine the CAC, which represent the threshold concentration above which aggregates are formed.

Herein, the aggregation behavior of the hydrophobically modified PGs from **Section 3.2.1.1** and **Section 3.2.1.2** in aqueous solution was studied by DLS as a function of polymer concentration, which allowed the determination of CAC. A dilution series from 300  $\mu\text{M}$  to 0.25  $\mu\text{M}$  of each polymer was generated and DLS measurements were performed. The results were evaluated in terms of the derived count rate (DCR) in kilo counts per second (kcps), which is representative of the light scattering intensity. In general, in the dilute regime, the larger the concentration, the larger the scattered intensity, showing a linear increase up to a certain concentration. For high concentrations, especially at which

molecules form aggregates, the scattering behavior changes, resulting in an abrupt increase in the DCR with increasing compound concentration.<sup>[422]</sup> In **Figure 39**, for each hydrophobic polymer the DCR was plotted against its related molarity, whereby **Figure 39a** shows the data of pentane (C5) functionalized PGs carrying one to four pentane chains, **Figure 39b** and **Figure 39c** of the respective polymers modified with decane (C10) and pentadecane (C15) units, while **Figure 39d** presents both cholesteryl-functionalized PGs. For better comparability, the axes were all scaled identically, whereby the inserts show the respective graphs with adjusted y-axis scaling.

First, it is noticed in **Figure 39** that the DCR increased especially at higher concentrations with increasing length of the attached alkyl chains, indicating an enhancement in hydrophobicity. While the difference between functionalization with C5 and C10 units is rather small, a much larger DCR is seen for C15 modification. As larger particles scatter more light than smaller ones, which implies a higher DCR, the results revealed, as expected, that more hydrophobic polymers have higher tendency to aggregate. Since cholesterol is a large, inflexible, and very hydrophobic molecule forming strong hydrophobic association, higher DCR values would have been expected. Thus, it appeared that in this case the influence of cholesterol functionalization was less crucial since these polymers carry only 0.5 cholesteryl units. However, it should also be noted that an exact comparison between the alkyl- and the cholesteryl-modified polymers is not feasible as they are based on PGs with different ratios (see **Section 3.2.1.1** and **Section 3.2.1.2**).

### 3 Results and discussion

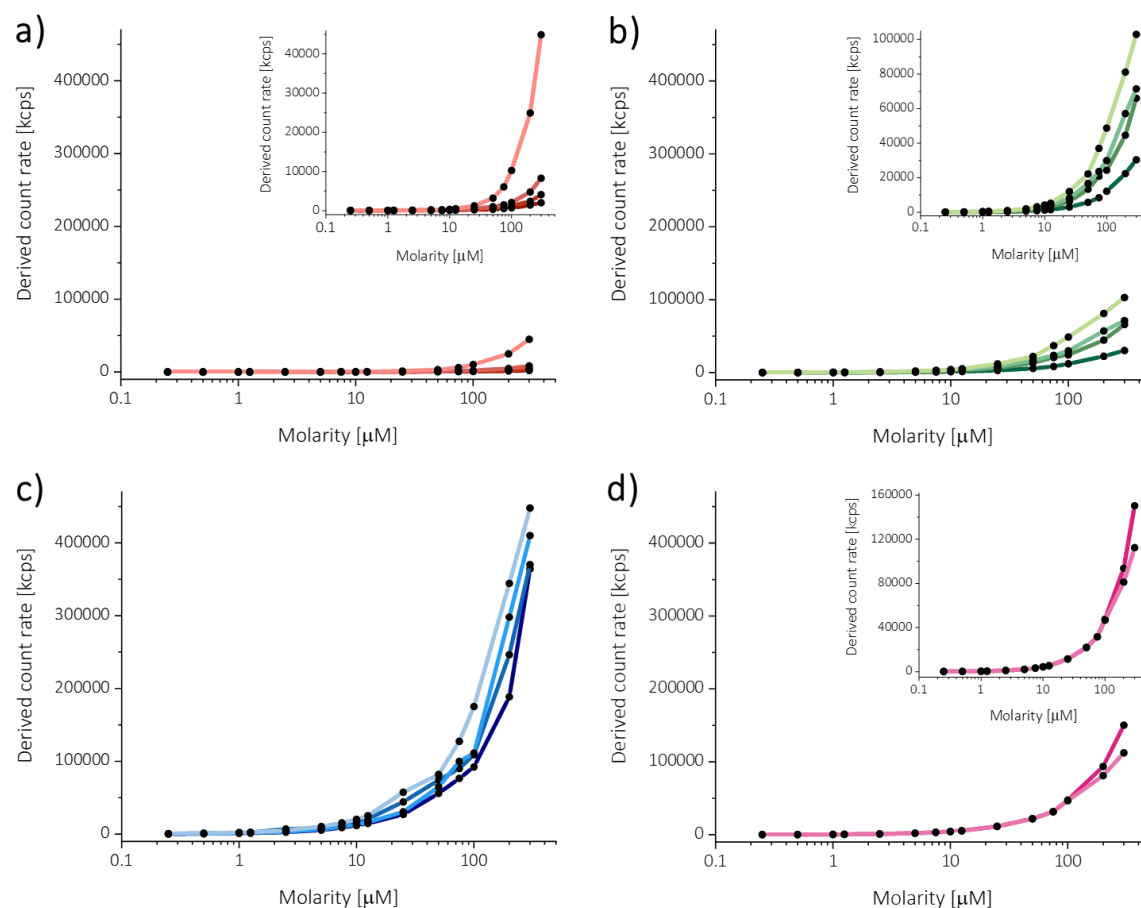


**Figure 39.** Derived count rate (DCR) as a function of various polymer molarities of a) pentane-functionalized PG with one (dark red), two (red), three (middle red) and four (light red) pentane units, b) decane-functionalized PG carrying one (dark green), two (green), three (middle green) and four (light green) decane moieties, c) pentadecane-functionalized PG carrying one (dark blue), two (blue), three (middle blue) and four (light blue) pentadecane groups and d) cholesteryl-functionalized PG with (light pink) and without (pink) PEG-linker. The inserts show the respective graphs with adjusted scaling of the y-axis.

Focusing on the various measurements with same functionality but different functionalization degree, a slight increase in light scattering intensity could be observed with increasing number of hydrophobic chains bound to the polymers. While this trend was only detectable at higher molarities, for higher dilutions no differences were apparent. Regarding  $P(\text{G}_{50}\text{-co-SEt}_{5.5}\text{-co-Chol}_{0.5})$  and  $P(\text{G}_{50}\text{-co-SEt}_{5.5}\text{-co-SPEG-Chol}_{0.5})$ , **Figure 39d** shows no, respectively no pronounced deviation of the DCR of the two polymers. Consequently, the hydrophilic PEG linker had rather no decisive influence on the water solubility, which was actually one of the reasons for the introduction of the PEG linker.

Having a look at the progression of the different measured values in **Figure 39**, at first linearity of DCR can be seen, whereas at a certain concentration the value increased abruptly. This increase was detected for each polymer at a specific molarity and indicated



the beginning of self-aggregation in aqueous solution, representing the CAC. In **Table 8**, the determined CAC values for each polymer are listed.

Differences between the different polymers and concentrations could also be detected optically. While clear polymeric solutions were evident for C5 modification over the entire molarity range used here, functionalization of PG with cholesteryl as well as three and four C10 units showed turbidity at higher concentrations. On the other hand, the polymers modified with the more hydrophobic C15 group were very cloudy at high molarities and became continuously clearer upon further dilution. These observations correlated with the higher light scattering intensities obtained via DLS measurements. However, an exact determination of the CAC was not feasible by optical evaluation.

**Table 8.** Values of CAC in  $\mu\text{M}$  of hydrophobic modified PGs used in this thesis, obtained by dLS investigations. For  $\text{P}(\text{G}_{50}\text{-co-SEt}_{12\text{-n-co-SPent}_n})$  with  $n = 1, 2, 3$  no CAC could be detected within the applied molarity range using the DLS method.

Sample	CAC [ $\mu\text{M}$ ]			
	n = 1	n = 2	n = 3	n = 4
$\text{P}(\text{G}_{50}\text{-co-SEt}_{12\text{-n-co-SPent}_n})$	-	-	-	200
$\text{P}(\text{G}_{50}\text{-co-SEt}_{12\text{-n-co-SDec}_n})$	75	50	50	50
$\text{P}(\text{G}_{50}\text{-co-SEt}_{12\text{-n-co-SPentadec}_n})$	12.5	12.5	12.5	10
$\text{P}(\text{G}_{50}\text{-co-SEt}_{5.5\text{-co-Chol}_{0.5}})$			25	
$\text{P}(\text{G}_{50}\text{-co-SEt}_{5.5\text{-co-SPEG-Chol}_{0.5}})$			25	

It was found in **Table 8**, that for  $\text{P}(\text{G}_{50}\text{-co-SEt}_{12\text{-n-co-SPent}_n})$  with  $n = 1, 2, 3$  no CAC could be detected within the applied molarity range using the DLS method. Furthermore, the CAC decreased in the order  $\text{P}(\text{G}_{50}\text{-co-SEt}_{8\text{-co-SPent}_4})$  ( $200 \mu\text{M}$ ) >  $\text{P}(\text{G}_{50}\text{-co-SEt}_{12\text{-n-co-SDec}_n})$  ( $75/50 \mu\text{M}$ ) >  $\text{P}(\text{G}_{50}\text{-co-SEt}_{5.5\text{-co-Chol}_{0.5}}) \approx \text{P}(\text{G}_{50}\text{-co-SEt}_{5.5\text{-co-SPEG-Chol}_{0.5}})$  ( $25 \mu\text{M}$ ) >  $\text{P}(\text{G}_{50}\text{-co-SEt}_{12\text{-n-co-SPentadec}_n})$  ( $12.5/10 \mu\text{M}$ ), indicating the highest tendency to form aggregates in C15 functionalization. The aggregation tendency was even higher than for the PGs modified with the bulky, very hydrophobic cholesteryl group, possibly due to the different degrees of functionalization. Moreover, these polymers were based on PGs with various backbones ( $\text{P}(\text{G}_{50}\text{-co-AGE}_{12})$  for alkyl versus  $\text{P}(\text{G}_{50}\text{-co-AGE}_6)$  for cholesteryl functionalization), meaning consequently different ratios between hydrophilic and

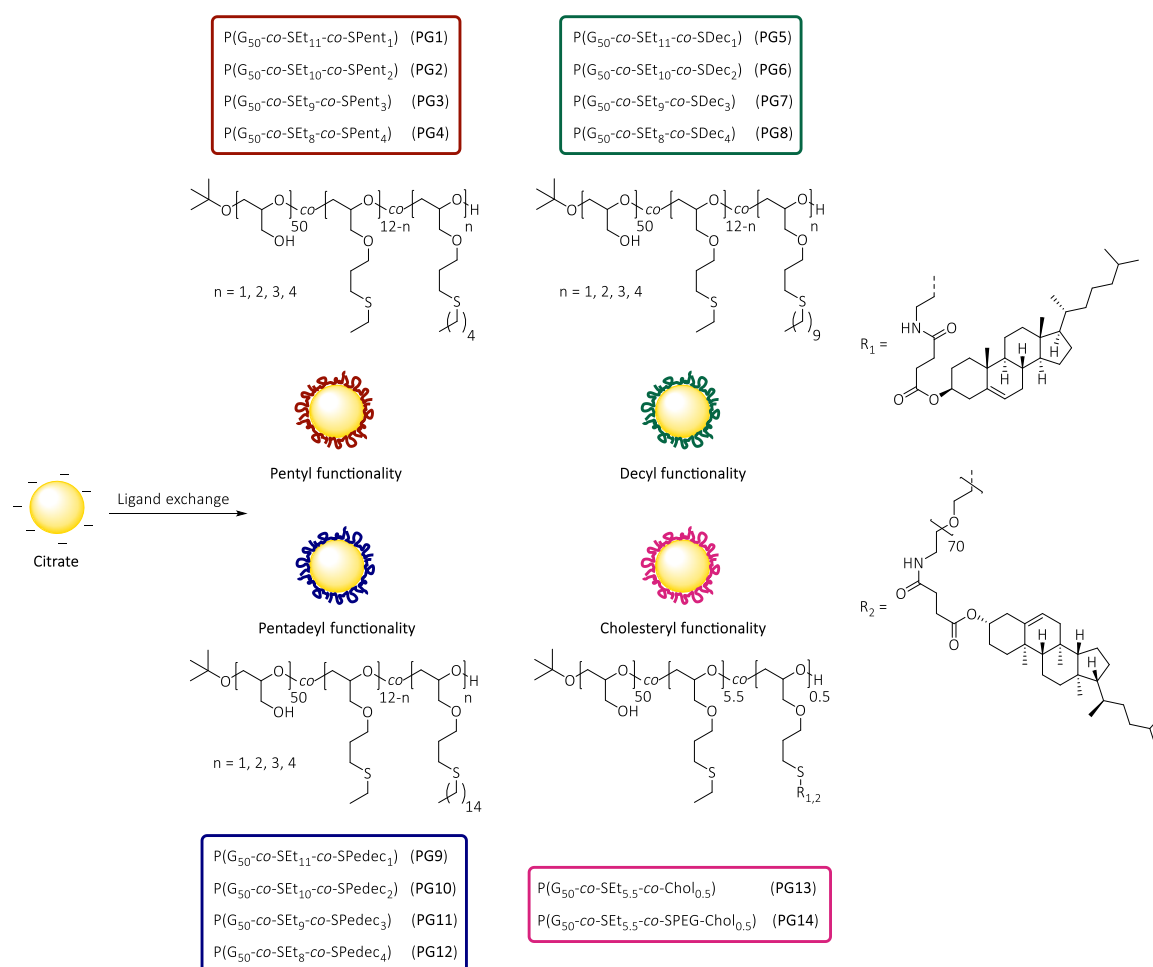
### 3 Results and discussion

hydrophobic moieties, especially after further modification. Focusing on the CAC values of PGs with same functionality but different degree of hydrophobicity, as expected, a reduction of functionalization degree led to a CAC shift to higher concentration. However, this effect was only observed at a certain level of functionalization.

After successful determination of the CAC, the polymers were subsequently attached to the AuNPs, whereby it was relevant ensuring an aggregate-free polymeric solution. Furthermore, aggregates should not be existent even after polymer binding, however, the coating layer should be thick enough to guarantee colloidal stability. Hence, it was of necessity to identify the optimal polymer concentration for particle modification receiving stable and aggregation-free coated AuNPs, which was abundantly examined in **Section 3.2.2.2.1** and **Section 3.2.2.2.2**.

## 3.2.2 Au surface modification with hydrophobic functionalized PGs

Surface functionalization of citrate-stabilized AuNPs with the in Section 3.2.1 described multifunctional hydrophobic modified polymers was performed by ligand exchange reaction under formation of stable quasi-covalent gold-sulfur bonds<sup>[189]</sup>. Since the polymer attachment and consequently the stability of the particles is dependent on their curvature<sup>[8,118]</sup>, two different particle diameter (15 nm and 30 nm) were utilized in this thesis. In this section, first the 15 nm and 30 nm citrate-AuNPs were investigated via SEM imaging, UV-Vis absorbance, DLS and zeta potential measurements as well as FT-IR spectroscopy, whereafter the successful polymer attachment was proven by same characterization methods. In order to obtain stable and aggregate-free coated AuNPs, systematic studies were performed to determine the optimal polymer concentration for particle functionalization and stabilization.



**Scheme 9.** Simplified illustration of AuNPs functionalized with multifunctional hydrophobic PGs via ligand exchange reaction.

### 3 Results and discussion

As depicted in **Scheme 9**, throughout this section pentyl functionalization was labeled in red, decyl functionalization in green, pentadecyl functionalization in blue and cholesteryl functionalization in pink. Citrate-stabilized AuNPs were marked in yellow (15 nm) and orange (30 nm), respectively.

#### 3.2.2.1 Citrate-stabilized AuNPs

Spherical AuNPs, suspended in an aqueous citrate solution, with particle diameter of 15 nm and 30 nm were commercially purchased. The citrate stabilization provided long term stability of the NPs and allowed a readily ligand exchange due to weak association of citrate with the particle surface, as already discussed in **Section 2.1.3**. Here, firstly the Au mass concentration of the colloidal solution was analyzed via ICP-MS, obtaining a particle concentration of 44.9 mg/L for 15 nm AuNPs as well as of 43.1 mg/L for 30 nm AuNPs. Furthermore, the NP size and shape were analyzed by using SEM imaging (see **Figure 40a** and **Figure 40b**). In consistency with the literature<sup>[355,356]</sup>, it was found that AuNPs are not all perfectly spherical and uniform in size, as marked for 30 nm AuNPs by red arrows in **Figure 40b**. In accordance with the supplier's specification, particles with size deviation of less than 8% were identified, yielding in diameters with deviation of  $14.5 \pm 1.1$  nm (15 nm AuNPs) and  $29.3 \pm 1.9$  nm (30 nm AuNPs). Afterwards, the citrate-stabilized AuNPs were investigated by DLS, UV-Vis absorbance and zeta potential measurements as well as FT-IR spectroscopy. **Figure 40** shows for 15 nm AuNPs a characteristic SPR band at 520 nm, a monodispersed curve progression with PDI = 0.061, a mean hydrodynamic diameter  $d$  (Z-average) of  $d = 18.7 \pm 0.9$  nm as well as a negative zeta potential value of  $\zeta = -31.7 \pm 1.3$  mV, which indicated that the surface of the AuNPs was capped with citric acid. Furthermore, for 30 nm AuNPs values of SPR = 524 nm, PDI = 0.173,  $d = 32.3 \pm 0.7$  nm and  $\zeta = -36.7 \pm 1.4$  mV were received. The before mentioned values are further listed in **Table 29** in **Section 5.4.1.1**, and compared with the manufacturer's specifications. The presence of the C=O-stretching vibrations at  $1583\text{ cm}^{-1}$  and  $1398\text{ cm}^{-1}$  as well as  $1591\text{ cm}^{-1}$  and  $1390\text{ cm}^{-1}$ , assigned to the carboxylate moiety, suggested that citrate is used as capping agent. As the particles were dispersed in aqueous solution, the FT-IR spectra consisted of a broad OH-stretching band centered at  $3375\text{ cm}^{-1}$  and  $3355\text{ cm}^{-1}$ , respectively, as displayed in **Figure 40e**.

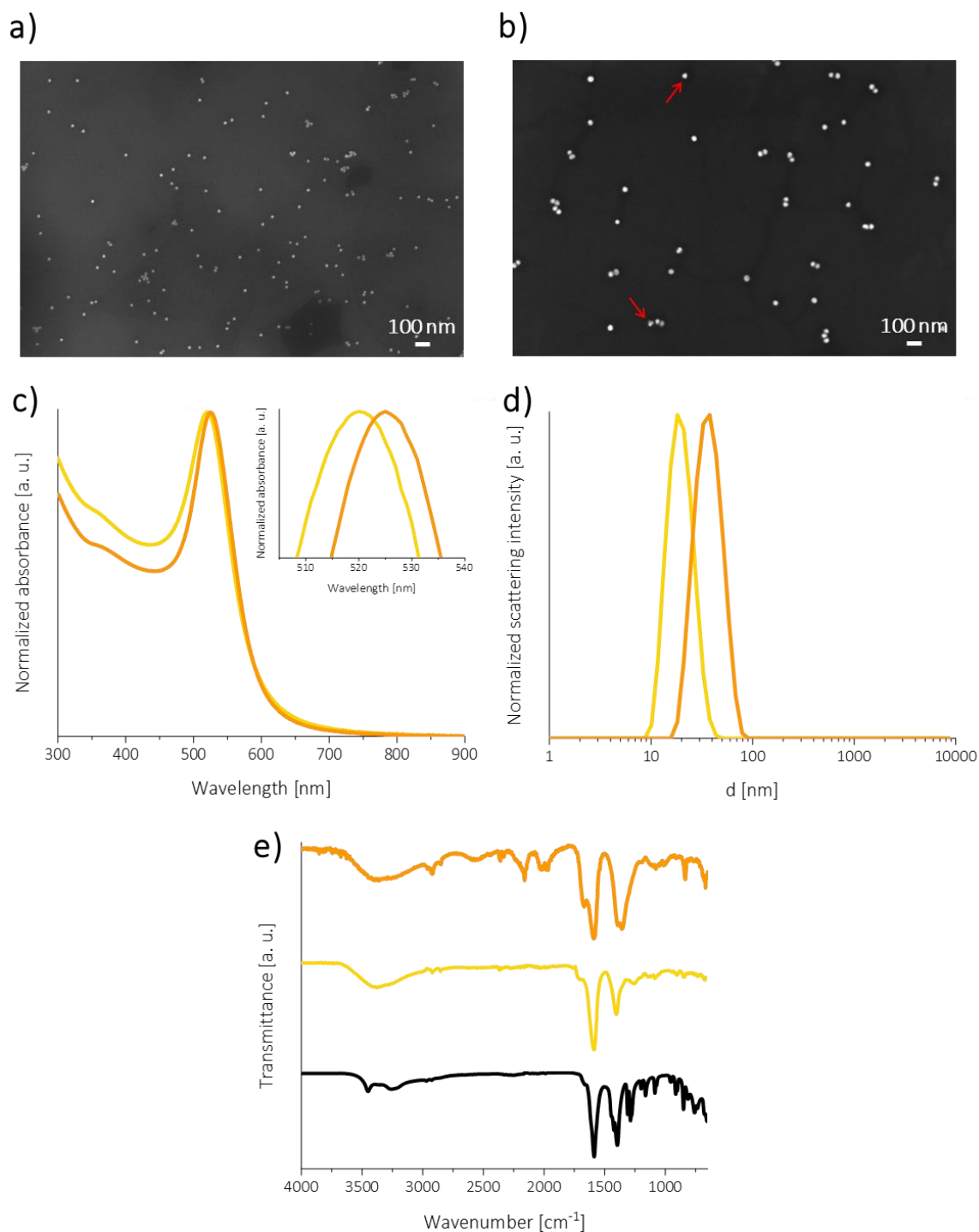


**Figure 40.** SEM images of a) 15 nm AuNPs and b) 30 nm AuNPs, c) normalized UV-Vis absorbance and d) normalized DLS spectra of 15 nm (yellow) and 30 nm (orange) citrate-AuNPs as well as e) FT-IR spectra of citrate-stabilized 15 nm AuNPs (middle, yellow) and 30 nm AuNPs (top, orange) compared to pure sodium citrate (bottom, black). The red arrows in the SEM image denote the particles that are not perfectly spherical. UV-Vis and DLS spectra show a SPR shift to higher wavelength respectively a larger  $d$  by increasing the particle size. The insert in (c) displays an enlarged part of the respective graph with adjusted scaling of both axes, to improve visualization of the SPR shift. In the FT-IR spectra, both AuNPs show characteristic C=O stretching as of pure citrate and an additional OH-vibration at  $3375\text{ cm}^{-1}$  respectively  $3355\text{ cm}^{-1}$  due to particle dispersion in water.

### 3 Results and discussion

#### 3.2.2.2 Adsorption of alkyl- and cholesteryl-functionalized PGs on citrate-AuNPs

In order to bind the multifunctional alkyl- and cholesteryl-modified polymers of **Section 3.2.1** to the particle surface, a ligand exchange reaction on citrate-AuNPs was conducted, resulting in sterically stabilized NPs. As described in **Section 2.1.3.4**, steric stabilization is dependent on various factors and that stability is only effective when the polymer layer on the surface of the particle is completely occupied, not exhibiting any gaps. Incomplete coverage of the NP surface may cause attraction of the colloids and in particular long-chain and high molecular weight polymers having multiple anchor groups may interact with more than one NP with a patchy surface coverage leading to aggregation, which is referred to as bridging flocculation.<sup>[157]</sup> Complete coverage, and thus stabilization, is dependent on the concentration of the adsorbed polymer in solution, as reported by Wang *et al.*<sup>[424]</sup> In this study it was shown, that at low concentrations one single polymer molecule could possibly bind to more than one NP nearby, leading to flocculation bridging, while a dense PEG layer was obtained at higher concentrations, preventing particle aggregation. Furthermore, the concentration of the polymeric solution also affects the arrangement of multifunctional polymers adsorbed on the NP surface. PVP at low concentrations adopted an arrangement on silica particles that is characterized by trains, whereas the conformation changed to loops and tails by increasing the concentration.<sup>[425]</sup> Latter causes not only an increase in layer thickness due to the more elongated polymer segments, but there is also the possibility that the long, extended loops and tails could reach other NPs and adsorb to them, resulting in bridging of the particles.<sup>[105,157]</sup> The concentration dependent conformational change may be explained by the enhanced competition for binding of the polymers to the particle surface. This competition occurs not only upon increasing the concentration, but also by reducing the surface area of the NPs.<sup>[426,427]</sup>

Consequently, to prevent aggregation, the optimal polymer concentration for particle coating has to be determined. Hence, in the following, two studies were performed analyzing the ideal concentration to maintain stable and aggregate-free polymer-modified AuNPs. Firstly, in this section, the concentration which is maximum possible obtaining particles without bridging was investigated via DLS (see **Section 3.2.2.2.1**). DLS is an established technique to estimate the aggregation state of the NPs, as this method allows

the measurement of the effective size of colloidal particles. Secondly, in **Section 3.2.2.2.2**, the minimal concentration leading to sufficiently dense adsorption layer was determined. This was proven by addition of a salt solution and subsequent absorbance measurements since an increase in ionic strength provokes aggregation. After the detailed studies on optimal polymer concentration for AuNP coating, the successful functionalization was verified using different spectroscopic methods such as DLS, UV-Vis and FT-IR (see **Section 3.2.2.2.3**).

#### *3.2.2.2.1 Determination of optimal polymer concentration for aggregate-free NPs via DLS*

To investigate the maximum possible concentration obtaining aggregate-free coated particles, a fixed volume of AuNPs was incubated with a fixed volume of polymeric solution. More precisely, 50  $\mu\text{L}$  of the different hydrophobic polymer solutions with various molarities around the in **Section 3.2.1.3** determined CAC were added to 500  $\mu\text{L}$  of 15 nm AuNPs (Au mass concentration of 44.7 mg/L as specified via ICP-MS). On the other hand, 520  $\mu\text{L}$  30 nm AuNPs (Au mass concentration of 43.1 mg/L as determined by ICP-MS), were incubated with 50  $\mu\text{L}$  polymeric solution to achieve identical Au mass concentrations, which was beneficial for further experiments throughout this thesis. After incubation overnight, two consecutive centrifugation and redispersion cycles were performed to remove unbound polymers, followed by analyzation via DLS measurements. As an example of concentration dependent aggregation behavior, **Figure 41** exemplarily reveals the normalized DLS spectra of 15 nm and 30 nm AuNPs modified with P(G<sub>50</sub>-co-SEt<sub>8</sub>-co-SPentadec<sub>4</sub>) in the range of 2.5  $\mu\text{M}$  to 12.5  $\mu\text{M}$  and 25  $\mu\text{M}$  to 150  $\mu\text{M}$ , respectively. While AuNP coating with higher polymeric molar concentrations resulted in detection of two peaks, whereas the peak at larger hydrodynamic diameters corresponds to aggregates, a unimodal size distribution was observed using lower molarities. In **Figure 41a** the intensity of the peak at larger hydrodynamic diameter decreased by decreasing the molar concentration for particle functionalization and was no longer detectable at a molarity of 5  $\mu\text{M}$ . With regard to the polymer arrangement, at this molar concentration, it seemed that the number of long extended tails and loops is probable sufficiently low preventing bridging flocculation, or their existence could even be excluded, and thus the polymer molecules can be expected to be close to the NP surface exhibiting train conformation. Since the size

### 3 Results and discussion

distribution depicted in the figure below is the intensity-weighted size distribution, the intensity decrease correlated with the reduction in the number of aggregates, as larger particles scatter more light. A similar concentration dependent trend could be observed for 30 nm AuNPs, receiving aggregate-free particle solutions using a molarity of 50  $\mu\text{M}$ , as depicted in **Figure 41b**. These results indicated, in accordance with literature, that a higher polymer amount per unit surface area can be adsorbed as the particle size increased.<sup>[428]</sup> However, the differences could also be related to the fact that the polymers may adopt a slightly different conformation on the various sized NPs.<sup>[118,427]</sup>

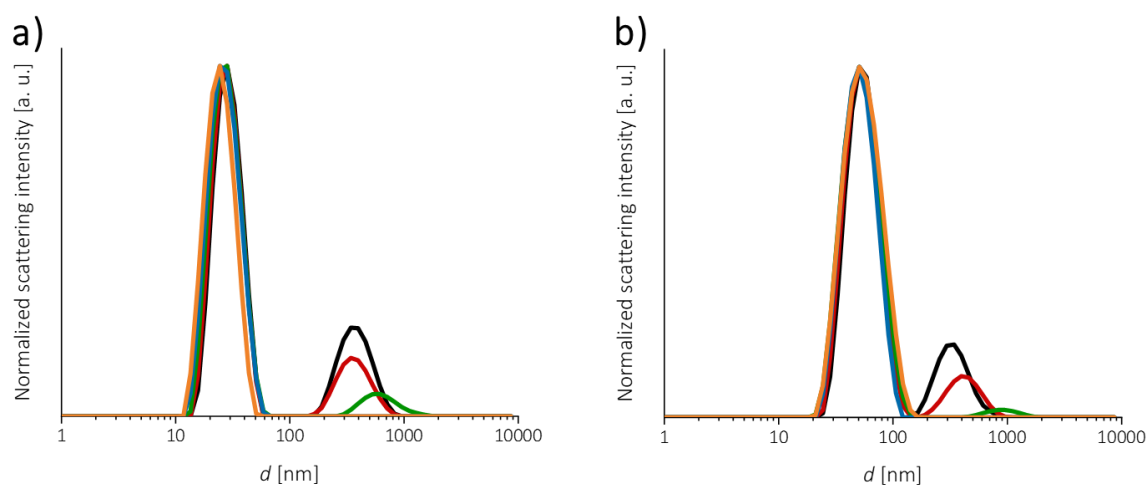


**Figure 41.** Normalized DLS spectra of a) 15 nm and b) 30 nm AuNPs modified with P(G<sub>50-co-SEt<sub>8</sub>-co-SPentadec<sub>4</sub></sub>) in the range of 5  $\mu\text{M}$  to 12.5  $\mu\text{M}$  and 25  $\mu\text{M}$  to 150  $\mu\text{M}$ , respectively. 15 nm AuNPs incubated with molar concentrations of 12.5  $\mu\text{M}$  (black), 10  $\mu\text{M}$  (red), 7.5  $\mu\text{M}$  (green), 5  $\mu\text{M}$  (blue) and 2.5  $\mu\text{M}$  (orange) are shown. For 30 nm AuNPs molarities of 150  $\mu\text{M}$  (black), 100  $\mu\text{M}$  (red), 75  $\mu\text{M}$  (green), 50  $\mu\text{M}$  (blue) and 25  $\mu\text{M}$  (orange) were used.

The maximum molarity values of the other hydrophobic PGs which allow to obtain aggregate-free AuNPs after polymer coating are presented in **Table 9**. By DLS measurements no aggregation formation for AuNP coating with P(G<sub>50-co-SEt<sub>12-n</sub>-co-SPent<sub>n</sub></sub>) and P(G<sub>50-co-SEt<sub>12-n</sub>-co-SDec<sub>n</sub></sub>) with  $n = 1, 2, 3, 4$  was determined even with the highest used polymeric molar concentration of 300  $\mu\text{M}$ . However, upon incubation of the particles with a 0.5  $\mu\text{M}$  polymeric solution only, in some cases a second peak was observed at larger hydrodynamic diameter, indicating agglomeration (data not shown). The reason that no aggregates were formed when using highest molarities, but the polymers, especially P(G<sub>50-co-SEt<sub>12-n</sub>-co-SDec<sub>n</sub></sub>) with  $n = 1, 2, 3, 4$ , exhibited a CAC in aqueous solution (see **Section 3.2.1.3**), may be explained by the fact that the colloidal NPs were already in a citrate-based solution and thus the polymer samples were further diluted after addition. In



contrast, modification with the polymer carrying the longest alkyl chain led to a concentration-dependent formation of aggregates, which is also contingent on the functionalization degree. This trend is in accordance with the results for CAC determination of **Section 3.2.1.3**, as more hydrophobic polymers have higher tendency to aggregate. Furthermore, it can be hypothesized that due to the longer alkyl side chains, which require more space on the particle surface, no close packing of adsorbed polymer sequences was present, but rather highly extended loops and tails allowing access to unoccupied surfaces, and thus enhancing bridging flocculation. The presence of more elongated segments strengthening this effect. In addition, aggregation could possibly also arise from attractive interactions between protruding alkyl chains of neighboring NPs. Consequently, lower polymer molarities were necessary to avoid this flocculation as the adsorption conformation changes within the concentration, which was referenced at the beginning of this **Section 3.2.2.2**. For 15 nm AuNPs coated with cholesteryl-modified PGs aggregate-free particles were obtained by adding a 50  $\mu\text{M}$  and 25  $\mu\text{M}$  polymeric solution, respectively. The extent of the bulky cholesteryl moiety, especially by the polymer with the long PEG linker, was not so significant due to the presence of just 0.5 hydrophobic units.

### 3 Results and discussion

**Table 9.** Maximum values of polymer solution molarities which allow to obtain aggregate-free AuNPs after coating with multifunctional hydrophobic polymers.

Sample	Molarity [ $\mu\text{M}$ ]			
	n = 1	n = 2	n = 3	n = 4
<b>15 nm AuNPs</b>				
P(G <sub>50</sub> -CO-SEt <sub>12-n</sub> -CO-SPent <sub>n</sub> )	300	300	300	300
P(G <sub>50</sub> -CO-SEt <sub>12-n</sub> -CO-SDec <sub>n</sub> )	300	300	300	300
P(G <sub>50</sub> -CO-SEt <sub>12-n</sub> -CO-SPentadec <sub>n</sub> )	10	7.5	5	5
P(G <sub>50</sub> -CO-SEt <sub>5.5</sub> -CO-Chol <sub>0.5</sub> )		50		
P(G <sub>50</sub> -CO-SEt <sub>5.5</sub> -CO-SPEG-Chol <sub>0.5</sub> )		25		
<b>30 nm AuNPs</b>				
P(G <sub>50</sub> -CO-SEt <sub>12-n</sub> -CO-SPent <sub>n</sub> )	300	300	300	300
P(G <sub>50</sub> -CO-SEt <sub>12-n</sub> -CO-SDec <sub>n</sub> )	300	300	300	300
P(G <sub>50</sub> -CO-SEt <sub>12-n</sub> -CO-SPentadec <sub>n</sub> )	100	75	75	50
P(G <sub>50</sub> -CO-SEt <sub>5.5</sub> -CO-Chol <sub>0.5</sub> )		300		
P(G <sub>50</sub> -CO-SEt <sub>5.5</sub> -CO-SPEG-Chol <sub>0.5</sub> )		200		

#### 3.2.2.2.2 Determination of optimal polymer concentration by addition of a salt solution

As previously described, the conformation of adsorbed polymers show dependency on the concentration, resulting in a dense coating layer due to predominant train conformation at a certain polymer concentration.<sup>[425]</sup> A close packing density, signifying high stability, is important to prevent anchoring ions to the NPs surface by dispersion of AuNPs in liquids with increased ionic strength since this provokes aggregation caused by to overweighing of van der Waals attraction compared to the polymer-induced steric repulsion. In addition to the possible adsorption of ions to the particle surface, the ionic strength is also known to affect the conformation of the bound polymers<sup>[118]</sup>, which in turn can alter the stability and flocculation behavior. In literature several examinations about salt-induced aggregation of metal NPs were found. Xie *et al.*<sup>[429]</sup>, for instance, investigated the relevant protein amount requiring stable AuNPs in a sodium chloride (NaCl) solution. Besides, the influence of ionic fluids on the stabilization of polymer-functionalized NPs has previously been studied in this thesis for AgNPs coated with thiol- and thioether-PEG as well as -PG (see

**Section 3.1.3.2).**<sup>[44]</sup> Similar investigations have already been carried out for various functionalized AuNPs.<sup>[17]</sup>

To receive quantitative data, herein, the molar concentration was determined, at which a sufficiently dense adsorption layer was formed to obtain stabilized particles upon addition of a salt solution provoking aggregation. Therefore, AuNPs of both sizes were incubated with polymeric solutions of the different hydrophobic PGs using various molarity ranges down to 1.25  $\mu\text{M}$  in the same way as described in **Section 3.2.2.2.1**. After purification by centrifugation, the colloidal solutions were treated with 1x PBS as well as 10% NaCl covering a broad range of ionic strength, followed by analyses via absorbance measurements in order to study their flocculation behavior. Since AuNPs exhibit a prominent SPR band in the UV-Vis spectrum, the stability of functionalized particles can in general be indicated by changes in the absorption spectrum, because agglomeration would cause, for instance, a broadening in the curve progression, a decrease in absorbance intensity, or a large shift of the SPR band.<sup>[11,115]</sup>

As exemplarily depicted for 15 nm AuNP modification with P(G<sub>50</sub>-co-SEt<sub>8</sub>-co-SPentadec<sub>4</sub>), the recorded spectra after adding ion-rich solutions are displayed in **Figure 42** and were compared to the untreated samples before salt addition. Depicted are particles incubated with molar concentrations between 10  $\mu\text{M}$  and 1.25  $\mu\text{M}$ , as both stable AuNPs and aggregation occurred in this molarity range. **Figure 42a** shows the absorbance spectra of the functionalized AuNPs, exhibiting a narrow curve progression. Only 15 nm AuNP incubated with a 1.25  $\mu\text{M}$  P(G<sub>50</sub>-co-SEt<sub>8</sub>-co-SPentadec<sub>4</sub>) solution resulted in a minor broadening in the wavelength range of 600 nm to 700 nm, not assumed to aggregation of the particles, as they demonstrated an intense red colored solution (see **Figure 42d**). After 2 h treatment with 10% NaCl solution, 15 nm AuNPs incubated with a molar concentration of 1.25  $\mu\text{M}$  displayed an extensive broadening of the SPR between 600 nm and 700 nm, indicating aggregation, while a small broadening was observed for particles pre-coated with a 2.5  $\mu\text{M}$  polymer solution. In contrast, the salt solution did not affect the plasmon band of the other samples (see **Figure 42b**). On the other hand, as displayed in **Figure 42c**, addition of 1x PBS to NPs previously incubated with this 1.25  $\mu\text{M}$  PG solution resulted in complete particle loss as can be seen by the significant shift of the absorbance maximum to higher wavelength and a notable decrease in the absorbance intensity. The latter is even

### 3 Results and discussion

recognizable, although the spectra were normalized. Due to the normalization, the spectra with low absorbance intensity did not exhibit a smooth curve progression, but rather a jagged line. In contrast to the treatment with NaCl, also particles pre-incubated with a 2.5  $\mu\text{M}$  polymeric solution exhibited a distinct broadening of the SPR band in the 600-700 nm range after addition of 1x PBS, owing to aggregation. These results could also be confirmed visually by the color change from red to blue or purple, as depicted in **Figure 42d**. It was demonstrated that 1x PBS has a stronger effect on the aggregation behavior than 10% NaCl, although the latter has a higher ionic strength. That the colloidal stability is not only dependent on the ionic strength, but on the type of salt solution as well as pH values, was reported by Fleer *et al.*<sup>[430]</sup> Moreover, it has been previously mentioned that the ionic strength can change the polymer conformation on the NPs<sup>[118]</sup>, suggesting that this may render the particle surface more or less accessible to ions.

Conclusively, these investigations demonstrated that at least a molar concentration of 5  $\mu\text{M}$  has to be used to functionalize the 15 nm AuNPs with P(G<sub>50</sub>-co-SEt<sub>8</sub>-co-SPentadec<sub>4</sub>) in order to obtain a particle solution stable in the different used ionic solutions. As figured out in the previous study for determining the optimal polymer concentration in **Section 3.2.2.2.1**, upon coating 15 nm AuNP with P(G<sub>50</sub>-co-SEt<sub>8</sub>-co-SPentadec<sub>4</sub>), the molar concentration of 5  $\mu\text{M}$  was also the maximum possible concentration to obtain aggregate-free particle solutions. This is rather challenging since small changes in the ratio of AuNP to polymer would lead to aggregation already in aqueous solution or later in this thesis during incubation with the protein solution.

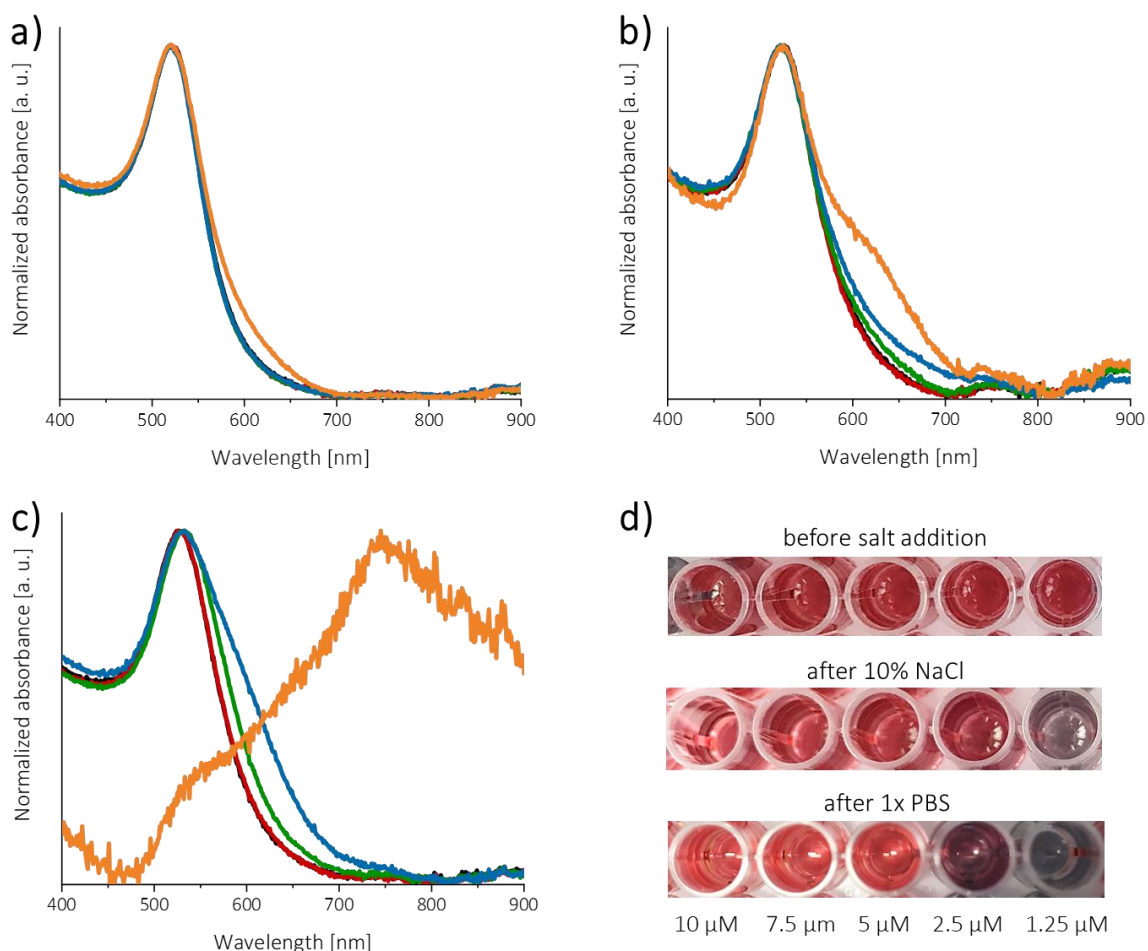


**Figure 42.** Normalized absorbance spectra of 15 nm AuNPs modified with P(G<sub>50</sub>-co-SEt<sub>8</sub>-co-SPentadec<sub>4</sub>) in different molarity ranges a) before salt addition, b) after treatment with 10% NaCl and c) after addition of 1x PBS. Particles incubated with molar concentrations of 10 μM (black), 7.5 μM (red), 5 μM (green), 2.5 μM (blue) and 1.25 μM (orange) are shown. d) Images of functionalized particle solutions before and after salt addition indicating aggregation by color change from red to blue or purple.

For the other multifunctional hydrophobic modified polymers, the same procedure was followed as for the example with P(G<sub>50</sub>-co-SEt<sub>8</sub>-co-SPentadec<sub>4</sub>) presented above. The complete data are not shown here due to their analogy. However, the minimum molarities required to obtain stable particles after salt incubation are listed in **Table 10**. All samples did not show any significant differences. For 15 nm AuNPs pre-coated with the four pentane-functionalized PGs as well as P(G<sub>50</sub>-co-SEt<sub>12-n</sub>-co-SDec<sub>n</sub>) and P(G<sub>50</sub>-co-SEt<sub>12-n</sub>-co-SPentadec<sub>n</sub>) both with  $n = 1$ , a molar concentration of 2.5 μM was adequate to maintain particle stability after treatment with salt solutions. For all other PGs used, coating with a 5 μM polymer solution was required.

In addition, examinations on 30 nm AuNPs incubated with polymeric solutions of various molar concentrations was conducted to figure out their stabilization against ion-rich

### 3 Results and discussion

solutions (see **Figure 43**). 30 nm AuNPs mixed with different molar concentrations between 10  $\mu\text{M}$  and 1.25  $\mu\text{M}$  displayed a strong SPR band and a narrow curve progression, as depicted in **Figure 43a**. As previously observed in case of 15 nm AuNPs, pre-incubation of 30 nm AuNPs with 1.25  $\mu\text{M}$  P(G<sub>50</sub>-co-SEt<sub>8</sub>-co-SPentadec<sub>4</sub>) also led to little broadening between 600-700 nm. However, the red colored particle solution as seen in **Figure 43d** did not indicate aggregation. Addition of 10% NaCl caused particle loss of NPs pre-incubated with a 1.25  $\mu\text{M}$  solution of P(G<sub>50</sub>-co-SEt<sub>8</sub>-co-SPentadec<sub>4</sub>) owing to aggregation, since a significant absorbance decrease in the plasmon band and a second maximum at wavelength between 700 nm and 800 nm was detected (see **Figure 43b**). The reduction in absorbance intensity was visible even despite the normalization of the spectra, which in turn resulted in a jagged curve shape. The absorbance spectrum of 30 nm AuNPs incubated with a molar concentration of 2.5  $\mu\text{M}$  displayed a strong SPR band after NaCl treatment but a slightly changed curve shape at higher wavelengths. Since the particle solution, as seen in **Figure 43d**, turned purple after addition of NaCl, these were indications of agglomeration. In addition, the nearly complete discoloration of the colloidal solution previously coated with a 1.25  $\mu\text{M}$  polymer solution suggested particle loss upon NaCl addition due to coagulation. As already observed for the smaller sized AuNPs, the 2 h treatment with 1x PBS affected the colloidal stability to a greater extent than the 10% NaCl addition, although the latter has a higher ionic strength. Precoating of 30 nm AuNPs with a polymeric solution of 1.25  $\mu\text{M}$  and 2.5  $\mu\text{M}$  P(G<sub>50</sub>-co-SEt<sub>8</sub>-co-SPentadec<sub>4</sub>) proved insufficient to keep the particles stable in 1x PBS solution. As seen in **Figure 43c**, a reduced absorbance intensity and a changed curve progression was observed for both samples. The decrease in absorbance intensity was moderate for NPs pre-incubated with a molar concentration of 2.5  $\mu\text{M}$ , however, a second maximum was clearly visible. Also, 30 nm AuNPs previously mixed with a 5  $\mu\text{M}$  polymer solution resulted in broadening of the absorbance curve in the wavelength range of 600-800 nm after addition of PBS, indicating agglomeration. Latter could not be confirmed visually by a color change, as depicted in **Figure 43d**. In conclusion, a molar concentration of at least 7.5  $\mu\text{M}$  P(G<sub>50</sub>-co-SEt<sub>8</sub>-co-SPentadec<sub>4</sub>) has to be used to provide an adequate surface coating for 30 nm AuNPs being stable in ion-rich solutions. Consequently, adsorption of a larger amount of P(G<sub>50</sub>-co-SEt<sub>8</sub>-co-SPentadec<sub>4</sub>) on 30 nm AuNPs than on 15 nm AuNPs was required to obtain stable particles after addition of the same salt solution. This is consistent with research on AuNPs coated with PEG. It was found

that with increasing particle size, a higher number of PEG molecules per AuNP was required to form stable colloidal solutions in NaCl.<sup>[431]</sup>

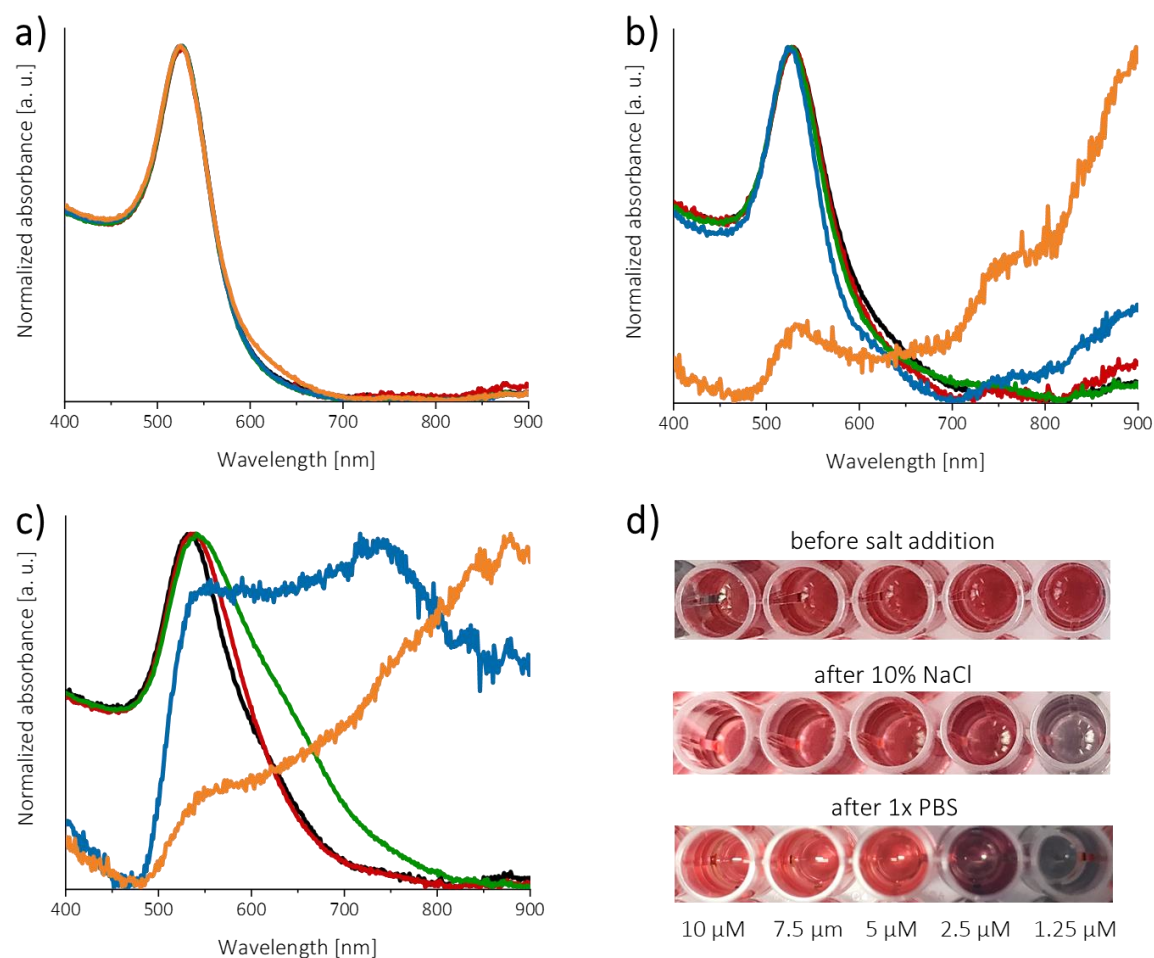


**Figure 43.** Normalized absorbance spectra of 30 nm AuNPs modified with P(G<sub>50</sub>-co-SEt<sub>8</sub>-co-SPentadec<sub>4</sub>) in different molarity ranges a) before salt addition, b) after treatment with 10% NaCl and c) after addition of 1x PBS. Particles incubated with molar concentrations of 10 μM (black), 7.5 μM (red), 5 μM (green), 2.5 μM (blue) and 1.25 μM (orange) are shown. d) Images of functionalized particle solutions before and after salt addition indicating aggregation by color change from red to blue or purple.

**Table 10** further shows the molar concentration of all other PGs used in this study that is needed to form stable 30 nm AuNPs in an ion-rich solution. It was expected that for larger particles a higher polymer concentration would be required to obtain a sufficient polymer layer, however, this was not found for all samples. Rather, for 30 nm AuNPs, stable particles were obtained using molarities between 2.5 μM and 7.5 μM.

### 3 Results and discussion

**Table 10.** Molarity values of polymer solutions added to 15 nm and 30 nm AuNPs to achieve colloidal stability even after addition of ion-rich solutions consisting of 10% NaCl and 1x PBS, respectively.

Sample	Molarity [ $\mu\text{M}$ ]			
	n = 1	n = 2	n = 3	n = 4
<b>15 nm AuNPs</b>				
P(G <sub>50</sub> -CO-SEt <sub>12-n</sub> -CO-SPent <sub>n</sub> )	2.5	2.5	2.5	2.5
P(G <sub>50</sub> -CO-SEt <sub>12-n</sub> -CO-SDec <sub>n</sub> )	2.5	5	5	5
P(G <sub>50</sub> -CO-SEt <sub>12-n</sub> -CO-SPentadec <sub>n</sub> )	2.5	5	5	5
P(G <sub>50</sub> -CO-SEt <sub>5.5</sub> -CO-Chol <sub>0.5</sub> )		5		
P(G <sub>50</sub> -CO-SEt <sub>5.5</sub> -CO-SPEG-Chol <sub>0.5</sub> )		5		
<b>30 nm AuNPs</b>				
P(G <sub>50</sub> -CO-SEt <sub>12-n</sub> -CO-SPent <sub>n</sub> )	2.5	2.5	2.5	5
P(G <sub>50</sub> -CO-SEt <sub>12-n</sub> -CO-SDec <sub>n</sub> )	5	5	2.5	5
P(G <sub>50</sub> -CO-SEt <sub>12-n</sub> -CO-SPentadec <sub>n</sub> )	5	5	7.5	7.5
P(G <sub>50</sub> -CO-SEt <sub>5.5</sub> -CO-Chol <sub>0.5</sub> )		5		
P(G <sub>50</sub> -CO-SEt <sub>5.5</sub> -CO-SPEG-Chol <sub>0.5</sub> )		2.5		

#### 3.2.2.2.3 Characterization of alkyl- and cholesteryl-functionalized AuNPs

The only negligible electrostatic stabilization with citrate compounds enables easy AuNP surface modification by ligand exchange reaction<sup>[181]</sup>, especially with sulfur-containing ligands under formation of a quasi-covalent gold-sulfur bond. Thus, in this study, the synthesized alkyl- and cholesteryl-functionalized PGs containing multiple thioether units (presented in detail in **Section 3.2.1**) were attached to citrate-stabilized 15 nm and 30 nm AuNPs, resulting in sterically stabilized particles. Therefore, 100  $\mu\text{L}$  of the polymeric solution (used molarities are listed in **Table 30**) was added to 1 mL of the purchased 15 nm citrate-AuNPs and 1.04 mL of the 30 nm AuNPs, in order to obtain similar Au mass concentration within in the colloidal solutions. After incubation overnight at RT under constant shaking (200 rpm), the colloidal solutions were purified by two successive centrifugation (20 000 g, 30 min, 4 °C) and redispersion cycles in milli-Q H<sub>2</sub>O in order to remove unbound polymers. Successful attachment of the different polymers to the particle



surface was confirmed by various methods (UV-Vis, DLS, zeta potential, FT-IR), which is presented in the following.

In the further course of this section, the alkyl- and cholesteryl-functionalized PGs P(G<sub>50</sub>-co-SEt<sub>11</sub>-co-SPent<sub>1</sub>), P(G<sub>50</sub>-co-SEt<sub>10</sub>-co-SPent<sub>2</sub>), P(G<sub>50</sub>-co-SEt<sub>9</sub>-co-SPent<sub>3</sub>), P(G<sub>50</sub>-co-SEt<sub>8</sub>-co-SPent<sub>4</sub>), P(G<sub>50</sub>-co-SEt<sub>11</sub>-co-SDec<sub>1</sub>), P(G<sub>50</sub>-co-SEt<sub>10</sub>-co-SDec<sub>2</sub>), P(G<sub>50</sub>-co-SEt<sub>9</sub>-co-SDec<sub>3</sub>), P(G<sub>50</sub>-co-SEt<sub>8</sub>-co-SDec<sub>4</sub>), P(G<sub>50</sub>-co-SEt<sub>11</sub>-co-SPentadec<sub>1</sub>), P(G<sub>50</sub>-co-SEt<sub>10</sub>-co-SPentadec<sub>2</sub>), P(G<sub>50</sub>-co-SEt<sub>9</sub>-co-SPentadec<sub>3</sub>), P(G<sub>50</sub>-co-SEt<sub>8</sub>-co-SPentadec<sub>4</sub>), P(G<sub>50</sub>-co-SEt<sub>5.5</sub>-co-Chol<sub>0.5</sub>) and P(G<sub>50</sub>-co-SEt<sub>5.5</sub>-co-SPEG-Chol<sub>0.5</sub>) are termed as PG1-PG14 in the order as indicated, and 15AuPG1-15AuPG14 after binding to 15 nm AuNPs and 30AuPG1-30AuPG14 after adsorption to 30 nm AuNPs, respectively.

Due to a change in the dielectric constant at the NP surface after polymer coating<sup>[358]</sup>, the SPR band displayed a shift to higher wavelength of about 1-5 nm compared to corresponding citrate-capped AuNPs (see **Table 11**, **Figure 44** and **Figure 45**). The narrow curve progression of the UV-Vis spectra suggested excellent colloidal stabilization.

Further characterization by DLS measurements proved successful polymer adsorption as modified 15 nm AuNPs show larger *d* values between 22.9 nm and 37.7 nm as well as *d* = 37.5-67.6 nm for functionalized 30 nm AuNPs compared to citrate-stabilized AuNPs (*d* = 18.7 ± 0.9 nm respective *d* = 32.3 ± 0.7 nm). Among all particles, AuNPs coated with PG14 displayed by far the largest hydrodynamic diameter, suggesting a thick polymer layer on the NP surface, which may be explained by the bulk side group functionalization owing to the PEG-linker of the polymer. Within the different PGs with same functionalities but various functionalization degrees (AuPG1-AuPG4, AuPG5-AuPG8 and AuPG9-AuPG12), *d* increased with the degree of functionalization, as listed in **Table 11** and depicted in **Figure 44** and **Figure 45**. Such a trend could not be observed as alkyl chain length increased. This is probably related to the fact that different polymer concentrations were required for coating the nanoparticles to obtain aggregate-free and stable particles. As it is known, steric stabilization is dependent on the concentration of the adsorbed polymer in solution. While at low concentrations one single polymer could possibly bind to more than one NP, leading to flocculation bridging, a dense polymer layer is obtained at higher concentrations, preventing particle aggregation. However, if the polymeric concentration is too high, such bridging can be occurred due to an increasing number of long, extended polymer

### 3 Results and discussion

sequences (loop and tails) which could reach other NPs and adsorb to them.<sup>[380,432]</sup> Hence, intensive examinations on AuNP incubation with polymeric solutions of various molar concentrations was conducted to figure out the molarity, which is high enough resulting in high stability, even after salt treatment, and simultaneously low enough to prevent aggregation by bridging flocculation. The complete data on these studies were previously shown in **Section 3.2.2.2.1** and **Section 3.2.2.2.2**. The final polymer molarities used for particle coating are listed in **Table 30**. For 15AuPG11 and 15AuPG12 the molar concentration of 5  $\mu\text{M}$  was both, the maximum possible molarity obtaining aggregate-free AuNPs in aqueous solution as well as the minimum required molarity to provide stable particle in ion-rich solutions. This posed a challenge as even small changes in the AuNP to polymer ratio resulted in aggregation already in aqueous solution or later during incubation with the protein solution. Also, for 15AuPG10 the margin between 5  $\mu\text{M}$  and 7.5  $\mu\text{M}$  was not that wide. The final molarities used (see **Table 30**) corresponded to a value between the maximum possible and minimum required molar concentration. Wherever possible, the polymer solutions with same molarities were used for particles of both sizes due to easier handling.

Successful ligand exchange with PGs was further confirmed by moderately negatively charged zeta potentials between -26.6 mV and -17.6 mV for all polymer-functionalized particles (see **Table 11**), which was already presented in literature<sup>[433]</sup>.

**Table 11.** Values of SPR, *d*, PDI and  $\zeta$  of citrate- and polymer-stabilized 15 nm and 30 nm AuNPs, determined by UV-Vis, DLS and zeta potential measurements.

	15 nm AuNPs			
	SPR [nm]	<i>d</i> [nm]	PDI	$\zeta$ [mV]
15Au-Citrate	520	18.7 ± 0.9	0.061	-31.7 ± 1.3
15AuPG1	521	29.4 ± 2.2	0.100	-23.2 ± 1.9
15AuPG2	521	25.7 ± 0.8	0.079	-24.4 ± 2.6
15AuPG3	522	29.3 ± 1.8	0.098	-24.2 ± 3.1
15AuPG4	522	32.6 ± 1.1	0.105	-23.0 ± 2.4
15AuPG5	522	27.9 ± 1.3	0.077	-22.1 ± 1.7
15AuPG6	522	32.1 ± 1.2	0.113	-24.1 ± 2.3
15AuPG7	522	28.0 ± 1.2	0.088	-23.7 ± 3.8
15AuPG8	522	33.9 ± 1.2	0.115	-24.0 ± 3.7
15AuPG9	522	22.9 ± 1.8	0.161	-24.7 ± 2.9
15AuPG10	522	24.0 ± 1.4	0.199	-24.8 ± 3.5
15AuPG11	522	26.8 ± 1.6	0.193	-23.1 ± 2.1
15AuPG12	522	25.2 ± 2.2	0.169	-26.6 ± 3.5
15AuPG13	522	25.4 ± 1.3	0.149	-20.8 ± 3.4
15AuPG14	523	37.7 ± 2.8	0.164	-18.2 ± 3.0
	30 nm AuNPs			
	SPR [nm]	<i>d</i> [nm]	PDI	$\zeta$ [mV]
30Au-Citrate	524	32.3 ± 0.7	0.173	-36.7 ± 1.4
30AuPG1	525	42.4 ± 0.9	0.174	-28.5 ± 0.6
30AuPG2	525	40.5 ± 0.6	0.188	-29.3 ± 1.5
30AuPG3	526	42.9 ± 1.1	0.195	-28.5 ± 1.3
30AuPG4	526	43.7 ± 1.4	0.168	-28.2 ± 2.0
30AuPG5	526	42.1 ± 0.9	0.170	-28.3 ± 2.7
30AuPG6	526	45.3 ± 0.6	0.191	-25.4 ± 3.5
30AuPG7	526	41.4 ± 0.7	0.184	-26.1 ± 2.5
30AuPG8	527	46.4 ± 1.5	0.167	-29.7 ± 1.8
30AuPG9	526	37.5 ± 0.6	0.199	-27.0 ± 2.7
30AuPG10	526	38.3 ± 1.0	0.198	-29.0 ± 2.9
30AuPG11	527	40.3 ± 1.3	0.181	-25.7 ± 3.6
30AuPG12	527	39.6 ± 1.1	0.196	-29.7 ± 2.4
30AuPG13	526	39.1 ± 1.4	0.180	-19.6 ± 2.8
30AuPG14	529	67.6 ± 1.4	0.214	-17.6 ± 1.3

### 3 Results and discussion

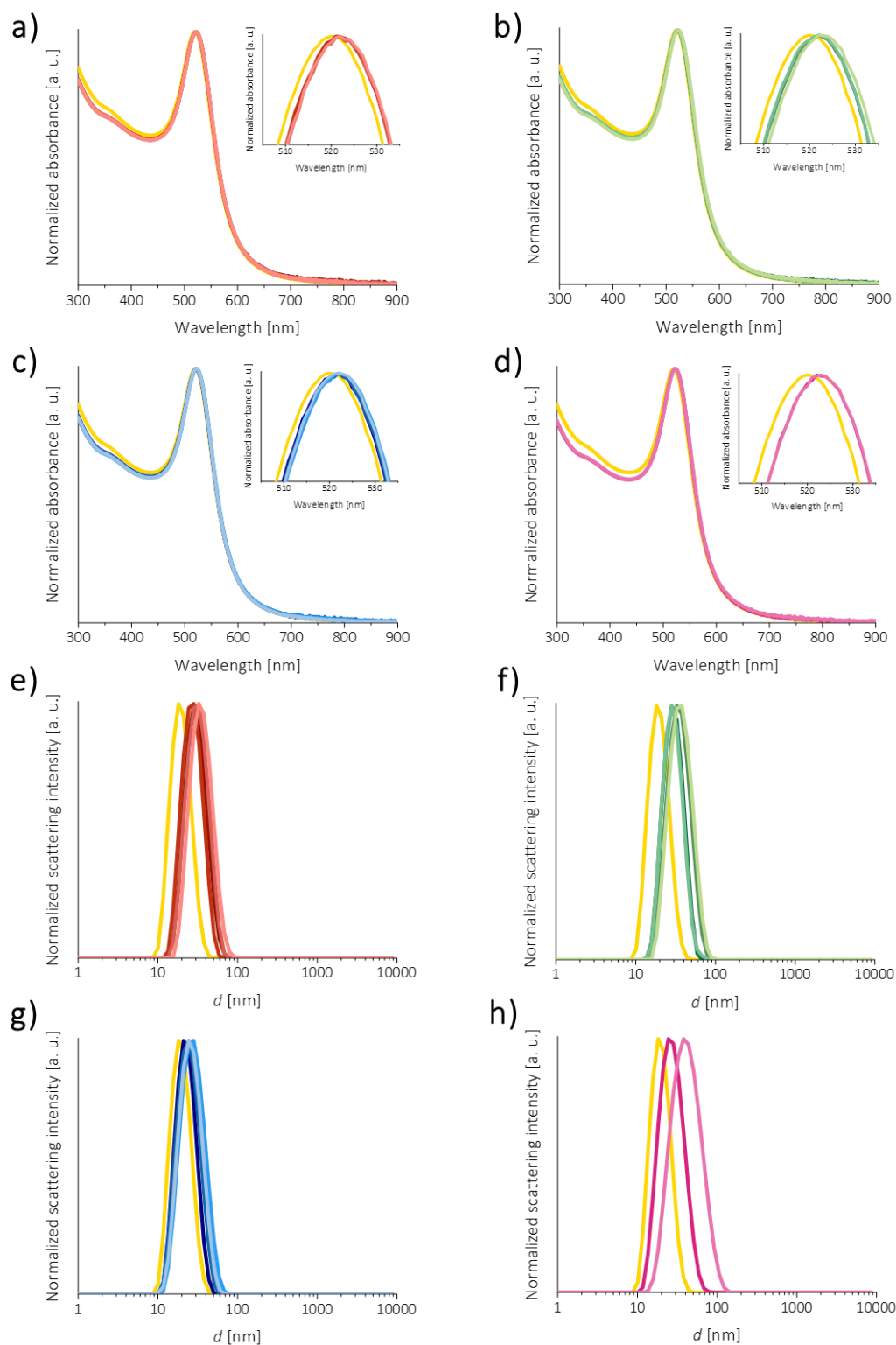


**Figure 44.** Normalized UV-Vis absorbance spectra of a) 15AuPG1 (dark red), 15AuPG2 (red), 15AuPG3 (middle red) and 15AuPG4 (light red), b) 15AuPG5 (dark green), 15AuPG6 (green), 15AuPG7 (middle green) and 15AuPG8 (light green), c) 15AuPG9 (dark blue), 15AuPG10 (blue), 15AuPG11 (middle blue) and 15AuPG12 (light blue) as well as d) 15AuPG13 (pink) and 15AuPG14 (light pink), compared to citrate-stabilized 15 nm AuNPs (yellow). The inserts display an enlarged part of the respective graph with adjusted scaling of both axes, to improve visualization of the SPR shift. And normalized DLS spectra of e) 15AuPG1 (dark red), 15AuPG2 (red), 15AuPG3 (middle red) and 15AuPG4 (light red), f) 15AuPG5 (dark green), 15AuPG6 (green), 15AuPG7 (middle green) and 15AuPG8 (light green), g) 15AuPG9 (dark blue), 15AuPG10 (blue), 15AuPG11 (middle blue) and 15AuPG12 (light blue) as well as h) 15AuPG13 (pink) and 15AuPG14 (light pink), compared to citrate-stabilized 15 nm AuNPs (yellow).

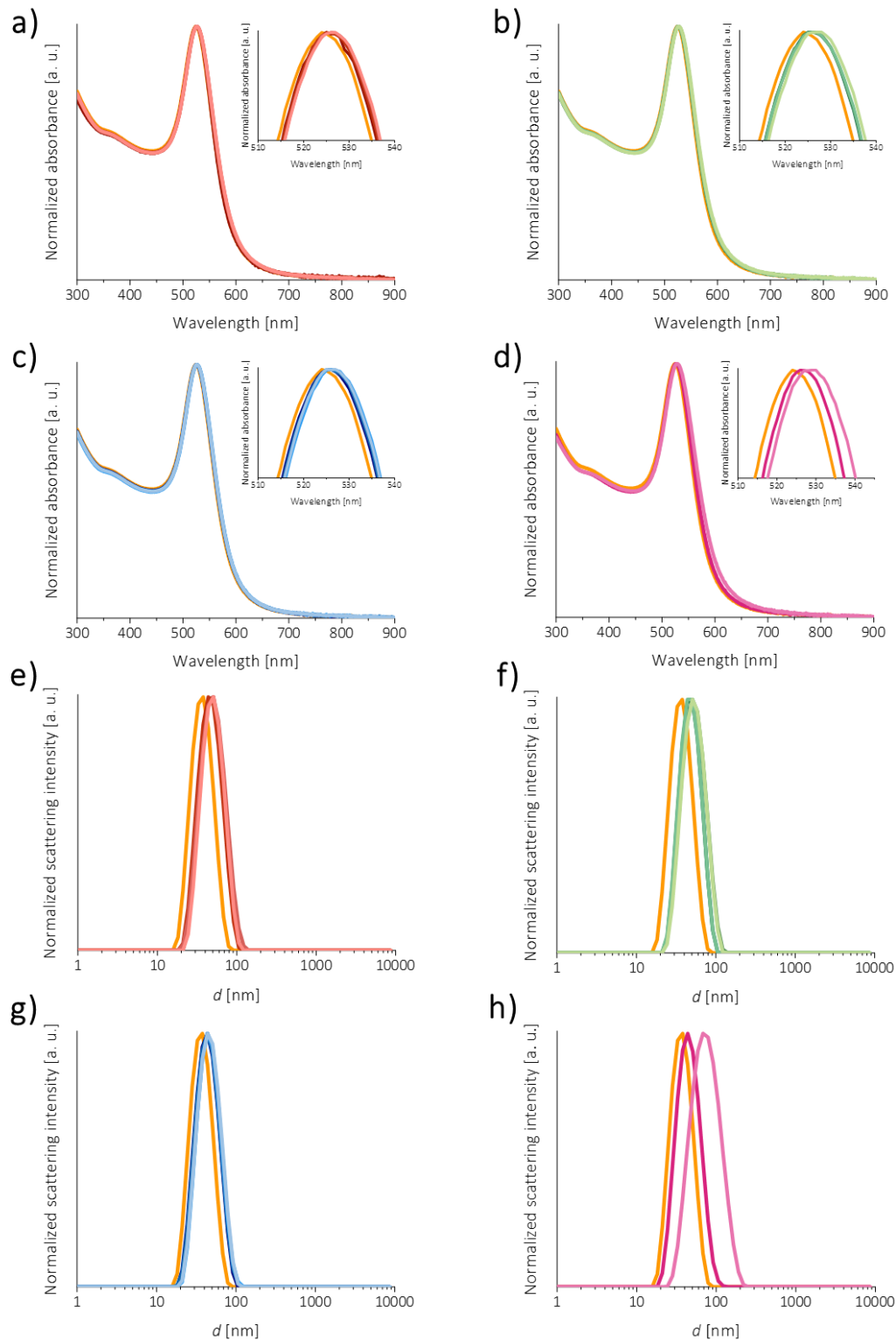


**Figure 45.** Normalized UV-Vis absorbance spectra of a) 30AuPG1 (dark red), 30AuPG2 (red), 30AuPG3 (middle red) and 30AuPG4 (light red), b) 30AuPG5 (dark green), 30AuPG6 (green), 30AuPG7 (middle green) and 30AuPG8 (light green), c) 30AuPG9 (dark blue), 30AuPG10 (blue), 30AuPG11 (middle blue) and 30AuPG12 (light blue) as well as d) 30AuPG13 (pink) and 30AuPG14 (light pink), compared to citrate-stabilized 30 nm AuNPs (orange). The inserts display an enlarged part of the respective graph with adjusted scaling of both axes, to improve visualization of the SPR shift. And normalized DLS spectra of e) 30AuPG1 (dark red), 30AuPG2 (red), 30AuPG3 (middle red) and 30AuPG4 (light red), f) 30AuPG5 (dark green), 30AuPG6 (green), 30AuPG7 (middle green) and 30AuPG8 (light green), g) 30AuPG9 (dark blue), 30AuPG10 (blue), 30AuPG11 (middle blue) and 30AuPG12 (light blue) as well as h) 30AuPG13 (pink) and 30AuPG14 (light pink), compared to citrate-stabilized 30 nm AuNPs (orange).

### 3 Results and discussion

In addition, attachment of multifunctional thioether-containing polymers to AuNPs was proven by FT-IR spectroscopy as exemplarily depicted for 15AuPG13 and 30AuPG3 in **Figure 46**, displaying transmission bands corresponding to the respective polymer vibrations. Both PG-coated AuNPs showed a broad signal at  $3386\text{ cm}^{-1}$  and  $3387\text{ cm}^{-1}$ , respectively, attributed to the OH stretching vibration. Since the modified particles were dissolved in aqueous solution, the higher intensity of the OH vibration compared to this of the pure polymers can be explained by the presence of water. Furthermore, functionalized AuNPs featured typical vibrations of CH, CH<sub>2</sub> and CH<sub>3</sub> units of the polymer backbone in wavelength ranges of  $2928\text{--}2876\text{ cm}^{-1}$  and  $1596\text{--}1254\text{ cm}^{-1}$ . Moreover, a signal at  $1074\text{ cm}^{-1}$  is seen, that can be assigned to the COC stretching vibration.

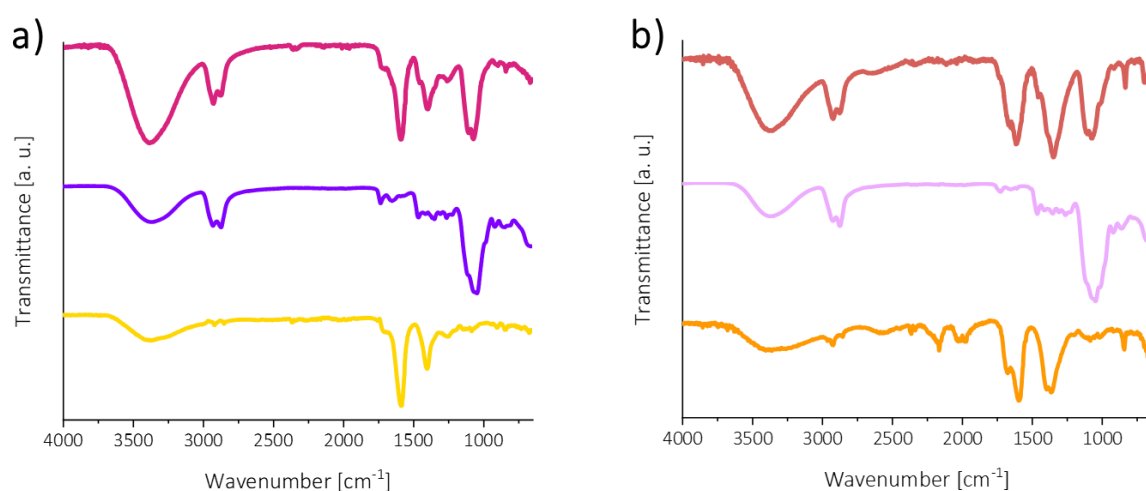


**Figure 46.** FT-IR transmittance spectra of a) 15AuPG13 (top, pink) compared to pure PG13 (middle, violet) and citrate-stabilized 15 nm AuNPs (bottom, yellow) as well as of b) 30AuPG3 (top, middle red) compared to pure PG3 (middle, light violet) and citrate-capped 30 nm AuNPs (bottom, orange). The measurements verified successful polymer attachment.

### 3.2.3 Serum protein adsorption on citrate-, alkyl- and cholesteryl-modified AuNPs

#### 3.2.3.1 Characterization of AuNPs after HS incubation

The before mentioned electrostatically and sterically stabilized 15 nm and 30 nm AuNPs were subsequently incubated in HS, to study the effect of surface functionalization on serum protein adsorption. After incubation with HS, UV-Vis and DLS measurements were performed, displaying a red-shift and larger  $d$  values compared to the particles without proteins (see values listed in **Table 12** and spectra depicted in **Figure 47** and **Figure 48**). The hydrodynamic diameter of unmodified AuNPs increased to a greater extent than the polymer-functionalized particles upon HS incubation, except of 30AuPG14HS, suggesting the adsorption of a thicker protein layer and thus possibly a higher protein amount. Within the PGylated AuNPs, 15AuPG14HS and 30AuPG14HS showed the largest size increase after incubation of 42 nm and 62 nm, respectively, which might possibly be due to a thicker protein layer and numerous bound proteins. This suggestion is examined and discussed in following parts of this thesis.

Furthermore, PDIs equal or less than 0.25 were present for all investigated AuNPs, except for 30AuPG14HS, indicating good dispersion in aqueous solution without aggregation. In contrast, citrate-AuNPs with both sizes and 30 nm AuNPs modified with PG14 showed after incubation with HS a PDI value around 0.27 and 0.38, respectively, suggesting aggregation. This assumption was strengthened by the large SPR shift compared to the samples before HS incubation, as well as the broadened curve progression in the range of 600-700 nm, as seen in **Figure 47** and **Figure 48**. Furthermore, the detection of very large hydrodynamic diameter of 80.3 nm for 15AuPG14HS, 84.8 nm for unmodified 15AuHS, 96.6 nm for 30AuHS and especially of 129.9 nm for 30AuPG14HS after incubation of the particles with HS indicated agglomeration.

In addition, protein binding yielded in less negative zeta potential values ( $\zeta = -22.5$  mV to  $-14.8$  mV for PGylated particles, and  $-24.5$  mV and  $-30.4$  mV, respectively, for ungrafted NPs) for all samples, shielding the surface charge of the AuNPs (see **Table 12**). Hence, the extent of the zeta potential change may be an indication on the amount of protein adsorption or whether negative or positively charged proteins have a higher affinity for the particle surface.

### 3 Results and discussion

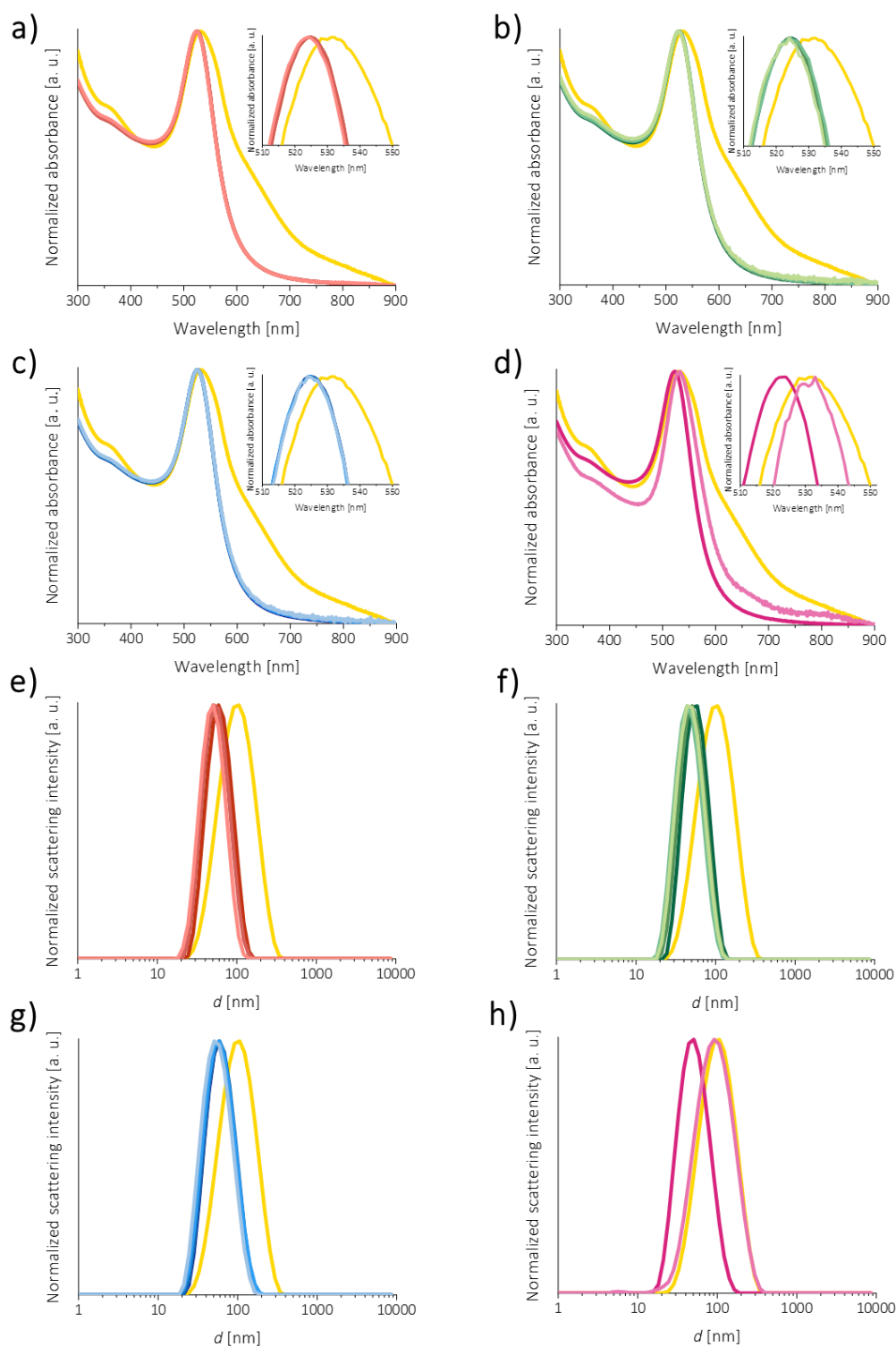


**Figure 47.** Normalized UV-Vis absorbance spectra of a) 15AuPG1HS (dark red), 15AuPG2HS (red), 15AuPG3HS (middle red) and 15AuPG4HS (light red), b) 15AuPG5HS (dark green), 15AuPG6HS (green), 15AuPG7HS (middle green) and 15AuPG8HS (light green), c) 15AuPG9HS (dark blue), 15AuPG10HS (blue), 15AuPG11HS (middle blue) and 15AuPG12HS (light blue) as well as d) 15AuPG13HS (pink) and 15AuPG14HS (light pink), compared to pure 15 nm AuNPs incubated with HS (yellow). The inserts display an enlarged part of the respective graph with adjusted scaling of both axes, to improve visualization of the SPR shift. And normalized DLS spectra of e) 15AuPG1HS (dark red), 15AuPG2HS (red), 15AuPG3HS (middle red) and 15AuPG4HS (light red), f) 15AuPG5HS (dark green), 15AuPG6HS (green), 15AuPG7HS (middle green) and 15AuPG8HS (light green), g) 15AuPG9HS (dark blue), 15AuPG10HS (blue), 15AuPG11HS (middle blue) and 15AuPG12HS (light blue) as well as h) 15AuPG13HS (pink) and 15AuPG14HS (light pink), compared to pure 15 nm AuNPs incubated with HS (yellow).



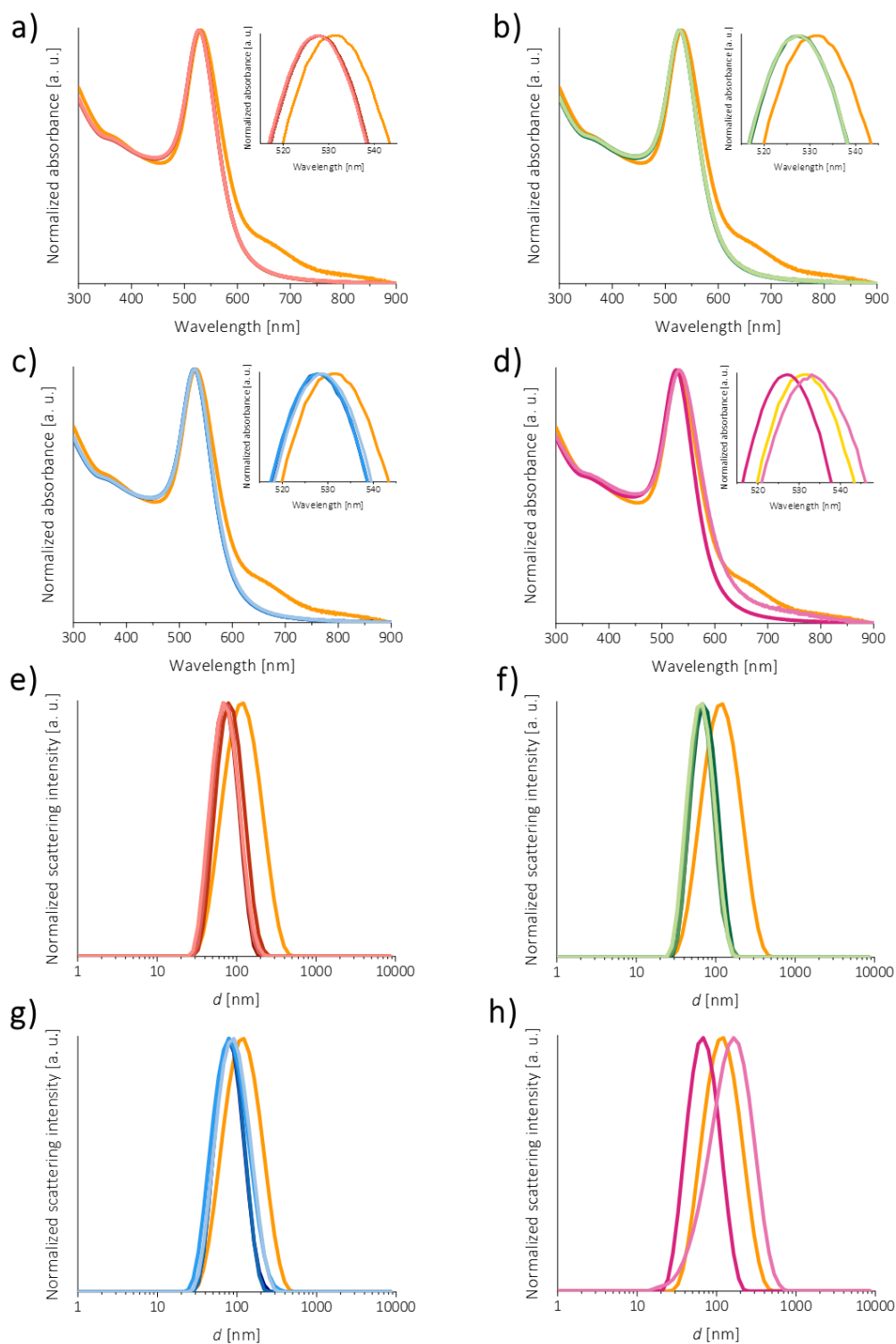


**Figure 48.** Normalized UV-Vis absorbance spectra of a) 30AuPG1HS (dark red), 30AuPG2HS (red), 30AuPG3HS (middle red) and 30AuPG4HS (light red), b) 30AuPG5HS (dark green), 30AuPG6HS (green), 30AuPG7HS (middle green) and 30AuPG8HS (light green), c) 30AuPG9HS (dark blue), 30AuPG10HS (blue), 30AuPG11HS (middle blue) and 30AuPG12HS (light blue) as well as d) 30AuPG13HS (pink) and 30AuPG14HS (light pink), compared to pure 30 nm AuNPs incubated with HS (orange). The inserts display an enlarged part of the respective graph with adjusted scaling of both axes, to improve visualization of the SPR shift. And normalized DLS spectra of e) 30AuPG1HS (dark red), 30AuPG2HS (red), 30AuPG3HS (middle red) and 30AuPG4HS (light red), f) 30AuPG5HS (dark green), 30AuPG6HS (green), 30AuPG7HS (middle green) and 30AuPG8HS (light green), g) 30AuPG9HS (dark blue), 30AuPG10HS (blue), 30AuPG11HS (middle blue) and 30AuPG12HS (light blue) as well as h) 30AuPG13HS (pink) and 30AuPG14HS (light pink), compared to pure 30 nm AuNPs incubated with HS (orange).

### 3 Results and discussion

**Table 12.** Values of SPR,  $d$ , PDI and  $\zeta$  of citrate- and polymer-stabilized 15 nm and 30 nm AuNPs after incubation with HS, determined by UV-Vis, DLS and zeta potential measurements.

	15 nm AuNPs			
	SPR [nm]	$d$ [nm]	PDI	$\zeta$ [mV]
15AuHS	532	84.8 ± 2.1	0.271	-24.5 ± 0.9
15AuPG1HS	525	50.5 ± 1.6	0.137	-17.4 ± 2.8
15AuPG2HS	525	55.3 ± 1.5	0.128	-18.1 ± 1.9
15AuPG3HS	525	50.4 ± 2.4	0.130	-18.6 ± 2.4
15AuPG4HS	524	48.9 ± 1.6	0.138	-19.9 ± 0.7
15AuPG5HS	524	52.1 ± 1.7	0.112	-19.6 ± 1.3
15AuPG6HS	524	47.1 ± 2.1	0.131	-17.0 ± 1.5
15AuPG7HS	524	42.6 ± 2.9	0.160	-16.8 ± 3.0
15AuPG8HS	524	45.1 ± 1.2	0.180	-14.8 ± 2.1
15AuPG9HS	525	56.9 ± 3.3	0.194	-17.2 ± 1.7
15AuPG10HS	525	58.4 ± 2.7	0.222	-16.1 ± 1.5
15AuPG11HS	525	54.6 ± 3.0	0.197	-20.1 ± 0.6
15AuPG12HS	524	50.7 ± 1.1	0.184	-21.5 ± 2.5
15AuPG13HS	524	49.9 ± 2.8	0.235	-16.9 ± 2.7
15AuPG14HS	532	80.3 ± 2.8	0.250	-16.0 ± 3.3
	30 nm AuNPs			
	SPR [nm]	$d$ [nm]	PDI	$\zeta$ [mV]
30AuHS	531	96.6 ± 2.5	0.275	-30.4 ± 0.8
30AuPG1HS	527	62.3 ± 4.1	0.172	-19.4 ± 2.0
30AuPG2HS	528	67.3 ± 6.5	0.194	-20.1 ± 3.6
30AuPG3HS	528	65.7 ± 3.6	0.160	-18.9 ± 1.3
30AuPG4HS	527	63.6 ± 4.4	0.183	-20.2 ± 1.4
30AuPG5HS	528	63.7 ± 2.1	0.155	-22.5 ± 2.5
30AuPG6HS	527	61.5 ± 1.4	0.185	-18.4 ± 1.4
30AuPG7HS	527	57.6 ± 1.9	0.170	-19.4 ± 2.5
30AuPG8HS	527	57.5 ± 1.3	0.171	-15.8 ± 0.6
30AuPG9HS	528	70.0 ± 1.8	0.186	-19.1 ± 3.2
30AuPG10HS	528	71.2 ± 1.5	0.172	-21.3 ± 1.1
30AuPG11HS	528	73.3 ± 2.9	0.211	-20.8 ± 2.4
30AuPG12HS	529	78.0 ± 1.6	0.223	-17.4 ± 1.4
30AuPG13HS	527	58.8 ± 1.8	0.218	-17.5 ± 1.8
30AuPG14HS	533	129.9 ± 3.2	0.380	-20.3 ± 1.6

Successful attachment of serum proteins to pure AuNPs and polymer-coated particles was further verified by FT-IR measurements as exemplarily depicted for 15AuHS, 15AuPG13HS, 30AuHS and 30AuPG3HS in **Figure 49**. Here, especially the prominent amide vibration bands of serum proteins around  $1644\text{ cm}^{-1}$  (amide band I) and  $1541\text{ cm}^{-1}$  (amide band II) were noticed<sup>[434]</sup>, consistent with the particles after HS incubation. However, due to the difference in band intensities among the various samples, neither an equal amount nor an equal composition of bound proteins is assumed. To reinforce this assumption, further investigations of the formed protein corona were carried out.

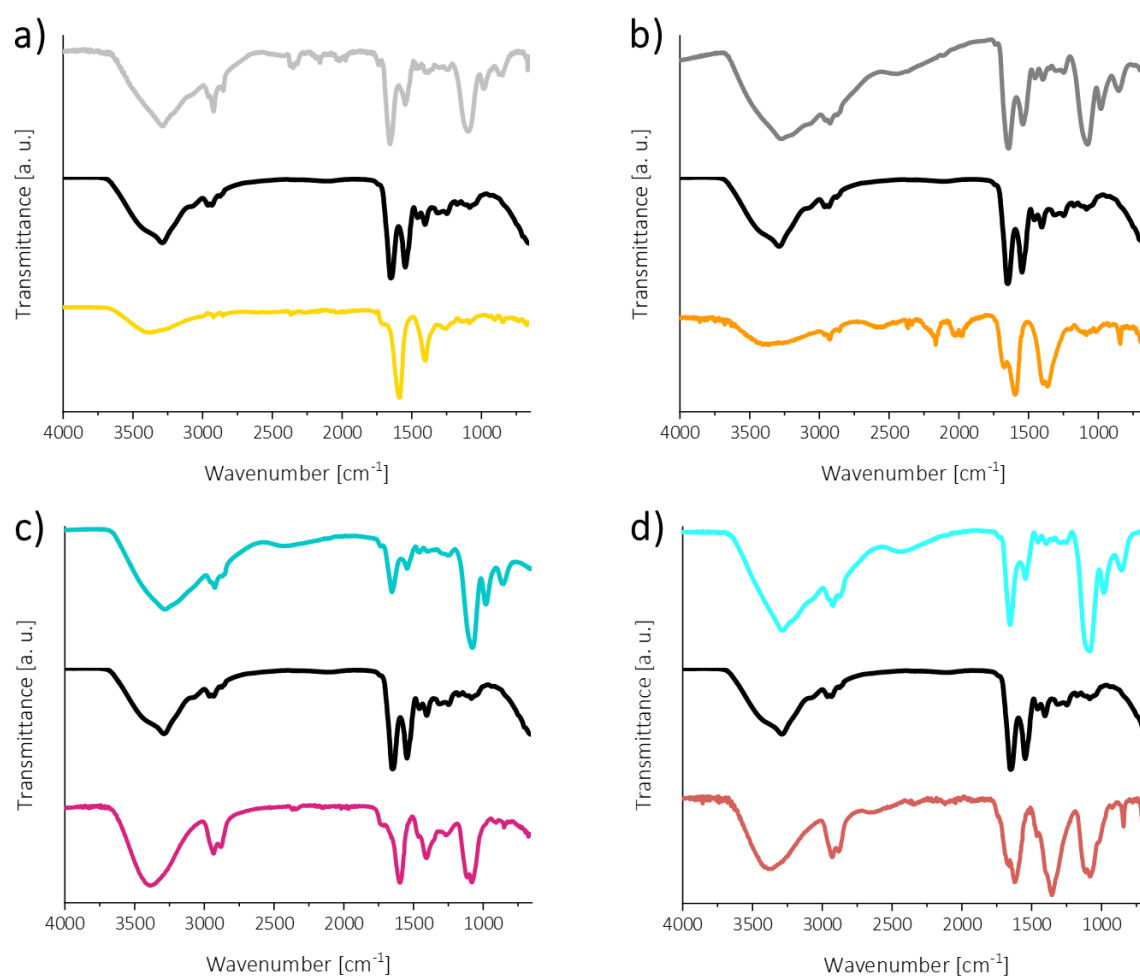


**Figure 49.** FT-IR transmittance spectra of a) 15AuHS (top, light grey) compared to pure HS (middle, black) and citrate-stabilized 15 nm AuNPs (bottom, yellow), b) 30AuHS (top, grey) compared to pure HS (middle, black) and citrate-stabilized 30 nm AuNPs (bottom, orange), c) 15AuPG13HS (top, cyan) compared to pure HS (middle, black) and 15AuPG13 (bottom, pink) as well as of d) 30AuPG3HS (top, light cyan) compared to pure HS (middle, black) and 30AuPG3 (bottom, middle red). The measurements verified successful serum protein attachment.

### 3 Results and discussion

#### 3.2.3.2 Quantification of total protein amount on AuNPs

For first examinations of the formed protein corona, the total amount of adsorbed proteins on each NP was quantitatively determined by micro-BCA assay, as displayed in **Figure 50**. To investigate the role of surface functionalization, same surface area of all particles was incubated with a corresponding volume of HS. The detailed procedure is described in **Section 5.4.1.4** and was used for all studies concerning the bound protein corona. However, it should be pointed out, when calculating the particle surface area per mL, as described in **Section 5.4.1.3**, the assumption was made that all particles are perfectly spherical and uniform in size. Hence, the formulas to calculate the volume ( $V = 4/3\pi r^3$ ) and the surface area ( $A = 4\pi r^2$ ) of a sphere were used. It should be further noted that the size, more precisely the radius, used in these equations is derived from the hydrodynamic diameter obtained by DLS measurements. After HS incubation and several washing steps, ensuring the absence of unbound proteins, the tightly coated proteins of the hard corona were dissociated from the NP surface by thermal stress in extraction buffer solution before performing the micro-BCA assay. **Figure 50** shows lower serum protein adsorption for particles with larger hydrodynamic diameter (**Figure 50b**) than for smaller ones (**Figure 50a**), with smaller NPs containing 1.7 to 2.8 times higher protein amounts, even though the same particle surface area was used for all samples. Reduced protein adsorption upon increasing the particle size, attributed to the difference in surface curvature, is consistent with literature.<sup>[210,435]</sup> In addition, a high amount of serum proteins attached to unfunctionalized AuNPs (26.5  $\mu\text{g}/10\text{ cm}^2$  for 15AuHS and 9.6  $\mu\text{g}/10\text{ cm}^2$  for 30AuHS), while PG modification resulted in suppressed protein binding (11.5-20.4  $\mu\text{g}/10\text{ cm}^2$  for polymer-modified 15 nm AuNPs and 4.6-8.7  $\mu\text{g}/10\text{ cm}^2$  for 30 nm AuNPs coated with multifunctional polymers). As mentioned before, a larger amount of adsorbed proteins after HS incubation of 15 nm and 30 nm citrate-AuNPs was already expected due to the increasing  $d$  values compared to the different functionalized particles incubated with HS. Although the hydrodynamic diameter of both unmodified NPs increased to the same extent post incubation with HS, differences in the number of bound proteins were obtained by micro-BCA assay, whereas the smaller particles displayed a higher protein amount, which is in accordance with literature.<sup>[210]</sup> Within polymer-functionalized AuNPs incubated with HS, only minor differences in the amount of bound proteins could be observed, with no discernible trend, except of AuNPs modified with PG carrying the

longest hydrophobic alkyl residue. Among this group, the amount of protein increased with increasing number of alkyl side chains. This finding is in accordance with literature since hydrophobicity enhances serum protein adsorption.<sup>[214,215]</sup> However, for the other functionalized particles investigated in this study, no statement can be given on the influence of the different hydrophobic units on protein adsorption with micro-BCA analysis. This might be because, as mentioned in **Section 2.2.1**, protein binding depends on many different factors, such as size and surface charge, which was not similar for all AuNPs studied in this work. Moreover, the polymer arrangement on the particle surface as well as the packing density probably played an even more important role in protein adsorption<sup>[436,437]</sup>, which is assumed to be different due to the variation in chemical structure and number of side chains on the polymer backbone.

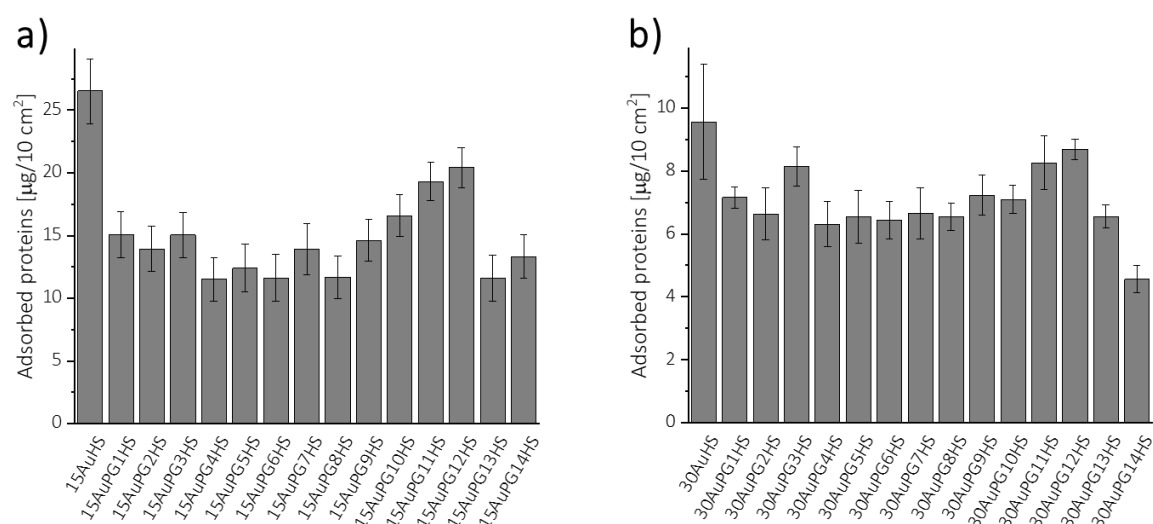


**Figure 50.** Quantitative characterization of the amounts of adsorbed proteins of a) 15 nm citrate-AuNPs as well as various PG-functionalized 15 nm AuNPs (15AuPG1-15AuPG14) and of b) 30 nm citrate-AuNPs as well as various PG-functionalized 30 nm AuNPs (30AuPG1-30AuPG14) after incubation with HS and several washing steps, using micro-BCA assay. The values are presented as mean  $\pm$  standard deviation ( $n = 3$ ).

### 3 Results and discussion

#### 3.2.3.3 Quantification of protein pattern

After quantification of the total amount of adsorbed proteins on each NP via micro-BCA assay, the adsorbed serum protein layers of 15AuHS and 30AuHS as well as of all polymer-functionalized particles were qualitatively quantified by SDS-PAGE resulted in different band patterns after Coomassie Blue staining (see **Figure 51**). Both pure HSA and HS were used as control samples. First, it could be observed that particles with a core of 15 nm (**Figure 51a**) showed a much stronger band intensity than the larger 30 nm AuNPs (**Figure 51b**), which is consistent with the above discussed results from the BCA assay, as the band intensity is related to the protein amount. A decreased total protein adsorption associated with larger particle sizes meaning smaller surface area is in accordance with the literature.<sup>[210,438]</sup> In addition, the different particle sizes as well as various PG coatings resulted in varied protein patterns, which showed differences not only in their band intensity, that can be related to the protein amount, but as well in the presence or absence of protein bands. A closer look at **Figure 51a** revealed that especially the protein isolate from unmodified particles (15AuHS) displayed a complex banding pattern, suggesting the composition of a large amount of different serum proteins. In accordance with the micro-BCA assay (**Figure 50**), functionalization with PG ligands (PGylation) led to a reduced protein adsorption, as indicated by a lower number of bands as well as decreased lane intensities compared to ungrafted AuNPs. Within the polymer-modified NPs, different band patterns and intensities can be recognized as well, showing for the lowest hydrophobic AuNPs (15AuPG1HS-15AuPG3HS) less protein bands or lanes with a significant lower intensity than for the more hydrophobic samples 15AuPG9HS-15AuPG12HS (see **Figure 51a**). In particular, the AuNPs functionalized with PGs containing a larger number of, and/or longer alkyl chains mainly displayed an intense band at a molecular weight of around 70 kDa, possibly attributable to the protein HSA (69 kDa), which is the most abundant protein (approximately 60% of total serum proteins, by mass) in human blood plasma<sup>[269]</sup>. Although HSA is the most abundant plasma protein, the associated protein band did not exhibit the greatest intensity in all protein patterns obtained by SDS-PAGE. The 15AuPG1HS-15AuPG3HS samples, for instance, showed a relatively less intense band in the 70 kDa region, and in addition, several other protein bands with similar intensity. This probably indicated that other proteins, present with lower abundance in HS, bound with higher affinity to the particle surface. By comparing the protein band pattern of pure

HS with those of the various AuNPs incubated with serum, this assumption can be strengthened, since the AuNPs studied displayed a complex protein composition with a variety of protein bands, while only one intense and few additional bands were detected for pure HS. However, it should be noted that due to the large number of proteins (approx. 3700)<sup>[439]</sup> present in HS, in addition other proteins with molecular weights around 70 kDa do exist and therefore the detected band cannot be solely attributed to HSA. Hence, a more detailed study of the adsorbed proteins was required and is presented in the following section.

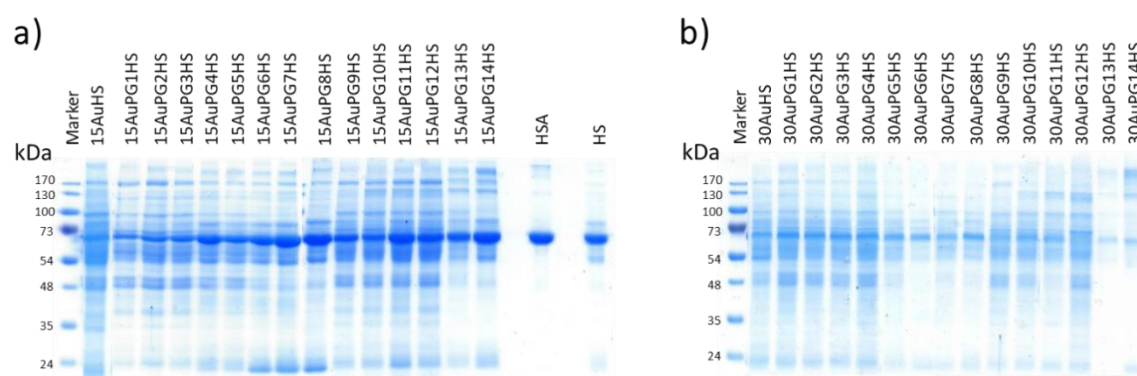


**Figure 51.** SDS-PAGE analysis for qualitative characterization of protein corona of a) 15 nm citrate-AuNPs as well as various hydrophobic functionalized 15 nm AuNPs (15AuPG1-15AuPG14) as well as of b) pure 30 nm AuNPs and polymer-coated 30 nm AuNPs (30AuPG1-30AuPG14) after incubation with HS and several washing steps. HSA and HS were used as control samples.

The larger particles in **Figure 51b** did not demonstrate the same trends as just described for the 15 nm AuNPs, although the NPs were coated with identical polymers and even the HS incubation was performed under similar conditions. This can possibly be explained by the fact that the particle size itself has an impact on the PG coating, with respect to the PG grafting density and conformation, which might subsequently affect the protein binding.

Since SDS-PAGE analysis is only a qualitative analysis, further investigations were mandatory to provide more detailed information of the protein composition of the various NPs. Owing to the costs and time constraints, only 15 nm AuNPs with selected coatings were investigated in more detail.

### 3 Results and discussion

#### 3.2.3.4 Investigation of protein corona composition of various coated AuNPs

To confirm the previous assumptions and to provide a more detailed statement of the protein composition of the different AuNPs, five samples were selected and analyzed under trypsin degradation of the detached proteins by LC-MS/MS. 15AuHS, 15AuPG1HS, 15AuPG6HS, 15AuPG12HS and 15AuPG13HS were chosen for LC-MS/MS analysis, covering the range to allow investigation of the general impact of PG as stealth-polymer as well as the influence of different hydrophobic units of PG attached AuNPs. Moreover, all these polymers exhibited stable particles after protein binding, as demonstrated in Section 3.2.3.1. HS was used as a reference in LC-MS/MS analysis.

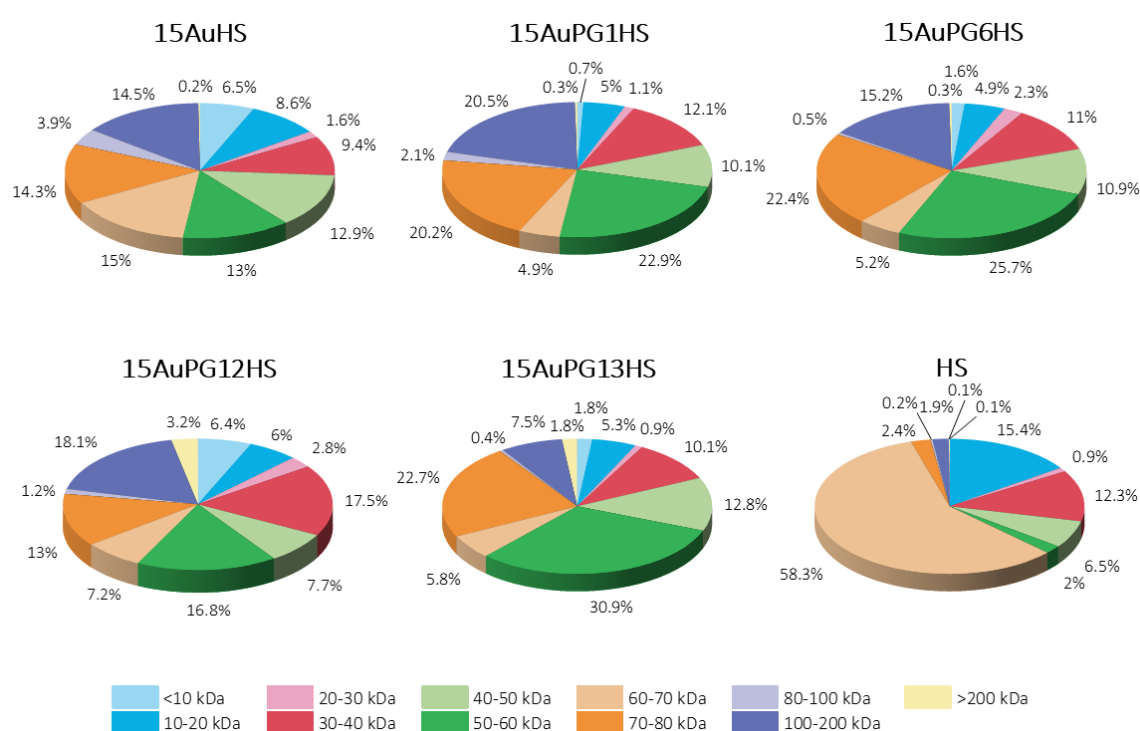


**Figure 52.** Classification of surface bound proteins on different modified AuNPs by quantitative LC-MS/MS analysis according to their molecular weight, compared to protein distribution of HS.

In accordance with micro-BCA assay, particle surface coating did not affect the number of attached proteins, but the total protein amount is decreased after PGylation compared to uncoated AuNPs. Both methods demonstrated that within the PG-modified AuNPs, 15AuPG12HS, being the most hydrophobic particle, which was proven by determination of the critical aggregation concentration of all polymeric solutions in water using DLS (see Section 3.2.1.3), had the highest amount of bound proteins. Increased protein amount on more hydrophobic compared to less hydrophobic particles is consistent with literature.<sup>[214]</sup>



It is hypothesized that hydrophobicity of a nanocarrier induces protein denaturation, leading to an exposure of the hydrophobic protein regions on the particle surface and thus may further influence the adsorption process.<sup>[440]</sup>

First, the proteins found in detectable quantity via LC-MS/MS analysis were sorted by their molecular weight, showing that different surface coatings affected the binding of proteins depending on their molecular weight. As seen in **Figure 52** all AuNPs showed low affinity for high molecular weight proteins, thus more than 97-99% of the total bound protein amount consisted of proteins with molecular weights below 200 kDa. Among the different protein binding profiles of the four PGylated AuNPs, there were no decisive differences regarding attached protein sizes, except of 15AuPG12HS. The distribution of protein molecular weights of 15AuPG1HS, 15AuPG6HS and 15AuPG13HS was similar with a deviation of 3% with exception for the proteins with 50-60 kDa as well as 100-200 kDa. While 15AuPG13HS adsorbed 5-8% more 50-60 kDa proteins than the other two mentioned samples, its enrichment of proteins with a molecular weight of 100-200 kDa was only half as low. Furthermore, 15AuPG12HS exhibited the most differences in the protein size binding profile between PG-coated AuNPs, attaching a lower amount of proteins with 50-60 kDa and 70-80 kDa, as well as showing higher affinity for proteins <10 kDa and 30-40 kDa, compared to 15AuPG1HS, 15AuPG6HS and 15AuPG13HS. In addition, this sample featured the largest amount of higher molecular weight proteins >200 kDa. Looking at the protein distribution of AuNPs without polymer coating, it was noticeable that no molecular weight region was prominent, which is in accordance with the SDS-PAGE results, demonstrating numerous protein bands with similar intensities. However, for 15AuHS the adsorption of 60-70 kDa proteins was with 15% up to three times higher than for the PGylated particles (about 5% to 7% of total bound proteins). These results indicated that the intense protein bands around 70 kDa in SDS-PAGE analysis of AuNPs functionalized with PGs (**Figure 50b**) was not attributed to the protein HSA (69 kDa), but rather to other proteins with a molecular weight of 70-80 kDa. In contrast, the control serum consisted of more than 95% proteins with a molecular weight smaller than 70 kDa, of which 58% were proteins between 60-70 kDa. This high percentage of identified proteins between 60-70 kDa is related to the existence of the most abundant protein HSA (approximately 60% of total plasma proteins, by mass) with a molecular weight of

### 3 Results and discussion

69 kDa.<sup>[269]</sup> Since the protein profiles of all AuNPs incubated with HS showed significantly lower adsorption of 60-70 kDa proteins and simultaneously higher binding of various other molecular weight proteins, the above-mentioned hypothesis that lower abundance serum proteins may bind with higher affinity to the particle surface can be confirmed.

Next, the identified proteins were classified by their biological function, divided in seven major protein groups: (i) acute phase proteins, (ii) coagulation proteins, (iii) lipoproteins, (iv) complement proteins, (v) immunoglobulins, (vi) tissue leakage proteins and (vii) other components (**Figure 53**), to represent the most abundant protein types. A full list of detected proteins grouped according to their biological function is displayed in **Table 80** in **Section 5.5**.

In order to get into more detail, **Figure 53b-h** displays the specific proteins of the different protein classes identified in the respective protein corona. **Figure 53b** shows that pure HS mainly consisted of the acute phase proteins alpha-1-antitrypsin (SERPINA1) (3%) and haptoglobin (HP) (2%), while the protein corona on AuNPs, especially on 15AuPG1HS (8%) and 15AuPG6HS (7%), was mainly enriched of inter-alpha-trypsin inhibitor heavy chain H4 (ITIH4). Proteins classified as coagulation proteins were barely existent in pure serum, as consistent with literature.<sup>[439]</sup> Mainly kininogen-1 (KNG1) (6% to 13%) and SERPINC1 (5% to 13%) were bound to the particles with different percentages depending on the surface coating (**Figure 53c**), both proteins had high affinity to PGylated particles, except of 15AuPG12HS. It is conspicuous that 15AuPG12HS bound much less coagulation proteins than the other AuNPs coated with PG containing hydrophobic residues, showing high similarity to unfunctionalized particles.

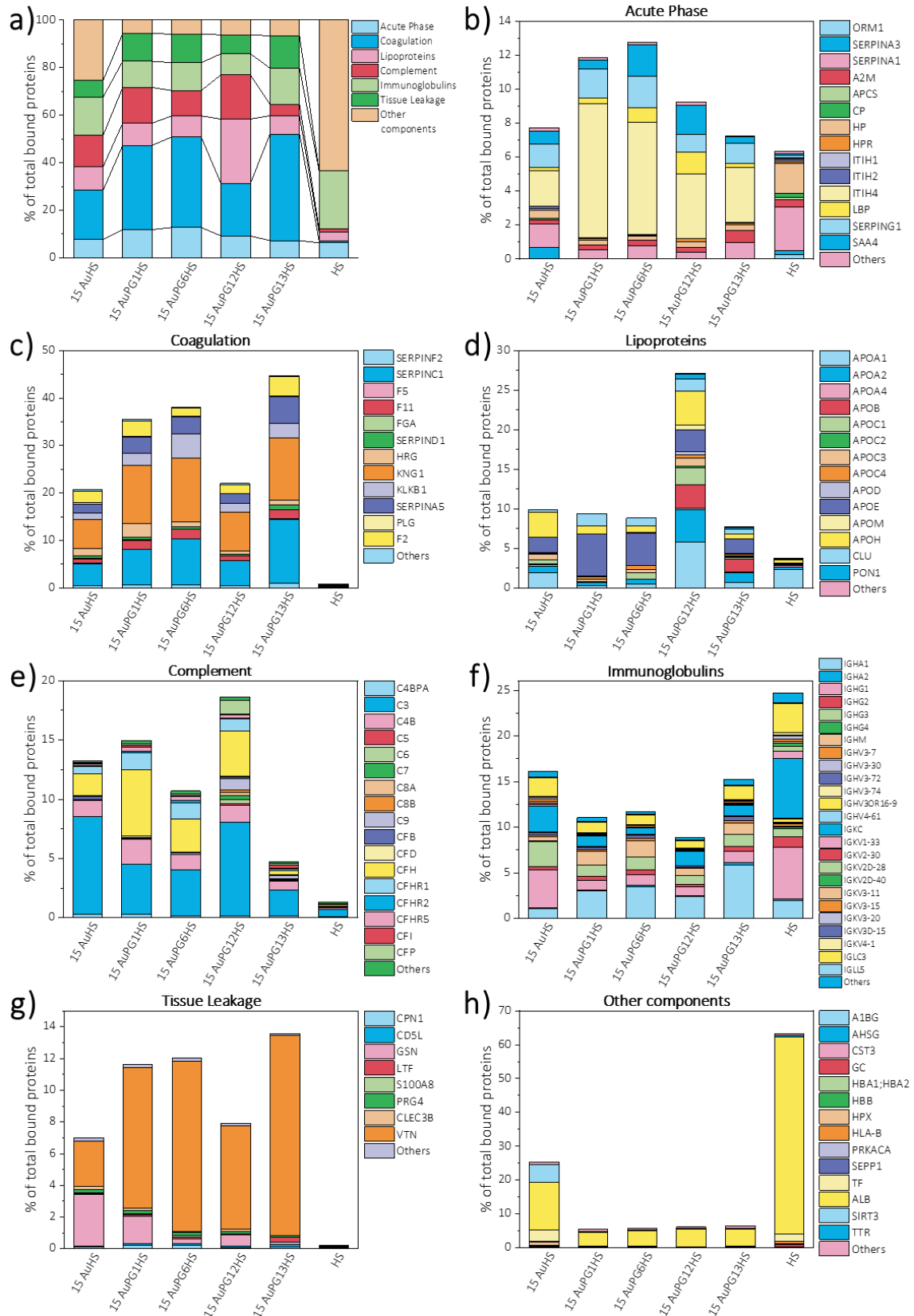


**Figure 53.** Classification of surface-bound proteins on different modified AuNPs by quantitative LC-MS/MS analysis according to their biological function divided in seven major protein groups, compared to protein distribution of HS. Proteins below 0.1% of total proteins in all samples were grouped together and reported as others.

### 3 Results and discussion

In contrast, as seen in **Figure 53d**, multiple lipoproteins were found in great extent in the protein corona of 15AuPG12HS, consisting of apolipoprotein A-I (APOA1) (6%), beta-2-glycoprotein 1 (APOH) (4%), apolipoprotein A-II (APOA2) (4%), apolipoprotein B-100 (APOB) (3%), apolipoprotein E (APOE) (3%) and some other lipoproteins between 1-3% of total bound proteins. Preferred adsorption of apolipoproteins on most hydrophobic nanocarriers is in accordance with literature<sup>[214]</sup> and is suggested owing to interactions between the hydrophobic NP surface and lipid-binding domains of apolipoproteins<sup>[441]</sup>. It was not surprising that such a variety of lipoproteins, even with much lower abundance, was in addition attached to the cholesteryl-functionalized particle 15AuPG13HS, since apolipoproteins are involved in the cholesterol transport<sup>[442]</sup>. Moreover, APOE was mainly adsorbed on 15AuPG1HS (5%) and 15AuPG6HS (4%). This example clearly demonstrated that the different surface coatings had an impact on protein binding, not only on number of attached proteins, but also on their abundance. Complement proteins were less abundant in HS compared to the identified proteins tethered to the particles, whereby the protein corona of 15AuPG12HS contained the highest amount of complement proteins (**Figure 53e**). Besides C3 (2-8%), which was most abundant in all samples, except of 15AuPG1HS, complement factor H (CFH) displayed high affinity on these particles but with lower concentrations. On the other hand, the protein corona of 15AuPG1HS exhibited with 6% of CFH a higher amount of adsorbed proteins than C3 (4%). In consistency with literature<sup>[443]</sup>, HS contained of a variety and high amount of immunoglobulins, which could in addition be observed in the protein corona on AuNPs used in this study (**Figure 53f**). 15AuHS and 15AuPG13HS exhibited the same percentage of immunoglobulins bound, presenting the highest amount among all samples. Enrichment of immunoglobulins to cholesteryl-functionalities was previously demonstrated by Caracciolo *et al.*<sup>[444]</sup> However, while 15AuHS mostly contained of Ig heavy constant gamma 1 (IGHG1) (4%), Ig heavy constant alpha 1 (IGHA1) was most abundant on 15AuPH13HS (6%). Moreover, IGHA1 represented the majority of adsorbed proteins on all PGylated particles, reaching 2-6% of total bound proteins. VTN was the tissue leakage protein having the highest affinity for all functionalized AuNPs (7% to 13%), although it was present only to a small extent in HS, as depicted in **Figure 53g**. While almost only VTN was detected in hydrophobic coated particles, gelsolin (GSN) was present in the protein corona as well, whereby latter bound with higher affinity to unmodified AuNPs. The highest percentage difference of detected

proteins was observed for proteins assigned to other components, as show in **Figure 53h**. According to LC-MS/MS measurements HS included 58% HSA and 2% transferrin (TF), which is consistent with the literature<sup>[439,445]</sup>. Protein corona of 15AuHS was mainly enriched of HSA (14%), sirtuin 3 (SIRT3) (5%) and TF (3%). In the protein class of other components, HSA was as well the highest abundant protein in adsorbed proteins on PG-functionalized particles, however, it accounts for only 4-5% of total proteins and is thus 3 times lower than on pure AuNPs. These results clearly demonstrated that the proteins most abundant in pure serum did not necessarily show the highest affinity for the particle surface and that the surface coating had an impact on protein adsorption, even though the protein corona composition was not always changed significantly with the various surface functionalities.

Besides the classification of the identified proteins according to their biological function, the most abundant proteins in the protein corona of AuNPs were summarized. **Figure 54a** shows the adsorbed proteins with relative abundances of 1% of total bound protein amount depicted in a heat map, and in the table in **Figure 54b** the 20 most abundant proteins are listed, with their abundance decreasing from top to bottom.

In **Figure 54a**, the protein HSA stands out with its highest abundance of 14% in the protein corona of 15AuHS, while this protein was enriched only to a lower percentage (4-5%) on the PG-modified particles. PG suppressed HSA attachment, consistent with literature<sup>[446]</sup>, but this protein was still among the most adsorbed protein on all four coated particles, with increased HSA binding as alkyl chain length as well as its number and thus the hydrophobicity increases, even if only to a small extent. Enhanced HSA adsorption with increasing alkyl chain length and increasing percentage of alkyl chains has already been shown in literature<sup>[398,447]</sup>, and can be explained as HSA is known to bind to hydrophobic components possessing special binding sites for fatty acid like alkyl chains<sup>[448,449]</sup> as well as for cholesterol<sup>[407]</sup>. In contrast to unmodified AuNPs, nanocarriers coated with polymers revealed a higher content of the coagulation protein KNG1, with the exception of 15AuPG12HS, exhibiting a similar amount of total bound proteins as 15AuHS. Thus, the prominent band around 70 kDa in the SDS-PAGE results (**Figure 50b**) of polymer-modified AuNPs can be assigned to KNG1 (72 kDa). In addition to KNG1, the tissue leakage protein VTN and the coagulation protein SERPINC1 could be found in high abundance in the protein

### 3 Results and discussion

corona of 15AuPG1HS, 15AuPG6HS and 15AuPG13HS, increasing in the order 15AuPG1HS < 15AuPG6HS < 15AuPG13HS. Upon looking at the heat-map illustration of 15AuPG12HS, it is clearly shown, that there was no protein predominant in the protein corona. Rather, several proteins with similar percentage of total bound proteins were present on this functionalized particle, where KNG1 and C3 were most abundant with approximately 8%, followed by VTN (6.5%), APOA1 (5.8%) and SERPINC1 (5.3%). Besides APOA1, further apolipoproteins were attached to the particle surface with abundances of less than or equal to 4% of total bound proteins. High enrichment of apolipoproteins on NPs with increasing hydrophobicity was already demonstrated by Gessner *et al.*<sup>[214]</sup>, suggesting that hydrophobic interactions between the nanocarrier and lipid-binding domains of apolipoproteins were probably the driving force for apolipoprotein adhesion<sup>[201]</sup>.

In addition, as seen in **Figure 54b**, eight of the 20 most abundant proteins were identified in the protein corona of ungrafted as well as PGylated AuNPs, although with different abundances. It seemed that the composition of the protein corona was not dramatically affected by the different surface hydrophobicities, but mainly had an impact on the amount of total proteins bound. Moreover, IGHA1 and KLKB1, which can be assigned to immunoglobulins and coagulation proteins, respectively, are two proteins that were only present in the top 20 of the polymer-modified nanocarriers. Complement protein CFH and lipoprotein APOE solely adsorbed on alkyl-PG-functionalized particles, showing highest affinity on 15AuPG1HS. Hence, it may be hypothesized that these proteins bind specifically to PG bearing alkyl functionalities. Furthermore, complement protein C3 was among the 10 most abundant proteins in all samples, which could be explained by the fact that C3 preferably binds to polyhydroxylated NPs<sup>[450]</sup> and the AuNPs used in this study were modified with PG, which is a multihydroxy-functional polymer.

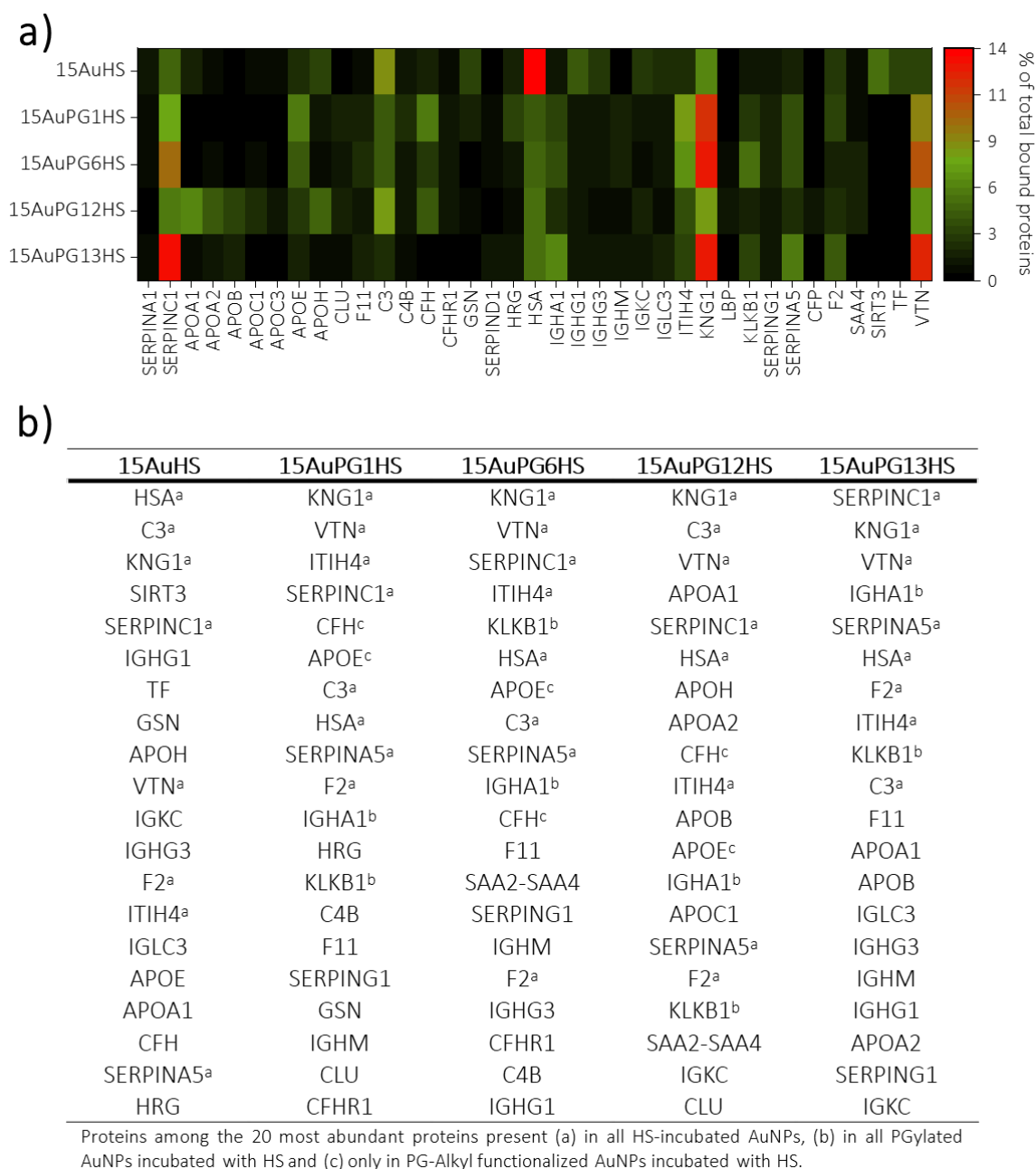


**Figure 54.** a) Heat map of the abundant proteins (> 1%) in the protein corona on all AuNPs. b) Top 20 most abundant proteins identified in the protein corona of all AuNPs incubated with HS, with its highest percentage starting at the top.

It was found that surface-coating on AuNPs generally affected the protein adsorption, although not to such a large extent as demonstrated by Schöttler *et al.*<sup>[30]</sup> on polystyrene nanocarriers. Especially HSA adsorption was reduced 3 times on polymer-modified particles, independent on their surface coating. In 15AuPG1HS and 15AuPG6HS, the protein composition of the corona was almost identical, wherein 17 of the 20 most abundant proteins were found on both AuNPs, with only minor variations in their abundance. Proteins were not observed to bind preferentially or less preferentially to the

### 3 Results and discussion

nanocarriers as their hydrophobicity increased from 15AuPG1 < 15AuPG6. This could possibly be related to the fact that the hydrophilic-hydrophobic ratio was not sufficiently different to dramatically affect protein adsorption. It is assumed that a greater effect may only occur with a larger fraction or higher length of alkyl side chains, since differences in most abundant proteins attached as well as in the amount of tethered proteins were already noticed for 15AuPG12HS. Moreover, cholesteryl functionality slightly affected the protein corona composition compared to alkyl moieties, with SERPINC1 showing highest affinity, followed by KNG1 and VTN, both are known to bind preferentially to cholesteryl-modified quantum dots<sup>[451]</sup>. Nevertheless, half of the 20 most abundant proteins in the protein corona were identified on all PGylated AuNPs, with KNG1 and VTN among the top 3. This could possibly be related to the identical polymer backbone, wherein only a certain number of side chains have been functionalized with various hydrophobic units.

However, it has explicitly to be mentioned that merely single measurements were conducted, impeding significant statements. Thus, the finding should be regarded as a proof of principle for determining the role of type and number of hydrophobic side chains on protein adsorption behavior.

Hereafter, the impact of the different protein corona compositions on a possible longer blood retention time is investigated by studying the AuNP uptake into human macrophages (see **Section 3.2.3.5**), since it is known that attached proteins influence cell internalization and thus the biological effect of NPs in the body. Depending on their biological function, proteins can either inhibit or promote cellular uptake once adsorbed on nanocarriers.<sup>[267,452]</sup>



### 3.2.3.5 Macrophage uptake of AuNPs with known protein corona composition

In order to prove the PG coating results in a stealth behavior of the particles and to investigate the impact of the different adsorbed proteins in a biological system, the in vitro interaction of the previously in detail discussed AuNPs with immune cells was studied. The four PGylated as well as the citrate-capped particles, before and after incubation with HS, were incubated with human monocyte-derived macrophages. Macrophages were used as they are important components of the immune defense and play an essential role in the clearance of foreign substances from the bloodstream.<sup>[243]</sup> Cellular uptake was determined by analyzing the amount of AuNPs not taken up by cells after 6 h of treatment using ICP-MS analysis.

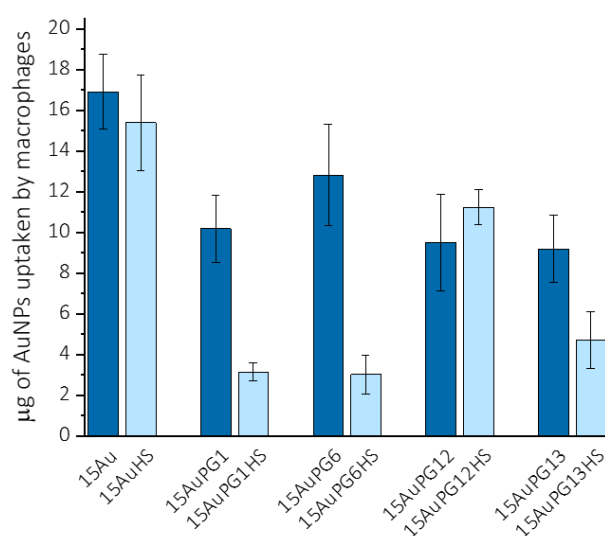


**Figure 55.** Macrophage uptake of unmodified and various PG-functionalized AuNPs, with and without pre-adsorption of HS proteins. Error bars represent the deviations from three experiments with macrophages isolated from buffy coat of one donor using one batch of functionalized AuNPs.

As seen in **Figure 55** ungrafted AuNPs displayed highest macrophage internalization independent on adsorbed proteins, while the PG-coated particles incubated in HS were less taken up than these without serum pre-treatment, except of 15AuPG12HS. Latter showed slightly increased cell uptake compared to 15AuPG12HS. Modification with PG reduced macrophage uptake compared to citrate-AuNPs, indicating the function of PG as a stealth polymer. However, since the effect of reduction could not be observed in such a great extent as for particles incubated with proteins, it was demonstrated that not PGylation itself but rather the adsorbed proteins were responsible for inhibited cell internalization.

### 3 Results and discussion

Enhanced cell uptake of 15AuHS compared to other particles incubated with HS could be explained due to its high protein amount present in the protein corona, as well as the fact that the complement protein C3, known to promote phagocytosis<sup>[27,290]</sup>, showed high affinity to the particle surface. Although the dysopsonin HSA, which prolongs blood circulation time<sup>[310]</sup>, was the most abundant protein on 15AuHS, these particles were highly taken up, suggesting that opsonizing effect of C3 is stronger than dysopsonizing character of HSA. Moreover, the attached immunoglobulins, as well as APOH, present in the top 20 proteins in the hard corona of bare AuNPs, enable the clearance of the particles by the immune system.<sup>[258,453]</sup> Since APOH is known to bind to negatively charged compounds<sup>[454]</sup>, the increased attachment of APOH on citrate-stabilized AuNPs compared to PGylated particles can possibly be attributed to the former displaying highest negative surface charge ( $-31.7 \pm 1.3$  mV), as determined by zeta potential measurements. The preferential binding to negatively charged surfaces could furthermore explain the interaction between the cell membrane and AuNPs, whose protein corona is enriched of APOH.

15AuPG1HS and 15AuPG6HS showed comparable low uptake by macrophages despite being coated with PGs bearing alkyl chains of different lengths as well as of different ratios, with both having similar protein corona composition, wherein KNG1 and VTN were the most abundant proteins and only half of the protein amount compared to bare AuNPs. KNG1 is known to bind to the surface receptor of macrophages, but not promote cell internalization. Rather, it supports the transport of nanocarriers to the site of inflammation.<sup>[455]</sup> Overexpression of KNG1, for instance, lead to suppressed tumor progression through inhibition of proliferation and promotion of apoptosis of tumor cells.<sup>[456]</sup> That internalization in immune cells is not affected by high KNG1 concentration in the protein corona has already been demonstrated by other research groups on silica and gold NPs.<sup>[27,444,457]</sup> In particular, high enrichment of VTN might play a decisive role in suppressed cell internalization, as it is known to reduce the affinity of extracellular nanocarriers to the surface of the cells.<sup>[458]</sup> In addition, the lipoprotein APOE, which was present on both PGylated AuNPs with 5% and 4 % of total bound proteins, respectively, probably played a role in inhibited macrophage uptake, as this transport protein is thought to enhance the passage of NPs across the blood-brain barrier<sup>[284,310]</sup>. Moreover, protein coronas of 15AuPG1HS and 15AuPG6HS contained complement protein C3, but to a 2-fold

decreased adsorption compared to ungrafted AuNPs, suggesting that PG suppressed specific C3 binding. Despite the presence of C3 in the top 10 of attached proteins, cell internalization was extremely low. However, it can be hypothesized, that the additionally abundant attached protein CFH as well as VTN, acting as complement inhibitors, affect the complement cascade, and thus regulate immune cell activation and consequently nanoparticle clearance and biodistribution.<sup>[458,459]</sup> Since the protein corona is composed of multiple layers rather than just one protein layer<sup>[460]</sup>, it is in addition possible that C3 was directly bound to the NP surface and surrounded by other proteins with dysopsonizing effects, thus forming a protective outer layer against recognition by macrophages<sup>[444]</sup>. For example, Zhang *et al.*<sup>[460]</sup> showed that proteins C3 and SERPINC1, which is high abundant in the protein corona of 15AuPG1HS and 15AuPG6HS, are strong binding pairs. SERPINC1 is an anticoagulant protein further possessing an anti-inflammatory function and hence be effective as therapeutic agent.<sup>[461,462]</sup> It is assumed that SERPINC1 did not enhance macrophage uptake, as already reported by Simon *et al.*<sup>[440]</sup>, who demonstrated low uptake of NPs by immune cells with SERPINC1 present in top 2 corona proteins.

In contrast, for 15AuPG12HS we observed a remarkable higher cellular uptake than the other particles functionalized with PG-containing alkyl moieties, possibly related to the high amount of complement protein C3, which was nearly the same as found in the protein corona on bare AuNPs. Thus, it was not the coating with PG per se that suppressed the specific C3 binding, as previously hypothesized, but rather this was dependent on the functionalization of the PG side chains. Just as in 15AuPG1HS and 15AuPG6HS, complement inhibitors CFH and VNT were proteins among the 10 most abundant proteins present in the protein corona of 15AuPG12HS, but exhibited a lower percentage. Thus, it can be suggested, that complement activation cannot be fully suppressed. Moreover, adsorbed APOH, which promotes particle internalization into cells<sup>[285]</sup>, might influence the biological behavior, leading to rapid clearance by macrophages. The increased binding affinity of APOH to 15AuPG12HS could in turn be related to its high negative surface charge of  $-26.6 \pm 3.5$  mV as well as to the fact that apolipoproteins bind preferentially to hydrophobic residues, as already mentioned in **Section 2.2.**<sup>[214,441,454]</sup> In addition to APOH, further lipoproteins such as APOA11, APOA2, APOB, APOE, APOC1 and APOJ were found in high abundance on 15AuPG12HS. However, in contrast to APOH, these lipoproteins are

### 3 Results and discussion

dysopsonins, increasing the blood circulation time of the nanocarriers.<sup>[266]</sup> Nevertheless, it seemed that the dysopsonizing effect of the aforementioned lipoproteins was not as strong as the opsonizing effect of APOH and C3. Furthermore, the high protein amount as well as the fact that no specific protein was enriched but the protein corona rather consisted of various proteins with similar amounts, suggested to play a crucial role in cell internalization. On top, hydrophobicity induces protein denaturation<sup>[463,464]</sup>, potentially affecting their function compared to NPs with less hydrophobic surface coatings.

Last, reduced macrophage uptake was realized for cholesteryl-functionalized particles even though not to such a great extent as recognized for 15AuPG1HS and 15AuPG6HS, although protein corona composition is similar, at least for most abundant proteins, whose functions are discussed previously. The fact that macrophage uptake was not as strongly suppressed as in 15AuPG1HS and 15AuPG6HS might be attributed to the enrichment of immunoglobulins, since this protein class possesses an opsonizing effect promoting phagocytosis<sup>[288,465]</sup>.

This indicated that NP-cell interaction is not only affected by most abundant proteins present in the protein corona, but rather is an effect of the interplay of the mixed corona, wherein some proteins enhance, and others inhibit cell internalization. These effects are pronounced to varying degrees, independent of the abundance of the attached proteins.

In order to investigate the cytotoxicity of these particles and to prove that the reduced cell uptake of HS-incubated AuNPs was not related to inactive macrophages, a LIVE/DEAD assay was performed. Fluorescence microscopy images show that AuNP incubation did not significantly influence macrophage viability, as depicted in **Figure 56**.

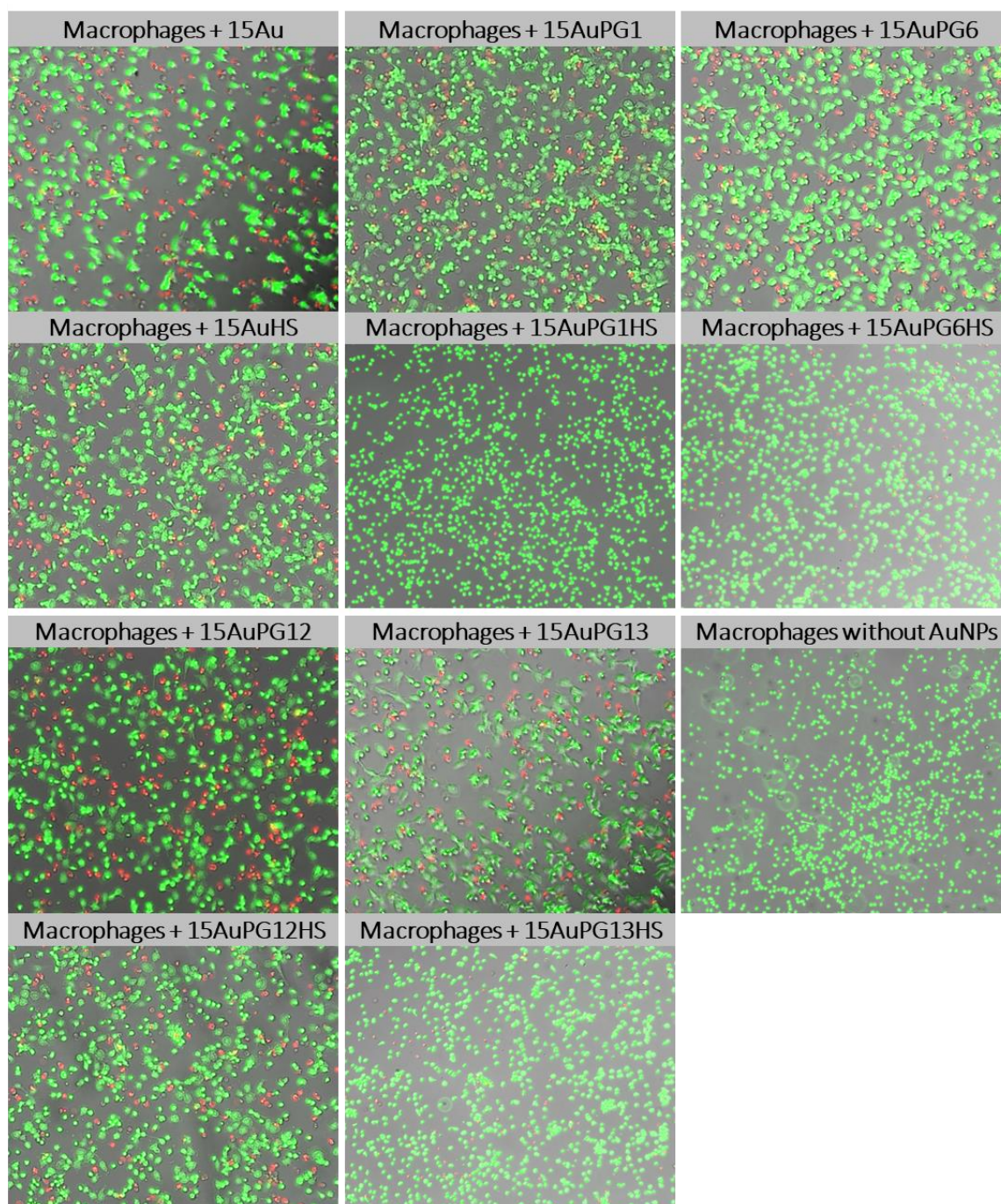


**Figure 56.** Fluorescence microscopy images of macrophages incubated with various 15 nm AuNPs after LIVE/DEAD staining.

However, it has to be explicitly pointed out that experiments were performed only with macrophages isolated from the buffy coat of one donor and just one batch of functionalized AuNPs was used. Thus, the results should be considered as proof of principle for evaluating the impact of the protein corona on immune response by macrophage internalization.

Taken together, AuNPs coated with multivalent PGs, side-chain functionalized with various hydrophobic units such as different alkyl functionalities with varying chain lengths as well

### 3 Results and discussion

as cholesteryl units, were prepared to investigate the effect of different surface hydrophobicities on serum protein adsorption and their subsequent cellular uptake by human monocyte-derived macrophages. After incubation of modified AuNPs with HS, attached proteins were quantitatively and qualitatively analyzed by micro-BCA assay and SDS-PAGE as well as LC-MS/MS, respectively. It was shown that the length and number of hydrophobic alkyl moieties influences protein adsorption, whereas high protein enrichment and a diverse protein pattern obtained for AuNPs coated with PG bearing the longest alkyl chain. In contrast, fewer proteins adsorbed on less hydrophobic particles, also exhibiting various protein corona composition that were examined in more detail. The differences in serum protein adsorption correlated with differences in cellular uptake of AuNPs by macrophages, with less hydrophobic NPs presenting significantly reduced cell internalization. These findings indicated that the hydrophobic side chains in PG, especially depending on the length and number of hydrophobic alkyls, played a crucial role in protein binding, which in turn affected macrophage uptake of AuNPs.

### 3.3 Impact of surface functionality on biodistribution of AuNPs in silkworms

To date, animal models are still indispensable for studying biodistribution and elimination of nanomaterials. However, the use of mammals for in vivo experiments faces various challenges including increasing regulatory hurdles and costs. In this study, the aim was to validate larvae of the domestic silkworm *Bombyx mori* as an alternative invertebrate model for preliminary in vivo research. Based on the in **Section 2.3.2** mentioned similarities between silkworm's hemolymph and mammalian blood, similar specialized major organ compartments, as well as common pharmacokinetics and a conserved innate immune system, it was hypothesized that the biodistribution of NPs may be comparable in silkworm and mammalian models. To address this assumption, in this study, the first comparison of differently polymer-coated AuNPs with respect to their biodistribution in silkworm organs following intra-hemolymph injection is presented. 6 h and 24 h after administration the Au content in different organ compartments was measured with ICP-MS.

Since surface functionalization and surface charge is known to affect biokinetics of NPs<sup>[20,308]</sup>, commercially available, citrate-capped 15 nm AuNPs were modified with four different surface coatings: one PEG-based modification and three PG-coatings with slightly hydrophobic functionalization, as well as positively and negatively charges. The various functionalities, more precisely distinct alkyl moieties as well as amine or carboxyl groups, were introduced to polymers by thiol-ene "click" reaction.<sup>[17,353]</sup>

The linear PG is a biocompatible polymer whose backbone matches the backbone of PEG, however containing a functional hydroxyl group in its every repeating unit. Thus, PG is considered as a multihydroxy-functional alternative to conventional PEG, making PGs interesting polymers in the drug delivery field.<sup>[466]</sup> Furthermore, due to the similar chemical structures, PG represents a good alternative as stealth polymer to PEG, showing comparable or more reduced protein adsorption.<sup>[33,34]</sup> Notably, in the present study, all polymers were thioether functionalized. Due to the non-nucleophilic and non-oxidative characteristics, such gold surface coating exhibits excellent colloidal stabilization and enables an easier chemical functionalization i.e., higher chemical stability compared to commonly used thiol-polymers.<sup>[17]</sup>

In this section, first the synthesis and characterization of the studied charged polymers P(G<sub>50</sub>-co-SEt<sub>5</sub>-co-NH<sub>2(1)</sub>) and P(G<sub>50</sub>-co-SEt<sub>5</sub>-co-COOH<sub>1</sub>) by <sup>1</sup>H-NMR, FT-IR and Raman

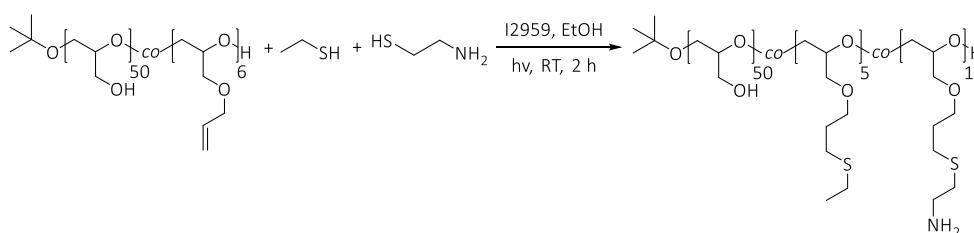
### 3 Results and discussion

spectroscopy as well as SEC analysis is described. Moreover, the number of amines within the PG was quantitatively determined by TNBSA assay. Only the synthesis and characterization of charged PGs bearing several thioether as well as amine and carboxylic units, respectively, is presented, since the synthesis of the other used polymers MeO-PEG-SPentyl and P(G<sub>50</sub>-co-SEt<sub>10</sub>-co-SDec<sub>2</sub>) has already been described thoroughly in **Section 3.1.1.1** and **Section 3.2.1.1**. Throughout this section the used polymers were named as MeO-PEG-SPentyl (PEG), P(G<sub>50</sub>-co-SEt<sub>10</sub>-co-SDec<sub>2</sub>) (PG(Alkyl)), P(G<sub>50</sub>-co-SEt<sub>5</sub>-co-NH<sub>2(1)</sub>) (PG(+)) and P(G<sub>50</sub>-co-SEt<sub>5</sub>-co-COOH<sub>1</sub>) (PG(-)), and in the further course of this section, only the abbreviations PEG, PG(Alkyl), PG(+)) and PG(-) were utilized for simplicity. Successful polymer adsorption to AuNPs by ligand exchange reaction was further proven by UV-Vis absorbance, DLS, zeta potential measurements and FT-IR spectroscopy. Subsequent injection of the different particle solutions into silkworm's hemolymph and incubation of 6 h or 24 h allowed to provide information about the biodistribution and elimination of AuNPs by using ICP-MS technique.

#### 3.3.1 PGs bearing charged functionalities

##### 3.3.1.1 Synthesis of amine-functionalized PG

Amine-functionalized PG, more specifically P(G<sub>50</sub>-co-SEt<sub>5</sub>-co-NH<sub>2(1)</sub>), was synthesized by thiol-ene reaction of P(G<sub>50</sub>-co-AGE<sub>6</sub>) with EtSH and cysteamine hydrochloride (see **Scheme 10**). The UV-light triggered reaction, initiated by addition of I2959, and subsequent purification by dialysis and freeze-drying yielded in a light-yellow oil.



**Scheme 10.** Synthesis of P(G<sub>50</sub>-co-SEt<sub>5</sub>-co-NH<sub>2(1)</sub>) via thiol-ene reaction of P(G<sub>50</sub>-co-AGE<sub>6</sub>) using EtSH and cysteamine.

<sup>1</sup>H-NMR, FT-IR and Raman spectroscopy as well as SEC measurements were conducted to confirm the introduction of ethyl and amine functionalities (see **Section 5.4.19**).



$^1\text{H-NMR}$  spectrum in **Figure 57** shows a multiplet at 3.80-3.66 ppm, corresponding to the polymer backbone. The triplets at 3.23 ppm and 2.88 ppm, respectively, were allocated to the methylene protons H-18 and H-20 next to the amine group of the bound cysteamine. Integration of these signals determined an introduction of one amine unit per polymer. The spectrum showed further methylene protons (H-15-17 and H-13,14) at a chemical shift of 2.70-2.59 ppm and 1.91 ppm, respectively. The signals between 1.30 ppm and 1.25 ppm were attributed to the methyl protons of the thioethyl units and the *tert*-butyl end group. Successful thiol-ene reaction was confirmed as no allylic signals were detected.

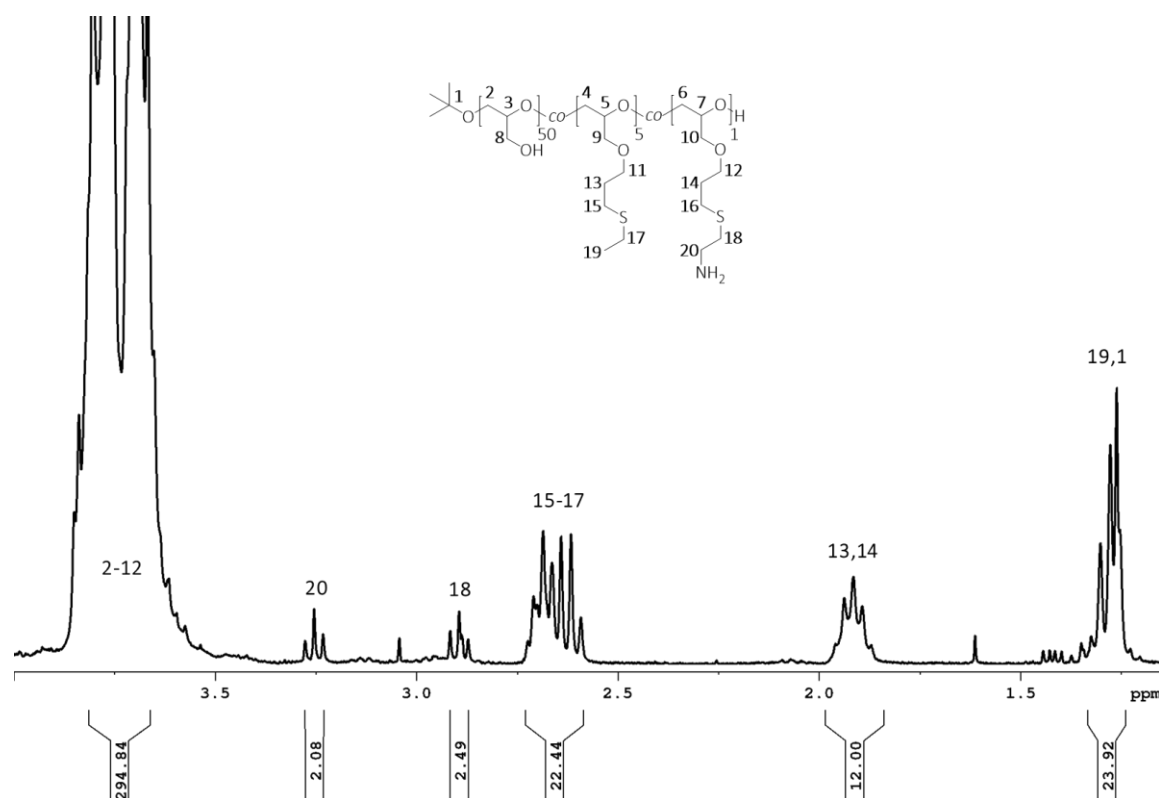


**Figure 57.**  $^1\text{H-NMR}$  spectrum of  $\text{P}(\text{G}_{50}\text{-co-SEt}_5\text{-co-NH}_{2(1)})$ , synthesized via bimolecular thiol-ene reaction of  $\text{P}(\text{G}_{50}\text{-co-AGE}_6)$  with EtSH and cysteamine.

Moreover, the number of amines within the PG was quantitatively determined by TNBSA assay. **Table 13** reveals that the values identified by the assay matched well with these maintained by  $^1\text{H-NMR}$  spectroscopy.

### 3 Results and discussion

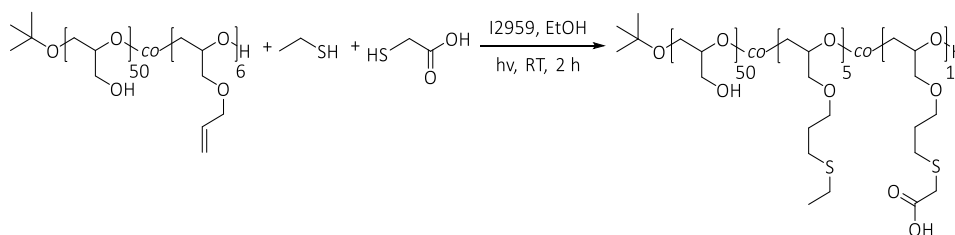
**Table 13.** Amine amount determined by TNBSA assay and  $^1\text{H-NMR}$  spectroscopy of  $\text{P}(\text{G}_{50}\text{-co-SEt}_5\text{-co-NH}_{2(1)})$  copolymer.

Polymer	Amine units per polymer chain	
	TNBSA assay	$^1\text{H-NMR}$ spectroscopy
$\text{P}(\text{G}_{50}\text{-co-SEt}_5\text{-co-NH}_{2(1)})$	1.1	1

FT-IR transmittance and Raman spectra of this amine-functionalized PG are not presented here as they are in analogy to  $\text{P}(\text{G}_{50}\text{-co-SEt}_{5.5}\text{-co-NH}_{2(0.5)})$  of **Section 3.2.1.2**, where the spectra of both spectroscopic methods were depicted.

#### 3.3.1.1 Synthesis of carboxyl-functionalized PG

Carboxyl-functionalized PG, more specifically  $\text{P}(\text{G}_{50}\text{-co-SEt}_5\text{-co-COOH}_1)$ , was received by adding EtSH and thioglycolic acid to  $\text{P}(\text{G}_{50}\text{-co-AGE}_6)$ , initiated with I2959 (see **Scheme 11**). After irradiation with UV light, and subsequent purification by dialysis and lyophilization the polymer was received as a yellowish oil.



**Scheme 11.** Synthesis of  $\text{P}(\text{G}_{50}\text{-co-SEt}_5\text{-co-COOH}_1)$  via bimolecular thiol-ene reaction of  $\text{P}(\text{G}_{50}\text{-co-AGE}_6)$  with EtSH and thioglycolic acid.

$^1\text{H-NMR}$ , FT-IR and Raman spectroscopy as well as SEC measurements were conducted to confirm the introduction of ethyl and carboxyl functionalities.

The multiplet displayed in the  $^1\text{H-NMR}$  spectrum in **Figure 58** at 3.81-3.68 ppm assigned to the protons of the polymer backbone. The singlet at a chemical shift of 3.37 ppm was allocated to the methylene protons H-18 next to the carboxyl group of the bound thioglycolic acid and further methylene protons (H-15-17 and H-13,14) were detected at a chemical shift of 2.73-2.60 ppm and 1.93 ppm, respectively. The multiplet between 1.38 ppm and 1.27 ppm and the significant peak at 1.28 ppm were attributed to the methyl protons of the thioethyl moieties (H-19) and to this of the *tert*-butyl end group (H-1).

Integrating these signals revealed introduction of one carboxyl unit per polymer. In addition, the absence of the allylic signals proved complete thiol-ene reaction.

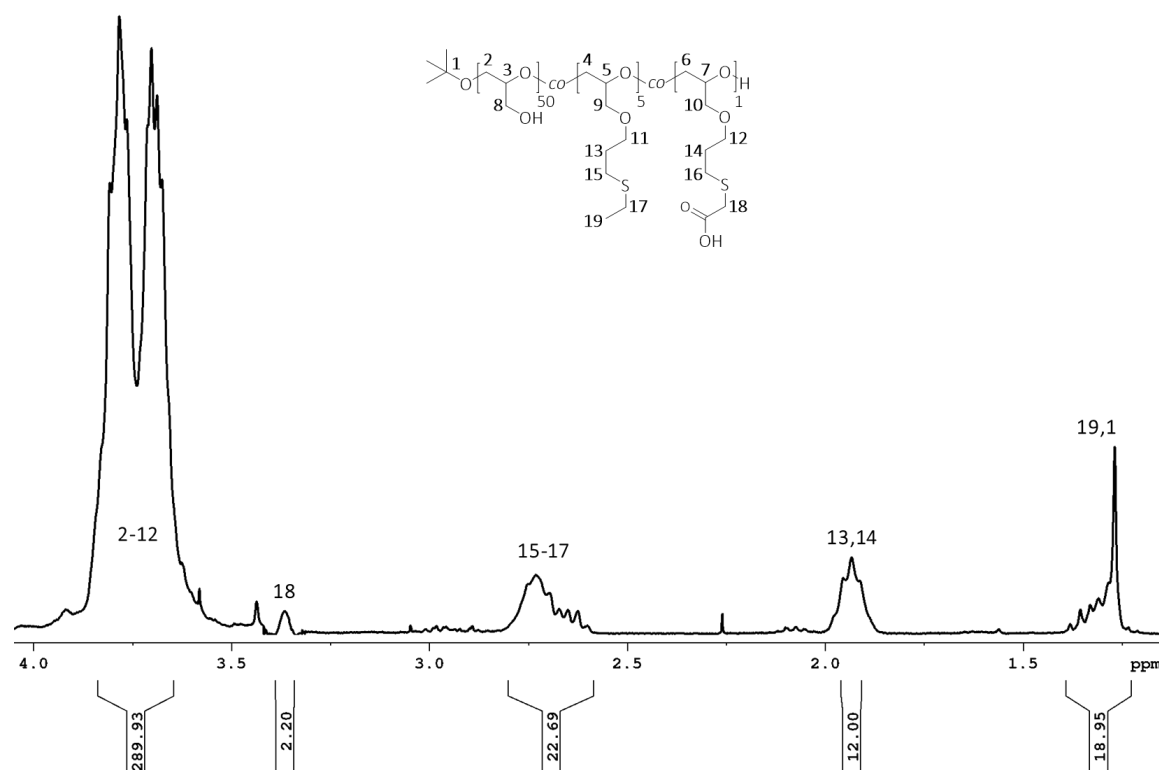


**Figure 58.**  $^1\text{H-NMR}$  spectrum of  $\text{P}(\text{G}_{50}\text{-co-SEt}_5\text{-co-COOH}_1)$ , synthesized via bimolecular thiol-ene reaction of  $\text{P}(\text{G}_{50}\text{-co-AGE}_6)$  with EtSH and thioglycolic acid.

Total conversion of allyl groups was further proven by FT-IR and Raman spectroscopy. The resulting polymer showed an intensive C=O-stretching band at  $1718\text{ cm}^{-1}$  instead of the previously existing band at  $1646\text{ cm}^{-1}$  attributed to allylic vibrations (see **Figure 59a**). In **Figure 59b** no more allylic C=C vibrations ( $1647\text{ cm}^{-1}$ ), but a C=O-stretching vibration at a wavelength of  $1737\text{ cm}^{-1}$ , indicating introduction of carboxyl functionalities. Moreover, the absence of the allyl signal ( $1644\text{ cm}^{-1}$ ) and the presence of the thioether stretching vibration ( $655\text{ cm}^{-1}$ ) indicated a successful functionalization with the thiol compounds thioglycolic acid. Relevant FT-IR and Raman bands were highlighted in light grey.

### 3 Results and discussion

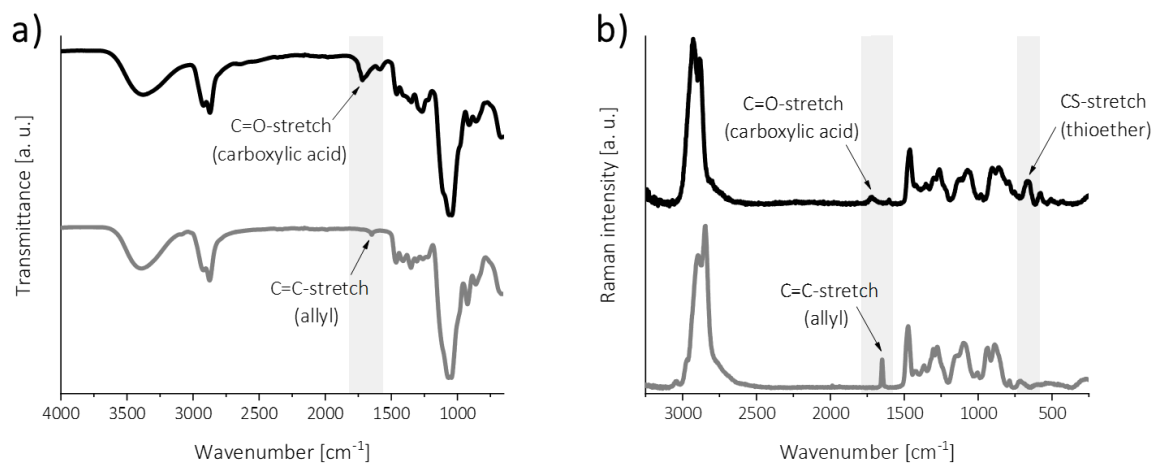


**Figure 59.** a) FT-IR transmittance and b) Raman spectra of P(G<sub>50</sub>-co-SEts-co-COOH<sub>1</sub>) (top, black) in comparison to P(G<sub>50</sub>-co-AGE<sub>6</sub>) (bottom, grey), displaying the absence of allyl vibration as well as the presence of carboxylic acid and thioether stretching after thiol-ene reaction.

### 3.3.2 Adsorption of PEG and PG carrying various functionalities on citrate-AuNPs

The four aforementioned polymers were attached to the surface of citrate-capped 15 nm AuNPs via ligand exchange reaction. As a result, sulfur containing polymers organized in a quasi-covalent coordination on the Au surface, a process solely driven by the miniscule electrostatic interaction of the citrate molecules on the particle surface.<sup>[181]</sup> As displayed in **Figure 60a**, citrate-stabilized AuNPs were labeled in yellow, AuNPs coated with MeO-PEG-SPentyl (PEG-AuNP) in blue, with P(G<sub>50-co</sub>-SEt<sub>10-co</sub>-SDec<sub>2</sub>) (PG(Alkyl)-AuNP) in cyan, with P(G<sub>50-co</sub>-SEt<sub>5-co</sub>-NH<sub>2(1)</sub>) (PG(+)-AuNP) in green and with P(G<sub>50-co</sub>-SEt<sub>5-co</sub>-COOH<sub>1</sub>) (PG(-)-AuNP) in red throughout this section.

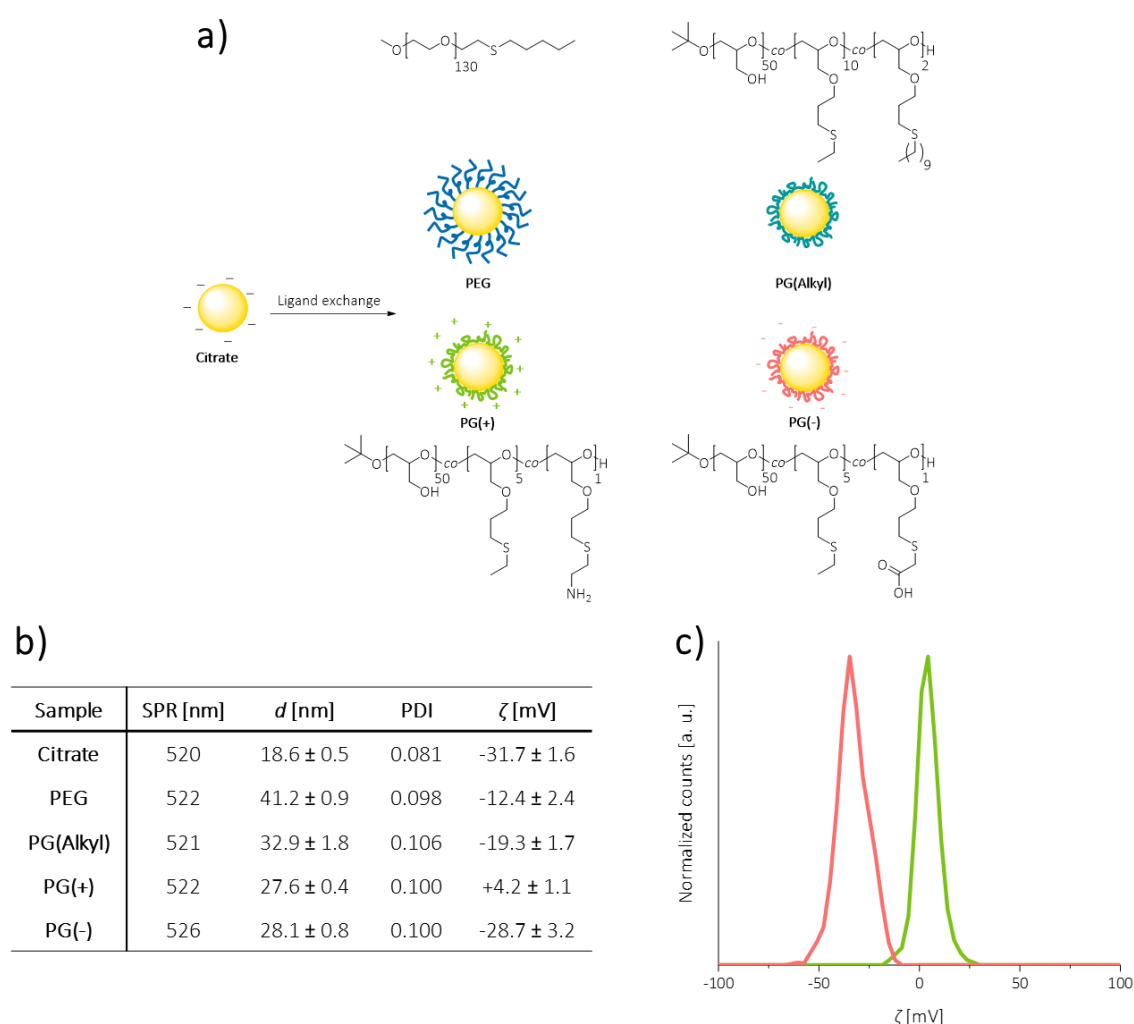


**Figure 60.** Polymeric functionalization of AuNPs. a) Simplified illustration of four different AuNPs coated with functionally distinct polymers. b) Values of SPR, *d*, PDI, and ζ of citrate- as well as PEG- or PG-coated AuNPs identified via UV-Vis, DLS and zeta potential analysis. c) Normalized zeta potential of PG(+)-AuNPs (green) and PG(-)-AuNPs (red), confirming positive (+4.2 mV) and negative (-28.7 mV) surface charges, respectively.

### 3 Results and discussion

Polymer attachment was verified by various spectroscopic data. UV-Vis absorbance and DLS spectroscopy proved that AuNPs were successfully modified, revealing a characteristic SPR red-shift and increased hydrodynamic diameter  $d$  compared to citrate-capped NPs (Figure 60b and Figure 61a-b). Larger  $d$  values were observed for PEG-coated AuNPs than for those coated with PG, which is in accordance with previous studies.<sup>[17,44]</sup> The polymer structure-dependency of  $d$  attributed to different polymer arrangements on the particle surface, displaying a brush-like conformation for PEG due to only end-grafting, while for configuration of multivalent PGs it has been hypothesized that they show trains, loops and tails (simplified illustration in Figure 60a).<sup>[8,374]</sup> All samples exhibited monodispersed curve progression with PDIs around 0.1.

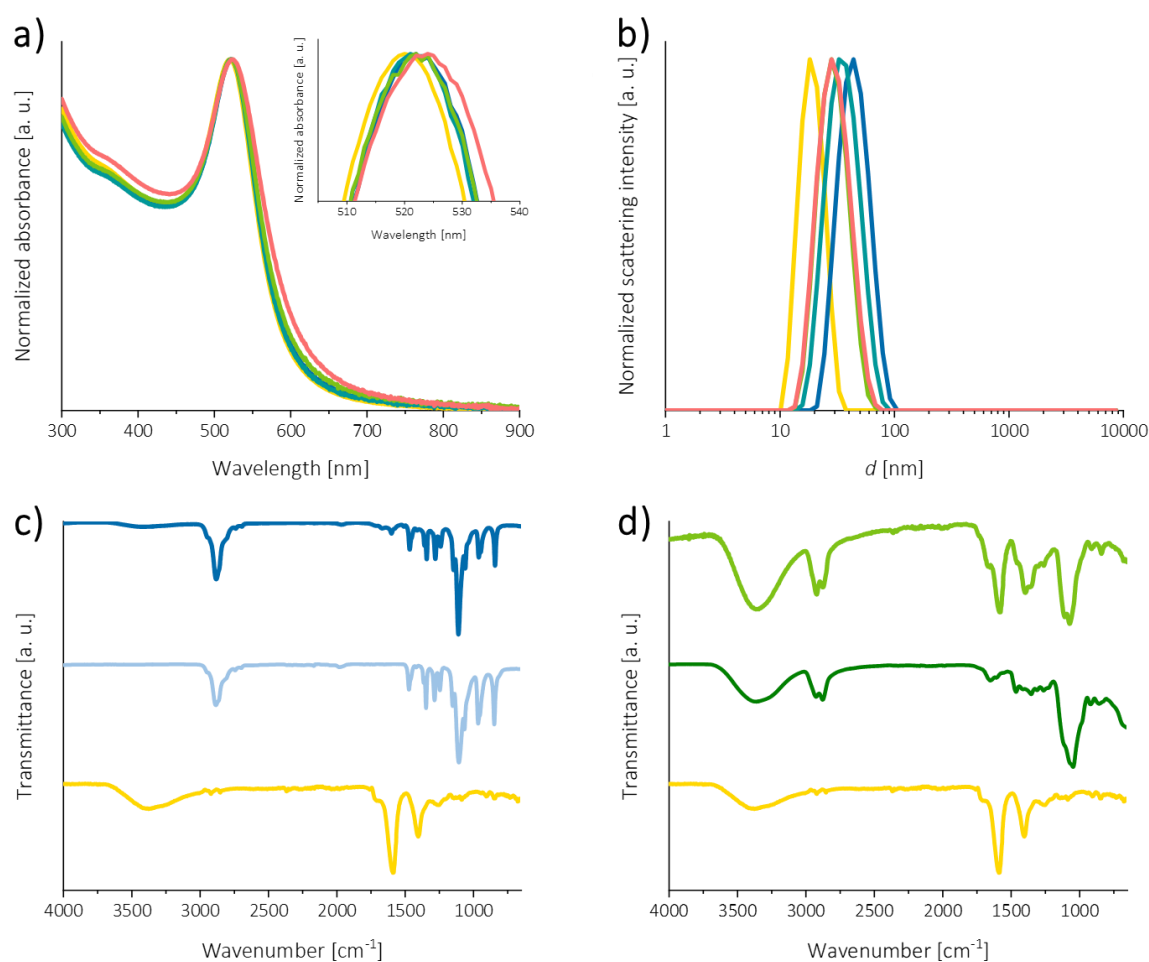


**Figure 61.** Normalized a) UV-Vis absorbance and b) DLS spectra of 15 nm citrate-capped AuNPs (yellow) compared to AuNPs modified with PEG (blue), PG(Alkyl) (cyan), PG(+) (green) and PG(-) (red). The insert in (a) displays an enlarged part of the respective graph with adjusted scaling of both axes, to improve visualization of the SPR shift. And c) and d) FT-IR transmittance spectrum of PEG- (c, top, blue) respective PG(+)- (d, top, green) functionalized AuNPs compared to this of pure PEG (c, middle, light blue) respective PG(+) (d, middle dark green) and citrate-AuNPs (both, bottom, yellow).

Furthermore, zeta potential measurements before and after polymer adsorption determined successful polymer attachment. Especially the positive zeta potential of +4.2 mV as well as the highly negative value of -28.7 mV verified charged AuNP surface modification with PG(+) and PG(-), respectively (**Figure 60c**). Zeta potential of AuNPs without charged functionalities showed less negative values of -12.4 mV for PEG and -19.3 mV for PG(Alkyl), which is in accordance with literature for PEG- and PG-modified AuNPs.<sup>[424,433]</sup>

In addition, FT-IR analysis of polymer-modified AuNPs revealed identical results compared to respective pure polymers, as exemplarily depicted for PEG and PG(-) in **Figure 61c-d**.

### 3 Results and discussion

#### 3.3.3 Biodistribution and accumulation of AuNPs in silkworms

Following the *in vitro* characterization of AuNPs with different surface functionalities, their toxicity in silkworms as well as their biodistribution and accumulation in silkworm larvae was investigated (detailed information of rearing summarized in **Section 5.1.2.21**).

For toxicity evaluation of the four differently functionalized AuNPs in silkworms ( $n = 5$  silkworms/group), 50  $\mu\text{L}$  of the respective colloidal AuNP solution (200  $\mu\text{g}/\text{mL}$  in 0.9% sodium chloride (NaCl)) were directly injected into the hemolymph. All silkworms survived even at 72 h post injection, proving that all AuNPs were nontoxic at the used concentration of 200  $\mu\text{g}/\text{mL}$ . In general, LD50 is used for determination of toxicity in animal models.<sup>[467]</sup> Namely a wide range of AuNP concentrations needs to be tested, to determine the dose at which 50% of silkworms do not survive. In this study the focus was put on biodistribution of NP in silkworms, and the toxic effect at higher concentrations was not further studied.

To study the biodistribution and accumulation of AuNPs in silkworm larvae, 50  $\mu\text{L}$  of the respective colloidal 200  $\mu\text{g}/\text{mL}$  AuNP solution were directly injected into the hemolymph, and silkworms were kept at 25 °C for 6 h or 24 h. At these two time points hemolymph, midgut, epidermis, and excrements (**Figure 62a**) were collected and analyzed these organ compartments by ICP-MS. Detailed procedures of AuNP injection and silkworm dissection are described in **Section 5.1.2.21** and **Section 5.1.2.22**. 6 h after administration the silkworm hemolymph from different treatment groups exhibited different colors (**Figure 62a**), depending on the AuNP coatings. Injection with the PG(+)-AuNPs resulted in a yellowish color of the hemolymph similar to the control group injected with pure 0.9% NaCl solution. The color of the hemolymph changed from yellowish to slightly red after injection with PEG-, PG(Alkyl)-, or PG(-)-functionalized AuNPs, the latter displaying the most intense red color. 24 h post injection, only PEG- and PG(-)-capped AuNPs caused the hemolymph to change from yellowish to light red (data not shown).



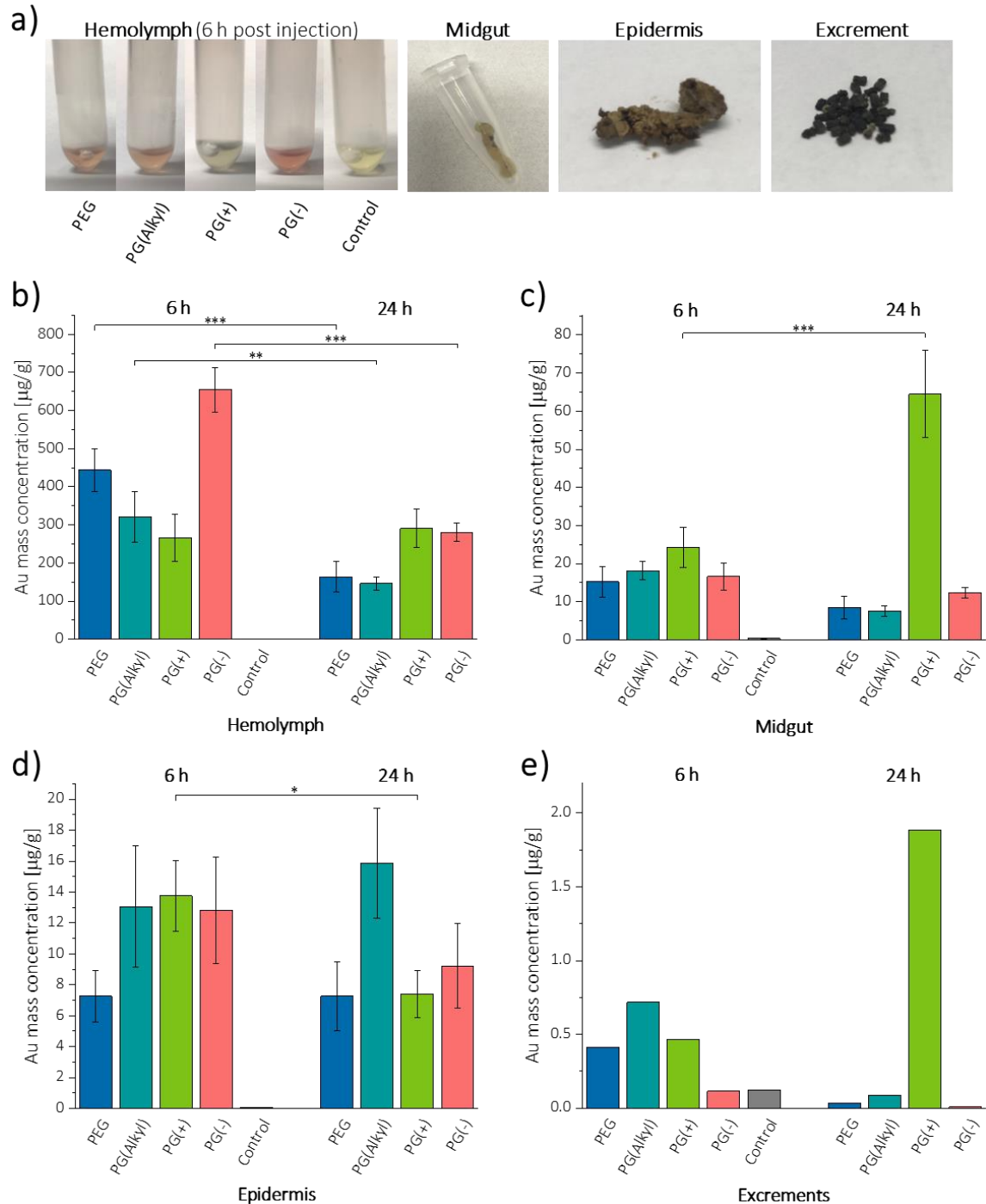


**Figure 62.** Biodistribution of functionalized AuNPs in silkworm (*Bombyx Mori*) larvae. a) Functionalized AuNPs change hemolymph color 6 h after incubation. b-d) Au mass concentration in silkworm samples 6 h and 24 h post injection of different AuNP solutions, including hemolymph (b), midgut (c), epidermis (d) and excrements (e). AuNPs coated with a PEG surface are marked in blue, with PG(Alkyl) in cyan, with PG(+) in green and PG(-) in red, while the control group is labelled in grey. Values are presented as the mean  $\pm$  standard deviation ( $n = 3$  silkworms/group), except for excrement analysis. Since the excrements were collected from all three silkworms of each group, only one measurement was performed. Statistical comparisons, using one-way ANOVA test, were performed for the same type of AuNPs at 6 h vs. 24 h post injection. Significances between the represented groups are assigned as \* ( $p < 0.05$ ), \*\* ( $p < 0.01$ ), and \*\*\* ( $p < 0.001$ ).

### 3 Results and discussion

Next, collected silkworm samples for ICP-MS measurements were prepared to identify the Au mass concentration in the hemolymph, midgut, epidermis, and excrements after injection of the differently functionalized AuNPs. Irrespective of the incubation time (6 h or 24 h), Au content per gram sample decreased in the different organ compartments in the following order hemolymph > midgut ≥ epidermis > excrements (**Figure 62b-e**), with values between 146 µg/g and 655 µg/g detected in the hemolymph, 8-65 µg/g in the midgut, 7-16 µg/g in the epidermis, and 0.01-1.88 µg/g in the excrements (see **Table 15** in **Section 5.1.2.23** for exact values). 6 h after injection, Au amounts were similar or higher compared to those incubated for 24 h, except for PG(+)-AuNPs, which showed three times higher concentrations in the midgut and excrements 24 h after administration. Lower Au concentrations at 24 h may have resulted from the distribution of AuNPs into other tissues such as the silk glands. Nevertheless, the high content of Au in the hemolymph for all groups, even after the 24 h exposure, indicated a prolonged retention of AuNPs in the hemolymph, which demonstrated the stealth effects of polymer coatings on AuNPs. Indeed, in mouse models longer blood circulation time of PEG-stabilized AuNPs had already been observed by other research groups.<sup>[308,468,469]</sup> In contrast, Lee *et al.* reported PEG-modified AuNPs that contained amine or carboxyl units to rapidly accumulate in mouse organs.<sup>[308]</sup> The fact that positively and negatively charged PEG-coated AuNPs spread rapidly into various organs in mice<sup>[308]</sup>, whereas PG(+)- and PG(-)-modified AuNPs used in this study mostly remained in the silkworms hemolymph, could possibly be explained by differences in polymer coating, since several factors such as surface thickness, density, charge, hydrophobicity, functional groups, and polymeric configuration play a role in adsorption of opsonin proteins.<sup>[211,214,470-473]</sup> However, since in the most studies with mice an accumulation into tissues is observed at the latest after an incubation time of more than one hour, it has to be further taken into account that the results of the experiments carried out with mammals and those using silkworms may not be transferable one to one.

Silkworm hemolymph contained the highest Au levels 6 h after injection of PG(-)-AuNPs (**Figure 62b**), followed by PEG-AuNPs, PG(Alkyl)-AuNPs, and PG(+)-AuNPs. Hemolymph Au mass concentration of 655 µg/g for PG(-)-AuNPs exceeded by 2.5-fold times PG(+)-AuNPs (266 µg/g). Au content corresponded to the different hemolymph colors 6 h after injection (**Figure 62a-b**), when hemolymph with the highest Au amount showed the most intensive

red color. However, 24 h post injection, this correlation between the Au content and the color of the hemolymph could not be observed anymore. At this time point, the Au amount already decreased in all groups, except for PG(+)-functionalized NPs. PG(+)-AuNPs exhibited a minimal higher Au amount of 291  $\mu\text{g/g}$  compared to 6 h exposure (266  $\mu\text{g/g}$ ), suggesting rapid initial biodistribution to other organs while reaching steady-state hemolymph levels. In contrast, the other coated AuNPs might have a time-dependent spreading, leading to a reduction of Au concentration in the hemolymph after 24 h, whereby the Au content of PG(-)-coated particles dropped to the same level as the PG(+)-functionalized particles. Based on these observations, it seems that both charged AuNPs display longer circulation time than PEG-AuNPs and PG(Alkyl)-AuNPs, suggesting a surface dependent reduced adsorption of proteins that are responsible for opsonization.<sup>[245]</sup>

PG(+)-AuNPs enriched in the midgut the strongest (24  $\mu\text{g/g}$ ) within 6 h incubation (**Figure 62c**) and increased 2.7-fold to 65  $\mu\text{g/g}$  by 24 h, in contrast to the other groups with slightly lower values at 6 h (15-18  $\mu\text{g/g}$ ), which even decreased in these other groups at 24 hours.

PEG functionality resulted in the lowest Au mass concentration in the epidermis after 6 h incubation (7  $\mu\text{g/g}$ ), while the other groups exhibited similar values (13-14  $\mu\text{g/g}$ , **Figure 62d**). 24 h post injection, PG(Alkyl)-modified AuNPs led to a slightly increased Au amount compared to that after 6 h (16  $\mu\text{g/g}$  vs. 13  $\mu\text{g/g}$ ), while the Au content decreased among the PG(+) and PG(-) groups (7-9  $\mu\text{g/g}$ ) or remained unchanged for PEG functionalization.

Silkworm excrements (**Figure 62e**) contained only very low amounts of Au (< 0.7  $\mu\text{g/g}$ ) at 6 h post injection and were at ICP-MS detection limit and were of or below 0.1  $\mu\text{g/g}$ , similar to the NaCl-injected negative controls. This indicates that the differently modified AuNPs still remained in the silkworm body at this time point. 24 h after injection, Au amounts slightly increased in the PG(+)-AuNP group (1.9  $\mu\text{g/g}$ ) but remained negative at or below limit of detection in the other groups. Elevated PG(+)-AuNPs in silkworm excrements at 24 h were in line with previously reported higher clearance rates of positively charged NPs in vivo studies of rats<sup>[309]</sup> in contrast to oppositely charged AuNPs.

All in all, organ distribution and elimination of AuNPs with four different surface functionalities in silkworms was investigated by ICP-MS 6 h and 24 h after AuNP

### 3 Results and discussion

administration. Independent on the surface functionalization, AuNP concentration was highest in the hemolymph, while especially 24 h post injection, the midgut und feces contained the highest concentration of positively charged particles. Compared to the different PG-functionalized AuNPs, only half the amount of PEG-capped particles accumulated in the epidermis after 6 h. These findings indicated a surface-dependent biodistribution and elimination of AuNPs in silkworms and confirmed the feasibility of using this inexpensive animal model for time- and cost-effective, preliminary in vivo studies of NPs.

---

# 4 Summary / Zusammenfassung

---

## 4 Summary / Zusammenfassung

### 4.1 Summary

Based on previous results showing that thioether modification of gold nanoparticles (AuNPs), especially coating with a multivalent system, yielded in excellent colloidal stability, the **first aim of this thesis** was to prove whether functionalization of silver nanoparticles (AgNPs) with thioether also has a comparable or even enhanced stabilization efficacy compared with the gold standard of coating with thiols and, particularly, whether the multivalency of polymers leads to stable AgNPs conjugates (see **Section 3.1**). For this purpose, in **Section 3.1.1** the synthesis of monovalent thioether-functionalized poly(ethylene glycol) (MeO-PEG-SPentyl) as well as its multifunctional analogue, linear side-chain functionalized poly(glycidol) (PG) with multiple ethylthioether ( $P(G_{50-co-SEt_6})$ ), as well as the synthesis of PG bearing multiple thiols along the backbone ( $P(G_{50-co-SH_6})$ ) was described. While the monovalent polymer was prepared from the purchased MeO-PEG-SH, which was also used in this study, the initial polymer PG of the multivalent system was also synthesized. Successful polymer synthesis was verified by  $^1H$ -NMR and FT-IR spectroscopy as well as SEC measurements. Furthermore, Raman spectroscopy and Ellman assay proved the presence or absence of thiols, whereas the latter was even used to determine the number of existing thiols. Surface modification of citrate-stabilized AgNPs with the aforementioned mono- and multivalent sulfur-containing polymers was carried out by ligand exchange reaction (see **Section 3.1.2**). Different physicochemical techniques (UV-Vis, DLS, zeta potential measurements and FT-IR spectroscopy) verified the successful thiol and thioether surface functionalization of AgNPs, whereas the number of polymer molecules loaded onto the particles as well as the conformation of PEG on the AgNPs surface was quantified via micro-TGA. Micro-TGA measurements revealed a higher number of polymers per nanoparticle (NP) for PEG than for the corresponding PG owing to their different structures with various numbers of anchor groups. Within the two PEGs, both demonstrating a brush-like configuration on the particle surface, MeO-PEG-SPentyl exhibited a lower grafting density than its thiol analogue caused by steric hindrance of the thioether anchor group, claiming more space on the particle surface. A similar trend could be observed for the polymer coverage with PG, even though the size difference between the thiol in  $P(G_{50-co-SH_6})$  and the thioether moieties of  $P(G_{50-co-SEt_6})$  was less distinct. Conversely to monovalent PEG, multivalent PG was assumed to be arranged as trains, loops

and tails. As previously reported for AuNPs,<sup>[17,385]</sup> thioether binding onto AgNPs is slower than the adsorption of analog thiols (see **Section 3.1.3.1**). However, the in **Section 3.1.3.2** presented study on the colloidal stabilization after centrifugation, high temperature treatment, and lyophilization suggested a thermodynamically stronger attachment for thioethers. Also, the aim of receiving stability in biological fluids could be reached after coating the AgNPs with these functional polymers except for particles capped with P(G<sub>50</sub>-*co*-SH<sub>6</sub>) suspended in phosphate buffered saline. In all studies using thioether as a binding agent, there are nearly similar results for PEGylated and PG-coated particles indicating no substantially stable silver–ligand interactions for multidental units.

The excellent stabilization efficacy of thioether-coated AgNPs in water as well as the good colloidal stability in biological environment and, especially, the ability of introducing different chemical or biological functionalities to the backbone of the thioether-PG make these NP systems of great interest in biomedical applications. Furthermore, it would be interesting to test the antibacterial activity of AgNPs modified with thioether-PG against various pathogens in **future** experiments.

As multivalent thioether-PG is already proven as a promising candidate for AuNP modification and stabilization,<sup>[17]</sup> the **second aim of this thesis** was to examine the stealth behavior of PG, side-chain functionalized with various hydrophobic units, to gain a deeper understanding of AuNP surface functionalization in terms of protein adsorption and their subsequent cellular uptake by human macrophages, which are important components of the immune defense and play an essential role in the clearance of foreign substances from the bloodstream. Since it is known that surface functionalization such as coating with hydrophilic polymers or hydrophobic ligands affects the protein corona formation and composition,<sup>[216]</sup> initially, twelve different alkyl-functionalized PG with varying chain lengths and varying ratios and of two cholesteryl-functionalized PG were synthesized and characterized within **Section 3.2.1**. The successful copolymer synthesis was confirmed by <sup>1</sup>H-NMR, FT-IR and Raman spectroscopy as well as TNBSA-assay and SEC analysis. In addition, these PGs were investigated regarding their critical aggregation concentration (CAC) via DLS analysis, since it is known that amphiphilic polymers can form soluble aggregates in aqueous solution above a certain concentration<sup>[390]</sup>, which has to be avoided to achieve attachment of these amphiphilic polymers to the NP surface. In **Section 3.2.2**

## 4 Summary / Zusammenfassung

surface functionalization of citrate-stabilized AuNPs of two different sizes with the before synthesized multifunctional hydrophobic modified polymers was performed by ligand exchange reaction. In this section, a thorough investigation on AuNP incubation with all polymeric solutions of various molar concentrations was conducted to figure out the molarity, which is high enough resulting in high stability, even after salt treatment, and simultaneously low enough to prevent aggregation by bridging flocculation. As suggested, especially for polymers carrying the longest alkyl chain, lower molar concentrations turned out to be ideal to obtain an aggregate-free particle solution, which was also dependent on the functionalization degree (see **Section 3.2.2.2.1**). Furthermore, it was found that larger particles compared to smaller ones could be incubated with a higher polymer molarity solution to achieve the aim of NPs devoid of agglomerates. On the other hand, in **Section 3.2.2.2.2** very low molar concentrations of 2.5  $\mu\text{M}$  to 5  $\mu\text{M}$  for 15 nm AuNPs and 2.5  $\mu\text{M}$  to 7.5  $\mu\text{M}$  for 30 nm AuNPs, respectively, were proven to be sufficient yielding stabilized particles even after addition of two different ion-rich solutions. In case of pentadecane-functionalized PG carrying three and four pentadecane chains, the molar concentration of 5  $\mu\text{M}$  was determined to be the optimal molarity for 15 nm AuNP in both studies, which became challenging since small changes in the AuNP to polymer ratio could lead to aggregation. After determining the optimal molar concentration for adsorption of each polymer to the different sized particles, successful surface coating was verified by various spectroscopic methods such as DLS, UV-Vis and FT-IR (see **Section 3.2.2.2.3**). In **Section 3.2.3** the various hydrophobic functionalized AuNPs were incubated in human serum (HS), and the effect of surface functionalization on protein corona composition and its impact on macrophage internalization was studied. Protein attachment to pure as well as PGylated AuNPs after incubation with HS was verified by various spectroscopic methods (UV-Vis, DLS, Zeta potential, FT-IR) (see **Section 3.2.3.1**). In **Section 3.2.3.2** the total amount of adsorbed proteins on each NP was quantitatively determined by micro-BCA assay, showing suppressed protein binding on PG-modified AuNPs compared to ungrafted particles, and reduced protein adsorption upon increasing the size of the NPs. Furthermore, the adsorbed serum protein layers were qualitatively quantified using SDS-PAGE resulted in different band patterns after Coomassie Blue staining (see **Section 3.2.3.3**). Furthermore, LC-MS/MS analysis in **Section 3.2.3.4** provided a more detailed investigation on the hard corona proteins of selected samples, and the impact of



the protein corona of these selected samples on immune response by macrophage internalization was evaluated (see **Section 3.2.3.5**). The findings appeared that thioether-containing hydrophobic PG acts as a stealth polymer, depending on the side-chain functionalization of the polymer backbone. Among tested AuNPs, AuNP modification with PG carrying the longest alkyl chain and simultaneously the highest number of alkyl moieties, exhibited high amount of attached proteins as well as high macrophage uptake, while less proteins adsorbed on all other PGylated particles, which were barely internalized. It seems that the protein corona as well as the biological fate of the nanocarrier is negatively affected only after a certain degree of functionalization with hydrophobic residues.

This study has indicated the relevance of the chemical design of polymers attached to AuNPs, which are expected to have a stealth effect, shielding them from being recognized by immune cells. However, these results further highlight that the protein corona is highly complex and not yet fully understood. Thus, further investigations on protein adsorption on various nanocarriers, the protein-protein interactions of corona proteins and their influence on cellular uptake have to be performed. Due to its dependency on various aspects, this will be a major challenge for the future. Since NP-cell interaction is not only dependent on different particle characteristics such as surface functionalization or size, but also on cell type<sup>[249]</sup>, for **future studies** it would be of interest to analyze the effect of protein corona on the uptake of different sized AuNPs by various cell lines. In this context, the comparison to non-phagocytic cells such as a carcinoma cell line would be particularly interesting. Since the introduction of more hydrophobic functionalities to PG limits their application owing to poor solubility in aqueous solutions, further **follow-up experiments** to this thesis could include AuNPs coated with PG bearing hydrophilic moieties in addition to ethyl thioether units, followed by investigation of these NPs in terms of protein adsorption and cellular uptake by immune cells. Anyway, PG containing only ethylthioether should be used for comparison. A **perspective** for such surface-functionalized NPs is that they have potential application as targeting materials. In this regard, the particle surface has to be tuned to enable not only reduced protein binding but, more importantly, adsorption of only specific proteins.

#### 4 Summary / Zusammenfassung

As the use of mammals for in vivo experiments faces various challenges including increasing regulatory hurdles and costs, the **third and last aim of this thesis** was to validate larvae of the domestic silkworm *Bombyx mori* as an alternative invertebrate model for preliminary in vivo research, using AuNPs with various surface chemistry for studying their biodistribution and elimination. In **Section 3.3.1**, firstly, two thioether-PGs bearing charged functionalities were synthesized and characterized by  $^1\text{H-NMR}$ , FT-IR and Raman spectroscopy as well as SEC analysis. Moreover, the number of amines within the polymer was quantitatively determined by TNBSA assay. Thereafter, various spectroscopic methods confirmed successful adsorption of the different surface functionalities to citrate-capped AuNPs, including monovalent PEG and multivalent PGs which were slightly hydrophobic, positively charged and negatively charged (see **Section 3.3.2**). Subsequently, the biodistribution of differently modified AuNPs in a silkworm model at two different time points was evaluated within **Section 3.3.3**, suggesting that surface chemistry affects the distribution and NP-cell interaction. ICP-MS measurements revealed the highest Au content in the hemolymph for all groups, even after 24 h incubation, indicating long retention time in the circulation and slow distribution of polymer-coated AuNPs into silkworm tissues and upon egestion in excrements. In this regard, it seemed that especially AuNPs modified with negatively charged PG were opsonized more slowly compared to particles coated with PEG and alkyl-functionalized PG. Among tested AuNPs, positively charged particles appeared to be eliminated most rapidly through the midgut, which plays a central role in detoxification, while the other three surface-functionalized AuNPs were barely detected in the midgut. Overall, it was hypothesized that the long-term bioavailability of AuNPs modified with PEG, alkyl-functionalized PG and negatively charged PG in the silkworm body would make silkworms as a potential alternative invertebrate model for in vivo testing. Furthermore, no toxicity of tested AuNPs in terms of silkworm survival was observed.

Taken together, these findings provided the first proof of principle that silkworms can be an attractive animal model for effectively evaluating the role of surface functionality on biodistribution and accumulation of AuNPs. However, it would be interesting to investigate by **follow-up experiments** whether AuNPs modified with PG carrying a larger number of charged moieties, would spread more rapidly into various silkworm organs such as midgut,

epidermis, and feces. In addition, a direct comparison of biodistribution and accumulation in silkworm larvae's and mice using the same surface-functionalized AuNPs would be of curiosity.

## 4 Summary / Zusammenfassung

### 4.2 Zusammenfassung

Basierend auf bereits vorliegenden Ergebnissen, die zeigten, dass die Thioether-Modifikation von Gold-Nanopartikeln (AuNPs), insbesondere die Beschichtung mit einem multivalenten System, zu einer herausragenden kolloidalen Stabilität führt, war das **erste Ziel dieser Arbeit** nachzuweisen, ob die Funktionalisierung von Silber-Nanopartikeln (AgNPs) mit Thioether-Polymeren ebenfalls eine vergleichbare oder sogar verbesserte Stabilisierungseffizienz im Vergleich zur Beschichtung mit Thiolen aufweist und ob insbesondere die Multivalenz der Polymere zu stabilen AgNP-Konjugaten führt (siehe **Abschnitt 3.1**) Hierfür wurde in **Abschnitt 3.1.1** die Synthese von monovalentem thioether-funktionalisierten Polyethylenglykol (MeO-PEG-SPentyl) sowie dessen multifunktionalen Polyglycidol (PG) Analogon P(G<sub>50-co</sub>-SEt<sub>6</sub>) beschrieben, das an den Seitenketten mehrere Ethylthioether-Gruppen trägt. Des Weiteren wurde in diesem Abschnitt die Synthese des multivalenten Thiol-Polymers P(G<sub>50-co</sub>-SH<sub>6</sub>) dargestellt, das mehrere Thiol-Einheiten entlang des Polymerrückgrates trägt. Während das monovalente thioether-Polymer aus dem gekauften MeO-PEG-SH hergestellt wurde, welches ebenfalls für diese Studie verwendet wurde, wurde das Ausgangspolymer PG des multivalenten Systems im Rahmen dieser Arbeit selbst synthetisiert. Die erfolgreiche Polymersynthese wurde mittels <sup>1</sup>H-NMR- und FT-IR-Spektroskopie sowie durch SEC-Messungen nachgewiesen. Darüber hinaus wurde das Vorhandensein beziehungsweise die Abwesenheit von Thiolen mittels Raman-Spektroskopie und Ellman-Assay überprüft, wobei letztere Methode auch zur Bestimmung der Anzahl der vorhandenen Thiol-Einheiten herangezogen wurde. Die anschließende Oberflächen-modifikation von Citrat-stabilisierten AgNPs mit den eben erwähnten mono- und multivalenten schwefelhaltigen Polymeren fand über eine Ligandenaustauschreaktion statt (siehe **Abschnitt 3.1.2**). Diverse physikochemische Analysemethoden (UV-Vis, DLS, Zeta-Potential-Messungen und FT-IR-Spektroskopie) bestätigten die erfolgreiche Anbindung der Thiol- und Thioether-Polymere an die Partikeloberfläche. Darüber hinaus wurde die Anzahl der auf die AgNPs geladenen Polymermoleküle sowie die Konformation von PEG auf der Partikeloberfläche mittels Mikro-TGA quantifiziert. Die Mikro-TGA-Messungen ergaben für PEG eine höhere Anzahl von Polymeren pro Partikel im Vergleich zum entsprechenden multivalenten Polymer, bedingt durch ihre unterschiedlichen Strukturen mit einer unterschiedlichen Anzahl von Ankergruppen. Innerhalb der beiden

PEGs, die beide eine bürstenartige Konfiguration auf der Partikeloberfläche aufweisen, wies MeO-PEG-SPentyl eine geringere Pflropfdichte auf als sein Thiol-Analogen, was auf die sterische Hinderung der Thioether-Ankergruppe zurückzuführen ist, die mehr Platz auf der Partikeloberfläche beansprucht. Eine ähnliche Tendenz konnte für die Polymerbedeckung mit PG beobachtet werden, obwohl der Größenunterschied zwischen dem Thiol in P(G<sub>50-co</sub>-SH<sub>6</sub>) und den Thioether-Einheiten von P(G<sub>50-co</sub>-SEt<sub>6</sub>) weniger ausgeprägt war. Im Gegensatz zu monovalentem PEG wurde angenommen, dass multivalentes PG in Form von Zügen, Schleifen und Schwänzen angeordnet ist. Wie bereits in vorherigen Untersuchung mit AuNPs festgestellt wurde,<sup>[17,385]</sup> ist auch bei AgNPs die Anbindung von Thioethern langsamer als die Adsorption von analogen Thiolen (siehe **Abschnitt 3.1.3.1**). Die in **Abschnitt 3.1.3.2** durchgeführte Studie zur Untersuchung der kolloidalen Stabilität nach Zentrifugation, Behandlung mit hohen Temperaturen und nach Gefriertrocknung lässt jedoch auf eine thermodynamisch stärkere Bindung für Thioether schließen. Zudem konnte durch die Beschichtung der AgNPs mit diesen funktionellen Polymeren die gewünschte Stabilität in biologischen Flüssigkeiten erzielt werden, mit Ausnahme der mit P(G<sub>50-co</sub>-SH<sub>6</sub>) beschichteten Partikel, die in Phosphat-gepufferter Salzlösung suspendiert wurden. In allen Versuchen in denen Thioether als Ankergruppe verwendet wurden, gab es annähernd identische Ergebnisse für PEGylierte und PG-beschichtete Partikel, was auf keine wesentlich stabileren Silber-Liganden-Wechselwirkungen für multivalente Verbindungen hinweist.

Die ausgezeichnete Stabilisierungseffizienz von Thioether-beschichteten AgNPs in Wasser, die gute kolloidale Stabilität in biologischer Umgebung und insbesondere die Möglichkeit, verschiedene chemische oder biologische Funktionalitäten in das Rückgrat von PG einzuführen, machen diese NP-Systeme für biomedizinische Anwendungen äußerst attraktiv. Ferner wäre es interessant, die antibakterielle Aktivität von AgNPs, die mit Thioether-PG modifiziert wurden, in **zukünftigen Experimenten** gegen verschiedene Krankheitserreger zu testen.

Nachdem sich multivalentes Thioether-PG bereits als vielversprechender Kandidat für die Modifizierung und Stabilisierung von AuNP erwiesen hat,<sup>[17]</sup> bestand das **zweite Ziel** dieser Arbeit darin, das „Stealth“-Verhalten von PG, das mit verschiedenen hydrophoben Einheiten funktionalisiert wurde, zu untersuchen. Dadurch sollte ein besseres Verständnis

## 4 Summary / Zusammenfassung

der AuNP-Oberflächenfunktionalisierung im Hinblick auf die Proteinadsorption und die anschließende zelluläre Aufnahme durch menschliche Makrophagen erlangt werden, die wichtige Komponenten der Immunabwehr sind und eine wesentliche Rolle bei der Beseitigung von Fremdstoffen aus dem Blutkreislauf spielen. Da bekannt war, dass eine Oberflächenfunktionalisierung wie die Beschichtung mit hydrophilen Polymeren oder hydrophoben Liganden die Bildung und Zusammensetzung der Proteinkorona beeinflusst,<sup>[216]</sup> wurden zunächst zwölf verschiedene alkyl-funktionalisierte PGs mit unterschiedlichen Kettenlängen und unterschiedlichen Verhältnissen synthetisiert und in **Abschnitt 3.2.1** charakterisiert. Daneben wurden außerdem auch zwei cholesteryl-funktionalisierte PGs untersucht. Die erfolgreiche Copolymersynthese wurde durch <sup>1</sup>H-NMR-, FT-IR- und Raman-Spektroskopie sowie durch TNBSA-Assay und SEC-Analyse bestätigt. Zusätzlich wurden diese PGs mittels DLS-Analyse auf ihre kritische Aggregationskonzentration (CAC) untersucht, da amphiphile Polymere bekannterweise in wässriger Lösung ab einer bestimmten Konzentration lösliche Aggregate bilden können<sup>[390]</sup>, was zu vermeiden galt, um die Anbindung dieser amphiphilen Polymere an die NP-Oberfläche zu realisieren. In **Abschnitt 3.2.2** wurde anschließend die Modifizierung von zwei unterschiedlich großen Citrat-stabilisierten AuNPs mit den zuvor synthetisierten Polymeren, die mit hydrophoben Einheiten funktionalisiert wurden, beschrieben. In diesem Abschnitt wurde zuerst eine ausführliche Untersuchung der Inkubation von AuNPs mit sämtlichen Polymerlösungen verschiedener molaren Konzentrationen durchgeführt, um die passende Molarität herauszufinden, die hoch genug ist, um eine kolloidale Stabilität auch nach Salzbehandlung zu garantieren, und gleichzeitig niedrig genug, um eine Aggregation durch Verbrückung zu verhindern. Wie vermutet, erwiesen sich insbesondere für Polymere mit der längsten Alkylkette niedrigere molare Konzentrationen als ideal, um eine aggregatfreie Partikellösung zu erhalten. Im Fall von pentadecyl-funktionalisiertem PG wurde hierbei außerdem eine Abhängigkeit vom Funktionalisierungsgrad beobachtet (siehe **Abschnitt 3.2.2.2.1**). Des Weiteren wurde festgestellt, dass größere Partikel im Vergleich zu kleineren mit einer Lösung mit höheren Polymermolarität inkubiert werden können, um das gewünschte Ziel von agglomeratfreien NPs zu erreichen. Andererseits hat sich in **Abschnitt 3.2.2.2.2** gezeigt, dass sehr niedrige molare Konzentrationen von 2.5  $\mu\text{M}$  bis 5  $\mu\text{M}$  für 15 nm AuNPs bzw. 2.5  $\mu\text{M}$  bis 7.5  $\mu\text{M}$  für 30 nm AuNPs ausreichen, um auch nach Zugabe von zwei verschiedenen ionenreichen Lösungen stabile Partikel zu erhalten.

Im Fall von  $P(G_{50}\text{-}co\text{-}SEt_{12\text{-}n}\text{-}co\text{-}SPentadec_n)$  mit  $n = 3$  und  $4$  wurde die molare Konzentration von  $5 \mu\text{M}$  als optimale Molarität für  $15 \text{ nm}$  AuNP in beiden Studien ermittelt, was eine Herausforderung darstellte, da kleine Änderungen des Verhältnisses von AuNP zu Polymer zur Aggregation führen konnten. Nach der Bestimmung der optimalen molaren Konzentration für die Adsorption jedes Polymers an die NP unterschiedlicher Größe wurde die erfolgreiche Oberflächenbeschichtung durch verschiedene spektroskopische Methoden wie DLS, UV-Vis und FT-IR überprüft (siehe **Abschnitt 3.2.2.2.3**). In **Abschnitt 3.2.3** wurden die verschiedenen hydrophob funktionalisierten AuNPs in menschlichem Serum (HS) inkubiert und die Auswirkung der Oberflächenfunktionalisierung auf die Zusammensetzung der gebildeten Proteinkorona sowie deren Einfluss auf die Internalisierung von Makrophagen untersucht. Die Anbindung von Proteinen an unbeschichtete sowie PGylierte AuNPs nach Inkubation mit HS wurde mit verschiedenen spektroskopischen Methoden (UV-Vis, DLS, Zeta-Potential, FT-IR) überprüft (siehe **Abschnitt 3.2.3.1**). In **Abschnitt 3.2.3.2** wurde die Gesamtmenge der adsorbierten Proteine auf den Partikeln mittels Mikro-BCA-Assay quantitativ bestimmt. Dabei zeigte sich, dass die Proteinanbindung auf PG-modifizierten AuNPs im Vergleich zu unbeschichteten Partikeln unterdrückt wurde und die Proteinadsorption mit zunehmender Größe der Partikel abnahm. Darüber hinaus wurden die adsorbierten Serumproteinschichten mittels SDS-PAGE qualitativ quantifiziert, was zu unterschiedlichen Bandenmustern nach Coomassie-Blau-Färbung führte (siehe **Abschnitt 3.2.3.3**). Die LC-MS/MS-Analyse ausgewählter Proben in **Abschnitt 3.2.3.4** lieferte eine detailliertere Untersuchung der Proteine der harten Proteinkorona. Anschließend wurde die Auswirkungen der Proteinkorona dieser ausgewählten Proben auf die Immunantwort durch die Internalisierung durch Makrophagen bewertet (siehe **Abschnitt 3.2.3.5**). Die Ergebnisse zeigten, dass thioetherhaltige hydrophobe PGs, in Abhängigkeit von der Seitenkettenfunktionalisierung des Polymerrückgrats, als „Stealth“-Polymere fungieren. Von den getesteten AuNPs wies die Modifikation mit PG, das die längste Alkylkette und gleichzeitig die größte Anzahl von Alkylresten trug, eine hohe Menge an gebundenen Proteinen sowie eine hohe Makrophagenaufnahme auf. An allen anderen PGylierten Partikel wurden hingegen weniger Proteine adsorbiert und diese NP wurden kaum in Makrophagen internalisiert. Es scheint, dass die Proteinkorona sowie das biologische Verhalten des Nanoträgers erst nach

#### 4 Summary / Zusammenfassung

einem bestimmten Grad der Funktionalisierung mit hydrophoben Resten negativ beeinflusst wird.

Diese Studie hat gezeigt, wie wichtig das chemische Design der an die AuNPs gebundenen Polymere ist, die einen Tarnkappeneffekt haben und so die Partikel vor der Erkennung durch Immunzellen schützen sollen. Die Ergebnisse machen jedoch auch deutlich, dass die Proteinkorona sehr komplex ist und noch nicht vollständig verstanden wurde. Daher müssen weitere Untersuchungen zur Proteinadsorption an verschiedenen Nanoträgern, zu den Protein-Protein-Wechselwirkungen von Corona-Proteinen und zu ihrem Einfluss auf die zelluläre Aufnahme durchgeführt werden. Aufgrund der Abhängigkeit von verschiedenen Aspekten wird dies eine große Herausforderung für die Zukunft sein. Da die NP-Zell-Interaktion nicht nur von verschiedenen Partikeleigenschaften wie der Oberflächenfunktionalisierung oder der Größe, sondern auch vom Zelltyp<sup>[249]</sup> abhängig ist, wäre es für **zukünftige Forschungsarbeiten** von Bedeutung, die Auswirkung der Proteinkorona auf die Aufnahme von AuNPs unterschiedlicher Größe durch verschiedene Zelllinien zu untersuchen. Hierbei wäre vor allem der Vergleich zu nicht-phagozytischen Zellen, wie etwa einer Krebszelllinie, besonders interessant. Aufgrund der Tatsache, dass die Einführung von hydrophoberen Funktionalitäten in PG die Anwendung aufgrund der schlechten Löslichkeit in wässrigen Lösungen einschränkt, könnten außerdem **Folgeexperimente** zu dieser Arbeit mit AuNPs durchgeführt werden, die mit PG beschichtet sind, das neben Ethylthioether-Einheiten auch hydrophile Gruppen trägt, und anschließend die Proteinadsorption und die zelluläre Aufnahme dieser NP durch Immunzellen untersuchen. In jedem Fall sollte PG, das nur Ethylthioether-Funktionalitäten enthält, zum Vergleich herangezogen werden. Eine **potenzielle Einsatzmöglichkeit** für solche oberflächenfunktionalisierten NPs ist, dass sie als Targeting-Materialien eingesetzt werden können. Für diesen Zweck muss die Partikeloberfläche so eingestellt werden, dass nicht nur eine geringere Proteinbindung, sondern vor allem die Adsorption nur bestimmter Proteine erzielt wird.

Da die Verwendung von Säugetieren für In-vivo-Experimente mit verschiedenen Herausforderungen verbunden ist, wie zum Beispiel zunehmender regulatorischer Hürden und Kosten, bestand das **dritte und letzte Ziel** dieser Arbeit darin, Larven des heimischen Seidenspinners *Bombyx mori* als alternatives wirbelloses Tiermodell für erste In-vivo-



Forschungen zu prüfen (siehe **Abschnitt 3.3**). Zur Untersuchung der Biodistribution und Eliminierung von NP in den Seidenspinnerraupen, wurden AuNPs mit unterschiedlicher Oberflächenchemie verwendet. In **Abschnitt 3.3.1** wurden zunächst zwei Thioether-PGs mit Ladungsfunktionalitäten synthetisiert und per  $^1\text{H-NMR}$ -, FT-IR- und Raman-Spektroskopie sowie SEC-Analyse charakterisiert. Darüber hinaus wurde die Anzahl der im Polymer vorhandenen Amine quantitativ anhand des TNBSA-Assay bestimmt. Anschließend wurden durch eine Ligandenaustauschreaktion verschiedenen Oberflächenfunktionalitäten, wie monovalentes PEG, sowie multivalente PGs, die leicht hydrophob, positiv und negativ geladen waren, auf Citrat-verkapselte AuNPs aufgebracht. Die erfolgreiche Adsorption konnte durch verschiedene spektroskopische Methoden bestätigt werden (siehe **Abschnitt 3.3.2**). Im nachfolgenden **Abschnitt 3.3.3** wurde die biologische Verteilung der unterschiedlich modifizierten AuNPs in einem Seidenraupenmodell in Abhängigkeit von zwei verschiedenen Inkubationszeiten untersucht, da anzunehmen war, dass die Oberflächenchemie die Verteilung und die Interaktion zwischen NP und Zelle beeinflusst. ICP-MS-Ergebnisse zeigten sogar nach einer Inkubation von 24 Stunden bei allen Partikeln den höchsten Au-Gehalt in der Hämolymphe, was auf eine lange Verweildauer im Blutkreislauf sowie eine langsame Verteilung der polymerbeschichteten AuNPs im Seidenraupengewebe und beim Ausscheiden über die Exkrementa hinweist. Offenbar wurden insbesondere die mit negativ geladenem PG modifizierten AuNPs langsamer opsonisiert als die mit PEG und alkylfunktionalisiertem PG beschichteten Partikel. Unter allen getesteten AuNPs schienen positiv geladene Partikel am schnellsten durch den Mitteldarm eliminiert zu werden, der eine zentrale Rolle bei der Entgiftung spielt, während die anderen drei oberflächenfunktionalisierten AuNPs im Mitteldarm kaum nachgewiesen wurden. Zusammenfassend kann angenommen werden, dass die Seidenraupen aufgrund der langfristige Bioverfügbarkeit von AuNPs, die mit PEG, alkylfunktionalisiertem PG und negativ geladenem PG modifiziert wurden, ein potenzielles alternatives Wirbellosenmodell für In-vivo-Tests darstellen würde. Darüber hinaus wurde bei den getesteten AuNPs in Hinblick auf das Überleben der Seidenraupen keine Toxizität festgestellt.

Diese Ergebnisse lieferten den ersten Beweis dafür, dass Seidenraupen ein attraktives Tiermodell sind, um die Rolle der Oberflächenfunktionalität für die biologische Verteilung

#### 4 Summary / Zusammenfassung

und Akkumulation von AuNPs effektiv zu untersuchen. Für **Folgeversuche** wäre es interessant zu testen, ob sich AuNPs die mit PGs funktionalisiert wurden, die eine größere Anzahl an geladenen Gruppen tragen, schneller in die verschiedenen Organe der Seidenraupen wie Mitteldarm, Epidermis und Exkrementen ausbreiten würden. Darüber hinaus wäre ein direkter Vergleich der Biodistribution und Akkumulation in Seidenraupenlarven und Mäusen unter Verwendung derselben oberflächenfunktionalisierten AuNPs von großem Interesse.

---

# 5 Experimental section

---

## 5 Experimental section

### 5.1 Materials and Methods

#### 5.1.1 Materials

Allyl glycidyl ether (AGE) ( $\geq 99\%$ ) from Sigma Aldrich, St. Louis, MO, USA was purified by drying over calcium hydride ( $\text{CaH}_2$ ) ( $92\%$ ) from abcr GmbH, Karlsruhe, Germany and distillation under reduced pressure. The purified monomer was stored under nitrogen ( $\text{N}_2$ ) atmosphere. The following chemicals were used as received. Cholesterol ( $\geq 99\%$ ), cysteamine hydrochloride ( $\geq 98\%$ ), 1-decanethiol ( $96\%$ ), diethylether ( $\text{Et}_2\text{O}$ ) ( $\geq 99\%$ ), 2,2-dimethoxy-2-phenylacetophenon (DMPA) ( $99\%$ ), 4-(dimethylamino)pyridine (DMAP) ( $\geq 99\%$ ), dry *N,N*-dimethylformamide (DMF) ( $99.8\%$ ), *N,N*-dimethylformamide (DMF) (for HPLC,  $\geq 99.9\%$ ) for SEC measurements, 5,5'-dithiobis(2-nitrobenzoic acid) (DTNB, Ellman's reagent) ( $99\%$ ), ethanethiol ( $\text{EtSH}$ ) ( $\geq 97\%$ ), ethanol ( $\text{EtOH}$ ) ( $99.8\%$ ), ethanolamine ( $\geq 98\%$ ), ethyl vinyl ether ( $99\%$ ,  $0.1\%$  KOH as stabilizer), glycidol ( $96\%$ ), human serum albumin (€) (lyophilized powder,  $\geq 96\%$  (agarose gel electrophoresis)), hydrochloride ( $\text{HCl}$ ) ( $37\%$ ), lithium bromide ( $\text{LiBr}$ ) ( $\geq 99\%$ ), magnesium sulfate ( $\text{MgSO}_4$ ), 2-mercaptoethanol ( $\geq 99\%$ ), *N*-hydroxysuccinimide (NHS) ( $> 98\%$ ), 1-petadecanethiol ( $\geq 97\%$ ), 1-pentanethiol ( $98\%$ ), 1-pentene ( $\geq 98.5\%$ ), phosphoric acid ( $\text{H}_3\text{PO}_4$ ) ( $85$  wt.% in  $\text{H}_2\text{O}$ ,  $99.99\%$  trace metals basis), poly(ethylene glycol) methyl ether thiol (MeO-PEG-SH), potassium *tert*-butoxide ( $\text{KO}^t\text{Bu}$ ) ( $1$  M in THF), sodium chloride ( $\text{NaCl}$ ) ( $\geq 99.5\%$ ), sodium hydroxide ( $\text{NaOH}$ ) ( $> 98\%$ ), sodium nitrate ( $\text{NaNO}_3$ ) ( $\geq 99\%$ ), tetramethylsilane (TMS) as analytical standard for NMR spectroscopy, thioacetic acid ( $96\%$ ), thioglycolid acid ( $\geq 99\%$ ), tris(2-carboxyethyl)phosphine hydrochloride (TCEP) ( $\geq 98\%$ ), TWEEN<sup>®</sup> 20 and water ( $\text{H}_2\text{O}$ ) (CHROMASOLV<sup>®</sup> Plus, for HPLC) for SEC measurements were purchased from Sigma Aldrich, St. Louis, MO, USA. Hydrogen peroxide solution ( $\text{H}_2\text{O}_2$ ) ( $30\%$ ), succinic anhydride ( $\geq 98\%$ ), toluene-4-sulfonic acid monohydrate (*p*TsOH) ( $\geq 99\%$ ), sodium azide ( $\text{NaN}_3$ ) and sodium hydrogen carbonate ( $\text{NaHCO}_3$ ) were obtained from Merck KGaA, Darmstadt, Germany. Alpha-mercapto-omega-amino poly(ethylene glycol) (HS-PEG-NH<sub>2</sub>) (Iris Biotech, Marktredwitz, Germany), gold nanoparticles (AuNPs) ( $15$  nm,  $30$  nm) (BBI, Cardiff, UK), 2-hydroxy-1-[4-(hydroxyethoxy)-phenyl]-2-methyl-1-propanone (I2959) (BASF, Ludwigshafen, Germany), *N*-(3-dimethylaminopropyl)-*N'*-ethylcarbodiimide hydrochloride (EDC) ( $\geq 98\%$ ) (Carbosynth, Compton, Berkshire, UK) and silver nanoparticles (AgNPs) ( $20$  nm) (nanoComposix Inc, San Diego, CA, USA) were used as received. *N,N*-dimethylformamide

## 5 Experimental section

(DMF) and dichloromethane (DCM) were purchased from VWR International S.A.S. (Fontenay-sous-Bois, France), deuterated chloroform ( $\text{CDCl}_3$ ) as well as deuterium oxide ( $\text{D}_2\text{O}$ ) for NMR spectroscopy were purchased from Deutero GmbH, Kastellaun, Germany and tetrahydrofuran (THF) from Bernd Kraft, Duisburg, Germany. Chloroform (ROTISOLV  $\geq 99.9\%$ , UV/IR-grade) for GPC measurements and nitric acid ( $\text{HNO}_3$ ) (ROTIPURAN®Supra 69%) were obtained from Carl Roth GmbH + Co. KG, Karlsruhe, Germany. Sodium borohydride ( $\text{NaBH}_4$ ) (99%) and 2,4,6-trinitrobenzene sulfonic acid (TNBSA) were purchased from Thermo Fisher, Waltham, MA, USA. Ammonium persulfate (APS) (assay (titr.): min. 98%), ammonium sulfate ( $(\text{NH}_4)_2\text{SO}_4$ ) (assay (titr.): min. 99.5%), dithiothreitol (DTT) (assay (iodometr.): min. 99.5%), Glycerol (assay (GC): min. 99.5%), methanol (MeOH) (assay (GC): min. 99.8%), *N,N,N',N'*-Tetramethyl ethylenediamine (TEMED) (assay (GC): min. 99%), sodium dodecyl sulfate (SDS) (assay (titr.): min. 99.0%), Tris-Hydrochloride (Tris-HCl) (assay (titr.): min. 99.9%) were purchased from AppliChem GmbH, Darmstadt, Germany. Acrylamide/bis-acrylamide solution (ROTIPHORESE®Gel30 (37,5:1)) was purchased from Bio-Rad Laboratories GmbH, Feldkirchen, Germany.

For preparing phosphate buffer (PB, 0.1 M, pH 7.5), 16 mL of a 0.2 M sodium dihydrogen phosphate solution ( $\text{NaH}_2\text{PO}_4$ ) was mixed with 84 mL of a 0.2 M disodium hydrogen phosphate dodecahydrate solution ( $\text{Na}_2\text{HPO}_4 \cdot 12\text{H}_2\text{O}$ ) and 100 mL of deionized water ( $\text{H}_2\text{O}$ ).

Phosphate buffer saline (1x PBS, pH 7.4) was prepared by dilution of sodium chloride ( $\text{NaCl}$ ) (8.00 g, 137 mmol), potassium chloride (KCl) (200 mg, 2.68 mmol), sodium phosphate dibasic dodecahydrate ( $\text{Na}_2\text{HPO}_4 \cdot 12\text{H}_2\text{O}$ ) (2.80 g, 7.82 mmol) and potassium dihydrogen phosphate ( $\text{KH}_2\text{PO}_4$ ) (200 mg, 1.47 mmol) in 1 L deionized water. All salts used for PB and PBS preparation were purchased from Merck GmbH, Darmstadt, Germany.

Dulbecco's Modified Eagle Medium (DMEM, GlutaMAX™) (Thermo Fisher Scientific, Waltham, MA, USA) was supplemented with 10% fetal calf serum (FCS) (Sigma Aldrich, St. Louis, USA) and 1% penicillin-streptomycin (Pen-Strep) (Thermo Fisher Scientific, Waltham, USA).

Human serum (HS) (from human male AB plasma, USA origin, sterile-filtered, hemoglobin,  $\leq 30$  mg/dL), purchased from Sigma Aldrich, St. Louis, USA, was stored at  $-20$  °C until use.

## 5 Experimental section

Before usage, HS was filtered with a 0.2  $\mu$ M syringe filter (Filtropur S 0.45, Sarstedt AG & Co. KG, Nümbrecht, Germany) and heated to 37 °C.

### 5.1.2 Methods

#### 5.1.2.1 Working techniques

Unless specifically stated in the description of the experimental procedure, all working steps were carried out at room temperature (RT) and deionized water was used for all synthesis and purification procedures. However, some working processes took place under oxygen free conditions. For this purpose, all reaction vessels were connected to a high vacuum Schlenk line, evacuated three times to a pressure of  $10^{-3}$  mbar and then put under argon atmosphere. The long-term storage and the weighted sample of air-sensitive substances such as KO<sup>t</sup>Bu, AGE and ethoxyethyl glycidyl ether (EEGE)<sup>[351]</sup> were carried out in a glovebox (GS Glovebox Systemtechnik GmbH) under a purified N<sub>2</sub> atmosphere. Also the copolymerization of EEGE and AGE was conducted in the glovebox.<sup>[353]</sup>

#### 5.1.2.2 UV-light triggered reactions

UV irradiation for thiol-ene click reactions were performed in EtOH or a mixture of H<sub>2</sub>O and DMF using I2959 as photo initiator and with an UV handlamp (A. Hartenstein Laborbedarf GmbH, 230 V, 50 Hz, 4 W 254 nm and 4 W 365 nm) at a wavelength of 365 nm for 2 h.

#### 5.1.2.3 Material purification via dialysis and lyophilization

For purification, the dissolved polymers were dialyzed against 2 L of a H<sub>2</sub>O-EtOH or H<sub>2</sub>O-DMF mixture (100:1) for 2 d and against pure H<sub>2</sub>O for further 2 d with a water change three times a day using dialysis membranes (Biotech, Rancho Dominguez, CA, USA) with a molecular weight cut-off (MWCO) value of 1000 Da (for PEG) and 3500 Da (for PG). Thiol-functionalized polymers were dialyzed against degassed milli-Q H<sub>2</sub>O (2 h Ar / 2 L solvent) to prevent oxidation. After dialysis, the polymers were freeze-dried at -57 °C and 1 bar using an Alpha 1-2 Ldplus from Christ, Osterode am Harz, Germany.

#### 5.1.2.4 <sup>1</sup>H-NMR spectroscopy

<sup>1</sup>H-NMR spectra were recorded on a Bruker Fourier 300 spectrometer (Billerica, MA, USA) at 300 MHz with 128 scans. The spectra were analyzed by using the TopSpin software from Bruker. The indicated chemical shifts  $\delta$  of the individual resonances are given in parts per million (ppm) and refer to the internal residual proton signal of the deuterated solvents used, CDCl<sub>3</sub> (<sup>1</sup>H,  $\delta$  = 7.26 ppm; <sup>13</sup>C,  $\delta$  = 77.36 ppm), D<sub>2</sub>O (<sup>1</sup>H,  $\delta$  = 4.79 ppm), DMSO (<sup>1</sup>H,

$\delta = 2.50$  ppm) with TMS as internal reference.<sup>[474]</sup> The following abbreviations were used for the multiplicities: s = singlet, d = doublet, dd = doublet of doublet, t = triplet, q = quartet, quin = quintet, m = multiplet, br = broad. The indentified hydrogen and carbon atoms were numbered for all substances.

### **5.1.2.5 FT-IR spectroscopy**

FT-IR experiments were performed with a Nicolet iS10 FT-IR spectrometer with Smart iTX accessories from Thermo Fisher Scientific (Waltham, MA, USA) measuring in a spectral range from  $4000\text{ cm}^{-1}$  to  $650\text{ cm}^{-1}$ . The samples were measured with a diamond attenuated total reflection (ATR) unit, a scan number of 16 and a resolution of 4. The spectra were analyzed by using the software OMNIC 8.2 from Thermo Fisher Scientific, Waltham, MA, USA. Characteristic peaks were allocated to the respective functional compounds.<sup>[475]</sup>

### **5.1.2.6 Raman spectroscopy**

Raman measurements were carried out with a DXR Raman microscope from Thermo Fisher Scientific, Waltham, MA, USA. The instrument has four Olympus objective lenses (4x, 10x, 20x, 50x) and an excitation laser with a wavelength of 780 nm and a maximum power of 24 mW. The measurements were performed in auto mode and with automatic fluorescence correction. Raman vibrational frequencies were assigned to the corresponding characteristic groups.<sup>[476,477]</sup>

### **5.1.2.7 SEC analysis**

For sample preparation approximately 2 mg of the samples were dissolved in 1 mL of the corresponding SEC eluent and then filtered through a cellulose or poly(tetrafluorethylene) (PTFE) syringe filter with  $0.45\text{ }\mu\text{m}$  pore size (Thermo Fisher Scientific, Waltham, USA). The received data were analyzed via OmniSEC 5.12 software from Thermo Fisher Scientific, Waltham, MA, USA.

#### *SEC in $\text{CHCl}_3$*

The device consists of a Viscotek SECmax system with a refractive index (RI) detector (Viscotek VE3580), both from Malvern. The column was a 30 cm long, linear (2) Phenogel  $5\text{ }\mu\text{m}$  with a width of 7.8 mm, heated up to  $35\text{ }^\circ\text{C}$  in a column oven. The column material was porous polystyrene (PS) with a pore diameter of  $13\text{ }\mu\text{m}$ . As solvent  $\text{CHCl}_3$  including 0.5-1% EtOH was used with a flow rate of 1.0 mL/min. For calibration, PS standards were used.

## 5 Experimental section

### *SEC in H<sub>2</sub>O*

A Viscotek GPCmax system from Malvern Panalytical (Malvern, Worcestershire, GBR) with a RI detector (Viscotek VE3580), a viscosity detector (Viscotek 270) and a multiple angle light scattering (MALS) detector (Viscotek SEC-MALS 20, laser wavelength 660 nm) were used. The columns were 30 cm long linear A2000 and A3000 columns from Viscotek with a width of 8 mm, which were filled with porous polymethylmethacrylate (PMMA) with a pore diameter of 13  $\mu\text{m}$ . The column oven kept a constant temperature of 35 °C. The measurements were performed in H<sub>2</sub>O by the addition of 0.1 M NaNO<sub>3</sub> and 0.02% NaN<sub>3</sub>, and with an elution rate of 0.7 mL/min. PEG standards from Malvern were used for calibration.

### *SEC in DMF*

SEC measurements were performed on an OmniSEC Resolve (Malvern) with a multi-detector system OmniSEC Reveal (Malvern) including two light scattering detectors (right angle light scattering (RALS) and low angle light scattering (LALS)), a RI detector and a viscosity detector. DMF with 1 g/L lithium bromide (LiBr) was used as solvent with a flow rate of 1 mL/min. The columns were two linear D2000 and D3000 columns from Malvern with a length of 30 cm and a width of 8 mm. The columns were heated to 45 °C in the column oven and the column material was cross-linked styrene-divinyl benzene (styrene-DVB) with a pore diameter of 6  $\mu\text{m}$ . Calibration was performed using PMMA as well as PEG standards from Malvern.

#### **5.1.2.8 Ellman Assay**

Thiol-functionalized polymers were quantitatively analyzed by Ellman assay using 2-mercaptoethanol as reference. Therefore, dilution series of the 2-mercaptoethanol standard as well as of the polymers were prepared in the range between 10  $\mu\text{M}$  and 300  $\mu\text{M}$ . In a 96 well plate (Thermo Scientific, Nunclon Delta Surface) 10  $\mu\text{L}$  of the standard or the polymer sample were added, followed by addition of 40  $\mu\text{L}$  NaBH<sub>4</sub> (1 M) in NaOH (0.01 M) and incubation for 1 h at RT. After carefully adding 24  $\mu\text{L}$  HCl (1 M) and 30 min incubation, the solution was mixed with 116  $\mu\text{L}$  PBS (0.8 M) and the absorbance was measured at 412 nm in a Tecan Spark<sup>®</sup> 20 M multimode microplate reader (Tecan, Crailsheim, Germany). Afterwards, 10  $\mu\text{L}$  Ellman's reagent (12.6 mM) in PBS (0.8 M) were added, mixed, and measured again at a wavelength of 412 nm. A linear calibration curve



was generated using the values of 2-mercaptoethanol, allowing the calculation of the number of thiol units per polymer.

### **5.1.2.9 TNBSA Assay**

Amine-functionalized polymers were quantitatively analyzed via TNBSA assay using ethanolamine as reference. Therefore, stock solutions (10 mg/mL) of the ethanolamine standard and the polymer samples were prepared. 50  $\mu$ L of the respective stock solutions were mixed with 50  $\mu$ L H<sub>2</sub>O<sub>2</sub> (0.3 M) in NaHCO<sub>3</sub> (0.1 M) and 4.95 mL NaHCO<sub>3</sub> (0.1 M) and incubated 1 h at 37 °C. Afterwards, dilution series with concentrations between 1  $\mu$ g/mL and 99  $\mu$ g/mL were created. In a 96 well plate 80  $\mu$ L of the standard or the polymer sample were added, followed by adding 80  $\mu$ L NaHCO<sub>3</sub> (0.1 M) and 40  $\mu$ L freshly prepared TNBSA solution (0.01%) in NaOH (0.01 M) and incubation for 2 h at 37 °C. After the addition of 40  $\mu$ L SDS (10%) and 20  $\mu$ L HCl (1 M), the plate was briefly mixed thoroughly and the absorbance at 335 nm was measured using a Tecan Spark® 20 M multimode microplate reader (Tecan, Crailsheim, Germany). A linear calibration curve was generated using the values of ethanolamine, allowing the calculation of the number of amine units per polymer.

### **5.1.2.10 ICP-MS**

ICP-MS measurements were performed on iCAP RQ from Thermo Fisher Scientific (Waltham, USA) to determine the Ag and Au mass concentration of the commercially purchased as well as of the polymer and HS attached colloidal solutions. For measuring, the purchased AgNP and AuNP solutions were diluted 1:100 with 0.69% nitric acid (HNO<sub>3</sub>) and the polymer- as well as protein-coated particle solutions were diluted 1:10000 with 0.69% HNO<sub>3</sub>. Au and Ag standard solutions (gold ICP standard and silver ICP standard, Merck KgaA, Darmstadt, Germany) of different dilutions (10, 1, 0.1 and 0.01 mg/L) were used as reference.

### **5.1.2.11 SEM**

To acquire SEM images of AgNPs and AuNPs, the particle solutions were dropped onto a silicon wafer, which was fixed with conductive silver to the SEM stubs. After evaporation of the water, the sample was placed inside the device from Carl Zeiss Microscopy (Göttingen, Germany) and measured with a secondary electron detector. ImageJ software was used for particle analyzing and area calculations.

## 5 Experimental section

### *5.1.2.12 DLS and zeta potential*

The hydrodynamic diameter and the zeta potential of the colloidal particles were determined via DLS measurement at 25 °C using a Zetasizer Nano ZSP from Malvern. The light source was a He-Ne laser with 633 nm wavelength and an intensity of 10 mW with a detection angle of 173 °. For measuring the colloidal NPs were dissolved in milli-Q water.

### *5.1.2.13 UV-Vis spectroscopy*

UV-Vis measurements were performed on a Genesys 10S Bio spectrophotometer (Thermo Fisher Scientific, Waltham, MA, USA), using UV-transparent plastic cuvettes (BRAND GmbH + Co KG, Wertheim, Germany) at RT. The device has a Xenon flashlight that covers a wavelength range from 190 nm to 1100 nm. Samples were prepared by diluting the purchased colloidal gold solution 1:10, while the concentrated functionalized AuNP solutions were diluted 2:800. In contrast, AgNP solution was characterized without any dilution. Absorption measurements of the used thiol- and thioether-polymers were conducted with 310 µM polymer solutions. Accordingly, milli-Q water was used as reference. UV-Vis absorbance scans of solutions consisting of AuNPs were recorded in the range of 300 nm to 900 nm, while these of AgNP solutions were taken in the range of 300–700 nm.

### *5.1.2.14 Micro-TGA*

Micro-TGA measurements were performed by NETZSCH GmbH (Selb, Germany) using a micro-TG 209 F1 Libra. For evaporating water, the samples were pre-dried at 80 °C in a compartment dryer. During the measurement, the samples were heated from 30 °C to 80 °C with a heating rate of 10 K/min under nitrogen atmosphere and retained 15 min at 80 °C, proving the complete removal of the water. Afterwards the samples were heated up to 900 °C with the same heating rate of 10 K/min. After reaching a temperature of 550 °C, the atmosphere was switched from nitrogen (N<sub>2</sub>) to oxygen (O<sub>2</sub>). The weight loss in the region of 230 °C to 320 °C was considered for PG bound to the AgNP surface, while attached PEG showed a weight loss between 320 °C and 430 °C. These temperature regions were used for calculating the polymer to AgNP ratio.<sup>[8]</sup>

### *5.1.2.15 Micro-BCA assay*

Micro-bicinchoninic acid (micro-BCA) Protein-Assay-Kit, purchased from Thermo Fisher Scientific, Waltham, USA, was used for two different purposes.

Firstly, micro-BCA assay was performed to determine how many purification steps by centrifugation are required ensuring no unbound proteins in the supernatant of the HS-incubated AuNPs. 150  $\mu\text{L}$  of the BSA standards in a concentration range between 0.5  $\mu\text{g}/\text{mL}$  and 200  $\mu\text{g}/\text{mL}$  as well as 150  $\mu\text{L}$  of the 4<sup>th</sup> and 5<sup>th</sup> supernatant after centrifugation of the protein-incubated AuNPs were added in a 96 well plate and mixed thoroughly with 150  $\mu\text{L}$  freshly prepared micro-BCA working reagent. After incubation for 2 h at 37 °C the absorbance at 562 nm was measured using a Tecan Spark® 20 M multimode microplate reader (Tecan, Crailsheim, Germany). All measurements were performed in triplicate. A linear calibration curve was generated using the values of BSA, allowing the calculation of the  $\epsilon$  amount. Secondly, micro-BCA assay was used to quantify the amount of adsorbed proteins on each AuNP after incubation with HS followed by several washing steps. After five washing steps, ensuring the absence of loose proteins, the remained sediment of different protein-coated AuNPs was redispersed in 500  $\mu\text{L}$  of 5% (w/v) SDS solution, followed by 5 min sonification and 10 min treatment at 95 °C, in order to release the proteins for the particle surface. After centrifugation, 150  $\mu\text{L}$  of the supernatant was transferred to a 96 well plate and mixed thoroughly with 150  $\mu\text{L}$  freshly prepared micro-BCA working reagent, following the same procedure as explained before.

#### 5.1.2.16 SDS-PAGE and Coomassie Brilliant Blue G-250 staining

SDS-PAGE analysis was performed according to procedure of Laemmli.<sup>[478]</sup>, employing 12.5% separating gel and 5% stacking gel which were prepared via polymerization reaction, consisting of components ascribed in the following **Table 14**.

**Table 14.** Composition of 12.5% separating gel and 5% stacking gel.

Composition of 12.5% separating gels		Composition of 5% stacking gels	
Components	Volume for two gels	Components	Volume for two gels
H <sub>2</sub> O	4.95 mL	H <sub>2</sub> O	5.80 mL
30% acrylamide and 0.8% bisacrylamide	6.30 mL	30% acrylamide and 0.8% bisacrylamide	1.66 mL
1.5 M Tris-HCl and 0.4% SDS, pH 8.8	3.75 mL	0.5 M Tris-HCl and 0.4% SDS, pH 6.8	2.5 mL
10% APS	150 $\mu\text{l}$	10% APS	80.0 $\mu\text{l}$
TEMED	10.0 $\mu\text{l}$	TEMED	12.0 $\mu\text{l}$

## 5 Experimental section

Protein samples for analysis were pretreated for 10 min at 95 °C in 30 µL sample buffer consisting of 60 mM Tris-HCl (pH 6.8), 2% (w/v) SDS, 7% (v/v) glycerol, and 100 mM DTT followed by separation via SDS-PAGE for 1 h at 200 volts in a Mini-PROTEAN® II slab gel apparatus (Bio-Rad, Hercules, California, USA). After migration the gels were washed in H<sub>2</sub>O, stained overnight with a colloidal Coomassie Brilliant Blue staining solution (10% (w/v) (NH<sub>4</sub>)<sub>2</sub>SO<sub>4</sub>, 10% (v/v) H<sub>3</sub>PO<sub>4</sub>, 20% (v/v) MeOH and 2% (w/v) Coomassie Blue G-250) according to Candiano *et al.*<sup>[479]</sup> and destained afterwards with H<sub>2</sub>O to remove background staining.

### 5.1.2.17 LC-MS/MS

#### *Gel electrophoresis*

Proteins in sample buffer were reduced with 50 mM DTT at 70 °C for 10 min and alkylated with 120 mM Iodoacetamide at RT for 20 min. Separation was performed on NuPAGE® Novex® 4-12% Bis-Tris gels (Life Technologies) with MOPS (3-(N-morpholino) propanesulfonic acid) buffer according to manufacturer's instructions. Gels were washed three times for 5 min with water and stained for 1 h with Simply Blue™ Safe Stain (Life Technologies). After washing with water for 1 h, each gel lane was cut into 15 slices.

#### *In-Gel Digestion*

The excised gel bands were destained with 30% acetonitrile in 0.1 M ammonium hydrogencarbonate (NH<sub>4</sub>HCO<sub>3</sub>) (pH 8), shrunk with 100% acetonitrile, and dried in a vacuum concentrator (Concentrator 5301, Eppendorf, Germany). Digests were performed with 0.1 µg trypsin per gel band overnight at 37 °C in 0.1 M NH<sub>4</sub>HCO<sub>3</sub> (pH 8). After removing the supernatant, peptides were extracted from the gel slices with 5% formic acid, and extracted peptides were pooled with the supernatant.

#### *NanoLC-MS/MS Analysis*

NanoLC-MS/MS analyses were performed on an LTQ-Orbitrap Velos Pro (Thermo Scientific) equipped with a PicoView Ion Source (New Objective) and coupled to an EASY-nLC 1000 (Thermo Scientific). Peptides were loaded on a trapping column (2 cm x 150 µm ID, PepSep) and separated on a capillary columns (30 cm x 150 µm ID, PepSep) both packed with 1.9 µm C18 ReproSil and separated with a 30-minute linear gradient from 3% to 30% acetonitrile and 0.1% formic acid and a flow rate of 500 nL/min. MS scans were acquired in the Orbitrap analyzer with a resolution of 30000 at m/z 400, MS/MS scans were acquired

in the Orbitrap analyzer with a resolution of 7500 at  $m/z$  400 using higher energy collisional dissociation (HCD) fragmentation with 30% normalized collision energy. A TOP5 data-dependent MS/MS method was used; dynamic exclusion was applied with a repeat count of 1 and an exclusion duration of 30 seconds; singly charged precursors were excluded from selection. Minimum signal threshold for precursor selection was set to 50000. Predictive automatic gain control (AGC) was used with AGC target a value of  $1e6$  for MS scans and  $5e4$  for MS/MS scans. Lock mass option was applied for internal calibration in all runs using background ions from protonated decamethylcyclopentasiloxane ( $m/z$  371.10124).

### *MS data analysis*

Raw MS data files were analyzed with MaxQuant version 1.6.2.2.<sup>[480]</sup> Database search was performed with Andromeda, which is integrated in the utilized version of MaxQuant. The search was performed against the UniProt Human reference proteome database (UP000005640). The search was performed with tryptic cleavage specificity with 3 allowed miscleavages. Protein identification was under control of the false-discovery rate (1% FDR on protein and peptide level). In addition to MaxQuant default settings, the search was performed against following variable modifications: Protein N-terminal acetylation, Gln to pyro-Glu formation (N-term. Gln) and oxidation (Met). Carbamidomethyl (Cys) was set as fixed modification.

#### **5.1.2.18 Macrophage isolation**

Macrophage experiments were carried out with the required approval of the local ethics committee of the University of Würzburg, using buffy coats obtained from the Bavarian Red Cross (Blood Donor Service, German Red Cross, Wiesentheid, Germany). Buffy coats were separated from the blood of healthy donors who had given their written informed consent.

Macrophage isolation from buffy coats was performed according to procedure of Tylek *et al.*<sup>[481]</sup> For human monocyte collection, first, peripheral blood mononuclear cells were isolated by density gradient centrifugation with Pancoll (Density: 1077 g/L; Pan-Biotech, Aidenbach, Germany), followed by separation via negative selection (Pan Monocyte Isolation Kit, Miltenyi Biotec, Gladbach, Germany).

## 5 Experimental section

### *5.1.2.19 AuNP uptake into macrophages*

$0.5 \times 10^6$  freshly collected monocytes suspended in 150  $\mu\text{L}$  RPMI-1640 medium (GlutaMAX™) (Thermo Fisher Scientific, Waltham, USA) containing 1% (v/v) 5000 U/mL Pen-Strep (Thermo Fisher Scientific, Waltham, USA) and 10% (v/v) human platelet lysate (hPL)<sup>[481]</sup> (PL Bioscience, Aachen, Germany) were placed in each well of tissue culture-treated 24-well plates (Nunc, Thermo Fisher Scientific, Waltham, USA). The well plates seeded with cells were then incubated in a humidified atmosphere at 37 °C and 5% CO<sub>2</sub> for 30 min to enable cell adhesion, before gently adding 1 mL macrophage culture medium. After a while, the monocytes differentiated spontaneously, i.e., without additional differentiation factors, into macrophages. On the next day, the medium was carefully replaced with fresh serum free medium, followed by cell treatment with 20  $\mu\text{g}/\text{mL}$  citrate-capped as well as PGylated AuNPs both with and without HS pre-adsorption. After addition of the different AuNPs to the cells, the well plates were briefly stirred gently to ensure dispersion of the particles in the culture medium before incubation for 6 h. Thereafter, cells were washed three times with 500  $\mu\text{L}$  PBS to remove free and weakly bound particles on the cell surface. The supernatants were collected and then the amount of cellular uptake was quantified by measuring the Au ion concentration of AuNPs not taken up via ICP-MS analysis. Macrophages which were not treated with AuNPs were used as reference. The experiment was performed in triplicates using monocytes from the same donor as well as AuNPs from the same coating procedure.

### *5.1.2.20 Live-Dead staining*

Using the LIVE/DEAD Viability/Cytotoxicity Kit for mammalian cells (Thermo Fisher Scientific, Waltham), the macrophage viability was evaluated after 6 h incubation with and without various AuNPs as described previously. After particle treatment, cells were incubated in the staining solution consisting of containing 1  $\mu\text{M}$  calcein acetoxymethyl ester (Calcein AM) and 2  $\mu\text{M}$  ethidium homodimer-1 in supplement-free RPMI-1640 media for 30 min at 37 °C with the exclusion of light. Cell visualization was acquired using a fluorescence microscopy (Axio Observer) from Carl Zeiss, Jena, Germany. The experiment was performed once.

### **5.1.2.21 Silkworm rearing and intra-hemolymph injection of AuNP solutions**

Four-way polyhybrid silkworm eggs (129 × 127) × (126 × 125) and dry fodder with preservatives were purchased from the Council for Agricultural Research and Economics – Research Centre for Agriculture and Environment (CREA-AA, Padova, Italy). Silkworm rearing in laboratory was performed as described before.<sup>[319]</sup> Silkworm diet was prepared according to the manufacturer's protocol. Briefly, silkworm larvae reaching the third day of their fifth instar were used for experiments.

Intra-hemolymph injection of AuNP solutions was performed using a 1-mL syringe with a 30-gauge needle (ø 0.30 × 12 mM; B. Braun, Melsungen AG, Melsungen, Germany) into the dorsal epidermis of the silkworm at the fifth segment.<sup>[317]</sup> 50 µL of a desired colloidal solution (200 µg/mL in 0.9% NaCl) or pure 0.9% NaCl as control was injected into each silkworm (n = 3 for ICP-MS analysis; n = 5 for toxicity test). Subsequently, silkworms were incubated at 25 °C for 6 h, 24 h (ICP-MS) or 72 h (toxicity) in petri dishes with vents (90 x 14 mm, Carl Roth GmbH + Co. KG, Karlsruhe, Germany).

### **5.1.2.22 Silkworm dissection**

Silkworms were anesthetized on ice for at least 30 s, followed by cutting one of the second abdominal prolegs to gently drain the hemolymph. For prevention of silkworms' hemolymph melanization, working solution of L-glutathione reduced (γ-L-Glutamyl-L-cysteinyl-glycin (GSH) (≥ 98.0%), Sigma Aldrich, St. Louis, USA) was freshly prepared prior to use at a concentration of 200 mM in 0.9% NaCl and was immediately added to the extracted hemolymph at a final concentration of 5 mM.<sup>[482,483]</sup>

For extraction of the midgut and epidermis, silkworms were further anesthetized under ice for 10-15 min. Subsequently, the head and tail of the larva (laying on its dorsal side) were fixed by needles on a styrofoam dissection plate. The abdominal epidermis was then carefully cut along the midline using dissection scissors, followed by fixation of cut epidermis on both sides with needles to expose the midgut underneath.<sup>[319]</sup> The whole midgut was first extracted. After removing other attaching tissues such as silk glands and trachea, the whole epidermis was collected for further analysis. Excrement of silkworms was directly collected from the petri dishes after incubation.

## 5 Experimental section

### 5.1.2.23 Au content in silkworm tissues

The samples obtained after dissection were dried overnight at 60 °C, followed by dissolving in 200  $\mu\text{L}$  69%  $\text{HNO}_3$ . After shaking overnight, the samples were further diluted with 1.8 mL milli-Q, receiving a 6.9%  $\text{HNO}_3$  solution. Before measuring the Au mass concentration in each organ by ICP-MS, the samples were filtered with a 0.45  $\mu\text{M}$  syringe filter (Flitropur S 0.45, Sarstedt AG & Co. KG, Nümbrecht, Germany). Au standards (10, 1, 0.1 and 0.01 mg/L) were also prepared in 6.9%  $\text{HNO}_3$ .

**Table 15.** Au content per gram tissue in the analyzed silkworm organs 6 h and 24 h post injection of the different polymer-functionalized AuNPs as well as the control group.

Sample		PEG-AuNP	PG(Alkyl) - AuNP	PG(+)-AuNP	PG(-)-AuNP	Control (no AuNPs)
Hemolymph [ $\mu\text{g/g}$ ]	6 h	427 $\pm$ 66.9	322 $\pm$ 66.6	266 $\pm$ 61.3	655 $\pm$ 58.6	0.60 $\pm$ 0.08
	24 h	164 $\pm$ 40.2	146 $\pm$ 17.8	291 $\pm$ 49.7	281 $\pm$ 24.6	-
Midgut [ $\mu\text{g/g}$ ]	6 h	15.3 $\pm$ 3.99	18.2 $\pm$ 2.43	24.3 $\pm$ 5.31	16.6 $\pm$ 3.48	0.34 $\pm$ 0.08
	24 h	8.39 $\pm$ 3.01	7.55 $\pm$ 1.33	64.5 $\pm$ 11.5	12.4 $\pm$ 1.37	-
Epidermis [ $\mu\text{g/g}$ ]	6 h	7.26 $\pm$ 1.67	13.1 $\pm$ 3.93	13.7 $\pm$ 2.28	13.0 $\pm$ 2.46	0.040 $\pm$ 0.004
	24 h	7.26 $\pm$ 2.25	15.9 $\pm$ 3.55	7.41 $\pm$ 1.53	9.21 $\pm$ 2.74	-
Excrements [ $\mu\text{g/g}$ ]	6 h	0.414 $\pm$ 0.011	0.716 $\pm$ 0.006	0.467 $\pm$ 0.040	0.115 $\pm$ 0.007	0.123 $\pm$ 0.004
	24 h	0.036 $\pm$ 0.001	0.088 $\pm$ 0.003	1.88 $\pm$ 0.029	0.009 $\pm$ 0.002	-

The values are presented as mean  $\pm$  standard deviation ( $n = 3$ ); (-) there was no control group for 24 h injection.

### 5.1.2.24 Statistical analysis

Statistical analysis was performed using one-way analysis of variance (one-way ANOVA) test with the GraphPad Prism (version 9.3.1). Significant differences between two represented groups are denoted as \* ( $p < 0.05$ ), \*\* ( $p < 0.01$ ) and \*\*\* ( $p < 0.001$ ).



## 5.2 Polymer synthesis and AgNP functionalization

In this section firstly general information about the used AgNPs are displayed, followed by the experimental procedures of polymer synthesis and the characterization of the respective polymer-modified AgNPs.

### 5.2.1 Citrate-AgNPs

20 nm Ag nanospheres stabilized with 2 mM sodium citrate tribasic were commercially purchased.

#### 5.2.1.1 Handling and characterization of citrate-AgNPs

Unless specifically mentioned, all characterization and reaction steps with AgNPs were conducted in milli-Q H<sub>2</sub>O.

**Table 16.** Particle and mass concentration as well as values of  $d$ , PDI,  $\zeta$ , and SPR of 20 nm citrate-stabilized AgNPs (BATCH TJC0126), defined by the manufacturer compared to own measurements.

	20 nm citrate-AgNPs	
Particle concentration [particles/mL]	$5.2 \cdot 10^{11(a)}$	$2.0 \cdot 10^{11\epsilon}$
Mass concentration [mg/mL]	$22.1^{(a)}$	$19.4^{(d)}$
$d$ [nm]	$19.9 \pm 2.8^{(b)}$	$21.3 \pm 2.7^l$
PDI	-	$0.229^{(f)}$
$\zeta$ [mV]	$-43^{(a)}$	$-36.5 \pm 2.5^{(g)}$
SPR [nm]	$392^{(a)}$	$400^{(h)}$

<sup>(a)</sup>defined by the manufacturer, <sup>(b)</sup>determined by the manufacturer via TEM analysis, <sup>(c)</sup>calculated via own measurements of the mass concentration and the hydrodynamic diameter  $d$ , <sup>(d)</sup>measured by ICP-MS, <sup>(e)</sup>calculated via SEM imaging, <sup>(f)</sup>measured via DLS, <sup>(g)</sup>determined by zeta potential measurements, <sup>(h)</sup>determined by UV-Vis

FT-IR (ATR):  $\tilde{\nu}_{\max} = 1579\text{-}1393$  ((C=O)O<sup>-</sup>), 1262 (CH<sub>2</sub>), 1080 (CO) cm<sup>-1</sup>.

#### 5.2.1.2 Polymer functionalization of citrate-AgNPs

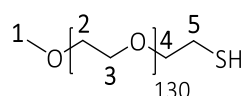
Via Ligand exchange reaction, citrate-AgNPs were functionalized with sulfur-containing polymers. Therefore, 100  $\mu$ L of the respective polymeric solution (310  $\mu$ M) was added to 1 mL of the purchased 20 nm citrate-stabilized AgNPs and incubated overnight. During the

## 5 Experimental section

incubation process, the colloidal solutions were shaken with 200 rpm at RT and covered with aluminum foil. The incubation was stopped by centrifugation (20 000 g, 25 min, 4 °C) (Mega Star 1.6R, Thermo Fisher Scientific, Waltham, MA, USA), the supernatant was removed, and the residue was redispersed in 1 mL milli-Q H<sub>2</sub>O. The purification step by centrifugation was performed twice.

### 5.2.2 MeO-PEG-SH

MeO-PEG-SH with a molecular weight of 6000 Da was commercially purchased.



<sup>1</sup>H-NMR (300 MHz, D<sub>2</sub>O):  $\delta$  = 3.74 (br, 520 H, H-2-4), 3.42 (s, 3 H, H-1), 2.77 (t, 2 H, H-5) ppm.

FT-IR (ATR):  $\tilde{\nu}_{\max}$  = 2882 (CH<sub>2</sub>, CH<sub>3</sub>), 1467-1240 (CH<sub>2</sub>, CH<sub>3</sub>), 1097 (COC), 958-842 (CC) cm<sup>-1</sup>.

Raman:  $\tilde{\nu}_{\max}$  = 2938-2835 (CH<sub>2</sub>, CH<sub>3</sub>), 2558 (SH), 1477-1229 (CH<sub>2</sub>, CH<sub>3</sub>), 1138-1058 (CC), 840 (COC) cm<sup>-1</sup>.

Ellman assay: 0.8 thiols per polymer

SEC (RI, H<sub>2</sub>O/DMF):

**Table 17.**  $\bar{M}_w$ ,  $\bar{M}_n$  and  $\mathfrak{D}$  determined by SEC as well as the via <sup>1</sup>H-NMR spectroscopy calculated molecular weight of MeO-PEG-SH.

	SEC	$\bar{M}_w$ [Da] <sup>(a)</sup>	$\bar{M}_n$ [Da] <sup>(a)</sup>	$\mathfrak{D}$ <sup>(a)</sup>	$M_{\text{exp.}}$ [Da] <sup>(b)</sup>
MeO-PEG-SH	H <sub>2</sub> O	5372	4212	1.28	6000

<sup>(a)</sup>determined by SEC in H<sub>2</sub>O, <sup>(b)</sup>defined by the manufacturer

#### 5.2.2.1 Ag–MeO-PEG-SH

UV-Vis, DLS, Zeta:

**Table 18.** Values of SPR,  $d$ , PDI and  $\zeta$  of MeO-PEG-SH-modified AgNPs, determined by UV-Vis, DLS and zeta potential measurements.

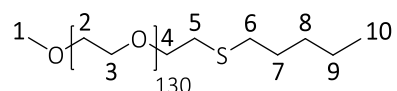
	SPR [nm]	$d$ [nm]	PDI	$\zeta$ [mV]
Ag–MeO-PEG-SH	407	48.8 ± 1.1	0.111	-16.8 ± 1.4

FT-IR (ATR):  $\tilde{\nu}_{\max} = 2882$  (CH<sub>2</sub>, CH<sub>3</sub>), 1468-1280 (CH<sub>2</sub>, CH<sub>3</sub>), 1110 (COC), 961-843 (CC) cm<sup>-1</sup>.

Micro-TGA (wt%): 47.4%<sub>polymer</sub>, 46.2%<sub>Ag</sub>.

### 5.2.3 MeO-PEG-SPentyl

MeO-PEG-SPentyl was synthesized according to literature.<sup>[17]</sup> Therefore, MeO-PEG-SH (150 mg, 25.0 μmol) was dissolved in 20 mL EtOH and the solution was degassed for 30 min. After adding 1-pentene (100 μl, 914 μmol) and I2959 (11.2 mg, 50.0 μmol) the mixture was stirred and irradiated with UV light at 365 nm for 2 h. The solvent was removed under vacuum and the remaining polymer was dissolved in 70 mL H<sub>2</sub>O. After dialyzing and lyophilization the polymer was received as a colorless powder.



<sup>1</sup>H-NMR (300 MHz, D<sub>2</sub>O):  $\delta = 3.74$  (br, 520 H, H-2-4), 3.41 (s, 3 H, H-1), 2.99 (t, 2 H, H-5), 2.97 (t, 2 H, H-6), 1.85-1.76 (m, 2 H, H-7), 1.43-1.36 (m, 2 H, H-8), 1.28-1.20 (m, 2 H, H-9), 0.94 (t, 3 H, H-10) ppm.

FT-IR (ATR):  $\tilde{\nu}_{\max} = 2881$  (CH<sub>2</sub>, CH<sub>3</sub>), 1467-1240 (CH<sub>2</sub>, CH<sub>3</sub>), 1101 (COC), 959-842 (CC) cm<sup>-1</sup>.

Raman:  $\tilde{\nu}_{\max} = 2941$ -2831 (CH<sub>2</sub>, CH<sub>3</sub>), 1477-1231 (CH<sub>2</sub>, CH<sub>3</sub>), 1138-1059 (CC), 840 (COC) cm<sup>-1</sup>.

SEC (RI, H<sub>2</sub>O):

**Table 19.**  $\bar{M}_w$ ,  $\bar{M}_n$  and  $\bar{D}$  determined by SEC analysis as well as the via <sup>1</sup>H-NMR spectroscopy calculated molecular weight of MeO-PEG-SPentyl.

	SEC	$\bar{M}_w$ [Da] <sup>(a)</sup>	$\bar{M}_n$ [Da] <sup>(a)</sup>	$\bar{D}$ <sup>(a)</sup>	$M_{\text{exp}}$ [Da] <sup>(b)</sup>
MeO-PEG-SPentyl	H <sub>2</sub> O	5160	4031	1.28	6070

<sup>(a)</sup>determined by SEC in H<sub>2</sub>O, <sup>(b)</sup>determined by <sup>1</sup>H-NMR spectroscopy in D<sub>2</sub>O

## 5 Experimental section

### 5.2.3.1 Ag–MeO–PEG–SPentyl

UV-Vis, DLS, Zeta:

**Table 20.** Values of SPR,  $d$ , PDI and  $\zeta$  of MeO-PEG-SPentyl-modified AgNPs, determined by UV-Vis, DLS and zeta potential measurements.

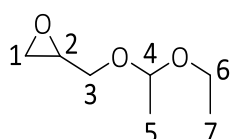
	SPR [nm]	$d$ [nm]	PDI	$\zeta$ [mV]
Ag–MeO–PEG–SPentyl	403	$42.8 \pm 0.9$	0.201	$-21.1 \pm 2.7$

FT-IR (ATR):  $\tilde{\nu}_{\max} = 2883$  (CH<sub>2</sub>, CH<sub>3</sub>), 1467-1241 (CH<sub>2</sub>, CH<sub>3</sub>), 1111 (COC), 961-843 (CC) cm<sup>-1</sup>.

Micro-TGA (wt%): 30.9%<sub>polymer</sub>, 63.1%<sub>Ag</sub>.

### 5.2.4 EEGE

The synthesis is based on a modified experimental procedure by Fitton *et al.*<sup>[351]</sup> Glycidol (72.0 mL, 1.08 mol) was mixed with ethyl vinyl ether (430 mL, 4.44 mol) and cooled down to 0 °C with an ice bath. *p*TsOH (2.00 g, 10.5 mmol) was slowly added to the stirring solution, keeping the temperature below 20 °C. After stirring for 1 h at 0 °C and further 2 h at RT, the mixture was washed three times with 50 mL of saturated NaHCO<sub>3</sub>. The organic phase was dried with MgSO<sub>4</sub>, filtered and the residual ethyl vinyl ether was removed under vacuum. The raw product was purified via pre-drying with CaH<sub>2</sub> overnight and fractionated distillation under Ar atmosphere and reduced pressure. EEGE monomer was received as a clear, colorless liquid.



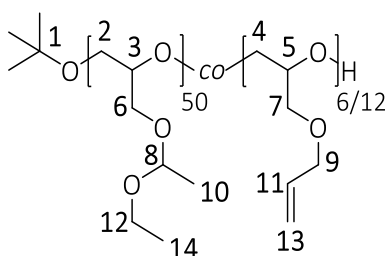
<sup>1</sup>H-NMR (300 MHz, CDCl<sub>3</sub>):  $\delta = 4.66$ -4.59 (m, 1 H, H-4), 3.70-3.25 (m, 2 H, H-3+6), 3.01-2.99 (m, 1 H, H-2), 2.67-2.64 (m, 1 H, H-1), 2.51-2.45 (m, 1 H, H-1), 1.18 (t, 3 H, H-5), 1.07 (t, 3 H, H-7) ppm.

5.2.5 P(EEGE<sub>50</sub>-co-AGE<sub>6/12</sub>)

Linear P(EEGE<sub>50</sub>-co-AGE<sub>6/12</sub>) was synthesized as described previously.<sup>[353]</sup> Therefore, EEGE, AGE and KO<sup>t</sup>Bu were mixed under inert atmosphere in the glovebox and the yellow solution was stirred at 60 °C for 19 h. The polymerization was terminated by adding 1 mL EtOH and the resulting copolymer was received as brownish oil. In this thesis two different allyl-functionalized PGs with various EEGE to AGE ratios were synthesized, named as P(EEGE<sub>50</sub>-co-AGE<sub>6</sub>) and P(EEGE<sub>50</sub>-co-AGE<sub>12</sub>). For this synthesis, the exact amounts of the used substances are listed in **Table 21**.

**Table 21.** Exact amounts of EEGE, AGE and KotBu used for copolymerization of P(EEGE<sub>50</sub>-co-AGE<sub>6</sub>) and P(EEGE<sub>50</sub>-co-AGE<sub>12</sub>).

	EEGE	AGE	KO <sup>t</sup> Bu
P(EEGE <sub>50</sub> -co-AGE <sub>6</sub> )	15.8 mL, 108 mmol	1.50 mL, 12.6 mmol	2.00 mL, 16.1 mmol
P(EEGE <sub>50</sub> -co-AGE <sub>12</sub> )	15.8 mL, 108 mmol	3.00 mL, 25.3 mmol	2.00 mL, 16.1 mmol



<sup>1</sup>H-NMR (300 MHz, CDCl<sub>3</sub>):  $\delta$  = 5.93-5.80 (m, 6/12 H, H-11), 5.19 (dd, 12/24 H, H-13), 4.67 (q, 50 H, H-8), 3.96 (d, 12/24 H, H-9), 3.72-3.38 (m, 380 H, H-2-7+12), 1.27 (d, 150 H, H-10), 1.22 (s, 9 H, H-1), 1.17 (t, 150, H-14) ppm.

FT-IR (ATR):  $\tilde{\nu}_{\max}$  = 2977-2873 (CH, CH<sub>2</sub>, CH<sub>3</sub>), 1668 (C=C), 1446-1262 (CH, CH<sub>2</sub>, CH<sub>3</sub>), 1129-1054 (COC), 999-875 (CC) cm<sup>-1</sup>.

Raman:  $\tilde{\nu}_{\max}$  = 3014-2881 (CH, CH<sub>2</sub>, CH<sub>3</sub>), 1646 (C=C), 1462-1261 (CH, CH<sub>2</sub>, CH<sub>3</sub>), 1119-1063 (CC), 909-832 (COC) cm<sup>-1</sup>.

## 5 Experimental section

SEC (RI, CHCl<sub>3</sub>/DMF):

**Table 22.**  $\bar{M}_w$ ,  $\bar{M}_n$  and  $\bar{D}$  determined by SEC analysis as well as the via <sup>1</sup>H-NMR spectroscopy calculated molecular weights of P(EEGE<sub>50-co</sub>-AGE<sub>6</sub>) and P(EEGE<sub>50-co</sub>-AGE<sub>12</sub>).

	Solvent	$\bar{M}_w$ [Da] <sup>(a)</sup>	$\bar{M}_n$ [Da] <sup>(a)</sup>	$\bar{D}$ <sup>(a)</sup>	$M_{exp.}$ [Da] <sup>(b)</sup>
P(EEGE <sub>50-co</sub> -AGE <sub>6</sub> )	CHCl <sub>3</sub> <sup>*</sup>	7676	4609	1.67	
	DMF <sup>*</sup>	2225	2533	1.14	8063
	DMF <sup>**</sup>	12110	9002	1.35	
P(EEGE <sub>50-co</sub> -AGE <sub>12</sub> )	CHCl <sub>3</sub> <sup>*</sup>	8531	6368	1.39	
	DMF <sup>*</sup>	2712	2415	1.12	8753
	DMF <sup>**</sup>	10730	9085	1.18	

<sup>(a)</sup>determined by SEC in CHCl<sub>3</sub>/DMF, <sup>(b)</sup>determined by <sup>1</sup>H-NMR spectroscopy in CDCl<sub>3</sub>, <sup>\*</sup>PEG calibration, <sup>\*\*</sup>PMMA calibration

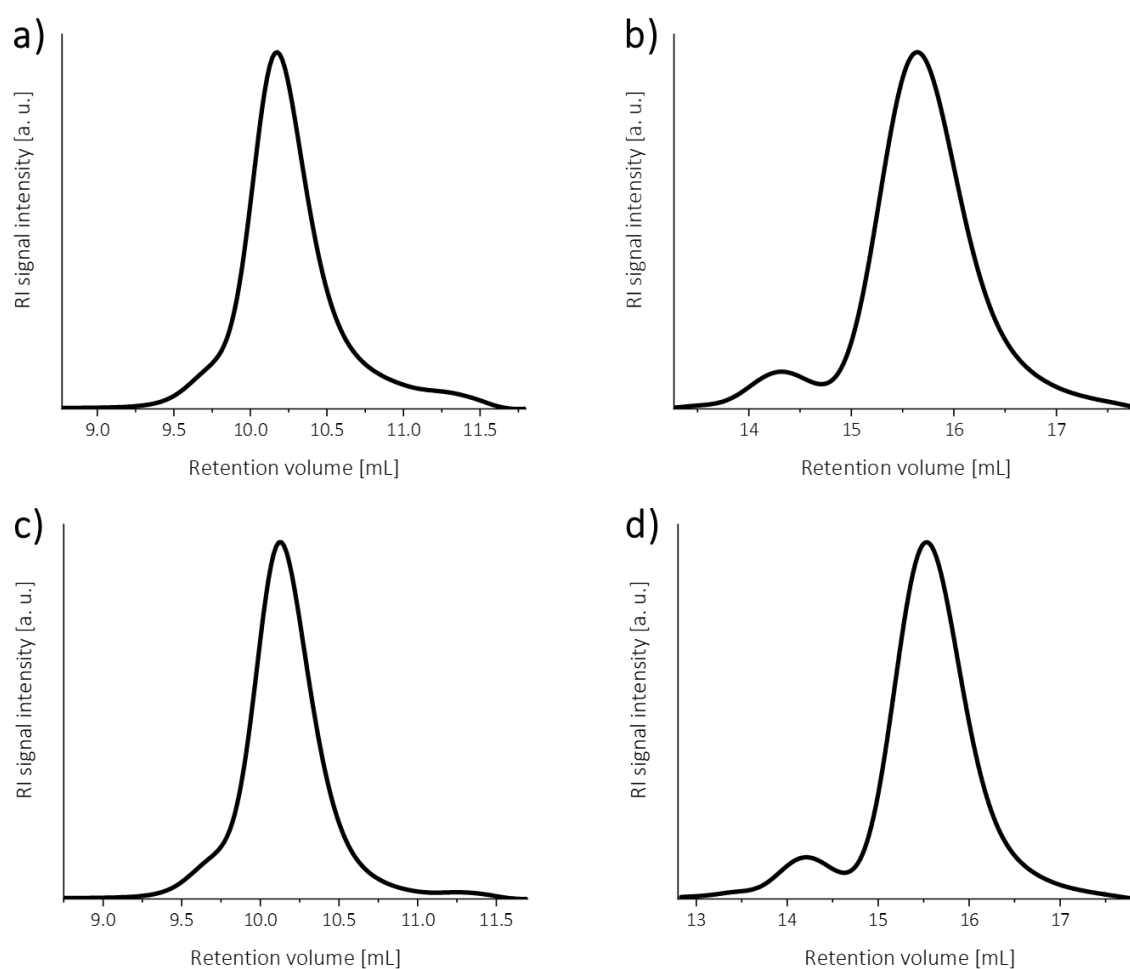


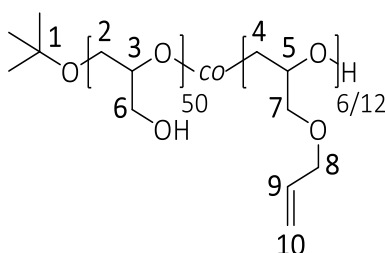
**Figure 63.** SEC elugram of P(EEGE<sub>50-co</sub>-AGE<sub>6</sub>) in a) CHCl<sub>3</sub> and b) DMF as well as of P(EEGE<sub>50-co</sub>-AGE<sub>12</sub>) in c) CHCl<sub>3</sub> and d) DMF, displaying a monomodal distribution with a high molecular weight shoulder and a low molecular weight tailing for analysis in CHCl<sub>3</sub> while a bimodal distribution is detected by SEC in DMF.

5.2.6 P(G<sub>50</sub>-co-AGE<sub>6/12</sub>)

In order to receive the copolymers P(G<sub>50</sub>-co-AGE<sub>6</sub>) and P(G<sub>50</sub>-co-AGE<sub>12</sub>), the acetal protection group of P(EEGE<sub>50</sub>-co-AGE<sub>6</sub>) and P(EEGE<sub>50</sub>-co-AGE<sub>12</sub>) was removed under acidic conditions.<sup>[353]</sup> The deprotection took place in THF and dropwise addition of 37% HCl, followed by stirring for 1 h at RT. The respective volumes of THF and HCl are shown in **Table 23**. Afterwards, THF was removed by decantation and the remaining polymer was dissolved in H<sub>2</sub>O and neutralized with NaOH. After dialysis and freeze-drying the polymer was received as a slightly yellow and highly viscous solid.

**Table 23.** Amounts of THF and 37% HCl for the synthesis of P(EEGE<sub>50</sub>-co-AGE<sub>6</sub>) and P(EEGE<sub>50</sub>-co-AGE<sub>12</sub>).

	THF	HCl
P(G <sub>50</sub> -co-AGE <sub>6</sub> )	300 mL	10.0 mL
P(G <sub>50</sub> -co-AGE <sub>12</sub> )	400 mL	15.0 mL

P(G<sub>50</sub>-co-AGE<sub>6</sub>):

<sup>1</sup>H-NMR (300 MHz, D<sub>2</sub>O):  $\delta$  = 6.08-5.96 (m, 6 H, H-9), 5.37 (dd, 12 H, H-10), 4.14 (d, 12 H, H-8), 3.82-3.69 (m, 280 H, H-2-7), 1.28 (s, 9 H, H-1) ppm.

FT-IR (ATR):  $\tilde{\nu}_{\max}$  = 3386 (OH), 2919-2872 (CH, CH<sub>2</sub>, CH<sub>3</sub>), 1646 (C=C), 1461-1222 (CH, CH<sub>2</sub>, CH<sub>3</sub>), 1042 (COC), 921-858 (CC) cm<sup>-1</sup>.

Raman:  $\tilde{\nu}_{\max}$  = 2931-2879 (CH, CH<sub>2</sub>, CH<sub>3</sub>), 1644 (C=C), 1462-1258 (CH, CH<sub>2</sub>, CH<sub>3</sub>), 1134-1063 (CC), 907-856 (COC) cm<sup>-1</sup>.

## 5 Experimental section

### P(G<sub>50-co</sub>-AGE<sub>12</sub>):

<sup>1</sup>H-NMR (300 MHz, D<sub>2</sub>O):  $\delta$  = 6.08-5.96 (m, 12 H, H-9), 5.37 (dd, 24 H, H-10), 4.14 (d, 24 H, H-8), 3.82-3.69 (m, 310 H, H-2-7), 1.28 (s, 9 H, H-1) ppm.

FT-IR (ATR):  $\tilde{\nu}_{\max}$  = 3372 (OH), 2922-2873 (CH, CH<sub>2</sub>, CH<sub>3</sub>), 1646 (C=C), 1461-1223 (CH, CH<sub>2</sub>, CH<sub>3</sub>), 1040 (COC), 919-856 (CC) cm<sup>-1</sup>.

Raman:  $\tilde{\nu}_{\max}$  = 2931-2881 (CH, CH<sub>2</sub>, CH<sub>3</sub>), 1646 (C=C), 1463-1261 (CH, CH<sub>2</sub>, CH<sub>3</sub>), 1135-1072 (CC), 909-859 (COC) cm<sup>-1</sup>.

### SEC (RI, H<sub>2</sub>O/DMF):

**Table 24.**  $\bar{M}_w$ ,  $\bar{M}_n$  and  $\bar{D}$  as well as the via <sup>1</sup>H-NMR spectroscopy calculated molecular weights of P(G<sub>50-co</sub>-AGE<sub>6</sub>) and P(G<sub>50-co</sub>-AGE<sub>12</sub>).

	SEC	$\bar{M}_w$ [Da] <sup>(a)</sup>	$\bar{M}_n$ [Da] <sup>(a)</sup>	$\bar{D}$ <sup>(a)</sup>	$M_{\text{exp}}$ [Da] <sup>(b)</sup>
P(G <sub>50-co</sub> -AGE <sub>6</sub> )	H <sub>2</sub> O*	2430	1561	1.56	
	DMF*	3930	3693	1.06	4461
	DMF**	5198	4100	1.27	
P(G <sub>50-co</sub> -AGE <sub>12</sub> )	H <sub>2</sub> O*	2248	1367	1.64	
	DMF*	4045	3761	1.08	5146
	DMF**	5718	4812	1.12	

<sup>(a)</sup>determined by SEC in H<sub>2</sub>O/DMF, <sup>(b)</sup>determined by <sup>1</sup>H-NMR spectroscopy in D<sub>2</sub>O, \*PEG calibration, \*\*PMMA calibration



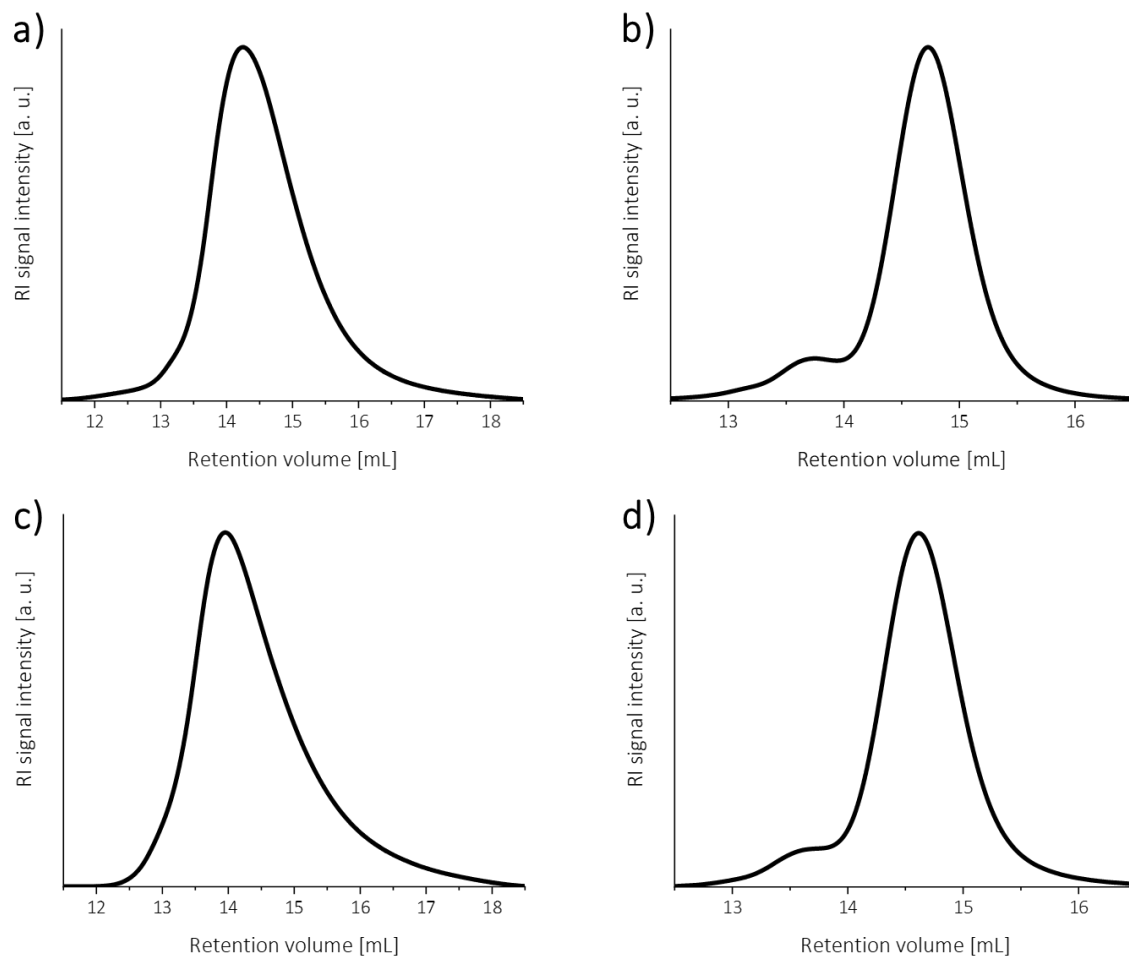
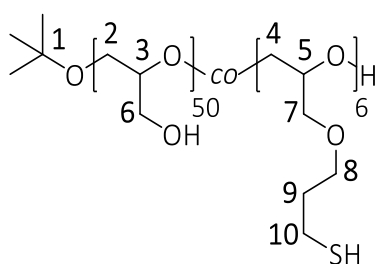


**Figure 64.** SEC elugram of P(G<sub>50</sub>-co-AGE<sub>6</sub>) in a) H<sub>2</sub>O and b) DMF respectively of P(G<sub>50</sub>-co-AGE<sub>12</sub>) in c) H<sub>2</sub>O and d) DMF, displaying a monomodal distribution with a low molecular weight tailing for analysis in H<sub>2</sub>O while a bimodal distribution is detected by SEC in DMF.

### 5.2.7 P(G<sub>50</sub>-co-SH<sub>6</sub>)

The synthesis is based on a modified experimental procedure by Stichler *et al.*<sup>[353]</sup> P(G<sub>50</sub>-co-AGE<sub>6</sub>) (1.45 g, 325 μmol) was dissolved in 200 mL EtOH and the solution was degassed for 40 min. After adding DMPA (449 mg, 1.75 mmol) and thioacetic acid (876 μL, 12.3 mmol) the mixture was stirred and irradiated with UV light at 365 nm for 2 h. The solvent was removed under vacuum and the remaining polymer was dissolved in 70 mL EtOH and precipitated in 700 mL cold Et<sub>2</sub>O. After removing Et<sub>2</sub>O under reduced pressure, the polymer was dissolved in 70 mL H<sub>2</sub>O with NaOH (7.00 g, 175 mmol) and the reaction solution was refluxed for 2.5 h. After cooling down to RT and neutralization with HCl, TCEP (1.11 g, 3.90 mmol) was added. The mixture was stirred for 12 h at RT, dialyzed for 3 d against degassed milli-Q H<sub>2</sub>O (2 L) with a water change four times a day. After lyophilization the polymer was received as a yellowish, viscous oil.

## 5 Experimental section



$^1\text{H-NMR}$  (300 MHz,  $\text{D}_2\text{O}$ ):  $\delta$  = 3.80-3.67 (m, 292 H, H-2-8), 2.65 (t, 12 H, H-10), 1.92 (quin, 12 H, H-9), 1.27 (s, 9 H, H-1) ppm.

FT-IR (ATR):  $\tilde{\nu}_{\text{max}}$  = 3363 (OH), 2923-2873 (CH,  $\text{CH}_2$ ,  $\text{CH}_3$ ), 1460-1226 (CH,  $\text{CH}_2$ ,  $\text{CH}_3$ ), 1039 (COC), 914-851 (CC)  $\text{cm}^{-1}$ .

Raman:  $\tilde{\nu}_{\text{max}}$  = 2928-2874 (CH,  $\text{CH}_2$ ,  $\text{CH}_3$ ), 2565 (SH), 1460-1258 (CH,  $\text{CH}_2$ ,  $\text{CH}_3$ ), 1116-1063 (CC), 900-845 (COC), 653 (CS)  $\text{cm}^{-1}$ .

Ellman assay: 5.6 thiols per polymer

SEC (RI,  $\text{H}_2\text{O}$ ):

**Table 25.**  $\bar{M}_w$ ,  $\bar{M}_n$  and  $\mathcal{D}$  as well as the via  $^1\text{H-NMR}$  spectroscopy calculated molecular weights of  $\text{P}(\text{G}_{50}\text{-co-SH}_6)$ .

	$\bar{M}_w$ [Da] <sup>(a)</sup>	$\bar{M}_n$ [Da] <sup>(a)</sup>	$\mathcal{D}$ <sup>(a)</sup>	$M_{\text{exp}}$ [Da] <sup>(b)</sup>
$\text{P}(\text{G}_{50}\text{-co-SH}_6)$	4388	1771	2.48	4664

<sup>(a)</sup>determined by SEC in  $\text{H}_2\text{O}$ , <sup>(b)</sup>determined by  $^1\text{H-NMR}$  spectroscopy in  $\text{D}_2\text{O}$

### 5.2.7.1 Ag-P( $\text{G}_{50}\text{-co-SH}_6$ )

UV-Vis, DLS, Zeta:

**Table 26.** Values of SPR,  $d$ , PDI and  $\zeta$  of  $\text{P}(\text{G}_{50}\text{-co-SH}_6)$ -modified AgNPs, determined by UV-Vis, DLS and zeta potential measurements.

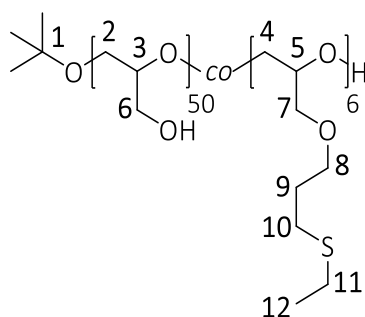
	SPR [nm]	$d$ [nm]	PDI	$\zeta$ [mV]
Ag-P( $\text{G}_{50}\text{-co-SH}_6$ )	406	$33.5 \pm 0.8$	0.213	$-19.8 \pm 1.3$

FT-IR (ATR):  $\tilde{\nu}_{\text{max}}$  = 3378 (OH), 2925-2876 (CH,  $\text{CH}_2$ ,  $\text{CH}_3$ ), 1461-1226 (CH,  $\text{CH}_2$ ,  $\text{CH}_3$ ), 1070 (COC), 916-855 (CC)  $\text{cm}^{-1}$ .

Micro-TGA (wt%): 34.6%<sub>polymer</sub>, 65.3%<sub>Ag</sub>.

5.2.8 P(G<sub>50</sub>-co-SEt<sub>6</sub>)

P(G<sub>50</sub>-co-SEt<sub>6</sub>) was synthesized according to literature.<sup>[17]</sup> Therefore, P(G<sub>50</sub>-co-AGE<sub>6</sub>) (700 mg, 147 μmol) was dissolved in 35 mL EtOH and degassed for 30 min. After adding I2959 (128 mg, 499 μmol) and EtSH (1.50 mL, 20.3 mmol) the solution was stirred and irradiated with UV light at 365 nm for 2 h. The solvent was removed under vacuum and the remaining polymer was dissolved in 160 mL H<sub>2</sub>O. After dialysis and freeze-drying the polymer was received as a slightly yellow, viscous oil.



<sup>1</sup>H-NMR (300 MHz, D<sub>2</sub>O): δ = 3.80-3.67 (m, 292 H, H-2-8), 2.71-2.59 (m, 24 H, H-10+11), 1.92 (quin, 12 H, H-10), 1.35-1.30 (m, 18 H, H-12), 1.27 (s, 9 H, H-1) ppm.

FT-IR (ATR):  $\tilde{\nu}_{\max}$  = 3362 (OH), 2924-2874 (CH, CH<sub>2</sub>, CH<sub>3</sub>), 1459-1223 (CH, CH<sub>2</sub>, CH<sub>3</sub>), 1041 (COC), 913-853 (CC) cm<sup>-1</sup>.

Raman:  $\tilde{\nu}_{\max}$  = 2928-2879 (CH, CH<sub>2</sub>, CH<sub>3</sub>), 1459-1258 (CH, CH<sub>2</sub>, CH<sub>3</sub>), 1119-1063 (CC), 907-851 (COC), 654 (CS) cm<sup>-1</sup>.

SEC (RI, H<sub>2</sub>O):

**Table 27.**  $\bar{M}_w$ ,  $\bar{M}_n$  and Đ as well as the via <sup>1</sup>H-NMR spectroscopy calculated molecular weights of P(G<sub>50</sub>-co-SEt<sub>6</sub>).

	$\bar{M}_w$ [Da] <sup>(a)</sup>	$\bar{M}_n$ [Da] <sup>(a)</sup>	Đ <sup>(a)</sup>	M <sub>exp</sub> [Da] <sup>(b)</sup>
P(G <sub>50</sub> -co-SEt <sub>6</sub> )	3230	1704	1.90	4833

<sup>(a)</sup>determined by SEC in H<sub>2</sub>O, <sup>(b)</sup>determined by <sup>1</sup>H-NMR spectroscopy in D<sub>2</sub>O

## 5 Experimental section

### 5.2.8.1 Ag-P(G<sub>50-co-SEt<sub>6</sub></sub>)

UV-Vis, DLS, Zeta:

**Table 28.** Values of SPR, *d*, PDI and  $\zeta$  of P(G<sub>50-co-SEt<sub>6</sub></sub>)-modified AgNPs, determined by UV-Vis, DLS and zeta potential measurements.

	SPR [nm]	<i>d</i> [nm]	PDI	$\zeta$ [mV]
Ag-P(G <sub>50-co-SEt<sub>6</sub></sub> )	403	36.2 ± 0.8	0.218	-25.4 ± 2.6

FT-IR (ATR):  $\tilde{\nu}_{\max}$  = 3379 (OH), 2925-2875 (CH<sub>2</sub>, CH<sub>3</sub>), 1459-1222 (CH<sub>2</sub>, CH<sub>3</sub>), 1072 (COC), 916-857 (CC) cm<sup>-1</sup>.

Micro-TGA (wt%): 20.0%<sub>polymer</sub>, 79.9%<sub>Ag</sub>.

### 5.3 Studies of thiol- and thioether-polymer-modified AgNPs

#### 5.3.1 Binding kinetics study

For studying the binding kinetics of the thiol- (MeO-PEG-SH and P(G<sub>50-co</sub>-SH<sub>6</sub>)) and thioether-polymers (MeO-PEG-SPentyl and P(G<sub>50-co</sub>-SEt<sub>6</sub>)) to the AgNP surface, the citrate-stabilized particles were modified with the respective polymeric solution as described earlier (see **Section 5.2.1.2**). After 5 min, 30 min, 2 h, 6 h and 12 h aliquots (220  $\mu$ L) of the particle solution were taken out, and the incubation was stopped by centrifugation (20 000 g, 25 min, 4 °C). The supernatant was removed, and the residue was redispersed in 800  $\mu$ L milli-Q H<sub>2</sub>O, followed by absorbance measurements.

#### 5.3.2 Colloidal stability studies

The stabilization effect of the different polymer modifications was examined under conditions provoking aggregation of the particles. For each stabilization test, 1 mL of the citrate-stabilized particles were incubated with 100  $\mu$ L of the respective 310  $\mu$ M polymeric solution by shaking overnight, followed by centrifugation and removal of the supernatant. For the centrifugation, temperature, and lyophilization studies, these concentrated modified AgNPs were suspended in milli-Q H<sub>2</sub>O and exposed to four centrifugation and resuspension cycles, to 80 °C for 12 h or were freeze-dried. In case of freeze-drying, the received pellets were once again dissolved in milli-Q H<sub>2</sub>O. Considering the colloidal stability studies in PBS, DMEM, and PB with different pH values, the concentrated functionalized AgNPs were suspended in the corresponding buffer or medium for 12 h. After centrifugation, the supernatants were removed, and the residues were resuspended again in PBS, DMEM, and PB, respectively. Investigating the colloidal stabilization efficacy for each mentioned procedure, the particle solutions before and after each treatment were measured via UV-Vis absorbance spectroscopy. To determine the stability in percent, the absorbance values at a wavelength of 410 nm obtained by UV-Vis before (mean 100%) and after were situated in relation.

## 5 Experimental section

### 5.4 Polymer synthesis and AuNP functionalization

In this section first general information about the used AuNPs are displayed, followed by the experimental procedures of polymer syntheses and the characterization of the respective polymer- and human serum (HS)-modified AuNPs.

#### 5.4.1 Citrate-AuNPs

15 nm and 30 nm Au nanospheres using sodium citrate as stabilizer, were commercially purchased.

##### 5.4.1.1 Handling and characterization of citrate-AuNPs

Unless specifically mentioned, all characterization and reaction steps with AuNPs were conducted in milli-Q H<sub>2</sub>O.

**Table 29.** Particle and mass concentration as well as values of  $d$ , PDI,  $\zeta$  and SPR of citrate-stabilized 15 nm AuNPs (Batch 20080130) and 30 nm AuNPs (Batch 20120098), defined by the manufacturer compared to own measurements.

	15 nm citrate-AuNPs	
Particle concentration [particles/mL]	$1.4 \cdot 10^{12(a)}$	$6.9 \cdot 10^{11(b)}$
Mass concentration [mg/mL]	47.7 <sup>(a)</sup>	44.9 <sup>(c)</sup>
$d$ [nm]	$14.7 \pm 1.2^{(a)}$	$14.5 \pm 1.1^{(d)}$ $18.7 \pm 0.9^{(e)}$
PDI	-	0.061 <sup>(e)</sup>
$\zeta$ [mV]	-	$-31.7 \pm 1.3^{(f)}$
SPR [nm]	-	520 <sup>(g)</sup>
	30 nm citrate-AuNPs	
Particle concentration [particles/mL]	$2.0 \cdot 10^{11(a)}$	$1.3 \cdot 10^{11(b)}$
Mass concentration [mg/mL]	54.6 <sup>(a)</sup>	43.1 <sup>(c)</sup>
$d$ [nm]	$29.8 \pm 2.4^{(a)}$	$29.3 \pm 1.9^{(d)}$ $32.3 \pm 0.7^{(e)}$
PDI	-	0.173 <sup>(e)</sup>
$\zeta$ [mV]	-	$-36.7 \pm 1.4^{(f)}$
SPR [nm]	-	524 <sup>(g)</sup>

<sup>(a)</sup>defined by the manufacturer, <sup>(b)</sup>calculated via own measurements of the mass concentration and the hydrodynamic diameter  $d$ , <sup>(c)</sup>measured by ICP-MS, <sup>(d)</sup>calculated via SEM imaging, <sup>(e)</sup>measured via DLS, <sup>(f)</sup>determined by zeta potential measurements, <sup>(g)</sup>determined by UV-Vis

FT-IR (ATR):

15 nm AuNP:  $\tilde{\nu}_{\max} = 1583\text{-}1398$  ((C=O)O<sup>-</sup>), 1248 (CH<sub>2</sub>), 1107 (CO) cm<sup>-1</sup>.

30 nm AuNP:  $\tilde{\nu}_{\max} = 1591\text{-}1390$  ((C=O)O<sup>-</sup>), 1260 (CH<sub>2</sub>), 1063 (CO) cm<sup>-1</sup>.

#### 5.4.1.2 Polymer functionalization of citrate-AuNPs

Citrate-AuNPs (15 nm and 30 nm) were modified with thioether-containing polymers via ligand exchange reaction. After adding 100  $\mu\text{L}$  of a polymeric solution (used molarities were previously determined by different experimental investigations (see Section 3.2.2.2) and were set as listed in Table 30) to 1 mL of the purchased citrate-stabilized 15 nm AuNPs, and to 1.04 mL of the purchased citrate-stabilized 30 nm AuNPs, respectively, to obtain similar Au mass concentration within in the colloidal solutions, the samples were incubated overnight at RT under constant shaking (200 rpm) (double block Thermomixer MHR23 (200-1500 rpm), Hettich AG, Bäch, Switzerland). After incubation, the NP solutions were purified by two successive centrifugation (22 000 g, 30 min, 4 °C) and redispersion cycles.

**Table 30.** Used polymer molarities of various alkyl- and cholesterol-modified PGs for functionalization of 15 nm AuNPs and 30 nm AuNPs.

Sample	Used polymer molarity [ $\mu\text{M}$ ]			
	n = 1	n = 2	n = 3	n = 4
<b>15 nm AuNPs</b>				
P(G <sub>50</sub> -CO-SEt <sub>12-n</sub> -CO-SPent <sub>n</sub> )	50	50	50	50
P(G <sub>50</sub> -CO-SEt <sub>12-n</sub> -CO-SDec <sub>n</sub> )	50	50	50	50
P(G <sub>50</sub> -CO-SEt <sub>12-n</sub> -CO-SPentadec <sub>n</sub> )	7.5	7.5	5	5
P(G <sub>50</sub> -CO-SEt <sub>5,5</sub> -CO-Chol <sub>0,5</sub> )		25		
P(G <sub>50</sub> -CO-SEt <sub>5,5</sub> -CO-SPEG-Chol <sub>0,5</sub> )		12.5		
<b>30 nm AuNPs</b>				
P(G <sub>50</sub> -CO-SEt <sub>12-n</sub> -CO-SPent <sub>n</sub> )	50	50	50	50
P(G <sub>50</sub> -CO-SEt <sub>12-n</sub> -CO-SDec <sub>n</sub> )	50	50	50	50
P(G <sub>50</sub> -CO-SEt <sub>12-n</sub> -CO-SPentadec <sub>n</sub> )	25	25	25	25
P(G <sub>50</sub> -CO-SEt <sub>5,5</sub> -CO-Chol <sub>0,5</sub> )		25		
P(G <sub>50</sub> -CO-SEt <sub>5,5</sub> -CO-SPEG-Chol <sub>0,5</sub> )		12.5		

## 5 Experimental section

### 5.4.1.3 Calculation of surface area

$$\begin{aligned} \text{Surface area per mL} &= \text{Surface area per particle} \cdot \text{Number of particle per mL} \\ &= 4\pi r^2 \cdot \frac{\text{Mass of Au per mL}}{\text{Mass of one particle}} \\ &= 4\pi r^2 \cdot \frac{\text{Mass of Au per mL}}{\text{Volume of one particle} \cdot \rho(\text{Au})} \\ &= 4\pi r^2 \cdot \frac{\text{Mass of Au per mL}}{\frac{4}{3}\pi r^3 \cdot \rho(\text{Au})} \end{aligned}$$

$r$ : radius determined via DLS (hydrodynamic diameter)

*Mass of Au per mL*: determined by ICP-MS (concentration of Au-ions)

$\rho(\text{Au}) = 19.3 \text{ g/cm}^3$

### 5.4.1.4 Incubation with human serum (HS)

HS was prepared as previously described in **Section 5.1.1** before transferring into an Eppendorf tube. Pure AuNPs as well as polymer-functionalized AuNPs with both sizes (15 nm and 30 nm) were added to HS, followed by short vortexing and incubation for 1 h at 37 °C, simulating body temperature. Here, the volume corresponding to a particle surface area of 10 cm<sup>2</sup> was added to 100 μL HS, inspired by literature<sup>[477]</sup>. Calculation of surface area was demonstrated in detail before. HS incubation was stopped by five centrifugation (20 000 g, 30 min, 4 °C) and redispersion cycles, whereby the pellet was resuspended in 1x PBS supplemented with 0.05% TWEEN® 20 after the first three cycles and in pure 1x PBS after the following centrifugation step. Upon final centrifugation, the supernatant was removed, and the pellet was used for subsequent analysis. Five centrifugation and redispersion cycles were sufficient for purification to ensure the absence of unbound serum proteins. This was confirmed by micro-BCA assay of the supernatants after successive centrifugations steps (data not shown).



## UV-Vis, DLS, Zeta:

**Table 31.** Values of SPR,  $d$ , PDI and  $\zeta$  of 15 nm and 30 nm citrate-AuNPs incubated with HS, determined by UV-Vis, DLS and zeta potential measurements.

	SPR [nm]	$d$ [nm]	PDI	$\zeta$ [mV]
15Au-HS	532	84.8 ± 2.1	0.271	-24.5 ± 0.9
30Au-HS	531	96.6 ± 2.5	0.275	-30.4 ± 0.8

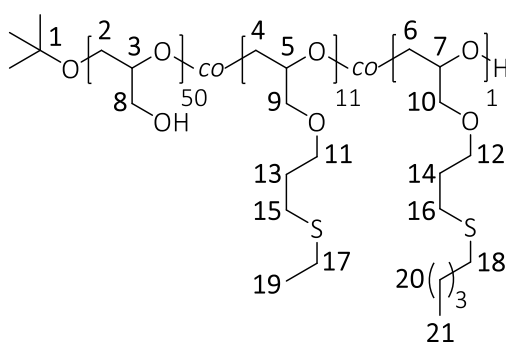
## FT-IR (ATR):

**15Au-HS:**  $\tilde{\nu}_{\max}$  = 3285 (OH), 2956-2873 (CH<sub>2</sub>, CH<sub>3</sub>), 1547-1246 (CH<sub>2</sub>, CH<sub>3</sub>), 1097 (COC), 984-854 (CC) cm<sup>-1</sup>.

**30Au-HS:**  $\tilde{\nu}_{\max}$  = 3273 (OH), 2956-2873 (CH<sub>2</sub>, CH<sub>3</sub>), 1539-1249 (CH<sub>2</sub>, CH<sub>3</sub>), 1077 (COC), 981-853 (CC) cm<sup>-1</sup>.

5.4.2 P(G<sub>50</sub>-co-SEt<sub>11</sub>-co-SPent<sub>1</sub>)

P(G<sub>50</sub>-co-AGE<sub>12</sub>) (50.0 mg, 9.72 μmol) was dissolved in 10 mL EtOH and degassed for 20 min. After adding EtSH (144 μL, 1.94 mmol), 1-pentanethiol (14.5 μL, 117 μmol) and I2959 (17.5 mg, 77.8 μmol) the solution was stirred and irradiated with UV light at 365 nm for 2 h. The solvent was removed under vacuum and the remaining polymer was dissolved in 90 mL H<sub>2</sub>O. After dialysis and lyophilization the polymer was received as a slightly yellow, viscous solid.



<sup>1</sup>H-NMR (300 MHz, D<sub>2</sub>O):  $\delta$  = 3.80-3.67 (m, 334 H, H-2-12), 3.14-2.85 (m, 48 H, H-15-18), 2.08 (quin, 24 H, H-13,14), 1.39-1.33 (m, 39 H, H-19,20), 1.26 (s, 9 H, H-1), 0.94 (t, 3 H, H-21) ppm.

FT-IR (ATR):  $\tilde{\nu}_{\max}$  = 3364 (OH), 2921-2872 (CH, CH<sub>2</sub>, CH<sub>3</sub>), 1458-1253 (CH, CH<sub>2</sub>, CH<sub>3</sub>), 1041 (COC), 914-855 (CC) cm<sup>-1</sup>.

## 5 Experimental section

**Raman:**  $\tilde{\nu}_{\max}$  = 2926-2881 (CH, CH<sub>2</sub>, CH<sub>3</sub>), 1461-1260 (CH, CH<sub>2</sub>, CH<sub>3</sub>), 1133-1056 (CC), 909-854 (COC), 646 (CS) cm<sup>-1</sup>.

**SEC (RI, H<sub>2</sub>O):**

**Table 32.**  $\bar{M}_w$ ,  $\bar{M}_n$  and  $\mathcal{D}$  as well as the via <sup>1</sup>H-NMR spectroscopy calculated molecular weight of P(G<sub>50-co</sub>-SEt<sub>11-co</sub>-SPent<sub>1</sub>).

	$\bar{M}_w$ [Da] <sup>(a)</sup>	$\bar{M}_n$ [Da] <sup>(a)</sup>	$\mathcal{D}$ <sup>(a)</sup>	$M_{\text{exp}}$ [Da] <sup>(b)</sup>
P(G <sub>50-co</sub> -SEt <sub>11-co</sub> -SPent <sub>1</sub> )	5256	2360	2.23	5931

<sup>(a)</sup>determined by SEC in H<sub>2</sub>O, <sup>(b)</sup>determined by <sup>1</sup>H-NMR spectroscopy in D<sub>2</sub>O

### 5.4.2.1 Au-P(G<sub>50-co</sub>-SEt<sub>11-co</sub>-SPent<sub>1</sub>)

**UV-Vis, DLS, Zeta:**

**Table 33.** Values of SPR,  $d$ , PDI and  $\zeta$  of P(G<sub>50-co</sub>-SEt<sub>11-co</sub>-SPent<sub>1</sub>)-modified 15 nm and 30 nm AuNPs, determined by UV-Vis, DLS and zeta potential measurements.

	SPR [nm]	$d$ [nm]	PDI	$\zeta$ [mV]
15Au-P(G <sub>50-co</sub> -SEt <sub>11-co</sub> -SPent <sub>1</sub> )	521	29.4 ± 2.2	0.100	-23.2 ± 1.9
30Au-P(G <sub>50-co</sub> -SEt <sub>11-co</sub> -SPent <sub>1</sub> )	525	42.4 ± 0.9	0.174	-28.5 ± 0.6

**FT-IR (ATR):**  $\tilde{\nu}_{\max}$  = 3383 (OH), 2922-2878 (CH, CH<sub>2</sub>, CH<sub>3</sub>), 1593-1257 (CH, CH<sub>2</sub>, CH<sub>3</sub>), 1073 (COC), 913-841 (CC) cm<sup>-1</sup>.

### 5.4.2.2 Au-P(G<sub>50-co</sub>-SEt<sub>11-co</sub>-SPent<sub>1</sub>)-HS

**UV-Vis, DLS, Zeta:**

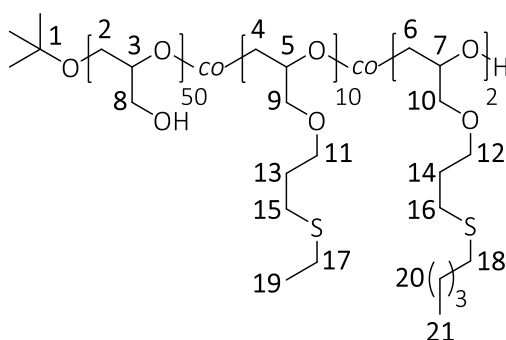
**Table 34.** Values of SPR,  $d$ , PDI and  $\zeta$  of 15 nm and 30 nm AuNP-P(G<sub>50-co</sub>-SEt<sub>11-co</sub>-SPent<sub>1</sub>) incubated with HS, determined by UV-Vis, DLS and zeta potential measurements.

	SPR [nm]	$d$ [nm]	PDI	$\zeta$ [mV]
15Au-P(G <sub>50-co</sub> -SEt <sub>11-co</sub> -SPent <sub>1</sub> )-HS	525	50.5 ± 1.6	0.137	-17.4 ± 2.8
30Au-P(G <sub>50-co</sub> -SEt <sub>11-co</sub> -SPent <sub>1</sub> )-HS	527	62.3 ± 4.1	0.172	-19.4 ± 2.0

**FT-IR (ATR):**  $\tilde{\nu}_{\max}$  = 3280 (OH), 2960-2880 (CH, CH<sub>2</sub>, CH<sub>3</sub>), 1541-1248 (CH, CH<sub>2</sub>, CH<sub>3</sub>), 1077 (COC), 984-861 (CC) cm<sup>-1</sup>.

5.4.3 P(G<sub>50</sub>-co-SEt<sub>10</sub>-co-SPent<sub>2</sub>)

P(G<sub>50</sub>-co-AGE<sub>12</sub>) (50.0 mg, 9.72 μmol) was dissolved in 10 mL EtOH and degassed for 20 min. After adding EtSH (144 μL, 1.94 mmol), 1-pentanethiol (24.1 μL, 194 μmol) and I2959 (17.5 mg, 77.8 μmol) the solution was stirred and irradiated with UV light at 365 nm for 2 h. The solvent was removed under vacuum and the remaining polymer was dissolved in 90 mL H<sub>2</sub>O. After dialyzing and freeze-drying the polymer was received as a slightly yellow, viscous solid.



<sup>1</sup>H-NMR (300 MHz, D<sub>2</sub>O): δ = 3.80-3.67 (m, 334 H, H-2-12), 3.14-2.82 (m, 48 H, H-15-18), 2.07 (quin, 24 H, H-13,14), 1.38-1.32 (m, 42 H, H-19,20), 1.26 (s, 9 H, H-1), 0.94 (t, 6 H, H-21) ppm.

FT-IR (ATR):  $\tilde{\nu}_{\max}$  = 3364 (OH), 2922-2873 (CH, CH<sub>2</sub>, CH<sub>3</sub>), 1458-1256 (CH, CH<sub>2</sub>, CH<sub>3</sub>), 1040 (COC), 915-854 (CC) cm<sup>-1</sup>.

Raman:  $\tilde{\nu}_{\max}$  = 2928-2882 (CH, CH<sub>2</sub>, CH<sub>3</sub>), 1463-1260 (CH, CH<sub>2</sub>, CH<sub>3</sub>), 1127-972 (CC), 907-850 (COC), 648 (CS) cm<sup>-1</sup>.

SEC (RI, H<sub>2</sub>O):

**Table 35.**  $\bar{M}_w$ ,  $\bar{M}_n$  and Đ as well as the via <sup>1</sup>H-NMR spectroscopy calculated molecular weight of P(G<sub>50</sub>-co-SEt<sub>10</sub>-co-SPent<sub>2</sub>).

	$\bar{M}_w$ [Da] <sup>(a)</sup>	$\bar{M}_n$ [Da] <sup>(a)</sup>	Đ <sup>(a)</sup>	$M_{\text{exp}}$ [Da] <sup>(b)</sup>
P(G <sub>50</sub> -co-SEt <sub>10</sub> -co-SPent <sub>2</sub> )	6456	2697	2.39	5974

<sup>(a)</sup>determined by SEC in H<sub>2</sub>O, <sup>(b)</sup>determined by <sup>1</sup>H-NMR spectroscopy in D<sub>2</sub>O

## 5 Experimental section

### 5.4.3.1 Au-P(G<sub>50-co-SEt<sub>10-co-SPent<sub>2</sub></sub>)</sub>

UV-Vis, DLS, Zeta:

**Table 36.** Values of SPR, *d*, PDI and  $\zeta$  of P(G<sub>50-co-SEt<sub>10-co-SPent<sub>2</sub></sub>)-modified 15 nm and 30 nm AuNPs, determined by UV-Vis, DLS and zeta potential measurements.</sub>

	SPR [nm]	<i>d</i> [nm]	PDI	$\zeta$ [mV]
15Au-P(G <sub>50-co-SEt<sub>10-co-SPent<sub>2</sub></sub>)</sub>	521	25.7 ± 0.8	0.079	-24.4 ± 2.6
30Au-P(G <sub>50-co-SEt<sub>10-co-SPent<sub>2</sub></sub>)</sub>	525	40.5 ± 0.6	0.188	-29.3 ± 1.5

FT-IR (ATR):  $\tilde{\nu}_{\max}$  = 3378 (OH), 2922-2878 (CH, CH<sub>2</sub>, CH<sub>3</sub>), 1593-1257 (CH, CH<sub>2</sub>, CH<sub>3</sub>), 1073 (COC), 913-844 (CC) cm<sup>-1</sup>.

### 5.4.3.2 Au-P(G<sub>50-co-SEt<sub>10-co-SPent<sub>2</sub></sub>)-HS</sub>

UV-Vis, DLS, Zeta:

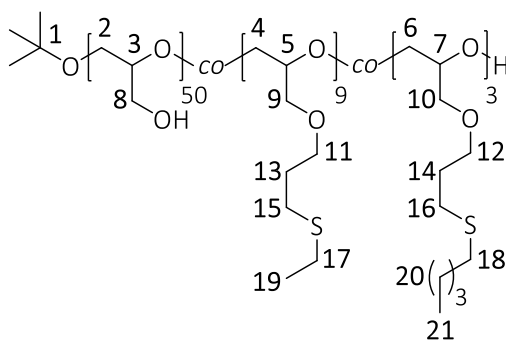
**Table 37.** Values of SPR, *d*, PDI and  $\zeta$  of 15Au- and 30Au-P(G<sub>50-co-SEt<sub>10-co-SPent<sub>2</sub></sub>) incubated with HS, determined by UV-Vis, DLS and zeta potential measurements.</sub>

	SPR [nm]	<i>d</i> [nm]	PDI	$\zeta$ [mV]
15Au-P(G <sub>50-co-SEt<sub>10-co-SPent<sub>2</sub></sub>)-HS</sub>	525	55.3 ± 1.5	0.128	-18.1 ± 1.9
30Au-P(G <sub>50-co-SEt<sub>10-co-SPent<sub>2</sub></sub>)-HS</sub>	528	67.3 ± 6.5	0.194	-20.1 ± 3.6

FT-IR (ATR):  $\tilde{\nu}_{\max}$  = 3261 (OH), 2960-2880 (CH, CH<sub>2</sub>, CH<sub>3</sub>), 1539-1248 (CH, CH<sub>2</sub>, CH<sub>3</sub>), 1077 (COC), 984-861 (CC) cm<sup>-1</sup>.

5.4.4 P(G<sub>50</sub>-co-SEt<sub>9</sub>-co-SPent<sub>3</sub>)

P(G<sub>50</sub>-co-AGE<sub>12</sub>) (50.0 mg, 9.72 μmol) was dissolved in 10 mL EtOH and degassed for 20 min. After adding EtSH (144 μL, 1.94 mmol), 1-pentanethiol (60.3 μL, 486 μmol) and I2959 (17.5 mg, 77.8 μmol) the solution was stirred and irradiated with UV light at 365 nm for 2 h. The solvent was removed under vacuum and the remaining polymer was dissolved in 90 mL H<sub>2</sub>O. After dialysis and lyophilization the polymer was received as a slightly yellow, viscous solid.



<sup>1</sup>H-NMR (300 MHz, D<sub>2</sub>O): δ = 3.80-3.67 (m, 334 H, H-2-12), 3.16-2.85 (m, 48 H, H-15-18), 2.07 (quin, 24 H, H-13,14), 1.39-1.32 (m, 45 H, H-19,20), 1.26 (s, 9 H, H-1), 0.94 (t, 9 H, H-21) ppm.

FT-IR (ATR):  $\tilde{\nu}_{\max}$  = 3372 (OH), 2922-2873 (CH, CH<sub>2</sub>, CH<sub>3</sub>), 1458-1227 (CH, CH<sub>2</sub>, CH<sub>3</sub>), 1041 (COC), 915-855 (CC) cm<sup>-1</sup>.

Raman:  $\tilde{\nu}_{\max}$  = 2925-2885 (CH, CH<sub>2</sub>, CH<sub>3</sub>), 1463-1258 (CH, CH<sub>2</sub>, CH<sub>3</sub>), 1066 (CC), 908-847 (COC), 644 (CS) cm<sup>-1</sup>.

SEC (RI, H<sub>2</sub>O):

**Table 38.**  $\bar{M}_w$ ,  $\bar{M}_n$  and Đ as well as the via <sup>1</sup>H-NMR spectroscopy calculated molecular weight of P(G<sub>50</sub>-co-SEt<sub>9</sub>-co-SPent<sub>3</sub>).

	$\bar{M}_w$ [Da] <sup>(a)</sup>	$\bar{M}_n$ [Da] <sup>(a)</sup>	Đ <sup>(a)</sup>	$M_{\text{exp}}$ [Da] <sup>(b)</sup>
P(G <sub>50</sub> -co-SEt <sub>9</sub> -co-SPent <sub>3</sub> )	8236	2869	2.87	6016

<sup>(a)</sup>determined by SEC in H<sub>2</sub>O, <sup>(b)</sup>determined by <sup>1</sup>H-NMR spectroscopy in D<sub>2</sub>O

## 5 Experimental section

### 5.4.4.1 Au-P(G<sub>50-co-SEt<sub>9</sub>-co-SPent<sub>3</sub>)</sub>

UV-Vis, DLS, Zeta:

**Table 39.** Values of SPR, *d*, PDI and  $\zeta$  of P(G<sub>50-co-SEt<sub>9</sub>-co-SPent<sub>3</sub>)-modified 15 nm and 30 nm AuNPs, determined by UV-Vis, DLS and zeta potential measurements.</sub>

	SPR [nm]	<i>d</i> [nm]	PDI	$\zeta$ [mV]
15Au-P(G <sub>50-co-SEt<sub>9</sub>-co-SPent<sub>3</sub>)</sub>	522	29.3 ± 1.8	0.098	-24.2 ± 3.1
30Au-P(G <sub>50-co-SEt<sub>9</sub>-co-SPent<sub>3</sub>)</sub>	526	42.9 ± 1.1	0.195	-28.5 ± 1.3

FT-IR (ATR):  $\tilde{\nu}_{\max}$  = 3386 (OH), 2921-2877 (CH, CH<sub>2</sub>, CH<sub>3</sub>), 1596-1254 (CH, CH<sub>2</sub>, CH<sub>3</sub>), 1074 (COC), 905-840 (CC) cm<sup>-1</sup>.

### 5.4.4.2 Au-P(G<sub>50-co-SEt<sub>9</sub>-co-SPent<sub>3</sub>)-HS</sub>

UV-Vis, DLS, Zeta:

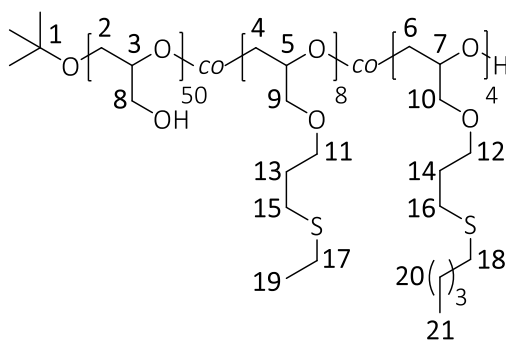
**Table 40.** Values of SPR, *d*, PDI and  $\zeta$  of 15Au- and 30Au-P(G<sub>50-co-SEt<sub>9</sub>-co-SPent<sub>3</sub>) incubated with HS, determined by UV-Vis, DLS and zeta potential measurements.</sub>

	SPR [nm]	<i>d</i> [nm]	PDI	$\zeta$ [mV]
15Au-P(G <sub>50-co-SEt<sub>9</sub>-co-SPent<sub>3</sub>)-HS</sub>	525	50.4 ± 2.4	0.130	-18.6 ± 2.4
30Au-P(G <sub>50-co-SEt<sub>9</sub>-co-SPent<sub>3</sub>)-HS</sub>	528	65.7 ± 3.6	0.160	-18.9 ± 1.3

FT-IR (ATR):  $\tilde{\nu}_{\max}$  = 3283 (OH), 2958-2879 (CH, CH<sub>2</sub>, CH<sub>3</sub>), 1546-1246 (CH, CH<sub>2</sub>, CH<sub>3</sub>), 1074 (COC), 982-858 (CC) cm<sup>-1</sup>.

5.4.5 P(G<sub>50</sub>-co-SEt<sub>8</sub>-co-SPent<sub>4</sub>)

P(G<sub>50</sub>-co-AGE<sub>12</sub>) (50.0 mg, 9.72 μmol) was dissolved in 10 mL EtOH and degassed for 20 min. After adding EtSH (144 μL, 1.94 mmol), 1-pentanethiol (72.4 μL, 583 μmol) and I2959 (17.5 mg, 77.8 μmol) the solution was stirred and irradiated with UV light at 365 nm for 2 h. The solvent was removed under vacuum and the remaining polymer was dissolved in 90 mL H<sub>2</sub>O. After dialysis and freeze-drying the polymer was received as a slightly yellow, viscous solid.



<sup>1</sup>H-NMR (300 MHz, D<sub>2</sub>O): δ = 3.80-3.67 (m, 334 H, H-2-12), 3.16-2.87 (m, 48 H, H-15-18), 2.07 (quin, 24 H, H-13,14), 1.39-1.33 (m, 48 H, H-19,20), 1.26 (s, 9 H, H-1), 0.95 (t, 12 H, H-21) ppm.

FT-IR (ATR):  $\tilde{\nu}_{\max}$  = 3372 (OH), 2923-2872 (CH, CH<sub>2</sub>, CH<sub>3</sub>), 1458-1222 (CH, CH<sub>2</sub>, CH<sub>3</sub>), 1042 (COC), 914-852 (CC) cm<sup>-1</sup>.

Raman:  $\tilde{\nu}_{\max}$  = 2924-2879 (CH, CH<sub>2</sub>, CH<sub>3</sub>), 1461-1258 (CH, CH<sub>2</sub>, CH<sub>3</sub>), 1061 (CC), 906-847 (COC), 644 (CS) cm<sup>-1</sup>.

SEC (RI, H<sub>2</sub>O):

**Table 41.**  $\bar{M}_w$ ,  $\bar{M}_n$  and Đ as well as the via <sup>1</sup>H-NMR spectroscopy calculated molecular weight of P(G<sub>50</sub>-co-SEt<sub>8</sub>-co-SPent<sub>4</sub>).

	$\bar{M}_w$ [Da] <sup>(a)</sup>	$\bar{M}_n$ [Da] <sup>(a)</sup>	Đ <sup>(a)</sup>	$M_{\text{exp}}$ [Da] <sup>(b)</sup>
P(G <sub>50</sub> -co-SEt <sub>8</sub> -co-SPent <sub>4</sub> )	7841	3647	2.15	6058

<sup>(a)</sup>determined by SEC in H<sub>2</sub>O, <sup>(b)</sup>determined by <sup>1</sup>H-NMR spectroscopy in D<sub>2</sub>O

## 5 Experimental section

### 5.4.5.1 Au-P(G<sub>50-co-SEt<sub>8</sub>-co-SPent<sub>4</sub>)</sub>

UV-Vis, DLS, Zeta:

**Table 42.** Values of SPR, *d*, PDI and  $\zeta$  of P(G<sub>50-co-SEt<sub>8</sub>-co-SPent<sub>4</sub>)-modified 15 nm and 30 nm AuNPs, determined by UV-Vis, DLS and zeta potential measurements.</sub>

	SPR [nm]	<i>d</i> [nm]	PDI	$\zeta$ [mV]
15Au-P(G <sub>50-co-SEt<sub>8</sub>-co-SPent<sub>4</sub>)</sub>	522	32.6 ± 1.1	0.105	-23.0 ± 2.4
30Au-P(G <sub>50-co-SEt<sub>8</sub>-co-SPent<sub>4</sub>)</sub>	526	43.7 ± 1.4	0.168	-28.2 ± 2.0

FT-IR (ATR):  $\tilde{\nu}_{\max}$  = 3370 (OH), 2925-2875 (CH, CH<sub>2</sub>, CH<sub>3</sub>), 1590-1247 (CH, CH<sub>2</sub>, CH<sub>3</sub>), 1072 (COC), 914-842 (CC) cm<sup>-1</sup>.

### 5.4.5.2 Au-P(G<sub>50-co-SEt<sub>8</sub>-co-SPent<sub>4</sub>)-HS</sub>

UV-Vis, DLS, Zeta:

**Table 43.** Values of SPR, *d*, PDI and  $\zeta$  of 15Au- and 30Au-P(G<sub>50-co-SEt<sub>8</sub>-co-SPent<sub>4</sub>) incubated with HS, determined by UV-Vis, DLS and zeta potential measurements.</sub>

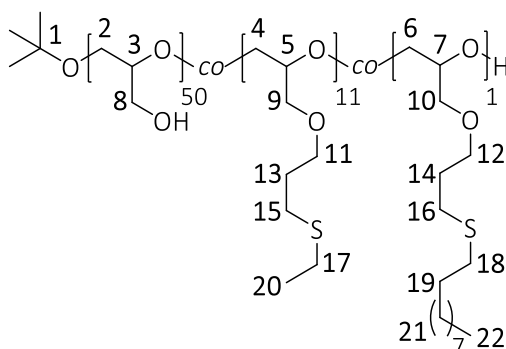
	SPR [nm]	<i>d</i> [nm]	PDI	$\zeta$ [mV]
15Au-P(G <sub>50-co-SEt<sub>8</sub>-co-SPent<sub>4</sub>)-HS</sub>	524	48.9 ± 1.6	0.138	-19.9 ± 0.7
30Au-P(G <sub>50-co-SEt<sub>8</sub>-co-SPent<sub>4</sub>)-HS</sub>	527	63.6 ± 4.4	0.183	-20.2 ± 1.4

FT-IR (ATR):  $\tilde{\nu}_{\max}$  = 3273 (OH), 2954-2872 (CH, CH<sub>2</sub>, CH<sub>3</sub>), 1541-1246 (CH, CH<sub>2</sub>, CH<sub>3</sub>), 1070 (COC), 983-856 (CC) cm<sup>-1</sup>.



5.4.6 P(G<sub>50</sub>-co-SEt<sub>11</sub>-co-SDec<sub>1</sub>)

P(G<sub>50</sub>-co-AGE<sub>12</sub>) (50.0 mg, 9.72 μmol) was dissolved in 10 mL EtOH and degassed for 20 min. After adding EtSH (180 μL, 2.43 mmol), 1-decanethiol (3.09 μL, 14.6 μmol) and I2959 (17.5 mg, 77.8 μmol) the solution was stirred and irradiated with UV light at 365 nm for 2 h. The solvent was removed under vacuum and the remaining polymer was dissolved in 90 mL H<sub>2</sub>O. After dialyzing and lyophilization the polymer was received as a slightly yellow, viscous solid.



<sup>1</sup>H-NMR (300 MHz, D<sub>2</sub>O): δ = 3.80-3.67 (m, 334 H, H-2-12), 3.16-2.87 (m, 46 H, H-15-17), 2.70 (t, 2 H, H-18), 2.07 (quin, 24 H, H-13,14), 1.73 (quin, 2 H, H-19), 1.39-1.32 (m, 47 H, H-20,21), 1.26 (s, 9 H, H-1), 0.95 (t, 3 H, H-22) ppm.

FT-IR (ATR):  $\tilde{\nu}_{\max}$  = 3371 (OH), 2922-2873 (CH, CH<sub>2</sub>, CH<sub>3</sub>), 1458-1256 (CH, CH<sub>2</sub>, CH<sub>3</sub>), 1041 (COC), 914-855 (CC) cm<sup>-1</sup>.

Raman:  $\tilde{\nu}_{\max}$  = 2925-2880 (CH, CH<sub>2</sub>, CH<sub>3</sub>), 1463-1259 (CH, CH<sub>2</sub>, CH<sub>3</sub>), 1051 (CC), 905-848 (COC), 643 (CS) cm<sup>-1</sup>.

SEC (RI, H<sub>2</sub>O):

**Table 44.**  $\bar{M}_w$ ,  $\bar{M}_n$  and Đ as well as the via <sup>1</sup>H-NMR spectroscopy calculated molecular weight of P(G<sub>50</sub>-co-SEt<sub>11</sub>-co-SDec<sub>1</sub>).

	$\bar{M}_w$ [Da] <sup>(a)</sup>	$\bar{M}_n$ [Da] <sup>(a)</sup>	Đ <sup>(a)</sup>	$M_{\text{exp}}$ [Da] <sup>(b)</sup>
P(G <sub>50</sub> -co-SEt <sub>11</sub> -co-SDec <sub>1</sub> )	6770	3155	2.15	6001

<sup>(a)</sup>determined by SEC in H<sub>2</sub>O, <sup>(b)</sup>determined by <sup>1</sup>H-NMR spectroscopy in D<sub>2</sub>O

## 5 Experimental section

### 5.4.6.1 Au-P(G<sub>50-co-SEt<sub>11-co-SDec<sub>1</sub></sub>)</sub>

UV-Vis, DLS, Zeta:

**Table 45.** Values of SPR, *d*, PDI and  $\zeta$  of P(G<sub>50-co-SEt<sub>11-co-SDec<sub>1</sub></sub>)-modified 15 nm and 30 nm AuNPs, determined by UV-Vis, DLS and zeta potential measurements.</sub>

	SPR [nm]	<i>d</i> [nm]	PDI	$\zeta$ [mV]
15Au-P(G <sub>50-co-SEt<sub>11-co-SDec<sub>1</sub></sub>)</sub>	522	27.9 ± 1.3	0.077	-22.1 ± 1.7
30Au-P(G <sub>50-co-SEt<sub>11-co-SDec<sub>1</sub></sub>)</sub>	526	42.1 ± 0.9	0.170	-28.3 ± 2.7

FT-IR (ATR):  $\tilde{\nu}_{\max}$  = 3388 (OH), 2921-2877 (CH, CH<sub>2</sub>, CH<sub>3</sub>), 1594-1246 (CH, CH<sub>2</sub>, CH<sub>3</sub>), 1073 (COC), 913-839 (CC) cm<sup>-1</sup>.

### 5.4.6.2 Au-P(G<sub>50-co-SEt<sub>11-co-SDec<sub>1</sub></sub>)-HS</sub>

UV-Vis, DLS, Zeta:

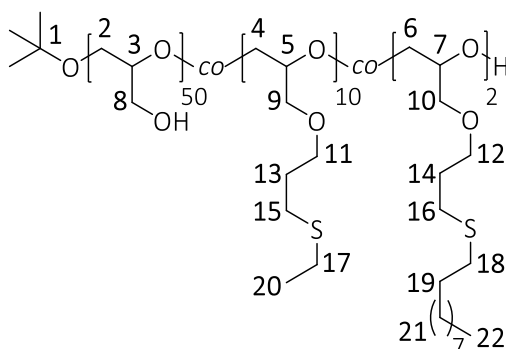
**Table 46.** Values of SPR, *d*, PDI and  $\zeta$  of 15Au- and 30Au-P(G<sub>50-co-SEt<sub>11-co-SDec<sub>1</sub></sub>) incubated with HS, determined by UV-Vis, DLS and zeta potential measurements.</sub>

	SPR [nm]	<i>d</i> [nm]	PDI	$\zeta$ [mV]
15Au-P(G <sub>50-co-SEt<sub>11-co-SDec<sub>1</sub></sub>)-HS</sub>	524	52.1 ± 1.7	0.112	-19.6 ± 1.3
30Au-P(G <sub>50-co-SEt<sub>11-co-SDec<sub>1</sub></sub>)-HS</sub>	528	63.7 ± 2.1	0.155	-22.5 ± 2.5

FT-IR (ATR):  $\tilde{\nu}_{\max}$  = 3287 (OH), 2957-2878 (CH, CH<sub>2</sub>, CH<sub>3</sub>), 1543-1245 (CH, CH<sub>2</sub>, CH<sub>3</sub>), 1078 (COC), 984-858 (CC) cm<sup>-1</sup>.

5.4.7 P(G<sub>50</sub>-co-SEt<sub>10</sub>-co-SDec<sub>2</sub>)

P(G<sub>50</sub>-co-AGE<sub>12</sub>) (50.0 mg, 9.72 μmol) was dissolved in 10 mL EtOH and degassed for 20 min. After adding EtSH (180 μL, 2.43 mmol), 1-decanethiol (4.10 μL, 19.4 μmol) and I2959 (17.5 mg, 77.8 μmol) the solution was stirred and irradiated with UV light at 365 nm for 2 h. The solvent was removed under vacuum and the remaining polymer was dissolved in 90 mL H<sub>2</sub>O. After dialyzation and freeze-drying the polymer was received as a slightly yellow, viscous solid.



<sup>1</sup>H-NMR (300 MHz, D<sub>2</sub>O): δ = 3.80-3.67 (m, 334 H, H-2-12), 3.16-2.87 (m, 44 H, H-15-17), 2.70 (t, 4 H, H-18), 2.07 (quin, 24 H, H-13,14), 1.73 (quin, 4 H, H-19), 1.39-1.33 (m, 58 H, H-20,21), 1.27 (s, 9 H, H-1), 0.95 (t, 6 H, H-22) ppm.

FT-IR (ATR):  $\tilde{\nu}_{\max}$  = 3372 (OH), 2923-2873 (CH, CH<sub>2</sub>, CH<sub>3</sub>), 1458-1255 (CH, CH<sub>2</sub>, CH<sub>3</sub>), 1040 (COC), 914-855 (CC) cm<sup>-1</sup>.

Raman:  $\tilde{\nu}_{\max}$  = 2930-2884 (CH, CH<sub>2</sub>, CH<sub>3</sub>), 1461-1256 (CH, CH<sub>2</sub>, CH<sub>3</sub>), 1115-971 (CC), 901-858 (COC), 642 (CS) cm<sup>-1</sup>.

SEC (RI, H<sub>2</sub>O):

**Table 47.**  $\bar{M}_w$ ,  $\bar{M}_n$  and Đ as well as the via <sup>1</sup>H-NMR spectroscopy calculated molecular weight of P(G<sub>50</sub>-co-SEt<sub>10</sub>-co-SDec<sub>2</sub>).

	$\bar{M}_w$ [Da] <sup>(a)</sup>	$\bar{M}_n$ [Da] <sup>(a)</sup>	Đ <sup>(a)</sup>	$M_{\text{exp}}$ [Da] <sup>(b)</sup>
P(G <sub>50</sub> -co-SEt <sub>10</sub> -co-SDec <sub>2</sub> )	8148	2744	2.97	6113

<sup>(a)</sup>determined by SEC in H<sub>2</sub>O, <sup>(b)</sup>determined by <sup>1</sup>H-NMR spectroscopy in D<sub>2</sub>O

## 5 Experimental section

### 5.4.7.1 Au-P(G<sub>50-co-SEt<sub>10-co-SDec<sub>2</sub></sub>)</sub>

UV-Vis, DLS, Zeta:

**Table 48.** Values of SPR, *d*, PDI and  $\zeta$  of P(G<sub>50-co-SEt<sub>10-co-SDec<sub>2</sub></sub>)-modified 15 nm and 30 nm AuNPs, determined by UV-Vis, DLS and zeta potential measurements.</sub>

	SPR [nm]	<i>d</i> [nm]	PDI	$\zeta$ [mV]
15Au-P(G <sub>50-co-SEt<sub>10-co-SDec<sub>2</sub></sub>)</sub>	522	32.1 ± 1.2	0.113	-24.1 ± 2.3
30Au-P(G <sub>50-co-SEt<sub>10-co-SDec<sub>2</sub></sub>)</sub>	526	45.3 ± 0.6	0.191	-25.4 ± 3.5

FT-IR (ATR):  $\tilde{\nu}_{\max}$  = 3380 (OH), 2921-2877 (CH, CH<sub>2</sub>, CH<sub>3</sub>), 1589-1245 (CH, CH<sub>2</sub>, CH<sub>3</sub>), 1073 (COC), 907-840 (CC) cm<sup>-1</sup>.

### 5.4.7.2 Au-P(G<sub>50-co-SEt<sub>10-co-SDec<sub>2</sub></sub>)-HS</sub>

UV-Vis, DLS, Zeta:

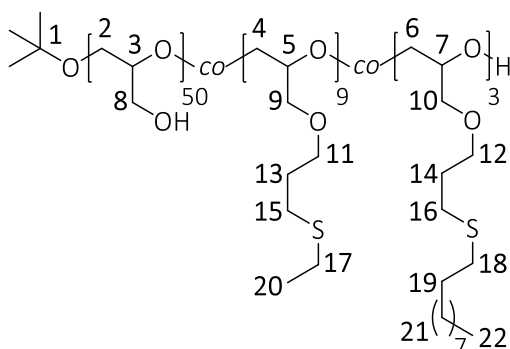
**Table 49.** Values of SPR, *d*, PDI and  $\zeta$  of 15Au- and 30Au-P(G<sub>50-co-SEt<sub>10-co-SDec<sub>2</sub></sub>) incubated with HS, determined by UV-Vis, DLS and zeta potential measurements.</sub>

	SPR [nm]	<i>d</i> [nm]	PDI	$\zeta$ [mV]
15Au-P(G <sub>50-co-SEt<sub>10-co-SDec<sub>2</sub></sub>)-HS</sub>	524	47.1 ± 2.1	0.131	-17.0 ± 1.5
30Au-P(G <sub>50-co-SEt<sub>10-co-SDec<sub>2</sub></sub>)-HS</sub>	527	61.5 ± 1.4	0.185	-18.4 ± 1.4

FT-IR (ATR):  $\tilde{\nu}_{\max}$  = 3286 (OH), 2957-2878 (CH, CH<sub>2</sub>, CH<sub>3</sub>), 1546-1245 (CH, CH<sub>2</sub>, CH<sub>3</sub>), 1077 (COC), 983-858 (CC) cm<sup>-1</sup>.

5.4.8 P(G<sub>50</sub>-co-SEt<sub>9</sub>-co-SDec<sub>3</sub>)

P(G<sub>50</sub>-co-AGE<sub>12</sub>) (50.0 mg, 9.72 μmol) was dissolved in 10 mL EtOH and degassed for 20 min. After adding EtSH (180 μL, 2.43 mmol), 1-decanethiol (6.18 μL, 29.2 μmol) and I2959 (17.5 mg, 77.8 μmol) the solution was stirred and irradiated with UV light at 365 nm for 2 h. The solvent was removed under vacuum and the remaining polymer was dissolved in 90 mL H<sub>2</sub>O. After dialysis and lyophilization the polymer was received as a slightly yellow, viscous solid.



<sup>1</sup>H-NMR (300 MHz, D<sub>2</sub>O): δ = 3.80-3.67 (m, 334 H, H-2-12), 3.16-2.85 (m, 42 H, H-15-17), 2.68 (t, 6 H, H-18), 2.07 (quin, 24 H, H-13,14), 1.70 (quin, 6 H, H-19), 1.39-1.32 (m, 69 H, H-20,21), 1.26 (s, 9 H, H-1), 0.93 (t, 9 H, H-22) ppm.

FT-IR (ATR):  $\tilde{\nu}_{\max}$  = 3364 (OH), 2923-2873 (CH, CH<sub>2</sub>, CH<sub>3</sub>), 1458-1251 (CH, CH<sub>2</sub>, CH<sub>3</sub>), 1042 (COC), 915-853 (CC) cm<sup>-1</sup>.

Raman:  $\tilde{\nu}_{\max}$  = 2923-2881 (CH, CH<sub>2</sub>, CH<sub>3</sub>), 1459-1230 (CH, CH<sub>2</sub>, CH<sub>3</sub>), 1112-973 (CC), 907-852 (COC), 642 (CS) cm<sup>-1</sup>.

SEC (RI, H<sub>2</sub>O):

**Table 50.**  $\bar{M}_w$ ,  $\bar{M}_n$  and Đ as well as the via <sup>1</sup>H-NMR spectroscopy calculated molecular weight of P(G<sub>50</sub>-co-SEt<sub>9</sub>-co-SDec<sub>3</sub>).

	$\bar{M}_w$ [Da] <sup>(a)</sup>	$\bar{M}_n$ [Da] <sup>(a)</sup>	Đ <sup>(a)</sup>	$M_{\text{exp}}$ [Da] <sup>(b)</sup>
P(G <sub>50</sub> -co-SEt <sub>9</sub> -co-SDec <sub>3</sub> )	6816	2759	2.47	6226

<sup>(a)</sup>determined by SEC in H<sub>2</sub>O, <sup>(b)</sup>determined by <sup>1</sup>H-NMR spectroscopy in D<sub>2</sub>O

## 5 Experimental section

### 5.4.8.1 Au-P(G<sub>50-co-SEt<sub>9</sub>-co-SDec<sub>3</sub>)</sub>

UV-Vis, DLS, Zeta:

**Table 51.** Values of SPR, *d*, PDI and  $\zeta$  of P(G<sub>50-co-SEt<sub>9</sub>-co-SDec<sub>3</sub>))-modified 15 nm and 30 nm AuNPs, determined by UV-Vis, DLS and zeta potential measurements.</sub>

	SPR [nm]	<i>d</i> [nm]	PDI	$\zeta$ [mV]
15Au-P(G <sub>50-co-SEt<sub>9</sub>-co-SDec<sub>3</sub>)</sub>	522	28.0 ± 1.2	0.088	-23.7 ± 3.8
30Au-P(G <sub>50-co-SEt<sub>9</sub>-co-SDec<sub>3</sub>)</sub>	526	41.4 ± 0.7	0.184	-26.1 ± 2.5

FT-IR (ATR):  $\tilde{\nu}_{\max}$  = 3379 (OH), 2921-2874 (CH, CH<sub>2</sub>, CH<sub>3</sub>), 1590-1246 (CH, CH<sub>2</sub>, CH<sub>3</sub>), 1076 (COC), 909-840 (CC) cm<sup>-1</sup>.

### 5.4.8.2 Au-P(G<sub>50-co-SEt<sub>9</sub>-co-SDec<sub>3</sub>)-HS</sub>

UV-Vis, DLS, Zeta:

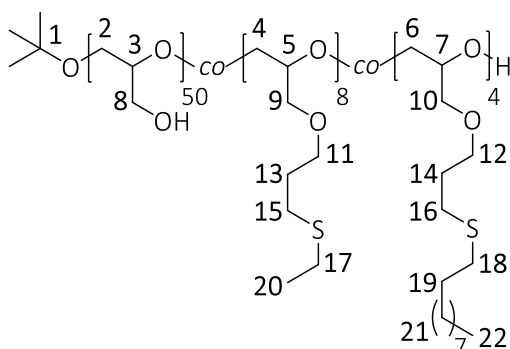
**Table 52.** Values of SPR, *d*, PDI and  $\zeta$  of 15Au- and 30Au-P(G<sub>50-co-SEt<sub>9</sub>-co-SDec<sub>3</sub>) incubated with HS, determined by UV-Vis, DLS and zeta potential measurements.</sub>

	SPR [nm]	<i>d</i> [nm]	PDI	$\zeta$ [mV]
15Au-P(G <sub>50-co-SEt<sub>9</sub>-co-SDec<sub>3</sub>)-HS</sub>	524	42.6 ± 2.9	0.160	-16.8 ± 3.0
30Au-P(G <sub>50-co-SEt<sub>9</sub>-co-SDec<sub>3</sub>)-HS</sub>	527	57.6 ± 1.9	0.170	-19.4 ± 2.5

FT-IR (ATR):  $\tilde{\nu}_{\max}$  = 3285 (OH), 2956-2873 (CH, CH<sub>2</sub>, CH<sub>3</sub>), 1544-1245 (CH, CH<sub>2</sub>, CH<sub>3</sub>), 1077 (COC), 983-859 (CC) cm<sup>-1</sup>.

5.4.9 P(G<sub>50</sub>-co-SEt<sub>8</sub>-co-SDec<sub>4</sub>)

P(G<sub>50</sub>-co-AGE<sub>12</sub>) (50.0 mg, 9.72 μmol) was dissolved in 10 mL EtOH and degassed for 20 min. After adding EtSH (180 μL, 2.43 mmol), 1-decanethiol (10.3 μL, 48.6 μmol) and I2959 (17.5 mg, 77.8 μmol) the solution was stirred and irradiated with UV light at 365 nm for 2 h. The solvent was removed under vacuum and the remaining polymer was dissolved in 90 mL H<sub>2</sub>O. After dialyzing and freeze-drying the polymer was received as a slightly yellow, viscous solid.



<sup>1</sup>H-NMR (300 MHz, D<sub>2</sub>O): δ = 3.80-3.67 (m, 334 H, H-2-12), 3.16-2.85 (m, 40 H, H-15-17), 2.67 (t, 8 H, H-18), 2.07 (quin, 24 H, H-13,14), 1.69 (quin, 8 H, H-19), 1.39-1.32 (m, 80 H, H-20,21), 1.26 (s, 9 H, H-1), 0.92 (t, 12 H, H-22) ppm.

FT-IR (ATR):  $\tilde{\nu}_{\max}$  = 3377 (OH), 2923-2873 (CH, CH<sub>2</sub>, CH<sub>3</sub>), 1458-1251 (CH, CH<sub>2</sub>, CH<sub>3</sub>), 1043 (COC), 914-856 (CC) cm<sup>-1</sup>.

Raman:  $\tilde{\nu}_{\max}$  = 2925-2885 (CH, CH<sub>2</sub>, CH<sub>3</sub>), 1458-1224 (CH, CH<sub>2</sub>, CH<sub>3</sub>), 1117-970 (CC), 907-845 (COC), 641 (CS) cm<sup>-1</sup>.

SEC (RI, H<sub>2</sub>O):

**Table 53.**  $\bar{M}_w$ ,  $\bar{M}_n$  and Đ as well as the via <sup>1</sup>H-NMR spectroscopy calculated molecular weight of P(G<sub>50</sub>-co-SEt<sub>8</sub>-co-SDec<sub>4</sub>).

	$\bar{M}_w$ [Da] <sup>(a)</sup>	$\bar{M}_n$ [Da] <sup>(a)</sup>	Đ <sup>(a)</sup>	$M_{\text{exp}}$ [Da] <sup>(b)</sup>
P(G <sub>50</sub> -co-SEt <sub>8</sub> -co-SDec <sub>4</sub> )	9823	2470	3.98	6338

<sup>(a)</sup>determined by SEC in H<sub>2</sub>O, <sup>(b)</sup>determined by <sup>1</sup>H-NMR spectroscopy in D<sub>2</sub>O

## 5 Experimental section

### 5.4.9.1 Au-P(G<sub>50-co-SEt<sub>8</sub>-co-SDec<sub>4</sub>)</sub>

UV-Vis, DLS, Zeta:

**Table 54.** Values of SPR, *d*, PDI and  $\zeta$  of P(G<sub>50-co-SEt<sub>8</sub>-co-SDec<sub>4</sub>)-modified 15 nm and 30 nm AuNPs, determined by UV-Vis, DLS and zeta potential measurements.</sub>

	SPR [nm]	<i>d</i> [nm]	PDI	$\zeta$ [mV]
15Au-P(G <sub>50-co-SEt<sub>8</sub>-co-SDec<sub>4</sub>)</sub>	522	33.9 ± 1.2	0.115	-24.0 ± 3.7
30Au-P(G <sub>50-co-SEt<sub>8</sub>-co-SDec<sub>4</sub>)</sub>	527	46.4 ± 1.5	0.167	-29.7 ± 1.8

FT-IR (ATR):  $\tilde{\nu}_{\max}$  = 3388 (OH), 2921-2874 (CH, CH<sub>2</sub>, CH<sub>3</sub>), 1589-1248 (CH, CH<sub>2</sub>, CH<sub>3</sub>), 1074 (COC), 914-842 (CC) cm<sup>-1</sup>.

### 5.4.9.2 Au-P(G<sub>50-co-SEt<sub>8</sub>-co-SDec<sub>4</sub>)-HS</sub>

UV-Vis, DLS, Zeta:

**Table 55.** Values of SPR, *d*, PDI and  $\zeta$  of 15Au- and 30Au-P(G<sub>50-co-SEt<sub>8</sub>-co-SDec<sub>4</sub>) incubated with HS, determined by UV-Vis, DLS and zeta potential measurements.</sub>

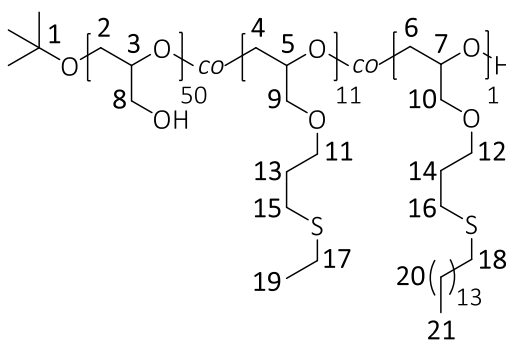
	SPR [nm]	<i>d</i> [nm]	PDI	$\zeta$ [mV]
15Au-P(G <sub>50-co-SEt<sub>8</sub>-co-SDec<sub>4</sub>)-HS</sub>	524	45.1 ± 1.2	0.180	-14.8 ± 2.1
30Au-P(G <sub>50-co-SEt<sub>8</sub>-co-SDec<sub>4</sub>)-HS</sub>	527	57.5 ± 1.3	0.171	-15.8 ± 0.6

FT-IR (ATR):  $\tilde{\nu}_{\max}$  = 3282 (OH), 2954-2871 (CH, CH<sub>2</sub>, CH<sub>3</sub>), 1545-1244 (CH, CH<sub>2</sub>, CH<sub>3</sub>), 1073 (COC), 984-853 (CC) cm<sup>-1</sup>.



5.4.10 P(G<sub>50</sub>-co-SEt<sub>11</sub>-co-SPentadec<sub>1</sub>)

P(G<sub>50</sub>-co-AGE<sub>12</sub>) (50.0 mg, 9.72 μmol) was dissolved in 10 mL EtOH and degassed for 20 min. After adding EtSH (144 μL, 1.94 mmol), 1-pentadecanethiol (14.0 μL, 97.2 μmol) and I2959 (17.5 mg, 77.8 μmol) the solution was stirred and irradiated with UV light at 365 nm for 2 h. The solvent was removed under vacuum and the remaining polymer was dissolved in 90 mL H<sub>2</sub>O. After dialysis and lyophilization the polymer was received as a slightly yellow, viscous solid.



<sup>1</sup>H-NMR (300 MHz, D<sub>2</sub>O): δ = 3.80-3.67 (m, 334 H, H-2-12), 3.16-2.85 (m, 48 H, H-15-18), 2.07 (quin, 24 H, H-13,14), 1.39-1.34 (m, 59 H, H-19,20), 1.26 (s, 9 H, H-1), 0.94 (t, 3 H, H-21) ppm.

FT-IR (ATR):  $\tilde{\nu}_{\max}$  = 3361 (OH), 2918-2850 (CH, CH<sub>2</sub>, CH<sub>3</sub>), 1461-1228 (CH, CH<sub>2</sub>, CH<sub>3</sub>), 1042 (COC), 915-849 (CC) cm<sup>-1</sup>.

Raman:  $\tilde{\nu}_{\max}$  = 2923-2884 (CH, CH<sub>2</sub>, CH<sub>3</sub>), 1463-1262 (CH, CH<sub>2</sub>, CH<sub>3</sub>), 1124-973 (CC), 909-844 (COC), 647 (CS) cm<sup>-1</sup>.

SEC (RI, H<sub>2</sub>O):

**Table 56.**  $\bar{M}_w$ ,  $\bar{M}_n$  and Đ as well as the via <sup>1</sup>H-NMR spectroscopy calculated molecular weight of P(G<sub>50</sub>-co-SEt<sub>11</sub>-co-SPentadec<sub>1</sub>).

	$\bar{M}_w$ [Da] <sup>(a)</sup>	$\bar{M}_n$ [Da] <sup>(a)</sup>	Đ <sup>(a)</sup>	M <sub>exp</sub> [Da] <sup>(b)</sup>
P(G <sub>50</sub> -co-SEt <sub>11</sub> -co-SPentadec <sub>1</sub> )	10427	3030	3.44	6071

<sup>(a)</sup>determined by SEC in H<sub>2</sub>O, <sup>(b)</sup>determined by <sup>1</sup>H-NMR spectroscopy in D<sub>2</sub>O

## 5 Experimental section

### 5.4.10.1 Au-P(G<sub>50-co-SEt<sub>11-co-SPentadec</sub><sub>1</sub></sub>)

UV-Vis, DLS, Zeta:

**Table 57.** Values of SPR, *d*, PDI and  $\zeta$  of P(G<sub>50-co-SEt<sub>11-co-SPentadec</sub><sub>1</sub></sub>)-modified 15 nm and 30 nm AuNPs, determined by UV-Vis, DLS and zeta potential measurements.

	SPR [nm]	<i>d</i> [nm]	PDI	$\zeta$ [mV]
15Au-P(G <sub>50-co-SEt<sub>11-co-SPentadec</sub><sub>1</sub></sub> )	522	22.9 ± 1.8	0.161	-24.7 ± 2.9
30Au-P(G <sub>50-co-SEt<sub>11-co-SPentadec</sub><sub>1</sub></sub> )	526	37.5 ± 0.6	0.199	-27.0 ± 2.7

FT-IR (ATR):  $\tilde{\nu}_{\max}$  = 3394 (OH), 2920-2851 (CH, CH<sub>2</sub>, CH<sub>3</sub>), 1591-1256 (CH, CH<sub>2</sub>, CH<sub>3</sub>), 1077 (COC), 905-839 (CC) cm<sup>-1</sup>.

### 5.4.10.2 Au-P(G<sub>50-co-SEt<sub>11-co-SPentadec</sub><sub>1</sub></sub>)-HS

UV-Vis, DLS, Zeta:

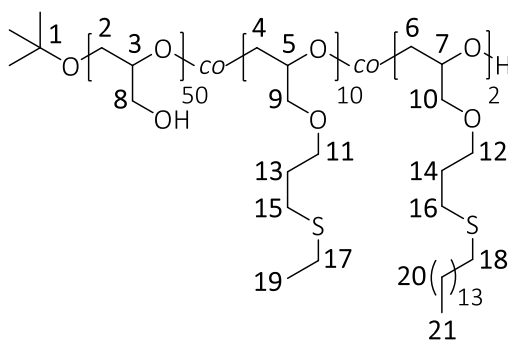
**Table 58.** Values of SPR, *d*, PDI and  $\zeta$  of 15Au- and 30Au-P(G<sub>50-co-SEt<sub>11-co-SPentadec</sub><sub>1</sub></sub>) incubated with HS, determined by UV-Vis, DLS and zeta potential measurements.

	SPR [nm]	<i>d</i> [nm]	PDI	$\zeta$ [mV]
15Au-P(G <sub>50-co-SEt<sub>11-co-SPentadec</sub><sub>1</sub></sub> )-HS	525	56.9 ± 3.3	0.194	-17.2 ± 1.7
30Au-P(G <sub>50-co-SEt<sub>11-co-SPentadec</sub><sub>1</sub></sub> )-HS	528	70.0 ± 1.8	0.186	-19.1 ± 3.2

FT-IR (ATR):  $\tilde{\nu}_{\max}$  = 3277 (OH), 2961-2877 (CH, CH<sub>2</sub>, CH<sub>3</sub>), 1544-1249 (CH, CH<sub>2</sub>, CH<sub>3</sub>), 1077 (COC), 983-860 (CC) cm<sup>-1</sup>.

5.4.11 P(G<sub>50</sub>-co-SEt<sub>10</sub>-co-SPentadec<sub>2</sub>)

P(G<sub>50</sub>-co-AGE<sub>12</sub>) (50.0 mg, 9.72 μmol) was dissolved in 10 mL EtOH and degassed for 20 min. After adding EtSH (144 μL, 1.94 mmol), 1-pentadecanethiol (56.1 μL, 194 μmol) and I2959 (17.5 mg, 77.8 μmol) the solution was stirred and irradiated with UV light at 365 nm for 2 h. The solvent was removed under vacuum and the remaining polymer was dissolved in 90 mL H<sub>2</sub>O. After dialyzing and lyophilization the polymer was received as a slightly yellow, viscous solid.



<sup>1</sup>H-NMR (300 MHz, D<sub>2</sub>O): δ = 3.80-3.67 (m, 334 H, H-2-12), 3.16-2.85 (m, 48 H, H-15-18), 2.07 (quin, 24 H, H-13,14), 1.38-1.34 (m, 82 H, H-19,20), 1.26 (s, 9 H, H-1), 0.94 (t, 6 H, H-21) ppm.

FT-IR (ATR):  $\tilde{\nu}_{\max}$  = 3359 (OH), 2918-2849 (CH, CH<sub>2</sub>, CH<sub>3</sub>), 1461-1224 (CH, CH<sub>2</sub>, CH<sub>3</sub>), 1044 (COC), 915-843 (CC) cm<sup>-1</sup>.

Raman:  $\tilde{\nu}_{\max}$  = 2921-2851 (CH, CH<sub>2</sub>, CH<sub>3</sub>), 1463-1262 (CH, CH<sub>2</sub>, CH<sub>3</sub>), 1127-997 (CC), 891-856 (COC), 647 (CS) cm<sup>-1</sup>.

SEC (RI, H<sub>2</sub>O):

**Table 59.**  $\bar{M}_w$ ,  $\bar{M}_n$  and Đ as well as the via <sup>1</sup>H-NMR spectroscopy calculated molecular weight of P(G<sub>50</sub>-co-SEt<sub>10</sub>-co-SPentadec<sub>2</sub>).

	$\bar{M}_w$ [Da] <sup>(a)</sup>	$\bar{M}_n$ [Da] <sup>(a)</sup>	Đ <sup>(a)</sup>	M <sub>exp</sub> [Da] <sup>(b)</sup>
P(G <sub>50</sub> -co-SEt <sub>10</sub> -co-SPentadec <sub>2</sub> )	11321	2586	4.38	6254

<sup>(a)</sup>determined by SEC in H<sub>2</sub>O, <sup>(b)</sup>determined by <sup>1</sup>H-NMR spectroscopy in D<sub>2</sub>O

## 5 Experimental section

### 5.4.11.1 Au-P(G<sub>50-co-SEt<sub>10-co-SPentadec<sub>2</sub></sub>)</sub>

UV-Vis, DLS, Zeta:

**Table 60.** Values of SPR, *d*, PDI and  $\zeta$  of P(G<sub>50-co-SEt<sub>10-co-SPentadec<sub>2</sub></sub>))-modified 15 nm and 30 nm AuNPs, determined by UV-Vis, DLS and zeta potential measurements.</sub>

	SPR [nm]	<i>d</i> [nm]	PDI	$\zeta$ [mV]
15Au-P(G <sub>50-co-SEt<sub>10-co-SPentadec<sub>2</sub></sub>)</sub>	522	24.0 ± 1.4	0.199	-24.8 ± 3.5
30Au-P(G <sub>50-co-SEt<sub>10-co-SPentadec<sub>2</sub></sub>)</sub>	526	38.3 ± 1.0	0.198	-29.0 ± 2.9

FT-IR (ATR):  $\tilde{\nu}_{\max}$  = 3405 (OH), 2919-2850 (CH, CH<sub>2</sub>, CH<sub>3</sub>), 1592-1254 (CH, CH<sub>2</sub>, CH<sub>3</sub>), 1076 (COC), 914-842 (CC) cm<sup>-1</sup>.

### 5.4.11.2 Au-P(G<sub>50-co-SEt<sub>10-co-SPentadec<sub>2</sub></sub>)-HS</sub>

UV-Vis, DLS, Zeta:

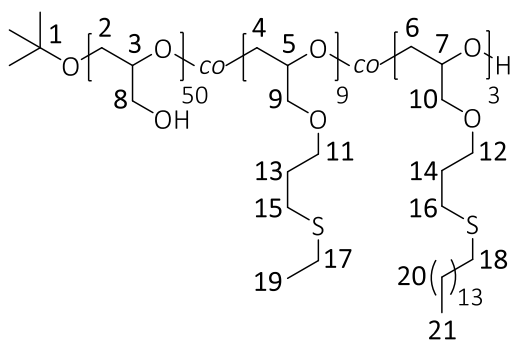
**Table 61.** Values of SPR, *d*, PDI and  $\zeta$  of 15Au- and 30Au-P(G<sub>50-co-SEt<sub>10-co-SPentadec<sub>2</sub></sub>) incubated with HS, determined by UV-Vis, DLS and zeta potential measurements.</sub>

	SPR [nm]	<i>d</i> [nm]	PDI	$\zeta$ [mV]
15Au-P(G <sub>50-co-SEt<sub>10-co-SPentadec<sub>2</sub></sub>)-HS</sub>	525	58.4 ± 2.7	0.222	-16.1 ± 1.5
30Au-P(G <sub>50-co-SEt<sub>10-co-SPentadec<sub>2</sub></sub>)-HS</sub>	528	71.2 ± 1.5	0.172	-21.3 ± 1.1

FT-IR (ATR):  $\tilde{\nu}_{\max}$  = 3281 (OH), 2956-2854 (CH, CH<sub>2</sub>, CH<sub>3</sub>), 1546-1249 (CH, CH<sub>2</sub>, CH<sub>3</sub>), 1081 (COC), 982-862 (CC) cm<sup>-1</sup>.

5.4.12 P(G<sub>50</sub>-co-SEt<sub>9</sub>-co-SPentadec<sub>3</sub>)

P(G<sub>50</sub>-co-AGE<sub>12</sub>) (50.0 mg, 9.72 μmol) was dissolved in 10 mL EtOH and degassed for 20 min. After adding EtSH (144 μl, 1.94 mmol), 1-pentadecanethiol (84.2 μL, 292 μmol) and I2959 (17.5 mg, 77.8 μmol) the solution was stirred and irradiated with UV light at 365 nm for 2 h. The solvent was removed under vacuum and the remaining polymer was dissolved in 90 mL H<sub>2</sub>O. After dialysis and freeze-drying the polymer was received as a slightly yellow, viscous solid.



<sup>1</sup>H-NMR (300 MHz, D<sub>2</sub>O): δ = 3.78-3.67 (m, 334 H, H-2-12), 3.17-2.85 (m, 48 H, H-15-18), 2.07 (quin, 24 H, H-13,14), 1.38-1.33 (m, 105 H, H-19,20), 1.27 (s, 9 H, H-1), 0.94 (t, 9 H, H-21) ppm.

FT-IR (ATR):  $\tilde{\nu}_{\max}$  = 3360 (OH), 2918-2849 (CH, CH<sub>2</sub>, CH<sub>3</sub>), 1462-1227 (CH, CH<sub>2</sub>, CH<sub>3</sub>), 1045 (COC), 915-843 (CC) cm<sup>-1</sup>.

Raman:  $\tilde{\nu}_{\max}$  = 2919-2849 (CH, CH<sub>2</sub>, CH<sub>3</sub>), 1462-1261 (CH, CH<sub>2</sub>, CH<sub>3</sub>), 1127-996 (CC), 890-856 (COC), 648 (CS) cm<sup>-1</sup>.

SEC (RI, H<sub>2</sub>O):

**Table 62.**  $\bar{M}_w$ ,  $\bar{M}_n$  and Đ as well as the via <sup>1</sup>H-NMR spectroscopy calculated molecular weight of P(G<sub>50</sub>-co-SEt<sub>9</sub>-co-SPentadec<sub>3</sub>).

	$\bar{M}_w$ [Da] <sup>(a)</sup>	$\bar{M}_n$ [Da] <sup>(a)</sup>	Đ <sup>(a)</sup>	M <sub>exp</sub> [Da] <sup>(b)</sup>
P(G <sub>50</sub> -co-SEt <sub>9</sub> -co-SPentadec <sub>3</sub> )	1330	2762	4.82	6436

<sup>(a)</sup>determined by SEC in H<sub>2</sub>O, <sup>(b)</sup>determined by <sup>1</sup>H-NMR spectroscopy in D<sub>2</sub>O

## 5 Experimental section

### 5.4.12.1 Au–P(G<sub>50-co-SEt<sub>9-co-SPentadec</sub><sub>3</sub>)</sub>

UV-Vis, DLS, Zeta:

**Table 63.** Values of SPR, *d*, PDI and  $\zeta$  of P(G<sub>50-co-SEt<sub>9-co-SPentadec</sub><sub>3</sub>)-modified 15 nm and 30 nm AuNPs, determined by UV-Vis, DLS and zeta potential measurements.</sub>

	SPR [nm]	<i>d</i> [nm]	PDI	$\zeta$ [mV]
15Au–P(G <sub>50-co-SEt<sub>9-co-SPentadec</sub><sub>3</sub>)</sub>	522	26.8 ± 1.6	0.193	-23.1 ± 2.1
30Au–P(G <sub>50-co-SEt<sub>9-co-SPentadec</sub><sub>3</sub>)</sub>	527	40.3 ± 1.3	0.181	-25.7 ± 3.6

FT-IR (ATR):  $\tilde{\nu}_{\max}$  = 3392 (OH), 2921-2886 (CH, CH<sub>2</sub>, CH<sub>3</sub>), 1590-1255 (CH, CH<sub>2</sub>, CH<sub>3</sub>), 1079 (COC), 904-846 (CC) cm<sup>-1</sup>.

### 5.4.12.2 Au–P(G<sub>50-co-SEt<sub>9-co-SPentadec</sub><sub>3</sub>)–HS</sub>

UV-Vis, DLS, Zeta:

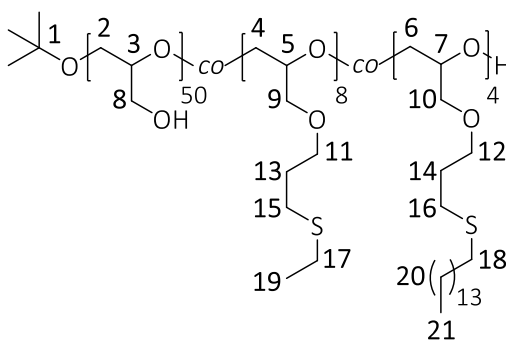
**Table 64.** Values of SPR, *d*, PDI and  $\zeta$  of 15Au– and 30Au–P(G<sub>50-co-SEt<sub>9-co-SPentadec</sub><sub>3</sub>) incubated with HS, determined by UV-Vis, DLS and zeta potential measurements.</sub>

	SPR [nm]	<i>d</i> [nm]	PDI	$\zeta$ [mV]
15Au–P(G <sub>50-co-SEt<sub>9-co-SPentadec</sub><sub>3</sub>)–HS</sub>	525	54.6 ± 3.0	0.197	-20.1 ± 0.6
30Au–P(G <sub>50-co-SEt<sub>9-co-SPentadec</sub><sub>3</sub>)–HS</sub>	528	73.3 ± 2.9	0.211	-20.8 ± 2.4

FT-IR (ATR):  $\tilde{\nu}_{\max}$  = 3270 (OH), 2955-2871 (CH, CH<sub>2</sub>, CH<sub>3</sub>), 1539-1244 (CH, CH<sub>2</sub>, CH<sub>3</sub>), 1069 (COC), 979-854 (CC) cm<sup>-1</sup>.

5.4.13 P(G<sub>50</sub>-co-SEt<sub>8</sub>-co-SPentadec<sub>4</sub>)

P(G<sub>50</sub>-co-AGE<sub>12</sub>) (50.0 mg, 9.72 μmol) was dissolved in 10 mL EtOH and degassed for 20 min. After adding EtSH (144 μL, 1.94 mmol), 1-pentadecanethiol (98.2 μL, 340 μmol) and I2959 (17.5 mg, 77.8 μmol) the solution was stirred and irradiated with UV light at 365 nm for 2 h. The solvent was removed under vacuum and the remaining polymer was dissolved in 90 mL H<sub>2</sub>O. After dialysis and lyophilization the polymer was received as a slightly yellow, viscous solid.



<sup>1</sup>H-NMR (300 MHz, D<sub>2</sub>O): δ = 3.80-3.67 (m, 334 H, H-2-12), 3.16-2.85 (m, 48 H, H-15-18), 2.07 (quin, 24 H, H-13,14), 1.38-1.35 (m, 105 H, H-19,20), 1.26 (s, 9 H, H-1), 0.95 (t, 128 H, H-21) ppm.

FT-IR (ATR):  $\tilde{\nu}_{\max}$  = 3375 (OH), 2918-2849 (CH, CH<sub>2</sub>, CH<sub>3</sub>), 1462-1226 (CH, CH<sub>2</sub>, CH<sub>3</sub>), 1044 (COC), 914 (CC) cm<sup>-1</sup>.

Raman:  $\tilde{\nu}_{\max}$  = 2918-2851 (CH, CH<sub>2</sub>, CH<sub>3</sub>), 1463-1260 (CH, CH<sub>2</sub>, CH<sub>3</sub>), 1127-1005 (CC), 891-856 (COC), 647 (CS) cm<sup>-1</sup>.

SEC (RI, H<sub>2</sub>O):

**Table 65.**  $\bar{M}_w$ ,  $\bar{M}_n$  and Đ as well as the via <sup>1</sup>H-NMR spectroscopy calculated molecular weight of P(G<sub>50</sub>-co-SEt<sub>8</sub>-co-SPentadec<sub>4</sub>).

	$\bar{M}_w$ [Da] <sup>(a)</sup>	$\bar{M}_n$ [Da] <sup>(a)</sup>	Đ <sup>(a)</sup>	M <sub>exp</sub> [Da] <sup>(b)</sup>
P(G <sub>50</sub> -co-SEt <sub>8</sub> -co-Pentadec <sub>4</sub> )	17821	2618	6.81	6618

<sup>(a)</sup>determined by SEC in H<sub>2</sub>O, <sup>(b)</sup>determined by <sup>1</sup>H-NMR spectroscopy in D<sub>2</sub>O

## 5 Experimental section

### 5.4.13.1 Au-P(G<sub>50-co-SEt<sub>8-co-SPentadec<sub>4</sub></sub>)</sub>

UV-Vis, DLS, Zeta:

**Table 66.** Values of SPR, *d*, PDI and  $\zeta$  of P(G<sub>50-co-SEt<sub>8-co-SPentadec<sub>4</sub></sub>)-modified 15 nm and 30 nm AuNPs, determined by UV-Vis, DLS and zeta potential measurements.</sub>

	SPR [nm]	<i>d</i> [nm]	PDI	$\zeta$ [mV]
15Au-P(G <sub>50-co-SEt<sub>8-co-SPentadec<sub>4</sub></sub>)</sub>	522	25.2 ± 2.2	0.169	-26.6 ± 3.5
30Au-P(G <sub>50-co-SEt<sub>8-co-SPentadec<sub>4</sub></sub>)</sub>	527	39.6 ± 1.1	0.196	-29.7 ± 2.4

FT-IR (ATR):  $\tilde{\nu}_{\max}$  = 3396 (OH), 2928-2876 (CH, CH<sub>2</sub>, CH<sub>3</sub>), 1590-1261 (CH, CH<sub>2</sub>, CH<sub>3</sub>), 1074 (COC), 899-843 (CC) cm<sup>-1</sup>.

### 5.4.13.2 Au-P(G<sub>50-co-SEt<sub>8-co-SPentadec<sub>4</sub></sub>)-HS</sub>

UV-Vis, DLS, Zeta:

**Table 67.** Values of SPR, *d*, PDI and  $\zeta$  of 15Au- and 30Au-P(G<sub>50-co-SEt<sub>8-co-SPentadec<sub>4</sub></sub>) incubated with HS, determined by UV-Vis, DLS and zeta potential measurements.</sub>

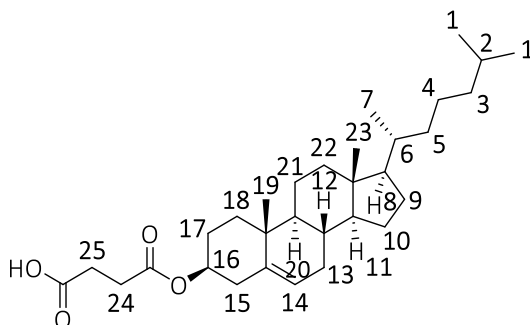
	SPR [nm]	<i>d</i> [nm]	PDI	$\zeta$ [mV]
15Au-P(G <sub>50-co-SEt<sub>8-co-SPentadec<sub>4</sub></sub>)-HS</sub>	524	50.7 ± 1.1	0.184	-21.5 ± 2.5
30Au-P(G <sub>50-co-SEt<sub>8-co-SPentadec<sub>4</sub></sub>)-HS</sub>	529	78.0 ± 1.6	0.223	-17.4 ± 1.4

FT-IR (ATR):  $\tilde{\nu}_{\max}$  = 3286 (OH), 2957-2854 (CH, CH<sub>2</sub>, CH<sub>3</sub>), 1547-1246 (CH, CH<sub>2</sub>, CH<sub>3</sub>), 1081 (COC), 981-859 (CC) cm<sup>-1</sup>.

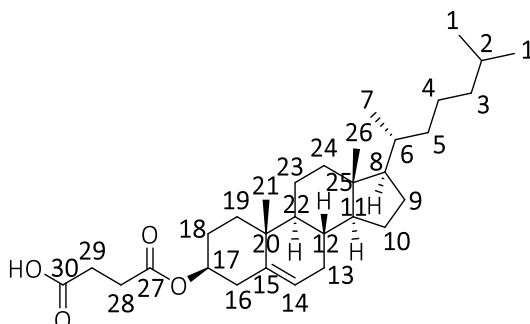


## 5.4.14 Carboxyl-functionalized Cholesterol (Chol-COOH)

Carboxyl-functionalized cholesterol (Chol-COOH) was synthesized by reaction of cholesterol with succinic anhydride in presence of 4-(dimethylamino)pyridine (DMAP) according to literature of Yang *et al.*<sup>[413]</sup> The reaction took place under oxygen free conditions. Cholesterol (100 mg, 259  $\mu\text{mol}$ ), succinic anhydride (51.8 mg, 517  $\mu\text{mol}$ ) and DMAP (15.8 mg, 129  $\mu\text{mol}$ ) as catalyst was dissolved in 20 mL DCM (dried overnight over molecular sieve 4Å) and refluxed overnight at 65 °C. After cooling in ice bath, the excessive succinic anhydride was removed by filtration and the solution was extracted three times with 40 mL H<sub>2</sub>O. The organic phase was dried with MgSO<sub>4</sub>, filtered and DCM was removed under vacuum. Drying several hours at 50 °C leads to a colorless solid with a yield of 82 wt%.



<sup>1</sup>H-NMR (300 MHz, CDCl<sub>3</sub>):  $\delta$  = 5.37 (d, 1 H, H-14), 4.69-4.58 (m, 1 H, H-16), 2.70-2.66 (m, 2 H, H-25), 2.63-2.58 (m, 2 H, H-24), 2.33-1.07 (m, 28 H, H-2-6,8-13,15,17,18+20-22), 1.02 (s, 3 H, H-7), 0.91 (d, 3 H, H-19), 0.86 (dd, 6 H, H-1), 0.68 (s, 3 H, H-23) ppm.



<sup>13</sup>C-NMR (300 MHz, CDCl<sub>3</sub>):  $\delta$  = 177.01 (C-30), 171.56 (C-27), 139.55 (C-15), 122.74 (C-14), 74.56 (C-17), 56.70 (C-11), 56.15 (C-8), 50.02 (C-22), 42.32 (C-25), 39.73 (C-3), 39.52 (C-24), 38.02 (C-16), 36.96 (C-20), 36.58 (C-19), 36.19 (C-5), 35.80 (C-6), 31.91 (C-13), 31.86 (C-12), 29.27 (C-28), 28.89 (C-29), 28.23 (C-18), 28.02 (C-2), 27.70 (C-10), 24.29

## 5 Experimental section

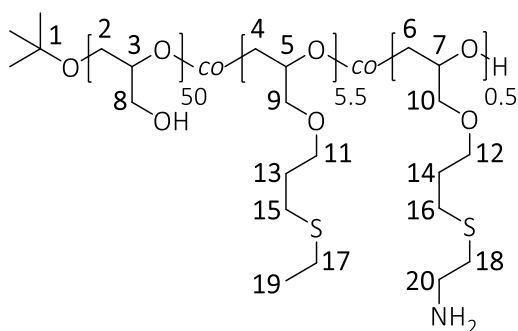
(C-9), 23.84 (C-4), 22.82 (C-1), 22.57 (C-1), 21.04 (C-23), 19.31 (C-7), 18.72 (C-21), 11.86 (C-26) ppm.

**FT-IR (ATR):**  $\tilde{\nu}_{\max}$  = 3430 (OH), 2934-2867 (CH, CH<sub>2</sub>, CH<sub>3</sub>), 1729 (C=O(OR)), 1708 (C=O(OH)), 1466-1259 (CH<sub>2</sub>, CH<sub>3</sub>), 1174 (COC), 1025 (CO), 957-737 (CC) cm<sup>-1</sup>.

**Raman:**  $\tilde{\nu}_{\max}$  = 2926-2863 (CH, CH<sub>2</sub>, CH<sub>3</sub>), 1727 (C=O(OR)), 1666 (C=C), 1638 (C=O(OH)), 1436-1253 (CH, CH<sub>2</sub>, CH<sub>3</sub>), 1195-696 (CC) cm<sup>-1</sup>.

5.4.15 P(G<sub>50</sub>-co-SEt<sub>5.5</sub>-co-NH<sub>2(0.5)</sub>)

In order to obtain P(G<sub>50</sub>-co-SEt<sub>5.5</sub>-co-NH<sub>2(0.5)</sub>), P(G<sub>50</sub>-co-AGE<sub>6</sub>) (350 mg, 78.5 μmol) was dissolved in 30 mL of a H<sub>2</sub>O-DMF mixture (1:1) and degassed for 30 min. After the addition of cysteamine hydrochloride (100 mg, 880 μmol), EtSH (300 μL, 4.06 mmol) and I2959 (58.0 mg, 259 μmol) the solution was stirred and irradiated with UV light at 365 nm for 2 h. The solvent was removed under vacuum and the remaining polymer was dissolved in 50 mL H<sub>2</sub>O. After purification by dialysis and freeze-drying the polymer was received as a slightly yellow, viscous solid. the polymer was received as a slightly yellow, viscous solid.



<sup>1</sup>H-NMR (300 MHz, D<sub>2</sub>O): δ = 3.79-3.65 (m, 292 H, H-2-12), 3.23 (t, 1 H, H-20), 2.87 (t, 1 H, H-18), 2.69-2.58 (m, 23 H, H-15-17), 1.90 (quin, 12 H, H-13,14), 1.30-1.25 (m, 16.5 H, H-19 and 9 H, H-1) ppm.

FT-IR (ATR):  $\tilde{\nu}_{\max}$  = 3372 (OH), 2922-2872 (CH, CH<sub>2</sub>, CH<sub>3</sub>), 1604 (NH<sub>2</sub>), 1459-1260 (CH, CH<sub>2</sub>, CH<sub>3</sub>), 1040 (COC), 913-856 (CC) cm<sup>-1</sup>.

Raman:  $\tilde{\nu}_{\max}$  = 2930-2882 (CH, CH<sub>2</sub>, CH<sub>3</sub>), 1462-1261 (CH, CH<sub>2</sub>, CH<sub>3</sub>), 1125-1062 (CC), 907-858 (COC), 655 (CS) cm<sup>-1</sup>.

TNBSA assay: 0.5 amines per polymer

SEC (RI, H<sub>2</sub>O):

**Table 68.**  $\bar{M}_w$ ,  $\bar{M}_n$  and Đ as well as the via <sup>1</sup>H-NMR spectroscopy calculated molecular weight of P(G<sub>50</sub>-co-SEt<sub>5.5</sub>-co-NH<sub>2(0.5)</sub>).

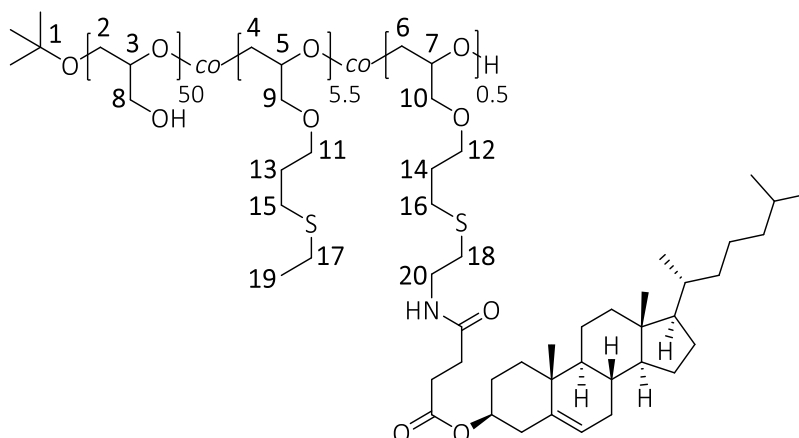
	$\bar{M}_w$ [Da] <sup>(a)</sup>	$\bar{M}_n$ [Da] <sup>(a)</sup>	Đ <sup>(a)</sup>	$M_{\text{exp}}$ [Da] <sup>(b)</sup>
P(G <sub>50</sub> -co-SEt <sub>5.5</sub> -co-NH <sub>2(0.5)</sub> )	2973	1192	1.54	4517

<sup>(a)</sup>determined by SEC in H<sub>2</sub>O, <sup>(b)</sup>determined by <sup>1</sup>H-NMR spectroscopy in D<sub>2</sub>O

## 5 Experimental section

### 5.4.16 P(G<sub>50</sub>-co-SEt<sub>5.5</sub>-co-Chol<sub>0.5</sub>)

The reaction of P(G<sub>50</sub>-co-SEt<sub>5.5</sub>-co-Chol<sub>0.5</sub>) took place under exclusion of air. P(G<sub>50</sub>-co-SEt<sub>5.5</sub>-co-SPEG-NH<sub>2(0.5)</sub>) (50 mg, 7.84 μmol), EDC (3.00 mg, 15.7 μmol), NHS (1.80 mg, 15.7 μmol) and Chol-COOH (7.63 mg, 15.7 μmol) were dissolved in 10 mL dry DMF. After stirring overnight at RT, DMF was removed under vacuum and the remaining polymer was dissolved in 90 mL H<sub>2</sub>O. After dialysis and freeze-drying the polymer was received as a slightly green, viscous solid.



<sup>1</sup>H-NMR (300 MHz, D<sub>2</sub>O): δ = 3.79-3.66 (m, 293 H, H-2-12,20), 2.70-2.58 (m, 24 H, H-15-18), 1.90 (quin, 12 H, H-13,14), 1.29-1.25 (m, 25.5 H, H-1+19) ppm. No signals of the cholesteryl units were detected in D<sub>2</sub>O.

FT-IR (ATR):  $\tilde{\nu}_{\max}$  = 3383 (OH), 2927-2880 (CH, CH<sub>2</sub>, CH<sub>3</sub>), 1731 (C=O(OR)), 1649 (C=O(NH)), 1588 (NH), 1465-1241 (CH, CH<sub>2</sub>, CH<sub>3</sub>), 1061 (COC), 962-842 (CC) cm<sup>-1</sup>.

Raman:  $\tilde{\nu}_{\max}$  = 2925-2874 (CH, CH<sub>2</sub>, CH<sub>3</sub>), 1665 (C=C), 1459-1258 (CH, CH<sub>2</sub>, CH<sub>3</sub>), 1120-1061 (CC), 889-861 (COC), 650 (CS) cm<sup>-1</sup>.

SEC (RI, H<sub>2</sub>O):

**Table 69.**  $\bar{M}_w$ ,  $\bar{M}_n$  and Đ as well as the via <sup>1</sup>H-NMR spectroscopy calculated molecular weight of P(G<sub>50</sub>-co-SEt<sub>5.5</sub>-co-Chol<sub>0.5</sub>).

	$\bar{M}_w$ [Da] <sup>(a)</sup>	$\bar{M}_n$ [Da] <sup>(a)</sup>	Đ <sup>(a)</sup>	M <sub>exp</sub> [Da] <sup>(b)</sup>
P(G <sub>50</sub> -co-SEt <sub>5.5</sub> -co-Chol <sub>0.5</sub> )	20676	2129	9.75	4986

<sup>(a)</sup>determined by SEC in H<sub>2</sub>O, <sup>(b)</sup>determined by <sup>1</sup>H-NMR spectroscopy in D<sub>2</sub>O

#### 5.4.16.1 Au-P(G<sub>50-co-SEt<sub>5.5-co-Chol</sub>0.5)</sub>

UV-Vis, DLS, Zeta:

**Table 70.** Values of SPR, *d*, PDI and  $\zeta$  of P(G<sub>50-co-SEt<sub>5.5-co-Chol</sub>0.5</sub>)-modified 15 nm and 30 nm AuNPs, determined by UV-Vis, DLS and zeta potential measurements.

	SPR [nm]	<i>d</i> [nm]	PDI	$\zeta$ [mV]
15Au-P(G <sub>50-co-SEt<sub>5.5-co-Chol</sub>0.5)</sub>	522	25.4 ± 1.3	0.149	-20.8 ± 3.4
30Au-P(G <sub>50-co-SEt<sub>5.5-co-Chol</sub>0.5)</sub>	526	39.1 ± 1.4	0.180	-19.6 ± 2.8

FT-IR (ATR):  $\tilde{\nu}_{\max}$  = 3387 (OH), 2928-2876 (CH, CH<sub>2</sub>, CH<sub>3</sub>), 1590-1261 (CH, CH<sub>2</sub>, CH<sub>3</sub>), 1074 (COC), 899-843 (CC) cm<sup>-1</sup>.

#### 5.4.16.2 Au-P(G<sub>50-co-SEt<sub>5.5-co-Chol</sub>0.5)-HS</sub>

UV-Vis, DLS, Zeta:

**Table 71.** Values of SPR, *d*, PDI and  $\zeta$  of 15Au- and 30Au-P(G<sub>50-co-SEt<sub>5.5-co-Chol</sub>0.5</sub>) incubated with HS, determined by UV-Vis, DLS and zeta potential measurements.

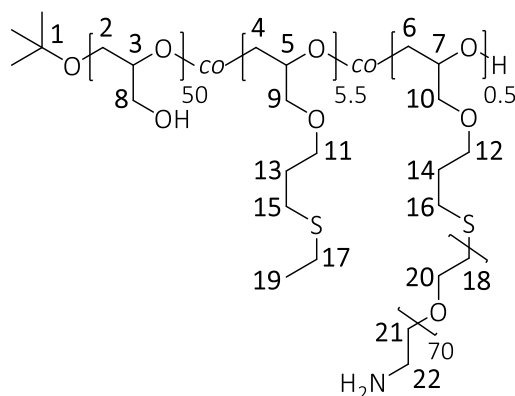
	SPR [nm]	<i>d</i> [nm]	PDI	$\zeta$ [mV]
15Au-P(G <sub>50-co-SEt<sub>5.5-co-Chol</sub>0.5)-HS</sub>	524	49.9 ± 2.8	0.235	-16.9 ± 2.7
30Au-P(G <sub>50-co-SEt<sub>5.5-co-Chol</sub>0.5)-HS</sub>	527	58.8 ± 1.8	0.218	-17.5 ± 1.8

FT-IR (ATR):  $\tilde{\nu}_{\max}$  = 3278 (OH), 2953-2872 (CH, CH<sub>2</sub>, CH<sub>3</sub>), 1546-1249 (CH, CH<sub>2</sub>, CH<sub>3</sub>), 1077 (COC), 981-857 (CC) cm<sup>-1</sup>.

## 5 Experimental section

### 5.4.17 P(G<sub>50</sub>-co-SEt<sub>5.5</sub>-co-SPEG-NH<sub>2(0.5)</sub>)

Receiving P(G<sub>50</sub>-co-SEt<sub>5.5</sub>-co-SPEG-NH<sub>2(0.5)</sub>), P(G<sub>50</sub>-co-AGE<sub>6</sub>) (250 mg, 56.0 μmol) was dissolved in 16 mL of a H<sub>2</sub>O-DMF mixture (15:1) and degassed for 30 min. After adding HS-PEG-NH<sub>2</sub> (175 mg, 55.5 μmol), EtSH (500 μL, 6.76 mmol) and I2959 (80.0 mg, 357 μmol) the solution was stirred and irradiated with UV light at 365 nm for 2 h. The solvent was removed under vacuum and the remaining polymer was dissolved in 50 mL H<sub>2</sub>O. After dialysis and lyophilization the polymer was received as a slightly yellow, viscous solid.



<sup>1</sup>H-NMR (300 MHz, D<sub>2</sub>O): δ = 3.78-3.65 (m, 432 H, H-2-12,18,20), 3.23 (t, 1 H, H-21), 2.96 (t, 1 H, H-22), 2.70-2.58 (m, 23 H, H-15-17), 1.90 (quin, 12 H, H-13,14), 1.29-1.25 (m, 25.5 H, H-1,19) ppm.

FT-IR (ATR):  $\tilde{\nu}_{\max}$  = 3383 (OH), 2924-2876 (CH, CH<sub>2</sub>, CH<sub>3</sub>), 1631 (NH<sub>2</sub>), 1465-1241 (CH, CH<sub>2</sub>, CH<sub>3</sub>), 1107 (COC), 962-842 (CC) cm<sup>-1</sup>.

Raman:  $\tilde{\nu}_{\max}$  = 2931-2886 (CH, CH<sub>2</sub>, CH<sub>3</sub>), 1471-1281 (CH, CH<sub>2</sub>, CH<sub>3</sub>), 1127-1064 (CC), 907-845 (COC), 657 (CS) cm<sup>-1</sup>.

TNBSA assay: 0.7 amines per polymer

SEC (RI, H<sub>2</sub>O):

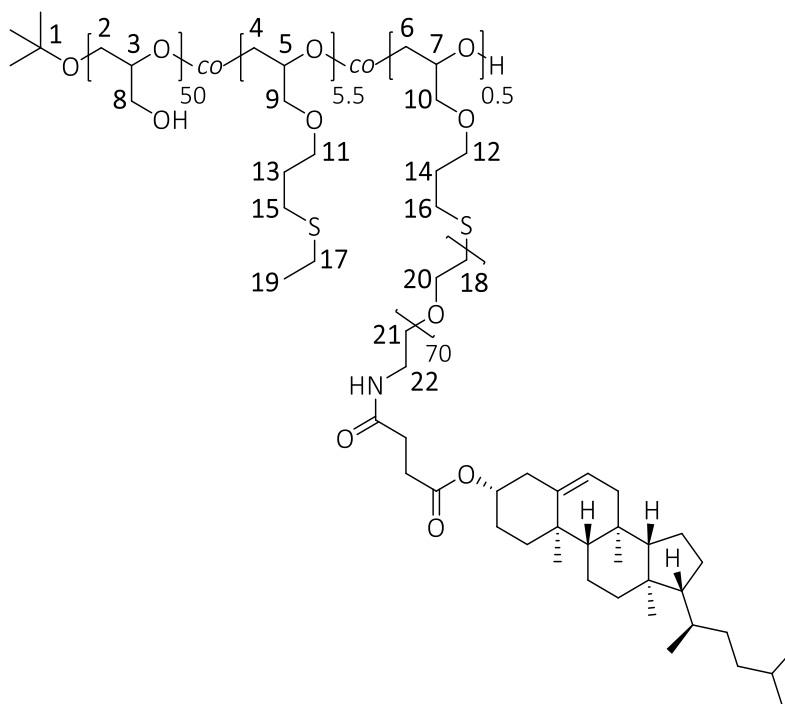
**Table 72.**  $\bar{M}_w$ ,  $\bar{M}_n$  and Đ as well as the via <sup>1</sup>H-NMR spectroscopy calculated molecular weight of P(G<sub>50</sub>-co-SEt<sub>5.5</sub>-co-SPEG-NH<sub>2(0.5)</sub>).

	$\bar{M}_w$ [Da] <sup>(a)</sup>	$\bar{M}_n$ [Da] <sup>(a)</sup>	Đ <sup>(a)</sup>	$M_{\text{exp}}$ [Da] <sup>(b)</sup>
P(G <sub>50</sub> -co-SEt <sub>5.5</sub> -co-SPEG-NH <sub>2(0.5)</sub> )	2804	1331	2.11	5913

<sup>(a)</sup>determined by SEC in H<sub>2</sub>O, <sup>(b)</sup>determined by <sup>1</sup>H-NMR spectroscopy in D<sub>2</sub>O

5.4.18 P(G<sub>50</sub>-co-SEt<sub>5.5</sub>-co-SPEG-Chol<sub>0.5</sub>)

P(G<sub>50</sub>-co-SEt<sub>5.5</sub>-co-SPEG-Chol<sub>0.5</sub>) was synthesized under oxygen free conditions. P(G<sub>50</sub>-co-SEt<sub>5.5</sub>-co-SPEG-NH<sub>2(0.5)</sub>) (50 mg, 7.84 μmol), EDC (3.00 mg, 15.7 μmol), NHS (1.80 mg, 15.7 μmol) and Chol-COOH (7.63 mg, 15.7 μmol) were dissolved in 10 mL dry DMF. After stirring overnight at RT, DMF was removed under vacuum and the remaining polymer was dissolved in 90 mL H<sub>2</sub>O. After purification via dialysis and lyophilization the polymer was received as a slightly green solid.



<sup>1</sup>H-NMR (300 MHz, D<sub>2</sub>O): δ = 3.80-3.67 (m, 433 H, H-2-12, 18,20,22), 2.71-2.60 (m, 24 H, H-15-17, 21), 1.91 (quin, 12 H, H-13,14), 1.38-1.27 (m, 25.5 H, H-1+19) ppm. No signals of the cholesteryl units were detected in D<sub>2</sub>O.

FT-IR (ATR):  $\tilde{\nu}_{\max}$  = 3381 (OH), 2926-2880 (CH, CH<sub>2</sub>, CH<sub>3</sub>), 1731 (C=O(OR)), 1648 (C=O(NH)), 1588 (NH), 1464-1240 (CH, CH<sub>2</sub>, CH<sub>3</sub>), 1108 (COC), 962-841 (CC) cm<sup>-1</sup>.

Raman:  $\tilde{\nu}_{\max}$  = 2949-2883 (CH, CH<sub>2</sub>, CH<sub>3</sub>), 1667 (C=C), 1458-1267 (CH, CH<sub>2</sub>, CH<sub>3</sub>), 1123-1062 (CC), 901-860 (COC), 653 (CS) cm<sup>-1</sup>.

## 5 Experimental section

SEC (RI, H<sub>2</sub>O):

**Table 73.**  $\bar{M}_w$ ,  $\bar{M}_n$  and Đ as well as the via <sup>1</sup>H-NMR spectroscopy calculated molecular weight of P(G<sub>50</sub>-co-SEt<sub>5.5</sub>-co-SPEG-Chol<sub>0.5</sub>).

	$\bar{M}_w$ [Da] <sup>(a)</sup>	$\bar{M}_n$ [Da] <sup>(a)</sup>	Đ <sup>(a)</sup>	$M_{exp}$ [Da] <sup>(b)</sup>
P(G <sub>50</sub> -co-SEt <sub>5.5</sub> -co-SPEG-Chol <sub>0.5</sub> )	36648	4308	8.51	6381

<sup>(a)</sup>determined by SEC in H<sub>2</sub>O, <sup>(b)</sup>determined by <sup>1</sup>H-NMR spectroscopy in D<sub>2</sub>O

### 5.4.18.1 Au-P(G<sub>50</sub>-co-SEt<sub>5.5</sub>-co-SPEG-Chol<sub>0.5</sub>)

UV-Vis, DLS, Zeta:

**Table 74.** Values of SPR, *d*, PDI and ζ of P(G<sub>50</sub>-co-SEt<sub>5.5</sub>-co-SPEG-Chol<sub>0.5</sub>)-modified 15 nm and 30 nm AuNPs, determined by UV-Vis, DLS and zeta potential measurements.

	SPR [nm]	<i>d</i> [nm]	PDI	ζ [mV]
15Au-P(G <sub>50</sub> -co-SEt <sub>5.5</sub> -co-SPEG-Chol <sub>0.5</sub> )	523	37.7 ± 2.8	0.164	-18.2 ± 3.0
30Au-P(G <sub>50</sub> -co-SEt <sub>5.5</sub> -co-SPEG-Chol <sub>0.5</sub> )	529	67.6 ± 1.4	0.214	-17.6 ± 1.3

FT-IR (ATR):  $\tilde{\nu}_{max}$  = 3375 (OH), 2927-2874 (CH, CH<sub>2</sub>, CH<sub>3</sub>), 1590-1257 (CH, CH<sub>2</sub>, CH<sub>3</sub>), 1080 (COC), 917-407 (CC) cm<sup>-1</sup>.

### 5.4.18.2 Au-P(G<sub>50</sub>-co-SEt<sub>5.5</sub>-co-SPEG-Chol<sub>0.5</sub>)-HS

UV-Vis, DLS, Zeta:

**Table 75.** Values of SPR, *d*, PDI and ζ of 15Au- and 30Au-P(G<sub>50</sub>-co-SEt<sub>5.5</sub>-co-SPEG-Chol<sub>0.5</sub>) incubated with HS, determined by UV-Vis, DLS and zeta potential measurements.

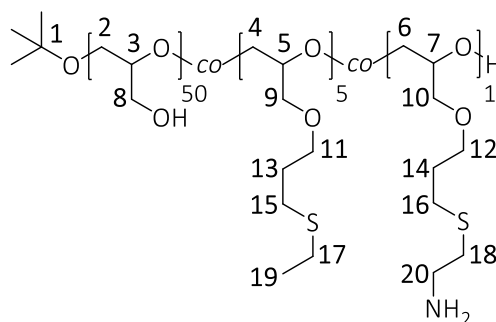
	SPR [nm]	<i>d</i> [nm]	PDI	ζ [mV]
15Au-P(G <sub>50</sub> -co-SEt <sub>5.5</sub> -co-SPEG-Chol <sub>0.5</sub> )-HS	532	80.3 ± 2.8	0.250	-16.0 ± 3.3
30Au-P(G <sub>50</sub> -co-SEt <sub>5.5</sub> -co-SPEG-Chol <sub>0.5</sub> )-HS	533	129.9 ± 3.2	0.380	-20.3 ± 1.6

FT-IR (ATR):  $\tilde{\nu}_{max}$  = 3277 (OH), 2922-2852 (CH, CH<sub>2</sub>, CH<sub>3</sub>), 1544-1292 (CH, CH<sub>2</sub>, CH<sub>3</sub>), 1073 (COC), 980-850 (CC) cm<sup>-1</sup>.



5.4.19 P(G<sub>50</sub>-co-SEt<sub>5</sub>-co-NH<sub>2</sub>(<sub>1</sub>))

To obtain P(G<sub>50</sub>-co-SEt<sub>5</sub>-co-NH<sub>2</sub>(<sub>1</sub>)), P(G<sub>50</sub>-co-AGE<sub>6</sub>) (500 mg, 105 μmol) was dissolved in 40 mL EtOH. The solution was degassed for 20 min. After adding cysteamine hydrochloride (143 mg, 1.26 mmol), EtSH (451 μL, 6.09 mmol) and I2959 (188 mg, 840 μmol) the solution was irradiated with UV light at 365 nm for 2 h. The solvent was removed under vacuum and the remaining polymer was dissolved in 90 ml H<sub>2</sub>O. After dialyzing and freeze-drying, the polymer was received as a light-yellow oil.



<sup>1</sup>H-NMR (300 MHz, D<sub>2</sub>O): δ = 3.80-3.66 (m, 292 H, H-2-12), 3.23 (t, 2 H, H-18), 2.88 (t, 2 H, H-20), 2.70-2.59 (m, 22 H, H-15-17), 1.91 (quin, 12 H, H-13,14), 1.30-1.25 (m, 24 H, H-1,19) ppm.

FT-IR (ATR):  $\tilde{\nu}_{\max}$  = 3363 (OH), 2921-2872 (CH, CH<sub>2</sub>, CH<sub>3</sub>), 1605 (NH<sub>2</sub>), 1458-1259 (CH, CH<sub>2</sub>, CH<sub>3</sub>), 1039 (COC), 915-857 (CC) cm<sup>-1</sup>.

Raman:  $\tilde{\nu}_{\max}$  = 2928-2886 (CH, CH<sub>2</sub>, CH<sub>3</sub>), 1461-1260 (CH, CH<sub>2</sub>, CH<sub>3</sub>), 1136-852 (CC), 907-858 (COC), 657 (CS) cm<sup>-1</sup>.

TNBSA assay: 1.1 amines per polymer

SEC (RI, H<sub>2</sub>O):

Table 76.  $\bar{M}_w$ ,  $\bar{M}_n$  and Đ as well as the via <sup>1</sup>H-NMR spectroscopy calculated molecular weight of P(G<sub>50</sub>-co-SEt<sub>5</sub>-co-NH<sub>2</sub>(<sub>1</sub>)).

	$\bar{M}_w$ [Da] <sup>(a)</sup>	$\bar{M}_n$ [Da] <sup>(a)</sup>	Đ <sup>(a)</sup>	$M_{\text{exp}}$ [Da] <sup>(b)</sup>
P(G <sub>50</sub> -co-SEt <sub>5</sub> -co-NH <sub>2</sub> ( <sub>1</sub> ))	4274	1977	2.16	4848

<sup>(a)</sup>determined by SEC in H<sub>2</sub>O, <sup>(b)</sup>determined by <sup>1</sup>H-NMR spectroscopy in D<sub>2</sub>O

## 5 Experimental section

### 5.4.19.1 Au-P(G<sub>50-co-SEt<sub>5-co</sub>-NH<sub>2(1)</sub>)</sub>

UV-Vis, DLS, Zeta:

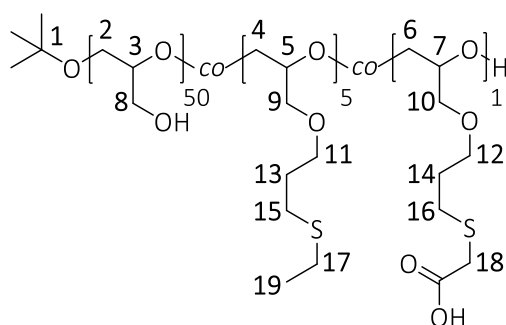
**Table 77.** Values of SPR, *d*, PDI and  $\zeta$  of P(G<sub>50-co-SEt<sub>5-co</sub>-NH<sub>2(1)</sub>)-modified 15 nm AuNPs, determined by UV-Vis, DLS and zeta potential measurements.</sub>

	SPR [nm]	<i>d</i> [nm]	PDI	$\zeta$ [mV]
15Au-P(G <sub>50-co-SEt<sub>5-co</sub>-NH<sub>2(1)</sub>)</sub>	522	27.6 ± 0.4	0.100	+4.2 ± 1.1

**FT-IR (ATR):**  $\tilde{\nu}_{\max}$  = 3365 (OH), 2921-2876 (CH, CH<sub>2</sub>, CH<sub>3</sub>), 1582 (NH<sub>2</sub>), 1458-1262 (CH, CH<sub>2</sub>, CH<sub>3</sub>), 1073 (COC), 912-841 (CC) cm<sup>-1</sup>.

### 5.4.20 P(G<sub>50-co-SEt<sub>5-co</sub>-COOH<sub>1</sub>)</sub>

To obtain P(G<sub>50-co-SEt<sub>5-co</sub>-COOH<sub>1</sub>), P(G<sub>50-co-AGE<sub>6</sub>) (500 mg, 105  $\mu$ mol) was dissolved in 30 mL EtOH. The solution was degassed for 20 min. After adding thioglycolic acid (50.9  $\mu$ L, 735  $\mu$ mol), EtSH (451  $\mu$ L, 6.09 mmol) and I2959 (188 mg, 840  $\mu$ mol) the solution was irradiated with UV light at 365 nm for 2 h. The solvent was removed under vacuum and the remaining polymer was dissolved in 100 mL H<sub>2</sub>O. After dialysis and lyophilization, the polymer was received as a yellowish oil.</sub></sub>



**<sup>1</sup>H-NMR** (300 MHz, D<sub>2</sub>O):  $\delta$  = 3.81-3.68 (m, 292 H, H-2-12), 3.37 (br, s, 2 H, H-18), 2.73-2.60 (m, 22 H, H-15-17), 1.93 (quin, 12 H, H-13,14), 1.38-1.27 (m, 15 H, H-1,19) ppm.

**FT-IR (ATR):**  $\tilde{\nu}_{\max}$  = 3378 (OH), 2921-2873 (CH, CH<sub>2</sub>, CH<sub>3</sub>), 1737 ((C=O)OH) 1459-1234 (CH, CH<sub>2</sub>, CH<sub>3</sub>), 1039 (COC), 914-857 (CC) cm<sup>-1</sup>.

**Raman:**  $\tilde{\nu}_{\max}$  = 2928-2885 (CH, CH<sub>2</sub>, CH<sub>3</sub>), 1695 ((C=O)OH) 1461-1261 (CH, CH<sub>2</sub>, CH<sub>3</sub>), 1114-859 (CC), 905-859 (COC), 655 (CS) cm<sup>-1</sup>.

SEC (RI, H<sub>2</sub>O):

**Table 78.**  $\bar{M}_w$ ,  $\bar{M}_n$  and Đ as well as the via <sup>1</sup>H-NMR spectroscopy calculated molecular weight of P(G<sub>50-co</sub>-SEt<sub>5-co</sub>-COOH<sub>1</sub>).

	$\bar{M}_w$ [Da] <sup>(a)</sup>	$\bar{M}_n$ [Da] <sup>(a)</sup>	Đ <sup>(a)</sup>	M <sub>exp</sub> [Da] <sup>(b)</sup>
P(G <sub>50-co</sub> -SEt <sub>5-co</sub> -COOH <sub>1</sub> )	2999	1487	2.02	4863

<sup>(a)</sup>determined by SEC in H<sub>2</sub>O, <sup>(b)</sup>determined by <sup>1</sup>H-NMR spectroscopy in D<sub>2</sub>O

#### 5.4.20.1 Au-P(G<sub>50-co</sub>-SEt<sub>5-co</sub>-COOH<sub>1</sub>)

UV-Vis, DLS, Zeta:

**Table 79.** Values of SPR, *d*, PDI and ζ of P(G<sub>50-co</sub>-SEt<sub>5-co</sub>-COOH<sub>1</sub>)-modified 15 nm AuNPs, determined by UV-Vis, DLS and zeta potential measurements.

	SPR [nm]	<i>d</i> [nm]	PDI	ζ [mV]
15Au-P(G <sub>50 co</sub> -SEt <sub>5-co</sub> -COOH <sub>1</sub> )	526	28.1 ± 0.8	0.100	-28.7 ± 3.2

FT-IR (ATR):  $\tilde{\nu}_{\max}$  = 3370 (OH), 2922-2876 (CH, CH<sub>2</sub>, CH<sub>3</sub>), 1686 ((C=O)OH), 1458-1259 (CH, CH<sub>2</sub>, CH<sub>3</sub>), 1074 (COC), 913-845 (CC) cm<sup>-1</sup>.

## 5 Experimental section

### 5.5 Full list of hard corona proteins adsorbed on 15 nm AuNPs identified by LC-MS/MS analysis

**Table 80.** Full list of hard corona proteins on 15Au–HS (15AuHS), 15Au–P(G<sub>50</sub>-co-SEt<sub>11</sub>-co-SPent<sub>1</sub>)–HS (15AuPG1HS), 15Au–P(G<sub>50</sub>-co-SEt<sub>10</sub>-co-SDec<sub>2</sub>)–HS (15AuPG6HS), 15Au–P(G<sub>50</sub>-co-SEt<sub>8</sub>-co-SPentadec<sub>4</sub>)–HS (15AuPG12HS) and 15Au–P(G<sub>50</sub>-co-SEt<sub>5.5</sub>-co-Chol<sub>0.5</sub>)–HS (15AuPG13HS) identified by LC-MS/MS analysis, grouped according to their biological function. In addition, proteins present in pure HS are listed. Relative amounts of total bound proteins were determined from one measurement of each sample, using intensity based absolute quantification (iBAQ) values. iBAQ values are proportional to the molar quantities of the proteins and help to estimate their relative abundance.

**iBAQ values of identified proteins**

		15AuHS	15AuPG1 HS	15AuPG6 HS	15AuPG12 HS	15AuPG13 HS	HS
<b>Acute Phase Proteins</b>							
Adiponectin	ADIPOQ	0	0	0	0	287390	334680
Alpha-1-Acid Glycoprotein 1	ORM1	3196100	0	0	1015600	0	58323000
Alpha-1-Acid Glycoprotein 2	ORM2	5723000	4483100	879030	8833300	2927500	15074000
Alpha-1- Antichymotrypsin	SERPINA3	31929000 0	12349000	698610	5486500	5160800	46473000
Alpha-1-Antitrypsin	SERPINA1	68240000 0	16106620 0	13142000 0	14186000 0	17439710 0	55331200 0
Alpha-2-Macroglobulin	A2M	97344000	96491000	57884000	10303000 0	14181000 0	90046000
Amyloid P Component, Serum	APCS	8361600	1365900	583670	4559200	873100	30216000
Beta-2-Microglobulin	B2M	9717100	0	0	0	0	387890
Ceruloplasmin	CP	47561360	1235000	161160	48777	290650	56831400
Fibronectin	FN1	16881000	8892800	2206600	7170400	1266400	11635000
Haptoglobin	HP	21447000 0	84151000	45555000	11820000 0	60861000	37816000 0
Haptoglobin Related Protein	HPR	10698000	42948000	8598400	65670000	15040000	14123000
Inter-Alpha-Trypsin Inhibitor Heavy Chain 1	ITIH1	49616000	7338800	0	3853700	3756900	21331000
Inter-Alpha-Trypsin Inhibitor Heavy Chain 2	ITIH2	56033000	7224200	2258500	5455000	9088000	26420000
Inter-Alpha-Trypsin Inhibitor Heavy Chain 3	ITIH3	855560	0	0	0	1188700	3214200
Inter-Alpha-Trypsin Inhibitor Heavy Chain 4	ITIH4	10223010 57	25691561 70	11482242 60	13948778 30	61090701 0	11970000
Lipocalin 1	LCN1	526000	888620	0	3479900	377270	0
Lipopolysaccharide Binding Protein	LBP	96545000	98213000	14452000 0	47321000 0	37925000	0
Plasma Protease C1 Inhibitor	SERPING1	65305000 0	56066000 0	31532000 0	37165000 0	23177000 0	25638000
Pro-Platelet Basic Protein	PPBP	14194000	7653000	3266600	3700800	0	0
Serum Amyloid A1	SAA1	20135000	16589000	7249600	34416000	0	333250

## 5 Experimental section

Serum Amyloid A2	SAA2	18376000	6087700	13165000	22412000	0	0
Serum Amyloid A4	SAA4	37245000 0	16615000 0	32400000 0	62358000 0	67583000	15986000
Transferrin Receptor	TFRC	174280	264140	2485900	184120	664460	0
<b>Coagulation Proteins</b>							
Alpha-2-Antiplasmin	SERPINF2	21389000 0	19980000 0	10635000 0	15071000 0	17927000 0	13215000
Antithrombin-III	SERPINC1	22361000 00	24213000 00	16687000 00	19307000 00	25474000 00	49328000
Carboxypeptidase B2	CPB2	17428000	5049900	874150	7396900	2846800	0
Coagulation Factor V	F5	32551000	44518000	18023000	31235000	19000000	30502
Coagulation Factor IX	F9	826500	70587	73431	280690	88776	0
Coagulation Factor XI	F10	0	0	0	0	0	775610
Coagulation Factor XI	F11	43474000 0	58297000 0	33250000 0	35989000 0	35317000 0	0
Coagulation Factor XII	F12	41295000	29309000	2311000	18334000	247440	3864300
Coagulation Factor XIII A Chain	F13A1	246700	97541	0	0	14186	0
Coagulation factor XIII B Chain	F13B	0	0	0	0	0	695680
Fibrinogen Alpha Chain	FGA	12759000 0	52351000	10840000	22419000	3266400	539960
Fibrinogen Beta Chain	FGB	7159800	2908000	1612000	1204700	3167100	160010
Fibrinogen Gamma Chain	FGG	12905000	11025000	1940900	4722100	7906400	195060
Fibulin-1	FBLN1	247460	0	0	0	0	778539
Heparin Cofactor 2	SERPIND1	20036000 0	18442000 0	94378000	10509000 0	18909000 0	6075700
Histidine Rich Glycoprotein	HRG	73282000 0	95079000 0	18162000 0	27801000 0	18954000 0	8783700
Hyaluronan Bbinding Protein 2	HABP2	0	0	0	0	0	1232400
Integrin Subunit Alpha 2b	ITGA2B	0	0	0	0	176600	0
Integrin Subunit Beta 3	ITGB3	43651	48288	36039	41380	37724	0
Kallistatin	SERPINA4	4961300	486510	0	1711200	0	1857200
Kininogen-1	KNG1	29676500 00	39635095 00	22953000 00	29688083 90	24785000 00	44581720
Matrix Gla Protein	MGP	2144400	0	792330	0	0	0
Plasma Kallikrein	KLKB1	68126000 0	83902000 0	89509000 0	65683000 0	58223000 0	2087500
Plasma Serine Protease Inhibitor	SERPINA5	86297000 0	11038000 00	63146000 0	75413000 0	10685000 00	834230
Plasminogen	PLG	17301000 0	41954000	9103600	25993000	42638000	26807000
Platelet Factor 4	PF4	28792000	19814000	16528000	23739000	8203800	0
Prothrombin	F2	11702000 00	10774000 00	29577000 0	71298000 0	77421000 0	17134000
Thrombospondin 1	THBS1	0	106600	7283,8	0	0	0
Tissue Factor Pathway Inhibitor	TFPI	1718100	856310	99369	964200	1220800	0
Vitamin K-Dependent Protein C	PROC	494340	0	0	0	0	258110

## 5 Experimental section

Vitamin K-Dependent Protein S	PROS1	4964200	3730000	1211400	806490	810700	1825200
Von Willebrand Factor	VWF	5507100	16077000	10326000	12368000	12810000	167330
<b>Lipoproteins</b>							
Apolipoprotein A-I	APOA1	89464000 0	78501000	81921000	21342000 00	12825000 0	49082000 0
Apolipoprotein A-II	APOA2	42071000 0	14337000 0	99917000	14817000 00	23195000 0	68310000
Apolipoprotein A-IV	APOA4	90708000	3823000	1214000	58386000	21526000	42674000
Apolipoprotein A-V	APOA5	1364800	1244400	517340	2344100	250670	0
Apolipoprotein B-100	APOB	24954000	14301000	10514000	10852000 00	30283000 0	8801500
Apolipoprotein C-I	APOC1	25450000 0	26092000	13878000 0	81769000 0	50269000	10122000
Apolipoprotein C-II	APOC2	25694000	764300	1753400	43981000	5891100	4332500
Apolipoprotein C-III	APOC3	31149000 0	81084000	60261000	38913000 0	27298000	17121000
Apolipoprotein C-IV	APOC4	95802000	11534000 0	93891000	14678000 0	25198000	1365000
Apolipoprotein D	APOD	8924900	6093000	2126900	14736000 0	30580000	7976000
Apolipoprotein E	APOE	95896000 0	17401000 00	69644000 0	10112000 00	34415000 0	16465000
Apolipoprotein F	APOF	0	0	0	0	0	688730
Apolipoprotein L1	APOL1	4383700	1037800	173960	12501000	13286000	4067800
Apolipoprotein M	APOM	1415500	340950	18269000	21852000 0	9744300	6123800
Apolipoprotein (A)	LPA	1756000	1541000	992040	22190000	4734600	156810
Beta-2-Glycoprotein 1	APOH	15034000 00	34781000 0	14041000 0	15979000 00	10429000 0	84674000
Clusterin	CLU	17054000 0	47974000 0	17549000 0	55913000 0	12378000 0	25737000
LDL Receptor Related Protein 1	LRP1	3919,8	21921	0	0	14191	0
Paraoxonase 1	PON1	6061200	3785400	2515400	21626000 0	37242000	15246000
Phospholipase A1 member A	PLA1A	0	791290	689520	741070	1069900	0
Phospholipid Transfer Protein	PLTP	0	0	0	818740	765140	0
<b>Complement Proteins</b>							
C4b-Binding Protein Alpha Chain	C4BPA	16084000 0	90570000	27541000	53438000	28722000	21523000
C4b-Binding Protein Beta Chain	C4BPB	2668400	818560	184180	0	283850	467220
Complement 4A	C4A	0	0	0	0	0	680630
Calmodulin-Like Protein 5	CALML5	45189	529190	932810	0	312990	641400
Complement C1q A Chain	C1QA	4313900	1553300	463200	3233500	0	448800
Complement C1q B Chain	C1QB	15277000	11766000	5630100	17566000	4169500	6491300
Complement C1q C Chain	C1QC	7777800	6423900	2269700	7005900	3658000	9732400

## 5 Experimental section

Complement C1q Tumor Necrosis Factor-Related Protein 3	C1QTNF3	9991600	14382000	9094600	7799000	3868500	0
Complement C1r	C1R	4839300	6579000	6320400	6198500	1128000	2505200
Complement C1s	C1S	4748000	4572100	3263600	7501300	958170	4236000
Complement C2	C2	0	0	0	0	0	457510
Complement C3	C3	39595500 00	13869000 00	66577000 0	29112000 00	42077000 0	12586000 0
Complement C4A	C4A	2168200	3930800	510780	3504600	1508700	0
Complement C4B	C4B	63579000 0	67829000 0	22775000 0	50243000 0	13790000 0	29678000
Complement C5	C5	2119900	1333000	828120	75777000	4752400	4203500
Complement C6	C6	15528000	3183600	1438700	11759000 0	7966600	4442700
Complement C7	C7	8543400	1278900	1010900	12571000 0	6153500	4720400
Complement C8 Alpha Chain	C8A	1366100	1443600	0	91603000	5639200	1067600
Complement C8 Beta Chain	C8B	1689400	2525100	589850	88874000	6806200	273120
Complement C8 Gamma Chain	C8G	2691100	1034700	260770	30453000	2071700	3329700
Complement C9	C9	14257000	11441000	20842000	33418000 0	54451000	3185000
Complement Factor B	CFB	13595533 2	34344209	637320	46354170	2594800	17086000
Complement Factor D	CFD	39385000	40944000	7842200	25523000	14061000	76817
Complement Factor H	CFH	87633040 0	18157985 00	48530572 0	14095414 00	60011000	29951245
Complement Factor H- Related Protein 1	CFHR1	28541000 0	46073000 0	23712000 0	35874000 0	25692000	3426100
Complement Factor H- Related Protein 2	CFHR2	29782000	50770000	29784000	25306000	2184900	882320
Complement Factor H- Related Protein 3	CFHR3	326510	15036000	6397400	7161800	793870	0
Complement Factor H- Related Protein 4	CFHR4	0	0	0	201320	0	0
Complement Factor H- Related Protein 5	CFHR5	86315000	11360000 0	63878000	10601000 0	13614000	0
Complement Factor I	CFI	37849000	38115000	11064000	24527000	44354000	4240500
Ficolin 1	FCN1	1297000	180370	0	911270	84889	0
Ficolin 2	FCN2	0	0	0	0	167600	0
Ficolin 3	FCN3	8226700	13961000	2491900	12143000	9737600	1345400
Mannan-Binding Lectin Serine Protease 1	MASP1	418890	593690	61232	150880	2305600	70406
Mannan-Binding Lectin Serine Protease 2	MASP2	0	0	0	0	0	206820
Properdin	CFP	19286000	51335000	25625000	42524000 0	31517000	175340
<b>Immunoglobulins</b>							
Ig Heavy Constant Alpha 1	IGHA1	51885000 0	97776000 0	60311000 0	86606000 0	10998000 00	41915000 0
Ig Heavy Constant Alpha 2	IGHA2	20512700	40420000	24278900	34898300	56900000	45156000

## 5 Experimental section

Ig Heavy Constant Delta	IGHD	22936000	1898600	43283	0	10477	3310900
Ig Heavy Constant Gamma 1	IGHG1	20437000 00	34364000 0	20484000 0	35485000 0	23637000 0	12154000 00
Ig Heavy Constant Gamma 2	IGHG2	14537000 0	12334000 0	81005000	11642000 0	94358000	24904000 0
Ig Heavy Constant Gamma 3	IGHG3	13474000 00	42771000 0	24401000 0	34619000 0	25554000 0	18196000 0
Ig Heavy Constant Gamma 4	IGHG4	39863000	2506600	2902200	5099900	1828800	37675000
Ig Heavy Constant Mu	IGHM	17752000 0	48365000 0	31177000 0	28351000 0	23856000 0	31180000
Ig Heavy Chain V-I Region V35	IGHV1-2	0	0	0	0	0	1559200
Ig Heavy Variable 1-18	IGHV1-18	14470000	0	0	0	0	3215800
Ig Heavy Chain V-I Region HG3	IGHV1-46	17464000	0	0	0	4619800	10714000
Ig Heavy Variable 1/OR15-1 (Non-Functional)	IGHV1OR 15-1	5196000	0	0	0	0	0
Ig Heavy Chain V-II Region OU	IGHV2-70	0	0	0	0	0	3188400
Ig Heavy Chain V-III Region JON	IGHV3-7	80746000	52184000	39738000	28778000	35188000	41845000
Ig Heavy Chain V-III Region DOB	IGHV3-9	0	0	0	0	0	4318800
Ig Heavy Variable 3-15	IGHV3-15	0	0	0	0	0	419320
Ig Heavy Chain V-III Region CAM	IGHV3-30	15289000	7702400	4500000	4827400	5642400	2515500
Ig Heavy Variable 3-35 (Non-Functional)	IGHV3-35	0	0	0	0	0	1343300
Ig Heavy Variable 3-38 (Non-Functional)	IGHV3-38	0	0	0	0	0	631840
Ig Heavy Variable 3-49	IGHV3-49	5938500	2474800	1497200	1720400	2367500	3793300
Ig Heavy Variable 3-72	IGHV3-72	11988000 0	87986000	53996000	70616000	77616000	13549000
Ig Heavy Variable 3-74	IGHV3-74	37710000	17626000	21735000	4823800	21966000	0
Ig Heavy Variable 3/OR16-9 (Non-Functional)	IGHV3OR 16-9	0	0	0	0	0	83262000
Ig Heavy Variable 3/OR16-12 (Non-Functional)	IGHV3OR 16-12	10959000	0	2207000	0	0	4885300
Ig Heavy Variable 4-28	IGHV4-28	0	0	0	0	0	2954600
Ig Heavy Variable 4-30-2	IGHV4- 30-2	0	0	0	0	0	810780
Ig Heavy Variable 4-61	IGHV4-61	21364000	4908200	3307700	0	5712300	23769000
Ig Heavy Variable 5-10-1	IGHV5- 10-1	1012500	0	0	0	0	0
Ig Heavy Variable 5-51	IGHV5-51	4687400	0	0	0	0	10116000
Ig J Chain	JCHAIN	6412700	22501000	12158000	24254000	14953000	4350500
Ig Kappa Constant	IGKC	13656000 00	36334000 0	11873000 0	57492000 0	21258000 0	14067000 00
Ig Kappa Chain V-I Region HK102	IGKV1-5	16636000	8447400	2947800	6970200	7151700	11756000
Ig Kappa Variable 1-6	IGKV1-6	0	0	0	0	0	311570



## 5 Experimental section

Ig Kappa Variable 1-8	IGKV1-8	0	0	0	0	0	5372300
Ig Kappa Variable 1-12	IGKV1-12	0	0	0	0	0	1143900
Ig Kappa Variable 1-13	IGKV1-13	0	0	0	0	0	2962500
Ig Kappa Chain V-I Region BAN	IGKV1-16	0	0	0	0	0	1021800
Ig Kappa Chain V-I Region Gal	IGKV1-17	0	0	0	0	0	4120700
Ig Kappa Chain V-I Region AU	IGKV1-33	10426000 0	12577000	2608800	27541000	13185000	16006000 0
Ig Kappa Chain V-I Region Daudi	IGKV1D-39	0	0	0	0	0	2511300
Ig Kappa Variable 2-24	IGKV2-24	0	5065500	0	6604600	3505700	13924000
Ig Kappa Chain V-II Region RPMI 6410	IGKV2-30	53933000	22275000	5686400	21875000	21680000	15771000
Ig Kappa Chain V-II Region FR	IGKV2D-28	21525000	8870200	1449200	12177000	4137400	38826000
Ig Kappa Variable 2D-29	IGKV2D-29	5117100	0	0	0	262860	3964700
Ig Kappa Chain V-II Region Cum	IGKV2D-40	0	0	0	0	0	73605000
Ig kappa chain V-III region VG	IGKV3-11	73789000	18168000	10532000	16922000	18040000	39663000
Ig Kappa Chain V-III Region POM	IGKV3-15	14904000 0	40087000	24929000	26714000	30447000	54796000
Ig Kappa Chain V-III Region B6	IGKV3-20	67051000	16879000	9757200	14870000	20786000	75820000
Ig Kappa Variable 3D-15	IGKV3D-15	3318800	814190	354640	1048800	1082200	22275000
Ig Kappa Variable 3D-20	IGKV3D-20	20208000	3755900	3403600	2943300	5099600	8981300
Ig Kappa Variable 4-1	IGKV4-1	26558000	9087700	859400	10809000	11431000	57911000
Ig Kappa Variable 6-21 (Non-Functional)	IGKV6-21	0	0	0	0	375140	0
Ig Kappa Variable 6D-21 (Non-Functional)	IGKV6D-21	3506400	398710	224070	0	755490	2764900
Ig Lambda Constant 3	IGLC3	97598000 0	37255000 0	18683000 0	30360000 0	28658000 0	67128000 0
Ig Lambda Constant 7	IGLC7	335540	380370	209870	247230	634500	0
Ig Lambda-Like Polypeptide 1	IGLL1	0	0	0	0	0	293410
Ig Lambda-Like Polypeptide 5	IGLL5	51369000	23195000	13954000	15669000	19345000	32872000
Ig Lambda Variable 1-36	IGLV1-36	0	0	0	0	0	613190
Ig Lambda Chain V-I Region NEWM	IGLV1-40	0	0	0	0	1334100	6390400
Ig Lambda Chain V-I Region HA	IGLV1-47	23321000	11331000	2902800	8981200	12378000	14558000
Ig Lambda Chain V-I Region NEW	IGLV1-51	11427000	4171900	0	4346200	2833900	5565700
Ig Lambda Chain V-II Region MGC	IGLV2-8	42332000	19340000	9449000	8920600	11237000	5031500
Ig Lambda Chain V-II Region BOH	IGLV2-11	3949500	1771600	1177900	1761100	1682500	3461800
Ig Lambda Chain V-II Region TOG	IGLV2-14	4752700	6204400	0	6078600	6305700	8342600
Ig Lambda Variable 3-10	IGLV3-10	17483000	3916200	2942600	3804300	4192100	0

## 5 Experimental section

Ig Lambda Chain V-III Region SH	IGLV3-19	12811000	6440600	2779400	4759000	5478900	7703000
Ig lambda chain V-III region LOI	IGLV3-21	9134200	2522000	594810	3111800	3569200	19629000
Ig Lambda Chain V-IV Region Hil	IGLV3-25	5336000	1151100	0	1034400	718800	0
Ig Lambda Chain V-IV Region Kern	IGLV3-27	0	0	0	0	0	4703500
Ig Lambda Variable 4-60	IGLV4-60	540290	456510	0	244700	272970	549400
Ig Lambda Variable 4-69	IGLV4-69	2571600	3162600	384250	3466800	4192000	4342200
Ig Lambda Variable 5-45	IGLV5-45	1093800	0	378780	0	780020	1135000
Ig Lambda Chain V-VI Region AR	IGLV6-57	1993900	0	0	0	1009400	0
Ig lambda chain V region 4A	IGLV7-43	11271000	6886600	0	5086600	7169700	0
Ig Lambda Variable 8-61	IGLV8-61	16537000	24554000	8249600	20008000	11848000	10837000
Ig Lambda Variable 9-49	IGLV9-49	584470	432990	0	367330	593210	394210
Ig Lambda Variable 10-54	IGLV10-54	978370	0	539510	0	811300	426250
Ig Like Domain Containing Protein	--	7404100	1369800	239450	0	1716100	2050600
<b>Tissue Leakage Proteins</b>							
Activation Protein Zeta	YWHAZ	0	1181000	1757800	313990	177360	0
Actin, Cytoplasmic 1	ACTB	2648400	5310800	7454000	2289900	3526400	226130
Actin Gamma 1	ACTG1	0	0	58706	0	0	0
Actin Gamma 2, Smooth Muscle	ACTG2	0	0	0	0	0	122740
Angiogenin	ANG	24457000	12389000	4485000	2642300	0	59864
Anthrax Toxin Receptor 1	ANTXR1	134700	99608	0	125920	112310	0
Anthrax Toxin Receptor 2	ANTXR2	0	0	0	696990	171520	0
Antileukoproteinase	SLPI	1265000	259190	144570	0	0	0
Attractin	ATRN	0	0	0	0	0	595660
Biliverdin Reductase B	BLVRB	1046200	811760	383100	910240	465520	0
Cadherin-1	CDH1	2809200	5015100	1818800	1407100	1812800	0
Calmodulin Regulated Spectrin Associated Protein Family Member 2	CAMSAP2	0	0	0	1578000	0	0
Calpain 1	CAPN1	241530	1885700	1810800	700260	651200	0
Calpain Small Subunit 1	CAPNS1	393440	0	0	367750	0	0
Calsyntenin 1	CLSTN1	0	76250	125600	0	0	0
Carboxypeptidase N Subunit 1	CPN1	65309000	77897000	35804000	26114000	25017000	619780
Cartilage Oligomeric Matrix Protein	COMP	411850	369540	44947	0	32489	42574
Cathelicidin Antimicrobial Peptide	CAMP	105010	185060	197060	2490100	863920	199840

## 5 Experimental section

Cathepsin D	CTSD	0	106650	0	853930	90454	0
Cathepsin S	CTSS	1672100	1698800	281350	1848600	778890	0
CD5 Antigen-Like	CD5L	9729500	27593000	16905000	29406000	30572000	10885000
Cofilin 1	CFL1	722310	248300	483830	152240	0	0
Collagen Type VI Alpha 3 Chain	COL6A3	0	0	20654	0	0	0
Collagen Type XVIII Alpha 1 Chain	COL18A1	10931000	6153100	2249900	4896200	1595200	0
Creatine Kinase M-type	CKM	566180	0	0	90520	0	0
Deleted In Malignant Brain Tumors 1	DMBT1	0	0	0	0	309690	0
Dermcidin	DCD	0	0	0	2700200	0	1509800
Desmocollin 1	DSC1	0	60807	66638	1948500	346540	0
Desmocollin 3	DSC3	602660	122130	0	0	0	0
Desmoplakin	DSP	7148	77171	458160	97219	274140	0
Dystonin	DST	1738700	1722800	630720	1878900	0	0
Enolase 1	ENO1	0	0	542350	0	0	0
Extracellular Matrix Protein 1	ECM1	1747100	191960	86145	0	38568	705560
Gelsolin	GSN	1579100000	559120000	54741000	267060000	20990000	13345000
Glyceraldehyde-3-Phosphate Dehydrogenase	GAPDH	2079100	4180800	4606500	7069100	3098800	0
Glycosylphosphatidylinositol Specific Phospholipase D1	GPLD1	0	0	0	0	0	628270
GTP-Binding Nuclear Protein Ran	RAN	0	0	313670	0	0	0
Heat Shock Protein Beta-1	HSPB1	0	150690	925110	0	0	0
Hepatocyte Growth Factor Activator	HGFAC	14290000	7131200	1124200	5995900	231770	62268
Histone H2B	HISTH2B	0	251100	0	0	0	54103
Histone H4	HIST1H4A	0	0	0	0	0	125340
Hornerin	HRNR	0	0	0	0	0	910670
Lactotransferrin	LTF	31693000	32899000	17845000	20755000	60858000	0
Lumican	LUM	0	0	0	0	0	170940
Macrophage Stimulation 1	MST1	3915900	2795500	215900	1704900	255030	0
Moesin	MSN	0	0	0	0	44260	0
Nucleoporin 214	NUP214	0	0	0	0	0	412030
Peptidoglycan Recognition Protein 2	PGLYRP2	15556000	602110	169020	551060	259720	2105700
Prenylcysteine Xxidase 1	PCYOX1	0	0	0	882900	190940	0
Profilin 1	PFN1	0	0	63129	0	0	0
Proline Rich Acidic Protein 1	PRAP1	386480	190570	634280	235640	0	0
Protein S100-A7	S100A7	3742100	5171000	1885300	4187700	877410	0

## 5 Experimental section

Protein S100-A8	S100A8	2426200	18903000	18265000	4195400	3250300	223650
Protein S100-A9	S100A9	0	4138000	1431900	1317800	0	0
Proteoglycan 4	PRG4	100152790	60158537	33558997	45374725	12233000	30564
Ras-Related C3 Botulinum Toxin Substrate 3	RAC3	0	235170	0	0	492930	0
Ras-Related Protein Rap-1b	RAP1B	378470	355650	0	496680	742780	0
Scavenger Receptor Cysteine Rich Family Member with 5 Domains	SSC5D	11216	16244	0	0	0	0
Spectrin Beta, Non-Erythrocytic 4	SPTBN4	269110	158550	0	1787100	479810	0
Stratifin	SFN	0	416500	2751100	0	0	0
Stomatin	STOM	0	142350	237370	0	223240	0
Sulfhydryl Oxidase 1	QSOX1	4248000	8424400	0	2089100	0	0
Tetranectin	CLEC3B	102820000	50850000	10257000	60012000	670060	2330700
Transforming Growth Factor Beta 1	TGFBI	287020	240430	201960	0	87387	0
Vitronectin	VTN	1384300000	2891000000	1856700000	2399600000	2393100000	10026000
<b>Other Components</b>							
Active Breakpoint Cluster Region-Related Protein	ABR	184390	269620	75485	0	0	0
ADAMTS Like Protein 4	ADAMTSL4	97406	84110	0	110100	0	0
Adipocyte Plasma Membrane Associated Protein	APMAP	0	0	0	930900	0	0
Afamin	AFM	1377600	128370	0	77897	205780	9044900
Alpha-1B-glycoprotein	A1BG	12873000	929070	1676200	0	0	38928000
Alpha-2-HS-Glycoprotein	AHSG	140580000	25022000	19497000	17802000	20832000	45744000
Alpha-mannosidase 2	MAN2A1	14323000	2176600	5549000	3954000	1320300	0
Angiopoietin Related Protein 3	ANGPTL3	1691600	541380	506790	164640	182600	0
Angiotensinogen	AGT	22237000	20086000	887470	766590	0	9535100
Annexin A2	ANXA2	0	161740	1076600	638200	0	0
Ankyrin Repeat And Sterile Alpha Motif Domain Containing Protein 1B	ANKS1B	0	0	0	115690	0	0
Arginase 1	ARG1	246000	376760	1199200	1820600	254530	0
Biotinidase	BTD	0	0	0	0	0	617560
Carbonic Anhydrase 2	CA2	454650	0	0	0	0	0
Carboxypeptidase N Subunit 2	CPN2	0	0	0	0	417860	820400
Caspase 14	CASP14	0	0	319800	0	923880	0
Catalase	CAT	0	0	161210	0	28200	0

## 5 Experimental section

Cathepsin H	CTSH	202010	558620	220410	167950	537560	0
C-C Motif Chemokine Ligand 14	CCL14	0	533750	0	643600	0	0
C-C Motif Chemokine Ligand 16	CCL16	722930	0	0	0	0	0
C-C Motif Chemokine Ligand 18	CCL18	2053600	1032200	2239500	618560	0	0
CD9 Antigen	CD9	471960	673210	148880	0	785730	0
Cholinesterase	BCHE	0	0	0	0	0	56482
Corticosteroid-binding globulin	SERPINA6	0	0	0	0	0	4214300
Cullin 1	CUL1	944000	0	530320	0	0	0
Cystatin A	CSTA	0	0	0	804220	0	0
Cystatin C	CST3	62403000	46093000	17890000	30819000	3078300	743220
Cystatin M	CST6	0	590450	0	0	0	0
Cysteine Rich Secretory Protein 3	CRISP3	0	0	0	0	0	215790
Desmoglein 1	DSG1	0	0	161770	420410	26137	0
DNA Cross-Link Repair 1C	DCLRE1C	0	19699000	0	0	0	0
Docking Protein 1	DOK1	5775700	2515300	3425700	333170	2940000	0
Endomucin	EMCN	0	89544	54371	0	83029	0
Fatty Acid Binding Protein 5	FABP5	613210	1874200	4052500	1192400	665470	72345
Fetuin B	FETUB	1922900	7188800	1543400	4105700	52958000	233670
Fibrillin 1	FBN1	508500	431360	243020	212500	150590	0
Filaggrin	FLG	241210	12103	171050	126920	13575	18272
Filaggrin 2	FLG2	0	114710	185700	318960	316210	0
Galectin 3 Binding Protein	LGALS3BP	0	0	0	98956	1008500	500880
Galectin 7	LGALS7	0	856270	1163900	0	0	0
Gamma-Glutamylcyclotransferase	GGCT	0	0	0	206310	157990	0
GC Vitamin D Binding Protein	GC	13274000 0	0	0	0	212260	12877000 0
Glutathione Peroxidase 3	GPX3	1889800	430750	0	3269000	213100	448820
Glycoprotein Ib Platelet Subunit Alpha	GP1BA	0	0	0	0	0	46308
Hemoglobin Subunit Alpha	HBA1; HBA2	14754000	3547800	2704700	6768800	2033700	36463000
Hemoglobin Subunit Beta	HBB	12421000	4604400	2281100	8861200	1649100	33073000
Hemoglobin Subunit Gamma 2	HBG2	0	0	0	0	0	104870
Hemopexin	HPX	47603000 0	5576800	0	903940	530010	14651000 0
HLA Class I Histocompatibility Antigen, B Alpha Chain	HLA-B	0	0	0	0	577160	0
Hornerin	HRNR	5563800	3166100	5454600	6558500	4366600	0

## 5 Experimental section

Insulin Like Growth Factor I	IGF1	17348000	11178000	4827900	7563200	0	0
Insulin Like Growth Factor II	IGF2	19664000	16167000	6720700	1340300	4498800	86988
Insulin Like Growth Factor Binding Protein 2	IGFBP2	19219000	22152000	6457600	14096000	9299500	0
Insulin Like Growth Factor Binding Protein 3	IGFBP3	15230000	9951000	3462900	4333600	1198700	296340
Insulin Like Growth Factor Binding Protein 4	IGFBP4	21198000	23315000	3577900	19179000	10647000	0
Insulin Like Growth Factor Binding Protein 5	IGFBP5	12746000	10701000	5378000	8178100	10063000	0
Insulin Like Growth Factor Binding Protein 6	IGFBP6	1999300	2222300	0	1008400	0	0
Insulin Like Growth Factor Binding Protein 7	IGFBP7	6501500	5475200	3628200	10772000	3819600	0
Insulin Like Growth Factor Binding Protein Acid Labile Subunit	IGFALS	6775700	3317800	901370	0	0	1304900
Intellectin 1	ITLN1	666090	795980	414980	1315800	733220	0
Junction Plakoglobin	JUP	0	96216	671840	281110	379200	0
Lactate Dehydrogenase A	LDHA	201680	557110	677670	484170	213730	0
Leucine Rich Alpha-2-Glycoprotein 1	LRG1	0	0	0	0	0	1756400
Leukocyte Cell Derived Chemotaxin 2	LECT2	6523100	4174100	2327700	1952700	238450	0
Lysozyme	LYZ	6303700	1616200	854300	3322300	2009500	563050
Macrophage Migration Inhibitory Factor	MIF	0	0	440870	0	0	0
Mediator of RNA Polymerase II Transcription Subunit 30	MED30	13508000	26575000	0	6225500	7886300	0
Microfibrillar Associated Protein 5	MFAP5	0	0	643620	0	0	0
Multimerin 2	MMRN2	0	0	0	0	0	13719
N-Acetylglucosamine-1-Phosphate Transferase Subunit Gamma	GNPTG	2988700	11258000	1182500	7870900	7382000	0
N-Acylsphingosine Amidohydrolase 1	ASAH1	0	0	0	0	0	68478
Neutrophil Defensin 3	DEFA3	6463600	2196800	1961400	3197100	2126900	98284
Peptidase M20 Domain Containing 1	PM20D1	0	0	0	0	1218000	0
Periostin	POSTN	255190	245490	87720	115760	0	0
Peroxiredoxin 2	PRDX2	0	0	0	0	0	34571
Phospholipase A2 Group VII	PLA2G7	0	0	0	7492900	0	0
Phosphoserine-TRNA Kinase	PSTK	0	0	0	0	0	5992300

## 5 Experimental section

Pigment Epithelium Derived Factor	SERPINF1	21363000	83576	0	429770	211950	7150800
Pleckstrin Homology Domain Containing Family G Member 1	PLEKHG1	0	692550	694730	1278800	0	0
Polyubiquitin B; Polyubiquitin C	UBB; UBC	0	0	0	2577900	1234100	0
Proprotein Convertase Subtilisin/Kexin Type 9	PCSK9	0	29314	0	0	0	0
Protein AMBP	AMBP	39057000	15938000	7048000	10009000	12386000	17545000
Protein Kinase CAMP-Activated Catalytic Subunit Alpha	PRKACA	49983000	6213200	2653000	786680	1993100	0
Protein Kinase CAMP-Activated Catalytic Subunit Gamma	PRKACG	325110	0	0	0	0	0
Protein Z-Dependent Protease Inhibitor	SERPINA10	0	185890	0	297360	406210	0
Resistin	RETN	0	0	0	491200	771030	0
Reticulon-3 (Isoform 5)	RTN3	0	0	2227000	0	1266900	0
Retinoic acid receptor responder protein 2	RARRES2	15122000	13410000	5938000	3937500	292870	87701
Retinol-binding protein 4	RBP4	1901000	194800	191960	77820	63142	8951100
Ribonuclease A Family Member 1, Pancreatic	RNASE1	4263500	3626700	581690	0	0	0
Ribonuclease A Family Member 4	RNASE4	15682000	13115000	5781600	3129600	459170	0
Secreted Phosphoprotein 2	SPP2	0	0	0	0	238200	192320
Selenoprotein P	SEPP1	33015000	39910000	19925000	20299000	30374000	0
Serpin Family B Member 3	SERPINB3	142330	539970	9139100	82183	564020	0
Serpin Family B Member 4	SERPINB4	0	0	1707400	0	77975	0
Serpin Family B Member 12	SERPINB12	0	0	0	662370	0	0
Serum Albumin	ALB	6874200000	1306600000	7716100000	1918100000	9415300000	12485400000
Sex Hormone Binding Globulin	SHBG	479120	0	0	0	0	228250
Sirtuin 3	SIRT3	2456900000	689300000	276060000	579350000	567560000	0
Sodium Channel Protein Type 8 Subunit Alpha	SCN8A	0	161940	0	0	166160	0
Solute Carrier Organic Anion Transporter Family Member 1C1	SLCO1C1	0	0	0	0	0	74619
Spondin-1	SPON1	389940	643460	110460	24164	213550	0
Stromal Cell-Derived Factor 1	CXCL12	363010	343680	0	958790	0	0
Suprabasin	SBSN	0	119950	0	106960	240890	0
Sushi, Nidogen And EGF-like Domain-Containing Protein 1	SNED1	3417000	2141500	1368300	1063900	1093800	0

## 5 Experimental section

Sushi, Von Willebrand Factor Type A, EGF And Pentraxin Domain-Containing Protein 1	SVEP1	0	28943	8476,2	0	0	0
Syntaxin-10	STX10	8400100	15419000	4581200	0	0	221630
Tenascin	TNC	0	0	11303	37809	0	0
Tenascin-XB	TNXB	197650	250170	136540	0	0	0
Thyroxine-Binding Globulin	SERPINA7	0	0	0	0	0	2312000
Titin	TTN	0	0	51370	0	1395.7	0
Transferrin	TF	158000000	48440000	24945000	39693000	28727000	47650000
Transgelin-2	TAGLN2	231690	530400	219460	89190	0	0
Transglutaminase 3	TGM3	0	0	107260	0	99558	0
Transmembrane protein 198	TMEM198	0	0	0	0	0	2648800
Transthyretin	TTR	47753000	16044000	8608000	21122000	10708000	11822000
Triosephosphate Isomerase	TPI1	0	0	1279400	0	0	0
Tsukushin	TSKU	0	0	0	152110	0	0
Tumor Necrosis Factor Receptor Superfamily Member 1A	TNFRSF1A	0	0	0	0	0	1286100
Tyrosine-Protein Kinase Transmembrane Receptor ROR2	ROR2	0	0	0	0	0	24265
Zinc-Alpha-2-Glycoprotein	AZGP1	7384800	0	0	1887800	903470	14453000



---

# 6 References

---

## 6 References

- [1] L. Kvítek, A. Panáček, J. Soukupová, M. Kolář, R. Večeřová, R. Prucek, M. Holecová, R. Zbořil, *J. Phys. Chem. C* **2008**, *112*, 5825.
- [2] I. H. El-Sayed, X. Huang, M. A. El-Sayed, *Nano Lett.* **2005**, *5*, 829.
- [3] S. Hwang, J. Nam, S. Jung, J. Song, H. Doh, S. Kim, *Nanomedicine* **2014**, *9*, 2003.
- [4] G. F. Paciotti, D. G. I. Kingston, L. Tamarkin, *Drug Dev. Res.* **2006**, *67*, 47.
- [5] G. Han, P. Ghosh, V. M. Rotello, *Nanomedicine* **2007**, *2*, 113.
- [6] S. M. Ansar, M. Gadogbe, K. Siriwardana, J. Y. Howe, S. Dogel, H. Hosseinkhannazer, W. E. Collier, J. Rodriguez, S. Zou, D. Zhang, *J. Phys. Chem. C* **2014**, *118*, 24925.
- [7] M. Popa, T. Pradell, D. Crespo, J. M. Calderón-Moreno, *Colloids Surf. Physicochem. Eng. Aspects* **2007**, *303*, 184.
- [8] K. Rahme, L. Chen, R. G. Hobbs, M. A. Morris, C. O'Driscoll, J. D. Holmes, *RSC Adv.* **2013**, *3*, 6085.
- [9] R. Javed, M. Zia, S. Naz, S. O. Aisida, N. u. Ain, Q. Ao, *J. Nanobiotechnology* **2020**, *18*, 172.
- [10] C. Brandenberger, C. Mühlfeld, Z. Ali, A.-G. Lenz, O. Schmid, W. J. Parak, P. Gehr, B. Rothen-Rutishauser, *Small* **2010**, *6*, 1669.
- [11] M. Tejamaya, I. Römer, R. C. Merrifield, J. R. Lead, *Environmental Science & Technology* **2012**, *46*, 7011.
- [12] X. D. Zhang, D. Wu, X. Shen, P. X. Liu, N. Yang, B. Zhao, H. Zhang, Y. M. Sun, L. A. Zhang, F. Y. Fan, *Int J Nanomedicine* **2011**, *6*, 2071.
- [13] H. Otsuka, Y. Nagasaki, K. Kataoka, *Adv. Drug Del. Rev.* **2003**, *55*, 403.
- [14] A. Abdelfattah, A. E. Aboutaleb, A. B. M. Abdel-Aal, A. A. H. Abdellatif, H. M. Tawfeek, S. I. Abdel-Rahman, *J. Drug Deliv. Sci. Technol.* **2022**, *71*, 103347.
- [15] G. Zhang, Z. Yang, W. Lu, R. Zhang, Q. Huang, M. Tian, L. Li, D. Liang, C. Li, *Biomaterials* **2009**, *30*, 1928.
- [16] S. Singh, F. Topuz, K. Hahn, K. Albrecht, J. Groll, *Angew. Chem. Int. Ed.* **2013**, *52*, 3000.
- [17] S. Feineis, J. Lutz, L. Heffele, E. Endl, K. Albrecht, J. Groll, *Adv. Mater.* **2018**, *30*, 1704972.
- [18] X. Duan, Y. Li, *Small* **2013**, *9*, 1521.
- [19] R. Augustine, A. Hasan, R. Primavera, R. J. Wilson, A. S. Thakor, B. D. Kevadiya, *Materials Today Communications* **2020**, *25*, 101692.
- [20] J. P. M. Almeida, A. L. Chen, A. Foster, R. Drezek, *Nanomedicine* **2011**, *6*, 815.
- [21] K. Partikel, R. Korte, D. Mulac, H.-U. Humpf, K. Langer, *Beilstein J. Nanotechnol.* **2019**, *10*, 1002.
- [22] S. Tenzer, D. Docter, J. Kuharev, A. Musyanovych, V. Fetz, R. Hecht, F. Schlenk, D. Fischer, K. Kiouptsi, C. Reinhardt, K. Landfester, H. Schild, M. Maskos, S. K. Knauer, R. H. Stauber, *Nat. Nanotechnol.* **2013**, *8*, 772.
- [23] T. Bewersdorff, E. A. Glitscher, J. Bergueiro, M. Eravci, E. Miceli, A. Haase, M. Calderón, *Mater. Sci. Eng. C* **2020**, *117*, 111270.
- [24] S. Schöttler, K. Landfester, V. Mailänder, *Angew. Chem. Int. Ed.* **2016**, *55*, 8806.
- [25] J. Lipka, M. Semmler-Behnke, R. A. Sperling, A. Wenk, S. Takenaka, C. Schleh, T. Kissel, W. J. Parak, W. G. Kreyling, *Biomaterials* **2010**, *31*, 6574.
- [26] M. Kumagai, T. K. Sarma, H. Cabral, S. Kaida, M. Sekino, N. Herlambang, K. Osada, M. R. Kano, N. Nishiyama, K. Kataoka, *Macromol. Rapid Commun.* **2010**, *31*, 1521.
- [27] C. D. Walkey, J. B. Olsen, H. Guo, A. Emili, W. C. W. Chan, *J. Am. Chem. Soc.* **2012**, *134*, 2139.
- [28] L. E. van Vlerken, T. K. Vyas, M. M. Amiji, *Pharm. Res.* **2007**, *24*, 1405.

- [29] M. Bauer, C. Lautenschlaeger, K. Kempe, L. Tauhardt, U. S. Schubert, D. Fischer, *Macromol. Biosci.* **2012**, *12*, 986.
- [30] S. Schöttler, G. Becker, S. Winzen, T. Steinbach, K. Mohr, K. Landfester, V. Mailänder, F. R. Wurm, *Nature nanotechnology* **2016**, *11*, 372.
- [31] D. J. Bharali, S. K. Sahoo, S. Mozumdar, A. Maitra, *J. Colloid Interface Sci.* **2003**, *258*, 415.
- [32] R. K. Kainthan, D. E. Brooks, *Biomaterials* **2007**, *28*, 4779.
- [33] J. Y. PY, R. K. Kainthan, Y. Zou, M. Chiao, J. N. Kizhakkedathu, *Langmuir* **2008**, *24*, 4907.
- [34] M. Weinhart, I. Grunwald, M. Wyszogrodzka, L. Gaetjen, A. Hartwig, R. Haag, *Chem. Asian J.* **2010**, *5*, 1992.
- [35] Y. Zou, S. Ito, F. Yoshino, Y. Suzuki, L. Zhao, N. Komatsu, *ACS nano* **2020**, *14*, 7216.
- [36] L. Wang, K. G. Neoh, E.-T. Kang, B. Shuter, *Biomaterials* **2011**, *32*, 2166.
- [37] H. S. Al-Maliki, S. Martinez, P. Piszczatowski, J. W. Bennett, *Mycobiology* **2017**, *45*, 233.
- [38] R. D. Rossoni, F. de Camargo Ribeiro, H. F. S. Dos Santos, J. D. Dos Santos, N. de Sousa Oliveira, M. T. dos Santos Dutra, S. A. B. de Lapena, J. C. Junqueira, *Arch. Oral Biol.* **2019**, *101*, 13.
- [39] P. Rajasekharreddy, P. U. Rani, S. Mattapally, S. K. Banerjee, *Mater. Sci. Eng. C* **2017**, *77*, 990.
- [40] Y. Orihara, H. Hamamoto, H. Kasuga, T. Shimada, Y. Kawaguchi, K. Sekimizu, *J. Gen. Virol.* **2008**, *89*, 188.
- [41] C. Kaito, K. Sekimizu, *Drug Discov. Ther.* **2007**, *1*, 89.
- [42] H. Hamamoto, R. Horie, K. Sekimizu, *Sci. Rep.* **2019**, *9*, 1.
- [43] S. Panthee, A. Paudel, H. Hamamoto, K. Sekimizu, *Front. Microbiol.* **2017**, *8*, 373.
- [44] J. Lutz, K. Albrecht, J. Groll, *Adv. NanoBiomed Res.* **2021**, 2000074.
- [45] I. Freestone, N. Meeks, M. Sax, C. Higgitt, *Gold bulletin* **2007**, *40*, 270.
- [46] R. H. Brill, **1965**.
- [47] D. J. Barber, I. C. Freestone, *Archaeometry* **1990**, *32*, 33.
- [48] M. Faraday, *Philos. Trans. R. Soc. London* **1857**, 145.
- [49] L. Lorenz, *AnP* **1880**, *247*, 70.
- [50] J. C. MAXWELL-GARNETT, *Phil. Trans. R. Soc. Lond, A* **1904**, *203*, 385.
- [51] G. Mie, *AnP* **1908**, *330*, 377.
- [52] U. Kreibig, M. Vollmer, *Optical properties of metal clusters, Vol. 25*, Springer Science & Business Media, **2013**.
- [53] U. Kreibig, P. Zacharias, *ZPhyA* **1970**, *231*, 128.
- [54] C. F. Bohren, D. R. Huffman, *Light by Small* **1983**.
- [55] K. L. Kelly, E. Coronado, L. L. Zhao, G. C. Schatz, ACS Publications, **2003**.
- [56] D. Paramelle, A. Sadovoy, S. Gorelik, P. Free, J. Hobley, D. G. Fernig, *Analyst* **2014**, *139*, 4855.
- [57] S. Link, M. A. El-Sayed, *J. Phys. Chem. B* **1999**, *103*, 4212.
- [58] J. Tan, B. Hao, C. Wang, Y. Ren, H. Hao, R. Yang, *Journal of Forensic Science and Medicine* **2016**, *2*, 195.
- [59] M. Garcia, J. De la Venta, P. Crespo, J. Llopis, S. Penadés, A. Fernández, A. Hernando, *PhRvB* **2005**, *72*, 241403.
- [60] Yu, S.-S. Chang, C.-L. Lee, C. R. C. Wang, *J. Phys. Chem. B* **1997**, *101*, 6661.
- [61] A. González, C. Noguez, *Journal of computational and theoretical nanoscience* **2007**, *4*, 231.
- [62] S. Underwood, P. Mulvaney, *Langmuir* **1994**, *10*, 3427.
- [63] K. H. Su, Q. H. Wei, X. Zhang, J. J. Mock, D. R. Smith, S. Schultz, *Nano Lett.* **2003**, *3*, 1087.

## 6 References

- [64] M. K. Kinnan, G. Chumanov, *J. Phys. Chem. C* **2010**, *114*, 7496.
- [65] S. M. Shawky, D. Bald, H. M. Azzazy, *Clin. Biochem.* **2010**, *43*, 1163.
- [66] R. Rojanathanes, A. Sereemasapun, N. Pimpha, V. Buasorn, P. Ekawong, V. Wiwanitkit, *Taiwanese Journal of Obstetrics and Gynecology* **2008**, *47*, 296.
- [67] B. Gosselin, M. Retout, R. Dutour, L. Troian-Gautier, R. Bevernaegie, S. Herens, P. Lefèvre, O. Denis, G. Bruylants, I. Jabin, *Analytical Chemistry* **2022**, *94*, 7383.
- [68] J. Wang, A. J. Drelich, C. M. Hopkins, S. Mecozzi, L. Li, G. Kwon, S. Hong, *WIREs Nanomedicine and Nanobiotechnology* **2022**, *14*, e1754.
- [69] S. Her, D. A. Jaffray, C. Allen, *Adv. Drug Del. Rev.* **2017**, *109*, 84.
- [70] K. A. Homan, J. Shah, S. Gomez, H. Gensler, A. B. Karpouk, L. Brannon-Peppas, S. Y. Emelianov, *Journal of biomedical optics* **2010**, *15*, 021316.
- [71] X. Huang, M. A. El-Sayed, *Journal of advanced research* **2010**, *1*, 13.
- [72] K. Tao, G. K. Murakonda, R. Jarubula, *Journal of Cluster Science* **2021**.
- [73] X. Huang, P. K. Jain, I. H. El-Sayed, M. A. El-Sayed, *Lasers Med. Sci.* **2007**, *23*, 217.
- [74] P. Bose, A. Priyam, R. Kar, S. P. Pattanayak, *RSC Adv.* **2020**, *10*, 31961.
- [75] V. O. Shipunova, M. M. Belova, P. A. Kotelnikova, O. N. Shilova, A. B. Mirkasymov, N. V. Danilova, E. N. Komedchikova, R. Popovtzer, S. M. Deyev, M. P. Nikitin, *Pharmaceutics* **2022**, *14*, 1013.
- [76] S. Haque, C. C. Norbert, R. Acharyya, S. Mukherjee, M. Kathirvel, C. R. Patra, *Cancers (Basel)* **2021**, *13*, 6114.
- [77] A. O. Elzoghby, A. L. Hemasa, M. S. Freag, *J. Control. Release* **2016**, *243*, 303.
- [78] P. Prasher, M. Sharma, H. Mudila, G. Gupta, A. K. Sharma, D. Kumar, H. A. Bakshi, P. Negi, D. N. Kapoor, D. K. Chellappan, M. M. Tambuwala, K. Dua, *Colloid and Interface Science Communications* **2020**, *35*, 100244.
- [79] E. C. Dreaden, A. M. Alkilany, X. Huang, C. J. Murphy, M. A. El-Sayed, *Chem. Soc. Rev.* **2012**, *41*, 2740.
- [80] D. Sun, W. Zhang, N. Li, Z. Zhao, Z. Mou, E. Yang, W. Wang, *Mater. Sci. Eng. C* **2016**, *63*, 522.
- [81] F. Rudnitski, S. Feineis, R. Rahmzadeh, E. Endl, J. Lutz, J. Groll, G. Hüttmann, *Journal of Biophotonics* **2018**, *11*, e201700329.
- [82] N. L. Rosi, D. A. Giljohann, C. S. Thaxton, A. K. R. Lytton-Jean, M. S. Han, C. A. Mirkin, *Science* **2006**, *312*, 1027.
- [83] X. Wu, L. Xu, W. Ma, L. Liu, H. Kuang, W. Yan, L. Wang, C. Xu, *Adv. Funct. Mater.* **2015**, *25*, 850.
- [84] N. Durán, C. P. Silveira, M. Durán, D. S. T. Martinez, *J. Nanobiotechnology* **2015**, *13*, 55.
- [85] D. V. Sotnikov, A. N. Berlina, V. S. Ivanov, A. V. Zherdev, B. B. Dzantiev, *Colloids Surf. B: Biointerfaces* **2019**, *173*, 557.
- [86] S. Patra, S. Mukherjee, A. K. Barui, A. Ganguly, B. Sreedhar, C. R. Patra, *Mater. Sci. Eng. C* **2015**, *53*, 298.
- [87] H. I. O. Gomes, C. S. M. Martins, J. A. V. Prior, *Nanomaterials* **2021**, *11*, 964.
- [88] L. A. Austin, M. A. Mackey, E. C. Dreaden, M. A. El-Sayed, *Archives of Toxicology* **2014**, *88*, 1391.
- [89] Y.-H. Chen, C.-Y. Tsai, P.-Y. Huang, M.-Y. Chang, P.-C. Cheng, C.-H. Chou, D.-H. Chen, C.-R. Wang, A.-L. Shiau, C.-L. Wu, *Mol. Pharm.* **2007**, *4*, 713.
- [90] A. Anwar, R. Siddiqui, M. A. Hussain, D. Ahmed, M. R. Shah, N. A. Khan, *Parasitology Research* **2018**, *117*, 265.

- [91] R. I. MacCuspie, *Journal of Nanoparticle Research* **2011**, *13*, 2893.
- [92] Â. Barreto, L. G. Luis, A. V. Girão, T. Trindade, A. M. V. M. Soares, M. Oliveira, *Journal of Nanoparticle Research* **2015**, *17*, 493.
- [93] H. Sharma, P. K. Mishra, S. Talegaonkar, B. Vaidya, *Drug Discovery Today* **2015**, *20*, 1143.
- [94] S. D. Brown, P. Nativo, J.-A. Smith, D. Stirling, P. R. Edwards, B. Venugopal, D. J. Flint, J. A. Plumb, D. Graham, N. J. Wheate, *J. Am. Chem. Soc.* **2010**, *132*, 4678.
- [95] R. Huschka, O. Neumann, A. Barhoumi, N. J. Halas, *Nano Lett.* **2010**, *10*, 4117.
- [96] L. Qiu, J.-W. Li, C.-Y. Hong, C.-Y. Pan, *ACS Appl. Mater. Interfaces* **2017**, *9*, 40887.
- [97] R. Hong, G. Han, J. M. Fernández, B.-j. Kim, N. S. Forbes, V. M. Rotello, *J. Am. Chem. Soc.* **2006**, *128*, 1078.
- [98] W. Eck, G. Craig, A. Sigdel, G. Ritter, L. J. Old, L. Tang, M. F. Brennan, P. J. Allen, M. D. Mason, *ACS Nano* **2008**, *2*, 2263.
- [99] S. Mukherjee, D. Chowdhury, R. Kotcherlakota, S. Patra, B. Vinothkumar, M. P. Bhadra, B. Sreedhar, C. R. Patra, *Theranostics* **2014**, *4*, 316.
- [100] R. Bardhan, S. Lal, A. Joshi, N. J. Halas, *Acc. Chem. Res.* **2011**, *44*, 936.
- [101] A. Sironmani, K. Daniel, *Drug discovery and development—present and future* **2011**, 463.
- [102] A.-C. Burduşel, O. Gherasim, A. M. Grumezescu, L. Mogoantă, A. Fikai, E. Andronescu, *Nanomaterials* **2018**, *8*, 681.
- [103] X.-F. Zhang, Z.-G. Liu, W. Shen, S. Gurunathan, *Int. J. Mol. Sci.* **2016**, *17*, 1534.
- [104] B. Derjaguin, L. Landau, *Progress in Surface Science* **1993**, *43*, 30.
- [105] A. V. Gurumoorthy, K. Khan, *Recent Research in Science and Technology* **2011**, *3*.
- [106] L. L. Rouhana, J. A. Jaber, J. B. Schlenoff, *Langmuir* **2007**, *23*, 12799.
- [107] J. Polte, *CrystEngComm* **2015**, *17*, 6809.
- [108] F. Matter, A. L. Luna, M. Niederberger, *Nano Today* **2020**, *30*, 100827.
- [109] J. Turkevich, P. C. Stevenson, J. Hillier, *Discuss. Faraday Soc.* **1951**, *11*, 55.
- [110] G. Frens, *NPhS* **1973**, *241*, 20.
- [111] N. G. Bastús, J. Comenge, V. Puntès, *Langmuir* **2011**, *27*, 11098.
- [112] J. Piella, N. G. Bastús, V. Puntès, *Chem. Mater.* **2016**, *28*, 1066.
- [113] Z. S. Pillai, P. V. Kamat, *J. Phys. Chem. B* **2004**, *108*, 945.
- [114] T. M. Tolaymat, A. M. El Badawy, A. Genaidy, K. G. Scheckel, T. P. Luxton, M. Suidan, *Science of the Total Environment* **2010**, *408*, 999.
- [115] T. L. Moore, L. Rodriguez-Lorenzo, V. Hirsch, S. Balog, D. Urban, C. Jud, B. Rothen-Rutishauser, M. Lattuada, A. Petri-Fink, *Chem. Soc. Rev.* **2015**, *44*, 6287.
- [116] J. Nam, N. Won, H. Jin, H. Chung, S. Kim, *J. Am. Chem. Soc.* **2009**, *131*, 13639.
- [117] D. H. Napper, *J. Colloid Interface Sci.* **1977**, *58*, 390.
- [118] S. M. Louie, R. D. Tilton, G. V. Lowry, *Environmental Science: Nano* **2016**, *3*, 283.
- [119] A. J. Worthen, V. Tran, K. A. Cornell, T. M. Truskett, K. P. Johnston, *Soft Matter* **2016**, *12*, 2025.
- [120] Z. Liu, L. Luo, Y. Dong, G. Weng, J. Li, *J. Colloid Interface Sci.* **2011**, *363*, 182.
- [121] R. Sardar, J.-W. Park, J. S. Shumaker-Parry, *Langmuir* **2007**, *23*, 11883.
- [122] S. Rucareanu, M. Maccarini, J. L. Shepherd, R. B. Lennox, *Journal of Materials Chemistry* **2008**, *18*, 5830.
- [123] R. G. Pearson, *Survey of Progress in Chemistry* **1969**, *5*, 1.
- [124] M. Brust, M. Walker, D. Bethell, D. J. Schiffrin, R. Whyman, *J. Chem. Soc., Chem. Commun.* **1994**, 801.

## 6 References

- [125] A. Badia, S. Singh, L. Demers, L. Cuccia, G. R. Brown, R. B. Lennox, *Chem. - Eur. J.* **1996**, *2*, 359.
- [126] I. Fratoddi, I. Venditti, C. Battocchio, G. Polzonetti, C. Cametti, M. V. Russo, *Nanoscale Research Letters* **2011**, *6*, 98.
- [127] A. Caragheorghopol, V. Chechik, *Physical Chemistry Chemical Physics* **2008**, *10*, 5029.
- [128] M. G. Bellino, E. J. Calvo, G. Gordillo, *Physical Chemistry Chemical Physics* **2004**, *6*, 424.
- [129] D. W. Jacobsen, *Clin. Chem.* **1998**, *44*, 1833.
- [130] A. Ravindran, N. Chandrasekaran, A. Mukherjee, *Current Nanoscience* **2012**, *8*, 141.
- [131] F. X. Zhang, L. Han, L. B. Israel, J. G. Daras, M. M. Maye, N. K. Ly, C.-J. Zhong, *Analyst* **2002**, *127*, 462.
- [132] R. Arvizo, R. Bhattacharya, P. Mukherjee, *Expert Opin. Drug. Deliv.* **2010**, *7*, 753.
- [133] C. G. England, J. S. Huang, K. T. James, G. Zhang, A. M. Gobin, H. B. Frieboes, *PLoS One* **2015**, *10*, e0129172.
- [134] P. Ionita, B. C. Gilbert, V. Chechik, *Angew. Chem.* **2005**, *117*, 3786.
- [135] M. Montalti, L. Prodi, N. Zaccheroni, R. Baxter, G. Teobaldi, F. Zerbetto, *Langmuir* **2003**, *19*, 5172.
- [136] A. Kassam, G. Bremner, B. Clark, G. Ulibarri, R. B. Lennox, *J. Am. Chem. Soc.* **2006**, *128*, 3476.
- [137] R. Hong, J. M. Fernández, H. Nakade, R. Arvizo, T. Emrick, V. M. Rotello, *Chemical Communications* **2006**, 2347.
- [138] M. J. Hostetler, A. C. Templeton, R. W. Murray, *Langmuir* **1999**, *15*, 3782.
- [139] A. Henglein, D. Meisel, *J. Phys. Chem. B* **1998**, *102*, 8364.
- [140] L. A. Porter Jr, D. Ji, S. L. Westcott, M. Graupe, R. S. Czernuszewicz, N. J. Halas, T. R. Lee, *Langmuir* **1998**, *14*, 7378.
- [141] T. Yonezawa, K. Yasui, N. Kimizuka, *Langmuir* **2001**, *17*, 271.
- [142] Y.-C. Chung, I. H. Chen, C.-J. Chen, *Biomaterials* **2008**, *29*, 1807.
- [143] E. J. Shelley, D. Ryan, S. R. Johnson, M. Couillard, D. Fitzmaurice, P. D. Nellist, Y. Chen, R. E. Palmer, J. A. Preece, *Langmuir* **2002**, *18*, 1791.
- [144] X.-M. Li, M. R. De Jong, K. Inoue, S. Shinkai, J. Huskens, D. N. Reinhoudt, *Journal of materials chemistry* **2001**, *11*, 1919.
- [145] S. Aryal, R. B. K.C, N. Bhattarai, B. M. Lee, H. Y. Kim, *Materials Chemistry and Physics* **2006**, *98*, 463.
- [146] N. Bloise, A. Massironi, C. Della Pina, J. Alongi, S. Siciliani, A. Manfredi, M. Biggiogera, M. Rossi, P. Ferruti, E. Ranucci, *Front. Bioeng. Biotechnol.* **2020**, *8*, 132.
- [147] B. Khan, M. Nawaz, R. Hussain, G. J. Price, M. F. Warsi, M. Waseem, *Chemical Papers* **2021**, *75*, 743.
- [148] S. Singh, F. Topuz, K. Hahn, K. Albrecht, J. Groll, *Angew. Chem. Int. Ed.* **2013**, *52*, 3000.
- [149] R. A. Sperling, W. J. Parak, *Philosophical Transactions of the Royal Society A: Mathematical, Physical and Engineering Sciences* **2010**, *368*, 1333.
- [150] J. Klein, *Journal of the Chemical Society, Faraday Transactions 1: Physical Chemistry in Condensed Phases* **1983**, *79*, 99.
- [151] R. R. Netz, D. Andelman, *Physics Reports* **2003**, *380*, 1.
- [152] G. Fleer, M. C. Stuart, J. M. Scheutjens, T. Cosgrove, B. Vincent, *Polymers at interfaces*, Springer Science & Business Media, **1993**.
- [153] A. M. Atta, H. A. Allohedan, A. O. Ezzat, Z. A. Issa, *Polym. Sci. Ser. B* **2014**, *56*, 762.

- [154] J. Liu, C. Detrembleur, M. Hurtgen, A. Debuigne, M.-C. De Pauw-Gillet, S. Mornet, E. Duguet, C. Jérôme, *Polymer Chemistry* **2014**, *5*, 5289.
- [155] C. Biver, R. Hariharan, J. Mays, W. B. Russel, *Macromolecules* **1997**, *30*, 1787.
- [156] M. J. Garvey, T. F. Tadros, B. Vincent, *J. Colloid Interface Sci.* **1976**, *55*, 440.
- [157] M. Elimelech, J. Gregory, X. Jia, *Particle deposition and aggregation: measurement, modelling and simulation*, Butterworth-Heinemann, **2013**.
- [158] H. S. Toh, C. Batchelor-McAuley, K. Tschulik, R. G. Compton, *Sci. China Chem.* **2014**, *57*, 1199.
- [159] D. J. Lavrich, S. M. Wetterer, S. L. Bernasek, G. Scoles, *J. Phys. Chem. B* **1998**, *102*, 3456.
- [160] M. A. Bryant, J. E. Pemberton, *J. Am. Chem. Soc.* **1991**, *113*, 8284.
- [161] E. B. Troughton, C. D. Bain, G. M. Whitesides, R. G. Nuzzo, D. L. Allara, M. D. Porter, *Langmuir* **1988**, *4*, 365.
- [162] M. D. Porter, T. B. Bright, D. L. Allara, C. E. Chidsey, *J. Am. Chem. Soc.* **1987**, *109*, 3559.
- [163] Z. Wang, J. Chen, S. Oyola-Reynoso, M. Thuo, *Coatings* **2015**, *5*, 1034.
- [164] J. B. Schlenoff, M. Li, H. Ly, *J. Am. Chem. Soc.* **1995**, *117*, 12528.
- [165] R. G. Nuzzo, B. R. Zegarski, L. H. Dubois, *J. Am. Chem. Soc.* **1987**, *109*, 733.
- [166] H. Sellers, A. Ulman, Y. Shnidman, J. E. Eilers, *J. Am. Chem. Soc.* **1993**, *115*, 9389.
- [167] J. Noh, H. S. Kato, M. Kawai, M. Hara, *J. Phys. Chem. B* **2002**, *106*, 13268.
- [168] C. D. Bain, E. B. Troughton, Y. T. Tao, J. Evall, G. M. Whitesides, R. G. Nuzzo, *J. Am. Chem. Soc.* **1989**, *111*, 321.
- [169] T. Hayashi, M. Hara, *Current Physical Chemistry* **2011**, *1*, 90.
- [170] I. Choi, H. Kang, S. Han, J. W. Han, J. Noh, *Bull. Korean Chem. Soc.* **2015**, *36*, 1067.
- [171] S. M. Wetterer, D. J. Lavrich, T. Cummings, S. L. Bernasek, G. Scoles, *J. Phys. Chem. B* **1998**, *102*, 9266.
- [172] E. Ito, H. Ito, H. Kang, T. Hayashi, M. Hara, J. Noh, *J. Phys. Chem. C* **2012**, *116*, 17586.
- [173] D. R. Lide, *CRC handbook of chemistry and physics, Vol. 85*, CRC press, **2004**.
- [174] C.-J. Zhong, M. D. Porter, *J. Am. Chem. Soc.* **1994**, *116*, 11616.
- [175] C. Sandroff, D. Herschbach, *The Journal of Physical Chemistry* **1982**, *86*, 3277.
- [176] M. W. J. Beulen, B.-H. Huisman, P. A. van der Heijden, F. C. J. M. van Veggel, M. G. Simons, E. M. E. F. Biemond, P. J. de Lange, D. N. Reinhoudt, *Langmuir* **1996**, *12*, 6170.
- [177] C. Jung, O. Dannenberger, Y. Xu, M. Buck, M. Grunze, *Langmuir* **1998**, *14*, 1103.
- [178] C.-J. Zhong, R. C. Brush, J. Anderegg, M. D. Porter, *Langmuir* **1999**, *15*, 518.
- [179] J. Noh, T. Murase, K. Nakajima, H. Lee, M. Hara, *J. Phys. Chem. B* **2000**, *104*, 7411.
- [180] M. J. Hostetler, J. E. Wingate, C.-J. Zhong, J. E. Harris, R. W. Vachet, M. R. Clark, J. D. Londono, S. J. Green, J. J. Stokes, G. D. Wignall, G. L. Glish, M. D. Porter, N. D. Evans, R. W. Murray, *Langmuir* **1998**, *14*, 17.
- [181] J. C. Love, L. A. Estroff, J. K. Kriebel, R. G. Nuzzo, G. M. Whitesides, *Chem. Rev.* **2005**, *105*, 1103.
- [182] A. A. Levchenko, C. K. Yee, A. N. Parikh, A. Navrotsky, *Chem. Mater.* **2005**, *17*, 5428.
- [183] D. B. Pedersen, S. Duncan, *J. Phys. Chem. A* **2005**, *109*, 11172.
- [184] P. Harder, M. Grunze, R. Dahint, G. M. Whitesides, P. E. Laibinis, *J. Phys. Chem. B* **1998**, *102*, 426.
- [185] V. Silin, H. Weetall, D. J. Vanderah, *J. Colloid Interface Sci.* **1997**, *185*, 94.
- [186] A. S. Karakoti, S. Das, S. Thevuthasan, S. Seal, *Angew. Chem. Int. Ed.* **2011**, *50*, 1980.

## 6 References

- [187] E. Pensa, E. Cortés, G. Corthey, P. Carro, C. Vericat, M. H. Fonticelli, G. Benítez, A. A. Rubert, R. C. Salvarezza, *Acc. Chem. Res.* **2012**, *45*, 1183.
- [188] J. R. Reimers, M. J. Ford, A. Halder, J. Ulstrup, N. S. Hush, *Proc. Natl. Acad. Sci.* **2016**, *113*, E1424.
- [189] H. Häkkinen, *Nat. Chem.* **2012**, *4*, 443.
- [190] M. Wu, J. Zhao, D. M. Chevrier, P. Zhang, L. Liu, *J. Phys. Chem. C* **2019**, *123*, 6010.
- [191] M. K. Corbierre, J. Beerens, R. B. Lennox, *Chem. Mater.* **2005**, *17*, 5774.
- [192] J. M. Forward, D. Bohmann, J. P. Fackler Jr, R. J. Staples, *Inorganic chemistry* **1995**, *34*, 6330.
- [193] J. R. Reimers, M. J. Ford, S. M. Marcuccio, J. Ulstrup, N. S. Hush, *Nature Reviews Chemistry* **2017**, *1*, 0017.
- [194] D. Kim, S. Park, J. H. Lee, Y. Y. Jeong, S. Jon, *J. Am. Chem. Soc.* **2007**, *129*, 7661.
- [195] W. Yang, H. Liang, S. Ma, D. Wang, J. Huang, *Sustain. Mater. Technol.* **2019**, *22*, e00109.
- [196] E. H. Jeong, G. Jung, C. A. Hong, H. Lee, *Arch. Pharm. Res.* **2014**, *37*, 53.
- [197] N. L. Anderson, N. G. Anderson, *Mol. Cell. Proteomics* **2002**, *1*, 845.
- [198] S. T. Yang, Y. Liu, Y. W. Wang, A. Cao, *Small* **2013**, *9*, 1635.
- [199] F. Darabi Sahneh, C. Scoglio, J. Riviere, *PLoS One* **2013**, *8*, e64690.
- [200] R. García-Álvarez, M. Vallet-Regí, *Nanomaterials* **2021**, *11*, 888.
- [201] C. D. Walkey, W. C. W. Chan, *Chem. Soc. Rev.* **2012**, *41*, 2780.
- [202] I. Lynch, T. Cedervall, M. Lundqvist, C. Cabaleiro-Lago, S. Linse, K. A. Dawson, *Adv. Colloid Interface Sci.* **2007**, *134-135*, 167.
- [203] G. Maiorano, S. Sabella, B. Sorce, V. Brunetti, M. A. Malvindi, R. Cingolani, P. P. Pompa, *ACS Nano* **2010**, *4*, 7481.
- [204] A. L. Barrán-Berdón, D. Pozzi, G. Caracciolo, A. L. Capriotti, G. Caruso, C. Cavaliere, A. Riccioli, S. Palchetti, A. Laganà, *Langmuir* **2013**, *29*, 6485.
- [205] R. García-Álvarez, M. Hadjidemetriou, A. Sánchez-Iglesias, L. M. Liz-Marzán, K. Kostarelos, *Nanoscale* **2018**, *10*, 1256.
- [206] M. Xu, M. G. Soliman, X. Sun, B. Pelaz, N. Feliu, W. J. Parak, S. Liu, *ACS Nano* **2018**, *12*, 10104.
- [207] M. P. Monopoli, D. Walczyk, A. Campbell, G. Elia, I. Lynch, F. Baldelli Bombelli, K. A. Dawson, *J. Am. Chem. Soc.* **2011**, *133*, 2525.
- [208] K. Kaur, J. A. Forrest, *Langmuir* **2012**, *28*, 2736.
- [209] J. Piella, N. G. Bastús, V. Puentes, *Bioconjug. Chem.* **2017**, *28*, 88.
- [210] M. A. Dobrovolskaia, A. K. Patri, J. Zheng, J. D. Clogston, N. Ayub, P. Aggarwal, B. W. Neun, J. B. Hall, S. E. McNeil, *Nanomedicine* **2009**, *5*, 106.
- [211] A. Gessner, A. Lieske, B. R. Paulke, R. H. Müller, *Eur. J. Pharm. Biopharm.* **2002**, *54*, 165.
- [212] A. Gessner, A. Lieske, B.-R. Paulke, R. H. Müller, *J. Biomed. Mater. Res. Part A* **2003**, *65A*, 319.
- [213] B. D. Johnston, W. G. Kreyling, C. Pfeiffer, M. Schäffler, H. Sarioglu, S. Ristig, S. Hirn, N. Haberl, S. Thalhammer, S. M. Hauck, M. Semmler-Behnke, M. Eppler, J. Hühn, P. Del Pino, W. J. Parak, *Adv. Funct. Mater.* **2017**, *27*, 1701956.
- [214] A. Gessner, R. Waicz, A. Lieske, B. R. Paulke, K. Mäder, R. H. Müller, *Int. J. Pharm.* **2000**, *196*, 245.
- [215] T. Cedervall, I. Lynch, S. Lindman, T. Berggård, E. Thulin, H. Nilsson, K. A. Dawson, S. Linse, *Proc. Natl. Acad. Sci.* **2007**, *104*, 2050.
- [216] Q. Yu, L. Zhao, C. Guo, B. Yan, G. Su, *Front Bioeng Biotechnol* **2020**, *8*, 210.
- [217] S. Lindman, I. Lynch, E. Thulin, H. Nilsson, K. A. Dawson, S. Linse, *Nano Lett.* **2007**, *7*, 914.



- [218] H. R. Kim, K. Andrieux, S. Gil, M. Taverna, H. Chacun, D. Desmaële, F. Taran, D. Georjin, P. Couvreur, *Biomacromolecules* **2007**, *8*, 793.
- [219] Z. Zhang, K. Van Steendam, S. Maji, L. Balcaen, Y. Anoshkina, Q. Zhang, G. Vanluchene, R. De Rycke, F. Van Haecke, D. Deforce, R. Hoogenboom, B. G. De Geest, *Adv. Funct. Mater.* **2015**, *25*, 3433.
- [220] A. Abuchowski, T. Van Es, N. Palczuk, F. Davis, *J. Biol. Chem.* **1977**, *252*, 3578.
- [221] A. Abuchowski, J. R. McCoy, N. C. Palczuk, T. van Es, F. F. Davis, *J. Biol. Chem.* **1977**, *252*, 3582.
- [222] M. Roberts, M. Bentley, J. Harris, *Adv. Drug Del. Rev.* **2002**, *54*, 459.
- [223] F. M. Veronese, *Biomaterials* **2001**, *22*, 405.
- [224] J. M. Harris, R. B. Chess, *Nat. Rev. Drug Discov.* **2003**, *2*, 214.
- [225] R. Haag, F. Kratz, *Angew. Chem. Int. Ed.* **2006**, *45*, 1198.
- [226] A. Kolate, D. Baradia, S. Patil, I. Vhora, G. Kore, A. Misra, *J. Control. Release* **2014**, *192*, 67.
- [227] F. M. Veronese, G. Pasut, *Drug Discovery Today* **2005**, *10*, 1451.
- [228] Y. Zhang, N. Kohler, M. Zhang, *Biomaterials* **2002**, *23*, 1553.
- [229] C. Brandenberger, C. Mühlfeld, Z. Ali, A. G. Lenz, O. Schmid, W. J. Parak, P. Gehr, B. Rothen-Rutishauser, *Small* **2010**, *6*, 1669.
- [230] I. Brigger, C. Dubernet, P. Couvreur, *Adv. Drug Del. Rev.* **2012**, *64*, 24.
- [231] J. V. Jokerst, T. Lobovkina, R. N. Zare, S. S. Gambhir, *Nanomedicine* **2011**, *6*, 715.
- [232] S. Jeon, J. Lee, J. Andrade, P. De Gennes, *J. Colloid Interface Sci.* **1991**, *142*, 149.
- [233] C. Fang, B. Shi, Y.-Y. Pei, M.-H. Hong, J. Wu, H.-Z. Chen, *Eur. J. Pharm. Sci.* **2006**, *27*, 27.
- [234] L. D. Unsworth, H. Sheardown, J. L. Brash, *Langmuir* **2005**, *21*, 1036.
- [235] A. Vonarbourg, C. Passirani, P. Saulnier, J.-P. Benoit, *Biomaterials* **2006**, *27*, 4356.
- [236] Q. Yang, S. W. Jones, C. L. Parker, W. C. Zamboni, J. E. Bear, S. K. Lai, *Mol. Pharm.* **2014**, *11*, 1250.
- [237] S. J. Sofia, V. Premnath, E. W. Merrill, *Macromolecules* **1998**, *31*, 5059.
- [238] R. Konradi, B. Pidhatika, A. Mühlebach, M. Textor, *Langmuir* **2008**, *24*, 613.
- [239] Q. Liu, A. Singh, R. Lalani, L. Liu, *Biomacromolecules* **2012**, *13*, 1086.
- [240] A. C. Engler, X. Ke, S. Gao, J. M. W. Chan, D. J. Coady, R. J. Ono, R. Lubbers, A. Nelson, Y. Y. Yang, J. L. Hedrick, *Macromolecules* **2015**, *48*, 1673.
- [241] L. Zhao, Y.-H. Xu, T. Akasaka, S. Abe, N. Komatsu, F. Watari, X. Chen, *Biomaterials* **2014**, *35*, 5393.
- [242] C. Siegers, M. Biesalski, R. Haag, *Chem. - Eur. J.* **2004**, *10*, 2831.
- [243] W. Ngo, S. Ahmed, C. Blackadar, B. Bussin, Q. Ji, S. M. Mladjenovic, Z. Sepahi, W. C. W. Chan, *Adv. Drug Del. Rev.* **2022**, *185*, 114238.
- [244] J. W. M. Bulte, D. L. Kraitchman, *NMR Biomed.* **2004**, *17*, 484.
- [245] P. Aggarwal, J. B. Hall, C. B. McLeland, M. A. Dobrovolskaia, S. E. McNeil, *Adv. Drug Del. Rev.* **2009**, *61*, 428.
- [246] A. Aderem, D. M. Underhill, *Annu. Rev. Immunol.* **1999**, *17*, 593.
- [247] H. Hillaireau, P. Couvreur, *Cellular and Molecular Life Sciences* **2009**, *66*, 2873.
- [248] P. Foroozandeh, A. A. Aziz, *Nanoscale Research Letters* **2018**, *13*, 339.
- [249] X. Cheng, X. Tian, A. Wu, J. Li, J. Tian, Y. Chong, Z. Chai, Y. Zhao, C. Chen, C. Ge, *ACS Appl. Mater. Interfaces* **2015**, *7*, 20568.
- [250] E. Brun, C. Sicard – Roselli, *Cancer Nanotechnol.* **2014**, *5*, 7.

## 6 References

- [251] S. Dominguez-Medina, J. Blankenburg, J. Olson, C. F. Landes, S. Link, *ACS Sustain. Chem. Eng.* **2013**, *1*, 833.
- [252] Y. Ma, J. Hong, Y. Ding, *Adv. Healthc. Mater.* **2020**, *9*, 1901448.
- [253] S. Neupane, Y. Pan, S. Takalkar, K. Bentz, J. Farmakes, Y. Xu, B. Chen, G. Liu, S. Y. Qian, Z. Yang, *J. Phys. Chem. C* **2017**, *121*, 1377.
- [254] A. Albanese, W. C. W. Chan, *ACS Nano* **2011**, *5*, 5478.
- [255] Y. T. Ho, N. A. Azman, F. W. Y. Loh, G. K. T. Ong, G. Engudar, S. A. Kriz, J. C. Y. Kah, *Bioconjug. Chem.* **2018**, *29*, 3923.
- [256] R. Cukalevski, S. A. Ferreira, C. J. Dunning, T. Berggård, T. Cedervall, *Nano Research* **2015**, *8*, 2733.
- [257] H. Cai, Y. Ma, Z. Wu, Y. Ding, P. Zhang, X. He, J. Zhou, Z. Chai, Z. Zhang, *NanoImpact* **2016**, *3-4*, 40.
- [258] S. M. Moghimi, A. C. Hunter, *Pharm. Res.* **2001**, *18*, 1.
- [259] P. Camner, M. Lundborg, L. Låstbom, P. Gerde, N. Gross, C. Jarstrand, *Journal of Applied Physiology* **2002**, *92*, 2608.
- [260] B. Muthusamy, G. Hanumanthu, S. Suresh, B. Rekha, D. Srinivas, L. Karthick, B. M. Vrushabendra, S. Sharma, G. Mishra, P. Chatterjee, K. S. Mangala, H. N. Shivashankar, K. N. Chandrika, N. Deshpande, M. Suresh, N. Kannabiran, V. Niranjana, A. Nalli, T. S. K. Prasad, K. S. Arun, R. Reddy, S. Chandran, T. Jadhav, D. Julie, M. Mahesh, S. L. John, K. Palvankar, D. Sudhir, P. Bala, N. S. Rashmi, G. Vishnupriya, K. Dhar, S. Reshma, R. Chaerkady, T. K. B. Gandhi, H. C. Harsha, S. S. Mohan, K. S. Deshpande, M. Sarker, A. Pandey, *Proteomics* **2005**, *5*, 3531.
- [261] M. S. Ehrenberg, A. E. Friedman, J. N. Finkelstein, G. Oberdörster, J. L. McGrath, *Biomaterials* **2009**, *30*, 603.
- [262] S. R. Saptarshi, A. Duschl, A. L. Lopata, *J. Nanobiotechnology* **2013**, *11*, 26.
- [263] H. Gao, Q. He, *Expert Opin. Drug. Deliv.* **2014**, *11*, 409.
- [264] R. H. Müller, K. H. Wallis, S. D. Tröster, J. Kreuter, *J. Control. Release* **1992**, *20*, 237.
- [265] H. Carrstensen, R. H. Müller, B. W. Müller, *Clin. Nutr.* **1992**, *11*, 289.
- [266] S. Ritz, S. Schöttler, N. Kotman, G. Baier, A. Musyanovych, J. Kuharev, K. Landfester, H. Schild, O. Jahn, S. Tenzer, V. Mailänder, *Biomacromolecules* **2015**, *16*, 1311.
- [267] D. R. Absolom, in *Methods in Enzymology*, Vol. 132, Academic Press, **1986**, pp. 281.
- [268] D. E. Owens III, N. A. Peppas, *Int. J. Pharm.* **2006**, *307*, 93.
- [269] S. Al-Harhi, J. I. Lachowicz, M. E. Nowakowski, M. Jaremko, Ł. Jaremko, *J. Inorg. Biochem.* **2019**, *198*, 110716.
- [270] K. Bolaños, M. J. Kogan, E. Araya, *Int. J. Nanomedicine* **2019**, *14*, 6387.
- [271] K. A. Majorek, P. J. Porebski, A. Dayal, M. D. Zimmerman, K. Jablonska, A. J. Stewart, M. Chruszcz, W. Minor, *Mol. Immunol.* **2012**, *52*, 174.
- [272] E. S. Lee, Y. S. Youn, *J. Pharm. Investig.* **2016**, *46*, 305.
- [273] F. Liu, J. Mu, B. Xing, *Curr. Pharm. Des.* **2015**, *21*, 000.
- [274] J. Young Yhee, J. Lee, H. Chang, J. Lee, I. Chan Kwon, K. Kim, *Curr. Pharm. Des.* **2015**, *21*, 1889.
- [275] P. Khullar, V. Singh, A. Mahal, P. N. Dave, S. Thakur, G. Kaur, J. Singh, S. Singh Kamboj, M. Singh Bakshi, *J. Phys. Chem. C* **2012**, *116*, 8834.
- [276] L. Rastogi, A. J. Kora, A. J., *Mater. Sci. Eng. C* **2012**, *32*, 1571.

- [277] M. Baneshi, S. Dadfarnia, A. M. H. Shabani, S. K. Sabbagh, S. Haghgoo, H. Bardania, *Int. J. Pharm.* **2019**, *564*, 145.
- [278] N. Fernández-Iglesias, J. Bettmer, *Nanoscale* **2015**, *7*, 14324.
- [279] E. Casals, T. Pfaller, A. Duschl, G. J. Oostingh, V. Puntès, *ACS Nano* **2010**, *4*, 3623.
- [280] W. Xiao, J. Xiong, S. Zhang, Y. Xiong, H. Zhang, H. Gao, *Int. J. Pharm.* **2018**, *538*, 105.
- [281] A. Albanese, C. D. Walkey, J. B. Olsen, H. Guo, A. Emili, W. C. W. Chan, *ACS Nano* **2014**, *8*, 5515.
- [282] A. Shamsian, M. R. Sepand, M. Javaheri Kachousangi, T. Dara, S. N. Ostad, F. Atyabi, M. H. Ghahremani, *Int. J. Nanomedicine* **2020**, *15*, 4063.
- [283] Z.-J. Zhu, T. Posati, D. F. Moyano, R. Tang, B. Yan, R. W. Vachet, V. M. Rotello, *Small* **2012**, *8*, 2659.
- [284] T. M. Göppert, R. H. Müller, *J. Drug Target.* **2005**, *13*, 179.
- [285] P. Thiagarajan, A. Le, C. R. Benedict, *Arterioscler. Thromb. Vasc. Biol.* **1999**, *19*, 2807.
- [286] A. Sasidharan, J. E. Riviere, N. A. Monteiro-Riviere, *J. Mater. Chem. B* **2015**, *3*, 2075.
- [287] A. Yang, W. Liu, Z. Li, L. Jiang, H. Xu, X. Yang, *Journal of nanoscience and nanotechnology* **2010**, *10*, 622.
- [288] S. Nagayama, K.-i. Ogawara, Y. Fukuoka, K. Higaki, T. Kimura, *Int. J. Pharm.* **2007**, *342*, 215.
- [289] C. M. Karsten, J. Köhl, *Immunobiology* **2012**, *217*, 1067.
- [290] M. Van Lookeren Campagne, C. Wiesmann, E. J. Brown, *Cell. Microbiol.* **2007**, *9*, 2095.
- [291] J. V. Sarma, P. A. Ward, *Cell and Tissue Research* **2011**, *343*, 227.
- [292] P. Ghosh, G. Han, M. De, C. K. Kim, V. M. Rotello, *Adv. Drug Del. Rev.* **2008**, *60*, 1307.
- [293] E. C. Dreaden, L. A. Austin, M. A. Mackey, M. A. El-Sayed, *Ther. Deliv.* **2012**, *3*, 457.
- [294] Y. Wang, E. C. Alcocilja, *J. Biol. Eng.* **2015**, *9*, 1.
- [295] L. C. Kennedy, L. R. Bickford, N. A. Lewinski, A. J. Coughlin, Y. Hu, E. S. Day, J. L. West, R. A. Drezek, *Small* **2011**, *7*, 169.
- [296] Q. Zhang, N. Iwakuma, P. Sharma, B. Moudgil, C. Wu, J. McNeill, H. Jiang, S. Grobmyer, *Nanotechnology* **2009**, *20*, 395102.
- [297] P. Decuzzi, B. Godin, T. Tanaka, S.-Y. Lee, C. Chiappini, X. Liu, M. Ferrari, *J. Control. Release* **2010**, *141*, 320.
- [298] C. He, Y. Hu, L. Yin, C. Tang, C. Yin, *Biomaterials* **2010**, *31*, 3657.
- [299] T. Maldiney, C. Richard, J. Seguin, N. Wattier, M. Bessodes, D. Scherman, *ACS nano* **2011**, *5*, 854.
- [300] H. Ou, T. Cheng, Y. Zhang, J. Liu, Y. Ding, J. Zhen, W. Shen, Y. Xu, W. Yang, P. Niu, J. Liu, Y. An, Y. Liu, L. Shi, *Acta Biomater.* **2018**, *65*, 339.
- [301] L. L. Estevanato, L. M. Lacava, L. C. Carvalho, R. B. Azevedo, O. Silva, F. Pelegrini, S. N. Bão, P. C. Morais, Z. G. Lacava, *J. Biomed. Nanotechnol.* **2012**, *8*, 301.
- [302] R. Qiao, C. Fu, Y. Li, X. Qi, D. Ni, A. Nandakumar, G. Siddiqui, H. Wang, Z. Zhang, T. Wu, *Adv. Sci.* **2020**, *7*, 2000406.
- [303] V. Patsula, D. Horák, J. Kučka, H. Macková, V. Lobaz, P. Francová, V. Herynek, T. Heizer, P. Páral, L. Šefc, *Sci. Rep.* **2019**, *9*, 10765.
- [304] G. Prencipe, S. M. Tabakman, K. Welsher, Z. Liu, A. P. Goodwin, L. Zhang, J. Henry, H. Dai, *J. Am. Chem. Soc.* **2009**, *131*, 4783.
- [305] J. Tan, D. Butterfield, C. Voycheck, K. Caldwell, J. Li, *Biomaterials* **1993**, *14*, 823.
- [306] W.-S. Cho, M. Cho, J. Jeong, M. Choi, B. S. Han, H.-S. Shin, J. Hong, B. H. Chung, J. Jeong, M.-H. Cho, *Toxicol. Appl. Pharmacol.* **2010**, *245*, 116.

## 6 References

- [307] L. Balogh, S. S. Nigavekar, B. M. Nair, W. Lesniak, C. Zhang, L. Y. Sung, M. S. Kariapper, A. El-Jawahri, M. Llanes, B. Bolton, *Nanomed. Nanotechnol. Biol. Med.* **2007**, *3*, 281.
- [308] J. K. Lee, T. S. Kim, J. Y. Bae, A. Y. Jung, S. M. Lee, J. H. Seok, H. S. Roh, C. W. Song, M. J. Choi, J. Jeong, *J. Appl. Toxicol.* **2015**, *35*, 573.
- [309] S. Hirn, M. Semmler-Behnke, C. Schleh, A. Wenk, J. Lipka, M. Schäffler, S. Takenaka, W. Möller, G. Schmid, U. Simon, W. G. Kreyling, *Eur. J. Pharm. Biopharm.* **2011**, *77*, 407.
- [310] M. Schäffler, F. Sousa, A. Wenk, L. Sitia, S. Hirn, C. Schleh, N. Haberl, M. Violatto, M. Canovi, P. Andreozzi, M. Salmona, P. Bigini, W. G. Kreyling, S. Krol, *Biomaterials* **2014**, *35*, 3455.
- [311] F. Sousa, S. Mandal, C. Garrovo, A. Astolfo, A. Bonifacio, D. Latawiec, R. H. Menk, F. Arfelli, S. Huewel, G. Legname, *Nanoscale* **2010**, *2*, 2826.
- [312] J. Kreuter, D. Shamenkov, V. Petrov, P. Ramge, K. Cychutek, C. Koch-Brandt, R. Alyautdin, *J. Drug Target.* **2002**, *10*, 317.
- [313] N. Levy, *Int. J. Stroke* **2012**, *7*, 440.
- [314] M. Ishii, Y. Matsumoto, K. Sekimizu, *Drug Discov. Ther.* **2015**, *9*, 234.
- [315] N. Abdelli, L. Peng, C. Keping, *Environ. Sci. Pollut. Res.* **2018**, *25*, 35048.
- [316] N. Sekimizu, A. Paudel, H. Hamamoto, *Drug Discov. Ther.* **2012**, *6*, 226.
- [317] Y. Matsumoto, K. Sekimizu, *Microbiol. Immunol.* **2019**, *63*, 41.
- [318] M. R. Kanost, in *Encyclopedia of Insects (Second Edition)* (Eds.: V. H. Resh, R. T. Cardé), Academic Press, San Diego, **2009**, pp. 446.
- [319] Y. Yu, A. K. Wolf, S. Thusek, T. Heinekamp, M. Bromley, S. Krappmann, U. Terpitz, K. Voigt, A. A. Brakhage, A. Beilhack, *J. Fungi (Basel)* **2021**, *7*.
- [320] C. Kaito, N. Akimitsu, H. Watanabe, K. Sekimizu, *Microb. Pathog.* **2002**, *32*, 183.
- [321] X. Meng, N. Abdelli, N. Wang, P. Lü, Z. Nie, X. Dong, S. Lu, K. Chen, *Biol. Trace Elem. Res.* **2017**, *180*, 327.
- [322] S. S. Fometu, G. Wu, L. Ma, J. S. Davids, *Beilstein J. Nanotechnol.* **2021**, *12*, 190.
- [323] Y. Wei, L. Quan, C. Zhou, Q. Zhan, *Nanomedicine* **2018**, *13*, 1495.
- [324] L. Cheng, K. Yang, M. Shao, X. Lu, Z. Liu, *Nanomedicine* **2011**, *6*, 1327.
- [325] R. R. Arvizo, O. R. Miranda, D. F. Moyano, C. A. Walden, K. Giri, R. Bhattacharya, J. D. Robertson, V. M. Rotello, J. M. Reid, P. Mukherjee, *PLoS One* **2011**, *6*, e24374.
- [326] J. Ke, Y. Zhu, J. Zhang, J. Yang, H. Guo, W. Zhao, C. Wen, L. Zhang, *ACS Sustain. Chem. Eng.* **2019**, *8*, 460.
- [327] L. Cheng, H. Huang, S. Chen, W. Wang, F. Dai, H. Zhao, *Mater. Des.* **2017**, *129*, 125.
- [328] L. Ma, V. Andoh, H. Liu, J. Song, G. Wu, L. Li, *JMatS* **2019**, *54*, 4997.
- [329] J. Soukupová, L. Kvítek, A. Panáček, T. Nevěčná, R. Zbořil, *Materials Chemistry and Physics* **2008**, *111*, 77.
- [330] C. P. Lau, M. F. Abdul-Wahab, J. Jaafar, G. F. Chan, N. A. A. Rashid, *J. Microbiol. Immunol. Infect.* **2017**, *50*, 427.
- [331] S. Ahlberg, A. Antonopoulos, J. Diendorf, R. Dringen, M. Epple, R. Flöck, W. Goedecke, C. Graf, N. Haberl, J. Helmlinger, *Beilstein J. Nanotechnol.* **2014**, *5*, 1944.
- [332] A. Manna, B. D. Kulkarni, K. Bandyopadhyay, K. Vijayamohan, *Chem. Mater.* **1997**, *9*, 3032.
- [333] R. C. Doty, T. R. Tshikhudo, M. Brust, D. G. Fernig, *Chem. Mater.* **2005**, *17*, 4630.
- [334] G. Mulley, A. T. A. Jenkins, N. R. Waterfield, *PLoS One* **2014**, *9*, e94409.
- [335] Z.-M. Xiu, J. Ma, P. J. J. Alvarez, *Environmental Science & Technology* **2011**, *45*, 9003.
- [336] D. A. Hutt, E. Cooper, G. J. Leggett, *J. Phys. Chem. B* **1998**, *102*, 174.

- [337] C. Battocchio, C. Meneghini, I. Fratoddi, I. Venditti, M. V. Russo, G. Aquilanti, C. Maurizio, F. Bondino, R. Matassa, M. Rossi, S. Mobilio, G. Polzonetti, *J. Phys. Chem. C* **2012**, *116*, 19571.
- [338] W. Gan, B. Xu, H.-L. Dai, *Angew. Chem. Int. Ed.* **2011**, *50*, 6622.
- [339] M. O. Awaleh, A. Badia, F. Brisse, X.-H. Bu, *Inorganic Chemistry* **2006**, *45*, 1560.
- [340] A. J. Blake, N. R. Champness, S. M. Howdle, P. B. Webb, *Inorganic Chemistry* **2000**, *39*, 1035.
- [341] J. A. Hubbell, J. P. Bearinger, A. Napoli, M. Textor, N. Tirelli, *US 7427410 B2*, **2008**.
- [342] H. Pletsch, A. Greiner, S. Agarwal, *Nanoscale* **2015**, *7*, 1977.
- [343] X. Huang, B. Li, H. Zhang, I. Hussain, L. Liang, B. Tan, *Nanoscale* **2011**, *3*, 1600.
- [344] J. P. Hermes, F. Sander, U. Fluch, T. Peterle, D. Thompson, R. Urbani, T. Pfohl, M. Mayor, *J. Am. Chem. Soc.* **2012**, *134*, 14674.
- [345] G. H. Woehle, L. O. Brown, J. E. Hutchison, *J. Am. Chem. Soc.* **2005**, *127*, 2172.
- [346] B. M. Barngrover, C. M. Aikens, *J. Phys. Chem. A* **2011**, *115*, 11818.
- [347] J. Liu, Z. Wang, F. D. Liu, A. B. Kane, R. H. Hurt, *ACS Nano* **2012**, *6*, 9887.
- [348] I. Römer, T. A. White, M. Baalousha, K. Chipman, M. R. Viant, J. R. Lead, *Journal of Chromatography A* **2011**, *1218*, 4226.
- [349] J. M. Zook, S. E. Long, D. Cleveland, C. L. A. Geronimo, R. I. MacCuspie, *Analytical and Bioanalytical Chemistry* **2011**, *401*, 1993.
- [350] S. Kittler, C. Greulich, J. Gebauer, J. Diendorf, L. Treuel, L. Ruiz, J. Gonzalez-Calbet, M. Vallet-Regi, R. Zellner, M. Köller, *Journal of Materials Chemistry* **2010**, *20*, 512.
- [351] A. O. Fitton, J. Hill, D. E. Jane, R. Millar, *Synthesis* **1987**, *1987*, 1140.
- [352] M. Erberich, H. Keul, M. Möller, *Macromolecules* **2007**, *40*, 3070.
- [353] S. Stichler, T. Jungst, M. Schamel, I. Zilkowski, M. Kuhlmann, T. Böck, T. Blunk, J. Teßmar, J. Groll, *Ann. Biomed. Eng.* **2017**, *45*, 273.
- [354] G. Lunn, E. B. Sansone, *Destruction of hazardous chemicals in the laboratory*, John Wiley & Sons, **2012**.
- [355] S. V. Sokolov, C. Batchelor-McAuley, K. Tschulik, S. Fletcher, R. G. Compton, *Chem. - Eur. J.* **2015**, *21*, 10741.
- [356] Á. I. López-Lorente, M. L. Soriano, M. Valcárcel, *Microchim. Acta* **2014**, *181*, 1789.
- [357] R. A. Bell, J. R. Kramer, *Environmental Toxicology and Chemistry* **1999**, *18*, 9.
- [358] P. Mulvaney, *Langmuir* **1996**, *12*, 788.
- [359] J. Manson, D. Kumar, B. J. Meenan, D. Dixon, *Gold Bulletin* **2011**, *44*, 99.
- [360] J. Lin, H. Zhang, V. Morovati, R. Dargazany, *J. Colloid Interface Sci.* **2017**, *504*, 325.
- [361] D. N. Benoit, H. Zhu, M. H. Lilierose, R. A. Verm, N. Ali, A. N. Morrison, J. D. Fortner, C. Avendano, V. L. Colvin, *Analytical chemistry* **2012**, *84*, 9238.
- [362] M. Maccarini, G. Briganti, S. Rucareanu, X.-D. Lui, R. Sinibaldi, M. Sztucki, R. B. Lennox, *J. Phys. Chem. C* **2010**, *114*, 6937.
- [363] T. Bewersdorff, J. Vonnemann, A. Kanik, R. Haag, A. Haase, *Int. J. Nanomedicine* **2017**, *12*, 2001.
- [364] H. D. Hill, J. E. Millstone, M. J. Banholzer, C. A. Mirkin, *ACS nano* **2009**, *3*, 418.
- [365] Y. Gong, T. Andelman, G. F. Neumark, S. O'Brien, I. L. Kuskovsky, *Nanoscale Research Letters* **2007**, *2*, 297.
- [366] V. B. Damodaran, C. J. Fee, T. Ruckh, K. C. Papat, *Langmuir* **2010**, *26*, 7299.
- [367] P. de Gennes, *Macromolecules* **1980**, *13*, 1069.
- [368] F. Meng, G. H. M. Engbers, J. Feijen, *J. Biomed. Mater. Res. Part A* **2004**, *70A*, 49.
- [369] H. Lee, A. H. de Vries, S.-J. Marrink, R. W. Pastor, *J. Phys. Chem. B* **2009**, *113*, 13186.

## 6 References

- [370] J. L. Perry, K. G. Reuter, M. P. Kai, K. P. Herlihy, S. W. Jones, J. C. Luft, M. Napier, J. E. Bear, J. M. DeSimone, *Nano Lett.* **2012**, *12*, 5304.
- [371] A. M. Smith, K. A. Johnston, S. E. Crawford, L. E. Marbella, J. E. Millstone, *Analyst* **2017**, *142*, 11.
- [372] K. Sebby, E. Mansfield, *Analytical and bioanalytical chemistry* **2015**, *407*, 2913.
- [373] K. A. Johnston, A. M. Smith, L. E. Marbella, J. E. Millstone, *Langmuir* **2016**, *32*, 3820.
- [374] J. A. Baker, J. C. Berg, *Langmuir* **1988**, *4*, 1055.
- [375] G. Fler, in *Nanoparticles in solids and solutions*, Kluwer Academic Publishers, **1996**, pp. 269.
- [376] T. Cosgrove, N. Finch, B. Vincent, J. Webster, *ColSu* **1988**, *31*, 33.
- [377] J. Scheutjens, G. Fler, *The Journal of Physical Chemistry* **1980**, *84*, 178.
- [378] G. Fler, L. Koopal, J. Lyklema, *Kolloid-Zeitschrift und Zeitschrift für Polymere* **1972**, *250*, 689.
- [379] D. Ciprari, K. Jacob, R. Tannenbaum, *Macromolecules* **2006**, *39*, 6565.
- [380] E. Dickinson, L. Eriksson, *Adv. Colloid Interface Sci.* **1991**, *34*, 1.
- [381] A. Albanese, W. C. Chan, *ACS nano* **2011**, *5*, 5478.
- [382] H. A. Biebuyck, C. D. Bain, G. M. Whitesides, *Langmuir* **1994**, *10*, 1825.
- [383] A. Ulman, *Chem. Rev.* **1996**, *96*, 1533.
- [384] W. Abdelwahed, G. Degobert, S. Stainmesse, H. Fessi, *Adv. Drug Del. Rev.* **2006**, *58*, 1688.
- [385] E. J. Shelley, D. Ryan, S. R. Johnson, M. Couillard, D. Fitzmaurice, P. D. Nellist, Y. Chen, R. E. Palmer, J. A. Preece, *Langmuir* **2002**, *18*, 1791.
- [386] V. Amendola, R. Pilot, M. Frasconi, O. M. Maragò, M. A. Iati, *J. Phys.: Condens. Matter* **2017**, *29*, 203002.
- [387] C.-k. Kim, P. Ghosh, V. M. Rotello, *Nanoscale* **2009**, *1*, 61.
- [388] H. J. Issaq, Z. Xiao, T. D. Veenstra, *Chem. Rev.* **2007**, *107*, 3601.
- [389] S. Schöttler, K. Klein, K. Landfester, V. Mailänder, *Nanoscale* **2016**, *8*, 5526.
- [390] K. Nakashima, P. Bahadur, *Adv. Colloid Interface Sci.* **2006**, *123-126*, 75.
- [391] F. Deubel, V. Bretzler, R. Holzner, T. Helbich, O. Nuyken, B. Rieger, R. Jordan, *Macromol. Rapid Commun.* **2013**, *34*, 1020.
- [392] A. B. Lowe, *Polymer Chemistry* **2010**, *1*, 17.
- [393] M. Fischer, C. P. Baptista, I. C. Gonçalves, B. D. Ratner, C. Sperling, C. Werner, C. L. Martins, M. A. Barbosa, *Biomaterials* **2012**, *33*, 7677.
- [394] M. Fischer, C. Sperling, P. Tengvall, C. Werner, *Biomaterials* **2010**, *31*, 2498.
- [395] K. Kottke-Marchant, J. M. Anderson, Y. Umemura, R. E. Marchant, *Biomaterials* **1989**, *10*, 147.
- [396] Y. J. Weng, R. X. Hou, G. C. Li, J. Wang, N. Huang, H. Q. Liu, *Applied Surface Science* **2008**, *254*, 2712.
- [397] J. F. C. Glatz, G. J. van der Vusse, *Progress in Lipid Research* **1996**, *35*, 243.
- [398] I. C. Gonçalves, M. C. L. Martins, M. A. Barbosa, B. D. Ratner, *Biomaterials* **2005**, *26*, 3891.
- [399] M. B. Gorbet, M. V. Sefton, *Biomaterials* **2004**, *25*, 5681.
- [400] K. M. Evans-Nguyen, M. H. Schoenfish, *Langmuir* **2005**, *21*, 1691.
- [401] P. L. Yeagle, *Biochimica et Biophysica Acta (BBA) - Reviews on Biomembranes* **1985**, *822*, 267.
- [402] M. S. Brown, P. T. Kovanen, J. L. Goldstein, *Science* **1981**, *212*, 628.
- [403] H. H. Wang, G. Garruti, M. Liu, P. Portincasa, D. Q. Wang, *Ann. Hepatol.* **2018**, *16*, 27.

- [404] Y. Zhao, Y. L. Marcel, *Biochemistry* **1996**, *35*, 7174.
- [405] G. Deliconstantinos, C. Tsopanakis, P. Karayiannakos, G. Skalkeas, *Atherosclerosis* **1986**, *61*, 67.
- [406] J.-S. Ha, C.-E. Ha, J.-T. Chao, C. E. Petersen, A. Theriault, N. V. Bhagavan, *Biochim. Biophys. Acta* **2003**, *1640*, 119.
- [407] L. Peng, H. Minbo, C. Fang, L. Xi, Z. Chaocan, *Protein Pept. Lett.* **2008**, *15*, 360.
- [408] M. A. Teir, J. GHITHAN, S. DARWISH, M. M. ABU-HADID, *Journal of Applied Biological Sciences* **2012**, *6*, 45.
- [409] C.-E. Ha, N. V. Bhagavan, *Biochimica et Biophysica Acta (BBA) - General Subjects* **2013**, *1830*, 5486.
- [410] Q. Zhou, J. Xiang, Y. Tang, J. Liao, C. Yu, H. Zhang, L. Li, Y. Yang, G. Xu, *Colloids Surf. B: Biointerfaces* **2008**, *61*, 75.
- [411] X. Wu, J. Liu, Q. Wang, W. Xue, X. Yao, Y. Zhang, J. Jin, *Spectrochim. Acta A Mol. Biomol. Spectrosc.* **2011**, *79*, 1202.
- [412] S. Curry, in *Adv Mol Cell Biol*, Vol. 33, Elsevier, **2003**, pp. 29.
- [413] D.-b. Yang, J.-b. Zhu, Z.-j. Huang, H.-x. Ren, Z.-j. Zheng, *Colloids Surf. B: Biointerfaces* **2008**, *63*, 192.
- [414] V. O. Aseyev, H. Tenhu, F. M. Winnik, *Conformation-Dependent Design of Sequences in Copolymers II* **2006**, *1*.
- [415] R. Tang, W. Ji, C. Wang, *Macromol. Biosci.* **2010**, *10*, 192.
- [416] S. Riemer, S. Prévost, M. Dzionara, M.-S. Appavou, R. Schweins, M. Gradzielski, *Polymer* **2015**, *70*, 194.
- [417] Y. Zhou, V. A. Briand, N. Sharma, S.-k. Ahn, R. M. Kasi, *Materials* **2009**, *2*, 636.
- [418] S.-i. Yusa, *International Journal of Polymer Science* **2012**, *2012*.
- [419] M. Chen, Y. Liu, W. Yang, X. Li, L. Liu, Z. Zhou, Y. Wang, R. Li, Q. Zhang, *Carbohydr. Polym.* **2011**, *84*, 1244.
- [420] Y.-S. Wang, L.-R. Liu, Q. Jiang, Q.-Q. Zhang, *Eur. Polym. J.* **2007**, *43*, 43.
- [421] S. K. Filippov, A. V. Lezov, O. Y. Sergeeva, A. S. Olifirenko, S. B. Lesnichin, N. S. Domnina, E. A. Komarova, M. Almgren, G. Karlsson, P. Štepanek, *Eur. Polym. J.* **2008**, *44*, 3361.
- [422] J. Wang, E. Matayoshi, *Pharm. Res.* **2012**, *29*, 1745.
- [423] C.-T. Lee, C.-P. Huang, Y.-D. Lee, *Biomacromolecules* **2006**, *7*, 1179.
- [424] W. Wang, Q.-Q. Wei, J. Wang, B.-C. Wang, S.-h. Zhang, Z. Yuan, *J. Colloid Interface Sci.* **2013**, *404*, 223.
- [425] B. Cattoz, T. Cosgrove, M. Crossman, S. W. Prescott, *Langmuir* **2012**, *28*, 2485.
- [426] J. A. Baker, R. A. Pearson, J. C. Berg, *Langmuir* **1989**, *5*, 339.
- [427] M. Aubouy, E. Raphaël, *Macromolecules* **1998**, *31*, 4357.
- [428] J.-T. Li, K. D. Caldwell, N. Rapoport, *Langmuir* **1994**, *10*, 4475.
- [429] H. Xie, A. G. Tkachenko, W. R. Glomm, J. A. Ryan, M. K. Brennaman, J. M. Papanikolas, S. Franzen, D. L. Feldheim, *Analytical chemistry* **2003**, *75*, 5797.
- [430] G. J. Fleer, J. Lyklema, *J. Colloid Interface Sci.* **1974**, *46*, 1.
- [431] Y. Liu, M. K. Sipton, J. Ryan, E. D. Kaufman, S. Franzen, D. L. Feldheim, *Analytical Chemistry* **2007**, *79*, 2221.
- [432] R. Elhaei, R. Kharrat, M. Madani, *J. Mol. Liq.* **2021**, *322*, 114572.
- [433] H. Du, F. A. de Oliveira, L. J. C. Albuquerque, G. Tresset, E. Pavlova, C. Huin, P. Guégan, F. C. Giacomelli, *Langmuir* **2020**, *36*, 1266.

## 6 References

- [434] F. Bonnier, M. J. Baker, H. J. Byrne, *Anal. Methods* **2014**, *6*, 5155.
- [435] S. Tenzer, D. Docter, S. Rosfa, A. Wlodarski, J. Kuharev, A. Reikik, S. K. Knauer, C. Bantz, T. Nawroth, C. Bier, J. Sirirattanapan, W. Mann, L. Treuel, R. Zellner, M. Maskos, H. Schild, R. H. Stauber, *ACS Nano* **2011**, *5*, 7155.
- [436] S. Sant, S. Poulin, P. Hildgen, *J. Biomed. Mater. Res. Part A* **2008**, *87A*, 885.
- [437] I. Firkowska-Boden, X. Zhang, K. D. Jandt, *Adv. Healthc. Mater.* **2018**, *7*, 1700995.
- [438] M. Schäffler, M. Semmler-Behnke, H. Sarioglu, S. Takenaka, A. Wenk, C. Schleh, S. M. Hauck, B. D. Johnston, W. G. Kreyling, *Nanotechnology* **2013**, *24*, 265103.
- [439] R. Pieper, C. L. Gatlin, A. J. Makusky, P. S. Russo, C. R. Schatz, S. S. Miller, Q. Su, A. M. McGrath, M. A. Estock, P. P. Parmar, M. Zhao, S.-T. Huang, J. Zhou, F. Wang, R. Esquer-Blasco, N. L. Anderson, J. Taylor, S. Steiner, *Proteomics* **2003**, *3*, 1345.
- [440] J. Simon, T. Wolf, K. Klein, K. Landfester, F. R. Wurm, V. Mailänder, *Angew. Chem. Int. Ed.* **2018**, *57*, 5548.
- [441] C. Vedhachalam, V. Narayanaswami, N. Neto, T. M. Forte, M. C. Phillips, S. Lund-Katz, J. K. Bielicki, *Biochemistry* **2007**, *46*, 2583.
- [442] R. W. Mahley, T. L. Innerarity, S. C. Rall, K. H. Weisgraber, *J. Lipid. Res.* **1984**, *25*, 1277.
- [443] J. R. Mills, D. R. Barnidge, D. L. Murray, *Methods* **2015**, *81*, 56.
- [444] G. Caracciolo, D. Pozzi, A. Capriotti, C. Cavaliere, S. Piovesana, H. Amenitsch, A. Laganà, *RSC Adv.* **2015**, *5*, 5967.
- [445] M. Zhou, D. A. Lucas, K. C. Chan, H. J. Issaq, E. F. Petricoin III, L. A. Liotta, T. D. Veenstra, T. P. Conrads, *Electrophoresis* **2004**, *25*, 1289.
- [446] R. K. Kainthan, Y. Zou, M. Chiao, J. N. Kizhakkedathu, *Langmuir* **2008**, *24*, 4907.
- [447] M. Zhang, Y. Wang, H. Zhang, J. Cao, Z. Fei, Y. Wang, *Spectrochim. Acta A Mol. Biomol. Spectrosc.* **2018**, *196*, 323.
- [448] S. Curry, P. Brick, N. P. Franks, *Biochim. Biophys. Acta* **1999**, *1441*, 131.
- [449] W. Pitt, S. Cooper, *J. Biomed. Mater. Res.* **1988**, *22*, 359.
- [450] S. T. Reddy, A. J. van der Vlies, E. Simeoni, V. Angeli, G. J. Randolph, C. P. O'Neil, L. K. Lee, M. A. Swartz, J. A. Hubbell, *Nat. Biotechnol.* **2007**, *25*, 1159.
- [451] K. Prapainop, P. Wentworth, *Eur. J. Pharm. Biopharm.* **2011**, *77*, 353.
- [452] E. Papini, R. Tavano, F. Mancin, *Front. Immunol.* **2020**, 2343.
- [453] A. Chonn, S. C. Semple, P. R. Cullis, *J. Biol. Chem.* **1995**, *270*, 25845.
- [454] S. Miyakis, B. Giannakopoulos, S. A. Krilis, *Thromb. Res.* **2004**, *114*, 335.
- [455] A. Barbasz, I. Guevara-Lora, M. Rapala-Kozik, A. Kozik, *Int. Immunopharmacol.* **2008**, *8*, 211.
- [456] J. Xu, J. Fang, Z. Cheng, L. Fan, W. Hu, F. Zhou, H. Shen, *J. Exp. Clin. Cancer Res.* **2018**, *37*, 180.
- [457] M. Brückner, J. Simon, S. Jiang, K. Landfester, V. Mailänder, *Acta Biomater.* **2020**, *114*, 333.
- [458] S. Wasmuth, K. Lueck, H. Baehler, A. Lommatzsch, D. Pauleikhoff, *Invest. Ophthalmol. Visual. Sci* **2009**, *50*, 5304.
- [459] V. P. Ferreira, M. K. Pangburn, C. Cortés, *Mol. Immunol.* **2010**, *47*, 2187.
- [460] Y. Zhang, J. L. Y. Wu, J. Lazarovits, W. C. W. Chan, *J. Am. Chem. Soc.* **2020**, *142*, 8827.
- [461] C. Oelschläger, J. r. Römisch, A. Staubitz, H. Stauss, B. Leithäuser, H. Tillmanns, H. Hölschermann, *Blood* **2002**, *99*, 4015.
- [462] J. H. Levy, R. M. Snieciński, I. J. Welsby, M. Levi, *Thromb. Haemost.* **2016**, *115*, 712.
- [463] S. Wei, L. S. Ahlstrom, C. L. Brooks III, *Small* **2017**, *13*, 1603748.
- [464] M. Kopp, S. Kollenda, M. Eppe, *Acc. Chem. Res.* **2017**, *50*, 1383.



- [465] J. A. Winkelstein, *J. Pediatr.* **1973**, *82*, 747.
- [466] A. Thomas, S. S. Müller, H. Frey, *Biomacromolecules* **2014**, *15*, 1935.
- [467] S. Saganuwan, *Bulgarian Journal of Veterinary Medicine* **2017**, *20*.
- [468] Y. Zhang, A. T. Liu, Y. R. Cornejo, D. Van Haute, J. M. Berlin, *PLoS One* **2020**, *15*, e0234916.
- [469] K. Kozics, M. Sramkova, K. Kopecka, P. Begerova, A. Manova, Z. Krivosikova, Z. Sevcikova, A. Liskova, E. Rollerova, T. Dubaj, V. Punttes, L. Wsolova, P. Simon, J. Tulinska, A. Gabelova, *Nanomaterials (Basel, Switzerland)* **2021**, *11*, 1702.
- [470] D. E. Owens, N. A. Peppas, *Int. J. Pharm.* **2006**, *307*, 93.
- [471] M. Lück, B. R. Paulke, W. Schröder, T. Blunk, R. Müller, *J. Biomed. Mater. Res.* **1998**, *39*, 478.
- [472] P. P. Karmali, D. Simberg, *Expert Opin. Drug. Deliv.* **2011**, *8*, 343.
- [473] C. E. Pedraza, L. G. Nikolcheva, M. T. Kaartinen, J. E. Barralet, M. D. McKee, *Bone* **2008**, *43*, 708.
- [474] G. R. Fulmer, A. J. M. Miller, N. H. Sherden, H. E. Gottlieb, A. Nudelman, B. M. Stoltz, J. E. Bercaw, K. I. Goldberg, *Organometallics* **2010**, *29*, 2176.
- [475] a. i. a. com, *Laborpraxis Band 4: Analytische Methoden* **2017**, 157.
- [476] D. Lin-Vien, N. B. Colthup, W. G. Fateley, J. G. Grasselli, *The handbook of infrared and Raman characteristic frequencies of organic molecules*, Elsevier, **1991**.
- [477] A. H. Kuptsov, G. N. Zhizhin, *Handbook of Fourier transform Raman and Infrared Spectra of Polymers, Vol. 45*, Elsevier, **1998**.
- [478] U. K. Laemmli, *Nature* **1970**, *227*, 680.
- [479] G. Candiano, M. Bruschi, L. Musante, L. Santucci, G. M. Ghiggeri, B. Carnemolla, P. Orecchia, L. Zardi, P. G. Righetti, *Electrophoresis* **2004**, *25*, 1327.
- [480] J. Cox, M. Mann, *Nat. Biotechnol.* **2008**, *26*, 1367.
- [481] T. Tylek, T. Schilling, K. Schlegelmilch, M. Ries, M. Rudert, F. Jakob, J. Groll, *Sci. Rep.* **2019**, *9*, 3533.
- [482] K. D. Clark, Z. Lu, M. R. Strand, *Insect biochemistry and molecular biology* **2010**, *40*, 460.
- [483] D. R. Phillips, K. D. Clark, *PLoS One* **2017**, *12*, e0171447.



## Acknowledgement / Danksagung

An dieser Stelle möchte ich mich bei all denjenigen bedanken, die mich in den vergangenen Jahren auf verschiedenste Art und Weise unterstützt haben und ohne die die Entstehung meiner Dissertation nicht möglich gewesen wäre.

Zuallererst möchte ich mich herzlichst bei Prof. Dr. Jürgen Groll dafür bedanken, dass er mir direkt im Anschluss meiner Masterarbeit die Möglichkeit gab, auch meine Dissertation am an seinem Lehrstuhl anzufertigen und dabei thematisch an meine Masterarbeit anzuknüpfen. Durch die Interdisziplinarität des Lehrstuhls konnte ich über meine ursprüngliche chemische Ausbildung hinausblicken, mich auch mit teilweise biologischen Fragestellungen auseinandersetzen und dadurch mein Wissen kontinuierlich erweitern. Danke für die Möglichkeit eigenständig zu arbeiten, eigene Ideen einzubringen und die von Ihnen mitgegeben Erfahrungen. Außerdem möchte ich mich gerne für die Teilnahme an wissenschaftlichen Konferenzen und vor allem für die großartige Möglichkeit zur Teilnahme am PONTEA-Seminar bedanken. Gerade die Ermöglichung des letztgenannten Kurses ist keine Selbstverständlichkeit. Dadurch habe ich nicht nur für die Doktorarbeit, sondern auch für die Zeit nach der Doktorarbeit viel gelernt, und mich vor allem persönlich weiterentwickelt.

Ich möchte mich herzlich bei Prof. Dr. Lutz Nuhn bedanken, dass er sich die Zeit zur Begutachtung meiner Thesis genommen hat.

Außerdem danke ich Prof. Dr. Andreas Beilhack für die angenehme Kooperation mit den *Silkworms*, und dass er die Rolle des Drittprüfers während meiner Doktorprüfung übernimmt.

An Dr. Krystyna Albrecht geht ein großer Dank für die Betreuung während meiner gesamten Promotion und dass sie wann immer von mir gewollt für Besprechungen der Ergebnisse oder Ideen zur Verfügung stand. Außerdem bedanke ich mich für das Korrekturlesen diverser Manuskripte sowie dieser Dissertation.

Danke an die guten Seelen des FMZs: Danke an Tanja Dambach und Birgit Langner-Bischof für die hervorragende Organisationen, die terminliche Koordination von Besprechungen mit Herrn Groll, aber auch für die netten Gespräche zwischendurch. Anton (Toni) Hofmann gilt mein Dank für die Fahrten nach Wiesentheid, um Buffy-Coat-Nachschub zu holen, damit

meine Kollegen mir Makrophagen bereitstellen konnten. Und bei IT-Problemen jeglicher Art hatte Harald Hümpfner stets eine Lösung parat.

An Dr. Tatjana Schilling, Alice Schaaf und Alevtina Rosenthal ein herzliches Dankeschön, dass ihr mich in der Zellkultur und bei biologischen Fragestellungen unterstützt habt.

Ein herzliches Dankeschön geht an Dr. Carina Blum, Dr. Tina Tylek und Dr. Annika Seifert, für die Bereitstellung der Makrophagen und die Einarbeitung sowie Hilfe bei der Durchführung von Mikroskopie- und Zellversuchen.

Besonders bedanken möchte ich mich außerdem bei Dr. Thorsten Keller für die Durchführung der SDS-PAGE Analysen, der Herstellung des Kontaktes für die LC-MS/MS-Analysen sowie Hilfestellung bei Fragen zu sämtlichen Assays.

Bei Dr. Philipp Stahlhut möchte ich mich für die SEM-Aufnahmen der Partikel bedanken.

Frederika Kaiser danke ich für die Einführung an der ICP-MS und der schnellen Klärung bei technischen Problemen an diesem Gerät.

Bei Dr. Yidong Yu bedanke ich mich herzlich für die sehr angenehme Zusammenarbeit sowie den netten und problemlosen Austausch. So eine motivierte und engagierte Kooperationspartnerin kann man nur jedem wünschen.

Ein Dankeschön außerdem an die FMZ-Oldies, dass ihr mich so herzlich aufgenommen habt und mir vor allem am Anfang meiner Zeit am FMZ mit Rat und Tat zu Seite gestanden wart. Danke für die lustigen Mittagspausen und Unternehmungen außerhalb der Arbeit. Ein besonderer Dank geht hierbei an Dr. Susanne Feineis, die mich in die Thematik der Polyglycidole und Nanopartikel eingeführt hat.

Ein sehr großer Dank geht an meine Bürokollegen Johannes Herbig und Dr. Christoph Böhm. Danke, dass ich die Temperatur in unserem Büro regeln durfte, dass ein Kaffee auf meinem Tisch stand, wenn ich müde war, für die Hilfe bei computer-/softwaretechnischen Fragen, und für die wissenschaftlichen Diskussionen oder auch netten privaten Gespräche über Freud und Leid.

Bei den Mädels aus dem Hühnerstall (Dr. Jessica Brand, Dr. Annika Seifert, Dr. Franziska Weigl, Theresa Vogel, Dr. Sonja Horvat und Dr. Carina Blum) bedanke ich mich recht herzlich für die Adoption in eurem Büro, wenn mich meine Jungs mal allein gelassen haben. Danke

für den Kaffeeklatsch, die Sporteinheiten und euer stets offenes Ohr für fachliche oder auch weniger fachliche Diskussionen. Ihr habt dazu beigetragen, dass meine Zeit am FMZ trotz all der Hürden in guter Erinnerung bleiben wird. Vor allem möchte ich mich von ganzen Herzen bei „BraLuWeSe“ (ohne Lu) bedanken, die im Laufe der Zeit zu großartigen Freundinnen geworden sind. Danke für die gegenseitige Unterstützung und Motivation, die Tränen wegen Freud und Leid, die aufbauenden Worte und nötigen Gespräche egal ob auf der Arbeit oder Privat.

Außerdem möchte ich mich bei Ilona Paulus, Viktoria Niklaus, Dr. Junwen Shan, Dr. Jessica Brand, Dr. Annika Seifert, Dr. Franziska Weigl, Theresa Vogel, Friederike Kaiser, Dr. Ib Holzmeister, Dr. Jan Weichhold, Dr. Christoph Böhm, Dr. Leonard Forster und Dr. Florian Pinzner für die gemeinsamen Mittags- und Kaffeepausen, abendliche Aktivitäten und allgemein für eine unvergessliche Zeit am FMZ bedanken. Auch bin ich froh, dass wir Mädels uns weiterhin noch regelmäßig treffen, obwohl unsere gemeinsame Zeit am FMZ vorüber ist.

Theresa Vogel danke ich herzlich für die Zeit mir des Öfteren das „Demo“-Wasserzeichen aus den Origin Grafiken zu entfernen.

Allen anderen nicht namentlich genannten „FMZlern“ möchte ich mich für die gute Zusammenarbeit, das angenehme Arbeitsklima und die schöne Zeit, die ich während meiner Promotion am FMZ hatte, bedanken.

Danke an Dr. Laura Kuehn, Dr. Matthias Ferger, Dr. Dominic Prieschl, Dr. Alexander Hermann, Dr. Moritz Dechant, Dr. Moritz Balkenhol, Dr. Uwe Schmidt und Patrick Forkel, die ich im ersten Semester kennengelernt habe und bis heute nicht aus den Augen verloren habe. Durch gemeinsames Lernen und gegenseitiges unterstützen habt ihr viel bis zum Weg zur Promotion beigetragen. Ich danke euch auch für die geile Zeit in Würzburg außerhalb der Uni oder auch bei gemeinsamen Urlauben.

Außerdem möchte ich mich herzlichst bei meinen Mädels von „zu Hause“ bedanken. Danke für eure bedingungslose Freundschaft, eure aufbauenden Worte und das Verständnis in stressigen Zeiten.

Ein besonderer Dank geht an meine Familie, die mir das Studium und letztlich auch die Doktorarbeit durch mentale und finanzielle Unterstützung überhaupt erst ermöglicht

haben. Danke für euer stets offenes Ohr, eure aufbauenden Worte, dass ihr mir in jeder Lebenssituation zur Seite standet, mich immer unterstützt hab und stolz auf mich wart und seid.

Zu guter Letzt möchte ich mich von Herzen bei Marcus bedanken, für die Geduld und Unterstützung vor allem in der Zeit des Schreibens. Danke dafür, dass du meine auch mal schlechten Launen ertragen hast, mich immer wieder aufgebaut hast und Verständnis hattest, wenn ich „lieber“ am Schreibtisch gesessen war als Zeit mit dir zu verbringen. Danke dass du an mich glaubst, mich unterstützt und immer für mich da bist. ♥